NBSIR 79-1609

NBS
Publi-
cations

NAT'L INST. OF STAND & TECH R.I.C.
A11104 514221

TECHNICAL REPORTS

MATERIALS STUDIES FOR MAGNETIC FUSION ENERGY APPLICATIONS AT LOW TEMPERATURES -II

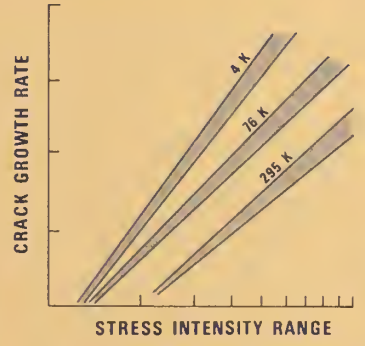

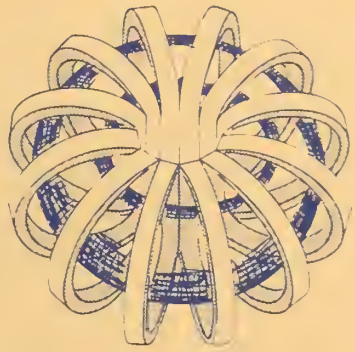

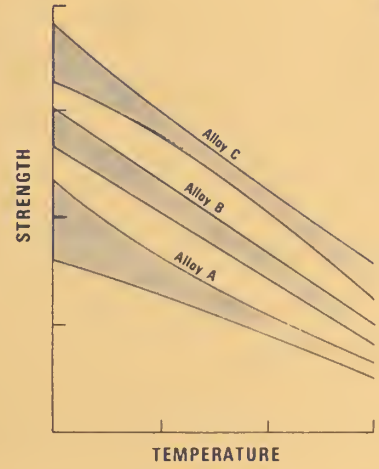

TO

DEPARTMENT OF ENERGY
OFFICE OF FUSION ENERGY
WASHINGTON, D.C. 20545

BY

FRACTURE AND DEFORMATION DIVISION
AND
THERMOPHYSICAL PROPERTIES DIVISION

NATIONAL BUREAU OF STANDARDS
BOULDER, CO 80303

QC
100
.U56
79-1609

NBSIR 79-1609

National Bureau of Standards
SEP 17 1979

UC 20 b,c

TECHNICAL REPORTS

MATERIALS STUDIES FOR MAGNETIC FUSION ENERGY APPLICATIONS AT LOW TEMPERATURES - II

Edited By

F.R. Fickett
Thermophysical Properties Division
and
R.P. Reed
Fracture and Deformation Division

National Bureau of Standards
Boulder, CO 80303

June 1979

Sponsored By

Department of Energy
Office of Fusion Energy
Washington, D.C. 20545

U.S. DEPARTMENT OF COMMERCE, Juanita M. Kreps, Secretary

Sidney Harman, Under Secretary
Jordan J. Baruch, Assistant Secretary for Science and Technology

NATIONAL BUREAU OF STANDARDS, Ernest Ambler, Director

CONTENTS

	Page
SUMMARY	v
ORGANIZATIONAL CONTACTS	vii
INTRODUCTION	1
PROGRAM DESCRIPTION	3
HIGHLIGHTS OF RESULTS	7
ALLOYS FOR LOW TEMPERATURE SERVICE	15
Testing of 2219-T87 Aluminum Alloy at 4 K - Martin Marietta	17
Low Cycle Fatigue Testing of 304LN Stainless Steel and 5083-O Aluminum Alloys - Martin Marietta	33
Fracture and Strength Properties of Selected Austenitic Stainless Steels at Cryogenic Temperatures - NBS	79
Heating and Strain Rate Effects in AISI 304L Stainless Steel at 4 K - NBS	123
Low Temperature Deformation of Fe-18Cr-8Ni Steel - NBS	149
PHYSICAL PROPERTIES OF STAINLESS STEELS	173
Elastic-Constant Variability in Stainless Steel 304 - NBS	175
Low Temperature Specific Heat of Two Stainless Steels - Wichita State Univ./NBS	197
Magnetic Susceptibility and Magnetization Studies of Some Commercial Austenitic Stainless Steels - Battelle Columbus	203
Some Magnetic Properties of the "Nonmagnetic" Stainless Steels - NBS	281
STAINLESS STEEL WELDING	295
Evaluation of Stainless Steel Weld Metals at Cryogenic Temperatures - NBS	297
Metallurgical Factors Affecting the Toughness of 316L SMA Weldments at Cryogenic Temperatures - NBS	313
Microstructure of Specific Stainless Steel Weldments being Evaluated for Cryogenic Service - Colorado School of Mines	353
NONMETALLICS FOR MAGNET STRUCTURES	401
Nonmetallics for Magnet Systems - NBS	403
TECHNOLOGY TRANSFER	453
Structural Alloys for Superconducting Magnets in Fusion Energy Systems - NBS	455
Handbook Preparation - MPDC/NBS	507
Vail Workshop	515

SUMMARY

The reports presented here summarize the work of the low temperature materials research project for the second year of the program. The various projects are outlined and the research results are presented. The major thrust of the measurements has been the evaluation of the low temperature mechanical and physical properties of stainless steel base metal and welds, with particular emphasis on the nitrogen strengthened stainless steels. Aluminum alloys have received some consideration also. Work has also been done on the production of nonmetallics, primarily industrial laminates, for low temperature applications and on the measurement of their properties at cryogenic temperatures. The second NBS/DOE Vail workshop was held in October 1978. A brief description is given of that program.

Note: The use of trade names of commercial materials is essential to the proper understanding of the work presented. This use in no way implies approval, endorsement or recommendation by the National Bureau of Standards. Contributions to this document by non-NBS authors have not been subjected to the usual NBS editorial review process.

ORGANIZATIONAL CONTACTS

Listed here are the people responsible for the various major aspects of the program so that those with specific technical questions may contact the individual directly.

Department of Energy, Office of Fusion Energy, Washington, D.C. 20545

Program Monitor	E. N. C. Dalder	(301) 353-4964 (FTS) 233-4964

National Bureau of Standards, Boulder, Colorado 80303

Program Manager	R. P. Reed	(303)499-1000 X3870
Program Coordinator and Magnetic Properties	F. R. Fickett	(FTS)323-1000 X3785
Welding	H. I. McHenry	X3268
Elastic Properties	H. M. Ledbetter	X3443
Nonmetallics	M. B. Kasen	X3558

Martin Marietta Aerospace, Denver Division, P.O. Box 31, Denver, Colorado 80201

Fatigue, Fracture	F. R. Schwartzberg J. A. Shepic	(303) 973-3225

Mechanical Properties Data Center, 13919 West Bay Shore Drive, Traverse City, Michigan 49684

Program Manager	R. C. Braden	(616) 947-4500
Data Evaluation	T. Moore	

Battelle Columbus Laboratories, 505 King Avenue, Columbus, Ohio 43201

Project Manager	E. W. Collings	(614) 424-4355 (FTS) 976-4355

INTRODUCTION

This report contains results of a research program to produce materials properties data to facilitate design and development of cryogenic structures for superconducting magnets, required for development of magnetic fusion energy. The program was conceived and developed jointly by the staffs of the National Bureau of Standards and the Office of Fusion Energy of the Department of Energy. This program, sponsored by DOE, is managed by NBS. Research is conducted at NBS and at various other laboratories, through subcontracts with NBS.

PROGRAM DESCRIPTION

The overall objective of the program is to assist in the design, construction and safe operation of low temperature magnetic fusion energy (MFE) systems, especially superconducting magnets, through effective materials research and materials technology transfer. The specific steps taken to achieve this objective are: (1) evaluation of low temperature materials research needs specific to MFE devices; (2) development and monitoring of a research program to acquire the necessary data; and (3) insuring rapid dissemination of the data to potential users through personal contacts, publications and workshops.

Accomplishment of the first specific objective started with the publication of the Survey of Low Temperature Materials for Magnetic Fusion Energy in March 1977. By continuing interactions with all low temperature design, construction and measurement programs, such as the Large Coil Project, we keep in touch with new problems as they arise. This year's contribution to accomplishment of the second objective is described here in Table 1 in the form of an outline of the research projects. The results are contained later in this report. The third objective is satisfied in part by these annual reports and by the handbook project as well as by the series of NBS-DOE Workshops on Materials at Low Temperatures which are held each fall.

Table 1. Outline of the NBS/DOE program on materials studies for magnetic fusion energy applications at low temperatures.

Program Area	Organization	Program Description
A. Alloys for Low Temperature Service		
1. Fatigue	Martin Marietta	Low cycle, strain controlled fatigue testing of 304LN stainless steel and 5083-0 aluminum at 295, 76 and 4 K.
2. Fracture	Martin Marietta	Fracture toughness, fatigue crack growth rate and tensile tests at 4 K on 2219-T87 aluminum alloy.
	NBS	Fracture toughness, fatigue crack growth rates and tensile tests at 295, 76 and 4 K on AISI 304, 316, 304LN, 316LN and Nitronic 50 alloys. A total of seven alloys were tested.
3. Test variables at 4 K	NBS	Effects of strain rate and discontinuous yielding on strength, temperature rise and martensitic products in selected stainless steels examined.
4. Effects of temperature on strength	NBS	Tensile tests of AISI 304L conducted at some 20 different temperatures between 4 and 295 K and results related to martensitic transformations.
B. Physical Properties of Stainless Steels		
1. Elastic properties	NBS	Measurement of the elastic properties of AISI 304, 304L, and 304N stainless steels to determine: within-specimen variability (anisotropy), heat-to-heat variability, effects of cooling to 4 K.
2. Magnetic properties	Battelle	Determination of the effect of magnetic field and temperature on the magnetization of austenitic stainless steels, and measurement of their magnetic susceptibilities.
	NBS	Evaluate the initial permeability, susceptibility and magnetic remanence of selected stainless steels and their welds at 4 K.
3. Thermal properties	Wichita State U/ NBS	Measure the low temperature specific heat of selected stainless steels.

Program Area	Organization	Program Description
	C. Stainless Steel Welding	
1. Metallurgical studies	Colo School of Mines	Characterize the microstructure, ferrite content and degree of sensitization of the 316L welds prepared by Arcos.
2. Toughness tests	NBS	Evaluate the fracture toughness of 316L as a function of ferrite content at 295, 76 and 4 K. Conduct tests on 308L and 316L weld specimens supplied by General Electric as part of their large coil program. Conduct tests at 295, 76 and 4 K on AWS 330 welds supplied by Teledyne-McKay.
	D. Nonmetallics for Magnet Stuctures	
1. Characterization	NBS	Characterization of the low-temperature mechanical, electrical, thermal and elastic properties of G-10CR and G-11CR industrial fiberglass-epoxy laminates including assessment of property variability among suppliers. Cooperation with National Laboratories in assessing radiation resistance of the CR grades. Subsequent studies will characterize less expensive NEMA laminates of the C and LE grades. A series of unreinforced nonmetallic materials will be selected for detailed cryogenic characterization.
	E. Technology Transfer	
1. Handbook preparation	MPDC/NBS	Production of a handbook containing low temperature mechanical and physical properties of materials of interest to the MFE community. Presently designated for inclusion: AISI 304, 316 and 21/6/9 stainless steels; 2219, 5083 and 6061 aluminum alloys.
2. NBS/DOE workshop	NBS	An annual workshop to present research results to the fusion community, to discuss new problems and to promote interaction between interested parties.

Highlights of Results

HIGHLIGHTS OF RESULTS

We present here a brief description of outstanding results from the project reports which follow in the next section.

Alloys for Low Temperature Service

Emphasis was placed on evaluation of the mechanical properties of nitrogen-strengthened stainless steels. Strain-controlled fatigue performance of AISI 304LN compares favorably with AISI 304 and 316 steels, especially in the high cycle range at low temperatures. Fracture toughness of AISI 304L and 316LN steels at 4 K remains high. The principal advantage of the nitrogen-strengthened austenitic steels is the increased yield strength at 4 K. Data were obtained documenting the effect of nitrogen additions on yield strength at 4 K. The dependence of flow strength on nitrogen concentration is stronger at lower temperatures.

Practical strain rates were shown to have little effect on 4 K tensile yield strengths. The discontinuous yielding phenomena observed in 4 K stress-strain behavior was confirmed to result from adiabatic heating of the specimens.

Physical Properties of Stainless Steels

Elastic-constant variability in stainless steel 304 alloys, including 304L and 304N, was determined experimentally using an ultrasonic pulse-echo-overlap method, which has an estimated uncertainty of $\pm$ 0.1 percent for these materials. Three kinds of variations -- sample-to-sample, directional within sample, and repeated measurements on a single sample -- were determined for four elastic constants: bulk modulus, Young's modulus, shear modulus, and Poisson's ratio. Based on 20 samples acquired randomly, the overall variabilities for these four elastic constants were 1.4, 0.9, 1.1, and 1.4 percent, respectively. Directional variations within a sample never exceeded 0.5 percent.

Upon cooling below room temperature, the elastic-stiffness constants increased regularly to about 40 K, where they decreased due to a Neel (paramagnetic-antiferromagnetic) transition. Poisson's ratio shows opposite behavior, first decreasing smoothly and then increasing near 40 K. Cooling curves for all studied samples were qualitatively similar, but showed measurable differences both in the high-temperature slope dC/dT and in the elastic-constant change ΔC due to the magnetic transition. The bulk modulus (reciprocal compressibility) changes much less with temperature than do the shear-type elastic constants.

Measurement of the magnetization and susceptibility of a large number of stainless steels as a function of temperature and magnetic field has led to a new interpretation of the magnetic state of these materials at low temperatures. They are apparently all spin-glass metals. In most cases the magnetization is not linear with field, which leads to some ambiguity in defining the permeability and, in some instances, significant amounts of hard ferromagnetism are found. Preliminary magnetic properties measurements have been made on a series of 316 and 316L weldments containing varying amounts of ferrite. The remanence and susceptibility values correlate well with magnegage measurements in most instances but some significant deviations have been observed probably resulting from a nonuniform ferrite distribution in the test specimens.

The specific heat of AISI 304 and 304L stainless steel over the temperature range 2-20 K was measured for the first time. The results indicate that, as expected, the specific heat is not greatly different from that observed for the other austenitic stainless steels.

Stainless Steel Welding

Research continued on the investigation of metallurgical factors contributing to the toughness (and degradation therof) of austenitic

stainless steel weld metals. Fracture toughness and metallurgical studies on the series of 316L test welds prepared by Arcos Corp. have been completed. The fracture toughness at 4 K ranged from 98 Mpa$\sqrt{m}$ (90 ksi$\sqrt{in}$) for the welds with 10% ferrite to 179 MPa$\sqrt{m}$ (162 ksi$\sqrt{in}$) for the ferrite-free welds; the toughness decrease was approximately linear with ferrite content between zero and 10%. Metallurgical studies were conducted by Colorado School of Mines and included microstructural characterization, ferrite content determination and sensitization studies. The fracture toughness evaluation of AWS 330 welds prepared by Teledyne-McKay at 295, 76 and 4 K was completed. The toughness at 4 K was 143 MPa$\sqrt{m}$ (130 ksi$\sqrt{in}$). Tests were conducted on shielded metal arc deposits of 308L and 316L weld metals using specimens provided by General Electric as part of their involvement in the Large Coil Project. The results were confusing in that the 308L weld had marginal Charpy impact toughness at 76 K (30 J; 22 ft lbs) yet the fracture toughness at 4 K was relatively high (156 MPa$\sqrt{m}$; 142 ksi$\sqrt{in}$). Furthermore, the Charpy toughness at 76 K of the 316L welds from GE was higher than the values for the 316L Arcos welds at the equivalent (zero) ferrite level, yet the fracture toughness at 4 K was significantly lower at 95 and 118 MPa$\sqrt{m}$ (86 and 107 ksi$\sqrt{in}$) for the GE welds and 178 MPa$\sqrt{m}$ (162 ksi$\sqrt{in}$) for the Arcos welds. Further work is needed to identify the cause of the reduced toughness.

Nonmetallics for Magnet Structures

A cooperative program between NBS and the U.S. laminating industry has been established to provide commercial availability of special grades of glass-epoxy, high-pressure industrial laminates intended for use in cryogenic magnet structures. These products, identified as G-10CR and G-11CR meet present NEMA and military specifications for G-10

and G-11 laminates. The essential difference is that the CR grades are produced to a common component and process specification so that property variability is minimized.

The specifications for producing the CR grade laminates have been provided to all U. S. laminating firms through the Industrial Laminates Subcommittee of the National Electrical Manufacturers Association. The CR grades are presently in commercial production. Production specifications will remain proprietary within the U. S. laminating industry. Inquiries about the specifications should be directed to Mr. H. Colin Smith, NEMA, Washington, D.C. (202-457-8419).

The mechanical, thermal and electrical properties of one lot of G-10CR and G-11CR have been measured at 295 K, 76 K and 4 K by NBS and by NBS subcontractors. The performance was found to equal that of the NEMA G-10 and G-11 products. The characterization program on the CR grades will continue in FY-79, including assessment to variability between manufacturers. The characterization will include studies to assess the benefits of fabricating the CR products with boron-free glass reinforcement for use in a neutron/gamma radiation environment.

Technology Transfer

Our major effort in this area is production of a handbook of low temperature data on the mechanical and physical properties of selected materials. The handbook is now in production, covers have been received, and a first chapter (AISI 316) draft has been evaluated.

Our annual NBS/DOE Workshop on Materials at Low Temperatures was attended by 70 people representing the materials and magnet design

communities. Indications are that the meeting was very productive for those concerned.

The preparation of papers reviewing the state of the art in low temperature materials selection and application is another aspect of technology transfer. One such paper, discussing a wide range of structural alloys, is included in this report.

Alloys for Low Temperature Service

TESTING OF 2219-T87 ALUMINUM ALLOY AT 4 K

Martin Marietta

TESING OF 2219-T87 ALUMINUM ALLOY AT 4 K

J. A. Shepic

Principal Investigator

C. F. Fiftal

Program Manager

MARTIN MARIETTA CORPORATION
Denver Division
Post Office Box 179
Denver, Colorado 80201

INTRODUCTION

Aluminum alloys have been proposed for structural applications in MFE magnet systems. One of the preferred alloys for cryogenic use is 2219 in either T87 or T851 condition, which represent solution annealed, cold worked to different strain values and aged. However, there is presently a lack of sufficient tensile and fracture data at 4K on this alloy, particularly for sections greater than 1 inch. The objective of this work was to characterize the tensile and fracture properties of heavy section (1.5 inches thick) 2219-T87 plate at 4K. Transverse and longitudinal crack growth parameters were also determined.

MATERIAL

The 1.5 inch thick 2219-T87 plate was procured from Martin Marietta inventory. Quality Control inspection of the material established 295K yield and ultimate at 55.1 ksi and 68.6 ksi, respectively, for the longitudinal grain direction. Elongation measured over a 2-inch gage length was 8%. Chemical analysis is as follows:

Element	Mn	Cu	Zn	Fe	Ti
Specification wt. %	0.20-0.40	5.8-6.8	0.10 max	0.30 max	0.02-0.10
Martin Marietta analysis wt. %	0.20	6.38	0.008	0.11	0.034

Hardness (average of 5 readings) is 78.4 R_B.

MECHANICAL TESTING

Tensile specimens were taken from L, T and ST orientations. The L and T specimens were of standard threaded-end configuration, utilizing a 0.31 inch gage diameter and a 1.5 inch gage length. The ST tensile specimens were miniatures, 1.5 inches in overall length with a gage length and diameter of 0.75 and 0.188 inches, respectively. The larger specimens were instrumented with nichrome element strain gages while a special remotely detachable 0.5 inch gage length extensometer was utilized on the

miniature specimens. Testing was performed in the cryostat and load frame assembly pictured in Figure 1. Tensile data at 4K are summarized in Table 1.

The K_{Ic} testing, 1.25-inch thick compact tension specimens were machined in the LT AND TL orientations. A WOL specimen configuration shown in Figure 2 was chosen for the SL orientation since plate thickness was a limiting factor in specimen design. The WOL specimen B dimension was nominally 0.75 inches. Precracking was done at 295K at a low stress intensity level in accordance with ASTM E399-74. The maximum stress intensity at the conclusion of precracking was less than 10 ksi$\sqrt{in.}$ (11 MPa$\sqrt{m}$) crack front curvature on all specimens was within the specification outlined in ASTM E399-74. Fracture testing of the compact tension specimens was performed in a 100 kip MTS testing machine equipped with a liquid nitrogen jacketed vacuum dewar (Figures 3, 4). The WOL specimens were tested in the small glass dewar system used for the previously described tensile tests.

Table 2 lists the results of the K_{Ic} tests. All specimens satisfied the validity criteria for K_{Ic} testing as specified in ASTM E399-74.

Fatigue crack growth rates were determined on TL and LT orientations utilizing 1-inch thick compact tension specimens. Testing was accomplished in the small test system since it allows easier access to the specimen and is more efficient in the use of He. A compliance gage was attached to integral knife edges machined in the face of the specimen to facilitate crack growth detection at 4K. The cyclic frequency was 9 Hz.

Figures 5 and 6 are plots of da/dN vs ΔK, the fatigue-crack growth data, which is summarized in Tables 3 and 4.

TABLE 1

MECHANICAL PROPERTIES OF 2219-T87 ALUMINUM ALLOY AT 4K

Specimen	Yield Strength (ksi)(MPa)	Ultimate Strength (ksi)(MPa)	Elongation (%)	Reduction of Area (%)	Elastic Modulus ($x10^3$ksi)(GPa)
Longitudinal	73.9	94.6	11.4	31	11.3
	74.5	94.1	12.1	32	11.5
Average	74.2 (512)	94.3 (650)	11.7	31	11.4 (78.6)
Transverse	72.2	94.3	10.2	25	12.2
	74.0	96.2	8.0	17	11.6
Average	73.1 (504)	95.2 (656)	9.1	21	11.9 (82.0)
Short Transverse	68.1	85.9	4.6	4.7	10.3
	69.5	85.2	5.0	3.6	11.1
Average	68.8 (474)	85.5 (589)	4.8	4.1	10.7 (73.8)

TABLE 2

FRACTURE PROPERTIES OF 2219-T87 ALUMINUM ALLOY AT 4K

Specimen Orientation	Load P_Q (kips)	Load Pmax (kips)	$\frac{Pmax}{P_Q}$	a (in.) (cm)	a/w	Y	K_Q (ksi$\sqrt{in}$)(MPa$\sqrt{m}$)	$2.5\frac{(K_Q)^2}{(Tys)}$	K_{Ic} (ksi$\sqrt{in}$)(MPa$\sqrt{m}$)
TL +	12.4	12.9	1.04	0.892 (2.27)	0.357	6.60	41.5 (45.6)	0.80	41.5
	12.5	12.8	1.02	0.874 (2.22)	0.350	6.50	41.3 (45.4)	0.80	41.3
									41.4 Avg (45.5)
LT +	12.7	13.6	1.07	0.900 (2.29)	0.360	6.65	42.8 (47.0)	0.83	42.8
	13.0	13.8	1.06	0.897 (2.28)	0.360	6.65	43.9 (48.2)	0.87	43.9
									43.4 Avg (47.7)
SL *	2.18	2.23	1.02	0.779 (1.98)	0.519		25.2 (27.7)	0.33	25.2
	2.29	2.29	1.06	0.785 (1.99)	0.523		26.7 (29.3)	0.38	26.7
									26.0 Avg (28.6)

\+ B = 1.25 in. (3.175 cm)

* B = 0.75 in. (1.905 cm)

TABLE 3

CRACK GROWTH RATE DATA AT 4K, TL ORIENTATION

Growth Band	Compliance (μ-in/lb)	a in (mm)	avg a/w	Δa in (mm)	ΔN	Δa/ΔN μ-in/cycle (μmm/cycle)	P_{max} lbs (KN)	Y	ΔK (ksi$\sqrt{in}$)*(MPa$\sqrt{m}$)
0	2.02	.627 (15.93)	.322	.033 (.83)	12,000	2.75 (69.9)	2500 (1.11)	6.11	10.26 (11.27)
1	2.12	.660 (16.76)	.344	.056 (1.43)	20,000	2.80 (71.1)	2500 (1.11)	6.41	10.76 (11.83)
2	2.38	.716 (18.19)	.373	.060 (1.52)	10,000	6.0 (152.4)	2800 (1.25)	6.85	12.9 (14.18)
3	2.70	.776 (19.71)	.401	.055 (1.40)	7,000	7.85 (199.4)	2800 (1.25)	7.34	13.8 (15.17)
4	3.03	.831 (21.11)	.431	.071 (1.80)	4,500	15.77 (400.6)	3000 (1.33)	7.93	16.0 (17.58)
5	3.50	.902 (22.91)	.471	.082 (2.09)	4,000	20.5 (520.7)	3000 (1.33)	8.83	17.8 (19.56)
6	4.15	.984 (25.00)	.510	.074 (1.87)	1,500	49.3 (1252)	3200 (1.42)	9.90	21.3 (23.41)
7	4.98	1.058 (26.87)							

* ΔK calculation is based on 95% of P_{max} since a P_{min} of 0.05 P_{max} was used throughout the test.

TABLE 4

CRACK GROWTH RATE DATA AT 4K, TL ORIENTATION

Growth Band	Compliance (μ-in/lb)	a in (mm)	avg a/w	Δa in (mm)	ΔN	μ-in/cycle (μmm/cycle)	P_{max} lbs (KN)	Y	ΔK (ksi$\sqrt{in}$)*(MPa$\sqrt{m}$)
0	2.02	.618 (15.69)	.318	.036 (0.92)	40,000	.9 (22.9)	2200 (.98)	6.06	8.96 (9.85)
1	2.17	.654 (16.61)	.338	.055 (1.40)	30,000	1.8 (45.7)	2200 (.98)	6.32	9.34 (10.3)
2	2.34	.709 (18.01)		.037 (0.94)	15,000	2.5 (63.5)	2400 (1.07)	6.70	10.8 (11.9)
3	2.58	.746 (18.95)	.387	.057 (1.45)	13,000	4.4 (111.8)	2400 (1.07)	7.09	11.4 (12.5)
4	2.88	.803 (20.40)	.419	.069 (1.75)	8,000	8.6 (218.4)	2600 (1.16)	7.68	13.4 (14.7)
5	3.30	.872 (22.15)	.456	.083 (2.11)	7,000	11.9 (302.3)	2600 (1.16)	8.47	14.8 (16.3)
6	3.96	.955 (24.26)	.496	.076 (1.93)	3,000	25.3 (642.6)	2800 (1.25)	9.49	17.8 (19.6)
7	4.68	1.031 (26.19)	.537	.087 (2.21)	2,000	43.5 (1105)	2800 (1.25)	11.54	21.7 (23.8)
8	5.68	1.118 (28.40)	.572	.053 (1.34)	600	88.3 (2243)	3000 (1.33)	12.17	24.5 (26.9)
9	6.44	1.171 (29.74)	.606	.038 (2.11)	400	207 (5258)	3000 (1.33)	13.87	27.95 (30.7)
10	7.57	1.254 (31.85)							

* ΔK calculation is based on 95% of P_{max} since a P_{min} of 0.05 P_{max} was used throughout the test.

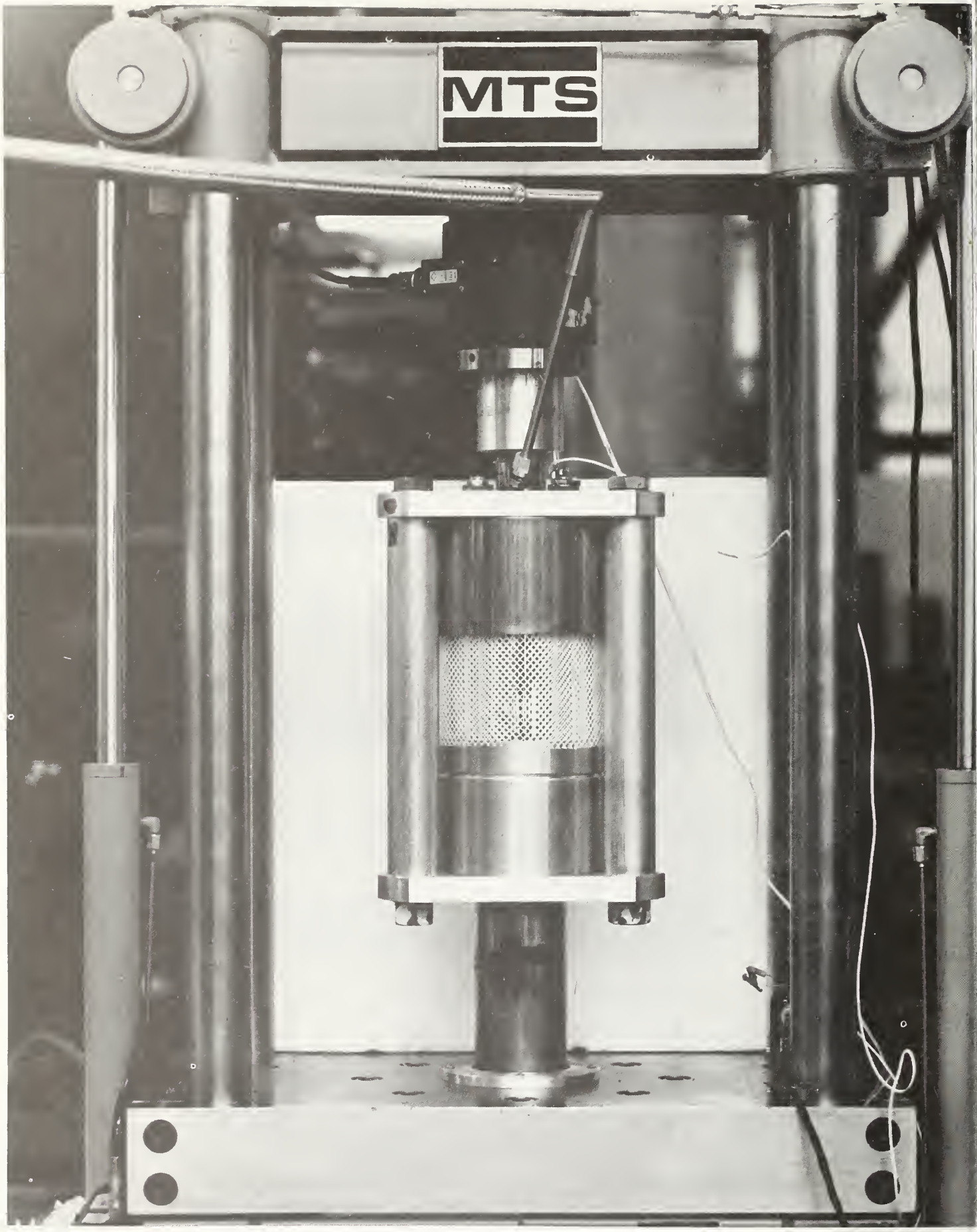

FIGURE 1 System for Tensile and Crack Growth Testing at 4K

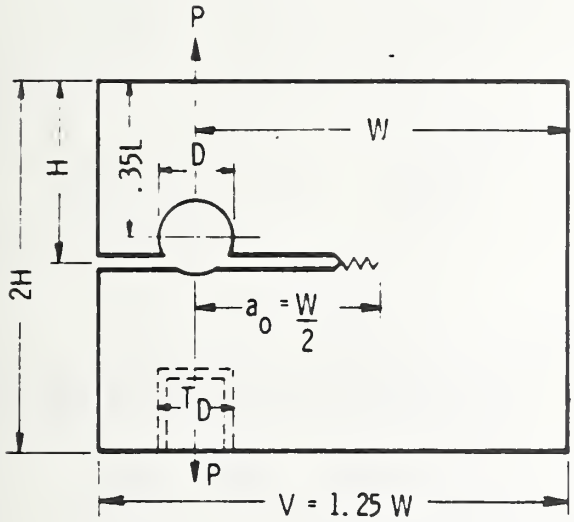

$B = a_o$

$W = 2H = 2.0B$

$D = .6B$

$T_D = .5B$

For a/W from 0.25 to 0.65

$$K_I = \frac{P}{B}\frac{a^{1/2}}{W}\left[39.70 - 294.2\left(\frac{a}{W}\right) + 1118\left(\frac{a}{W}\right)^2 - 1842\left(\frac{a}{W}\right)^3 + 1159\left(\frac{a}{W}\right)^4\right]$$

Notch Details

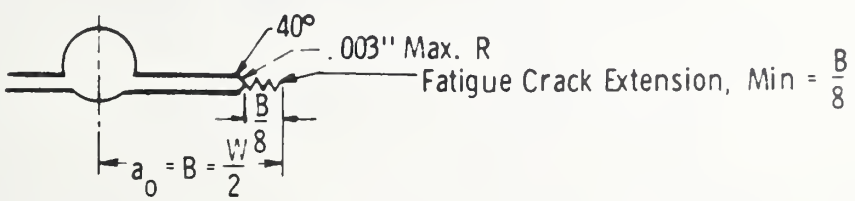

Figure 2 WOL Specimen Configuration

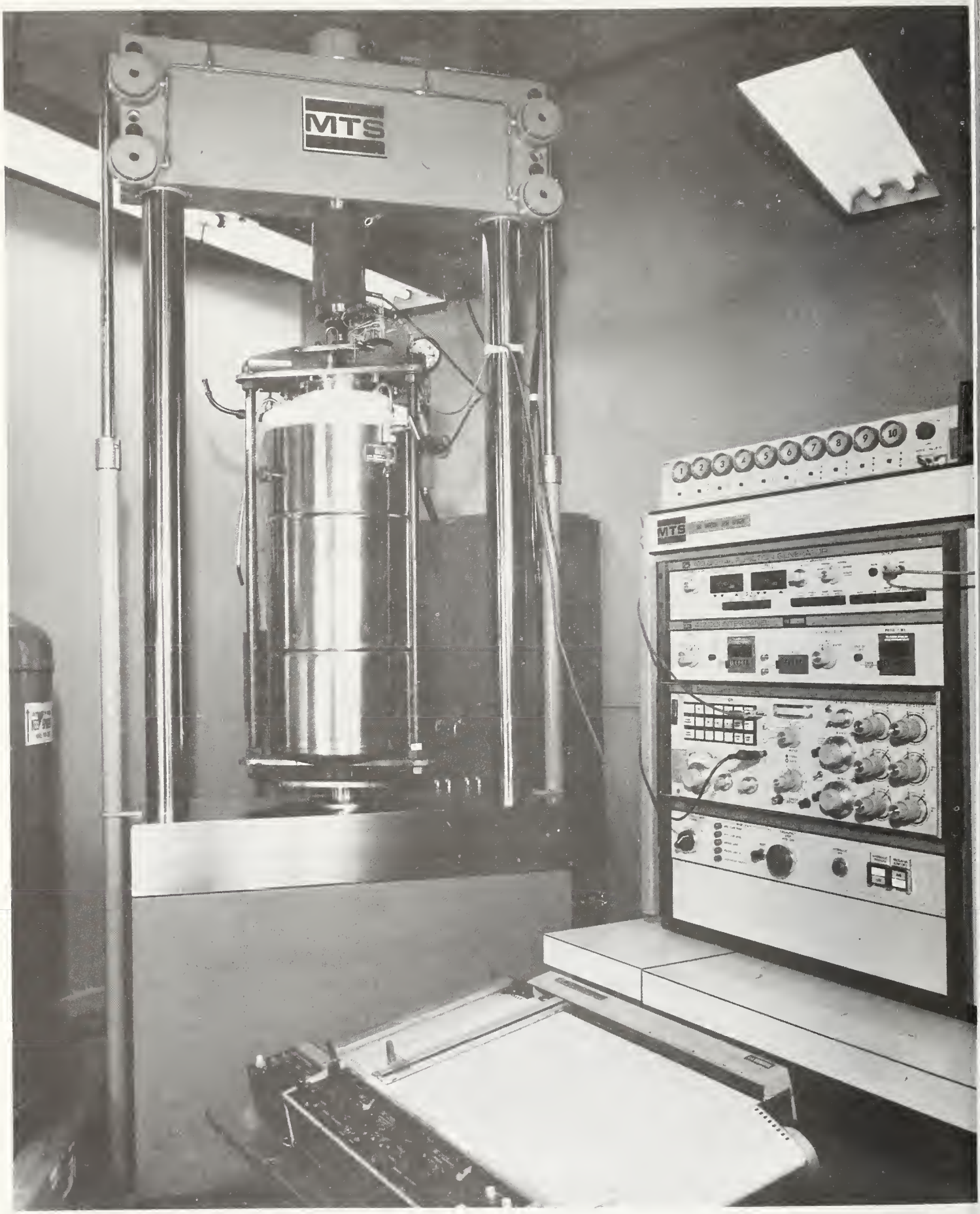

FIGURE 3 Overall View of Liquid Helium Testing System

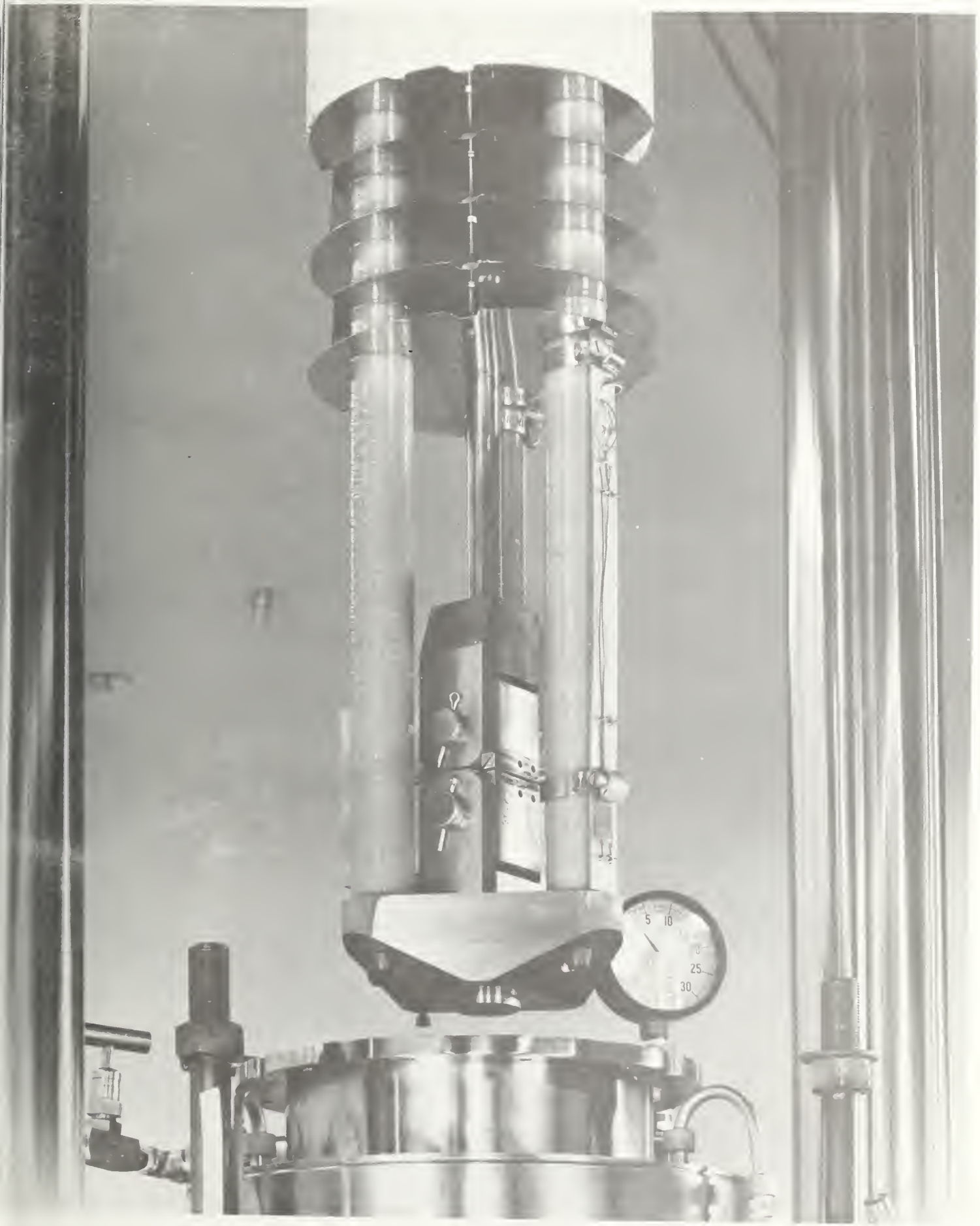

FIGURE 4 Close-Up View of Load Train for Liquid Helium Testing System

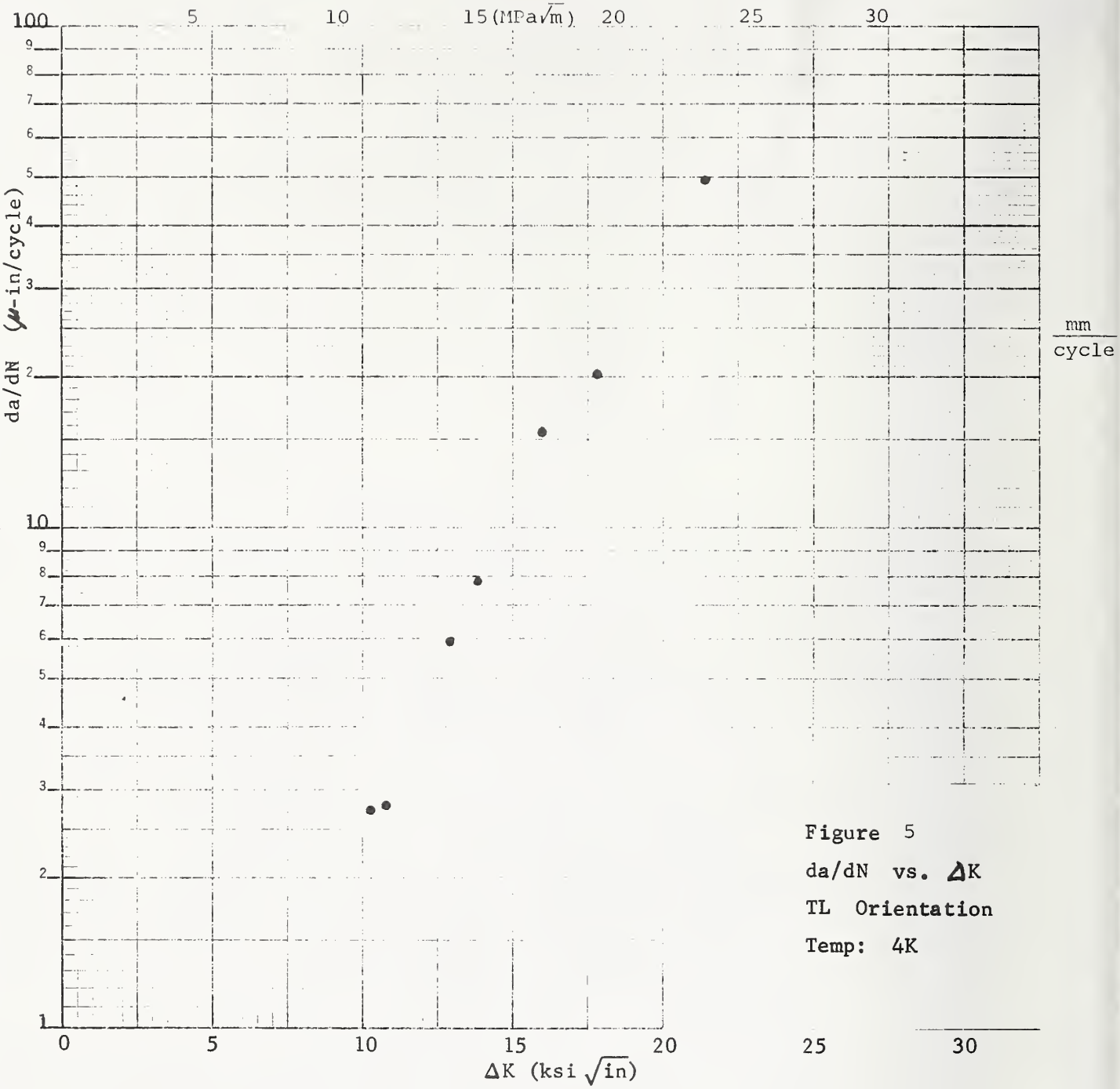

Figure 5
da/dN vs. ΔK
TL Orientation
Temp: 4K

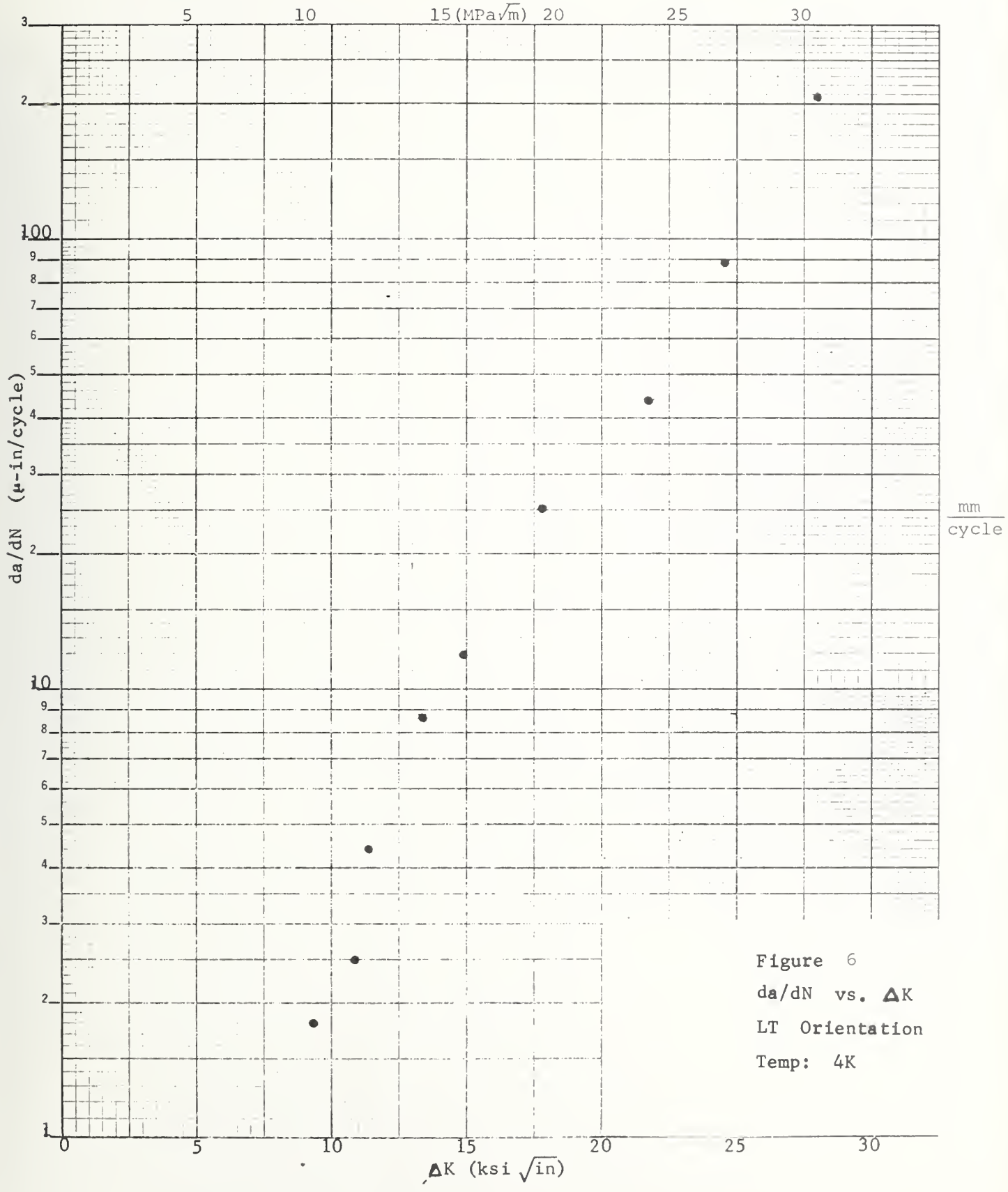

Figure 6
da/dN vs. ΔK
LT Orientation
Temp: 4K

LOW CYCLE FATIGUE TESTING OF 304LN STAINLESS STEEL AND 5083-O ALUMINUM ALLOYS

Martin Marietta

LOW CYCLE FATIGUE TESTING OF 304LN STAINLESS AND 5083-O ALUMINUM ALLOYS

J. A. Shepic
Principal Investigator

H. J. Brown
Program Manager

MARTIN MARIETTA CORPORATION
Denver Division
P.O. Box 179
Denver, Colorado

FOREWORD

This report describes technical activities conducted by the Denver Division of Martin Marietta from 26 July 1978 through 26 November 1978 under National Bureau of Standards (NBS) contract CST-8455.

The views and conclusions contained in this document are those of the authors and should not be interpreted as necessarily representing the official policies either expressed or implied, of the United States Government.

INTRODUCTION

Superconducting machinery will be subjected to cyclic loading at temperatures down to 4 K. Fatigue data for candidate materials are sparse below 20 K. At 4 K, most fatigue data are embodied in four papers (references 1, 2, 3, and 4).

Stainless alloy AISI 304LN and aluminum alloy 5083-0 were evaluated. No previous fatigue data for either alloy at 4 K were available.

MATERIALS

Each alloy was supplied by NBS as plate stock. The 304LN was obtained as 3.8 cm (1.5 in.) thick plate. The 5083-0 aluminum alloy was supplied in 2.5 cm (1.0 in.) thickness.

Chemistry and mechanical properties for 304LN, heat number 25397, are given below:

C = 0.024 w/o

Mn = 1.74 w/o

P = 0.035 w/o

S = 0.005 w/o

Si = 0.51 w/o

Ni = 8.60 w/o

Cr = 18.85 w/o

Mo = 0.38 w/o

Co = 0.23 w/o

Cu = 0.30 w/o

N = 0.13 w/o

Fe = Balance

	Temperature, K		
	293	77	4
Ultimate strength, MN/m^2 (ksi)	617 (90)	1541 (223)	1686 (245)
Yield strength, 0.2% offset MN/m^2 (ksi)	283 (41)	655 (95)	771 (112)
Elongation, %	63	47	37
Reduction of area, %	84	58	52

TESTING TECHNIQUE AND APPARATUS

This chapter describes the specimen geometry, testing apparatus, and technique used to obtain the fatigue data presented in this report.

The fatigue specimen configuration used for this program is similar to that used by Martin Marietta in previous fatigue studies (references 1, 2 and 5). The design incorporates a smooth gage section with a mild radius and a bearing shoulder at the end of the threaded section for alignment and locking, as opposed to aligning on the threads. This system is advantageous because only two close-tolerance alignment surfaces are required and failure within the prescribed area of the gage is assured. When locked with a nut at each end of the threaded bar, the specimen can be subjected to a fully reversed loading cycle that is continuous through zero load. Figure 1 gives the specifications for the specimen.

Fatigue specimens were polished after machining using 240 to 320 grit polishing paper (the coarseness of the initial rough polishing paper depended on the alloy hardness and machined surface roughness in the gage section) and then using 320 and 600 grit paper followed by a felt wheel and Tripoli polishing compound. The polishing paper was bonded to a rubber sanding disc mounted in a small Dumore grinding tool.

As the specimen is rotated at approximately 350 rpm between lathe centers, the periphery of the spinning (approximately 20,000 rpm) sanding disc contacts the specimen gage section with axial

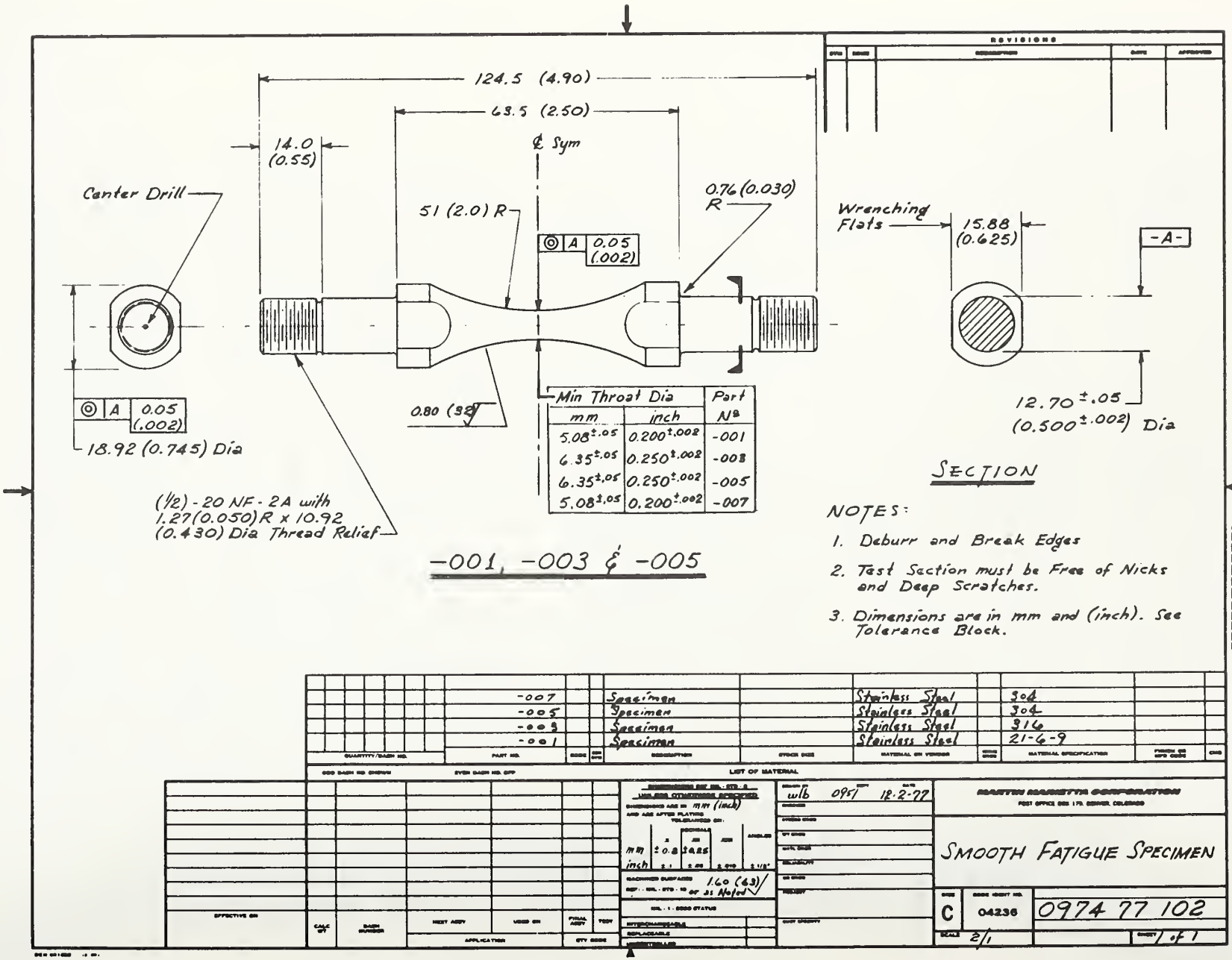

Figure 1 Specifications for Fatigue Specimen

strokes. (The same procedure was used with all grits). The final polish uses a 2 in. diameter felt wheel mounted in a Dumore grinding tool and loaded with Tripoli polishing compound. As the specimen is rotated between lathe centers at approximately 150 rpm, the spinning (approximately 20,000 rpm) impregnated felt wheel contacts the specimen gage section with axial strokes. This polishing technique produces a mirror finish in which any remaining polishing marks are in an axial direction that will have minimal effect on axial fatigue test results.

Because of the nonuniform cross section area of the specimen, it is necessary to control total strain based on diametral deflection rather than axial deflection. A diametral strain extensometer was designed and built specially for this work. This device is a one-piece aluminum ring with integral strain beams instrumented with nichrome resistance strain gauges. The beam ends are machined with knife edges to grip the specimen. The knife edge separation distance is controlled to provide good gripping action on the gage section. The gauge grips the specimen tight enough that it remains in the horizontal plane during filling of the cryostat and subsequent cycling loading. Figure 2 gives a closeup view of the extensometer.

The test configuration for 293 K evaluation was conventional. As shown in Figure 3, the specimen is installed in adapters that permit the shoulder to be preloaded. Adapters are then installed in the testing machine.

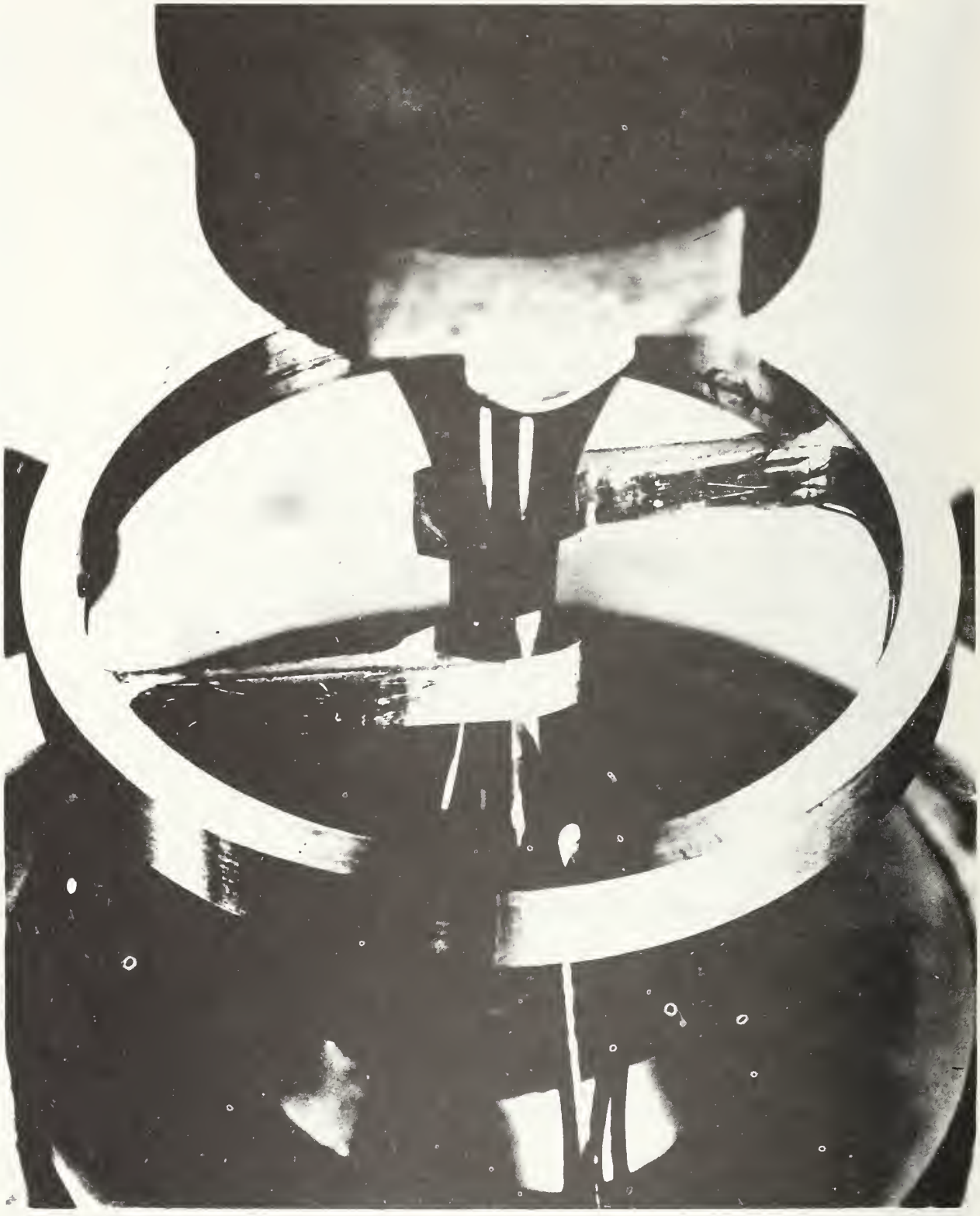

Figure 2 Diametral Strain Extensometer

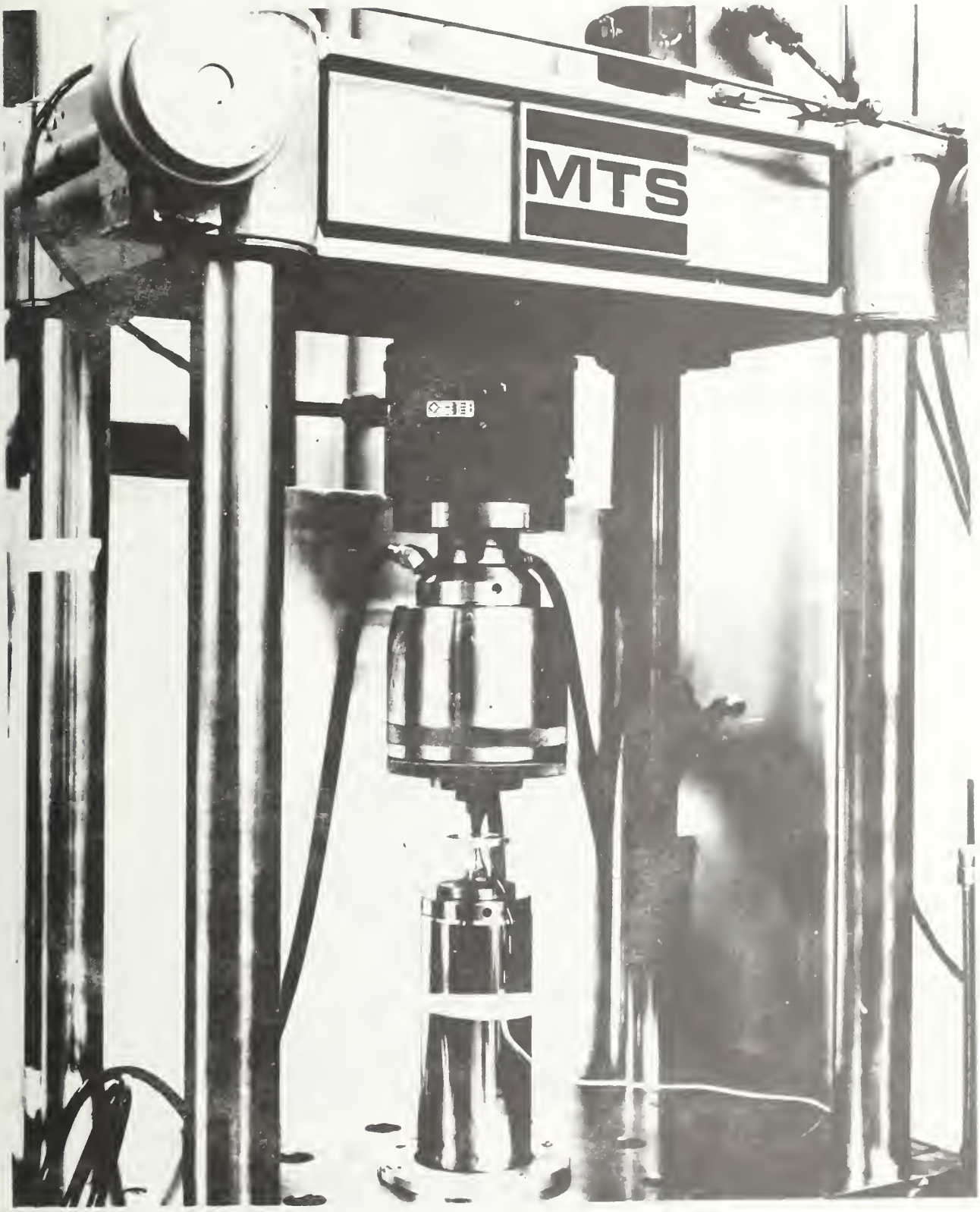

Figure 3 Apparatus for 293 K Testing

Testing at 77 K and 4 K was performed in a cryostat system prepared for low-cycle fatigue testing. Loading was achieved through two concentric frames shown in Figure 4. The smaller frame surrounding the specimen is constructed from titanium alloy. Note that a specimen adapter plate is used at the top of the specimen. At the bottom, the specimen shoulder bears against the triangular plate. The remainder of the frame is constructed from aluminum alloy. A glass vacuum dewar is used to provide environmental control. Figure 5 shows the load frame installed in the machine, both with and without the dewar in place.

The liquid helium system is designed so testing can be achieved with minimum cryogen consumption. The titanium frame and specimen are first precooled to 77 K and placed in a liquid nitrogen filled dewar on the bottom platen. After cooling, the head is raised and a liquid helium filled dewar replaces the liquid nitrogen dewar. A liquid level sensor is used to monitor level, and refilling is performed as required.

Fatigue testing was performed in a 222 kN (50 kip) closed-loop servo-controlled testing machine. Operation was in the strain-control mode. The relationship between total axial strain amplitude and total diametral strain amplitude is as follows:

$$\Delta\lambda_l = 2\Delta\lambda_d + \frac{\Delta P}{AE}(1-2\mu)$$

where λ_l = total axial or longitudinal strain amplitude

λ_d = total diametral strain amplitude

ΔP = load amplitude at half-life

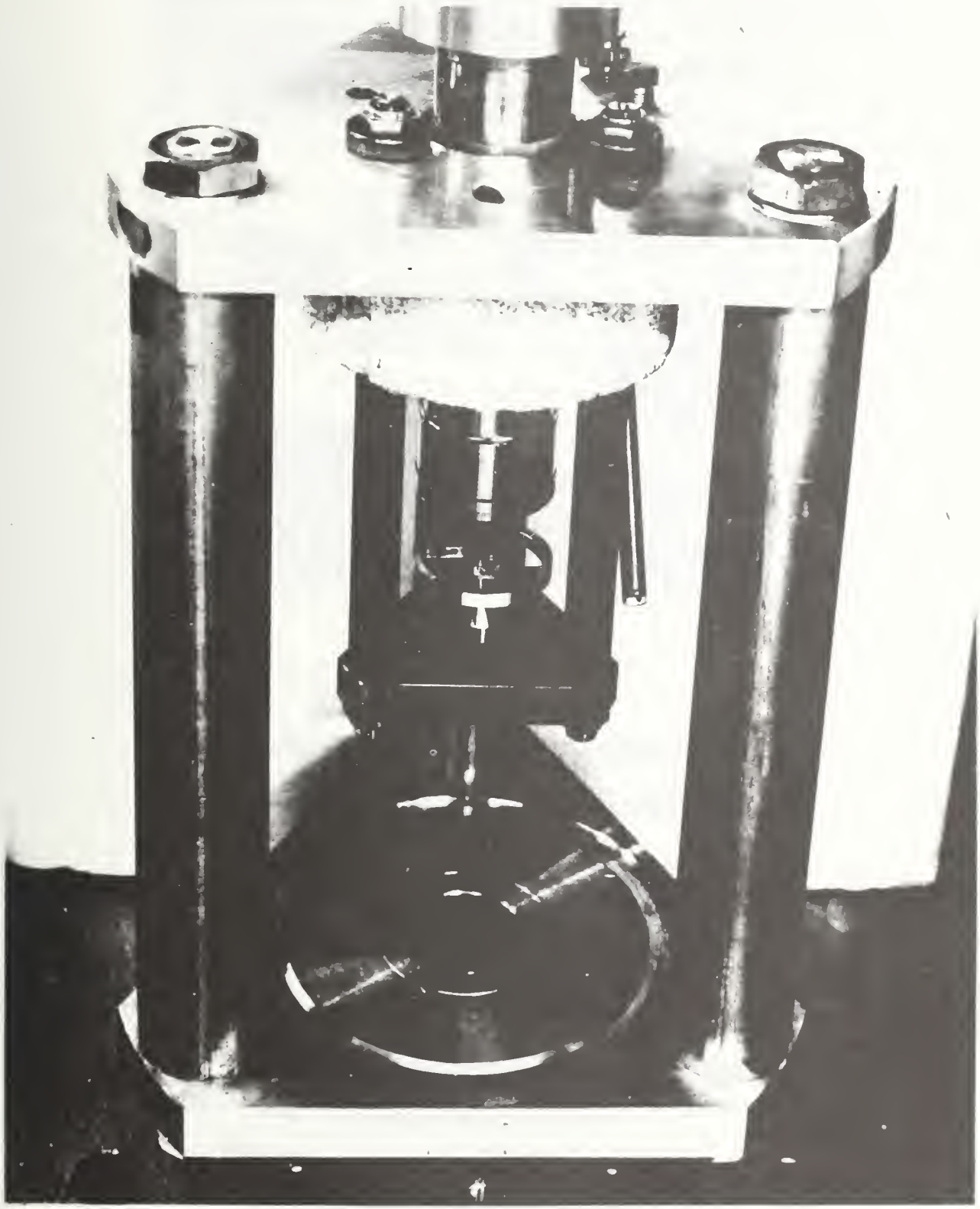

Figure 4 Load Train for 4K Testing

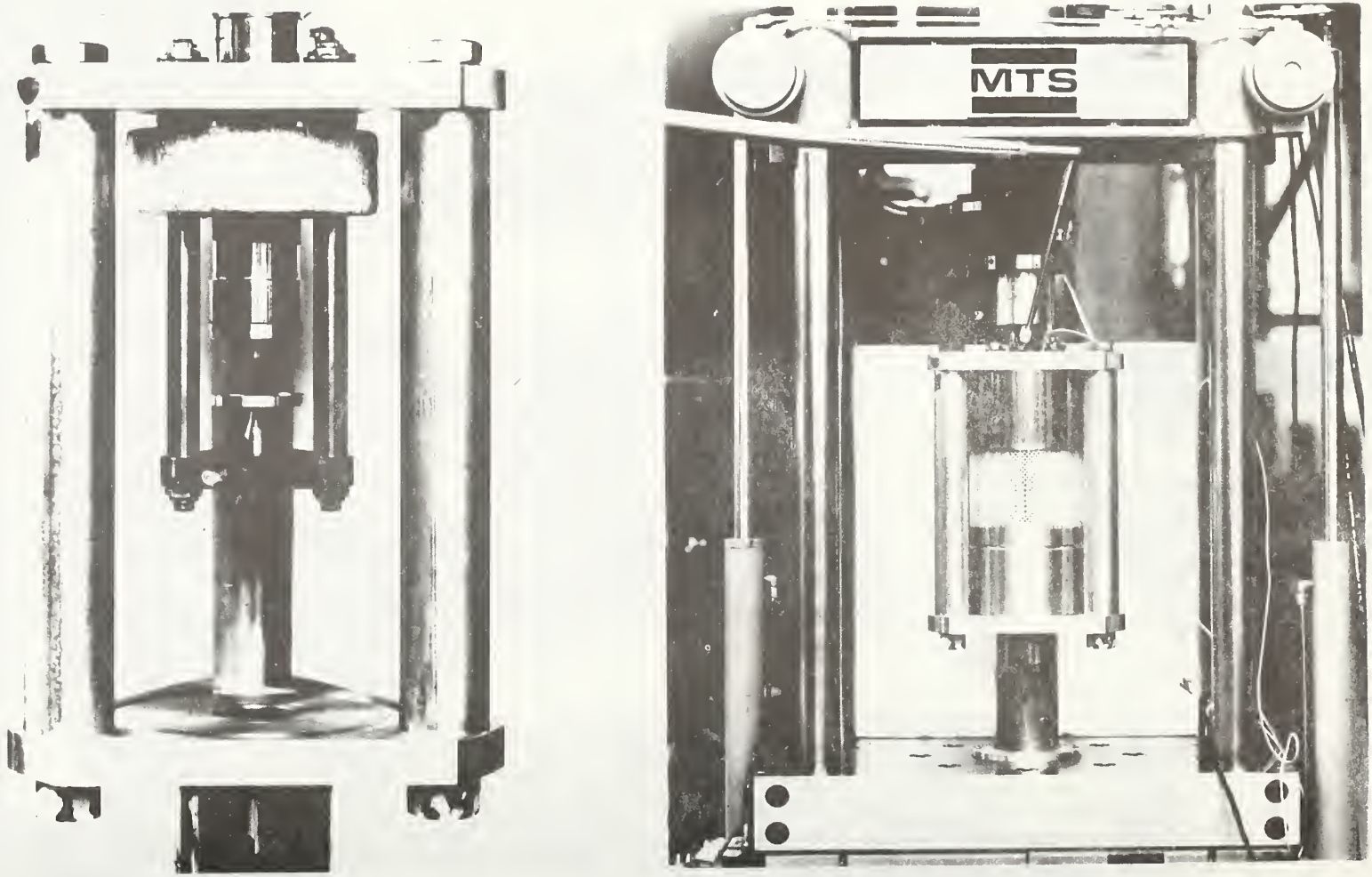

Figure 5 Apparatus for 4 K Testing

A = cross-sectional area

E = Young's modulus

μ = Poisson's ratio

To calculate the diametral strain amplitude required to achieve a desired axial strain amplitude, an approximate value for ΔP was selected. Following completion of the test, a more accurate value of ΔP was selected from the load vs strain hysteresis curves and the actual total axial strain amplitude value was recalculated. Accuracy of the ΔP estimation improved with each succeeding test and, as a result, actual values were close to desired values. The elastic component of the total strain was calculated using the ΔP value read from the test record and the appropriate value of Young's modulus. The plastic component of strain was calculated by subtracting the elastic strain from the total strain.

EXPERIMENTAL TEST RESULTS

Fatigue behavior of each of the two alloys was characterized at 293, 77, and 4 K. Because of the extreme high cost of liquid helium and the large quantities required to obtain long-time fatigue data, only a limited number of 4 K tests were conducted beyond 10^4 cycles.

304LN Stainless Steel - This alloy exhibits a significant amount of discontinuous yielding at 4 K, as shown by prior tensile test investigations. During cyclic loading, it is possible that the heat generated in the plastic range can cause vaporization of

the low heat capacity liquid helium and a resultant elevation of the test temperature. This situation should be rate sensitive and could be reduced by cycling at slow rates. Rate sensitivity measurements made by Martin Marietta in previous work on 304 stainless (reference 1) show a frequency dependency above 0.1 Hz at high cyclic strain amplitudes (1.5%). Cyclic frequencies on the 304LN fatigue tests discussed here were held at or below 0.1 Hz for strain amplitudes exceeding 1.0% in liquid helium.

Experimental data for the 304LN alloy exhibited a temperature dependency of life in the low cycle range in which life decreased with decreasing temperature. Below strain amplitudes of approximately 0.8%, life increased with decreasing temperature. Figure 6 graphically depicts the fatigue life as a function of strain. Table 1 gives detailed information on the diametral and longitudinal strains, stress amplitude, cyclic rate, and cycles to failure.

Figure 7 illustrates typical cyclic behavior of 304LN at room temperature and a strain amplitude of 1.52%, fully reversed (R = -1). Loading was initiated in compression to reduce the possibility of developing a local necked region during the first tensile loading. Materials that strain soften are especially susceptible to necking if tensile loading is appplied initially. Diametral deflection is plotted on the x-axis vs load on the y-axis. The calibrations for each are shown on the graph. The first cycle starts in compression at the center of the hysteresis loop. Note that the load increases with each successive cycle as a result of strain hardening. The degree of strain hardening is dependent on strain amplitude and test temperture.

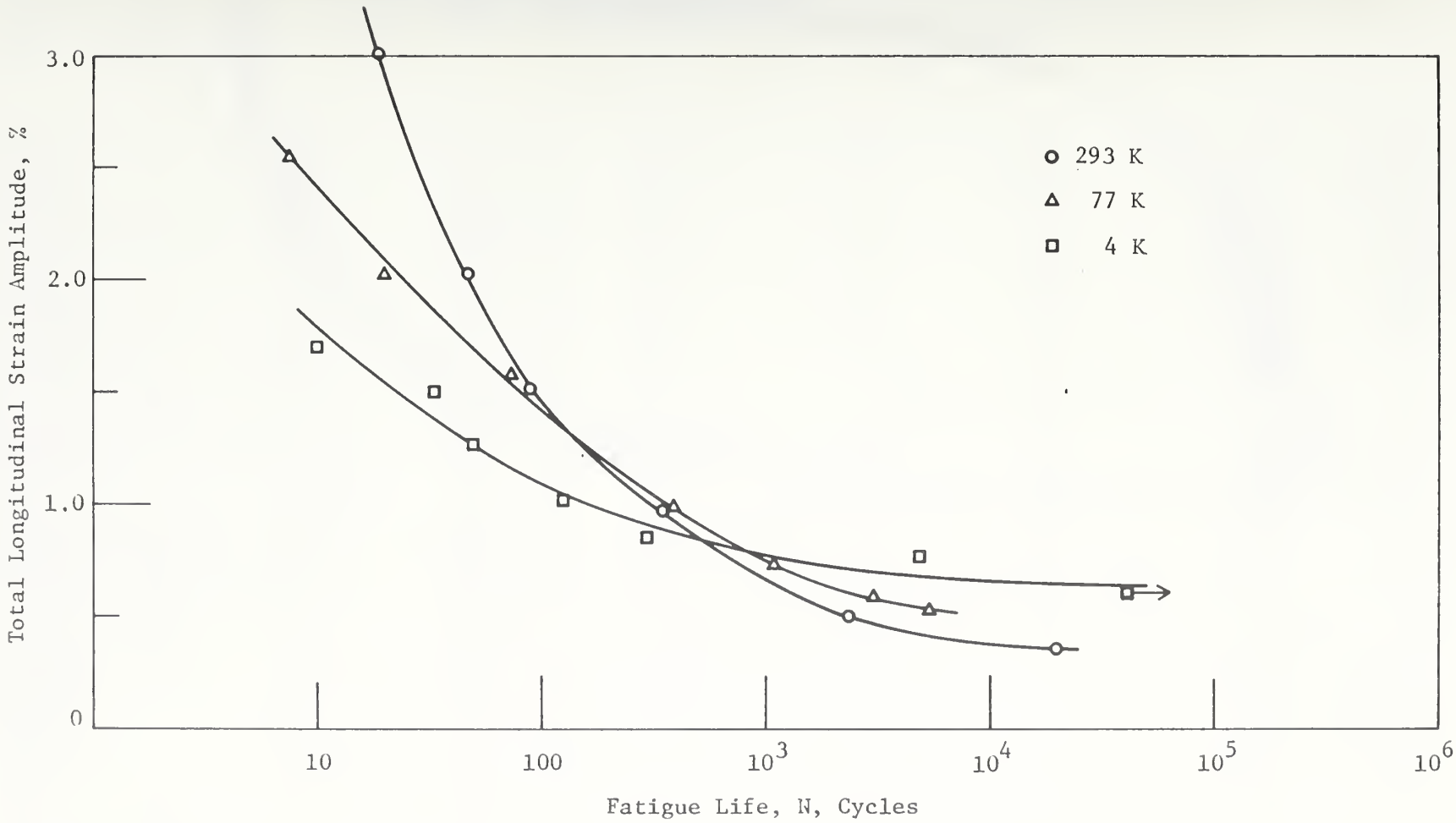

Figure 6 Fatigue Life Curves for 304LN

Table 1. Fatigue Data for 304LN Stainless Steel

Specimen Number	Temperature, K	Diametral Total Strain Amplitude, $\Delta\lambda d$,%	Stress Amplitude at Half-Life, $\Delta\sigma$, MN/m^2 (ksi)	Longitudinal Elastic Strain Amplitude, Δe_l, %	Longitudinal Plastic Strain Amplitude, $\Delta\varepsilon_l$, %	Longitudinal Total Strain Amplutude, $\Delta\lambda_l$, %	Cyclic Rate, Hz	Fatigue Life, N Cycles
304LN-1	300	0.95	655 (95)	0.34	1.70	2.04	0.10	475
304LN-2		0.45	379 (55)	0.20	0.78	0.98	0.50	3440
304LN-3		1.43	690 (100)	0.37	2.65	3.02	0.05	187
304LN-4		0.22	276 (40)	0.16	0.35	0.51	1.00	23,100
304LN-5		0.15	242 (35)	0.13	0.23	0.36	3.00	194,280
304LN-6		1.92	931 (135)	0.50	3.55	4.05	0.05	98
304LN-7		0.70	517 (75)	0.28	1.24	1.52	0.20	870
304LN-8	77	0.60	1793 (260)	0.87	0.70	1.57	0.20	730
304LN-9		1.07	1896 (275)	0.92	1.62	2.54	0.05	76
304LN-10		0.35	1275 (185)	0.61	0.37	0.98	0.50	3820
304LN-11		0.21	758 (110)	0.37	0.21	0.58	3.00	29,920
304LN-12		0.18	758 (110)	0.36	0.16	0.52	6.00	52,500
304LN-13		0.26	965 (140)	0.46	0.26	0.72	2.00	10,900
304LN-15		0.80	1896 (275)	0.91	1.10	2.01	0.10	201
304LN-14	4	0.55	1793 (260)	0.86	0.64	1.50	0.05	327
304LN-16		0.37	1275 (185)	0.61	0.40	1.01	0.20	1140
304LN-17		0.27	1103 (160)	0.54	0.23	0.77	0.50	4850
304LN-18		0.80	1310 (190)	0.64	1.36	2.00	0.04	19*
304LN-19		0.80	1310 (190)	0.64	1.36	2.00	0.03	25*
304LN-20		0.47	1482 (215)	0.71	0.55	1.26	0.09	490
304LN-21		0.30	1171 (170)	0.57	0.28	0.85	0.40	1970
304LN-22		0.20	931 (135)	0.45	0.15	0.60	1.00	40,070†
304LN-23		0.65	1861 (270)	0.90	0.80	1.70	0.04	100

*Specimen Buckled
†Test Discontinued

Temperature, K	293	77	4
Modulus, GN/m^2 (10^6 psi)	195 (28)	209 (30)	207 (29.7)
Possion's Ratio	0.290	0.279	0.271

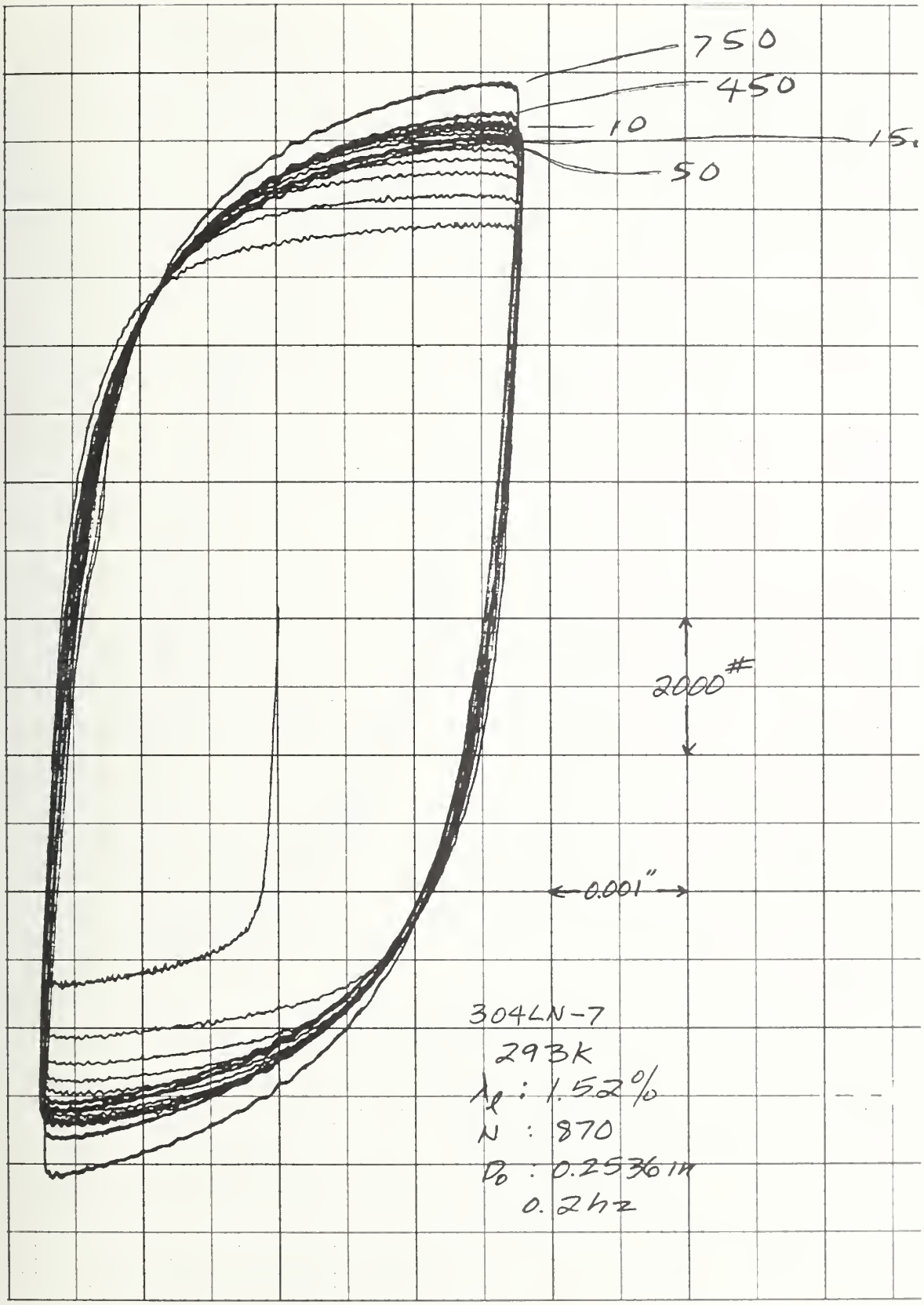

Figure 7 Load-Deflection Curve for Specimen 304 LN-7

Figure 8 illustrates a strain softening effect. Note that the load excursion is lower at 4800 cycles than at the start of the test. The strain amplitude was 0.51% and the test was conducted at room temperature.

A marked change in behavior occurs when the test temperature is reduced. Figure 9 shows a hysteresis plot of a 304LN specimen tested at 77 K at a strain amplitude of 1.57%; the same strain amplitude as Figure 7. The high degree of strain hardening is the result of strain - induced martensitic transformation.

Results obtained at 4 K for 304LN exhibit discontinuous yielding behavior. Figure 10 illustrates the first two cycles of a test at 4 K and a strain amplitude of 2.0%. The discontinuous yielding is pronounced. Note that load drops occur only after a small amount of initial yielding. This discontinuous behavior is a result of adiabatic heating of the specimen due to straining, causing a loss of strength.

Figure 11 illustrates behavior at a lower strain amplitude. The load drops are not as severe and control of the test is improved. After 100 cycles have elapsed, the hysteresis curve is smooth.

Figures 12 and 13 illustrate test results of even lower strain amplitudes. Strain hardening is still taking place, however, discontinuous yielding is not apparent at the 0.5% strain level (Figure 13).

5083-O Aluminum Alloy

Figure 14 summarizes the strain vs life data at the three

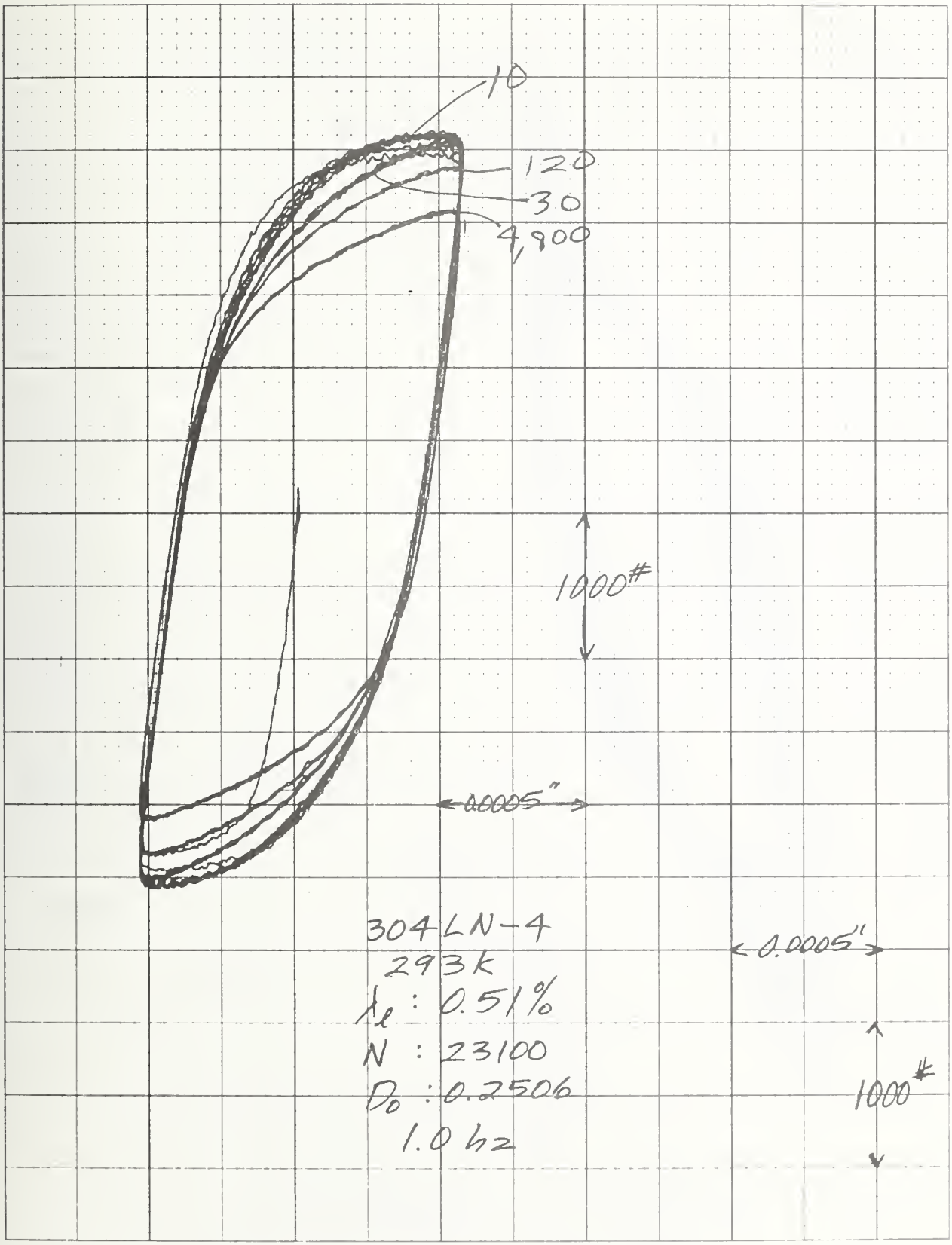

Figure 8 Load-Deflection Curve for Specimen 304LN-8

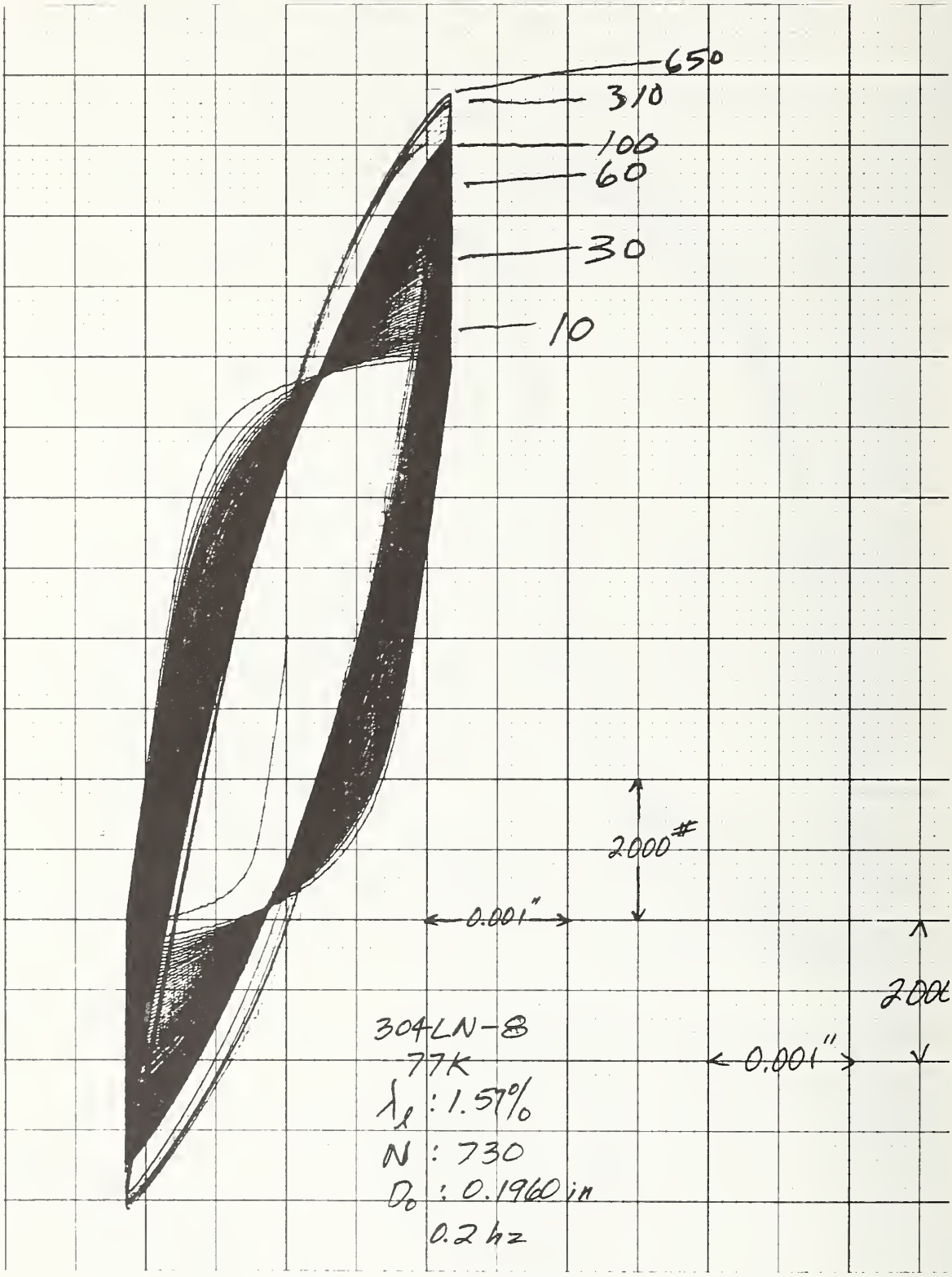

Figure 9 Load-Deflection Curve for Specimen 304LN-8

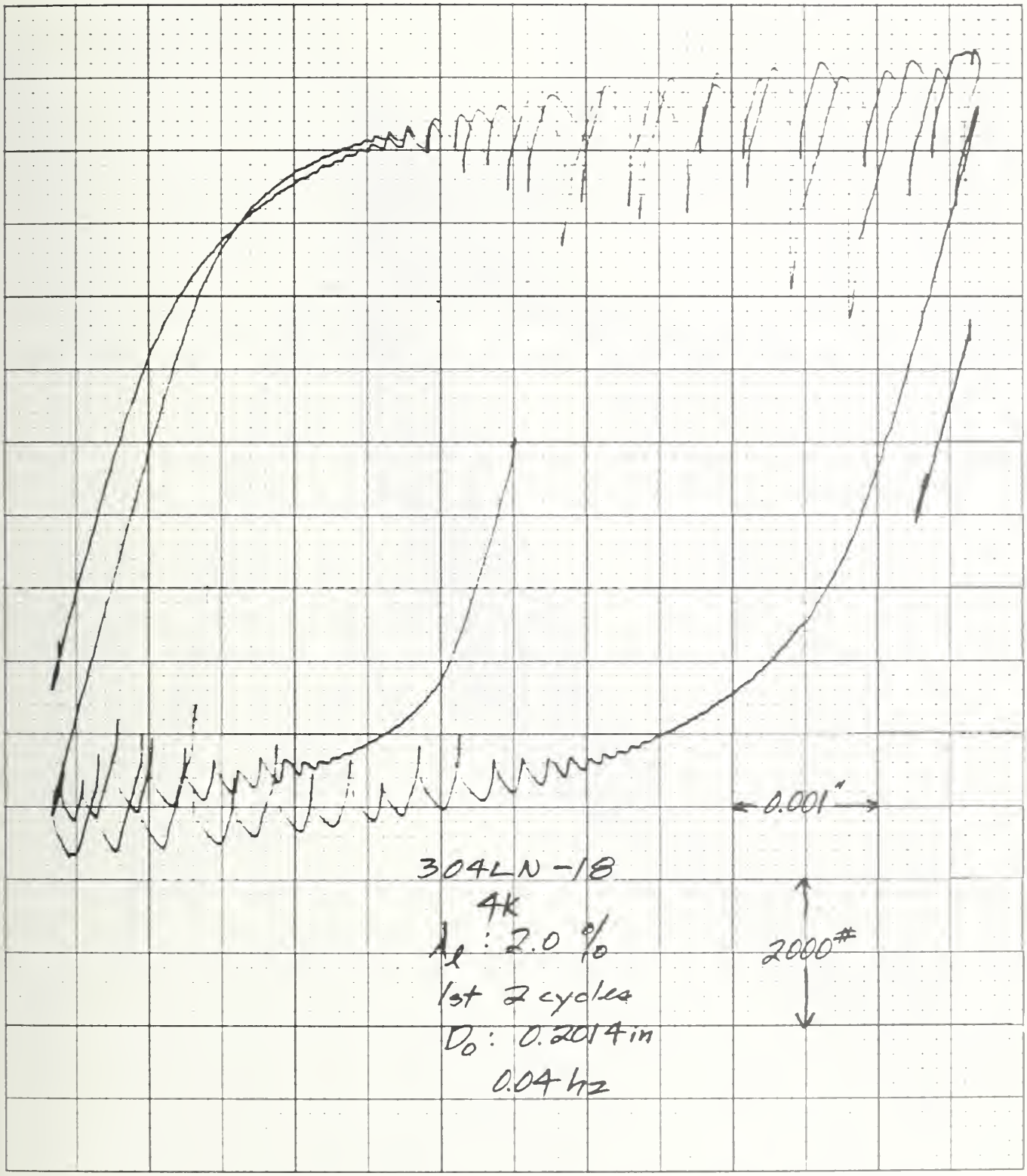

Figure 10 Load-Deflection Curve for Specimen 304LN-18 (First 2 Cycles)

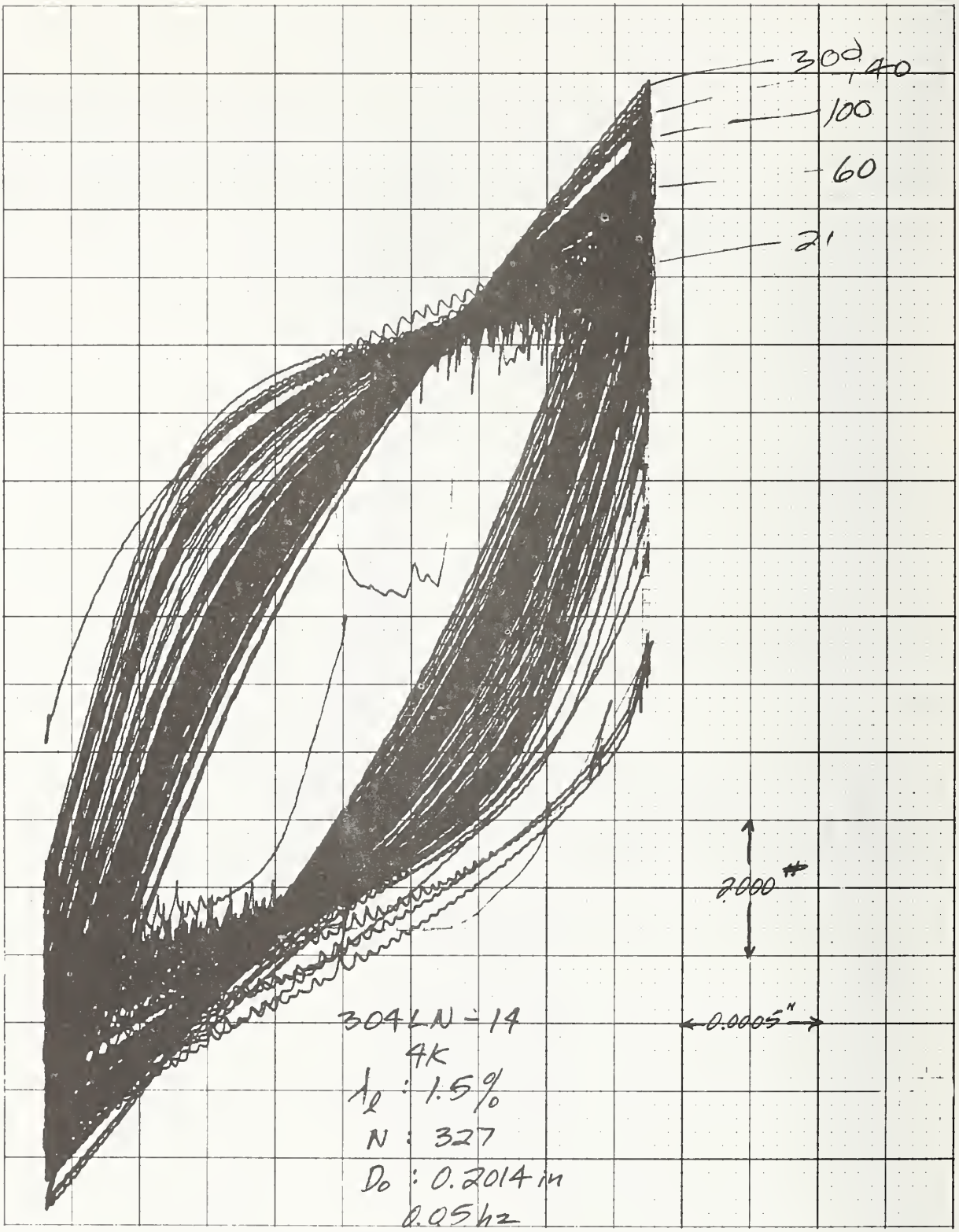

Figure 11 Load-Deflection Curve for Specimen 304LN-14

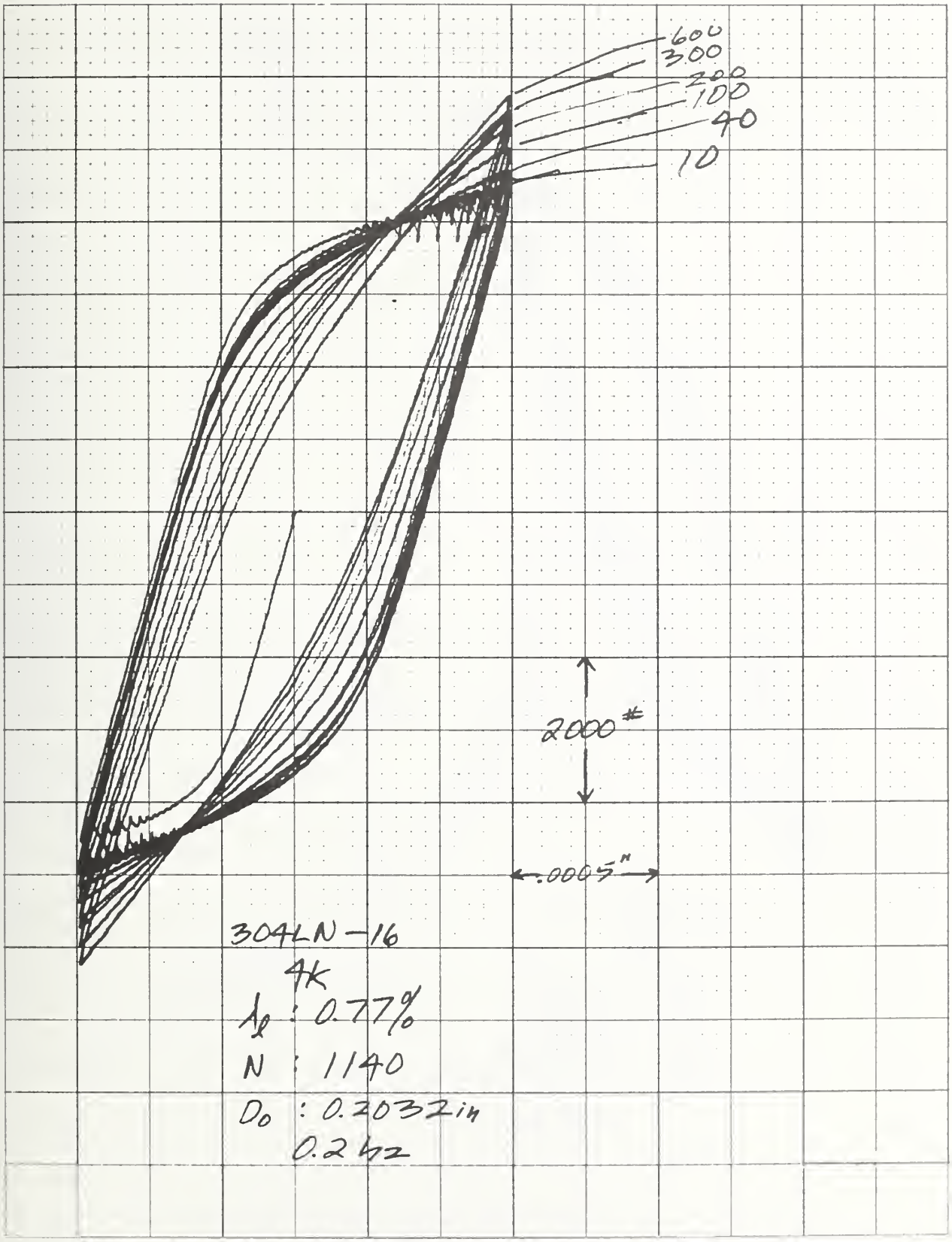

Figure 12 Load-Deflection Curve for Specimen 304LN-16

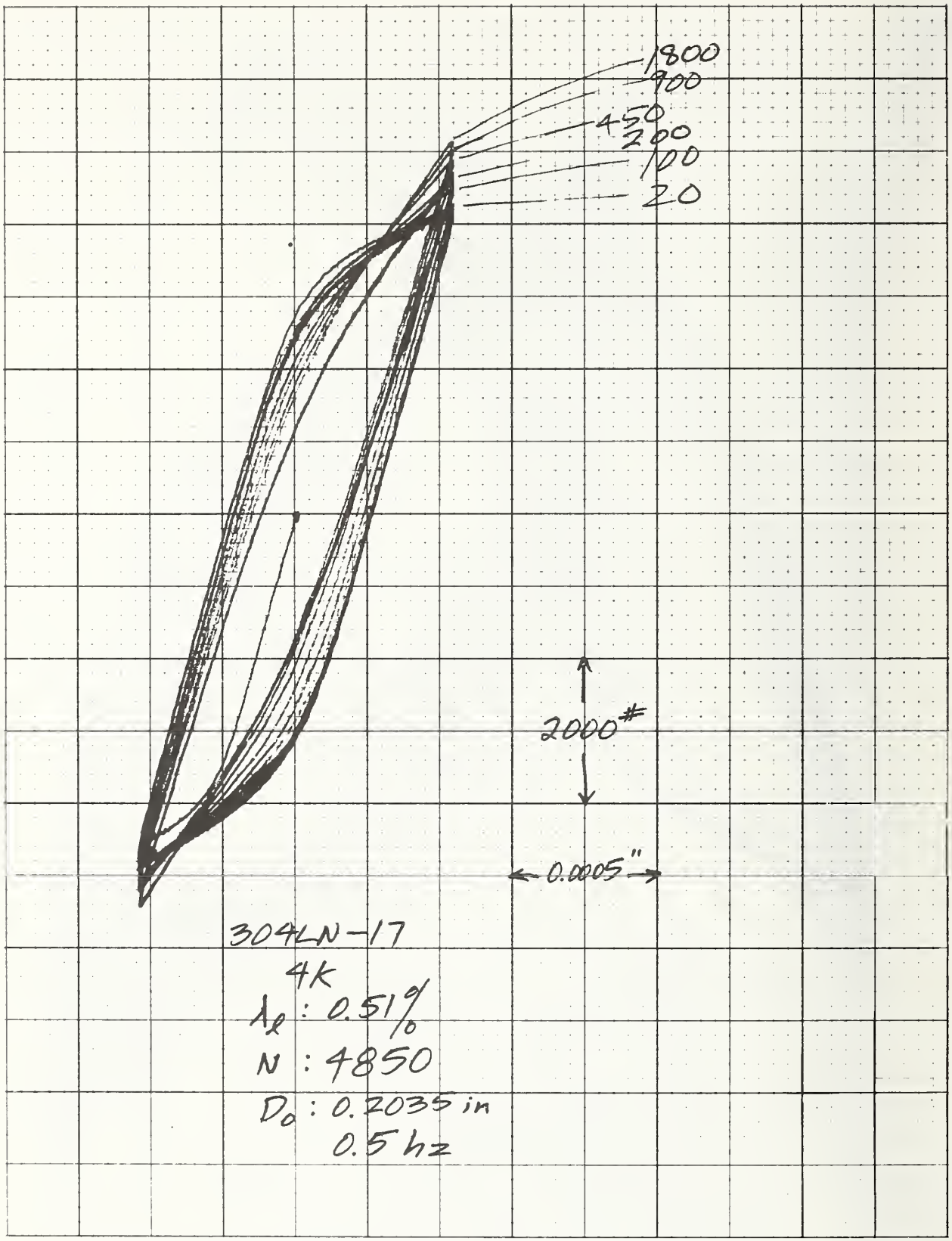

Figure 13 Load-Deflection Curve for Specimen 304LN-17

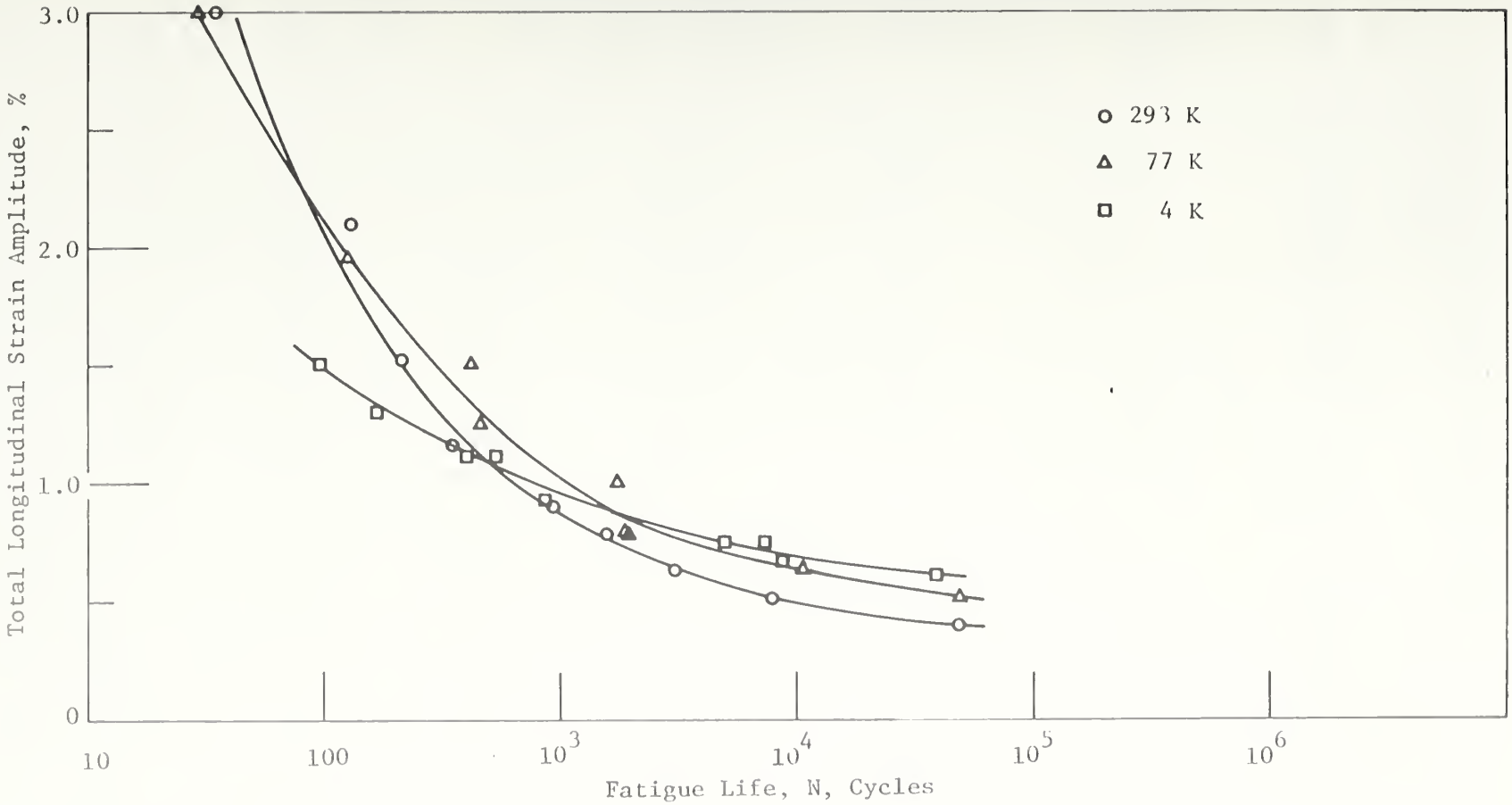

Figure 14 Fatigue Life Curves for 5083-0

temperatures. The trend is similar to the tested stainless alloys with a decrease in cyclic life at 4 K and high strain amplitudes with a reversal of this behavior at strain amplitudes below 0.9%. The 293 K and 77 K data at strain amplitudes above 1.5% are similar. These data are given in Table 2.

Figures 15 and 16 are typical hysteresis curves for this alloy at ambient temperature, strain softening was not apparent at any of the strain amplitudes tested.

Figures 17 and 18 are indicative of cyclic behavior at 77 K.

Tests conducted at 4 K exhibit extensive discontinuous yielding (Figure 19). Changes in cyclic frequency by a factor of 5 between specimens 21 and 33 (that were tested at a strain amplitude of 1.11%) did not show a significant degree of frequency dependency. The same was done with specimens 23 (Figure 20) and 24 at 0.75% strain amplitude with no significant difference in cycles to failure. It can be reasoned that the aluminum alloy, because of its higher thermal conductivity, will not be as susceptible to cyclic frequency as the stainless.

Failure modes of the aluminum alloy are interesting. The specimens fail in shear at strain amplitudes above 1% at 293 K and 77 K. Failure is abrupt, with load decay occurring one or two cycles before failure. Slight evidence of fatigue cracking is apparent on visual examination of the fracture surface.

The 4 K specimens that were tested at strain amplitudes above 1%, exhibit delamination, much like a high strength, precipation hardened aluminum alloy tensile tested at 4 K or 20 K.

Table 2. Fatigue Data for 5083-0 Aluminum Alloy

Specimen Number	Temperature, K	Diametral Total Strain Amplitude, $\Delta\lambda_d$, %	Stress Amplitude at Half-Life, $\Delta\sigma$ MN/m^2 (ksi)	Longitudinal Elastic Strain Amplitude, Δe_l, %	Longitudinal Plastic Strain Amplitude, $\Delta\varepsilon_l$, %	Longitudinal Total Strain Amplitude, $\Delta\lambda_l$, %	Cyclic Rate, Hz	Fatigue Life, N Cycles
5083-1	300	0.95	413 (60)	0.58	1.52	2.10	0.05	130
5083-2		0.49	386 (56)	0.54	0.62	1.16	0.20	350
5083-3		0.31	351 (51)	0.49	0.29	0.78	0.50	1550
5083-4		0.24	338 (49)	0.47	0.16	0.63	0.80	3010
5083-5		0.14	269 (39)	0.37	0.03	0.40	2.00	48,030
5083-6		1.40	420 (61)	0.59	2.41	3.00	0.03	35
5083-7		0.19	310 (45)	0.43	0.08	0.51	2.00	7920
5083-8		0.67	393 (57)	0.55	0.97	1.52	0.10	214
5083-9		0.37	365 (53)	0.51	0.39	0.90	0.05	920
5083-10	77	0.86	551 (80)	0.69	1.26	1.95	0.10	128
5083-11		1.36	585 (85)	0.73	2.27	3.00	0.03	29
5083-12		0.39	469 (68)	0.59	0.41	1.00	0.10	1720
5083-13		0.30	462 (67)	0.58	0.21	0.78	1.50	1920
5083-15		0.64	531 (77)	0.66	0.84	1.50	1.50	421
5083-16		0.28	469 (68)	0.59	0.18	0.77	1.00	1890
5083-17		0.17	372 (54)	0.47	0.04	0.51	3.00	49,050
5083-19		0.52	517 (75)	0.65	0.60	1.25	0.30	460
5083-20		0.23	414 (60)	0.52	0.11	0.63	2.00	10,790
5083-21	4	0.41	675 (98)	0.84	0.27	1.11	0.10	401
5083-22		0.41	662 (96)	0.82	0.29	1.11	0.50	527
5083-23		0.25	558 (81)	0.69	0.06	0.75	0.50	4930
5083-24		0.25	544 (79)	0.68	0.07	0.75	2.50	7230
5083-25		0.20	482 (70)	0.60	0.01	0.61	2.50	37,820
5083-26		0.49	689 (100)	0.85	0.45	1.30	0.10	167
5083-27		0.59	724 (105)	0.90	0.60	1.50	0.06	97
5083-28		0.32	641 (93)	0.79	0.13	0.92	0.40	870

Temperature, K	293	77	4
Modulus, GN/m^2 (10^6 psi)	71.6 (10.4)	80 (11.6)	81 (11.7)
Poission's Ratio	0.333	0.320	0.318

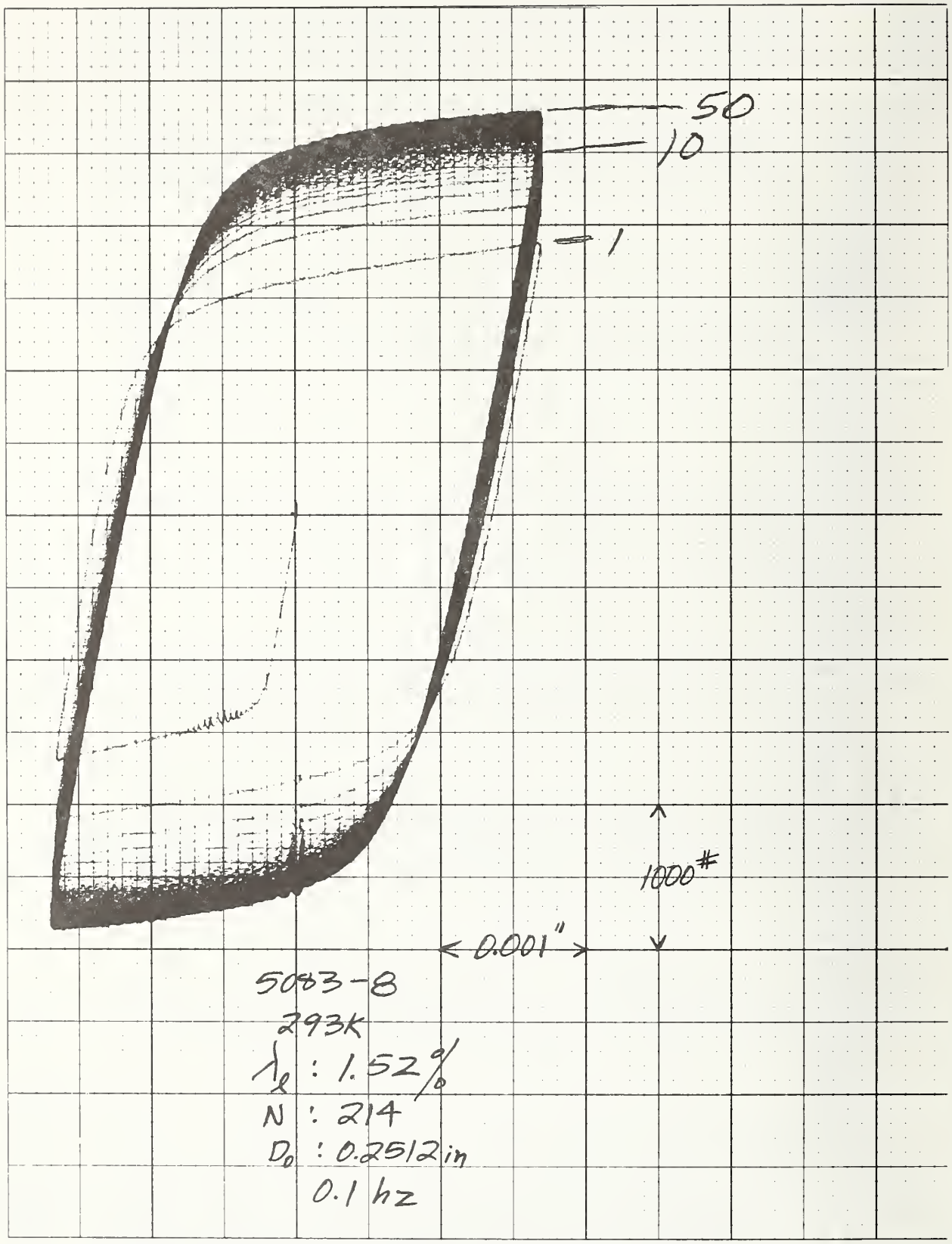

Figure 15 Load-Deflection Curve for Specimen 5083-8

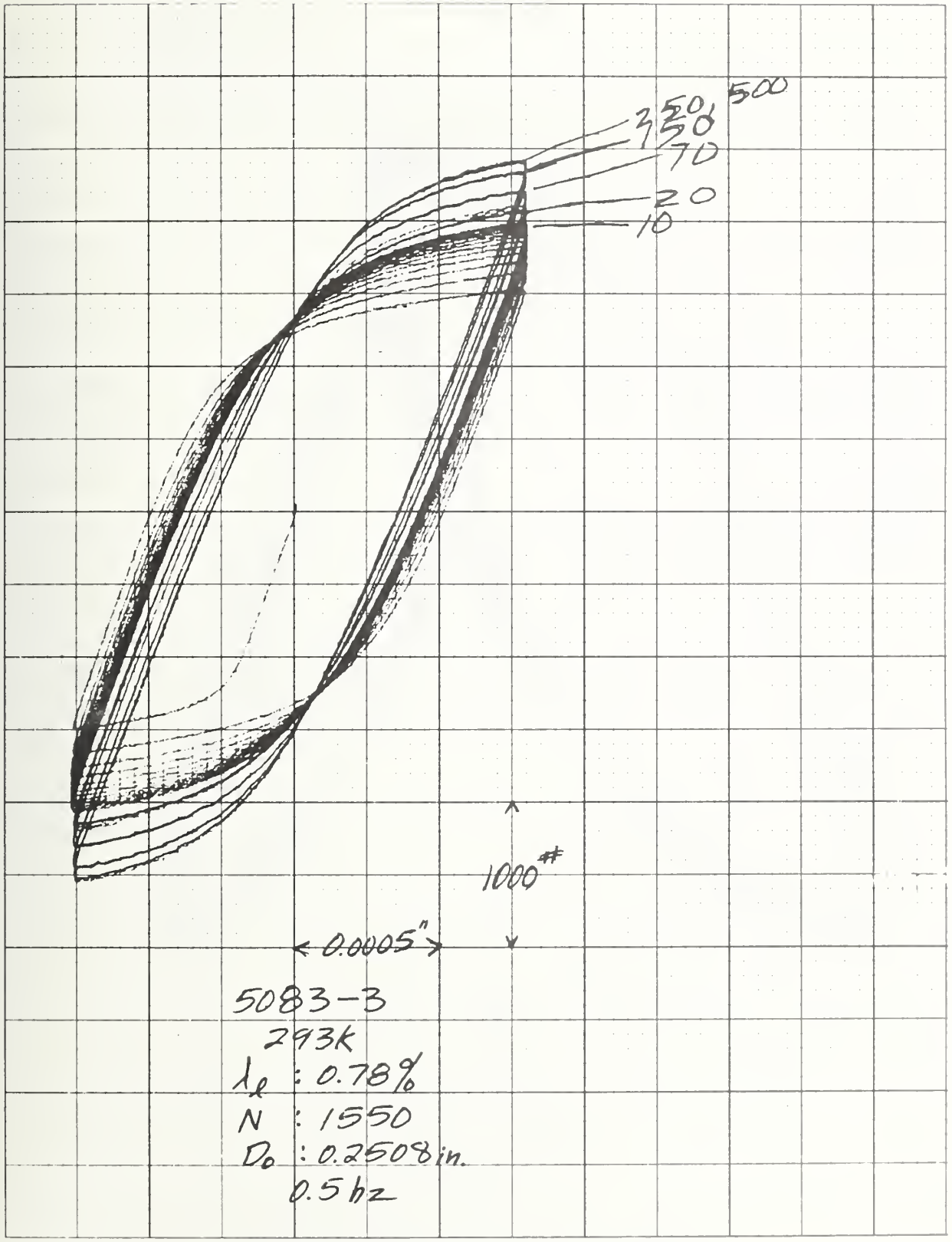

Figure 16 Load-Deflection Curve for Specimen 5083-3

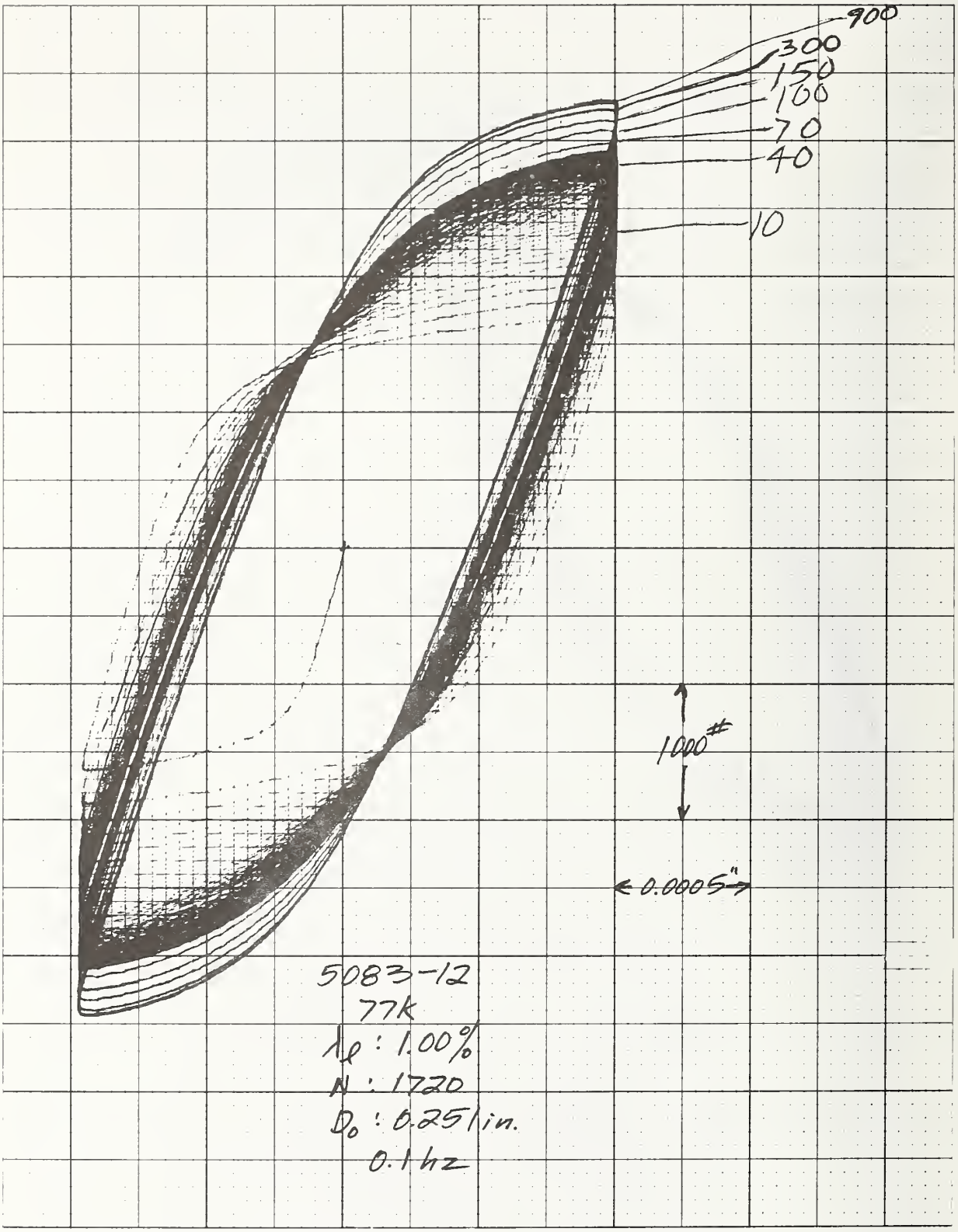

Figure 17 Load-Deflection Curve for Specimen 5083-12

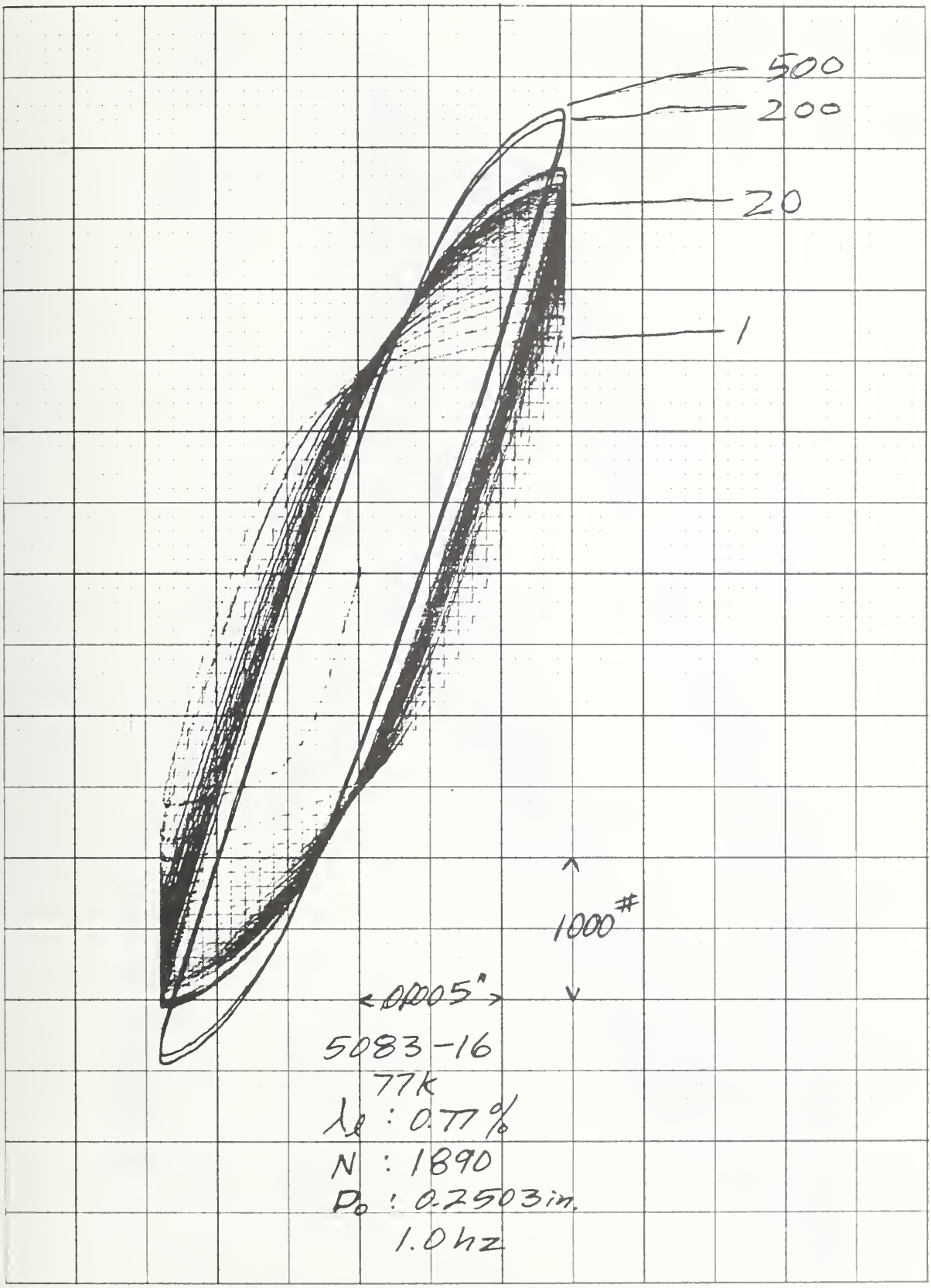

Figure 18 Load-Deflection Curve for Specimen 5083-16

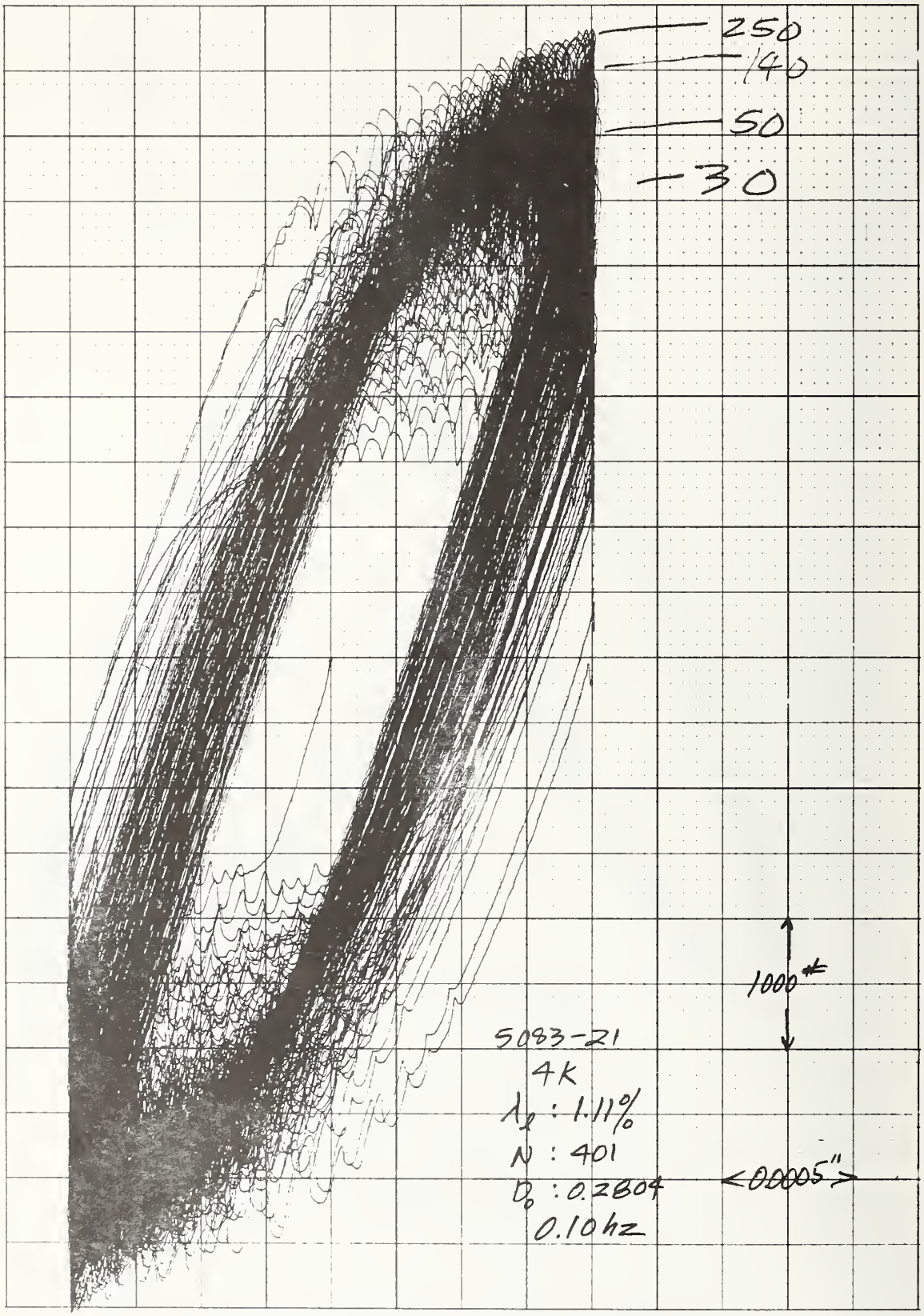

Figure 19 Load-Deflection Curve for Specimen 5083-21

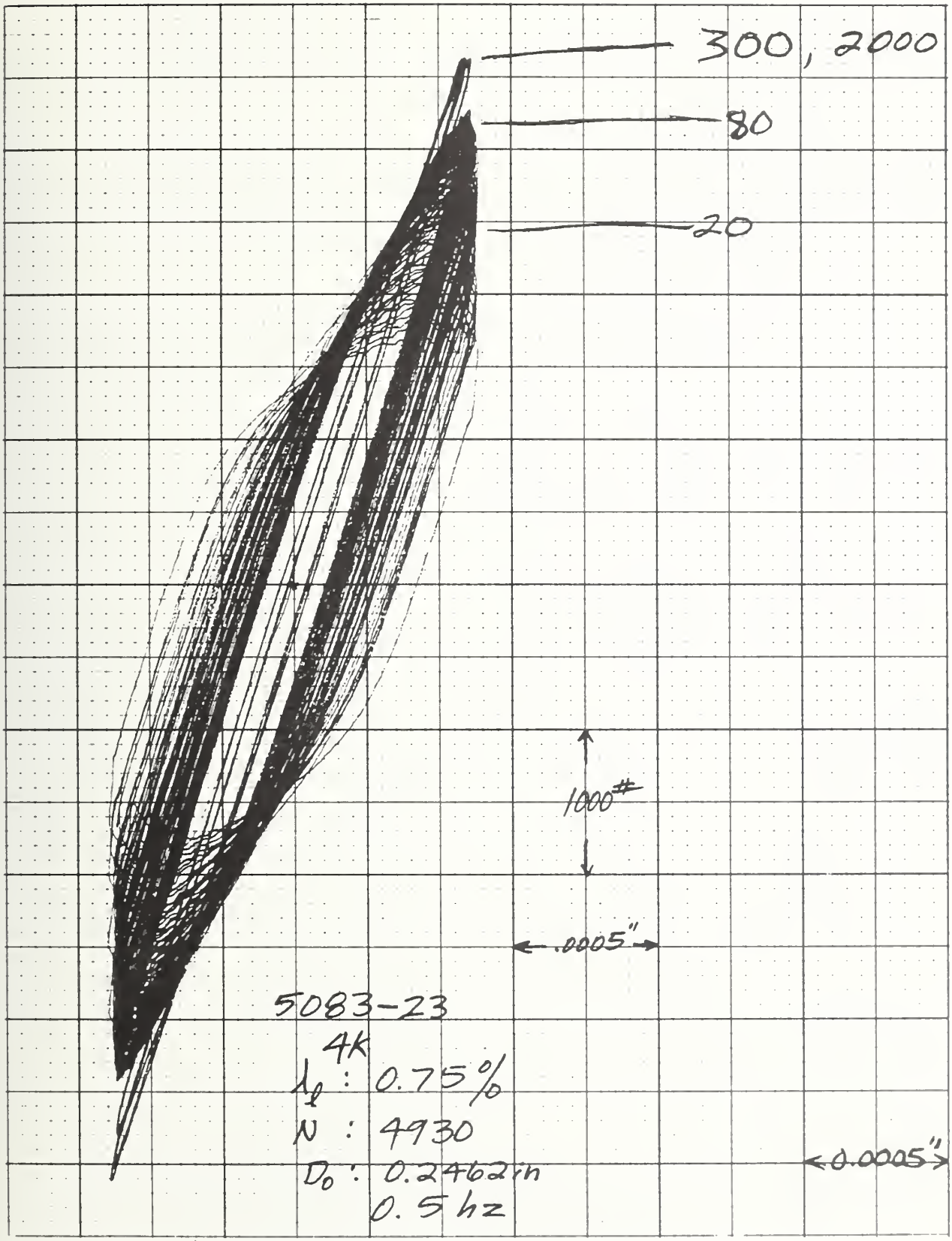

Figure 20 Load-Deflection Curve for Specimen 5083-23

At all temperatures and strain amplitudes near 0.6% or less, fatigue cracking normal to the axis of loading takes place, followed by failure of the remaining ligament.

Discussion of Results

Data obtained from this work were compared with other available information to obtain a comparison with alternate candidate materials.

For the 304LN alloy, the strain controlled data obtained from this work were plotted with strain controlled data obtained for 304, 316, and 21-6-9 stainless alloys in a previous Martin Marietta test program (Reference 1). A comparison of the fatigue strength of 304LN with the other three alloys was performed at 293 K (Figure 21). 304LN is similar in behavior to the 21-6-9 alloy. 304LN has better fatigue life than 304 at strain amplitudes above 1.0%. At 77 K (Figure 22), 304LN has lower fatigue life than 316 or 21-6-9 at strain amplitudes above 1.0% but is still better than 304. At higher cyclic lives (above 10,000 cycles), 304LN is superior to the other three alloys. Above 0.8% strain amplitude at 4 K (Figure 23), the cyclic life of 304LN is similar to that of 304 and 21-6-9, with 316 superior in this range. However, at strain amplitudes below 0.8% (cyclic life greater than 10,000 cycles), 304LN is superior to 304 and 21-6-9. Insufficient data on alloy 316 at high cyclic life prevent a comparison.

Figure 24 illustrates the strain hardening or strain softening response as a function of temperature and strain amplitude for the stainless alloys discussed above.

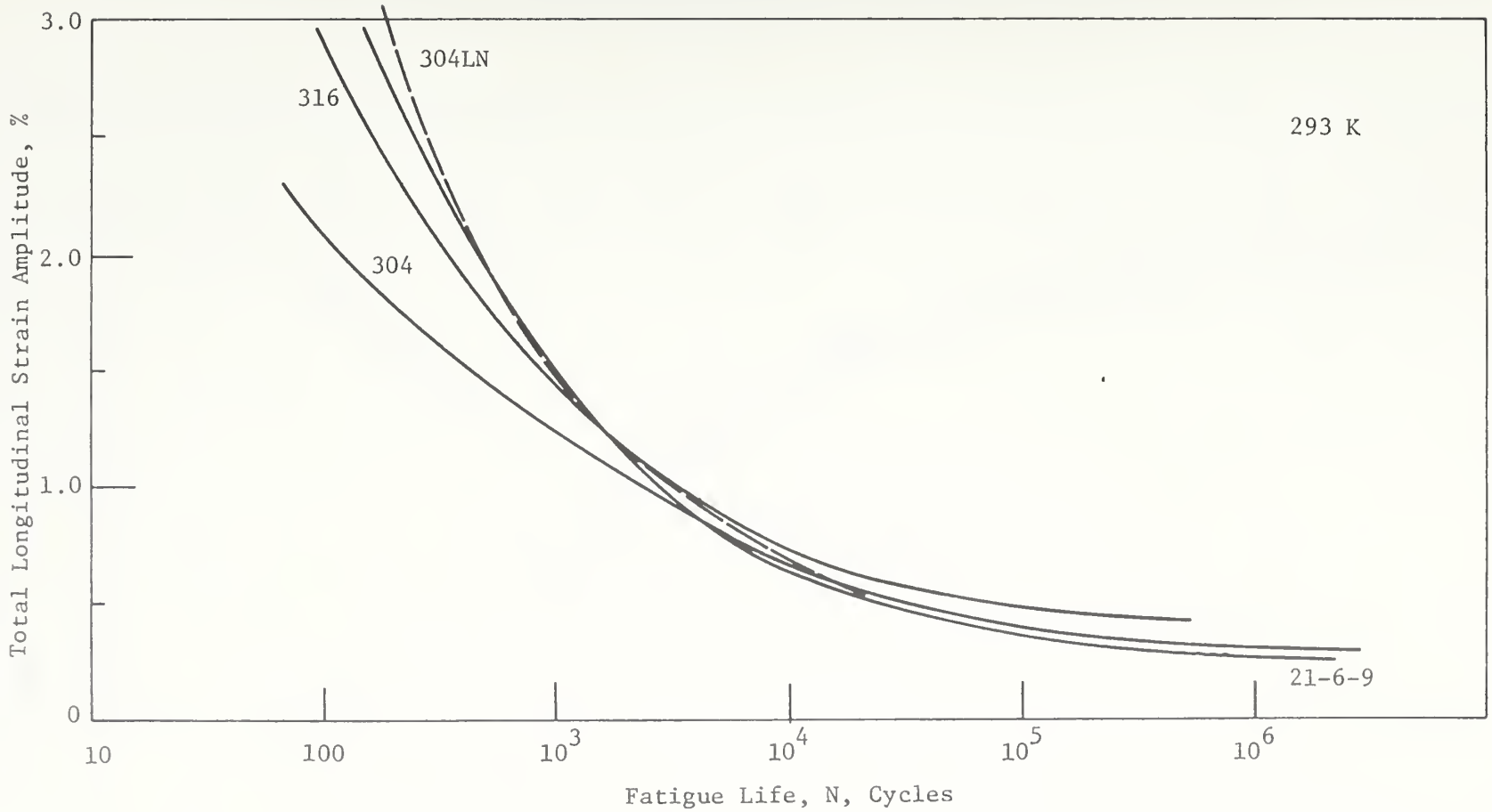

Figure 21 Comparison of Fatigue Data at 293 K

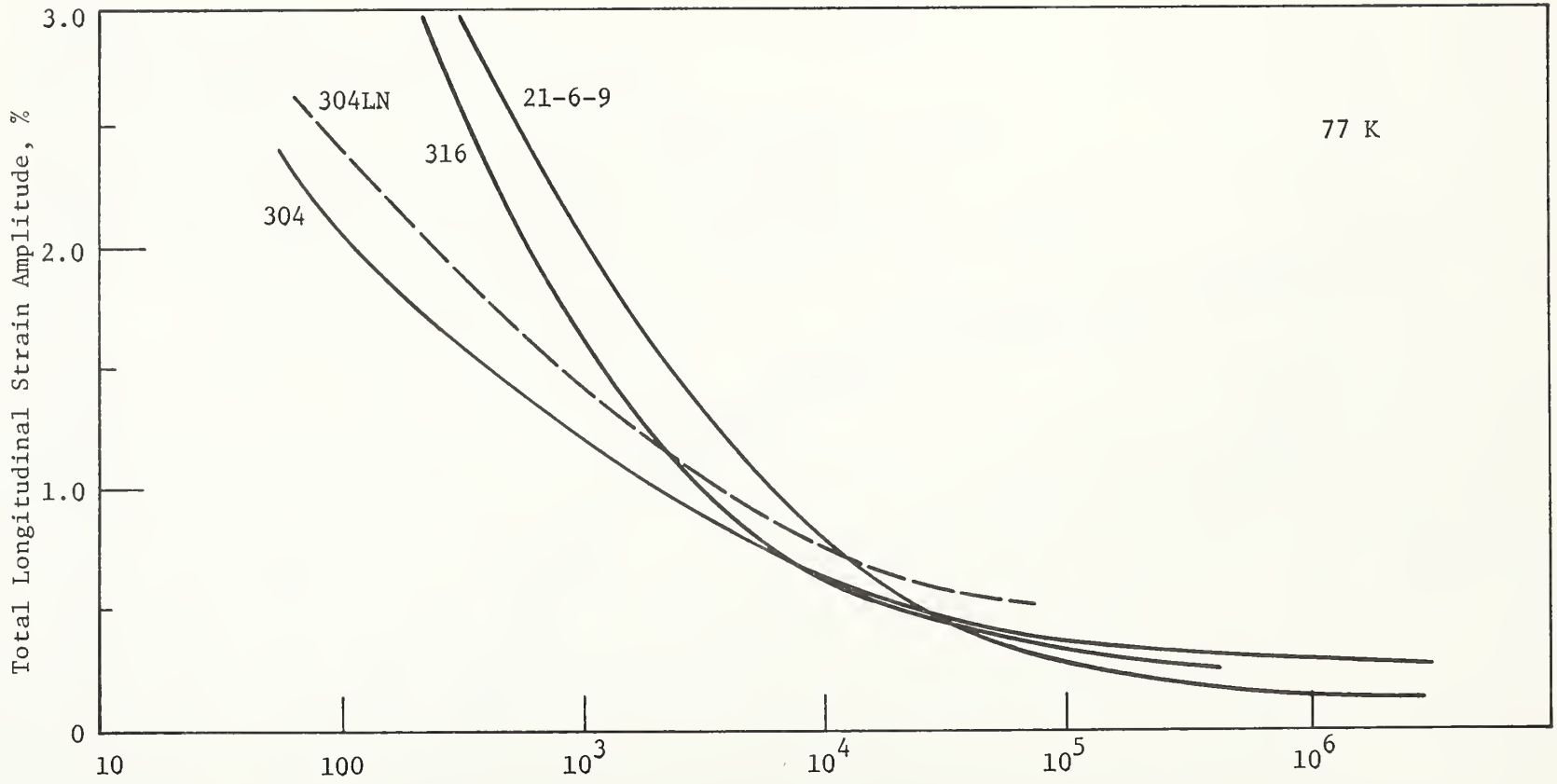

Figure 22 Comparison of Fatigue Data at 77 K

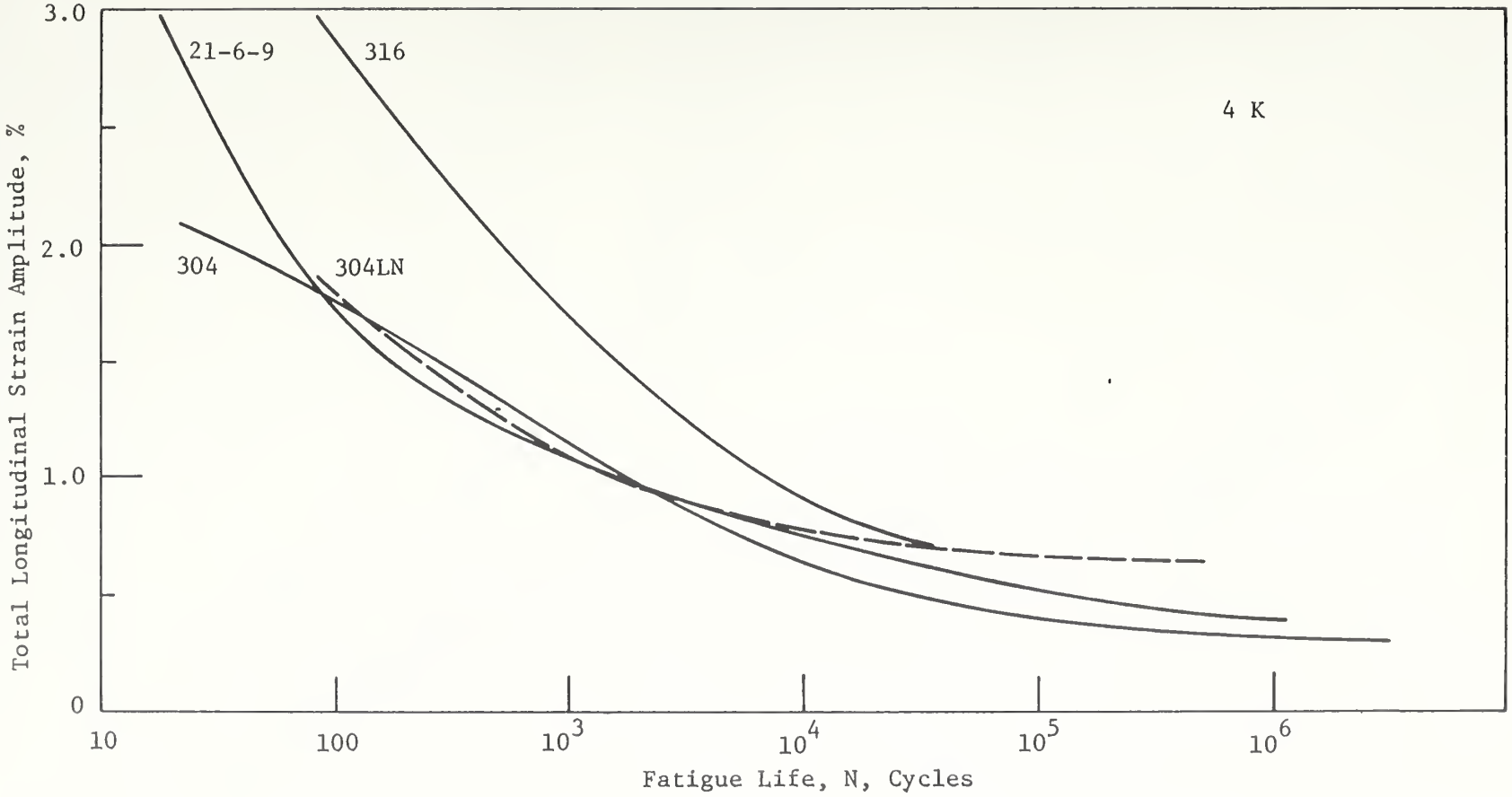

Figure 23 Comparison of Fatigue Data at 4 K

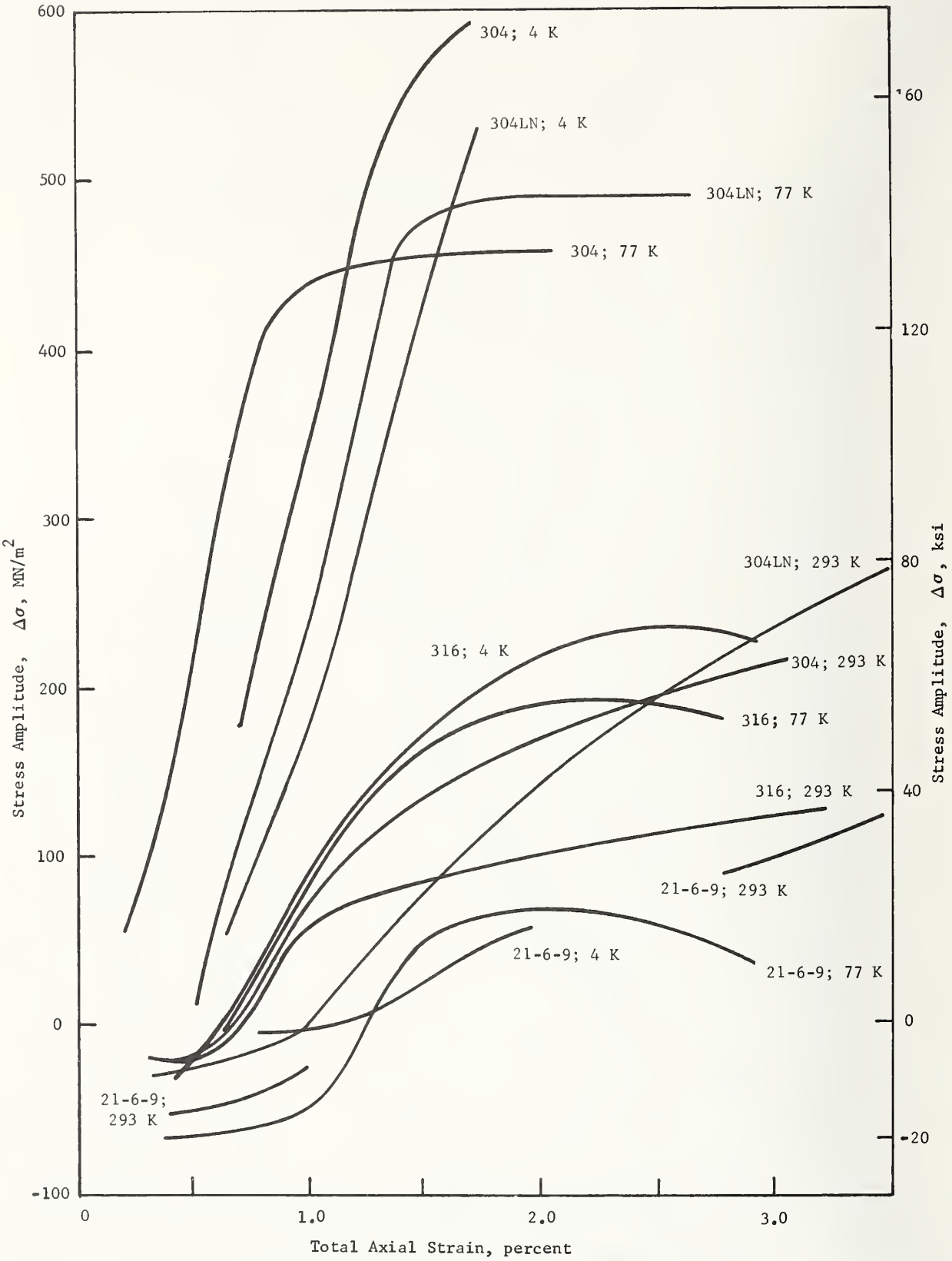

Figure 24 Effect of Strain Amplitude on Change in Stress Amplitude

The 5083-0 fatigue data generated from this work were compared with strain-controlled fatigue data determined for aluminum alloys 2014-T6 and 2219-T851 by Nachtigall in 1974 (Reference 3). This comparison is shown graphically at each test temperature in Figures 25, 26, and 27. In all cases, at the higher strain levels (low cyclic lives), 5083-0 has higher fatigue life than 2014-T6 but is lower than 2219-T851. At low strain levels (high cyclic lives), the alloys are comparable, with 2014-T6 having a slight advantage in fatigue life.

Fatigue behavior of the 304LN and 5083-0 alloys do not display qualities that should affect their candidacy for service at 4 K.

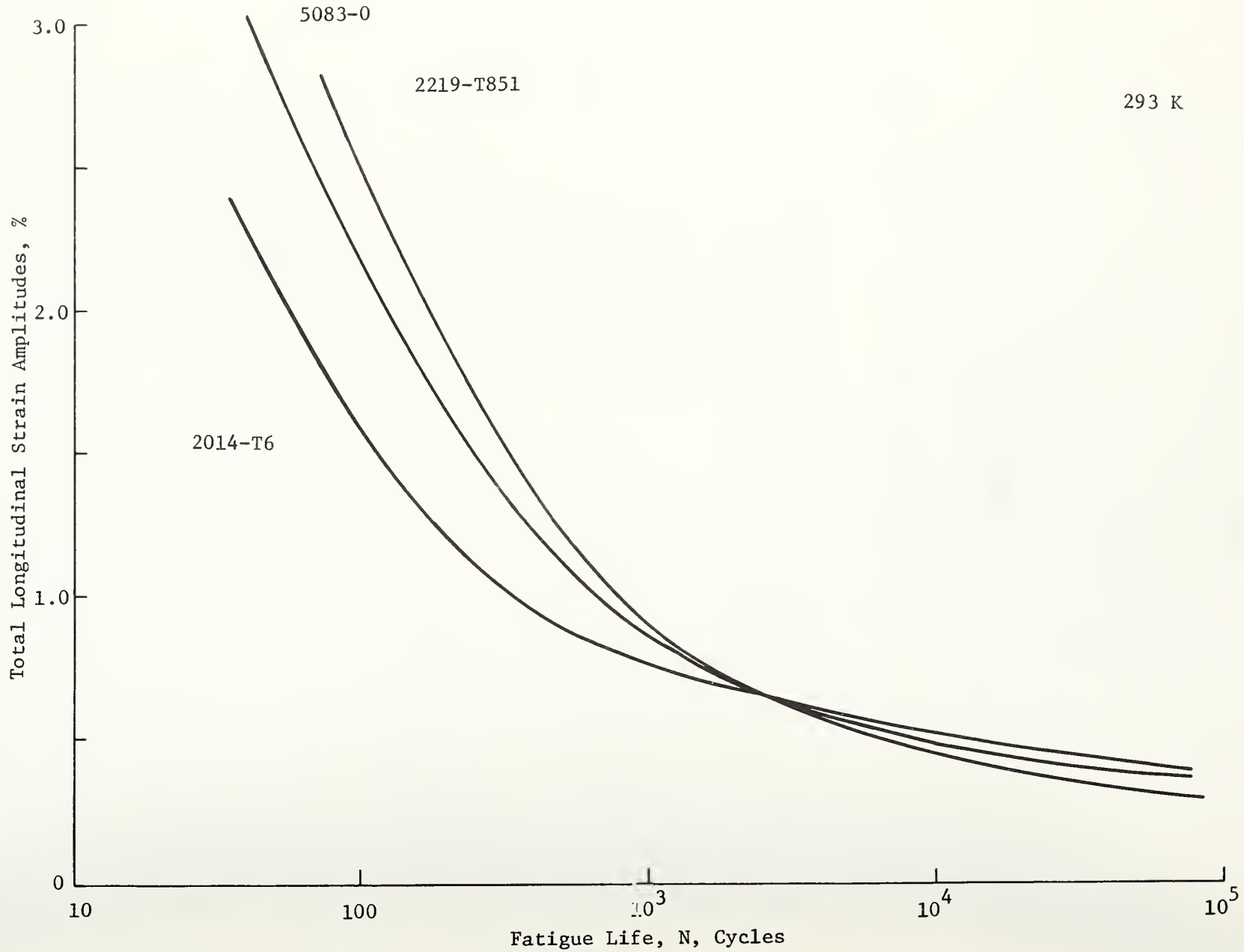

Figure 25 Comparison of Fatigue Data at 293 K

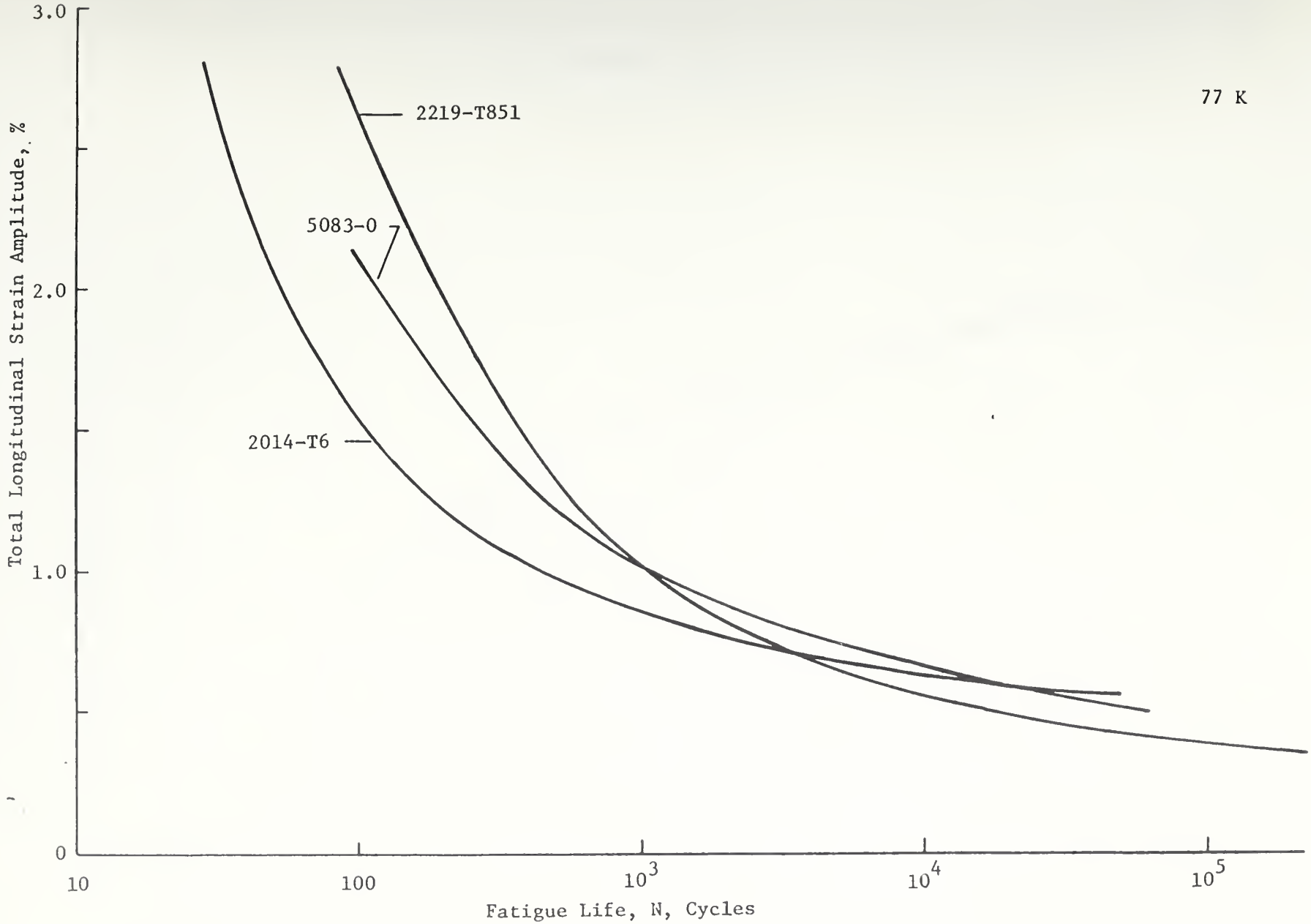

Figure 26 Comparison of Fatigue Data at 77 K

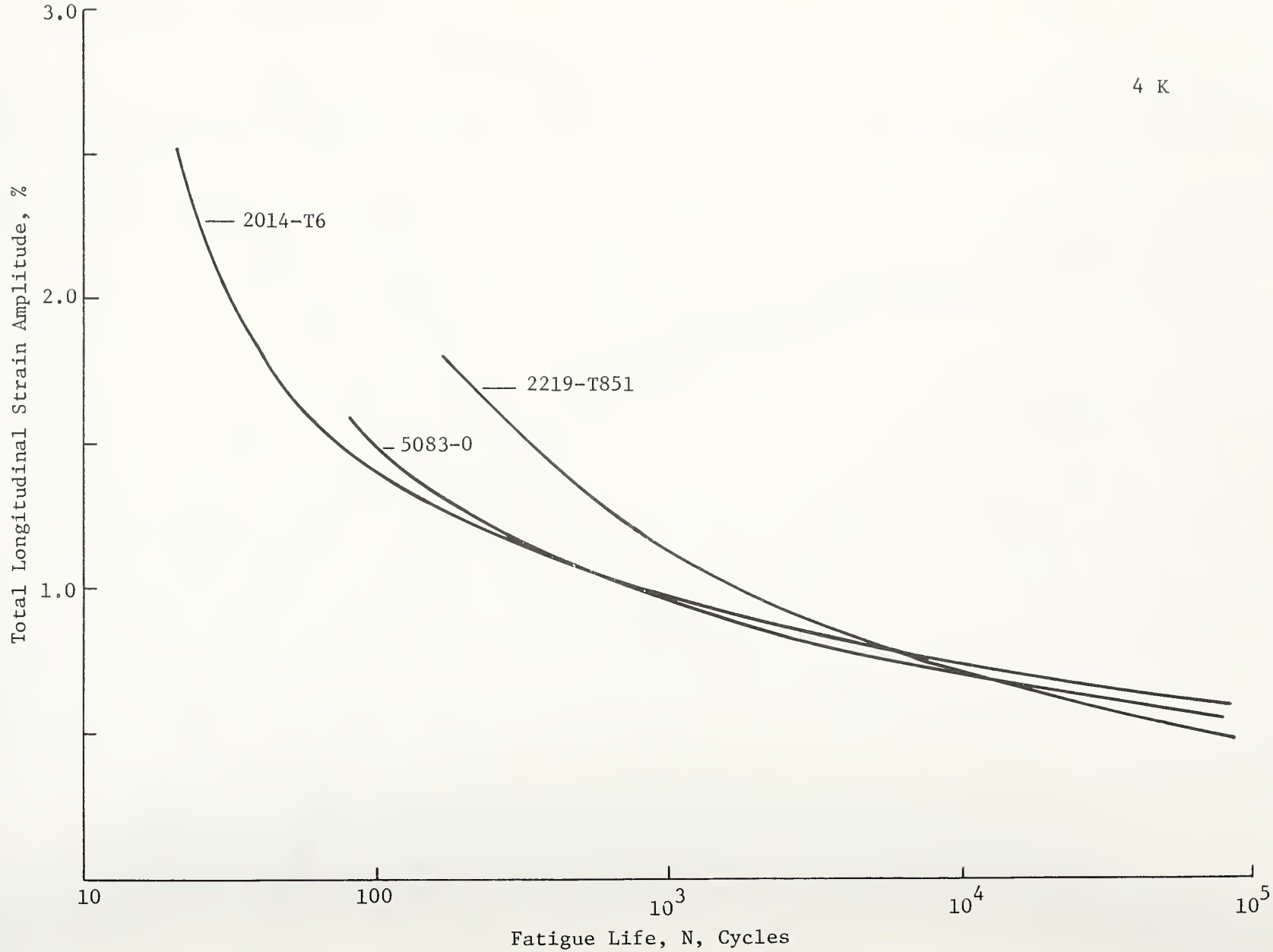

Figure 27 Comparison of Fatigue Data at 4 K

REFERENCES

1. F. R. Schwartzberg and J. A. Shepic, "Fatigue Testing of Stainless Steels", Materials Studies for Magnetic Fusion Energy Applications at Low Tempertures, Volume I, April 1978, National Bureau of Standards, Boulder, Colorado.

2. F. R. Schwartzberg and T. F. Kiefer, "Study of Fracture Behavior of Metals for Superconducting Applications", Materials Research for Superconducting Machinery, Semi-Annual Technical Report IV, October 1975, National Bureau of Standards, Boulder, Colorado.

3. A. J. Nachtigall, "Strain-Cycling Fatigue Behavior of Ten Structural Metals Tested in Liquid Helium, in Liquid Nitrogen, and in Ambient Air", NASA TN D-7532, February 1974.

4. A. J. Nachtigall, S. J. Klima, and J. C. Freche, "Fatigue of Liquid Rocket Engine Metals at Cryogenic Temperatures to -452F", NASA TN D-4274, December 1967

5. E. J. Beck "Effect of Beta Processing and Fabrication on Axial Loading Fatigue Behavior of Titanium", AFFDL-TR-69-108, Martin Marietta Corporation, June 1969.

FRACTURE AND STRENGTH PROPERTIES OF SELECTED AUSTENITIC STAINLESS STEELS AT CRYOGENIC TEMPERATURES

National Bureau of Standards

FRACTURE AND STRENGTH PROPERTIES OF SELECTED AUSTENITIC STAINLESS STEELS AT CRYOGENIC TEMPERATURES*

D. T. Read and R. P. Reed

Fracture and Deformation Division

National Bureau of Standards

Boulder, Colorado 80303

*Work supported by DOE/OFE. Contributions of NBS, not subject to Copyright.

ABSTRACT

Austenitic stainless steels have an excellent combination of mechanical and physical properties for load-bearing structures of large superconducting magnets for plasma containment in magnetic fusion experiments. To assess their relative suitability, fracture toughness, fatigue crack growth, and tensile properties data for five austenitic stainless steels at 295, 76, and 4 K have been obtained. The steels were AISI 304, 316, 304LN, and 316LN, and an Fe-21Cr-12Ni-5Mn alloy with a higher nitrogen content than the other four grades. Tensile properties were measured at 4 K for two additional AISI 304L alloys with higher than usual nitrogen contents. At 4 K the yield strength ranged from 350 to 1330 MPa (49 to 188 Ksi). This wide spread in yield strength was attributed to composition variations, especially nitrogen. A correspondingly large spread was observed in fracture toughness, from 131 to 328 MPa$\sqrt{m}$ (119 to 298 ksi $\sqrt{in}$). The two principal findings were the systematic variation of yield strength with nitrogen content and the systematic inverse correlation between fracture toughness and yield strength. Data from previous studies are reviewed which confirm the trends of the present data. These results permit the selection of the optimum combination of properties for a specific structural application.

INTRODUCTION

Nitrogen-strengthened austenitic stainless steels have attracted interest as possible cryogenic structural materials because of their superior strength [1-4]; but data on their toughness at cryogenic temperatures are generally lacking, except for a few studies [5-7]. The availability of high-strength, high-toughness alloys for cryogenic service would contribute to increased structural safety and economy in devices such as magnetic-fusion-energy systems [8]. As cryogenic structures become larger and magnetic fields more intense, materials with higher strengths than the widely used alloy AISI 304 are necessary. In fact, nitrogen-strengthened AISI 304LN and 316LN have been selected for respectively, the magnet cases for the Magnetic Fusion Test Facility at Lawrence Livermore Laboratory and the toroidal field coil being built by General Electric Company for the Large Coil Project. Clearly, development of a data base on the structural properties of nitrogen-strengthened austenitic stainless steels is needed to support materials selection and design for the large cryogenic magnet structures of the near future.

MATERIALS

All materials in this study are candidate materials for cryogenic structures. Chemical compositions are given in Table 1. The AISI 304 and 316 are from the Oak Ridge National Laboratory reference heats whose mechanical properties have been extensively characterized [9,10] at room and higher temperatures for several product forms. The AISI 304L, 304LN and 316LN are from commercial heats. The Fe-21Cr-12Ni-5Mn alloy (designated Nitronic 50 by the manufacturer**) was solutioned-annealed in the laboratory before specimens were machined. Final heat-treatment parameters

**This tradename is used only for clarity. No approval or endorsement of any commercial product by NBS is implied.

and measured grain sizes and hardnesses are given in Table 2. Representative microstructures are shown in Figs. 1-5. All microstructures appear very similar. The grain size of the AISI 304 was large (grain diameter 210 microns).

SPECIMENS

Fracture toughness and fatigue crack growth data were obtained using compact specimens of the type shown in Fig. 6. All specimens were 2.54 cm (1 in) thick. Small, round tensile specimens oriented transverse to the rolling direction were used. Their gage length was 2.54 cm (1 in) and the diameter of the gage section was 0.4 cm (.15 in). The orientations of fracture toughness (TL) and tensile specimens relative to the original alloy plate are shown in Fig. 7.

TECHNIQUES

Toughness

All toughness data reported here were obtained using a variant of the single specimen J-integral technique [11], with at least two complete tests for each material and temperature. It has been shown [12,13] that the critical stress intensity values obtained using the J-integral technique (denoted $K_{Ic}(J)$) are equal to or less than those obtained using the conventional technique for critical plane strain stress intensity, called the K_{Ic} test and described in ASTM Standard Test Method E-399 [14]. The value of $K_{Ic}(J)$ is given by [15]:

$$K_{Ic}(J) = \sqrt{EJ_{Ic}/(1-\nu^2)} \qquad (1)$$

where E is Young's modulus, J_{Ic} is the measured critical J-integral value, and ν is Poisson's ratio. The advantage of the J-integral

technique is the comparatively small specimen size required compared to the K_{Ic} test. Specimen size requirements for the J-integral test are[15]:

$$B, b, a, \geq 25\ J/\bar{\sigma} \tag{2}$$

where B and a are as shown in Fig. 6, b = W-a, J is the J-integral value, and $\bar{\sigma}$ is the flow strength, here taken as the mean of the yield and tensile strength. For the K_{Ic} test, the requirement is[14]:

$$B \geq 2.5\left(\frac{K_{Ic}}{\sigma_y}\right)^2 \tag{3}$$

where σ_y is the yield strength.

For the AISI 304 alloy, the minimum specimen thickness required for a valid J_{Ic} test at 4 K was approximately 2.5 cm (1 in), while a valid K_{Ic} test required a thickness of about 220 cm (85 in). This is an extreme case because this alloy has a very high toughness and a very low yield strength. Nevertheless the thickness requirements for the J_{Ic} test are generally much less severe than for the K_{Ic} test.

Despite the comparatively small specimen thicknesses required for J-integral testing, none of the room temperature tests proved valid because of insufficient specimen thickness. Similarly, many of the liquid nitrogen temperature tests were invalid. The requirement on specimen thickness [15] may be recast as a requirement on the J values:

$$J \leq B\bar{\sigma}/25 \tag{4}$$

where B is the specimen thickness and $\bar{\sigma}$ is the flow strength, the average of the yield and ultimate strengths. For a given specimen thickness the maximum valid J value may then be calculated. If the measured J value turns out to be less than the maximum valid J value, then the test is valid. If the measured J value is higher than the maximum valid value, the test is invalid. The calculated maximum value from Eq. (4) then becomes lower bound of the range of possible actual values. In the Results section, any lower bound value calculated in this way will be designated "Lower bound value calculated from the validity requirement using the controlling specimen dimension." Note that a test must be conducted for this conclusion; a test produces either a valid J_{Ic} value or a lower bound value.

A significant increase in the efficiency of J-integral testing resulted from the use of the single-specimen method [12]. This technique allows a critical J value to be derived from a test using one specimen, rather than at least four specimens as required in the multiple-specimen technique [15]. Although each single specimen J-integral test should be duplicated, a significant reduction in test time and number of specimens is realized.

In the single-specimen J-integral technique the specimen is precracked in tension-tension fatigue to a predetermined crack length. The specimen is loaded quasistatically (load line displacement rate 50 μm/s or less) under displacement control to a point well within the elastic region. The specimen is than partially unloaded, and the incremental compliance curve is recorded with appropriate amplification and signal conditioning. A signal proportional to the change in load is subtracted (electronically in the present case) from the load-line-displacement-

change signal; the proportionality factor is adjusted so that the unloading compliance before crack extension is displayed as a vertical line on the graph of load change against load line displacement change. The usual graph of load against load line displacement is recorded on another x-y plotter. The specimen is gradually extended, with several stops for recording the unloading compliance. Typically, ten to twenty unloading compliances are recorded. The magnitude of the decrease in load during the unloadings is restricted to ten percent of the total load. J-integral values are calculated in the usual way [16] from the load vs. load-line-displacement record at each unloading point. Crack extension values, Δa, are calculated from all unloading compliance curves except the first one, which is used to evaluate the compliance at $\Delta a=0$. The $(\Delta a,J)$ data are then plotted, and J_{Ic} is evaluated graphically as the intersection of a curve through the data with the theoretical blunting line given by $J=2\bar{\sigma}\Delta a$ where $\bar{\sigma}$ is the arithmetic mean of the yield strength and the ultimate tensile strength. Often the data followed the theoretical blunting line. Deviations were not systematic, and were due to data scatter or experimental error. An example of the J-Δa curves obtained is shown in Fig 8. The offset of the data from the theoretical blunting line through $\Delta a = 0$ is artificial; for evaluation of J_{Ic}, a blunting line parallel to the theoretical line but passing through the data is used. In this technique, scatter cannot be introduced into the J-Δa curve by specimen-to-specimen variability. Such variability was an unknown factor in tests using the multiple specimen technique.

The main disadvantage of the single-specimen method is that the Δa values obtained from the unloading compliance are systematically lower

than those found by direct measurement of the fracture surface and are scattered. The bias can be seen to have a small effect on the evaluation of J_{Ic}, typically 2 to 10%, although the slope of the J-Δa curve will not be given accurately. The bias is believed to be caused by the curved crack front which is formed during crack extension. The scatter tends to be counteracted by the large number of data points available in these tests. This scatter may be decreased in the future by more advanced test techniques, especially digital acquisition of the data.

Experimental Uncertainties in Toughness

Uncertainties in toughness data are of three kinds: first, those associated with the quantities directly measured, such as load, crack length, and displacement; second, those which arise from specimen to specimen and heat to heat material variability; and third, those associated with the procedure used to infer toughness values from the measured quantities. Errors of measurement are readily assessed by repeated measurement, measurement of standard loads or dimensions, and other usual calibration procedures. Errors associated with material variability may be the most severe. Evaluation of material properties for structural design requires careful consideration of uncertainties due to material variability, through understanding of its causes and extensive data on its magnitude. The consistency obtained by establishment of standard procedures for toughness tests reduces relative measurement errors. Since the standard procedures for elastic-plastic fracture toughness testing are still evolving, however, a limited discussion of the inherent measurement errors in these tests is helpful.

Measurement uncertainties in individual J values are considered to be of the order of 5% or less, from accumulated uncertainties in load

cell and displacement gauge calibrations and measurements of the area under the load-displacement record. Values of crack extension, Δa, from partial unloading compliances for the single specimen J-integral test averaged about 70% of the actual Δa value, with a standard deviation of around 0.7 mm. The bias is believed to contribute an uncertainty of 10% or less to the J_{Ic} measurement. The scatter is compensated by taking many data points, and does not further increase the uncertainty in J_{Ic}. The cumulative uncertainty in J_{Ic} values is estimated to be $\pm$15% or less, so the measurement uncertainty in K_{Ic} values inferred is 8% or less since K_{Ic} is proportional to $\sqrt{J_{Ic}}$. Data for comparison of the single specimen J-integral technique to the multiple-specimen technique were obtained at 76 and 4 K for AISI 304N. The 76 and 4 K single specimen J_{Ic} values were 2 and 13%, respectively, lower than the previously obtained values [7], in agreement with the $\pm$15% cumulative error in J_{Ic} estimated. Errors in fracture toughness associated with material variability may also be large. Data reported here are, in general, not applicable to materials with different chemical composition or thermochemical processing.

Fatigue

Fatigue crack growth rates were also measured using compact specimens. The specimen is loaded repeatedly (at a frequency of 20 Hz) with the minimum load one tenth of the maximum. The compliance, the reciprocal slope of a plot of load against load-line-displacement, is recorded periodically at intervals ranging from 100 to 20,000 cycles depending on the rate of crack growth. The compliance data are converted to crack lengths using the formula [17]

$$a = W[-.9505 + .3447(EBC)^{1/6} + .5654(EBC)^{1/3} - .1748(EBC)^{1/2}] \quad (5)$$

where C = displacement/load and E and B have been previously defined. This equation is a least squares fit, developed in our laboratory, to compliance data given in a proposed ASTM test method [18]. The crack length is also used in calculating the applied stress intensity factor range using the formula [14]

$$\Delta K = (P_{max}-P_{min})\frac{a^{1/2}}{BW}[29.6-185(\frac{a}{W})+655.7(\frac{a}{W})^2-1017(\frac{a}{W})^3+638.9(\frac{a}{W})^4] \quad (6)$$

where P_{max} and P_{min} are the maximum and minimum loads.

Strain gage, clamp-on extensometers were used in tensile measurements. Yield strength values at 0.2% offset are reported. The flow strength is taken as the average of the yield and ultimate strengths.

Uncertainties associated with inferring property values from measured quantities are not a problem in fatigue and tensile property measurements, because standard test procedures are widely accepted. However uncertainties of measurement and material variability remain. Standard deviations of 20 to 40% from the average value were typical in the fatigue crack growth data. Fatigue data are not considered to be as sensitive to material variability as toughness data, and in fact data from two or three specimens are usually consistent. Measurement uncertainties in tensile properties are estimated to be 3% or less; these are due to uncertainties in specimen dimensions, load values as read from analog recorder traces, and (for the yield strength) specimen strains from the calibrated extensometer.

For all tests, temperature control was achieved by immersing the specimen in liquid helium or liquid nitrogen at local atmospheric

pressure* or by testing in laboratory air. The apparatus used for these tests has been described by Fowlkes and Tobler [19].

RESULTS AND DISCUSSION

Fracture toughness results are listed in Table 3 as critical plane strain stress intensity values calculated from J-integral test results, denoted $K_{Ic}(J)$ using Eq. (1). The 4 K fracture toughness results for AISI 304 and 316 are significantly lower than some reported earlier [20], but these two stainless steels remain tougher at 4 K than any other material. Two possible reasons for the discrepancy are heat to heat material variability and changes in test procedures. The previously tested materials had the same orientation as the present study. The AISI 304 in the present study had lower hardness and lower yield strength at 295 and 76 K; the AISI 316 in the present study had lower hardness and lower yield strength at 295 K, but higher yield strength at 76 and 4 K. A thorough assessment of the heat to heat J-integral variability between materials cannot be made because in the present test program the Δa values obtained are rather small, 6 mm or less, while in the previous test program only a few of the directly measured Δa values were comparably small. Some overlap in Δa values between those of the present and previous studies is present for both AISI 304 and 316, and in both cases the J-integral values obtained in the present study were significantly less than those obtained at comparable Δa levels in the previous study. The regions of overlap were around Δa=6 mm, while the critical J values were determined from Δa values of about 2 mm and less in the present study. It is concluded that the discrepancy in results

*Typically .082 MPa. At this pressure, helium boils at 4 K and nitrogen at 76 K.

between present and previous studies is at least partially due to material variability, and may also be due in part to the changes in the J-integral test procedure which now tend to restrict attention to relatively small values of the crack extension.

Fracture toughness is plotted against yield strength for selected stainless steels [7,20] at 4 K in Fig. 9. Both fracture toughness and tensile data for this plot were obtained on specimens from the same plate. The selected data represent wrought and annealed austenitic stainless steels. No weldments nor sensitized nor otherwise improperly heat-treated alloys have been included. Fig. 9 shows that there is a linear relationship between yield strength and fracture toughness for austenitic stainless steels at 4 K. All weldments fall well below the trend line shown in Fig. 9.

The relationship between fracture toughness and yield strength has been reported by other observers [21-25]. The trend lines reported by Pellini are shown in Fig. 10 along with the same data shown in Fig. 9. The agreement between the trends is quite good, and probably fortuitous, especially when it is noted that Pellini's data are for body-centered-cubic materials at room temperature while the data of the present study are for face-centered-cubic materials at the temperature of liquid helium. No satisfactory explanation for the relationship between strength and toughness shown in Fig. 10 has been offered. However this trend may be significant if it represents, for 4 K use, the metal quality attainable with current metallurgical techniques. Perhaps better properties will be attainable or perhaps the trend represents the limit of what can be achieved in wrought, annealed stainless steels. Further research is needed to determine whether and how better combinations of strength and toughness can be obtained.

Fatigue crack growth results at 4 K are indicated schematically in Fig. 11. The complete list of fatiguq crack growth results is given in Table 4. The rates for AISI 304LN are higher than those for the other materials. Comparison of AISI 304LN and 304N [7] rates with 304L and 304 rates at 4 K indicate that the nitrogen addition increases the fatigue crack growth rates by a factor of 4 to 5. However, this effect is not observed in AISI 316 as both 316LN and 316 have equivalent rates at 4 K. All the fatigue crack growth rates observed in the present study were within the band of previously observed results for austenitic stainless steels [7].

Tensile test results are listed in Table 5. Temperature dependences of the yield and ultimate strengths are shown in Fig. 12. The alloys that have higher 4 K yield strengths have stronger temperature dependences. Elongations and reductions of area are plotted against temperature in Fig. 13. The general tendency of these quantities to decrease with decreasing temperature is evident.

The effect of nitrogen content on the 4 K yield strength is displayed in Fig. 14. Data are included from other studies [7,20,26]. At higher temperatures the solid solution strengthening effect is not as pronounced. A consistent increase in yield strength with increasing nitrogen content is apparent [27].

SUMMARY AND CONCLUSIONS

1. Fracture toughness, yield and ultimate tensile strength, and fatigue crack growth rates at 295, 76, and 4 K have been obtained for five austenitic stainless steels. Tensile data at 4 K were obtained for two additional stainless steels.
2. At 4 K, the yield strengths ranged from 350 to 1330 MPa (49 to 188 ksi), while the fracture toughness ranged from 138 to 321 MPa $\sqrt{m}$ (119 to 298 ksi $\sqrt{in}$).
3. At 4 K, fracture toughness decreased linearly with increasing yield strength.
4. At 4 K, yield strength increases linearly with nitrogen content. This dependency on nitrogen concentration becomes very significant at low temperatures. It appears that austenitic stainless steels can be "tailor-made" for 4 K applications by adjusting the nitrogen concentration to produce a desired yield strength-fracture toughness combination.

REFERENCES

1. D. C. Larbalestier and D. Evans, "High Strength Austenitic Stainless Steels for Cryogenic Use," Sixth International Cryogenic Engineering Conference, Grenoble, France (1976), IPC Science and Technology Press Ltd., Surrey, England, pp. 345-347.

2. J. W. Montano, "Stress Corrosion Resistance and Cryogenic Temperature Mechanical Behavior of 18-3Mn (Nitronic 33) Stainless Steel Parent and Welded Material," NASA TM X-73309, Marshall Space Flight Center, AL (1976).

3. C. E. Spaeder, Jr., and W. F. Domis, "Cryogenic and Elevated-Temperature Mechanical Properties of a High-Nitrogen Type 304 Stainless Steel," Report No. 44012-062-2, United States Steel Corporation, Pittsburgh, PA (1969).

4. R. B. Gunia and G. R. Woodrow, "Nitrogen Improves Engineering Properties of Chromium-Nickel Stainless Steels," J. of Materials, JMLSA, 5, (June 1970), pp. 413-430.

5. R. L. Tobler and R. P. Reed, "Tensile and Fracture Behavior of a Nitrogen-Strengthened, Chromium-Nickel-Manganese Stainless Steel at Cryogenic Temperatures," Symposium on Elastic-Plastic Fracture, American Society for Testing and Materials, Atlanta, GA (Nov. 1977).

6. P. P. Dessau, "LN_2 and LH_2 Fracture Toughness of Armco Alloy 22-13-5," Report No. TID/SNA-2083, Aerojet Nuclear Systems Co., Sacramento, CA (1971).

7. D. T. Read and R. P. Reed, "Toughness, Fatigue Crack Growth, and Tensile Properties of Three Nitrogen-Strengthened Stainless Steels at Cryogenic Temperatures," in Materials Studies for Magnetic Fusion Energy Applications at Low Temperatures-I, NBSIR 78-884 (1978), pp. 93-154.

8. R. P. Reed, F. R. Fickett, M. B Kasens, and H. I. McHenry, "Magnetic Fusion Energy Low Temperature Materials Program: A Survey, " in Materials Studies for Magnetic Fusion Energy Applications at Low Temperatures-I, NBSIR 78-884 (1978), pp. 245-335.

9. R. W. Swindeman, W. J. McAfee, and V. K. Sikka, "Product Form Variability in the Mechanical Behavior of Type 304 Stainless Steel at 593°C," in Reproductibility and Accuracy of Mechanical Tests, ASTM STP 626, American Society for Testing and Materials, Philadelphia, PA (1977), pp. 41-64.

10. V. K. Sikka, "Product Form Characterization of Reference Heat of Type 316 Stainless Steel, ORNL-5384, Oak Ridge National Laboratory, Oak Ridge, TN (1978).

11. G. A. Clarke, W. R. Andrews, P. C. Paris, and D. W. Schmidt, "Single Specimen Tests for J_{Ic} Determindtion," in Mechanics of Crack Growth, ASTM STP 590, American Society for Testing and Materials, Philadelphia, PA (1976), pp. 27-42.

12. W. A. Logsdon, "Elastic Plastic (J_{Ic}) Fracture Toughness Values: Their Experimental Determination and Comparison with Conventional Linear Elastic (K_{Ic}) Fracture Toughness Values for Five Materials," in Mechanics of Crack Growth, ASTM STP 590, American Society for Testing and Materials, Philadelphia, PA (1976), pp. 43-60.

13. D. T. Read and R. P. Reed, "Effects of Specimen Thickness on Fracture Toughness of an Aluminum Alloy," Intn. J. Fracture 13 (1977), pp. 201-213.

14. Standard Method of Test for Plane Strain Fracture Toughness of Metallic Materials (Designation E399-74), 1974 Annual Book of ASTM Standards, Part 10 (1974) 432-451.

15. J. D. Landes and J. A. Begley, "Test Results form J-Integral Studies: An Attempt to Establish a J_{Ic} Testing Procedure," in Fracture Analysis, ASTM STP 560, American Society for Testing and Materials, Philadelphia, PA (1974), pp. 170-186.

16. J. G. Merkle and H. T. Corten, "A J-Integral Analysis for the Compact Specimen, Considering Axial Force as Well as Bending Effects," J. Pressure Vessel Tech., Trans ASME, No 6 (1974), pp. 1-7.

17. H. I. McHenry, National Bureau of Standards, Boulder, CO, private communication.

18. Proposed Recommended Practice for R-Curve for R-Curve Determination, 1974 Annual Book of ASTM Standards, Part 10, American Society for Testing and Materials, Philadelphia, PA (1974), pp. 669-683.

19. C. W. Fowlkes and R. L. Tobler, "Fracture Testing and Results for a Ti-6Al-4V Alloy at Liquid Helium Temperature," Eng. Frac. Mech. 8 (1976), pp. 487-500.

20. Materials Research for Superconducting Machinery (I-VI, edited by R. P. Reed, A. F. Clark, E. C. van Reuth and H. M. Ledbetter. NTIS Order Numbers AD780596, ADA004586, ADA012365, ADA019230, ADA030170, and ADA036919, National Technical Information Service, Springfield, VA (1973-1977).

21. R. J. H. Wanhill, "Microstructural Influences on Fagigue and Fracture Resistance in High Strength Structural Materials," Engr. Fracture Mech. 10, (1978), pp. 337-357.

22. J. P. Hirth and F. H. Froes, "Interactions Between Fracture Toughness and Other Mechanical Properties in Titanium Alloys," Metall. Trans. 8A, (1977), pp. 1165-1176.

23. G. T. Hahn and A. R. Rosenfield, "Metallurgical Factors Affecting Fracture Toughness of Aluminum Alloys," Metall. Trans. 6A (1975), pp. 653-670.

24. M. G. Stout and W. W. Gerberich, "Structure/Property/Continuum Synthesis of Ductile Fracture in Inconel Alloy 718," Metall. Trans. 9A (1978), pp. 649-658.

25. W. S. Pellini, R. J. Goode, P. P. Puzak, E. A. Lange, and R. W. Huber, "Review of Concepts and Status of Procedures for Fracture-Safe Design of Complex Welded Structures Involving Metals of Low to Ultra-High Strength Levels," U.S. Naval Research Laboratory Report 6300, Washington, D.C. (1965).

26. R. Voyer and L. Weil, "Tensile and Creep Properties of a High Nitrogen Content 18/10 (AISI 304L) Stainless Steel at Cryogenic Temperatures," Adv. Cryo. Eng. 11 (1965), pp. 447-452.

27. L.-Å Norström, "The Influence of Nitrogen and Grain Size on Yield Strength in Type A.I.S.I 316L Austenitic Stainless Steel," Metal Science 11 (1977), pp. 208-212.

LIST OF TABLES

Table 1. Chemical compositions of the materials used in the present study in weight percent, as supplied by the manufacturers except for AISI 304, supplied by ORNL analysis.[9]

Table 2. Hardnesses and grain sizes of the materials used in the present study.

Table 3. Fracture toughness results obtained in the present study.

Table 4. Paris law fatigue crack growth rate parameters for the annealed austenitic stainless steels. The fatigue crack growth rate da/dN is given by $da/dN = C(\Delta K)^n$, where ΔK is the stress intensity range.

Table 5. Tensile properties at 295, 76, and 4 K for the annealed austenitic stainless steels.

Table 1. Chemical compositions of the materials used in the present study in weight percent, as supplied by the manufacturers except for AISI 304, supplied by ORNL analysis.

Designation	Cr	Ni	Mn	Mo	P	S	Si	C	N	Fe
A.I.S.I. 304*	18.44	9.72	1.28	0.32	0.030	0.016	0.48	0.051	0.031	bal
A.I.S.I. 304LN	18.85	8.60	1.74	0.38	0.38	0.003	0.51	0.24	0.13	bal
A.I.S.I. 316	17.25	13.48	1.86	2.34	0.024	0.019	0.58	0.057	0.030	bal
A.I.S.I. 316LN	17.40	13.90	1.58	2.50	0.021	0.021	0.48	0.016	0.16	bal
Fe-21Cr-12Ni-5Mn	21.15	12.37	4.96	2.17	0.026	0.015	0.49	0.041	0.310	bal
A.I.S.I. 304L	18.54	9.27	1.78	n.a.	0.019	0.012	0.50	0.021	0.075	bal
A.I.S.I. 304L	18.7	9.2	1.74	0.38	0.029	0.006	0.37	0.021	0.096	bal

*Data from Ref. 9.

Table 2. Hardnesses and Grain Sizes of the Materials Studies

Designation	Hardness (Rockwell B)	Grain Diameter[+] (microns)	ASTM Grain Size Number
A.I.S.I. 304	75	210	1.5
A.I.S.I. 304LN	79	57	5.5
A.I.S.I. 316	79	65	5.0
A.I.S.I. 316LN	83	105	3.5
Fe-25Cr-12Ni-5Mn*	93	160	2.4

[+]Measured by the intercept method.

*A non-standard heat treatment was used for this material. It was annealed for 1.5 hr at 1150°C and water quenched.

Table 3. Fracture Toughness Results Obtained in the Present Study in MPa$\sqrt{m}$ (ksi$\sqrt{in}$).

Material	Temperature (K) 295	76	4
A.I.S.I. 304	368[a] (335) 365[a] (332) 544[a] (500) 264[b] (240)	393[c] (358) 404[c] (368) 399[c] (363)	317 (288) 338 (308 328 (298)
A.I.S.I. 304LN	>608[a] (553) 557[a] (507) 284[b] (258)	310 (282) 376 (342) 343 (312)	213 (194) 195 (177) 221 (201) 210 (191)
A.I.S.I. 316	371[a] (338) 486[a] (442) 387[a] (352) 271[b]	351[c] (319) 418[c] (380) 436[c] (397) 402[c] (366)	280 (255) 267 (243) 256 (233) 268 (244)
A.I.S.I. 316LN	328[a] (298) 278[a] (253) 286[b] (260)	255 (232) 277 (252) 266 (242)	210 (191) 225[d] (205) 275[d] (259) 203 (185)
Fe-21Cr-12Ni-5Mn (Nitronic 50)	287[a] (352) 337[a] (307 321[b] (292)	268 (244) 270 (246) 255 (232) 264 (240)	114 (104) 147 (134) 131 (119)

[a]Invalid result according to the thickness criterion for a valid J-integral test.

[b]A toughness lower limit J_{lim} from $J_{lim} = B\bar{\sigma}/25$ where B = specimen ligament and σ = flow strength.

[c]Marginally invalid result according to the thickness criterion for a valid J_{Ic} test. Ligament is within 10% of the required value.

[d]Result from multiple-specimen analysis using an insufficient number of specimens.

Table 4. Paris law fatigue crack growth rate parameters C and n for annealed austenitic stainless steels. The fatigue crack growth rate da/dN in mm/cycle (in/cycle) is given by $da/dN = C(\Delta K)^n$, where ΔK is the stress intensity in $MPa\sqrt{m}$ ($ksi\sqrt{in}$). The C values enclosed in parentheses are to be used when ΔK and da/dN are in English units.

Material	Temperature	C		n
A.I.S.I. 304	304	6.58×10^{-10}	(3.76×10^{-11})	3.64
	76	9.51×10^{-12}	(5.83×10^{-13})	4.34
	4	3.26×10^{-10}	(1.84×10^{-11})	3.49
A.I.S.I. 304LN	295	3.01×10^{-9}	(1.69×10^{-10})	3.17
	76	2.67×10^{-9}	(1.45×10^{-10})	3.17
	4	1.69×10^{-10}	(1.02×10^{-11})	4.25
A.I.S.I. 316	295	6.89×10^{-12}	(4.44×10^{-13})	4.84
	76	4.41×10^{-8}	(2.19×10^{-9})	2.25
	4	8.33×10^{-9}	(4.33×10^{-10})	2.71
A.I.S.I. 316LN	295	5.66×10^{-10}	(3.17×10^{-11})	3.43
	76	3.01×10^{-8}	(1.49×10^{-9})	2.24
	4	7.56×10^{-10}	(4.15×10^{-11})	3.26
Fe-21Cr-12Ni-5Mn (Nitronic 50)	295	3.46×10^{-14}	(2.49×10^{-15})	5.91
	76	1.05×10^{-12}	(6.73×10^{-14})	4.79
	4	1.94×10^{-13}	(1.32×10^{-14})	5.33

Table 5. Tensile Properties at 295, 76, and 4 K for the Materials of the Present Study.

Material	Temperature	Yield Strength 0.2% offset MPa (ksi)	Tensile Strength MPa (ksi)	Flow Strength* MPa (ksi)	Elongation 2.5 cm gage length (%)	Reduction of Area (%)
A.I.S.I. 304	295	212.6 (30.8)	600.9 (87.2)	406.8 (59.0)	73	67
		218.2 (31.6)	567.3 (82.3)	392.8 (57.0)	62	71
		217.9 (31.6)	630.1 (91.4)	424.0 (61.5)	66	66
		216.2 (31.4)	599.4 (86.9)	407.8 (59.1)	67	68
	76	255.6 (37.1)	1455.7 (211)	855.7 (124)	41	67
		263.5 (38.2)	1414.1 (205)	838.8 (122)	42	61
		259.6 (37.7)	1434.9 (208)	847.2 (123)	42	65
	4	357.6 (51.9)	1589.3 (231)	973.4 (141)	36	49
		338.2 (49.1)	1600.7 (232)	969.5 (141)	42	47
		347.9 (50.5)	1595.0 (232)	971.5 (141)	38	48
A.I.S.I. 304LN	295	283.4 (41.1)	630.9 (91.5)	457.1 (66.3)	64	84
		284.1 (41.2)	604.0 (87.6)	444.0 (64.4)	62	84
		283.7 (41.1)	617.4 (89.5)	450.6 (65.4)	63	84
	76	644.0 (93.4)	1558.3 (226)	1101.1 (160)	49	61
		666.1 (96.6)	1524.5 (221)	1095.3 (159)	45	56
		655.0 (95.0)	1541.4 (224)	1098.2 (159)	47	58
	4	760.5 (110)	1701.0 (247)	1230.8 (179)	37	52
		781.9 (113)	1672.0 (242)	1227.0 (178)	37	53
		771.2 (112)	1686.5 (245)	1228.9 (178)	37	52

Table 5. Tensile Properties at 295, 76, and 4 K for the Materials of the Present Study (continued).

Material	Temperature	Yield Strength 0.2% offset MPa (ksi)	Tensile Strength MPa (ksi)	Flow Strength* MPa (ksi)	Elongation 2.5 cm gage length (%)	Reduction of Area (%)
A.I.S.I. 316	295	224.3 (32.5)	573.5 (83.2)	401.4 (58.2)	56	73
		231.5 (33.6)	573.3 (83.1)	402.4 (58.4)	57	73
		227.9 (33.0)	575.9 (83.5)	401.9 (58.3)	56	73
	76	586.7 (85.1)	1228.7 (178)	907.7 (132)	64	67
		629.3 (91.3)	1256.6 (182)	943.0 (137)	60	72
		608.0 (88.2)	1242.6 (180)	925.3 (134)	62	70
	4	717.7 (104)	1291.6 (187)	1004.7 (146)	45	60
		703.7 (102)	1310.5 (190)	1007.1 (146)	50	54
		710.7 (103)	1301.0 (189)	1005.9 (146)	48	57
A.I.S.I. 316LN (transverse)	295	277.9 (40.3)	615.7 (89.3)	446.8 (64.8)	55	71
		283.4 (41.1)	612.3 (88.8)	447.8 (64.9)	57	74
		275.8 (40.0)	615.7 (89.3)	445.8 (64.7)	58	71
		279.0 (40.5)	614.6 (89.1)	446.8 (64.8)	57	72
	76	726.7 (105)	1209.4 (175)	968.0 (140)	61	66
		724.0 (105)	1220.4 (177)	972.2 (141)	61	68
		724.0 (105)	1217.7 (177)	970.9 (141)	61	65
		724.9 (105)	1215.8 (176)	970.4 (141)	61	66
	4	1062.5 (154)	1388.7 (201)	1225.6 (178)	31	47
		1019.8 (148)	1390.7 (202)	1205.2 (175)	34	47
		992.2 (144)	1384.5 (201)	1188.4 (172)	41	53
		1024.8 (149)	1388.0 (201)	1205.4 (175)	35	50

Table 5. Tensile Properties at 295, 76, and 4 K for the Materials of the Present Study (continued).

Material	Temperature	Yield Strength 0.2% offset MPa (ksi)	Tensile Strength MPa (ksi)	Flow Strength* MPa (ksi)	Elongation 2.5 cm gage length (%)	Reduction of Area (%)
Fe-21Cr-12Ni-5Mn-X	295	426.1 (61.8)	766.1 (111)	596.1 (86.5)	45	69
	76	916.0 (133)	1512.8 (219)	1213.9 (176)	76	62
	4	1307 (190)	1842 (267)	1576 (229)	17	36
		1353 (196)	1853 (269)	1604 (233)	15	41
		1330 (193)	1848 (268)	1589 (231)	16	38
A.I.S.I. 304L (.096 wt % N)	4	618.5 (89.7)	1514.1 (220)	1066.3 (155)	32	57
		643.3 (93.3)				
		619.2 (89.8)	1494.1 (217)	1056.7 (153)	32	51
		627.0 (90.9)	1504.1 (218)	1061.5 (154)	32	54
A.I.S.I. 304L (.075 % N)	4	503.3 (73.0)	1539.0 (223)	1021.1 (148)	37	44
		499.2 (72.4)	1565.9 (227)	1032.6 (150)	36	45
		500.6 (72.6)	1534.8 (223)	1017.7 (148)	34	51
		501.0 (72.7)	1546.6 (224)	1023.8 (148	36	47

*Flow strength = 1/2 (yield strength + tensile strength).

LIST OF FIGURES

Fig. 1. Composite 3-dimensional photomicrograph of the AISI 304 alloy.

Fig. 2. Composite 3-dimensional photomicrograph of the AISI 304LN alloy.

Fig. 3. Composite 3-dimensional photomicrograph of the AISI 316 alloy.

Fig. 4. Composite 3-dimensional photomicrograph of the AISI 316LN alloy.

Fig. 5. Composite 3-dimensional photomicrograph of the Fe-21Cr-12Ni-5Mn (Nitronic 50) alloy.

Fig. 6. Specimen geometry.

Fig. 7. Orientations of compact and tensile specimens.

Fig. 8 Typical J-Δa curve obtained using the single-specimen J-integral method. Inferred Δa values are systematically lower than actual values after accounting for the zero shift.

Fig. 9. Fracture toughness at 4 K of selected wrought and annealed austenitic stainless steels plotted against their 4 K yield strengths. The line is a linear least squares fit.

Fig. 10. Fracture toughness at 4 K of selected wrought and annealed austenitic stainless steels plotted against their 4 K yield strengths with least squares fit line and Pellini's data band centers (dashed lines) for "old" and "new" ferritic steels at room temperature.

Fig. 11. Best-fit lines for 4 K fatigue crack growth rate data for selected wrought, annealed stainless steels.

Fig. 12. Temperature dependences of the yield and ultimate strengths of the annealed austenitic stainless steels.

Fig. 13. Temperature dependences of the elongation and reduction of area of the annealed austenitic stainless steels.

Fig. 14. Yield strength at 4 K for annealed austenitic stainless steels plotted against weight percent nitrogen. Behavior trends at 76 and 295 K are roughly indicated by the dashed lines.

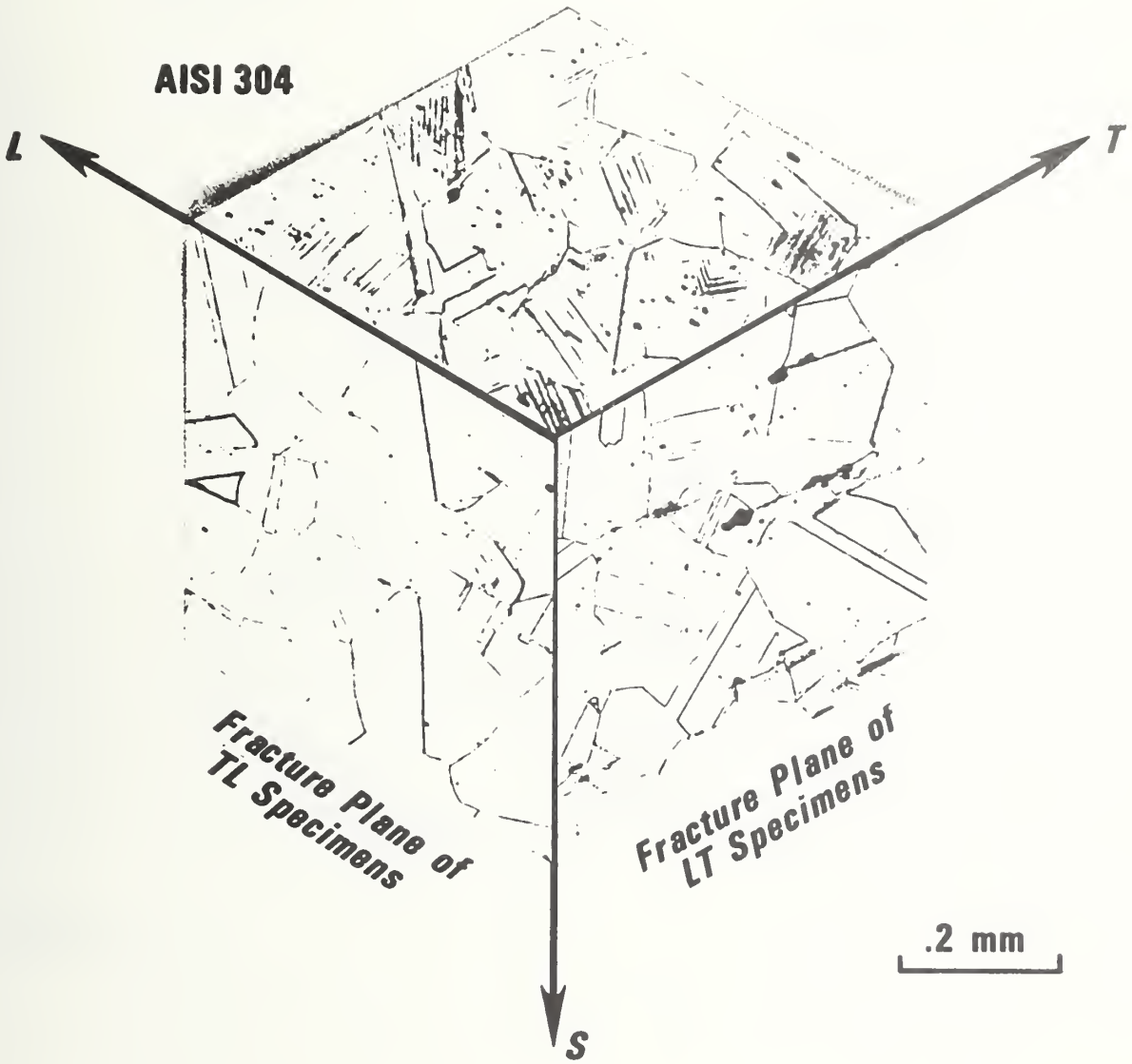

L - Longitudinal or rolling direction

T - Long transverse or width direction

S - Short transverse or plate thickness direction

Fig. 1. Composite 3-dimensional photomicrograph of the AISI 304 alloy.

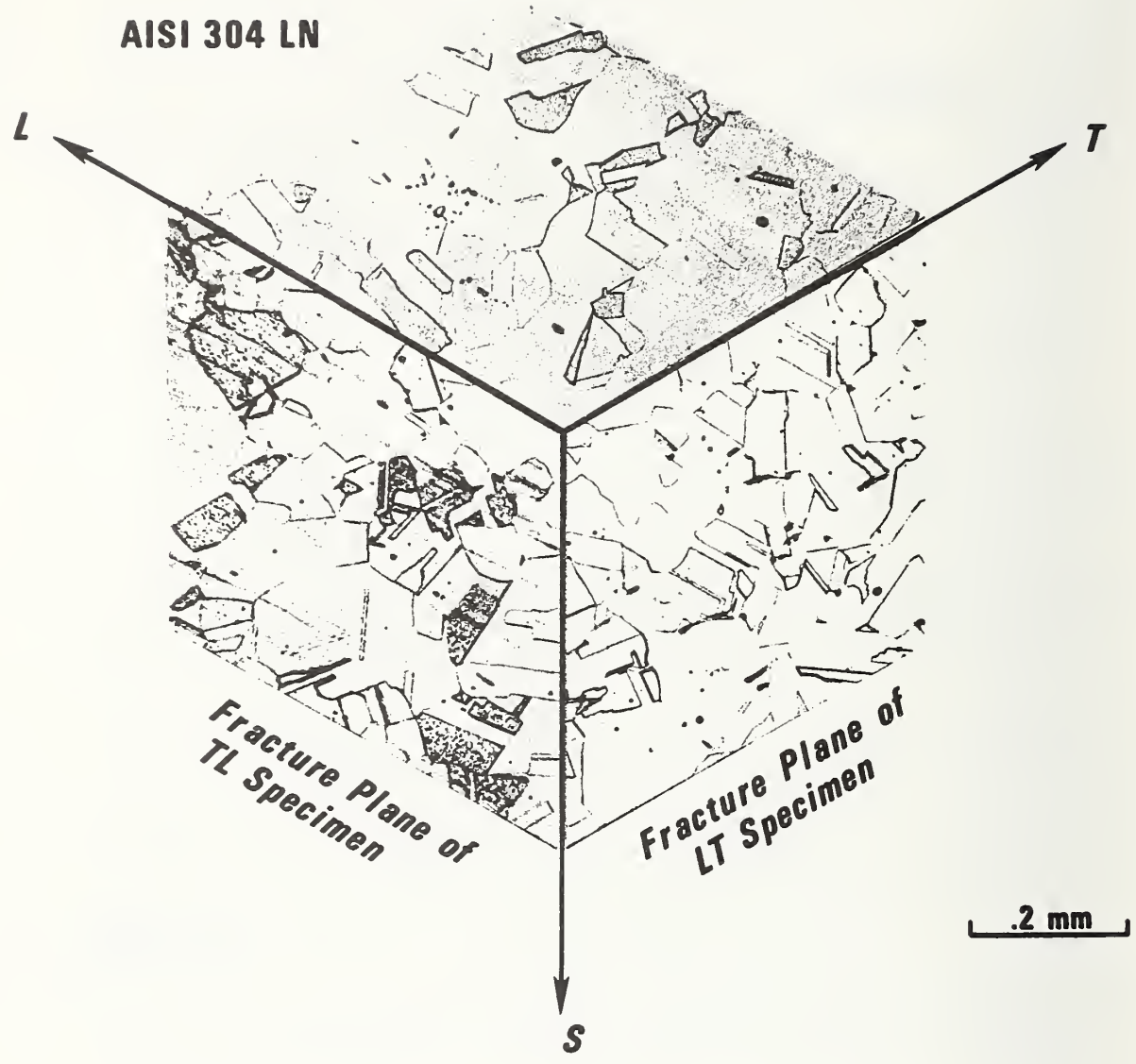

L - Longitudinal or rolling direction

T - Long transverse or width direction

S - Short transverse or plate thickness direction

Fig. 2. Composite 3-dimensional photomicrograph of the AISI 304LN alloy.

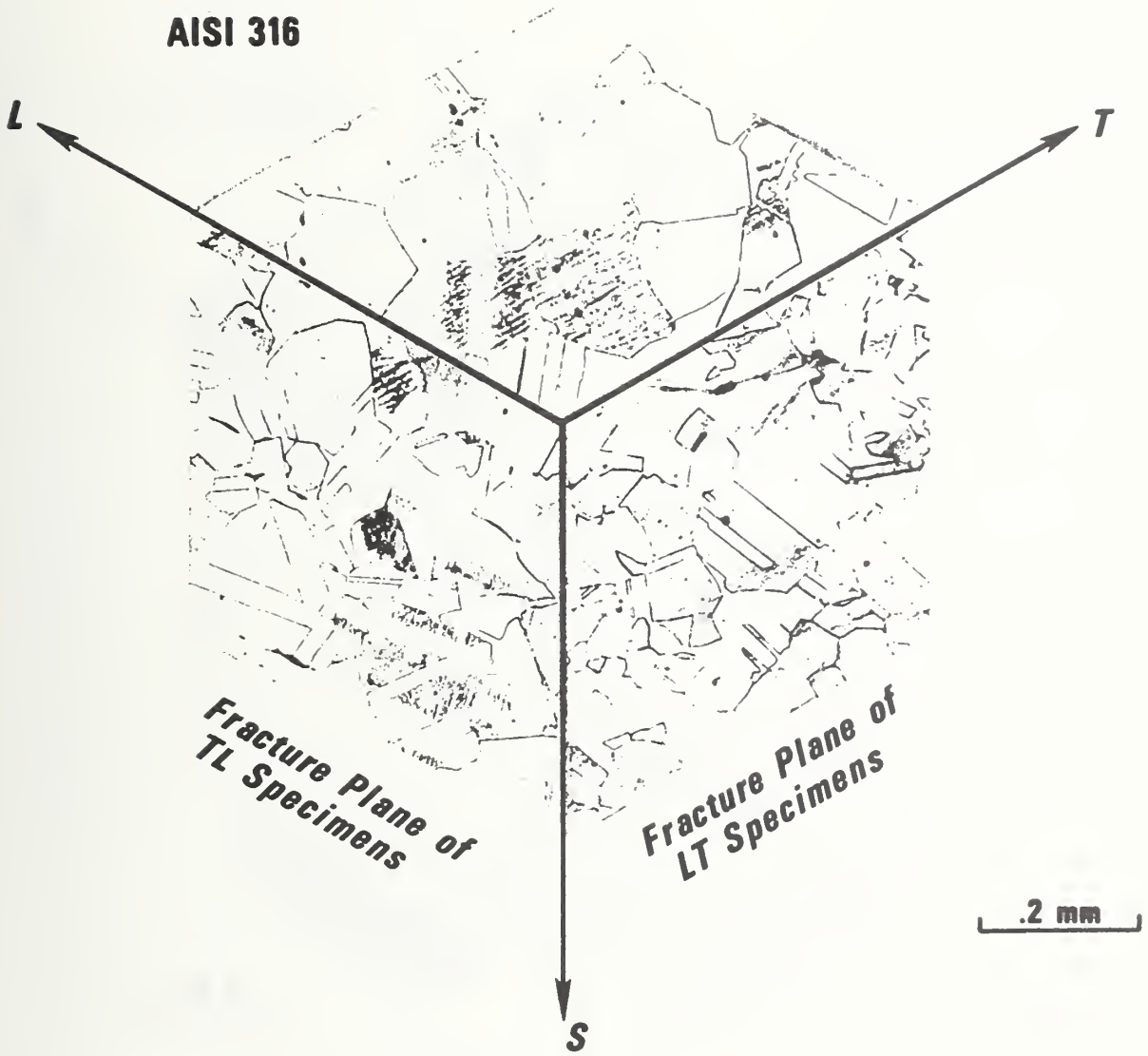

L - Longitudinal or rolling direction

T - Long transverse or width direction

S - Short transverse or plate thickness direction

Fig. 3. Composite 3-dimensional photomicrograph of the AISI 316 alloy.

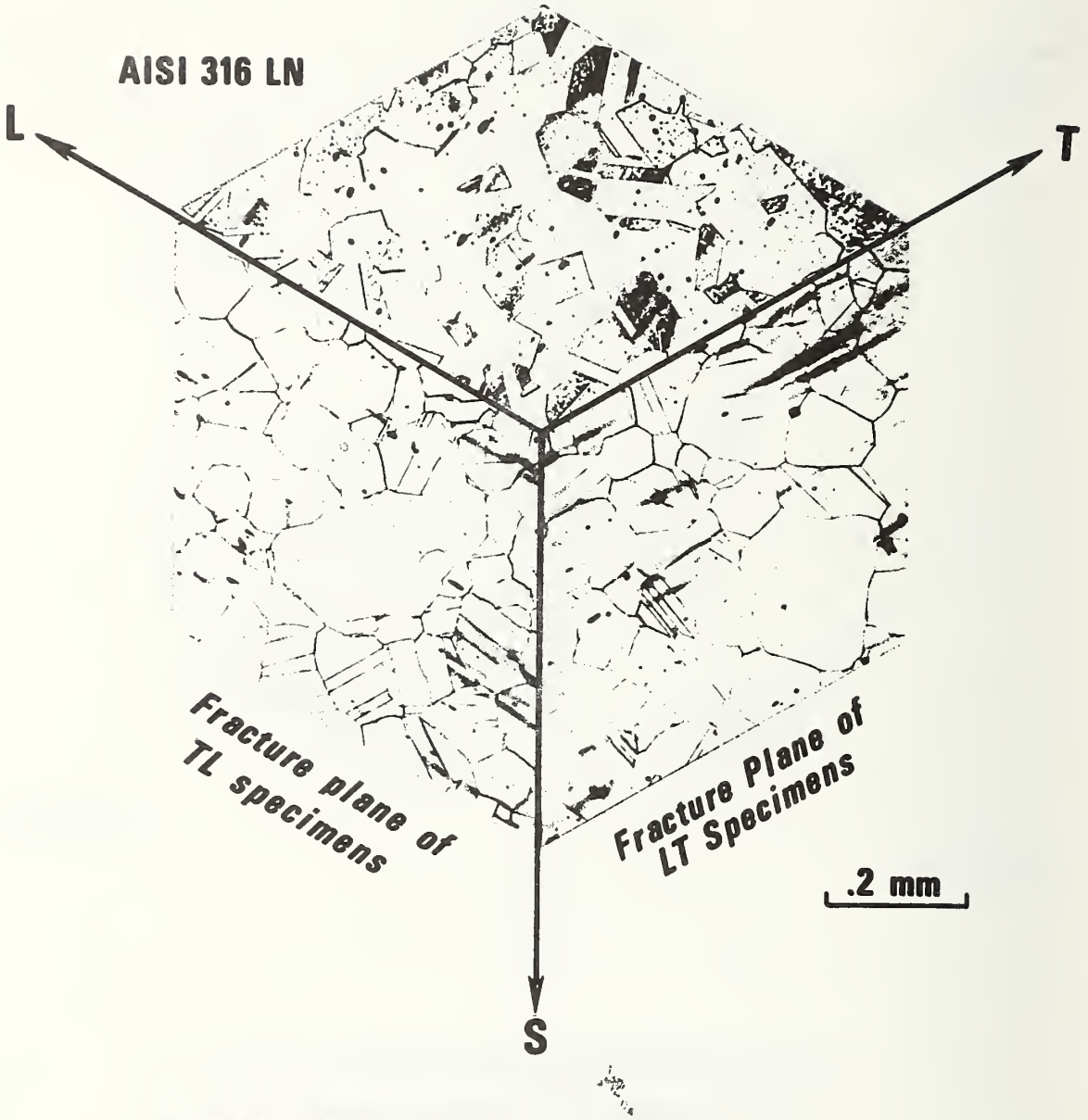

Fig. 4. Composite 3-dimensional photomicrograph of the AISI 316LN alloy.

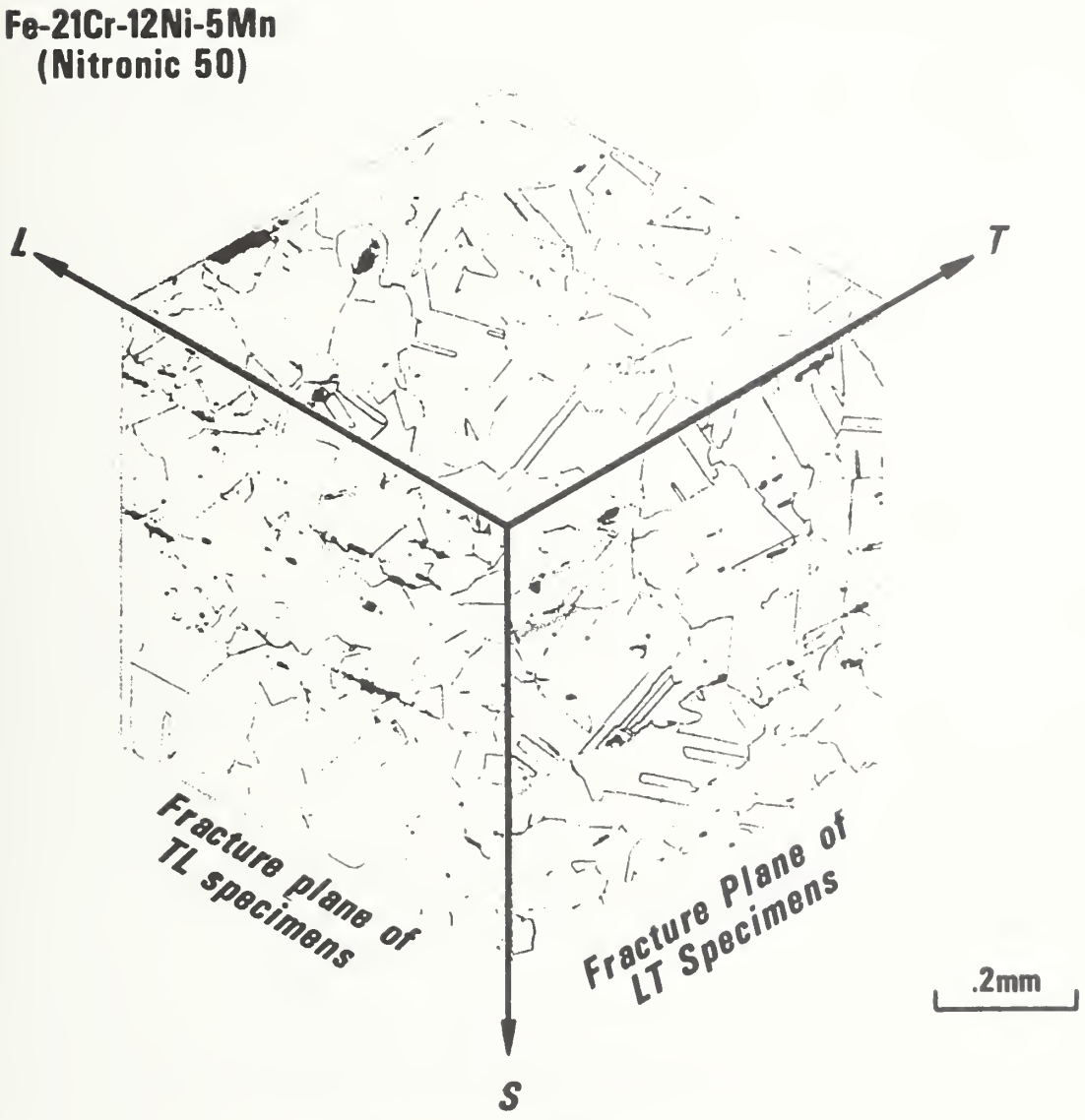

L - Longitudinal or rolling direction

T - Long transverse or width direction

S - Short transverse or plate thickness direction

Fig. 5. Composite 3-dimensional photomicrograph of the Fe-21Cr-12Ni-5Mn (Nitronic 50) alloy.

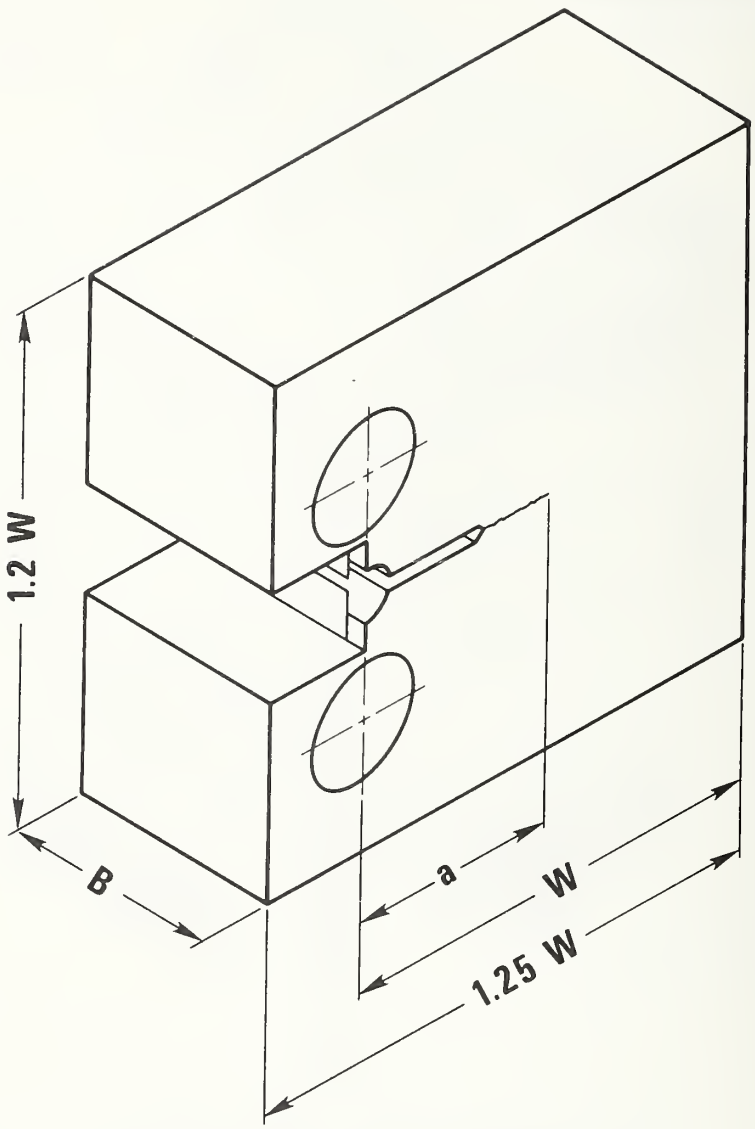

Fig. 6. Specimen geometry.

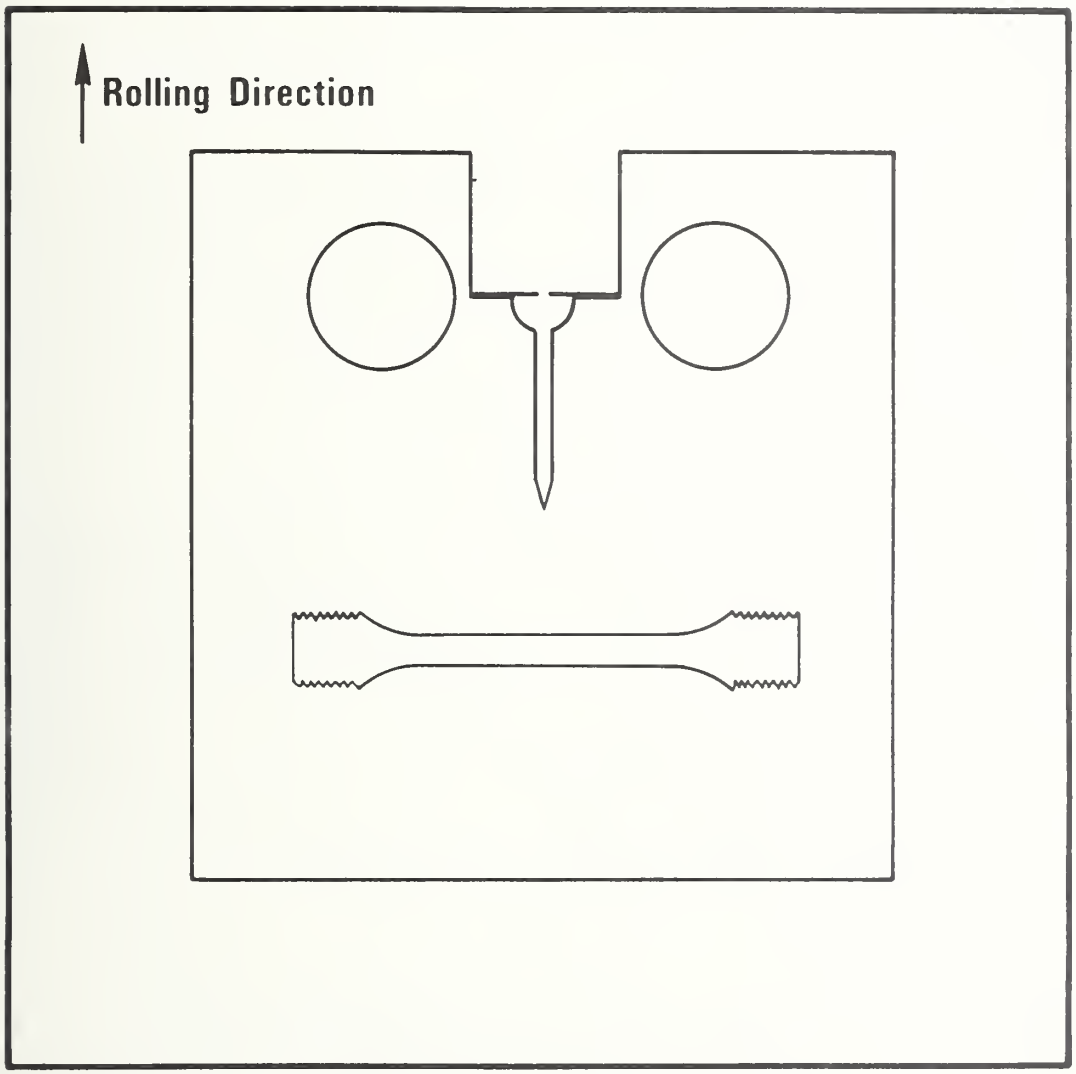

Fig. 7. Orientations of compact and tensile specimens.

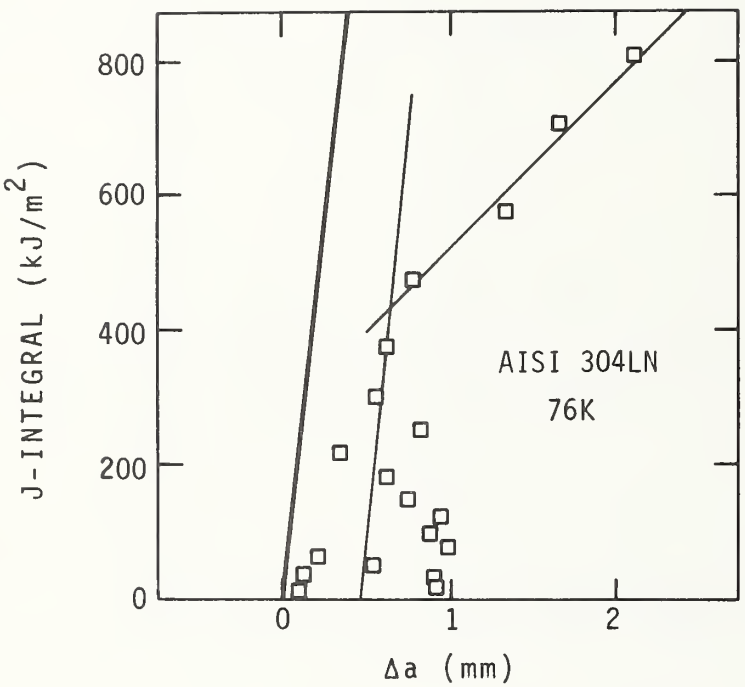

Fig. 8 Typical J-Δa curve obtained using the single-specimen J-integral method. Inferred Δa values are systematically lower than actual values after accounting for the zero shift.

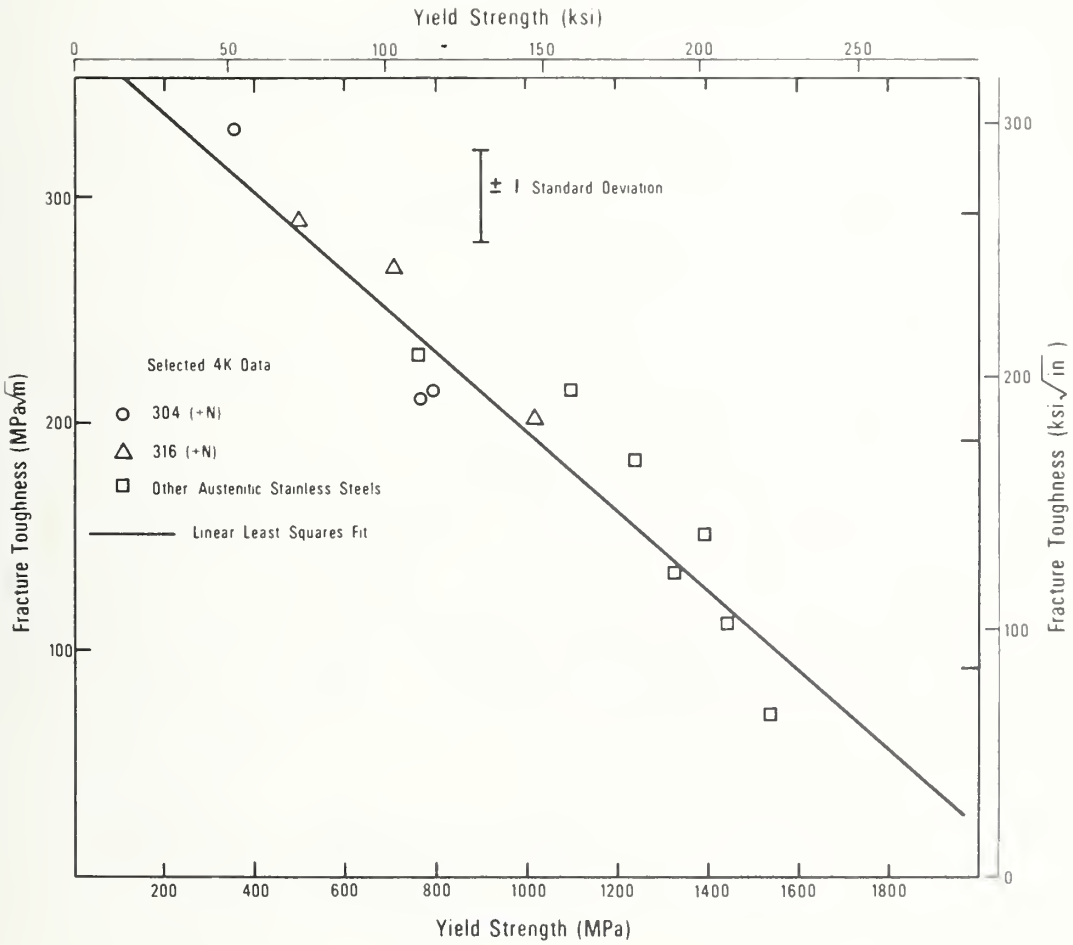

Fig. 9. Fracture toughness at 4 K of selected wrought and annealed austenitic stainless steels plotted against their 4 K yield strengths. The line is a linear least squares fit.

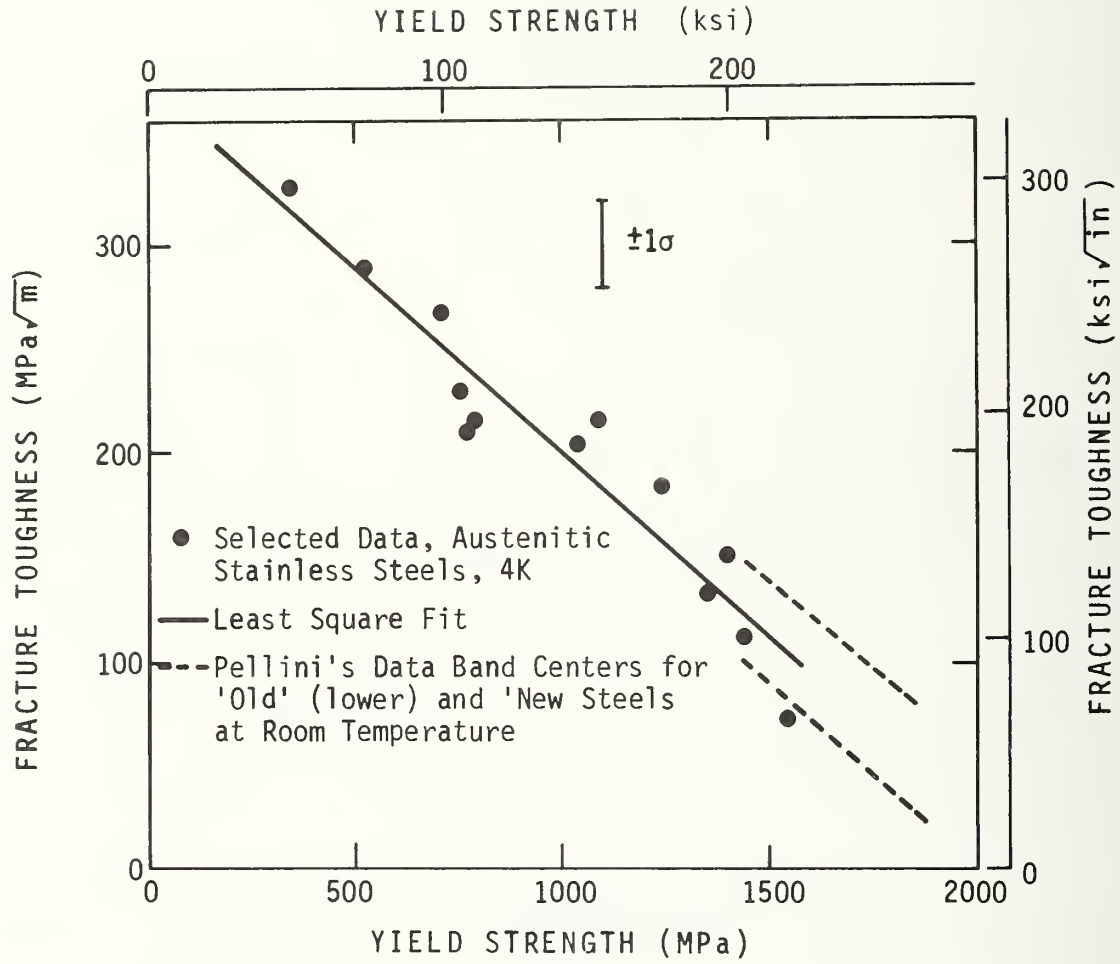

Fig. 10. Fracture toughness at 4 K of selected wrought and annealed austenitic stainless steels plotted against their 4 K yield strengths with least squares fit line and Pellini's data band centers (dashed lines) for "old" and "new" ferritic steels at room temperature.

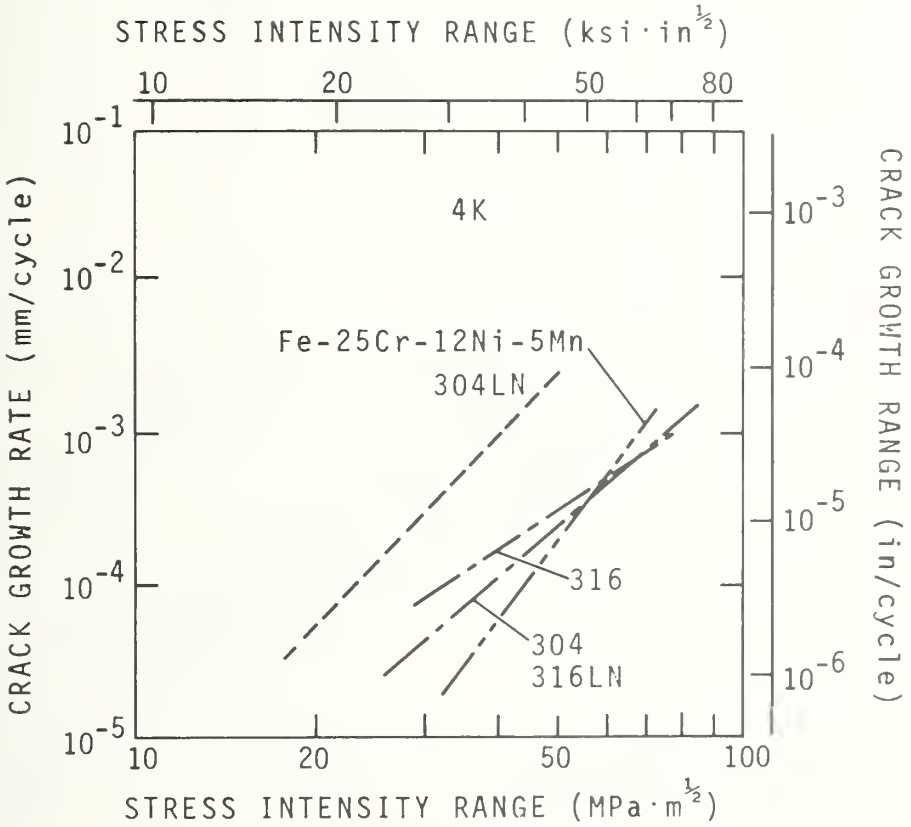

Fig. 11. Best-fit lines for 4 K fatigue crack growth rate data for selected wrought, annealed stainless steels.

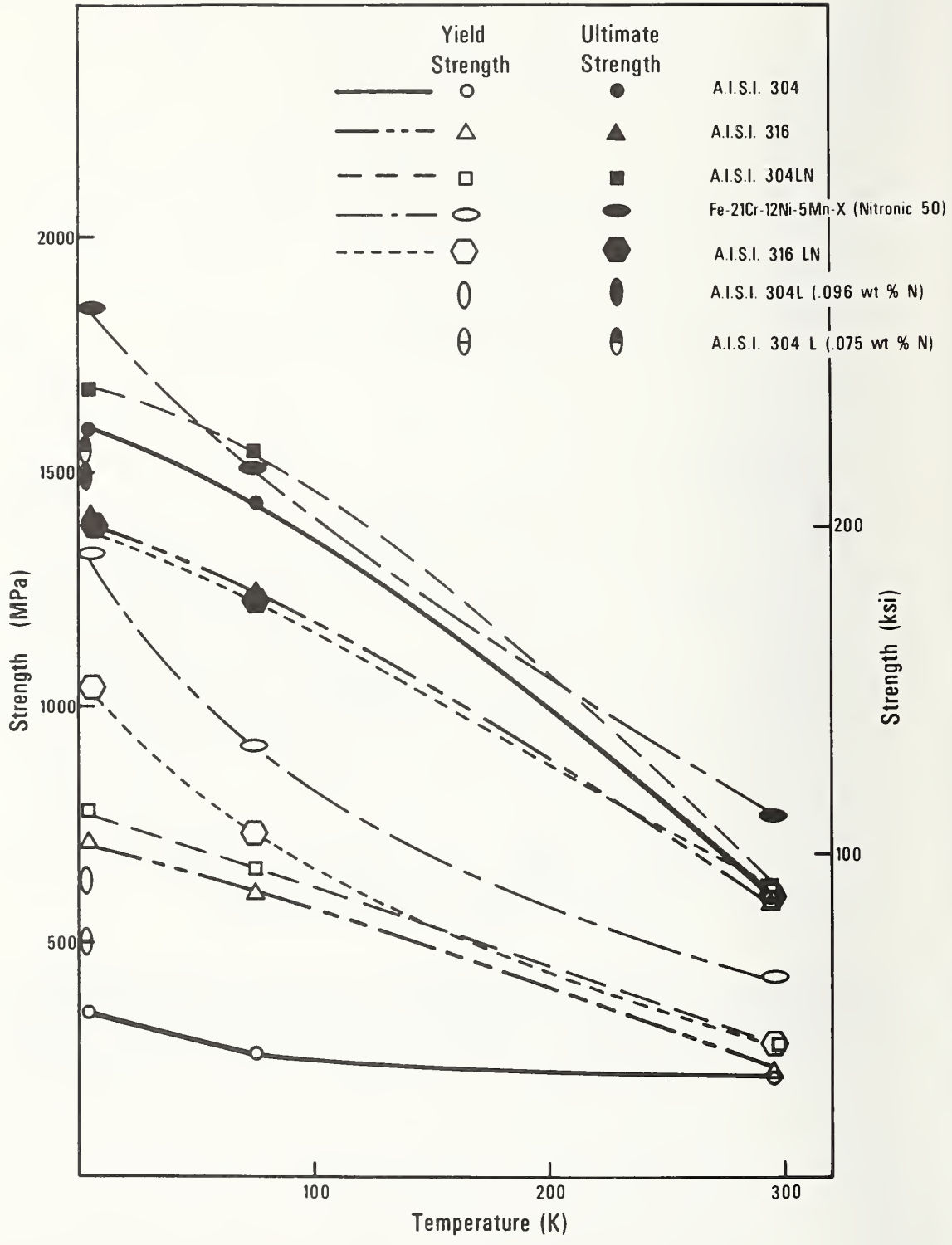

Fig. 12. Temperature dependences of the yield and ultimate strengths of the annealed austenitic stainless steels.

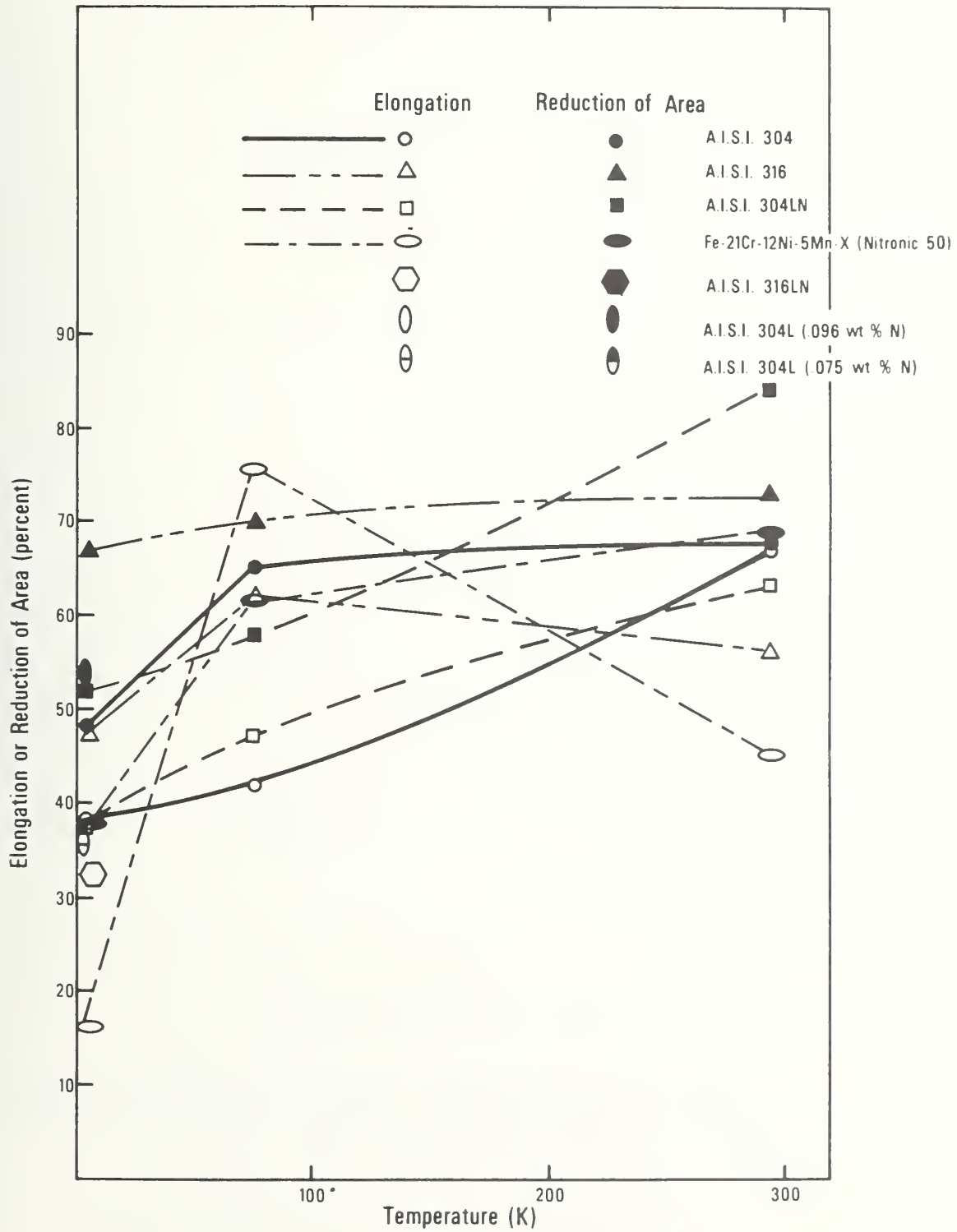

Fig. 13. Temperature dependences of the elongation and reduction of area of the annealed austenitic stainless steels.

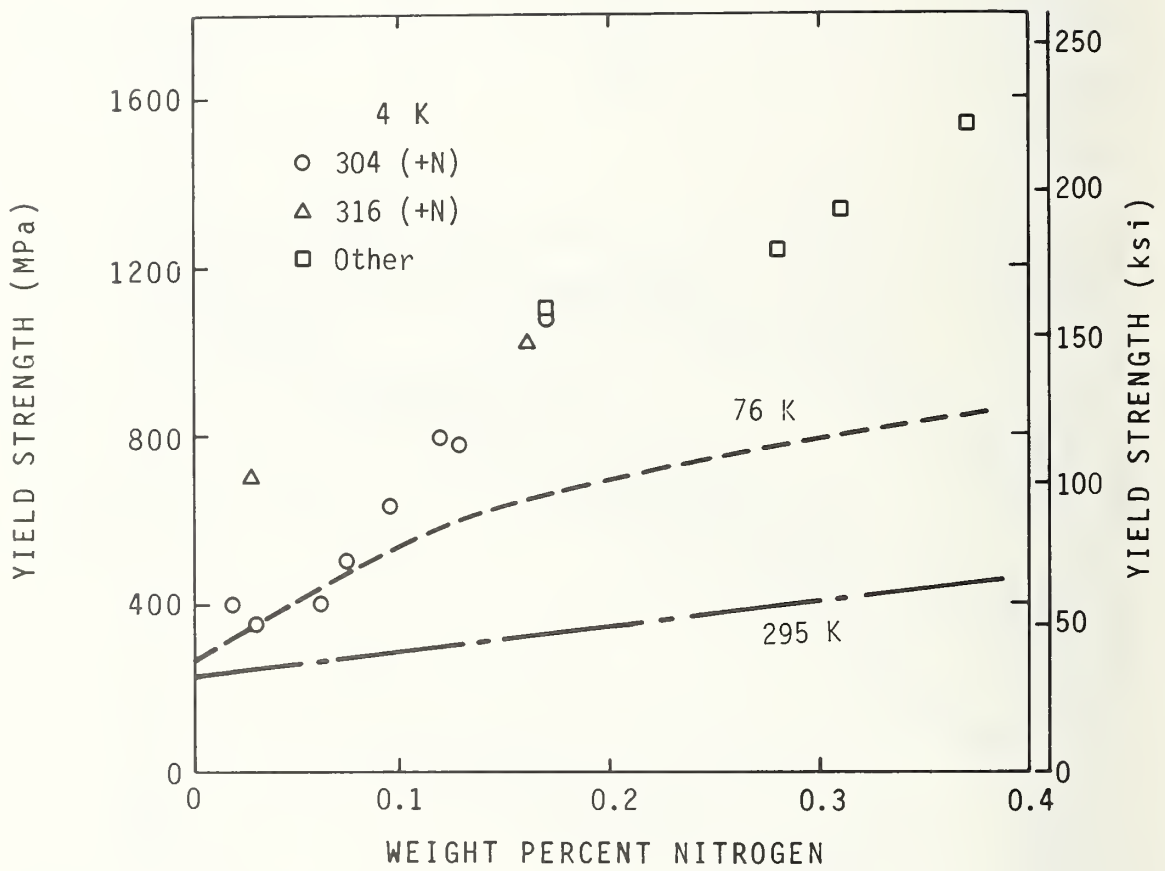

Fig. 14. Yield strength at 4 K for annealed austenitic stainless steels plotted against weight percent nitrogen. Behavior trends at 76 and 295 K are roughly indicated by the dashed lines.

HEATING AND STRAIN RATE EFFECTS IN AISI 304L STAINLESS STEEL AT 4 K

National Bureau of Standards

HEATING AND STRAIN RATE EFFECTS IN AISI 304L STAINLESS STEEL AT 4 K*

D. T. Read and R. P. Reed
Fracture and Deformation Division
National Bureau of Standards
Boulder, CO 80303

*Work sponsored by DOE/MFE. Contribution of NBS, not subject to copyright.

ABSTRACT

In structural alloy tensile specimens undergoing mechanical work in a liquid helium (4 K) bath, internal temperature increases are favored by low specimen specific heat and thermal conductivity. Indeed, the well-known phenomenon of serrated yielding is considered to be due to adiabatic heating of the specimen. Besides being of scientific interest, the possible occurrence of such heating must be accounted for in testing structural materials for liquid helium temperature applications. Therefore, temperatures of small tensile specimens of AISI 304L stainless steel were measured during straining at 4 K at several strain rates. Stress-strain curves were obtained at three strain rates. Serrated yielding was observed at all strain rates. Temperatures above 4 K were detected only during and immediately following the individual load drops. The maximum temperature rise detected was 52 K. No effect of crosshead speed was detected. Examination of a specimen which was deformed only until one load drop occurred showed that during the load drop only a small portion of the specimen deformed. Analysis of the relative number of occurrences of temperature rises of different magnitudes showed that only a small portion of the specimen was heated during a given load drop. The calculated size of the heated portion of the specimen agreed with the visually observed size of the severely deformed portion. The value of the maximum temperature attained was calculated from the load drop, volume of specimen material heated, and the physical properties of the specimen material; the calculated value agreed well with the measured value.

INTRODUCTION

In structural alloy tensile specimens undergoing mechanical work in a liquid helium (4 K) bath, internal temperature increases are favored by low specimen specific heat and thermal conductivity. Indeed, the well-known phenomenon of serrated yielding is considered to be due to adiabatic heating [1,2] of the specimen. Besides scientific interest, the possible occurrence of such heating must be accounted for in testing structural materials for liquid helium temperature applications. Therefore, temperatures of small tensile specimens of AISI 304L stainless steel were measured during straining at 4 K at several strain rates. Stress-strain curves were obtained at three strain rates.

MATERIAL

The material used in this study was a 2.5 cm (1 inch) plate, A.I.S.I. 304L stainless steel obtained commercially in the mill-annealed condition. Its chemistry is shown in Table 1. Flat tensile specimens in the longitudinal orientation with a gage section 2.5 mm (0.1 inch) thick by 4.8 mm (.19 inch) wide by 30 mm (1.2 inch) long were used for all tests. The nominal grain diameter was 70 μm and the hardness Rockwell B-83.

TECHNIQUES AND APPARATUS

The mechanical property tests were carried out using a screw-driven tensile machine with the capability for variable crosshead speeds, adapted for low temperature testing as described by Reed [3]. The strain rates are obtainable directly from the crosshead speeds and gage length under the assumption of negligible work hardening and negligible strain rate outside the reduced section. Table 2 gives the strain rates which correspond to the crosshead speeds. When the work hardening

coefficient is nonzero, the actual strain rates are less than those calculated from the crosshead speeds. During load drops, the actual strain rates are quite rapid, and, as far as is known, are independent of crosshead speed. Therefore, crosshead speeds will be given rather than strain rates when describing experiments and data. Displacement gages as described by Reed and Mikesell [4] were used to measure specimen strain.

For detection of temperature rises during deformation, the specimen was instrumented as shown in Fig. 1. A NbTi superconducting wire with a transition temperature of about 10 K was bonded into a slot milled into the specimen. This allowed detection of the occurrence of temperature rises along the whole length of the specimen, but provided no information on their magnitude. An Au-.05 at % Fe versus chromel thermocouple was soldered to the specimen. This allowed measurement of the amplitude of the temperature rise a specific location, and, as discussed below, allowed calculation of the temperature profile of the load drops. Electrical signals corresponding to the resistance rises in the superconducting wire or emf's from the thermocouple were plotted using an x-y plotter with a response time of a few tenths of a second.

Martensitic transformation is associated with plastic deformation at low temperatures in AISI 304L. Since the martensitic, body-centered cubic phase is ferromagnetic, local regions of deformation along the specimen were conviently decorated with iron powder.

RESULTS AND DISCUSSION

Serrated yielding occurred at all crosshead speeds for specimens immersed in liquid helium. A typical stress-strain curve is shown in Fig. 2. Because temperature rises occurred simultaneously with the

load drops, the specimens did not remain at 4 K. The strain required to initiate serrated yielding decreased as the crosshead speed increased, and the magnitude of the first detectable load drop also decreased with crosshead speed, as shown in Fig. 3. No systematic effect of crosshead speed on the yield strength was detected, Fig. 4.

The load drops were distributed in stress up to about 200 MPa, which was over ten percent of the ultimate strength for this material. A histogram showing the distribution of the magnitudes of the load drops is shown in Fig. 5.

The maximum temperature rise observed was 52 K. A histogram of the number of temperature rises in each of 11 temperature intervals, measured using one thermocouple on one specimen strained to failure at 4 K, is shown in Fig. 6. Many load drops occurred with no indication of a temperature rise at the thermocouple because in these cases the temperature rises were localized in a small region of the specimen volume away from the thermocouple. Assuming that the total number of temperature rises in a given temperature interval detected for all load drops was proportional to the extent of specimen length attaining that temperature interval during a single load drop, a temperature profile of a load drop was constructed, as shown in Fig. 7. The smooth curve is a hand-drawn interpolation of the calculated stepped curve. The width at half maximum of the calculated temperature profile was about 0.5 cm. This agrees well with the value of specimen length involved in the load drop obtained by visual observation of a specimen which was strained through only one load drop, Fig. 8. By sprinkling this specimen with iron powder, the region which was deformed during the load drop was decorated because it contained more α' martensite than the part of the

specimen which had deformed uniformly. Visual observation of the specimen surface before decoration also showed the severely deformed region because its surface was visually deformed and the specimen was necked. The deformed region appeared about 0.5 cm long, in agreement with other observations.

The crosshead speed dependence of the strain at which the first load drop occurred is consistent with expectations. The strain values at which the first load drop occurred were different from those found by Reed and Guntner [5]. This discrepancy is believed to be due to differences in chemical composition between the specimen materials of the two studies, and confirms that the deformation process at 4 K in these metastable austenitic stainless steel is quite sensitive to small changes in chemical composition.

The widely accepted explanation of the phenomenon of discontinuous yielding is adiabatic heating [1,2]. In this mechanism, the heat produced in the specimen when it strains a small amount raises the specimen temperature and lowers its strength enough for more deformation to occur, and the process continues. The localized temperature instability at 4 K is caused by very low heat capacity and reduced thermal conductivity. This cyclic process manifests itself in the stress strain curve as a sudden load drop, accompanied by sudden specimen elongation. The adiabatic heating model was tested by calculating the temperature rise, the load drop, and the conditions for unstable plastic flow and comparing the results with experimental data. The calculations follow Basinski [1,2], but the discussion of unstable plastic flow differs in detail. One assumes essentially adiabatic conditions, in which all mechanical work is converted to heat, negligible conduction of heat away

from the deformed region, and negligible energy used in the generation of lattice defects.

The temperature rise was calculated using the expression

$$P\Delta x = \rho v \int_{T_{init}}^{T_{max}} C dT \qquad (1)$$

where P was the load on the specimen, Δx its length change, ρ its mass density, v the specimen volume heated, C the specimen material specific heat in -J/kg, T the temperature, T_{init} the specimen temperature before the load drop (= 4 K), and T_{max} the maximum specimen temperature attained. Values for the parameters used in this and the following calculations are listed in Table 3. A graph of the specific heat over the requisite temperature range was constructed using data from Ho, King, and Fickett [6], Corsan and Mitchem [7] , and Jelinek and Collings [8]. The effect of the approximate nature of the specific heat curve used on calculated temperatures is insignificant due to the strong temperature dependence of the specific heat in the requisite temperature range. From Eq. (1), the calculated value of T_{max} was 58 K, which agrees quite well with the measured value, 56 K. The close agreement is probably fortuitous due to the approximations involved. These include: assuming that only a constant volume v is heated, and the temperature everywhere else remains at 4 K, when actually a distribution of temperatures through the specimen exists; and assuming that conditions are fully adiabatic. The close agreement between measured and calculated T_{max} provides assurance that these two approximations are reasonably accurate.

The magnitude of the load drop was calculated from the expression

$$\Delta\sigma = (\partial\sigma/\partial T)\Delta T + (\partial\sigma/\partial\varepsilon)\,\Delta\varepsilon \qquad (2)$$

where the first term on the right represents thermal softening and the second accounts for strain hardening during the load drop, σ denoting stress and ε strain. Note that $\Delta\sigma$ and $\partial\sigma/\partial T$ are negative quantities, while ΔT and $\Delta\varepsilon$ are positive, so that the thermal softening is opposed by work hardening, as must be the case. If work hardening is ignored ($\partial\sigma/\partial\varepsilon = 0$) we calculate $\Delta\sigma = -130$ MPa for a temperature rise of 52 K. Thus, thermal softening alone is more than enough to account for a typical stress drop of 75 MPa. The appropriate value for the work hardening coefficient $\partial\sigma/\partial\varepsilon$ is an average over strain and temperature. If $\partial\sigma/\partial\sigma$ is approximated as the average over the strain range of the load drops at 4 K, the calculated stress drop becomes 96 MPa, which is closer to the typical value and within the observed range of stress drops. The agreement between the calculated value (96 MPa) and the observed value (typically 75 MPa) is considered adequate considering the approximations involved.

The conditions for unstable plastic flow are given by

$$Pk/\rho v\partial P/\partial T \cdot 1/(1 + k/\ell\cdot\partial P/\partial\varepsilon) \geq C(T) \qquad (3)$$

where k is the mechanical compliance of the load train, P is the load on the specimen, and $\partial P/\partial T$ and $\partial P/\partial\varepsilon$ are related, respectively, to $\partial\sigma/\partial T$ and $\partial\sigma/\partial\varepsilon$ by multiplying the latter by the specimen cross sectional area. Table 3 gives a complete list of the meanings of the symbols. This equation signifies that the load drop and heating continue up to the temperature at which the specific heat C(T) is equal to

the heat produced for a small increment of strain divided by the mass of heated specimen material. If work hardening is again ignored, we calculate a maximum specimen temperature of 58 K in good agreement with the observed value 56 K. If work hardening is included using the approximation previously discussed for the work hardening coefficient, a maximum temperature of 44 K, which is considered adequate agreement with experiment. It is concluded that comparison of the temperature rises measured during load drops to those calculated using the magnitude of the load drops, the load, the specific heat, the temperature dependence of the yield strength, and the volume of the specimen participating in the temperature rises confirmed adiabatic heating as the mechanism of the load drops.

The crosshead speed independence of martensite contents[9] and yield strength is consistent with the absence of deviations of specimen temperature from 4 K except during load drops. All these results indicate that no dynamic effects were occurring, except during load drops.

The fact that no temperature rises were observed except during load drops provides assurance that typical liquid helium temperature test specimens and procedures do indeed yield 4 K data.

CONCLUSIONS

The following may be concluded from this study of the variability of the yield strength and deformation behavior of A.I.S.I. 304L stainless steel.

1) Adiabatic heating is confirmed as the mechanism for load drops; at higher strain rates, load drops occur at lower strains.
2) Small tensile specimens immersed in liquid helium remain at 4 K during straining except during load drops.
3) During load drops, localized regions of the specimen deform.

REFERENCES

1. Z. S. Basinski, "The Instability of Plastic Flow of Metals at Very Low Temperatures," Proc. Roy. Soc. A240 (1957) pp. 229-242.

2. Z. S. Basinski, "The Instability of Plastic Flow of Metals at Very Low Temperatures," Austral. J. Phys. 13 (1960) pp. 354-358.

3. R. P. Reed, "A Cryostat for Tensile Tests in the Temperature Range 300 to 4 K," Adv. Cryo. Eng. 7 (1961) pp. 448-454.

4. R. P. Reed and R. P. Mikesell, "Low Temperature Properties of Selected Copper Alloys", J. Mat. 2 (1967) pp. 370-392.

5. R. P. Reed and C. J. Guntner, "Stress-Induced Martensitic Transformations in 18Cr-Ni Steel," Trans. Met. Soc. AIME 230 (1964), pp. 1713-1720.

6. J. C. Ho, G. B. King, and F. R. Fickett, "Low Temperature Specific Heat of Two Stainless Steels," Cryogenics 18 (1978) pp. 296-298.

7. J. M. Corsan and N. I. Mitchem, "The Specific Heat of Stainless Steels Between 4 K and 300 K," in Proceedings of the Sixth International Cryogenics Engineering Conference (IPC Science and Technology, Surrey, England, 1976) pp. 342-344.

8. F. J. Jelinek and E. W. Collings, "Low-Temperature Thermal Expansion and Specific Heat Properties of Structural Materials," in Materials Research for Superconducting Machinery - Part 4 (1975). Available from NTIS, Order Number ADA 019230.

9. D. T. Read, R. P. Reed, and R. E. Schramm, "Low Temperature Deformation of Fe-18CR-8Ni Steel, in this volume.

LIST OF TABLES

Table 1. Chemical composition as supplied by the manufacturer of the AISI 304L alloy used in the present study.

Table 2. Strain rates used, as calculated from crosshead speeds and effective gage length used in the present study, assuming no work hardening.

Table 3. Parameters used in adiabatic heating calculations.

Table 1. Chemical computation, as supplied by the manufacturer, of the AISI 304L alloy used in the present study.

Cr	Ni	Mn	Mo	Ph	Si
18.5	8.75	1.43	.29	.025	.31

S	C	N	Co	Cu	Fe
.013	.030	.061	.18	.14	bal

Table 2. Strain rates as calculated from crosshead speeds and gage effective length used in the present study, assuming no work hardening.

Crosshead Speed (cm/min)	Strain Rate (per second)
5×10^{-4}	2×10^{-6}
2×10^{-2}	8×10^{-5}
5×10^{-1}	2×10^{-3}

Table 3. Parameters used in adiabatic heating calculations.

Symbol	Meaning	Value
P	load	8 kN
ΔX	specimen length change	1.27×10^{-4} m
ℓ	specimen length heated	5×10^{-3} m
A	cross sectional area	1.2×10^{-5} m^2
ν	specimen volume heated = $\ell \cdot A$	6×10^{-8} m^3
ρ	specimen density	7.9×10^{-3} kg/m^3
$\partial\sigma/\partial T$	thermal softening coefficient	2.5 MPa/K
$\partial\sigma/\partial\varepsilon$	work hardening coefficient	1500 MPa
κ	load train compliance	2.6×10^{-7} m/N
C (50K)	specific heat at 50 K	88 J/kg K

LIST OF FIGURES

Figure 1. Flat tensile specimen with thermocouple and superconductive wire for detection of temperature rises.

Figure 2. Typical stress strain curve for AISI 304L at 4 K.

Figure 3. Strain required to initiate serrated yielding and magnitude of the first detectable load drop, as a function of crosshead speed.

Figure 4. Yield strength at 4 K plotted against crosshead speed.

Figure 5. Histogram showing the frequency of stress drop magnitudes for one specimen strained to failure at 4 K.

Figure 6. Histogram showing the frequency of temperature rise magnitudes recorded by thermocouple in one specimen strained to failure at 4 K.

Figure 7. Profile of the temperature rise which occurs during a load drop, as calculated from the distribution of temperature rises occurring at one point. The smooth curve is a hand-drawn interpolation.

Figure 8. Photograph of a tensile specimen strained through one load drop, decorated with iron powder.

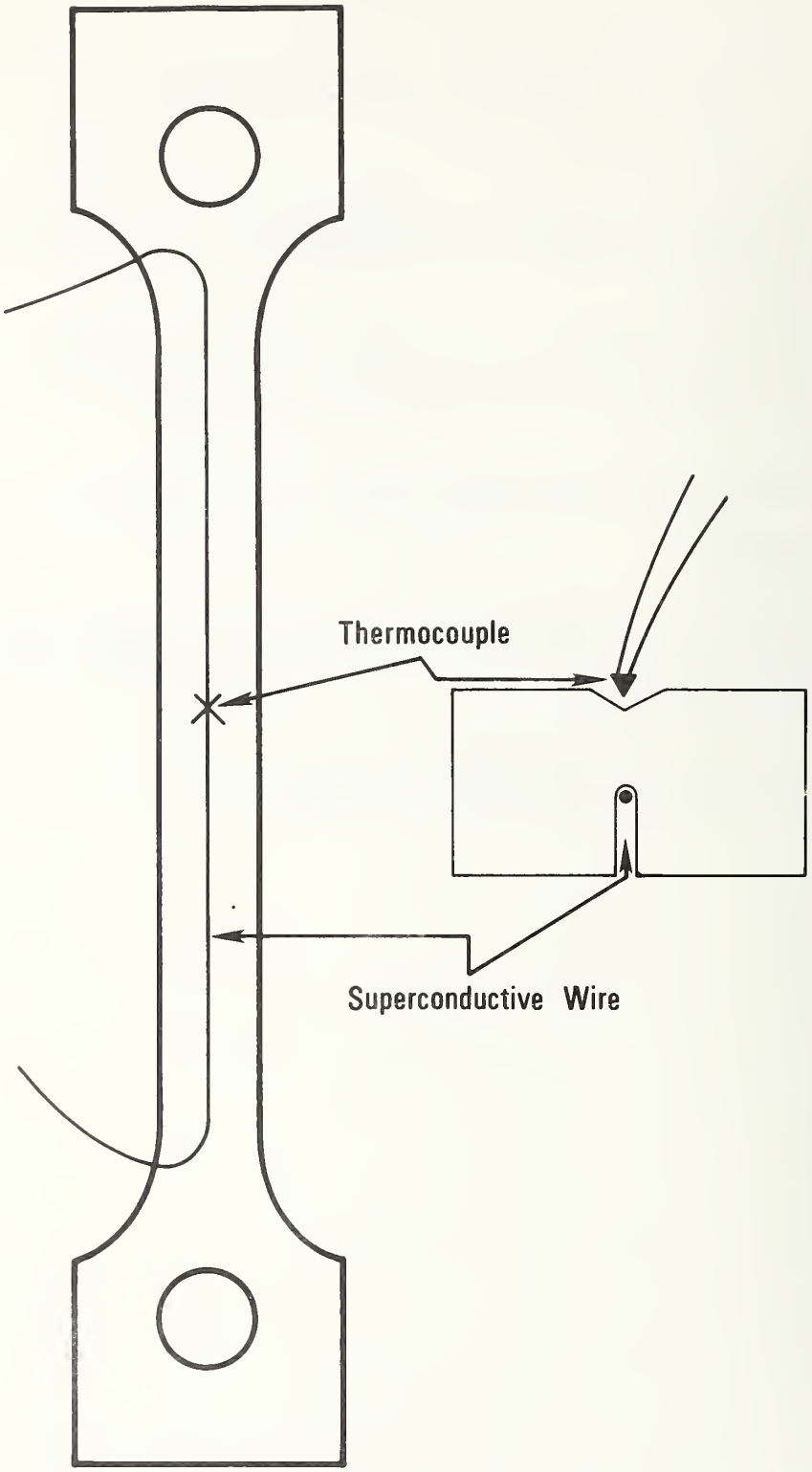

Figure 1. Flat tensile specimen with thermocouple and superconductive wire for detection of temperature rises.

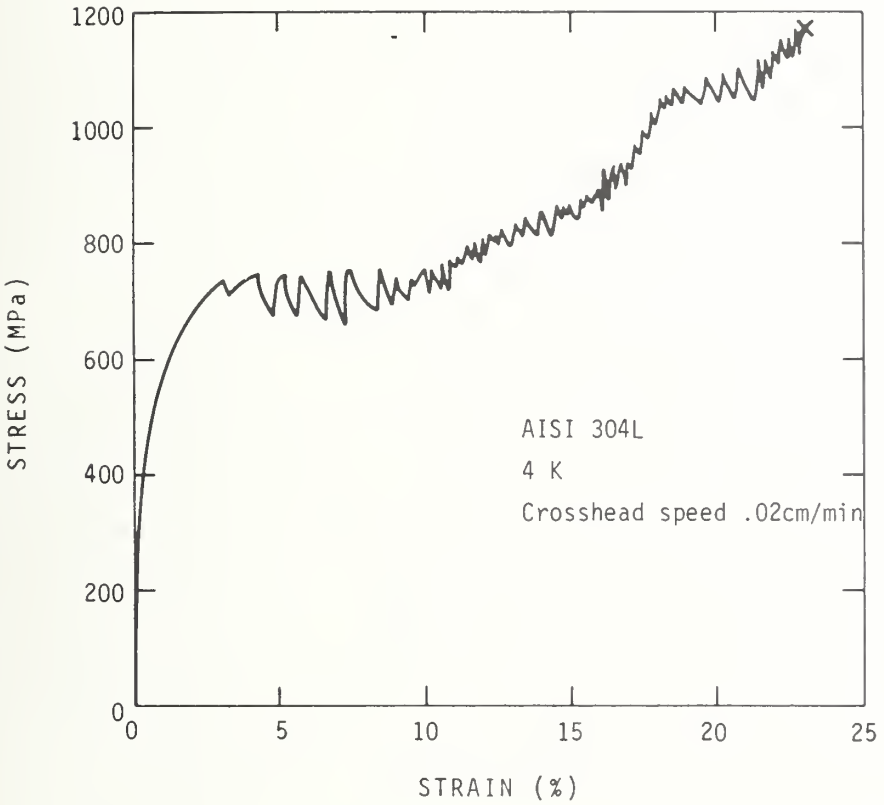

Figure 2. Typical stress-strain curve for AISI 304L at 4 K.

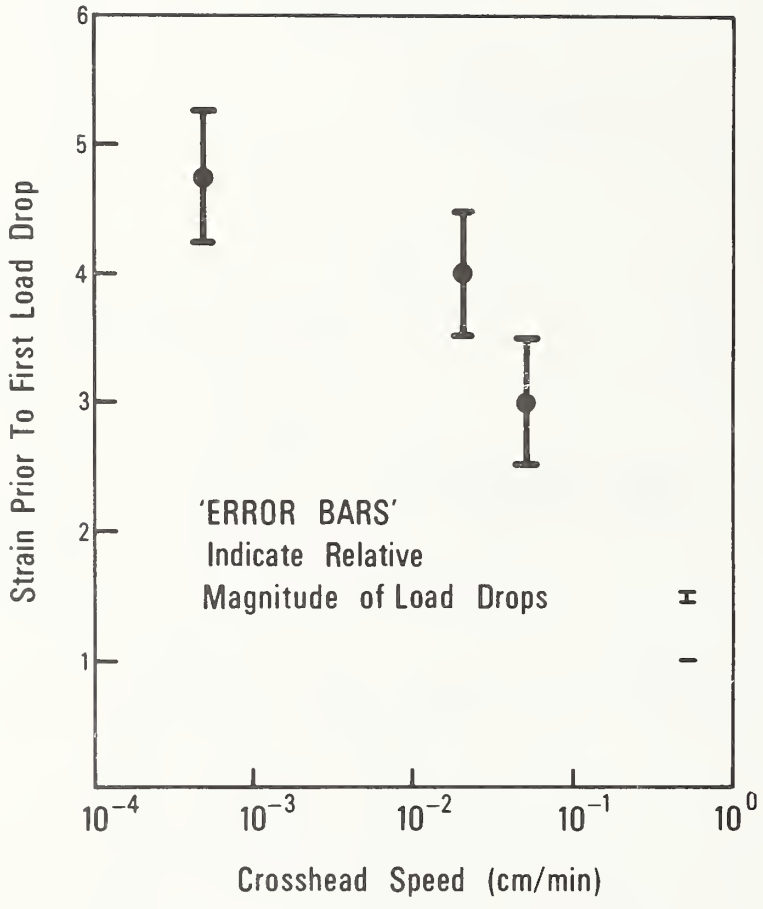

Figure 3. Strain required to initiate serrated yielding and magnitude of the first detectable load drop, as a function of crosshead speed.

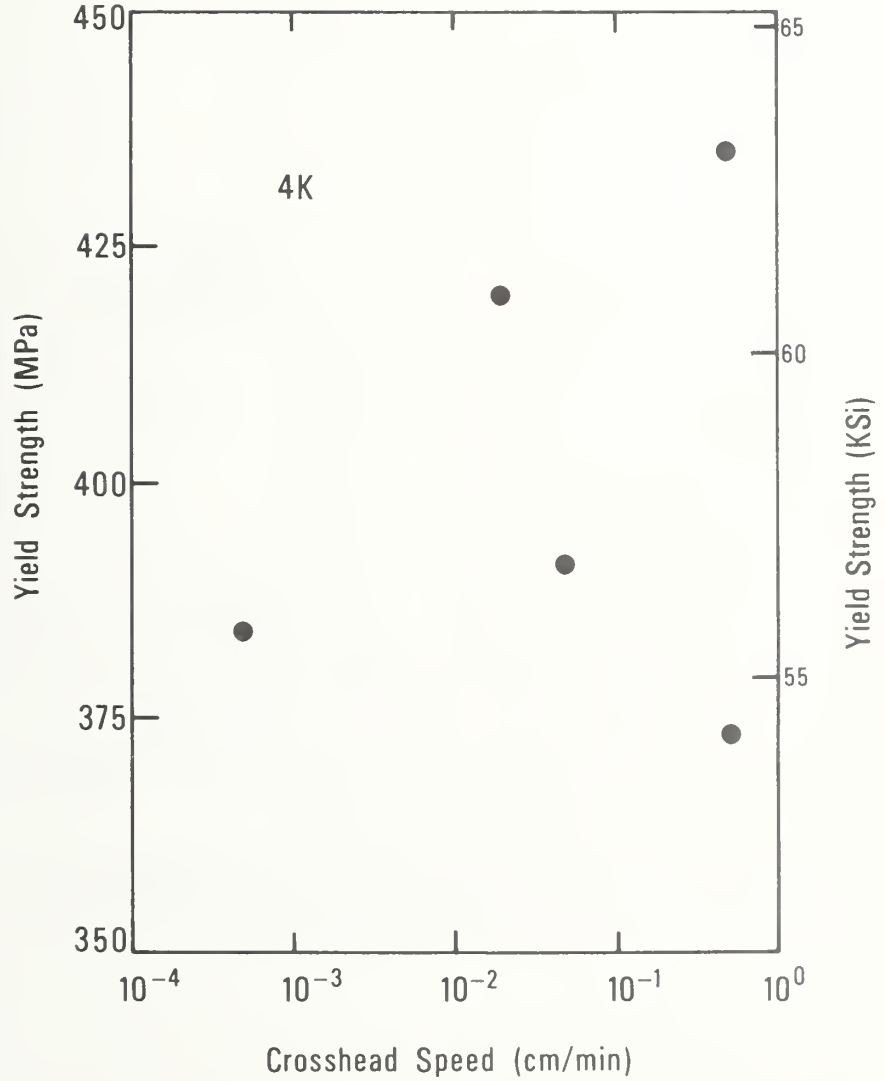

Figure 4. Yield strength at 4 K plotted against crosshead speed.

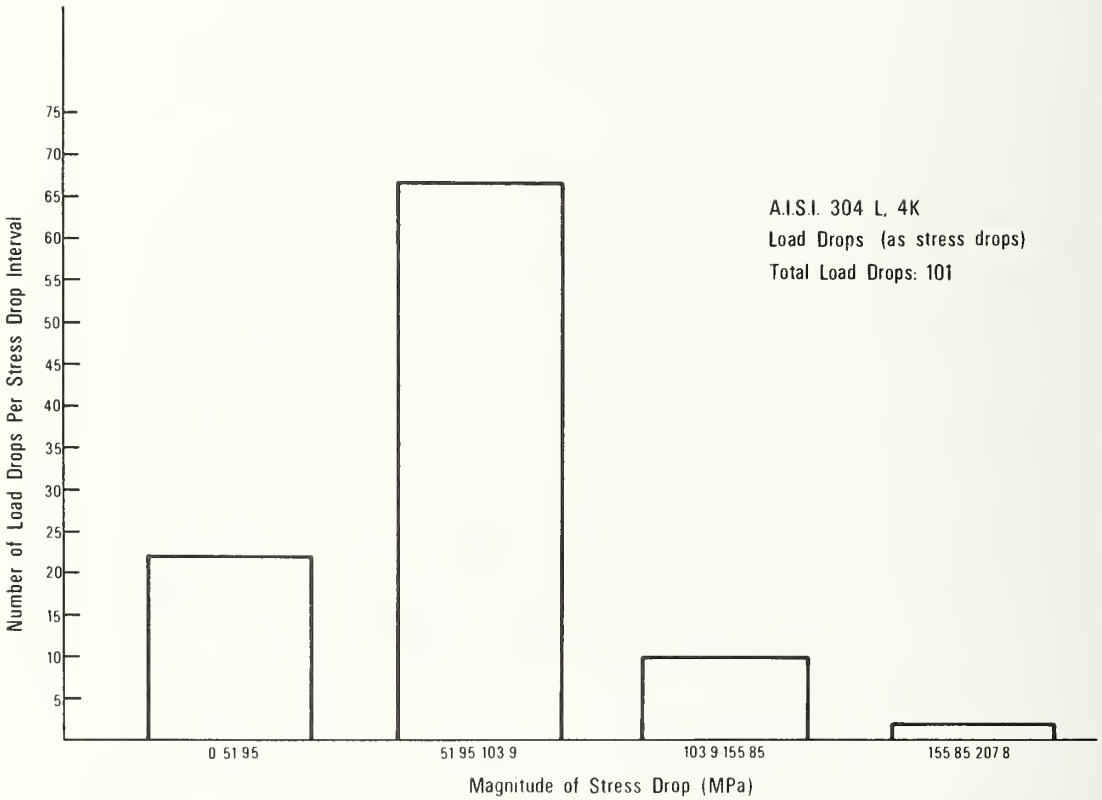

Figure 5. Histogram showing the frequency of stress drop magnitudes for one specimen strained to failure at 4 K.

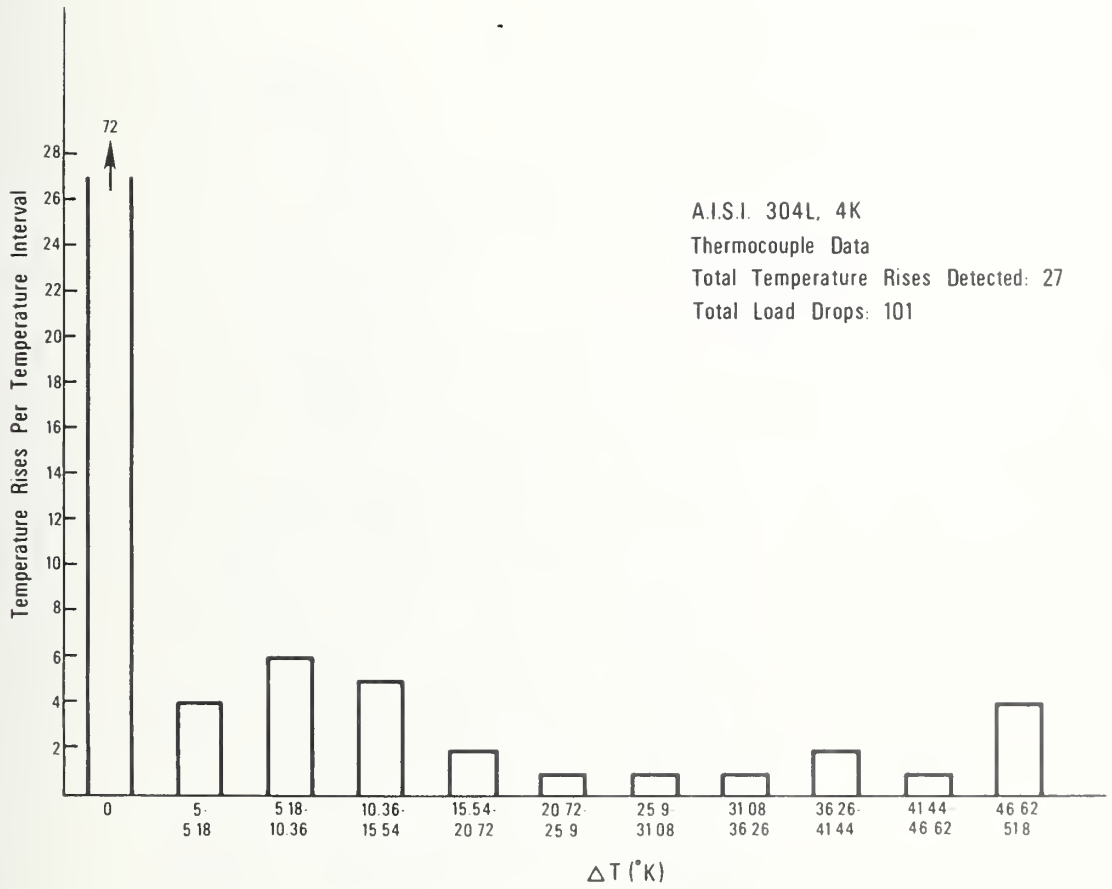

Figure 6. Histogram showing the frequency of temperature rise magnitudes recorded by thermocouple in one specimen strained to failure at 4 K.

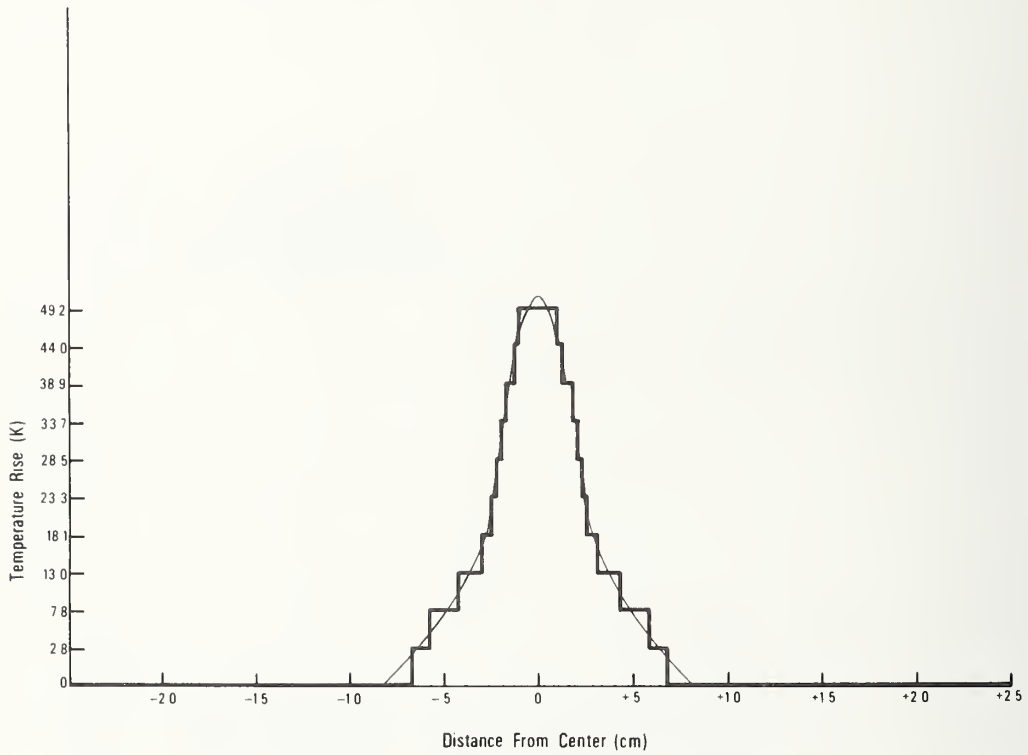

Figure 7. Profile of the temperature rise which occurs during a load drop, as calculated from the distribution of temperature rises occurring at one point. The smooth curve is a hand-drawn interpolation.

Figure 8. Photograph of a tensile specimen strained through one load drop, decorated with iron powder.

LOW TEMPERATURE DEFORMATION OF Fe-18Cr-8Ni STEEL

National Bureau of Standards

LOW TEMPERATURE DEFORMATION OF Fe-18Cr-8Ni STEEL*

D. T. Read, R. P. Reed, and R. E. Schramm
Fracture and Deformation Division
National Bureau of Standards
Boulder, CO 80303

*Work supported by DOE/OFE. Contribution of NBS, not subject to copyright.

ABSTRACT

The flow strengths of an Fe-18Cr-8Ni austenitic alloy were measured over the temperature range 4-300 K. This alloy did not transform martensitically on cooling but did transform to two martensitic products α' (body-centered-cubic, ferromagnetic) and ε (hexagonal-close-packed, non-ferromagnetic) during deformation. Volume percentages of the austenite and martensite phases which formed during deformation and stacking fault and twin fault probabilities of the austenite were measured as a function of strain at 4 K using x-ray and magnetic techniques. The flow strengths were measured over the temperature range 4-320 K at constant strain rate. The temperature dependence of the yield strength was anomalous, with a peak near 200 K and a minimum near 100 K, followed by steadily increasing strength to 4 K. These features have been attributed to the formation during deformation of the martensitic phases. Similar to previous results, the hexagonal-close packed phase (ε) increased to a maximum of about 20 percent at about 10 percent strain, then decreased with additional deformation. The body-centered phase (α') increased continuously as a function of strain. Stacking fault probability decreased as the ε martensite content increased. Martensite contents and fault probabilities were found to be independent of strain rate at 4 K. Discussion is presented on the role of the martensitic transformation in affecting deformation of austenitic alloys.

INTRODUCTION

Despite widespread use and study of metastable austenitic stainless steels at cryogenic temperatures, the tensile behavior of these alloys under various conditions of temperature, strain rate and cold work are not understood. These steels are extremely complex. Lower nickel, Fe-Cr-Ni austenitic steels have a magnetic transformation from paramagnetic to antiferromagnetic states with the Néel temperature usually near 60 K. Higher nickel, Fe-Cr-Ni austenitic steels have a more complex magnetic transformation; the low temperature state is now thought to represent a spin-glass type condition of localized ferromagnetic spins, dispersed randomly. Most AISI 300 series grades of austenitic stainless steels do not transform martensitically on cooling (i.e. M_s temperature < 0 K) but do transform on deformation at low temperatures to two martensitic products: (1) α' (body-centered cubic, ferromagnetic) and (2) ε (hexagonal close packed, either paramagnetic, antiferromagnetic or spin-glass magnetic state). Furthermore, in the Fe-18Cr-8Ni grades the stacking fault energy (γ) is low at room temperature ($\sim$ 20 erg/cm^2) and decreases toward zero at low temperatures. This low stacking fault energy insures the formation of many stacking faults during low temperature deformation.

Some studies have reported anomalous flow strength behavior for Fe-Cr-Ni base austenitic steels at low temperatures. Breedis and Robertson[1] found that as the M_s (α') temperature (241 K) of Fe-16Cr-12Ni single crystals was approached from higher temperatures the critical resolved shear stress decreased to zero. Deviations from the normal temperature dependence were apparent up to about 100 K above the M_s temperature. Stone and Thomas[2] also reported decreased critical resolved shear stress

at low temperatures (180-190 K) for Fe-15Cr-15Ni single crystals. Sato et al[3] conducted a series of tensile tests on Fe-18Cr-14Ni single crystals in the temperature range 170-430 K. Their tensile measurements indicate a clearly defined temperature (243 K) at which the flow stress begins to decrease. This decrease was attributed to hexagonal martensite formation, and 243 K was described as the $M_d(\varepsilon)$ temperature. From examination of specimen surface morphology, Sato et al concluded that below 243 K the dominant shear system was $\{111\}\ \langle 11\bar{2}\rangle$ and at higher temperatures the more conventional $\{111\}\ \langle 1\bar{1}0\rangle$ system was observed. Higo et al[4], working with perhaps the same Fe-18Cr-14Ni single crystals, had earlier found the same flow-strength temperature trends and postulated $\{111\}\ \langle 11\bar{2}\rangle$ shear systems in the austenite.

Measurements by Ilichev and Skibina, described by Verkin[5], from 4 to 300 K on Fe-18Cr-8Ni, Fe-18Cr-10Ni and Fe-18Cr-20Ni single crystals indicate the possibility for three separate dips of the yield-strength temperature dependence.

Measurements indicating strength reductions at lower temperatures for polycrystalline Fe-Cr-Ni austenitic stainless steels have been performed by Mirzayev et al[5] and Suzuki et al[7,8]. Tensile yield strengths of the alloys Fe-18Cr-10Ni and Fe-18Cr-13Ni alloys were measured from 77 to 670 K by Mirzayev et al. Above the $M_s(\alpha')$ temperature, a reduction of yield strength of about 20 percent was observed from higher temperature values. Contrasted to the single crystal results, as the $M_s(\alpha')$ temperature was approached, the yield strength again started to rise. The resultant yield strength temperature dependence was a dip (of about 20 percent) between the $M_s(\alpha')$ temperature and about 50 to 100 K above this temperature. This decrease of flow strength at low temperatures was

attributed to the transformation to ε martensite. Suzuki et al[7,8] also have conducted tensile measurements between 77 and 400 K on polycrystalline Fe-18Cr-9Ni alloys. Within the temperature interval where the flow stress is decreasing with decreasing temperature they have identified two distinct flow stresses. The lower stress corresponds to the proportional limit and to the stress at which ε martensite forms (although the technique for ε martensite observation is not clear). The higher stress corresponds to the stress at which α' martensite is first detected magnetically. The yield strength (0.2% offset) corresponds to the temperature dependence of the lower, ε-associated stress.

On the other hand, most research on TRIP steels, in which flow stress decreases at decreasing temperatures have also been identified, correlate flow strength with α' martensite content. Olsen and Azrin[9], working with a polycrystalline Fe-9Cr-8Ni-2Si-0.2, 0.3C alloy have associated the flow strength (0.2%) with the stress necessary to form 0.01 volume fraction α'. Below the temperature (∿ 320 K) at which the strength begins to decrease, the temperature dependence of both stresses coincide.

This paper measures the low temperature dependence of the flow strengths for a standard, commercially available AISI 304L. In this alloy the flow strengths were also found to dip at intermediate low temperatures. Associated magnetic and x-ray data are presented to identify the controlling transformation for low temperature deformation of this alloy.

MATERIAL

The material was a 2.5 cm (1 inch) plate of AISI 304L stainless steel obtained in the mill-annealed condition. Its chemistry is shown

in Table 1. Flat tensile specimens in the longitudinal orientation with a gage section 2.5 mm (0.1 inch) thick by 4.8 mm (.19 inch) wide by 30 mm (1.2 inch) were used for all tests. The nominal grain diameter was 45 μm and the hardness Rockwell B-79.

After machining, tensile specimens were annealed in vacuum, at 1000°C for 1 hour to remove possible cold work. The specimens were removed from the furnace still under vacuum and allowed to cool. These specimens were used for measurements of yield strength versus temperature. After testing to one percent strain, the specimens were reannealed under the same conditions and retested. Some specimens were tested and annealed a total of four times. Grain sizes ranged from 40 to 60 μm after the initial anneal to 60 to 80 μm after four anneals. Some flow strength (0.2% offset) dependence on grain size was detected at temperatures lower than 100 K, but little dependence was apparent above 100 K. All data points, independent of grain size (40-80 μm), are included in this report.

The observed $M_s(\alpha')$ and $M_s(\varepsilon)$ temperatures were below 4 K for this alloy. A calculated transition temperature of $M_s(\alpha') = 53$ K was obtained, following Larbalestier and King[10] who used the work of Eichelman and Hull and Hammond on austenitic ($\gamma \rightarrow \alpha'$) stability equations for Fe-Cr-Ni steels. The calculated $M_d(\alpha')$ temperatures, using the formula developed by Angel[11] for 30 to 50 percent tensile deformation, is 288 K.

TECHNIQUES AND APPARATUS

The tensile tests were carried out using a standard tensile machine with the capability for variable crosshead speeds. A cryostat arrangement developed by Reed[12] was used for tensile tests at 4 K. Displacement

gages as described by Reed and Mikesell[13] were used to measure specimen strain. This system was modified for use from 4-320 K with the addition of a reservoir for liquid nitrogen or liquid helium on the upper pull rod, heaters on both the upper and lower specimen grips, and electrical resistance thermometers (platinum for temperatures above 76 K, carbon for lower temperatures). The apparatus is shown in Fig. 1. Liquid level sensors, variable-output power supplies for the heaters, and amplification and readout electronics for the thermometers were used with the equipment shown in Fig. 1. All x-ray and magnetic measurements were conducted at room temperature. The body-centered cubic, ferromagnetic, α' martensite, was measured using both x-ray diffraction and magnetic techniques. The hexagonal close packed, ε martensite was only measured by x-ray techniques.

Magnetic measurements were carried out using a commercially-supplied apparatus incorporating a permanent bar magnet on an adjustable helical spring. From these measurements the α' concentration can be calculated, using a previously established relationship between α' and magnetic susceptibility[6].

The x-ray measurements were conducted as follows. The integrated intensity of x-ray diffraction lines is an indicator of the volume fraction of each crystallographic phase present. Assumming random orientation[15-17]:

$$I_{x\beta} = [A\, m_{x\beta}(LP)\, F^2_{x\beta}\, e^{-2M}/v^2_{\beta}]V_{\beta} \qquad (1)$$

where $I_{x\beta}$ = diffracted intensity for line x of the β-phase, A = constant, $m_{x\beta}$ = multiplicity factor, LP = Lorentz-polarization factor =

$1 + \cos^2 2\theta/\sin^2 \theta\cos\theta$ where θ = Bragg angle for line x, $F_{x\beta}$ = structure factor for line x of phase β, e^{-2M} = temperature factor, v_β = volume of unit cell of phase β and V_β = volume of phase β.

For convenience the above equation can be abbreviated

$$I_{x\beta} = K_\beta V_\beta \tag{2}$$

where K_β is a constant for each diffraction line of phase β.

The diffraction lines used for the three phases are: $(200)\gamma$, $(200)\alpha'$ and $(10\bar{1}1)\varepsilon$. The radiation was Co Kα. Hence, the calculated values of K_γ and K_ε relative to K_α, are

$$K_\varepsilon = 4.5K_\alpha, \tag{3a}$$

and

$$K_\gamma = 2.3K_\alpha, \tag{3b}$$

where γ refers to the austenite phase. Lattice parameter values used to obtain these ratios were 2.866 Å, for α'3.589 Å for α and a = 2.54 Å and c = 4.15 Å for ε[15]. Dispersion by the K electrons caused corrections to the atomic scattering factor (contained within $F_{x\beta}$) estimated as -3.9% for all phases[18]. Estimates of temperature factors and atomic scattering factors were from Cullity[16].

With the volume of α' known from magnetic measurements, the volume of ε can be obtained from

$$V_\varepsilon = I_{x\varepsilon}/K_\varepsilon = I(10\bar{1}1)_\varepsilon /4.5\, K_{\alpha'} = [I(10\bar{1}1)_\varepsilon/I(200)_{\alpha'}V_{\alpha'}/4.5] \tag{4}$$

and the volume of retained austenite is easily obtained using

$$V_\gamma = 1 - V_\varepsilon - V_{\alpha'}, \qquad (5)$$

Discrete intensity measurements were made at 0.04° 2θ intervals on a diffractometer across entire diffraction lines. The background was computed from a straight line fitted to average intensity values on either extreme of the lines. Numerical integration by the trapezoidal rule provided the diffraction peak area. Three separate independent background and intensity measurements were averaged.

Errors in the magnetic measurement of α' volume are about ± 2% and the x-ray measurements are estimated to have a precision of about ± 6%. Analysis of repeated measurements of ε at two strains led to a probable error in γ of less than ± 7%.

Stacking faults on the (111) plane in austenite result in a decreased separation of the peak positions of the (111) and (200) diffraction lines. A quantitative measure of the probability of these defects, α, comes from comparing this line separation between annealed and cold-worked specimens[19]

$$(2\theta_{200} \; 2\theta_{111})_{CW} \; (2\theta_{200} \; 2\theta_{111})_{AM} = 45\sqrt{3}/\pi^{-2}(\tan\theta_{200} + 1/2 \tan\theta_{111})\alpha \qquad (6)$$

Peak positions were determined by measuring diffracted intensity at five to seven 2θ positions centered around the peak, fitting this data to a parabola and calculating its maximum. Probable imprecision on stacking fault probability is ± 4 x 10^{-3}.

Twin faults produce an asymmetry of the diffraction line as measured by the difference between the center of gravity and the position of the peak maximum[20]. Here

$$\Delta CG(^\circ 2\theta)_{111} - \Delta CG(^\circ 2\theta)_{200} = (11 \tan\theta_{111} + 14.6 \tan\theta_{200})\beta \qquad (7)$$

where ΔCG = center of gravity - peak maximum and β = twin fault probability. Because of instrumental asymmetry, the values of ΔCG need correction by comparison with an annealed standard[21]. The center of gravity calculation came from the profile measurements noted above[22]. An error estimate of β is $\pm 7 \times 10^{-3}$.

RESULTS AND DISCUSSION

Temperature Dependence of the Flow Strength

The temperature dependence of the flow strength at 0.2 percent strain (corresponding to the conventional yield strength) is shown in Fig. 2. There is a pronounced decrease in flow strength beginning on cooling at about 200 K. A minimum is reached near 100 K, about 15 percent lower than the 200 K flow strength. Below 100 K, the flow strength at 0.2 percent strain rises very steeply to 4 K. Although there is some data scatter, the possibility for the existence of three dips in the temperature dependence of the flow strength reported by Verkin[5] seems remote.

The anomalous flow strength behavior at low temperatures is primarily confined to low plastic strains. The temperature dependence of the flow strength at 1.0 percent strain is presented in Fig. 3. While

the trend continues with the temperature dependence changing near 200 K on cooling, there is no longer a decrease in strength from 200 to 100 K. At higher strains the plateau of strength versus temperature observed between 100 to 200 K becomes more obscure.

As discussed earlier, other studies have identified either the hexagonal close packed (ε) phase[5-8] or the body-centered cubic (α') phase[9] as the transformation product controlling the early stages of deformation in polycrystalline austenitic alloys. Any model must explain two phenomena: (1) the abrupt decrease of the flow strength at about 200 K with decreasing temperature and (2) the abrupt increase of the flow strength near 100 K with decreasing temperature. X-ray and magnetometry experiments are now in progress to measure the amounts of austenite and ε and α' during the early stages of deformation at 200, 100 and 4 K. These measurements are not easy since the amounts of ε and α' are of the order of 1 percent.

Dependence of Martensitic Transformations on Plastic Deformation at 4 K

The volume percentages of austenite, ε and α' as a function of plastic deformation at 4 K were estimated using x-ray (ε) and magnetic measurements (α'). The results are presented in Fig. 4.

There is a linear dependence of percent α' formed at low temperatures as a function of strain. If the data of earlier measurements[9,15,23-24] on austenitic Fe-Cr-Ni alloys at 4 and 77 K are evaluated, the same conclusion is reached. However, there is marked quantitative discrepancy in the dependence of α' formation on deformation that cannot be adequately explained through use of current stability equations for M_s[10] or M_d[11] temperatures. There is no apparent correlation strain between either calculated $M_s(\alpha')$ or $M_d(\alpha')$ temperatures and percent α' formed at constant strain.

The hexagonal close-packed martensite phase initially increases with increased strain, then decreases at higher strains. The decrease of ε has led many to conclude that the ε phase transforms to α'. Presumably at higher strains (above approximately 10 percent elongation) the effects of higher flow stresses and austenite partitioning combine to retard the austenite to ε transformation.

The dependence of the stacking fault and twin fault probabilities on plastic deformation at 4 K, shown in Fig. 5, have not been previously reported. The stacking fault probability decreases at low strains, reaches a minimum at approximately 10 percent strain and increases at higher strains. These data correspond very well with the dependence of the volume percent hexagonal phase on strain; the presence of stacking faults and hexagonal phase are inversely related. A net reduction in the number of stacking faults present in a deformed material implies that these existing stacking faults are forming hexagonal martensite (or, less likely, α' martensite) faster than they are being generated. However, at higher strains, the process is reversed; presumably the newly formed stacking faults are not acting as nuclei for either ε or α' martensite and, thus, increase in density. Furthermore, the rate of ε formation is now exceeded by the rate of formation of α' martensite from ε.

Deformation twin fault density is shown in Fig. 5 to remain constant with strain. The magnitude of twin fault density scatters about the value for the annealed condition (3×10^3), indicating the absence of measurable formation of deformation twins in this alloy. However, examples of twin fault formation have been reported in an Fe-18Cr-7Ni-0.18C steel deformed 20 percent at 380 K[25].

CONCLUSIONS

The following may be concluded from this study of the temperature dependence of flow strength and deformation behavior of an Fe-18Cr-8Ni stainless steel:

(1) The temperature dependence of the flow strength is anomalous, with a peak near 200 K and a minimum near 100 K.

(2) The volume percent of strain-induced body-centered cubic martensite is linearly dependent on strain and independent of strain rate at 4 K.

(3) The volume percent of strain-induced hexagonal close-packed martensite at 4 K reaches a maximum near 10 percent strain.

(4) The number of strain-induced stacking faults at 4 K reach a minimum near 10 percent strain.

ACKNOWLEDGEMENTS

The authors wish to express their thanks to David Burkhalter, who conducted many of the tensile tests in this study. The work was supported by the Office of Fusion Energy, Department of Energy.

REFERENCES

1. J. F. Breedis and W. D. Robertson, "Martensitic transformation and plastic deformation in iron alloy single crystals," Acta Met. 11 (1963), pp. 547-559.

2. G. Stone and G. Thomas, "Deformation induced alpha and epsilon martensites in Fe-Ni-Cr single crystals," Metall. Trans. 5 (1974), pp. 2095-2102.

3. A. Sato, Y. Sunaga and T. Mori, "Contribution of the $\gamma \rightarrow \varepsilon$ transformation to the plastic deformation of stainless steel single crystals," Acta Met. 25 (1977), pp. 627-634.

4. Y. Higo, F. LeCroisey and T. Mori, "Relation between applied stress and orientation relationship of α' martensite in stainless steel single crystals," Acta Met. 22 (1974), pp. 313-323.

5. B. I. Verkin, "The development of cryogenic materials science in the USSR," Advances in Cryogenic Engineering, Vol. 24, R. P. Reed, A. F. Clark, K. Timmerhaus, Editors, Plenum Press, New York (1977).

6. D. A. Mirzayev, Yu. N. Goykdenberg, M. M. Shteynberg and S. V. Rushchin, "The elasto-plastic strain effects in alloys with low stacking fault energy at temperatures above M_s," Phys. Metals Metalloy. 35, No. 6 (1973) pp, 81-87.

7. T. Suzuki, H. Kojima, K. Suzuki, T. Hashimato, S. Koike and M. Ichihara, "Plastic deformation and martensitic transformation in an iron-base alloy," Sripta Met. 10 (1976), pp. 353-358.

8. T. Suzuki, H. Kojima, K. Suzuki, H. Hashimato and M. Ichihara, "An experimental study of the martensite nucleation and growth in 18/8 stainless steel," Acta Met. 25 (1977), pp. 1151-1162.

9. G. B. Olson and M. Azrin, "Transformation behavior of TRIP steels," Metall. Trans. A. 9A (1978), pp. 713-721.

10. D. C. Larbalestier and H. W. King, "Prediction of the low-temperature stability of type 304 stainless steel from a room temperature deformation test," Proc. Intn. Cryogenic Engr. Conf., IV, Eniehoven, Netherlands (May 1972).

11. T. Angel, "Formation of martensite in austenitic stainless steels," J. Iron Steel Inst. 177 (1954), pp. 165-174.

12. R. P. Reed, "A cryostat for tensile tests in the temperature range 300 to 4 K," Adv. Cryo. Eng. 7 (1961), pp. 448-454.

13. R. P. Reed and R. P. Mikesell, "Low temperature properties of selected copper alloys," J. Mat. 2 (1967), pp. 370-392.

14. R. P. Reed and R. P. Mikesell, "The stability of austenitic stainless steels at low temperatures as determined by magnetic measurements," Adv. Cryo. Eng. 4 (1960), pp. 84-100.

15. R. P. Reed and C. J. Guntner, "Stress-inducted martensitic transformations in 18Cr-8Ni steel," Trans. Met. Soc. AIME 230 (1964), pp. 1713-1720.

16. B. D. Cullity, Elements of X-ray Diffraction, Addison-Wesley Pub. Co., Inc., Reading, MA (1956), pp. 389, 395, 460, 475 and 477.

17. B. L. Averbach, M. F. Camerford and M. B. Bever, "An x-ray method for the determination of beta phase in a titanium alloy," Trans. Met. Soc. AIME 215 (1959), pp. 682-685.

18. R. W. James, The Optical Principles of the Diffraction of X-rays, G. Bell & Sons, Ltd., London (1954), p. 608.

19. R. E. Schramm and R. P. Reed, "Stacking fault energies of fcc Fe-Ni alloys by x-ray diffraction line profile analysis," Met. Trans. 7A (1976), pp. 359-363.

20. J. B. Cohen and C. N. J. Wagner, "Determination of twin fault probabilities from the diffraction patterns of fcc-metals and alloys," J. Appl. Phys. 33 (1962), pp. 2073-2077.

21. E. N. Aqua and C. N. J. Wagner, "An x-ray diffraction study of the effect of rhenium on the occurence of faulting in refractory alloys," Office of Naval Research, Tech Rep. No. 11, Contract NONOR609(43), 1964.

22. R. E. Schramm, "Corrections and calculations on an x-ray diffraction line profile: a computer program," National Bureau of Standards, Boulder, CO.

23. G. Blanc, R. Tricot and R. Castro, "Transformations martensitiques dans les aciers inoxydables austenitiques Fe-Cr-Ni," Mem. Sci. Rev. Metall. 70 (1973), pp. 527-541.

24. H. C. Fielder, B. L. Averbach and M. Cohen, "The effect of deformation on the martensitic transformation in austenitic stainless steel," Trans. ASM 47 (1954), pp. 267-286.

25. L. Remay and A. Pineau, "Observation of stacked layers of twins and ε martensite in a deformed austenitic stainless steel," Metall. Trans. 5 (1974), pp. 963-965.

Table 1. Chemical composition, as supplied by the manufacturer, of the AISI 304L.

Cr	Ni	Mn	Mo	Ph	Si
18.5	8.75	1.43	.29	.025	.31

S	C	N	Co	Cu	Fe
.013	.030	.061	.18	.14	bal

LIST OF FIGURES

Fig. 1 Apparatus used for variable temperature tensile tests.

Fig. 2 Yield strength (0.2 percent strain) of AISI 304L in the temperature range 4-320 K. The minimum near 100 K and the peak near 200 K are anomalous features.

Fig. 3 Flow strength at 1 percent strain of AISI 304L in the temperature range 4-320 K.

Fig. 4 Martensite and parent phase contents as functions of strain at 4 K for three crosshead speeds, with hand-drawn trend lines.

Fig. 5 Stacking and twin fault probabilities as functions of strain at 4 K for three crosshead speeds, with hand-drawn trend lines.

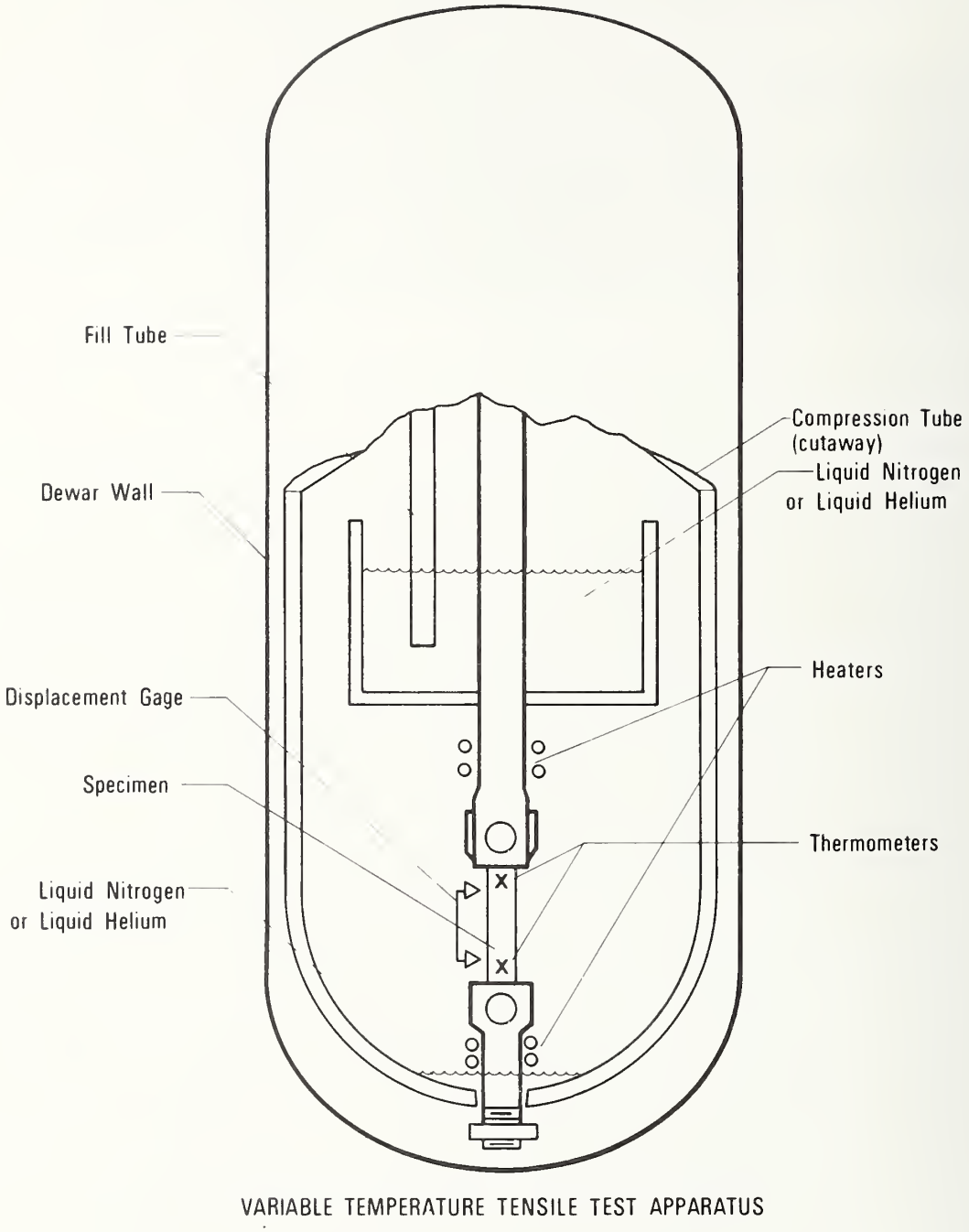

Fig. 1 Apparatus used for variable temperature tensile tests.

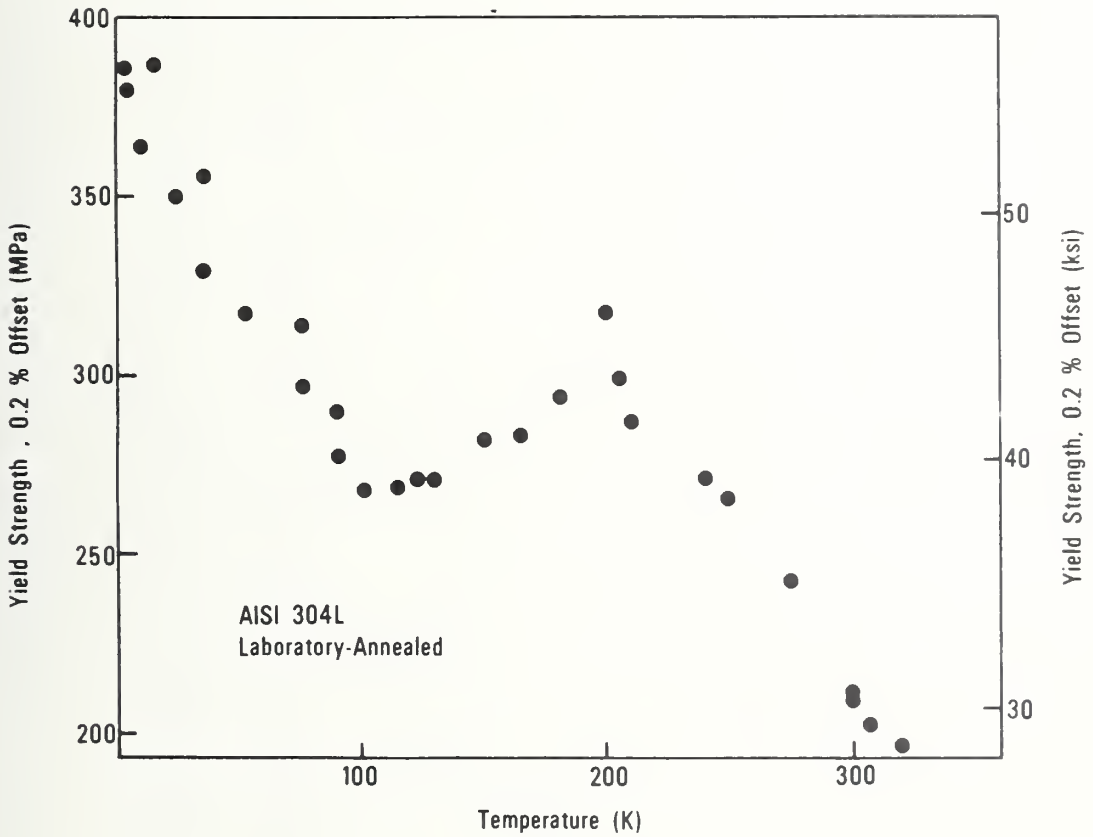

Fig. 2 Yield strength (0.2 percent strain) of AISI 304L in the temperature range 4-320 K. The minimum near 100 K and the peak near 200 K are anomalous features.

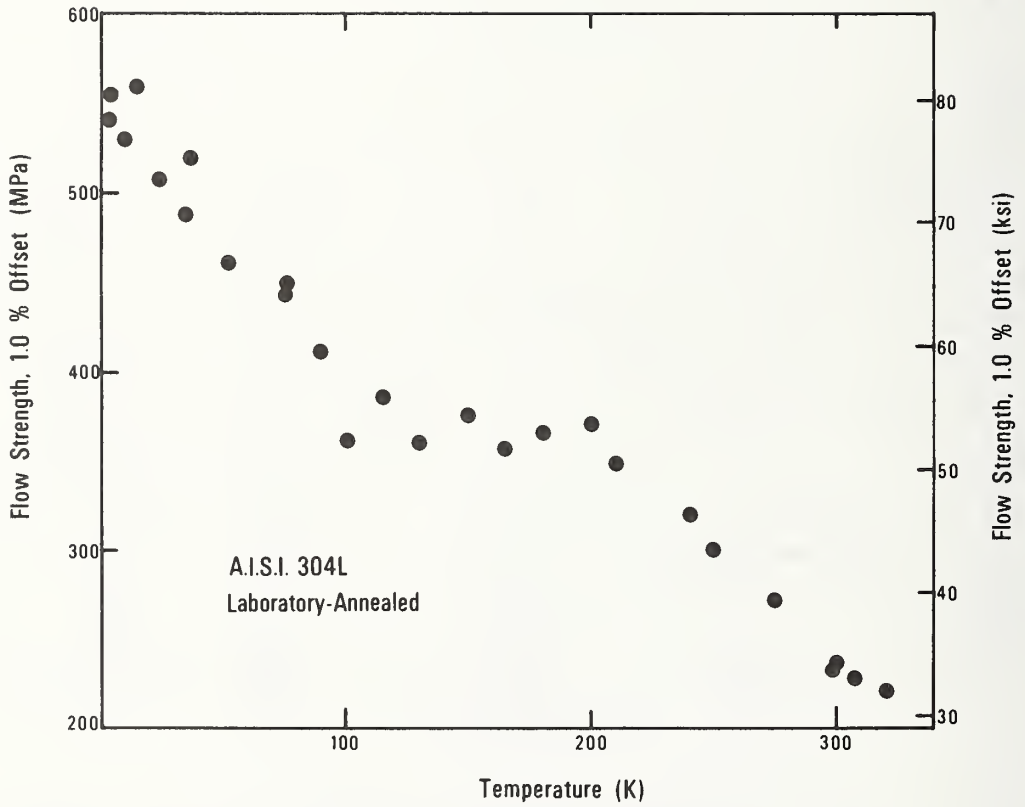

Fig. 3 Flow strength at 1 percent strain of AISI 304L in the temperature range 4-320 K.

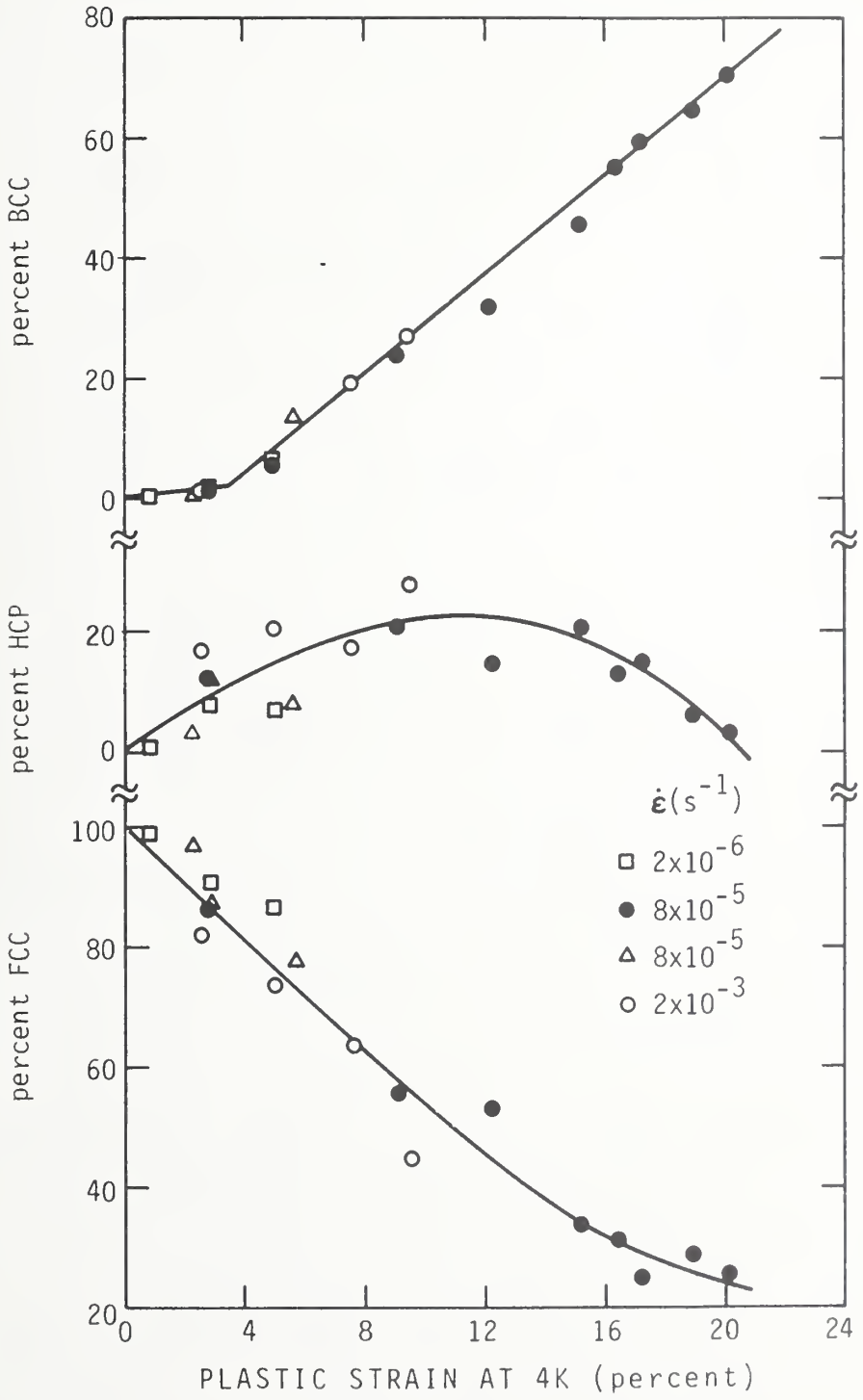

Fig. 4 Martensite and parent phase contents as functions of strain at 4 K for three crosshead speeds, with hand-drawn trend lines.

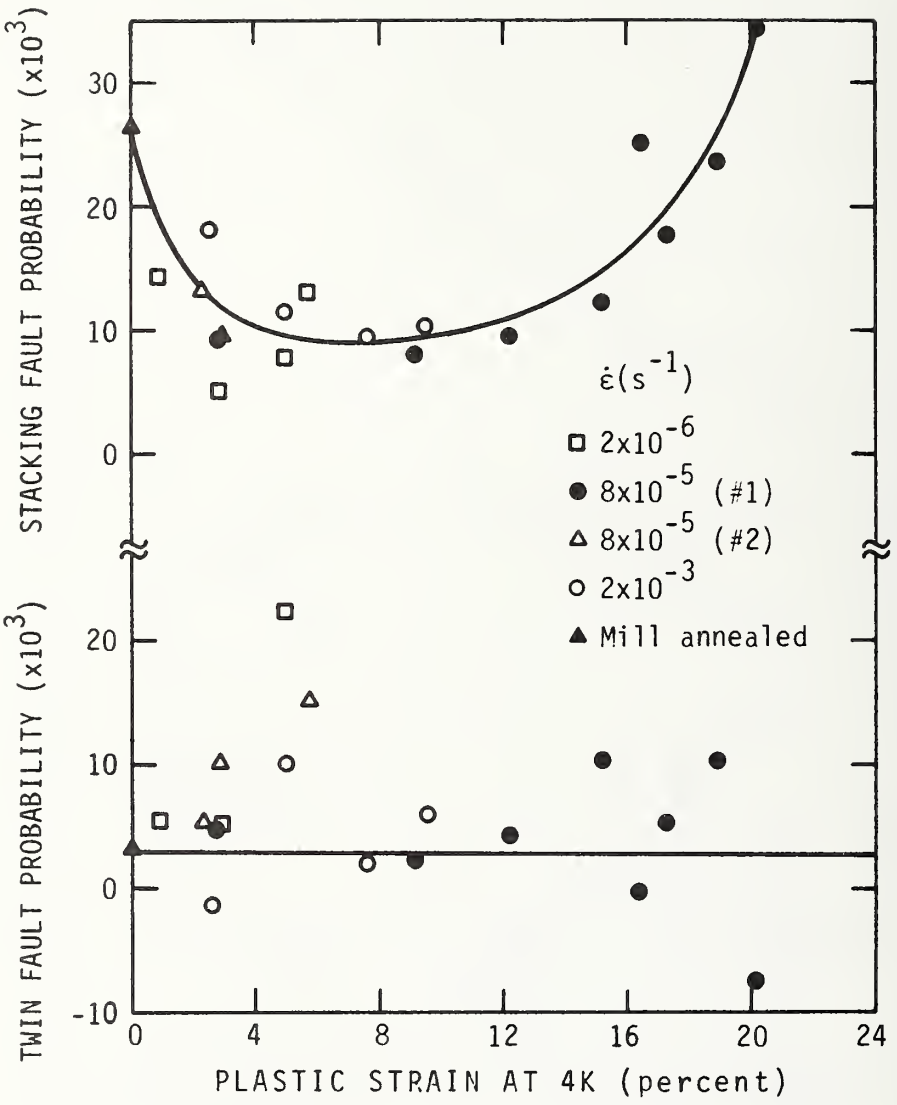

Fig. 5 Stacking and twin fault probabilities as functions of strain at 4 K for three crosshead speeds, with hand-drawn trend lines.

Physical Properties of Stainless Steels

ELASTIC-CONSTANT VARIABILITY IN STAINLESS STEEL 304

National Bureau of Standards

Elastic-Constant Variability in Stainless Steel 304*

H. M. Ledbetter
Fracture and Deformation Division
National Bureau of Standards
Boulder, Colorado 80303

N. V. Frederick
Electromagnetic Technology Division
National Bureau of Standards
Boulder, Colorado 80303

M. W. Austin
Fracture and Deformation Division
National Bureau of Standards
Boulder, Colorado 80303

ABSTRACT

Variability of elastic constants in stainless steel 304 was determined by measuring longitudinal and transverse ultrasonic velocities in twenty samples acquired randomly. Three kinds of variations - - sample-to-sample, directional within a sample, and repeated measurements on a single sample - - are reported for four elastic constants: the bulk modulus, Young's modulus, shear modulus, and Poisson's ratio. Because of surprisingly small variations, 1 percent or less, the principal problem became measurement sensitivity and reproducibility. To overcome this problem, an inexpensive high-resolution measurement system was devised using general-purpose equipment augmented with a very simple impedance-transforming amplifier and a broadband detector. With this system the often-reported, troublesome transit-time correction disappeared. Effects due to frequency and directionality were negligible.

*Contribution of the U. S. Government, not subject to copyright.

I. INTRODUCTION

For stainless steel 304, the presently reported study sought to determine the variability of elastic constants such as the bulk modulus, Young's modulus, shear modulus, and Poisson's ratio from sample to sample, directionally within a sample, for repeated measurements, and as a function of sound-wave frequency.

Elastic constants of technological materials fill many needs. They become vital in problems such as load-deflection, thermoelastic stress, elastic instability, and fracture mechanics. Empirical correlations occur between elastic constants and technologically important properties such as strength, hardness, and wear. Because they relate intimately to both the interatomic potential and the lattice-vibrational spectrum, elastic constants relate in turn to various fundamental solid-state phenomena such as diffusion, theoretical strength, and lattice defects. Since elastic constants occur as parameters in thermodynamic equations of state, well-defined relationships exist between elastic constants and free energy, specific heat, and thermal expansivity. Knowledge of the elastic constants allows one to compute the elastic Debye temperature, which equals the specific-heat Debye temperature at zero temperature. The Debye temperature characterizes crystalline solids better perhaps than any other single parameter.

Although usually expected, random variability of physical and, especially, mechanical properties of technological materials is seldom characterized quantitatively. A recent study[1] considered the mechanical-property variability among fifteen product forms from a single lot of stainless steel 304. Variability arises from three principal causes: chemical composition, thermomechanical treatment, and testing methods.

The present study used a single testing method, thus obviating the third cause.

Five types of statistical-data samples suggest themselves for a property variability study: (1) lot-to-lot; (2) sample-to-sample, within lot; (3) within sample, directional; (4) within sample, repeated measurements; (5) within sample, various test methods. The present study considers statistical samples (1), (3), and (4), and the results of the study show that studying statistical sample (2) seems seldom worthwhile in the case of elastic properties.

The most accurate elastic constants, C, usually follow from determining ultrasonic velocities, v, and using the general relationship $C = \rho v^2$, where ρ denotes mass density. The present study used a simple pulse-echo method to determine velocity $v = 2\ell/t$, where ℓ denotes the specimen length and t denotes the round-trip time for an ultrasonic pulse between two flat-and-parallel specimen faces. As described below, high accuracy in the present measurement results from four features: narrow pulse width, broad bandwidth, unrectified echoes, and cycle-to-cyle time measurements using consecutive echoes.

Ultrasonic-velocity determinations of elastic constants in stainless-steel-304-type alloys have been reported previously. In 1960, Fahey[2] reported ultrasonic elastic constants for stainless steel 303 at four temperatures between ambient and liquid-helium. Haskins[3] reported a similar study for stainless steels 303 and 321 down to 77 K and 23 K, respectively. Armstrong and Eash[4] used a thin-rod resonance method to measure ultrasonic velocities in stainless steel 303 between 4 K and 320 K. Ledbetter, Naimon, and Weston[5] reported the 4 to 300 K ultrasonic velocities for four stainless steels: A286, 304, 310, and 316. Hammond,

Moyer, and Brinkman[6] reported ultrasonic elastic constants for stainless 304 between 300 and 1000 K. Bates[7] recently correlated ultrasonic shear modulus with irradiation-induced swelling in stainless steel 316, and he reported the effect of Mo, P, and Si compositional variations on the elastic constants.

The present report represents one of the first detailed studies of elastic-constant variability for a technological material. Richards[8] reported a variability study of several static and dynamic experimental methods for determining elastic moduli in beryllium-copper rod.

II. EXPERIMENT

A. Materials

Twenty samples of stainless steel 304 were obtained effectively randomly from various sources in various forms, including bar, pipe, and plate. No laboratory treatments were performed on the alloys; they were tested in their as-acquired conditions. Table I gives chemical composition, hardness, and mass density.

Ultrasonic-velocity specimens were prepared by grinding flat and parallel surfaces (within 3 μm). Specimens studied for directionality variations were ground as rectangular prisms (Fig. 1).

B. Electronic system

The studied materials exhibit some dispersion, as shown by the pulse-echo pattern in Fig. 2. Since the specimen heavily loads the quartz transducer, the bandwidth of repeated echoes is limited mainly by the impedance-matching network connected to the transducer. Consistent with the common knowledge that time resolution varies inversely with the bandwidth of the measuring system, a wide-bandwidth system was devised. The bandwidth was about 20 times that of commercially available measurement systems used previously in our laboratory. Figure 3 shows the

circuit diagram of this new system. Note the absence of a variable tuning circuit. Note also that the quartz crystal is loaded by a very low capacitance cable and an FET source follower. This arrangement allows a good match to the high output impedance of the quartz transducer capacitance without sacrificing bandwidth. This approach to receiver design allowed the use of a low-power general-purpose oscillator as a signal source.

C. Velocity measurements

Velocities were determined by measuring the time difference between consecutive echoes in a pulse-echo pattern using a dual-channel sweep-delayed time-interval-microprocessor-equipped oscilloscope with typically a 0.001 μs resolution. Thus, for a 5 μs transit time the best resolution in the velocity is 2 parts in 10,000. Neglecting density error this amounts typically to a 0.04 percent error in the elastic constant. This resolution can be improved, but it serves adequately in most cases. It becomes more efficient to 'clean up' the echoes so they can be interpreted and measured more accurately. And this was achieved with the system described above. Figure 2 shows an oscilloscope display of the pulse and the first two echoes. Time measurements were made between the crests of leading cycles in consecutive echoes. Since the leading cycle attenuates strongly, care was needed when measuring between nonconsecutive echoes to guarantee a correct cycle matchup.

D. Transit-time error

Many authors[9-11] have reported a transit-time error due to the transducer and bond thicknesses. Previous publications from our laboratory corrected for this error by either a two-transducer method or by a multiple-specimen-length method.

The new measurement system eliminates the transit-time error, identifying it as an artifact due to attenuation of an echo's leading cycle and accumulation of spurious trailing cycles due either to the specimen and the transducer or to the electronics.

Attempts to make a transit-time-error correction using the procedure suggested by Neighbours, Bratten, and Smith[10] using four different-length specimens always resulted in corrections corresponding closely to an integral number of cycles. This was confirmed at quartz-crystal-transducer fundamental resonance frequencies of 4, 5, 7, and 10 MHz for the longitudinal case and at 4 and 8 MHz for the transverse case.

Correction attempts using a two-transducer method gave less well-defined echoes. But even these could be measured reasonably well by cycle-cycle overlap to give zero transit-time error.

Perhaps the most convincing evidence for zero transit-time error is shown in Table II, which shows velocities determined on a single specimen for a series of 180 measurements. For each measurement the transducer seal was broken and remade.

The careful reader has probably already noted that the conclusions given here concerning transit-time error are essentially a rediscovery of those given 20 years ago by Eros and Reitz[12].

III. RESULTS

Table II shows the effects of repeated measurements. Each entry in Table II represents the arithmetic average of 10 measurements, each with a different bond between specimen and transducer. Table II also shows effects of using transducers with different fundamental frequencies: 3, 5, and 7 MHz.

Table III shows effects of changing frequency in another way. A single 5 MHz transducer was driven off its resonant frequency between 2.5 and 7 MHz.

Table IV shows for a typical case the variation of velocity with direction within a single specimen, from a 3.8-cm 304L plate. Here, 001 denotes the rolling direction and 100 denotes the short-transverse direction.

Table V gives the main results of the study--the longitudinal and transverse sound velocities together with five derived elastic constants:[13]

$$\text{longitudinal modulus} = C_\ell = \rho v_\ell^2 \quad , \tag{1}$$

$$\text{shear modulus} = G = \rho v_t^2 \quad , \tag{2}$$

$$\text{bulk modulus} = B = \rho \left(v_\ell^2 - \frac{4}{3} v_t^2\right) \quad , \tag{3}$$

$$\text{Young's modulus} = E = 3 \rho v_t^2 \left(v_\ell^2 - \frac{4}{3} v_t^2\right)/\left(v_\ell^2 - v_t^2\right) \quad , \tag{4}$$

and

$$\text{Poisson's ratio} = \nu = \frac{1}{2} \left(v_\ell^2 - 2v_t^2\right)/\left(v_\ell^2 - v_t^2\right) \quad , \tag{5}$$

together with their standard deviations.

IV. DISCUSSION

Results in Table II show that longitudinal and transverse ultrasonic velocities in commercial stainless steels can be measured to an imprecision of about 1 part in 1000, or 0.1 percent. Using familiar error-propagation formulas, this translates approximately to imprecisions of 0.2 percent in C_ℓ, 0.2 percent in G, 0.3 percent in B, 0.5 percent in E, and 0.5

percent in ν. While such low imprecisions are claimed often in single-crystal experiments, the authors are unaware of a similar claim for commercial-alloy polycrystals.

Measuring between different pairs of echoes (1 and 2, 2 and 3, 3 and 4 in Table II) does not affect the measured velocity beyond the present resolution capability, typically 0.05 percent for v_ℓ and 0.03 percent fo v_t. This means the first echo is unaffected by the proximity of a large pulse. (Wider pulse widths may negate this conclusion.)

Changing measurement frequency between 3 and 7 MHz does not affect the measured velocity beyond the resolution capability, as shown in Table II. This means that dispersion effects are either absent or quite small, and except for familar adiabatic-isothermal corrections, elastic constants measured at high frequencies apply also to static cases.

The 180 measurements summarized in Table II represent 180 different transducer-specimen bonds as well as 6 different transducers. Thus, the effects of changing transducers and bonds are also negligible. These results show conclusively that transit-time errors discussed above (section II.D) are nonexistent.

The only 'tuning' in the present measurement system consists of changing the frequency. This was sometimes useful for improving the echo-pattern quality, best-quality echo patterns being obtained at frequencies between 2.5 and 7.5 MHz. For v_t the effect is nonmeasurable; v_ℓ changes smoothly only about 0.2 percent over this frequency range. Thus, the present measurement system responds reproducibly over a moderately large frequency range. This contrasts sharply with our laboratory's previous experience with measurement systems that contained tuning (impedance-matching) circuits that gave measurable echo patterns only over a narrow frequency range, about 0.5 MHz or less.

Directional variations of elastic constants within a sample are quite small, as shown in Table IV. Other specimens studied similarly also showed small directional variations. This means that textures are nearly nonexistent in these alloys because single-crystal elastic constants for stainless steels[14] show a Zener anisotropy $2C_{44}/(C_{11} - C_{12})$ between 3 and 4, which would cause measurable elastic-constant variations if crystallites were oriented nonrandomly. This lack of texture may be ascribed to the thermomechanical treatment: annealing after hot deformation. Textures caused by cold deformation are less easily removed by annealing.

The most important, and perhaps most surprising, results of the present study are shown in Table V, which gives the lot-to-lot variability of the sound velociites and the elastic constants. Velocity variations are quite small, 0.3 percent for v_ℓ and 0.6 percent for v_t. Coupled with a 0.6 percent density variations, this leads to elastic-constant variations of 0.9 percent for E, 1.2 percent for ν, and 1.4 percent for both B and ν. All these are much smaller than variations implied by elastic constants reported in the literature for these alloys. Thus, reported variabilites in these elastic constants must arise from experimental measurement errors, not from the material itself. Considering differences among these alloys that must exist in composition, microstructure, grain size, and carbon distribution, the low elastic-constant variability is indeed surprising. And it would be interesting to study this problem in other types of alloys: aluminum, copper, ferritic steel, and others.

V. CONCLUSIONS

The following principal results and conclusions emerge from the present study:

1. A new pulse-echo elastic-constant measurement system permits both longitudinal and shear velocity measurements to be made within 0.1 percent on materials such as commercial stainless steels.

2. Between 3 and 7 MHz the velocities are frequency independent within this system's resolution capability.

3. Transit-time error, usually ascribed to bond and transducer thickness, was found to be nonexistent.

4. Elastic constants of stainless steel 304 show surprisingly little lot-to-lot variation, 0.9 to 1.4 percent depending on the elastic constant. Larger variations reported in the literature are due mainly to experimental measurement errors.

ACKNOWLEDGMENT

This study was supported by the U.S. Department of Energy, Office of Fusion Energy.

REFERENCES

1. R. W. Swindeman, W. J. MacAfee, and V. K. Sikka, in Reproducibility and Accuracy of Mechanical Tests, STP 626 (Amer. Soc. Test. Mater., Phila., 1977), pp. 41-64.

2. N. H. Fahey, Watertown Arsenal Laboratories Report WAL TR 118 (1960).

3. J. F. Haskins, General Dynamics Report ERR-AN-055 (1961).

4. P. E. Armstrong and D. T. Eash, in Advances in Cryogenic Engineering, Volume 14 (Plenum, New York, 1969), pp. 64-70.

5. H. M. Ledbetter, W. F. Weston, and E. R. Naimon, J. Appl. Phys., 3855-3860 (1975).

6. J. P. Hammond, M. W. Moyer, and C. R. Brinkman, in Proceedings Second International Conference on Mechanical Behavior of Materials (Amer. Soc. Metals, Metals Park, Ohio, 1976), pp. 1037-1041.

7. J. F. Bates, Hanford Engineering Development Laboratory Report HEDL-SA-1068 (1976).

8. J. T. Richards, in Symposium on Determination of Elastic Constants, STP 129 (Amer. Soc. Test. Mater., Phila., 1952), pp. 71-100.

9. D. Lazarus, Phys. Rev. 76, 545-553 (1949).

10. J. R. Neighbours, F. W. Bratten, and C. S. Smith, J. Appl. Phys, 23, 389-393 (1952).

11. C. S. Smith and J. W. Burns, J. Appl. Phys. 24, 15-18 (1953).

12. S. Eros and J. R. Reitz, J. Appl. Phys. 29, 683-686 (1958).

13. L. D. Landau and E. M. Lifshitz, Theory of Elasticity (Pergamon, London, 1959), p. 13, p. 99.

14. M. Kikuchi, Trans. Jap. Inst. Met. 12, 417-421 (1971).

TABLE I. Chemical compositions (weight percent), hardness, and mass density.

	Cr	Ni	Mn	Si	C	P	S	N	Cu	Mo	V	Co	Hardness (Rockwell B)	Mass Density (g/cm^3)
1													72	7.851
2	18.4	9.7	1.4	.6	.02	.02	.01						87	7.923
3													76	7.930
4													96	7.910
5	18.84	10.18	1.65	.82	.026	.022	.010		.28	.27			62	7.856
6													76	7.816
7													76	7.876
8													76	7.812
9													82	7.921
10	18.30	8.45	0.82	.59	.061	.020	.017						92	7.927
11	18.5	8.75	1.43	.31	.030	.025	.013	.061					73	7.940
12	18.65	9.49	1.88	.38	.048	.019	.024	.12	.07	.52	.03	.06	75	7.860
13	18.66	8.51	0.44	.53	.06	.03			.15	.09			75	7.894
14	18.76	9.69	1.14	.58	.04	.02	.01	.02	.22	.21			74	7.895
15													79	7.883
16													78	7.915
17													77	7.817
18													76	7.826
19													93	7.814
20	18.52	9.68	1.23	.48	.051	.027	.017	.046		.33			74	7.935

Table II. Reproducibility and frequency effects for longitudinal and shear velocities in specimen 5. Each entry is an average of 10 measurements.

Frequency (MHz)	Echoes	v_ℓ (cm/μs)	v_t (cm/μs)
3	1-2	.5762	.3127
	2-3	.5763	.3126
	3-4	.5761	.3126
5	1-2	.5752	.3123
	2-3	.5754	.3123
	3-4	.5757	.3124
7	1-2	.5750	.3126
	2-3	.5751	.3127
	3-4	.5752	.3128
Mean (1-2)		.5755 ± .0006	.3125 ± .0002
Mean (1-3)		.5756 ± .0006	.3125 ± .0002
Mean (3-4)		.5757 ± .0005	.3126 ± .0002
Mean (3 MHz)		.5762 ± .0001	.3126 ± .0001
Mean (5 MHz)		.5754 ± .0003	.3123 ± .0001
Mean (7 MHz)		.5751 ± .0001	.3127 ± .0001
Mean (overall)		.5756 ± .0005	.3126 ± .0002

TABLE III. Effects of nonresonant driving frequency on measured ultrasonic velocities in specimen 5.

Frequency (MHz)	v_ℓ (cm/μs)	v_t (cm/μs)
2.5	.5759	[a]
3.0	.5761	.3127
3.5	.5758	.3125
4.0	.5756	.3126
4.5[b]	.5756	.3126
5.0	.5754	.3125
5.5	.5754	.3127
6.0	.5754	.3126
6.5	.5753	.3126
7.0	.5751	.3125
Mean	.5755	.3128
Std. dev.	.0003	.0005

[a] Irreproducible due to poor echo pattern.

[b] Fundamental frequency.

TABLE IV. Directional variation of ultrasonic wave velocities in specimen 5.

Propagation Direction	Polarization Direction	v_ℓ (cm/μs)	v_t (cm/μs)
100	100	.5760	
	010		.3126
	001		.3123
010	010	.5756	
	100		.3125
	001		.3123
001	001	.5761	
	100		.3122
	010		.3124
Mean		.5759	.3124
Std. dev.		.0003	.0001
Pct. std. error		.5	.03

TABLE V. Ultrasonic velocities and elastic constants for 20 randomly selected stainless-steel-304 samples.

Specimen	v_ℓ (cm/μs)	v_t (cm/μs)	B (10^{11} N/m^2)	E (10^{11} N/m^2)	G (10^{11} N/m^2)	ν
1	.5772	.3144	1.581	2.001	.776	.289
2	.5746	.3122	1.586	1.993	.772	.291
3	.5749	.3131	1.584	2.004	.777	.289
4	.5752	.3108	1.598	1.977	.764	.294
5	.5756	.3126	1.582	1.981	.767	.291
6	.5745	.3182	1.524	2.024	.791	.279
7	.5775	.3134	1.595	1.998	.774	.291
8	.5786	.3131	1.594	1.980	.766	.293
9	.5762	.3161	1.574	2.034	.791	.285
10	.5759	.3108	1.608	1.983	.766	.295
11	.5764	.3137	1.596	2.015	.781	.290
12	.5760	.3152	1.567	2.009	.781	.286
13	.5781	.3123	1.612	1.993	.770	.294
14	.5786	.3126	1.615	1.997	.772	.294
15	.5746	.3118	1.581	1.979	.766	.291
16	.5761	.3131	1.592	2.002	.776	.290
17	.5752	.3125	1.568	1.970	.763	.291
18	.5746	.3129	1.570	1.985	.770	.289
19	.5736	.3138	1.545	1.980	.770	.286
20	.5740	.3147	1.567	2.020	.786	.285
Mean	.5759	.3134	1.582	1.996	.774	.290
Std. dev.	.0015	.0018	.022	.017	.009	.004
Pct. std. error	0.3	0.6	1.4	0.9	1.1	1.4

FIGURE CAPTIONS

Figure 1. Nine sound-velocity modes for an orthogonal system, where $\underline{n}$ denotes propagation vector and $\underline{p}$ denotes polarization vector, indicated by arrows in diagram.

Figure 2. Composite oscilloscope display showing pulse and first two echoes. As described in text, transit-time measurements were made between crests of leading cycles of consecutive echoes.

Figure 3 Schematic circuit diagram of ultrasonic pulse-echo velocity-measurement system.

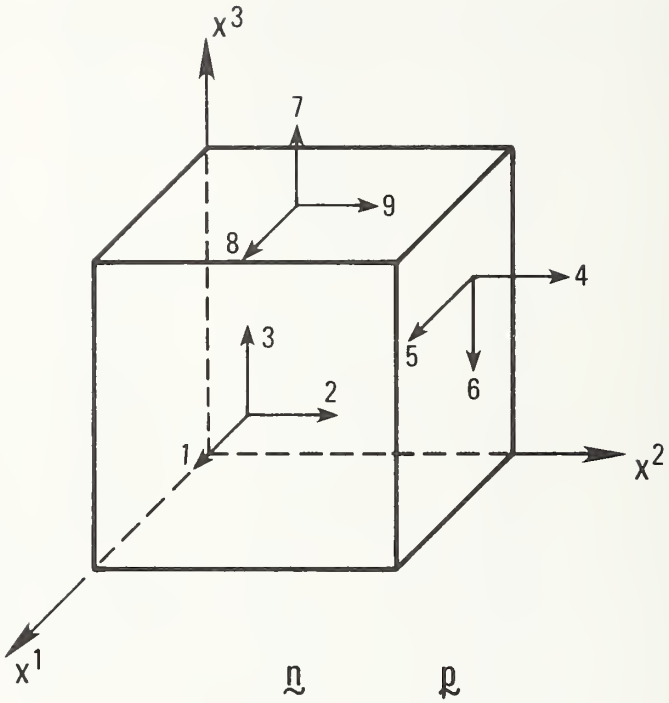

	$\underset{\sim}{n}$	$\underset{\sim}{p}$
1	1 0 0	1 0 0
2		0 1 0
3		0 0 1
4	0 1 0	0 1 0
5		1 0 0
6		0 0 1
7	0 0 1	0 0 1
8		1 0 0
9		0 1 0

Figure 1. Nine sound-velocity modes for an orthogonal system, where $\underset{\sim}{n}$ denotes propagation vector and $\underset{\sim}{p}$ denotes polarization vector, indicated by arrows in diagram.

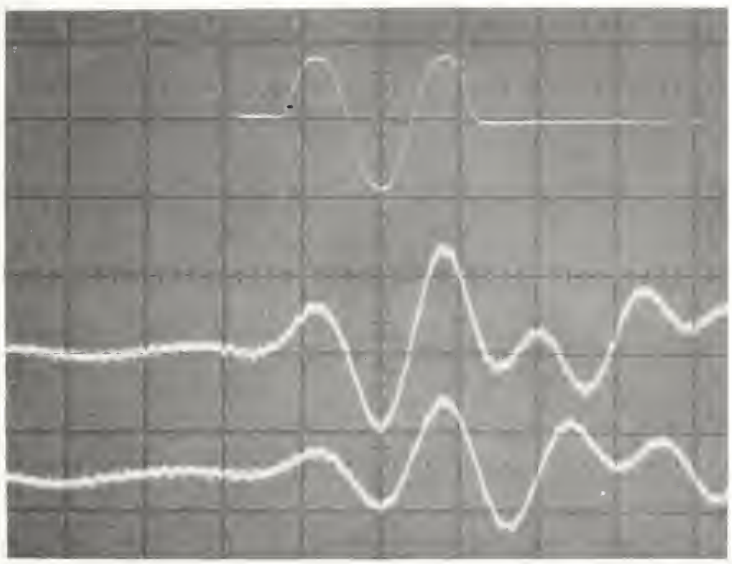

Figure 2. Composite oscilloscope display showing pulse and first two echoes. As described in text, transit-time measurements were made between crests of leading cycles of consecutive echoes.

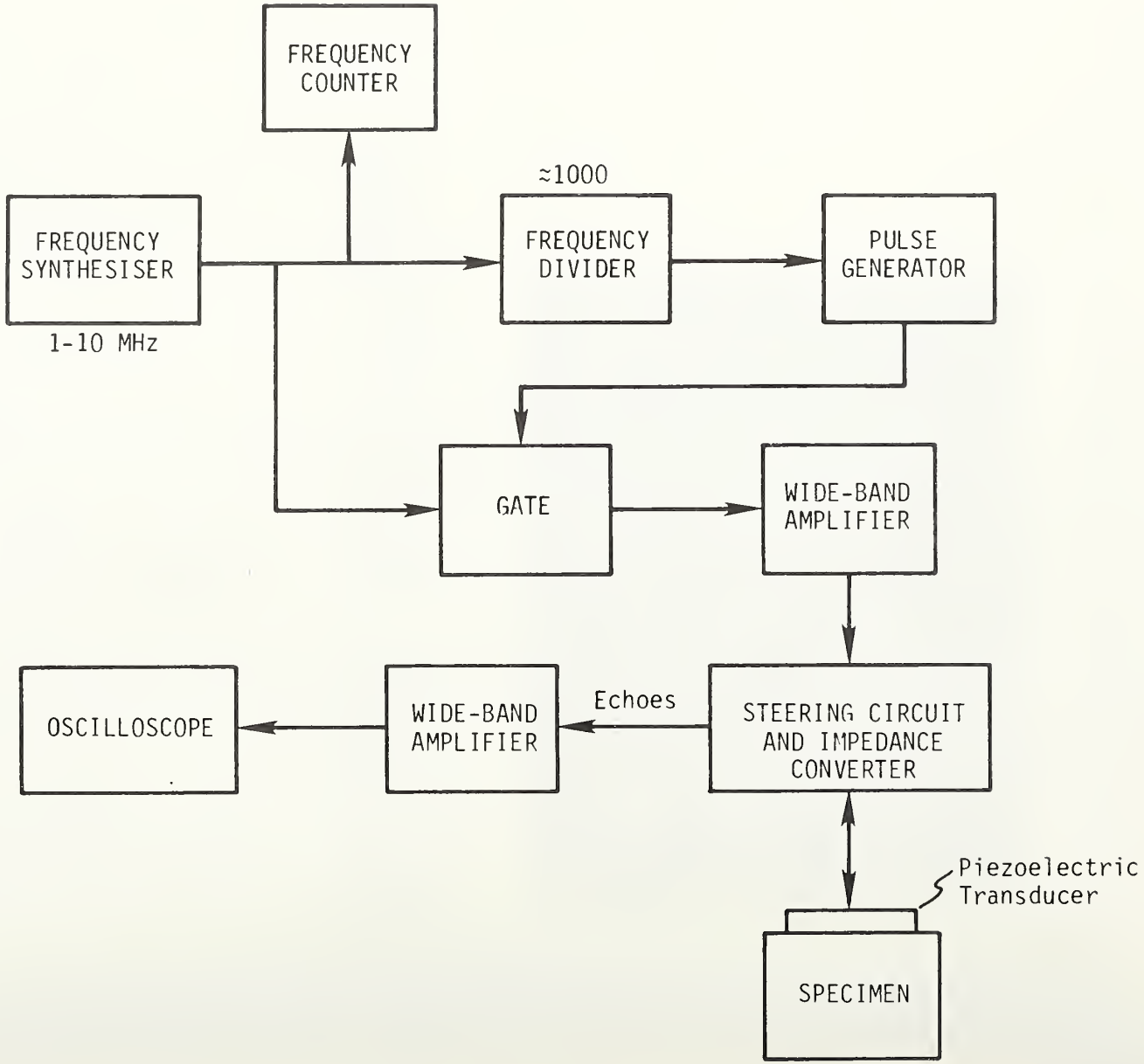

Figure 3 Schematic circuit diagram of ultrasonic pulse-echo velocity-measurement system.

LOW TEMPERATURE SPECIFIC HEAT OF TWO STAINLESS STEELS

Wichita State University

National Bureau of Standards

Specific heat values between 2 and 20 K are reported for the two stainless steels AISI 304 and AISI 304L. Measurements were made by standard adiabatic calorimetry. The results suggest that the thermal properties are roughly comparable to AISI 310S, but the absence of magnetic clusters implies that they are more appropriate for low temperature work.

Low temperature specific heat of two stainless steels

J.C. Ho, G.B. King and F.R. Fickett

Stainless steel is often used as a structural material in cryogenic systems. For many large-scale, low temperature applications, knowledge of specific heat values for such alloys is essential for proper design. Collings et al[1] have recently made calorimetric measurements on AISI 310S stainless steel. These measurements indicate the occurrence of superparamagnetism, presumably associated with magnetic clusters, by a temperature-independent contribution to the specific heat. Corsan and Mitchem[2] have recently reported specific heat measurements from 4 K to room temperature on a series of laboratory-produced Fe-Cr-Ni alloys with chromium contents ranging from 12–24 wt.% and nickel contents in the range 12–20 wt.%. Differences of up to 30% were observed in the specific heats as measured at 4 K. However, to the best of our knowledge, no data previously existed on the most common low temperature structural stainless steel - AISI 304. This note describes the results of low temperature specific heat measurements on AISI 304 and AISI 304L stainless steels. L designates low carbon content.

Experimental

The experimental materials were obtained from commercial suppliers. The chemical analyses made on these specific materials are given in Table 1. The specimens were machined from the stock as received and were given no further heat treatments. The specimens were cylinders 2.54 cm long and 2.22 cm in diameter with a mass of ~ 0.080 kg.

The specific heat measurements were made between 2 and 20 K by standard adiabatic calorimetry. The sample temperature determinations were based on the electrical resistance of a commercial germanium thermometer. Pulsed Joule heating was obtained by passing a current through a manganin wire which, along with the thermometer, was thermally anchored to the sample. The heat capacity of the thermometer-heater assembly was separately measured for addenda corrections. The performance of the calorimeter was checked by measuring the specific heat of a high-purity copper sample; the data were in good agreement with literature values.

Results and discussion

The specific heat data are presented in Figs 1 and 2 in the format of C/T versus T^2, where C is the specific heat and T is the absolute temperature. The solid lines, represented by the equations given on the figures are obtained by least-squares fit with a standard deviation of 0.17%. The linear term is due to the conduction electrons, while the others are lattice contributions.[3] The fact that one needs more than just the T^3 term reflects the contribution of higher-frequency phonons at finite temperatures.[4] The overall uncertainty in the specific heat is estimated to be

James C. Ho and Galen B. King are at the Physics Department, Wichita State University, Wichita, Kansas 67208, USA. Fred R. Fickett is at the Cryogenics Division, National Bureau of Standards, Boulder, Colorado 80302, USA. The work was sponsored by the Division of Magnetic Fusion Energy of the Department of Energy. Received 15 February 1978.

Table 1. Chemical analysis of steels

	Wt% of listed element									
AISI No	C	Mn	P	S	Si	Cr	Ni	N	Mo	Co
304	0.061	0.820	0.020	0.017	0.590	18.30	8.45	–	–	–
304L	0.030	1.430	0.025	0.013	0.031	18.50	8.75	0.061	0.29	0.18

0011-2275/78/1805-0296 $01.00

Table 2. Heat capacity, entropy and enthalpy of AISI 304 and AISI 304L stainless steel

Temperature, K	Heat capacity, J kg^{-1} K^{-1}		Entropy, J kg^{-1} K^{-1}		Enthalpy, J kg^{-1}	
	304	304L	304	304L	304	304L
2.0	0.936	0.843	0.0	0.0	0.0	0.0
3.0	1.41	1.27	0.469	0.422	1.17	1.06
4.0	1.89	1.70	0.939	0.847	2.82	2.54
5.0	2.37	2.15	1.41	1.27	4.95	4.47
6.0	2.87	2.60	1.88	1.70	7.57	6.84
7.0	3.37	3.07	2.37	2.14	10.7	9.67
8.0	3.89	3.56	2.85	2.58	14.3	13.0
9.0	4.43	4.06	3.34	3.03	18.5	16.8
10.0	4.99	4.59	3.84	3.48	23.2	21.1
11.0	5.57	5.14	4.34	3.95	28.5	26.0
12.0	6.18	5.73	4.85	4.42	34.4	31.4
13.0	6.82	6.35	5.37	4.90	40.8	37.4
14.0	7.51	7.00	5.90	5.40	48.0	44.1
15.0	8.23	7.70	6.44	5.90	55.9	51.5
16.0	9.00	8.45	7.00	6.43	64.5	59.5
17.0	9.83	9.25	7.57	6.96	73.9	68.4
18.0	10.7	10.1	8.16	7.52	84.2	78.1
19.0	11.7	11.0	8.76	8.09	95.4	88.6
20.0	12.7	12.0	9.39	8.68	108	100

within 1%. Fig. 3 shows the temperature variation of the specific heat directly.

Based on the experimental specific heat equations, entropy and enthalpy (heat content) values at temperatures up to 20 K have been calculated, with reference to 2 K. They are summarized in Table 2. The results thus obtained suggest that, as far as thermal properties are concerned, AISI 304 and AISI 304L are roughly comparable to AISI 310S.[1] However, the absence of magnetic clusters in these materials suggests that they are more appropriate in those low temperature applications where magnetic properties are critical. We have also calculated values of the Debye temperature with the results: θ_D = 496 K for 304 and θ_D = 457 K for 304L.

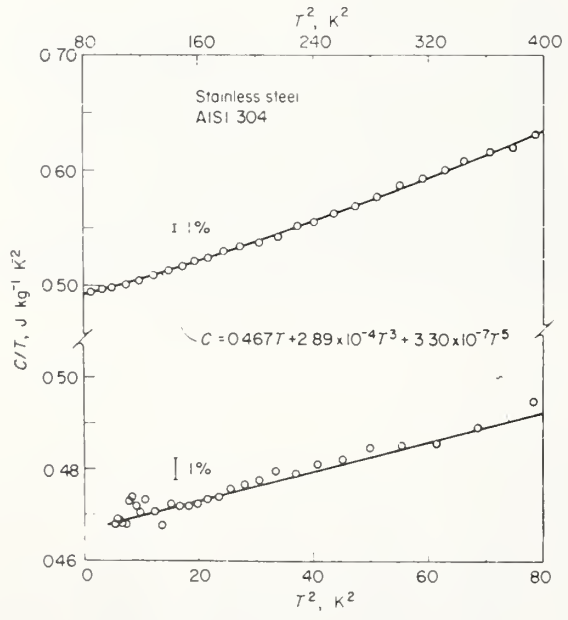

Fig. 1 C/T versus T^2 for AISI 304

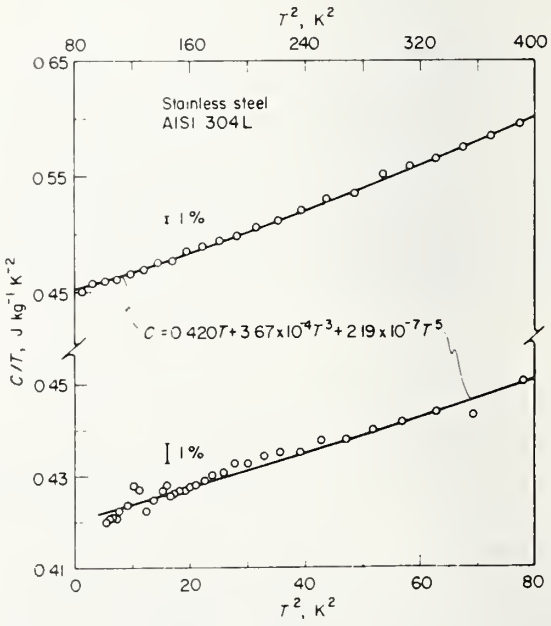

Fig. 2 C/T versus T^2 for AISI 304L

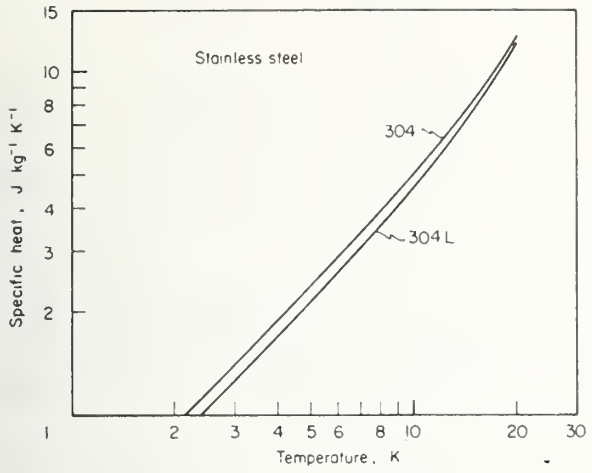

Fig. 3 Specific heat of AISI 304 and AISI 304L as a function of temperature

It is also interesting to note that the data presented here agree quite well with those for the 24Cr-12Ni alloy measured by Corsan and Mitchem,[2] which is the only one of their alloys with the same Ni : Cr ratio as AISI 304. This seems to bear out their observation that it is this ratio which is correlated with the variation in specific heat among the alloys, a high ratio leading to a relatively high specific heat.

References

1 **Collings, E.W., Jelinek, F.J., Ho, J.C., Mathur, M.P.** *Advances in Cryogenic Engineering*, Ed K.D. Timmerhaus, R.P. Reed and A.F. Clark, **22** (Plenum Publishing Corp, NY 1977) 159

2 **Corsan, J.M., Mitchen, N.I.** Proc 6th Int Cryo Eng Conf (IPC Sci and Tech Press, Guildford, Surrey, England 1976) 342

3 1 see eg, **Kittel, C.** Introduction to Solid State Physics, 4th Ed, (John Wiley and Sons, NY 1971) 252

4 **Barron, T.H.K., Morrison, J.A.** *Can J Phys* **35** (1957) 799

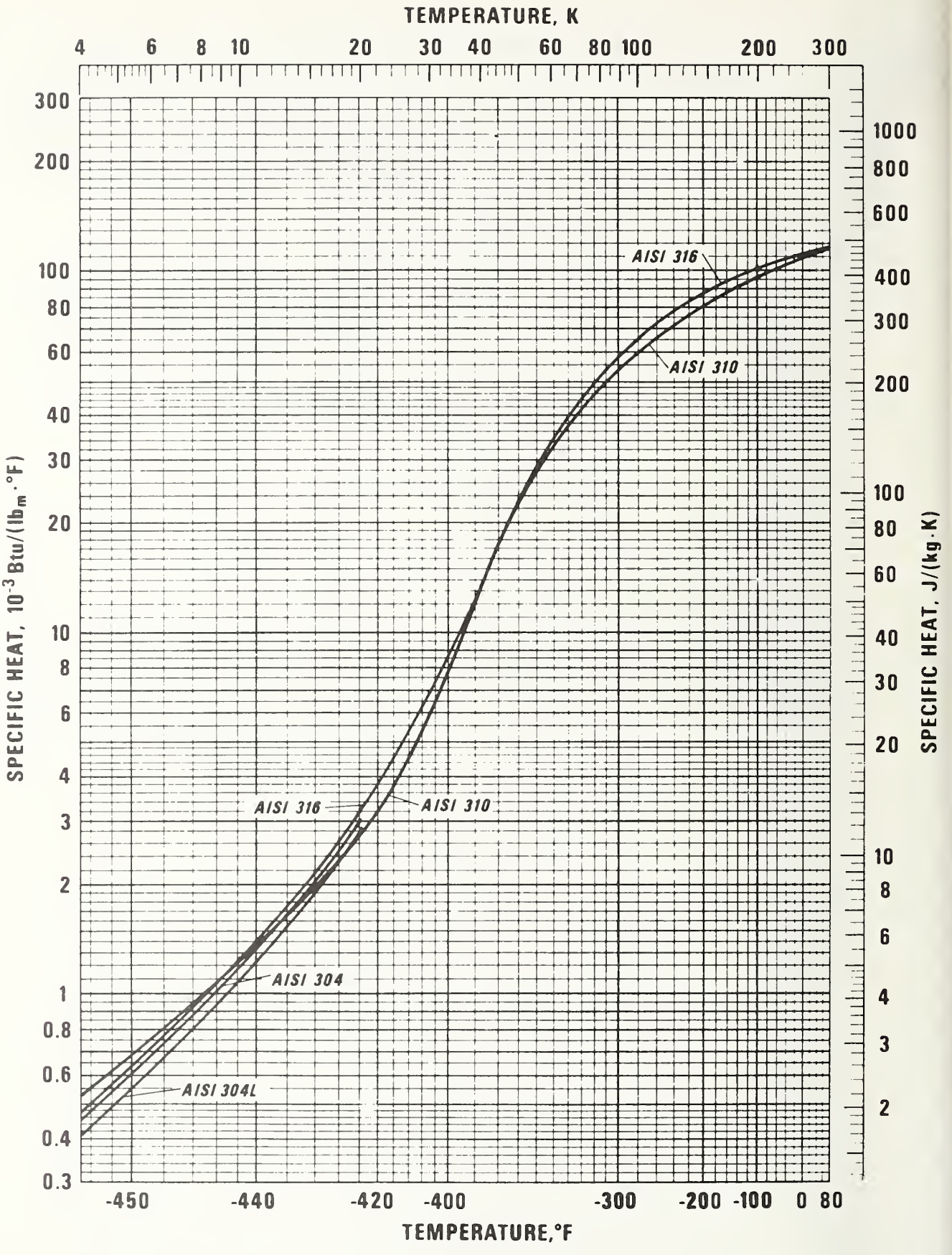

Figure 4. This graph, from the NBS handbook LNG Materials and Fluids (1977), shows how the data determined here for AISI 304 and 304L fit with specific heat data for other stainless steels.

MAGNETIC SUSCEPTIBILITY AND MAGNETIZATION STUDIES OF SOME COMMERCIAL AUSTENITIC STAINLESS STEELS

Battelle Columbus Laboratories

FOREWORD

Magnetic susceptibility measurements were carried out at Battelle by R. D. Smith, and the magnetization measurements were performed at The Ohio State University by S. C. Hart. The work was carried out under the auspices of the Thermophysical Properties Division, National Bureau of Standards, Boulder, Colorado, F. R. Fickett, program monitor.

E. W. Collings
Principal Investigator
BATTELLE

MAGNETIC SUSCEPTIBILITY AND MAGNETIZATION STUDIES
OF SOME COMMERCIAL AUSTENITIC STAINLESS STEEL ALLOYS

to

THE THERMOPHYSICAL PROPERTIES DIVISION
NATIONAL BUREAU OF STANDARDS
BOULDER, COLORADO 80302

INTRODUCTION

Magnetic susceptibility measurements, using the Curie magnetic force technique, and magnetization measurements, using a vibrating-sample magnetometer have been carried out on six AISI 300-series alloys 310S, 304, 304L, 304N, 316, 316L; as well as AWS 330 weld metal and Inconel 625, over the temperature ranges listed in Table 1.

TABLE 1. TEMPERATURE RANGES OF THE SUSCEPTIBILITY AND MAGNETIZATION STUDIES

Alloy Name	Temperature Range of Susceptibility Study (K)	Temperature Range of Magnetization Study (K)
AISI 310S	77-414	4-75
AISI 304	9-408	4-143 plus 297
304L	77-410	4-112 plus 200, 296
304N	77-403	4-114 plus 294
AISI 316	77-407	3-110 plus 296
316L	77-413	4- 80 plus 181, 286
AWS 330	77-416	4-65 plus 187, 295
In 625	5-412	--

After listing alloy compositions, describing sample preparation procedures and so on, the numerical results of the study will be presented

in two separate sections, the first dealing with the susceptibility results, and the second with the magnetization. The report concludes with a summary of the magnetic characteristics of austenitic stainless steels with reference to the four principal types studied.

SPECIMEN MATERIALS

Sources and Compositions

In Table 2 are listed the vendors and available specifications of the alloys investigated. In Table 3, vendor-supplied compositions are listed together with average atomic weights (AW) calculated using the expression $AW = 100/\Sigma_i(x_i/w_i)$, where x_i is the abundance in weight percent of a constituent of atomic weight w_i.

TABLE 2. VENDORS AND AVAILABLE SPECIFICATIONS OF THE ALLOYS INVESTIGATED

Alloy Name	Supplier and Available Specifications
AISI 310S	Rolled Alloys, Inc., Heat No. 20,650 HRAP Plate, as-received
AISI 304	Armco Steel Corp., Heat No. 546,314 7/8-in. diameter bar, as-received
AISI 304L	Jessop Steel Co., Heat No. 14,768 1-in. plate, received as 1900-1950 F (1038-1066 C), 1/2 h, water quench
AISI 304N	Cameron Iron Works, Inc., CIW Serial No. 12585Z Heat No. K2980, received as 1925 F (1052 C), 2-1/2 h, water quench
AISI 316	Commercial source 3/4-in. diameter bar, as-received
AISI 316L	Armco Steel Corp., Heat No. 55,603, 1-in. diameter bar, as-received
AWS 330	Weld test pad, hence as-cast, rapidly chilled from melt

TABLE 3. VENDOR-SUPPLIED COMPOSITIONS OF ALLOYS LISTED IN WGT PERCENT

Element (Atomic Wgt)	Fe* (55.85)	Cr (52.00)	Ni (58.71)	Mn (54.94)	Mo (95.94)	V (50.94)	Cu (63.54)	Co (58.93)	C (12.01)	N (14.01)	P (30.97)	S (32.06)	Si (28.09)	Average Atomic Wgt
Alloy Name														
AISI 310S	52.47	24.65	20.40	1.41	0.13	--	0.14	--	0.038	--	0.023	0.016	0.72	54.94
AISI 304	71.74	18.30	8.45	0.82	--	--	--	--	0.061	--	0.020	0.017	0.59	54.87
AISI 304L	70.27	18.5	8.75	1.43	0.29	--	0.14	0.18	0.030	0.061	0.025	0.013	0.31	55.05
AISI 304N	68.71	18.65	9.49	1.88	0.52	0.03	0.07	0.06	0.048	0.12	0.019	0.024	0.38	54.93
AISI 316	66.8	16.8	11.7	1.9	2.1	--	0.2	--	0.05	--	0.03	0.02	0.4	55.62
AISI 316L	64.54	17.58	13.29	1.69	2.25	--	--	--	0.023	--	0.02	0.018	0.59	55.61
AWS 330	42.28	17.81	34.38	4.59	0.25	--	--	--	0.142	0.044	0.019	0.007	0.48	55.43

* Balance.

Specimen Preparation

Samples were removed from the supplied material using a carborundum cutoff wheel, care being taken to prevent plastic (bulk) damage during handling, and to remove surface damage by etching with "glyceregia"*. The effect of bulk and surface damage on the magnetic susceptibility of AISI 304N, for example, is discussed in Appendix A. Table 4 lists the degrees of etching administered, and the final specimen weight prior to measurement of magnetic susceptibility and magnetization, respectively. As can be seen from the table, surface layers of thickness 0.010-0.015 cm were removed from the susceptibility samples; after which an attempt was made to etch to about the same extent the larger (1/3 to 1/2-g) magnetization samples.

TABLE 4. DEGREE OF ETCHING AND SPECIMEN WEIGHTS IN MAGNETIC SUSCEPTIBILITY MEASUREMENT

Alloy Name	Amount Removed (%)	Final Specimen Weight (mg)
AISI 310S	23	8.85
AISI 304	46	3.725
304L	40	4.99
304N	23	4.37
AISI 316	39	11.51
316L	33	11.50
AWS 330	17	4.95
In 625	--	24.54

* 10 ml HNO_3, 20-50 ml HCl, 30 ml glycerol.

MAGNETIC SUSCEPTIBILITY STUDIES

Measuring Procedure

Magnetic susceptibilities were measured as functions of temperature by the Curie technique using an electronic microbalance and an electromagnet fitted with 18-cm diameter "constant-force" pole caps. The vertical magnetic force field at the sample position ($H \cdot \partial H/\partial z$) was calibrated at room temperature using a ½-g sample of high-purity Pt whose susceptibility and susceptibility temperature dependence are well known. Ferromagnetic contamination of the specimen could be detected, as well as corrected for, by the Honda-Owen method in which the matrix susceptibility is obtained as the intercept, χ_∞, of a reciprocal-field plot based on the equation

$$\chi = \chi_\infty + M/H \quad ,$$

in which M represents the magnetization (which must always be saturated) of the ferromagnetic impurity.

If the parasitic ferromagnetic moment is zero or temperature independent (as would be the case for Fe itself at temperatures below about 500K*) the force-balance data are analysed by computor. On the other hand if the reciprocal-field plots are non-linear, or if the slopes turn out to be temperature dependent, the data are analyzed graphically. Examples are given below.

Data Reduction

Graphical Analysis--AWS 330

Since AWS 330 showed evidence of superparamagnetism within the liquid nitrogen temperature range (77-100K) the data were analysed by

---

* The saturated moment of Fe decreases by about 4% between 0 and 500K.

hand and presented as plots of χ versus 1/H--Figures 1(a) and (b) Since the plots seemed linear in the temperature range 129.5K-414.5K extrapolated values of χ_∞ were acquired. These are presented in Table 5. Attempts were then made to computer fit the susceptibility temperature dependence within this temperature range to the relationship

$$\chi = C/(T-\theta)$$

Only by restricting the data to the temperature range above 172K could an acceptable coefficient of variability (in this case 0.5%) be obtained. The fitting parameters were then C = 11,214 ± 53 $10^{-6} cm^3 Kg^{-1}$, and θ = 111.8 ± 0.6 K, the latter value revealing the need for the reduced temperature range, and indicating the advent of superparamagnetism at about that temperature, which presumably represents the Curie point of pre-existing chemical clusters.

Hand Calculation--AISI Type 304 (8.7-65.6K)

As indicated in Table 1, only for AISI 304 and In 625 were force balance measurements extended into the liquid He range. In the case of case of AISI 304, since the susceptibility began to exhibit some field dependence in that range, the force balance data were reduced by hand and presented under the headings "high" (10.0 kOe) and "low" (3.75 kOe) fields, as in Table 6, and plotted as in Figure 2.

Computer Analysis of Data, Mostly Within the Temperature Range 77-400K

If inspection of the data indicated that the slopes of the reciprocal-field plots would be either zero or temperature independent they were analyzed by computer according to the algorithm illustrated in Figure 3. An index of the data-sets analyzed in this way is given in Table 7. The susceptibility temperature dependences themselves are presented numerically in Tables 8 through 14, and graphically for several representative alloys in Figure 4.

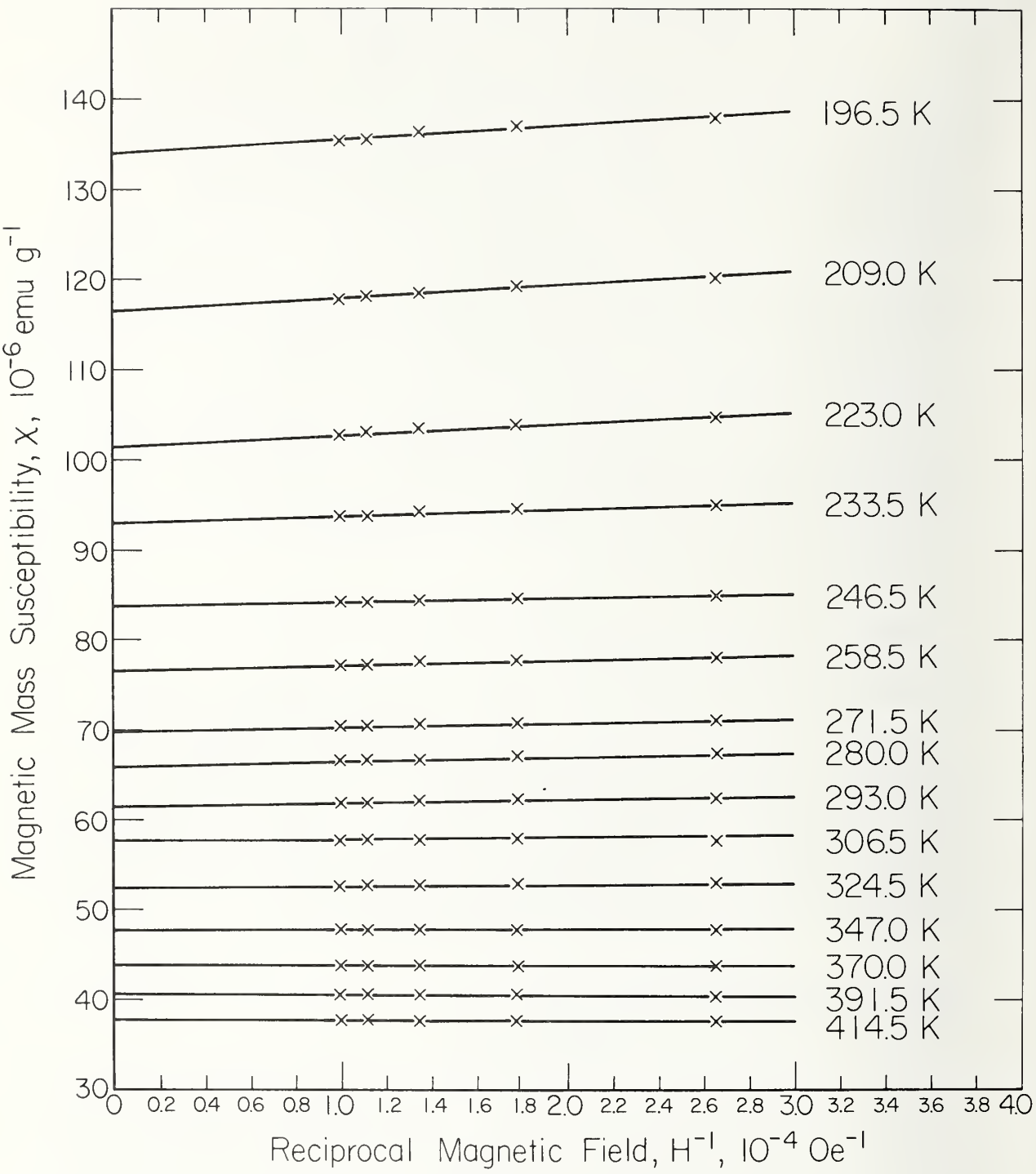

FIGURE 1(a). MAGNETIC SUSCEPTIBILITY OF AWS 330. RECIPROCAL FIELD PLOTS FOR THE TEMPERATURE RANGE 414.5-196.5K. THE GRADUAL DEVELOPMENT OF "FERROMAGNETIC SLOPE" IS EVIDENT.

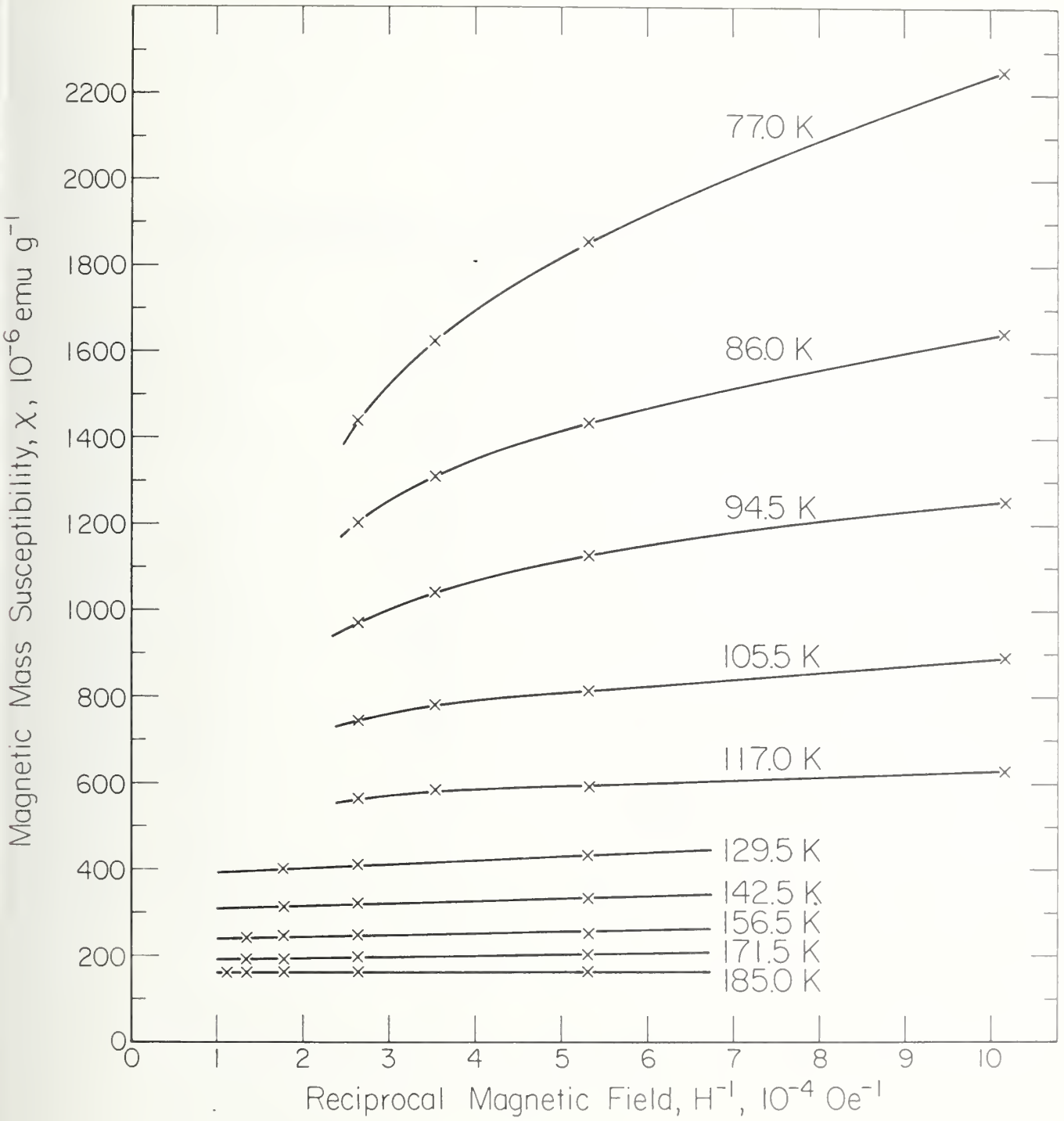

FIGURE 1(b). MAGNETIC SUSCEPTIBILITY OF AWS 330--CONTINUED. RECIPROCAL FIELD PLOTS FOR THE TEMPERATURE RANGE 185-77K. THE ONSET OF SUPERPARAMAGNETISM AT TEMPERATURES NEAR 100K IS EVIDENT.

TABLE 5. MAGNETIC SUSCEPTIBILITY OF AWS 330. GRAPHICALLY EXTRAPOLATED χ_∞ VALUES FOR THE TEMPERATURE RANGE 414.5-129.5K

Temperature (K)	Magnetic Susceptibility ($10^{-6}cm^3g^{-1}$)	Temperature (K)	Magnetic Susceptibility ($10^{-6}cm^3g^{-1}$)
414.5	37.8	258.5	77.0
391.5	40.6	246.5	83.5
370.0	43.8	233.5	92.4
347.0	47.0	223.0	101.1
324.5	52.5	209.0	116.0
306.5	57.5	196.5	132.7
297.0	60.1	185.0	155.3
296.5	60.2	171.5	185.7
		156.5	233.5
293.0	61.5		
280.0	65.9	142.5	303.3
272.0	69.1	129.5	383.0

TABLE 6. MAGNETIC SUSCEPTIBILITY OF AISI TYPE 304 IN THE TEMPERATURE RANGE 8.7-65.6K

Magnetic Field, 10.0 kOe		Magnetic Field, 3.75 kOe	
Temperature (K)	Magnetic Susceptibility ($10^{-6}cm^3g^{-1}$)	Temperature (K)	Magnetic Susceptibility ($10^{-6}cm^3g^{-1}$)
8.7	69.8	8.9	71.7
9.3	69.9	9.5	72.1
9.4	69.9	9.5	71.3
10.6	70.1	10.7	72.2
11.6	70.3	11.5	71.3
12.3	70.4	12.4	72.4
13.7	70.8	14.1	72.9
15.4	71.0	15.2	72.3
17.2	71.6	16.9	72.8
18.9	72.1	18.5	73.2
20.7	72.7	20.2	74.1
24.1	74.3	23.7	75.8
26.1	75.2	25.6	76.2
31.4	78.1	30.1	78.2
34.5	81.2	33.5	81.7
38.1	84.4	37.5	83.7
40.0	85.2	40.0	87.8
45.2	82.8	45.1	86.4
51.7	75.6	50.7	78.6
64.7	63.6	65.6	64.3

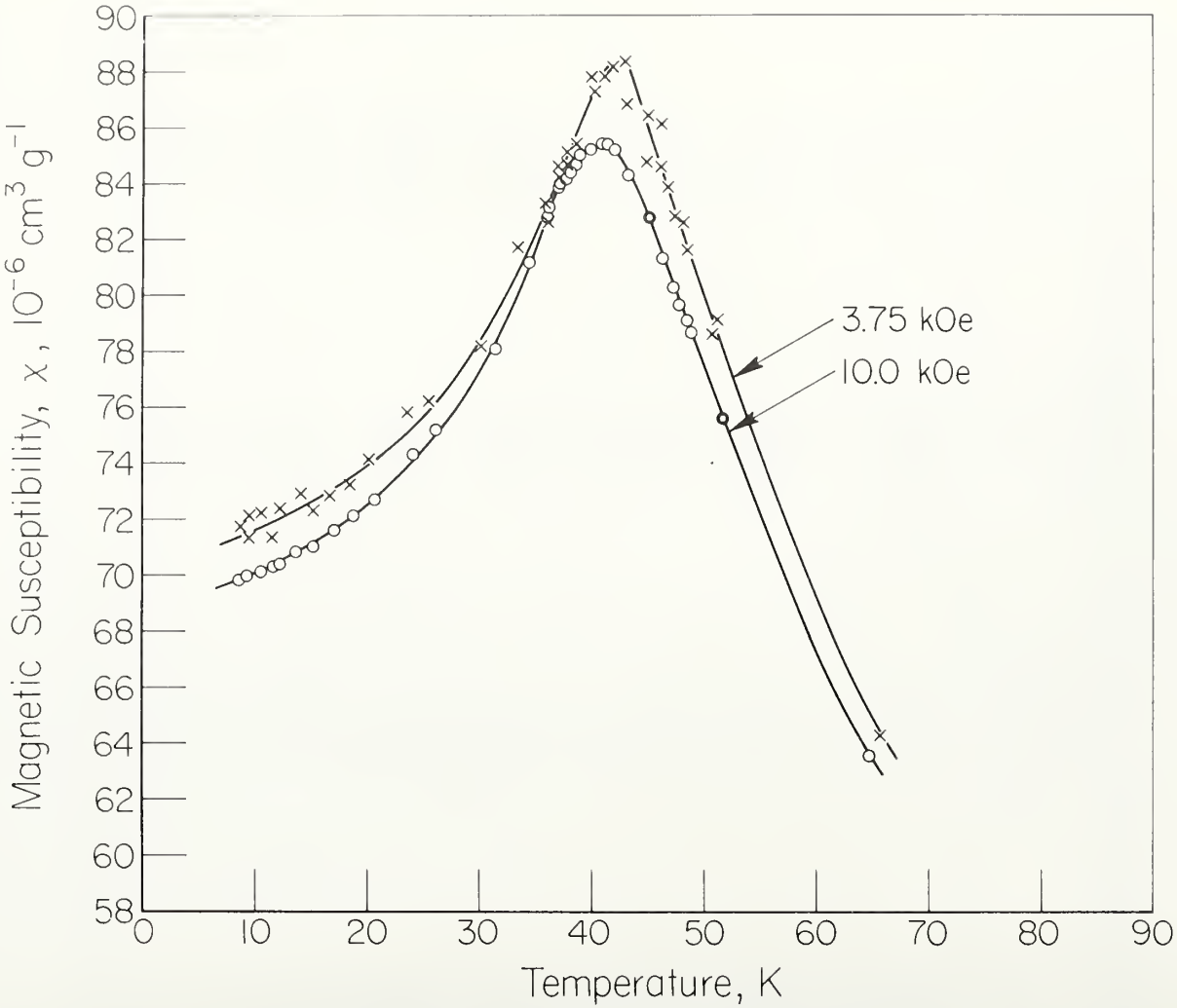

FIGURE 2. MAGNETIC SUSCEPTIBILITY TEMPERATURE DEPENDENCE OF AISI TYPE 304, AT TWO MAGNETIC FIELDS LEVELS, WITHIN THE TEMPERATURE RANGE 8.7-65.6K.

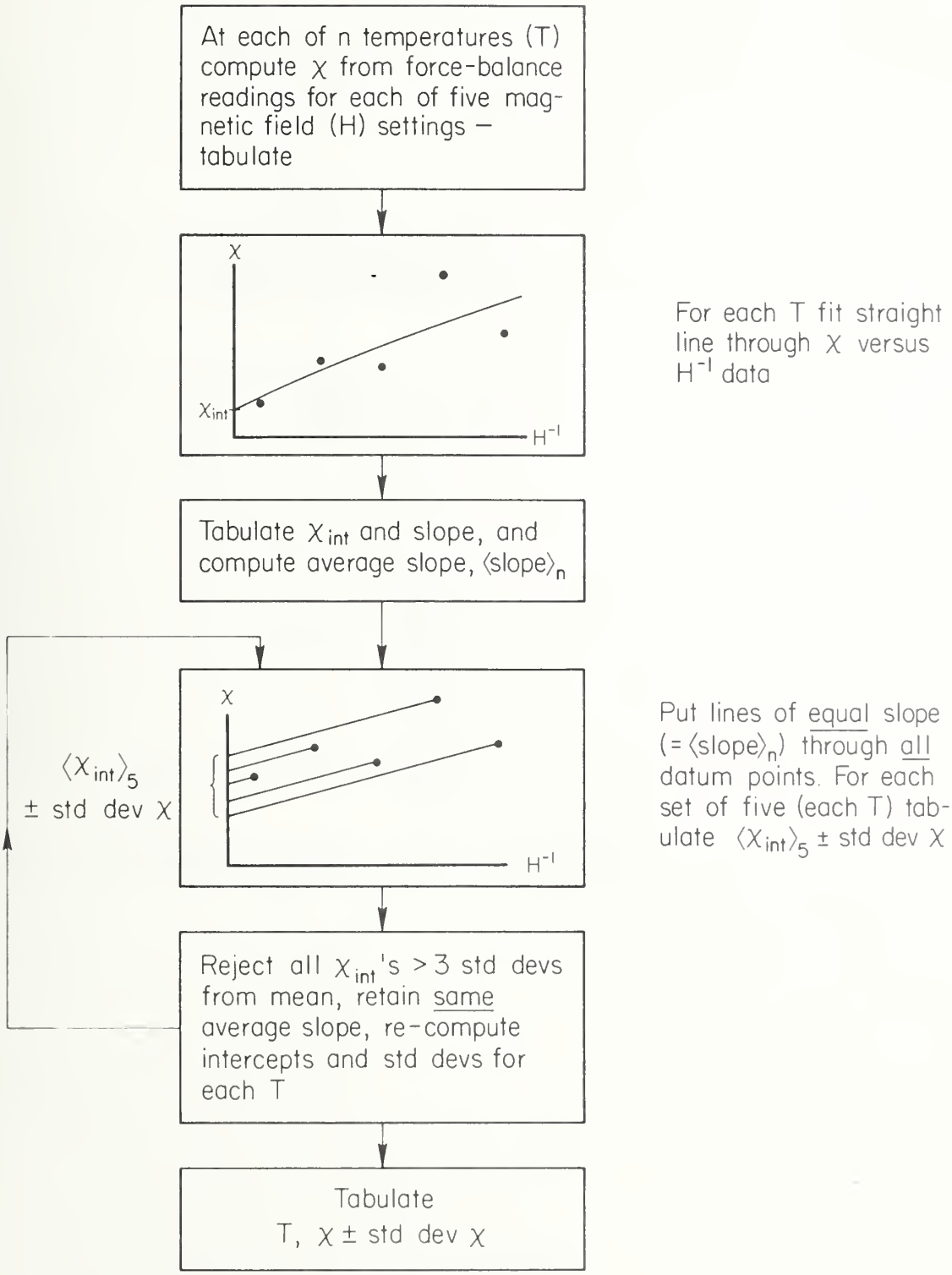
At each of n temperatures (T) compute χ from force-balance readings for each of five magnetic field (H) settings – tabulate
χ
χ_{int}
H^{-1}
For each T fit straight line through χ versus H^{-1} data
Tabulate χ_{int} and slope, and compute average slope, $\langle slope \rangle_n$
χ
H^{-1}
$\langle \chi_{int} \rangle_5$ ± std dev χ
Put lines of equal slope (= $\langle slope \rangle_n$) through all datum points. For each set of five (each T) tabulate $\langle \chi_{int} \rangle_5$ ± std dev χ
Reject all χ_{int}'s > 3 std devs from mean, retain same average slope, re-compute intercepts and std devs for each T
Tabulate
T, χ ± std dev χ

FIGURE 3. ALGORITHM FOR THE COMPUTER REDUCTION OF SUSCEPTIBILITY FORCE BALANCE DATA

TABLE 7. INDEX OF COMPUTER-PRODUCED SUSCEPTIBILITY TEMPERATURE DEPENDENCE DATA TABLES

Alloy Name	Temperature Range of Computer Analysis (K)	Table Number
AISI 310S	77-414	8
AISI 304	77-408	9
304L	77-410	10
304N	77-403	11
AISI 316	77-407	12
316L	77-413	13
In 625	9-80*	14(a)
	77-412	14(b)

* Results normalized at 77K to those of the higher temperature run.

TABLE 8. MAGNETIC SUSCEPTIBILITY TEMPERATURE DEPENDENCE OF AISI 310S OVER THE TEMPERATURE RANGE 77-414K

Temperature (K)	Susceptibility at Intercept	Number of Points Accepted	Standard Deviation of Intercept
77.0	86.015	4	0.053
87.0	76.787	3	0.142
85.0	77.670	3	0.132
96.5	67.705	4	0.095
106.0	61.112	4	0.099
118.5	54.540	4	0.030
129.5	49.934	5	0.081
142.5	45.891	5	0.079
153.0	42.927	5	0.055
166.0	40.057	5	0.056
177.5	37.891	5	0.051
189.0	36.056	5	0.053
202.5	34.278	5	0.061
217.5	32.433	5	0.085
231.5	31.072	5	0.057
245.0	29.975	5	0.057
257.0	28.964	5	0.048
271.0	28.002	5	0.046
281.5	27.335	5	0.036
293.5	26.605	5	0.070
298.5	26.241	5	0.084
305.5	25.990	5	0.069
326.5	24.918	5	0.064
347.5	24.081	5	0.050
371.0	23.196	5	0.042
391.0	22.523	5	0.079
414.0	21.865	5	0.040

TABLE 9. MAGNETIC SUSCEPTIBILITY TEMPERATURE DEPENDENCE OF AISI 304 OVER THE TEMPERATURE RANGE 77-408K

Temperature (K)	Susceptibility at Intercept	Number of Points Accepted	Standard Deviation of Intercept
77.0	55.349	4	0.066
93.5	48.675	4	0.036
103.5	45.610	4	0.034
118.5	42.033	4	0.106
131.5	39.060	5	0.074
143.5	37.598	5	0.070
152.5	36.046	5	0.046
166.5	34.870	5	0.057
182.0	33.430	5	0.084
194.0	32.286	5	0.092
203.0	31.599	5	0.144
213.5	30.897	5	0.087
228.5	30.125	4	0.092
241.0	29.401	5	0.039
251.0	28.851	5	0.082
265.5	28.165	5	0.105
277.5	27.710	5	0.076
289.0	27.221	5	0.103
300.5	26.930	5	0.092
302.0	26.786	5	0.090
322.5	26.095	5	0.099
344.0	25.519	5	0.063
366.0	24.939	5	0.133
388.0	24.421	5	0.064
408.0	24.004	5	0.076

TABLE 10. MAGNETIC SUSCEPTIBILITY TEMPERATURE DEPENDENCE OF AISI 304L OVER THE TEMPERATURE RANGE 77-410K

Temperature (K)	Susceptibility at Intercept	Number of Points Accepted	Standard Deviation of Intercept
77.0	50.460	4	0.041
94.0	44.752	3	0.031
107.0	41.268	5	0.070
125.0	38.038	5	0.077
141.0	35.625	5	0.078
158.0	33.698	4	0.027
172.5	32.328	5	0.042
189.0	31.106	4	0.048
202.0	30.266	5	0.063
213.0	29.527	5	0.057
223.5	28.972	5	0.073
236.0	28.277	5	0.041
248.5	27.692	5	0.050
261.0	27.232	5	0.064
274.0	26.629	5	0.067
287.0	26.181	5	0.037
298.5	25.888	5	0.078
302.0	25.738	5	0.083
321.5	25.065	5	0.049
343.5	24.411	4	0.062
367.0	23.848	5	0.083
387.5	23.362	5	0.043
409.5	22.954	4	0.060

TABLE 11. MAGNETIC SUSCEPTIBILITY TEMPERATURE DEPENDENCE OF AISI 304N OVER THE TEMPERATURE RANGE 77-403K

Temperature (K)	Susceptibility at Intercept	Number of Points Accepted	Standard Deviation of Intercept
77.0	52.388	5	0.084
90.5	47.291	5	0.061
104.5	43.122	4	0.033
116.0	40.438	5	0.065
126.5	38.366	5	0.090
138.0	36.600	5	0.043
152.5	34.814	5	0.046
168.0	33.103	5	0.063
183.5	31.801	4	0.062
197.0	30.747	5	0.086
211.5	29.765	5	0.093
226.0	28.915	5	0.064
239.5	28.152	5	0.107
251.5	27.651	5	0.082
266.5	27.019	4	0.098
280.5	26.527	4	0.072
296.5	25.972	5	0.064
298.5	26.004	5	0.040
298.5	25.958	5	0.065
312.5	25.550	5	0.041
336.5	24.840	4	0.056
358.0	24.261	5	0.080
380.5	23.787	5	0.079
402.5	23.406	5	0.087

TABLE 12. MAGNETIC SUSCEPTIBILITY TEMPERATURE DEPENDENCE OF AISI 316 OVER THE TEMPERATURE RANGE 77-407K

Temperature (K)	Susceptibility at Intercept	Number of Points Accepted	Standard Deviation of Intercept
77.0	75.446	4	0.030
96.5	62.727	4	0.034
110.5	55.576	4	0.082
124.0	50.688	5	0.042
136.5	47.005	5	0.031
149.5	43.967	5	0.045
164.0	41.348	5	0.044
178.0	39.143	5	0.046
189.0	37.706	5	0.058
198.5	36.602	5	0.065
209.5	35.461	5	0.050
222.0	34.304	5	0.034
233.0	33.366	5	0.049
243.0	32.608	5	0.063
254.5	31.838	5	0.053
264.0	31.250	5	0.041
278.0	30.425	5	0.047
291.5	29.753	5	0.042
300.0	29.345	5	0.054
306.5	28.980	5	0.059
319.0	28.446	5	0.065
344.0	27.462	4	0.056
366.0	26.683	5	0.042
386.5	26.051	5	0.053
407.0	25.482	5	0.061

TABLE 13. MAGNETIC SUSCEPTIBILITY TEMPERATURE DEPENDENCE OF AISI 316L OVER THE TEMPERATURE RANGE 77-413K

Temperature (K)	Susceptibility at Intercept	Number of Points Accepted	Standard Deviation of Intercept
77.0	78.875	5	0.085
89.5	69.635	3	0.073
102.5	61.671	5	0.057
116.0	55.031	5	0.060
127.0	51.395	4	0.026
137.0	48.159	4	0.016
148.0	45.371	5	0.030
160.0	42.993	5	0.054
169.5	41.313	5	0.042
179.0	39.785	5	0.041
190.0	38.301	4	0.054
203.0	36.869	5	0.038
214.5	35.666	5	0.046
224.5	34.733	5	0.043
234.0	33.857	5	0.039
247.0	32.883	5	0.030
258.0	32.145	4	0.013
270.5	31.327	5	0.060
281.5	30.666	5	0.051
295.0	29.958	5	0.059
297.0	29.766	5	0.042
309.0	29.275	5	0.034
324.0	28.583	5	0.034
346.0	27.755	5	0.047
368.5	26.936	5	0.053
390.0	26.236	5	0.052
413.0	25.582	5	0.038

TABLE 14(a). MAGNETIC SUSCEPTIBILITY TEMPERATURE DEPENDENCE OF INCONEL 625 OVER THE TEMPERATURE RANGE 9-80K

Temperature (K)	Susceptibility at Intercept*	Number of Points Accepted	Standard Deviation of Intercept
9.5	33.923	5	0.065
9.5	34.170	3	0.087
10.1	32.564	4	0.081
10.5	31.774	4	0.069
11.3	29.971	5	0.095
12.5	28.058	5	0.102
13.4	26.629	5	0.037
15.8	23.718	5	0.030
19.9	20.287	5	0.066
23.8	17.904	5	0.016
29.4	15.481	5	0.074
34.3	13.692	5	0.044
38.2	12.740	4	0.053
42.8	11.806	5	0.077
48.7	10.897	5	0.055
56.0	10.083	5	0.054
61.3	9.490	5	0.035
62.5	9.412	5	0.062
68.1	8.995	5	0.042
74.2	8.510	5	0.039
79.6	8.249	4	0.056

* After normalization, at 77K, to the data of Table 14(b) (normalization factor: 1.1152).

TABLE 14(b). MAGNETIC SUSCEPTIBILITY TEMPERATURE DEPENDENCE OF INCONEL 625 OVER THE TEMPERATURE RANGE 77-412K

Temperature (K)	Susceptibility at Intercept	Number of Points Accepted	Standard Deviation of Intercept
77.0	8.354	5	0.035
90.0	7.784	5	0.027
97.0	7.540	5	0.018
98.5	7.466	5	0.019
110.0	7.083	4	0.022
110.0	7.091	4	0.011
121.0	6.790	5	0.024
122.0	6.761	5	0.020
131.5	6.557	5	0.026
141.5	6.363	5	0.028
153.0	6.134	5	0.034
161.0	6.014	5	0.033
170.0	5.874	5	0.031
180.0	5.746	5	0.054
194.0	5.608	5	0.024
203.0	5.506	5	0.039
211.5	5.450	4	0.018
226.0	5.294	4	0.033
233.5	5.236	5	0.047
242.5	5.189	5	0.037
250.5	5.139	5	0.033
259.5	5.096	4	0.023
270.0	5.032	4	0.027
282.0	4.961	5	0.039
294.0	4.910	4	0.019
296.5	4.916	5	0.026
320.0	4.792	5	0.028
343.0	4.698	5	0.037
366.0	4.616	5	0.023
388.0	4.559	4	0.017
412.0	4.479	5	0.023

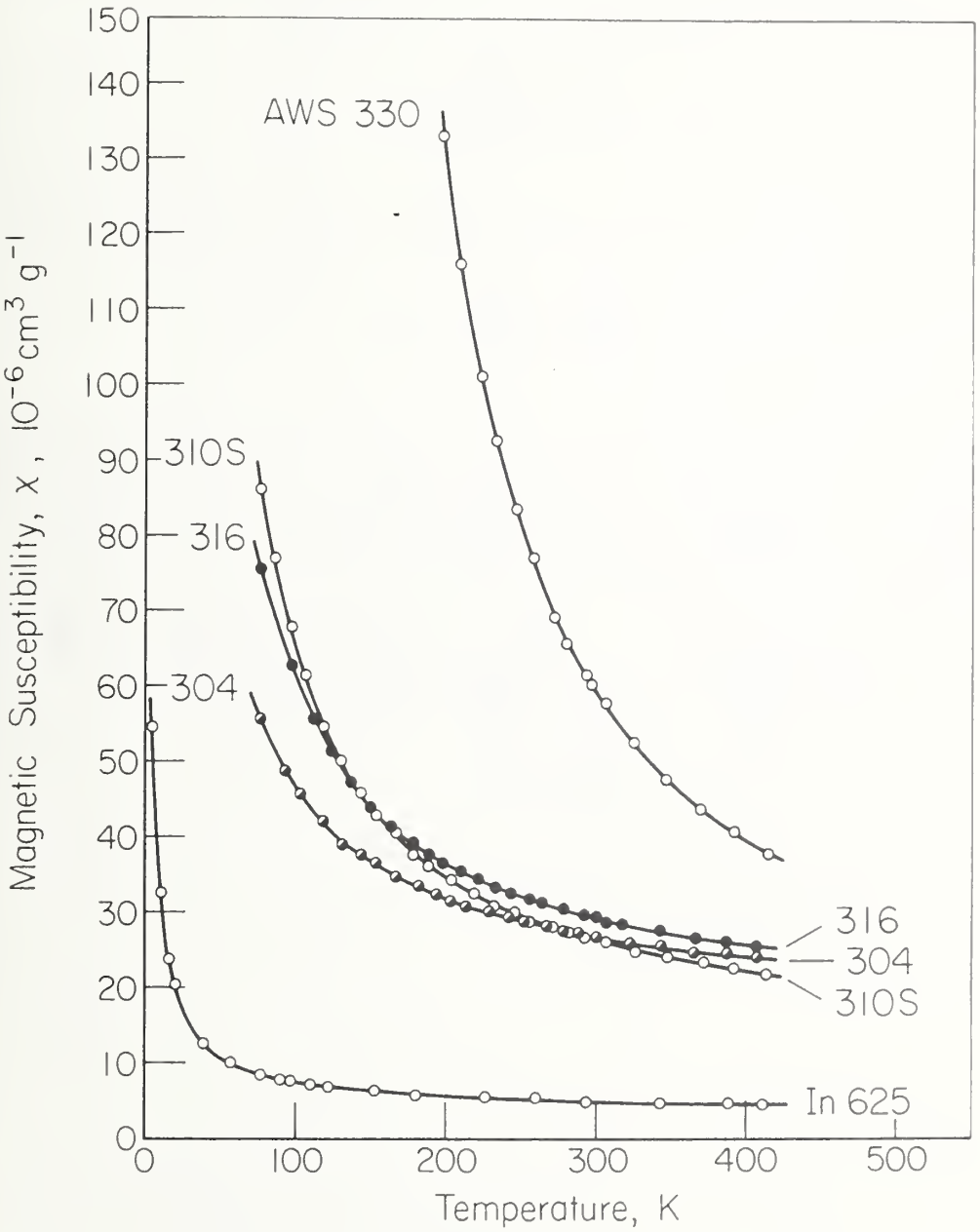

FIGURE 4. MAGNETIC SUSCEPTIBILITY TEMPERATURE DEPENDENCES FOR AISI 310 S, AISI 304, AISI 316, AWS 330, AND In 625

Curve Fitting

With the aid of the well-known SPSS (1967) package* the data of Tables 8 through 14 were fitted to the relationship

$$\chi = \chi_o + C/(T-\theta) \quad .$$

In addition, as has been mentioned, those of Table 5 (AWS 330) were fitted to

$$\chi = C/(T-\theta) \quad .$$

Usually three iterations were employed in order to improve the goodness of fit (expressed in terms of the coefficient of variability) by reducing the temperature range and eliminating what appeared to be bad data. The coefficients of the equations are listed in Table 15. Also listed in the table is an average (over all atoms in the alloy) effective moment per atom, p, in Bohr magnetons, calculated from the relationship

$$p^2 = 799.5 \left(\frac{\text{av. at. wgt.}}{100}\right) C \times 10^{-6} cm^3 Kg^{-1} \quad ,$$

where C is the so-called "Curie constant".

---

* Statistical Package for the Social Sciences, Northwestern University, Version 6.5, April 1, 1976.

TABLE 15. COEFFICIENTS OF THE SUSCEPTIBILITY TEMPERATURE DEPENDENCES OF SOME 300-SERIES STAINLESS STEELS AND INCONEL 625

Alloy Name	Temperature Range (K)	Number of Datum Points	Coefficient of Variability (%)	χ_o ($10^{-6}cm^3g^{-1}$) ($10^{-9}m^3kg^{-1}$)	θ (K)	C ($10^{-6}cm^3Kg^{-1}$) ($10^{-9}m^3Kkg^{-1}$)	Average Atomic Wgt. of Alloy	Average Effective Magnetic Moment/atom, p (Bohr magnetons)
AISI 310S	85-414	25	0.2	11.42±0.06	+23.5±0.4	4093±32	54.94	1.341±0.005
AISI 304	77-400	24	0.3	16.6±0.1	-2.2±1.0	3081±71	54.87	1.163±0.013
AISI 304L	94-367	19	0.4	15.7±0.2	-16.6±2.9	3172±184	55.05	1.182±0.034
304N	77-403	20	0.2	16.37±0.07	-2.6±0.8	2863±53	54.93	1.121±0.010
AISI 316	77-407	24	0.2	15.8±0.1	+13.6±1.0	3864±77	55.62	1.311±0.013
316L	116-390	23	0.2	15.7±0.1	+14.3±1.3	3992±97	55.61	1.332±0.016
AWS 330	172-415	18	0.5	0	111.8±0.6	11,213±53	55.43	2.229±0.005
In 625	4.6-79	22	0.5	3.89±0.04	-2.3±0.1	358±3	--	--
	77-412	30	0.2	3.42±0.01	-14.2±1.3	454±15	--	--

MAGNETIZATION STUDIES

Measuring Procedure

Magnetization was measured as a function of field and temperature using a vibrating-sample magnetometer. Prior to the commencement of each temperature run, which lasted about eight to ten hours, the magnetometer was calibrated and aligned using an NBS-traceable sample of pure Ni.

Magnetization Results

An index of the temperature and field ranges covered in this study is given in Table 16, while the results themselves are presented numerically in Table 17 through 23 and graphically in Figures 5 through 11.

TABLE 16. INDEX OF THE TEMPERATURE AND MAGNETIC FIELD RANGES COVERED

Alloy Name	Temperature Range (K)	Magnetic Field Range (kOe)
AISI 310S	4-75	0.5-13.33
AISI 304	4-143 plus 297	0.5-13.20
304L	4-112 plus 200, 296	0.05-13.00
304N	4-114 plus 294	0.01-13.00
AISI 316	3-110 plus 296	0.5-13.33
316L	4- 80 plus 181, 286	0.05-13.00
AWS 330	4- 65 plus 187,295	0.01-13.20

TABLE 17. MAGNETIZATION TEMPERATURE (T) AND FIELD (H) DEPENDENCES OF AISI TYPE 310S

Sample 310-S Magnetization v.s. Temperature v.s. Applied Field. Units=emu/gram page 1

H \ T	4.2	7.0	10.0	15.0	20.0	25.0	30.0	35.0
500	0.717	0.711	0.637	0.444	0.325	0.236	0.175	0.136
1000	1.256	1.246	1.106	0.833	0.629	0.463	0.341	0.267
1111	1.362	1.349	1.195	0.912	0.693	0.510	0.378	0.295
1250	1.492	1.473	1.307	1.010	0.775	0.571	0.426	0.333
1429	1.634	1.613	1.433	1.124	0.870	0.648	0.481	0.376
1667	1.822	1.812	1.600	1.277	1.002	0.754	0.558	0.436
2000	2.060	2.026	1.804	1.468	1.169	0.883	0.664	0.521
2500	2.372	2.330	2.089	1.735	1.407	1.082	0.820	0.645
3333	2.814	2.761	2.497	2.124	1.767	1.396	1.076	0.852
5000	3.499	3.444	3.155	2.766	2.386	1.955	1.547	1.248
10000	4.893	4.840	4.549	4.179	3.756	3.261	2.743	2.309
13333	5.554	5.501	5.210	4.840	4.443	3.967	3.393	2.923

Units are: Magnetization, cm^3g^{-1}; Temperature, K; Magnetic field, Oe.

TABLE 17 continued

Sample 310-S Magnetization v.s. Temperature v.s. Applied Field. Units=emu/gram page 2

H \ T	40.0	45.0	50.0	55.0	60.0	65.0	70.0	75.0
500	0.109	0.092	0.078	0.068	0.060	0.055	0.049	0.045
1000	0.215	0.181	0.154	0.135	0.120	0.108	0.098	0.089
1111	0.239	0.202	0.172	0.150	0.134	0.120	0.108	0.099
1250	0.268	0.227	0.193	0.171	0.151	0.135	0.123	0.112
1429	0.305	0.257	0.220	0.192	0.171	0.153	0.139	0.127
1667	0.355	0.303	0.257	0.225	0.199	0.185	0.163	0.148
2000	0.421	0.358	0.308	0.268	0.238	0.213	0.194	0.177
2500	0.524	0.444	0.381	0.334	0.296	0.267	0.241	0.221
3333	0.701	0.590	0.505	0.444	0.391	0.354	0.321	0.294
5000	1.026	0.875	0.756	0.664	0.587	0.529	0.479	0.439
10000	1.957	1.701	1.484	1.312	1.166	1.053	0.955	0.878
13333	2.528	2.211	1.947	1.724	1.547	1.399	1.272	1.172

TABLE 18. MAGNETIZATION TEMPERATURE (T) AND FIELD (H) DEPENDENCES OF AISI 304

Sample T-304 Magnetization v.s. Temperature v.s. Applied Field. Units=emu/gram page 1

H \ T	4.2	7.0	10.0	15.0	20.0	25.0	30.0	35.0
500	0.036	0.037	0.039	0.039	0.039	0.040	0.041	0.043
667	0.051	0.052	0.050	0.051	0.051	0.052	0.055	0.056
1000	0.071	0.072	0.073	0.074	0.074	0.077	0.079	0.083
1111	0.079	0.080	0.081	0.081	0.083	0.084	0.088	0.092
1250	0.088	0.089	0.090	0.091	0.092	0.094	0.098	0.102
1429	0.099	0.101	0.102	0.103	0.105	0.107	0.111	0.116
1667	0.117	0.117	0.118	0.119	0.122	0.125	0.129	0.135
2000	0.137	0.139	0.140	0.141	0.145	0.148	0.153	0.160
2500	0.170	0.172	0.173	0.175	0.179	0.183	0.189	0.198
3333	0.225	0.227	0.229	0.231	0.236	0.242	0.251	0.263
5000	0.335	0.337	0.340	0.344	0.352	0.360	0.374	0.392
7500	0.498	0.502	0.505	0.511	0.523	0.536	0.558	0.586
10000	0.664	0.670	0.673	0.682	0.698	0.716	0.748	0.782
12500	0.829	0.838	0.841	0.857	0.875	0.900	0.941	0.984
13200	0.878	0.885	0.891	0.907	0.925	0.953	0.997	1.044

Units are: Magnetization, cm^3g^{-1}; Temperature, K; Magnetic field, Oe.

TABLE 18 continued

Sample T-304 Magnetization v.s. Temperature v.s. Applied Field. Units=emu/gram page 2

H	T	38.0	41.0	44.0	47.0	50.0	55.0	60.0	70.0
500		0.046	0.047	0.045	0.044	0.042	0.039	0.036	0.032
667		0.060	0.061	0.059	0.058	0.055	0.052	0.047	0.041
1000		0.087	0.089	0.087	0.084	0.082	0.075	0.068	0.060
1111		0.096	0.098	0.097	0.094	0.091	0.083	0.076	0.067
1250		0.106	0.110	0.108	0.107	0.102	0.093	0.085	0.075
1429		0.119	0.124	0.123	0.121	0.116	0.105	0.097	0.084
1667		0.139	0.144	0.143	0.139	0.134	0.123	0.112	0.100
2000		0.167	0.170	0.170	0.164	0.159	0.145	0.134	0.118
2500		0.207	0.211	0.211	0.204	0.198	0.181	0.166	0.147
3333		0.273	0.279	0.281	0.270	0.261	0.239	0.220	0.195
5000		0.406	0.414	0.415	0.402	0.387	0.355	0.327	0.902
7500		0.604	0.617	0.614	0.595	0.573	0.526	0.486	0.430
10000		0.807	0.819	0.813	0.788	0.757	0.692	0.642	0.573
12500		1.012	1.019	1.009	0.978	0.928	0.872	0.804	0.713
13200		1.069	1.075	1.065	1.031	0.981	0.922	0.850	0.757

TABLE 18 continued

Sample T-304 Magnetization v.s. Temperature v.s. Applied Field. Units=emu/gram page 3

H	T	100.0	143.0	296.5
500		0.028	0.021	0.017
667		0.037	0.027	0.023
1000		0.051	0.039	0.032
1111		0.055	0.043	0.036
1250		0.063	0.049	0.039
1429		0.071	0.055	0.044
1667		0.082	0.064	0.051
2000		0.097	0.076	0.059
2500		0.116	0.094	0.073
3333		0.156	0.124	0.096
5000		0.230	0.184	0.141
7500		0.341	0.275	0.209
10000		0.449	0.369	0.278
12500		0.564	0.467	0.348
13200		0.595	0.492	0.369

TABLE 19. MAGNETIZATION TEMPERATURE (T) AND FIELD (H) DEPENDENCES OF AISI 304L

Sample 304-L Magnetization v.s. Temperature v.s. Applied Field. Units=emu/gram page 1

H	T	4.2	15.0	25.0	30.0	40.0	50.0	60.0	70.0
50		0.0214	0.0236	0.0237	0.0242	0.0242	0.0232	0.0236	0.0233
100		0.0409	0.0430	0.0437	0.0437	0.0436	0.0420	0.0422	0.0415
200		0.0741	0.0760	0.0764	0.0768	0.0765	0.0740	0.0743	0.0735
500		0.166	0.168	0.170	0.171	0.170	0.166	0.166	0.166
667		0.211	0.215	0.216	0.216	0.216	0.212	0.214	0.211
1000		0.298	0.298	0.298	0.301	0.301	0.299	0.299	0.294
1111		0.320	0.322	0.322	0.323	0.323	0.323	0.321	0.316
1250		0.345	0.348	0.348	0.349	0.349	0.348	0.345	0.342
1429		0.370	0.375	0.376	0.377	0.377	0.376	0.376	0.370
1667		0.400	0.408	0.408	0.408	0.410	0.411	0.410	0.403
2000		0.443	0.448	0.449	0.450	0.450	0.454	0.455	0.444
2500		0.493	0.499	0.502	0.502	0.505	0.509	0.511	0.497
3333		0.563	0.569	0.571	0.574	0.578	0.586	0.589	0.570
5000		0.666	0.675	0.679	0.682	0.691	0.707	0.710	0.683
7500		0.790	0.802	0.808	0.814	0.830	0.857	0.860	0.820
10000		0.908	0.920	0.929	0.938	0.962	1.001	1.003	0.949
12500		1.021	1.039	1.053	1.064	1.092	1.144	1.142	1.079
13000		1.045	1.062	1.079	1.087	1.118	1.172	1.170	1.104

Units are: Magnetization, cm^3g^{-1}; Temperature, K; Magnetic field, Oe.

TABLE 19 continued

Sample 304-L Magnetization v.s. Temperature v.s. Applied Field. Units-emu/gram page 2

H	T	88.0	112.0	200.0	295.5
50		0.0236	0.0234	0.0254	0.0281
100		0.0417	0.0417	0.0459	0.0519
200		0.0616	0.0736	0.0813	0.0921
500		0.165	0.164	0.175	0.187
667		0.209	0.206	0.215	0.226
1000		0.292	0.287	0.284	0.288
1111		0.314	0.309	0.303	0.305
1250		0.338	0.330	0.322	0.322
1429		0.362	0.355	0.344	0.343
1667		0.392	0.384	0.370	0.367
2000		0.432	0.421	0.403	0.398
2500		0.482	0.467	0.443	0.436
3333		0.550	0.530	0.495	0.484
5000		0.650	0.620	0.567	0.549
7500		0.770	0.725	0.649	0.622
10000		0.882	0.824	0.726	0.691
12500		0.993	0.920	0.799	0.752
13000		1.015	0.940	0.814	0.769

TABLE 20. MAGNETIZATION TEMPERATURE (T) AND FIELD (H) DEPENDENCES OF AISI 304N

Sample 304-N Magnetization v.s. Temperature v.s. Applied Field. Units=emu/gram page 1

H \ T	4.2	10.0	15.0	20.0	25.0	30.0	35.0	40.0
10	0.0006	0.0006	0.0005	0.0005	0.0006	0.0006	0.0005	0.0006
20	0.0012	0.0010	0.0010	0.0011	0.0011	0.0011	0.0011	0.0011
30	0.0015	0.0016	0.0015	0.0016	0.0016	0.0017	0.0017	0.0017
50	0.0028	0.0025	0.0026	0.0027	0.0026	0.0027	0.0028	0.0028
100	0.0058	0.0051	0.0051	0.0052	0.0053	0.0054	0.0055	0.0057
200	0.0112	0.0101	0.0102	0.0104	0.0106	0.0108	0.0111	0.0115
300	0.0161	0.0154	0.0154	0.0156	0.0161	0.0164	0.0166	0.0173
500	0.0250	0.0252	0.0256	0.0260	0.0263	0.0271	0.0276	0.0287
667	0.0329	0.0335	0.0340	0.0344	0.0352	0.0358	0.0370	0.0385
1000	0.0499	0.0512	0.0517	0.0525	0.0535	0.0548	0.0562	0.0583
1111	0.0557	0.0567	0.0573	0.0586	0.0592	0.0609	0.0628	0.0648
1250	0.0622	0.0638	0.0644	0.0655	0.0667	0.0683	0.0703	0.0729
1429	0.0708	0.0725	0.0733	0.0746	0.0758	0.0778	0.0802	0.0830
1667	0.0823	0.0843	0.0854	0.0868	0.0882	0.0909	0.0933	0.0965
2000	0.0983	0.101	0.102	0.104	0.106	0.109	0.112	0.116
2500	0.122	0.126	0.127	0.130	0.132	0.135	0.139	0.144
3333	0.163	0.167	0.169	0.171	0.175	0.179	0.185	0.192
5000	0.242	0.250	0.252	0.258	0.262	0.270	0.277	0.288
7500	0.365	0.375	0.380	0.387	0.394	0.405	0.417	0.434
10000	0.488	0.501	0.508	0.518	0.527	0.541	0.557	0.581
12500	0.613	0.630	0.639	0.649	0.662	0.680	0.701	0.732
13000	0.638	0.654	0.663	0.676	0.689	0.708	0.731	0.762

Units are: Magnetization, cm^3g^{-1}; Temperature, K; Magnetic field, Oe.

TABLE 20 continued

Sample 304-N Magnetization v.s. Temperature v.s. Applied Field. Units=emu/gram page 2

H / T	45.0	50.0	52.0	55.0	60.0	65.0	80.0	114.0
10	0.0006	0.0006	0.0006	0.0006	0.0005	0.0004	0.0004	0.0003
20	0.0011	0.0012	0.0012	0.0011	0.0011	0.0010	0.0009	0.0006
30	0.0017	0.0018	0.0019	0.0017	0.0017	0.0016	0.0013	0.0010
50	0.0029	0.0030	0.0031	0.0030	0.0028	0.0026	0.0022	0.0018
100	0.0059	0.0062	0.0063	0.0061	0.0058	0.0053	0.0045	0.0036
200	0.0119	0.0125	0.0127	0.0123	0.0115	0.0108	0.0092	0.0074
300	0.0181	0.0189	0.0191	0.0185	0.0175	0.0164	0.0140	0.0112
500	0.0302	0.0314	0.0316	0.0310	0.0292	0.0274	0.0235	0.0187
667	0.0400	0.0417	0.0426	0.0412	0.0389	0.0366	0.0311	0.0251
1000	0.0613	0.0640	0.0644	0.0630	0.0596	0.0560	0.0478	0.0382
1111	0.0680	0.0713	0.0715	0.0699	0.0664	0.0621	0.0533	0.0426
1250	0.0767	0.0798	0.0807	0.0787	0.0748	0.0700	0.0596	0.0478
1429	0.0871	0.0909	0.0917	0.0895	0.0848	0.0797	0.0681	0.0546
1667	0.102	0.106	0.107	0.104	0.0989	0.0926	0.0795	0.0638
2000	0.122	0.127	0.128	0.125	0.119	0.111	0.0952	0.0763
2500	0.152	0.157	0.159	0.156	0.147	0.139	0.119	0.0952
3333	0.201	0.211	0.212	0.207	0.197	0.185	0.158	0.127
5000	0.302	0.316	0.318	0.310	0.295	0.276	0.237	0.190
7500	0.455	0.473	0.475	0.464	0.441	0.415	0.356	0.285
10000	0.609	0.630	0.633	0.619	0.589	0.554	0.475	0.382
12500	0.768	0.787	0.790	0.771	0.735	0.692	0.596	0.478
13060	0.799	0.819	0.821	0.802	0.764	0.721	0.621	0.499

TABLE 20 continued

Sample 304-N Magnetization v.s. Temperature v.s. Applied Field. Units=emu/gram page 3

H	T 294.0
10	0.0003
20	0.0005
30	0.0008
50	0.0012
100	0.0025
200	0.0049
300	0.0074
500	0.0124
667	0.0164
1000	0.0249
1111	0.0278
1250	0.0313
1429	0.0357
1667	0.0417
2000	0.0499
2500	0.0612
3333	0.0829
5000	0.124
7500	0.187
10000	0.247
12500	0.310
13000	0.323

TABLE 21. MAGNETIZATION TEMPERATURE (T) AND FIELD (H) DEPENDENCES OF AISI 316

Sample 316 Magnetization v.s. Temperature v.s. Applied Field. Units=emu/gram page 1

H \ T	3.0	5.0	10.0	15.0	20.0	25.0	30.0	35.0
500	0.078	0.089	0.089	0.091	0.096	0.103	0.103	0.091
667	0.106	0.114	0.117	0.121	0.128	0.136	0.138	0.121
1000	0.154	0.163	0.173	0.177	0.186	0.202	0.203	0.179
1111	0.170	0.181	0.191	0.196	0.207	0.225	0.227	0.202
1250	0.191	0.201	0.213	0.220	0.232	0.252	0.253	0.226
1429	0.218	0.228	0.242	0.251	0.268	0.287	0.288	0.256
1667	0.255	0.265	0.282	0.294	0.311	0.335	0.337	0.298
2000	0.303	0.314	0.337	0.347	0.366	0.399	0.399	0.355
2500	0.377	0.391	0.418	0.434	0.456	0.497	0.494	0.437
3333	0.000	0.514	0.554	0.579	0.612	0.664	0.653	0.579
5000	0.000	0.773	0.836	0.877	0.931	0.992	0.956	0.852
7500	0.000	1.175	1.284	1.355	1.423	1.464	1.385	1.251
10000	0.000	1.609	1.778	1.849	1.896	1.898	1.781	1.617
12500	0.000	2.079	2.289	2.333	2.338	2.297	2.152	1.964
13333	0.000	2.238	2.456	2.489	2.478	2.422	2.275	2.076

Units are: Magnetization, cm^3g^{-1}; Temperature, K; Magnetic field, Oe.

TABLE 21 continued

Sample 316 Magnetization v.s. Temperature v.s. Applied Field. Units=emu/gram page 2

H	T	40.0	45.0	50.0	55.0	60.0	65.0	70.0	75.0
500		0.078	0.069	0.062	0.056	0.051	0.047	0.044	0.040
667		0.105	0.093	0.083	0.075	0.069	0.063	0.059	0.054
1000		0.157	0.138	0.124	0.111	0.101	0.093	0.087	0.081
1111		0.174	0.154	0.138	0.123	0.113	0.104	0.097	0.090
1250		0.195	0.173	0.155	0.139	0.127	0.119	0.110	0.102
1429		0.222	0.197	0.176	0.159	0.144	0.133	0.124	0.116
1667		0.259	0.230	0.205	0.185	0.169	0.155	0.145	0.135
2000		0.309	0.275	0.246	0.221	0.202	0.186	0.173	0.161
2500		0.382	0.343	0.307	0.275	0.253	0.232	0.216	0.201
3333		0.508	0.453	0.404	0.366	0.337	0.309	0.289	0.269
5000		0.757	0.677	0.606	0.546	0.500	0.459	0.429	0.399
7500		1.117	1.008	0.904	0.817	0.748	0.688	0.645	0.601
10000		1.461	1.325	1.196	1.090	0.997	0.921	0.860	0.803
12500		1.795	1.636	1.491	1.360	1.246	1.150	1.073	1.005
13333		1.907	1.734	1.584	1.443	1.327	1.225	1.148	1.073

TABLE 21 continued

Sample 316 Magnetization v.s. Temperature v.s. Applied Field. Units=emu/gram page 3

H \ T	80.0	90.0	100.0	110.0	296.0
500	0.038	0.034	0.031	0.029	0.015
667	0.051	0.046	0.042	0.038	0.020
1000	0.076	0.068	0.061	0.057	0.030
1111	0.084	0.075	0.068	0.063	0.034
1250	0.095	0.086	0.077	0.071	0.038
1429	0.108	0.097	0.088	0.081	0.043
1667	0.126	0.113	0.103	0.094	0.050
2000	0.151	0.135	0.123	0.113	0.060
2500	0.188	0.169	0.152	0.140	0.075
3333	0.251	0.225	0.202	0.187	0.100
5000	0.374	0.333	0.303	0.281	0.150
7500	0.560	0.503	0.456	0.421	0.225
10000	0.751	0.672	0.609	0.560	0.300
12500	0.937	0.836	0.762	0.702	0.374
13333	0.999	0.890	0.811	0.748	0.396

TABLE 22. MAGNETIZATION TEMPERATURE (T) AND FIELD (H) DEPENDENCES OF AISI 316L

Sample 316 L Magnetization v.s. Temperature v.s. Applied Field. Units=emu/gram page 1

H	T	4.2	5.3	10.0	15.0	20.0	25.0	30.0	35.0
50		0.0121	0.0079	0.0081	0.0088	0.0096	0.0101	0.0096	0.0082
100		0.0198	0.0150	0.0160	0.0177	0.0188	0.0202	0.0199	0.0170
200		0.0364	0.0310	0.0320	0.0341	0.0367	0.0405	0.0399	0.0343
500		0.0831	0.0755	0.0796	0.0852	0.0913	0.101	0.100	0.0862
667		0.108	0.100	0.105	0.112	0.120	0.134	0.133	0.115
1000		0.159	0.152	0.161	0.169	0.183	0.204	0.199	0.173
1111		0.178	0.169	0.178	0.189	0.203	0.226	0.222	0.192
1250		0.198	0.191	0.201	0.213	0.228	0.253	0.249	0.217
1429		0.226	0.217	0.231	0.242	0.261	0.290	0.283	0.246
1667		0.263	0.254	0.269	0.282	0.305	0.336	0.328	0.287
2000		0.316	0.305	0.318	0.340	0.367	0.405	0.394	0.343
2500		0.394	0.385	0.400	0.425	0.460	0.504	0.489	0.427
3333		0.525	0.514	0.539	0.570	0.619	0.672	0.644	0.567
5000		0.791	0.777	0.819	0.875	0.949	0.994	0.939	0.836
7500		1.212	1.190	1.270	1.346	1.440	1.447	1.350	1.218
10000		1.642	1.645	1.767	1.855	1.893	1.855	1.730	1.578
12500		2.131	2.143	2.269	2.319	2.306	2.231	2.081	1.918
13000		2.219	2.256	2.357	2.407	2.382	2.306	2.156	1.980

Units are: Magnetization, cm^3g^{-1}; Temperature, K; Magnetic field, Oe.

TABLE 22 continued

Sample 316-L Magnetization v.s. Temperature v.s. Applied Field. Units=emu/gram page 2

H	T	40.0	50.0	60.0	80.0	181.0	286.0
50		0.0072	0.0055	0.0045	0.0034	0.0018	0.0014
100		0.0147	0.0115	0.0094	0.0070	0.0039	0.0029
200		0.0297	0.0233	0.0189	0.0139	0.0078	0.0059
500		0.0748	0.0589	0.0481	0.0358	0.0197	0.0149
667		0.0990	0.0781	0.0637	0.0474	0.0256	0.0198
1000		0.150	0.118	0.0968	0.0721	0.0387	0.0300
1111		0.167	0.132	0.108	0.0801	0.0425	0.0335
1250		0.188	0.149	0.121	0.0901	0.0485	0.0375
1429		0.214	0.168	0.138	0.103	0.0552	0.0430
1667		0.248	0.196	0.161	0.120	0.0643	0.0500
2000		0.300	0.236	0.193	0.144	0.0775	0.0600
2500		0.374	0.295	0.241	0.179	0.0969	0.0751
3333		0.498	0.394	0.322	0.239	0.129	0.100
5000		0.740	0.589	0.484	0.360	0.194	0.151
7500		1.091	0.880	0.725	0.542	0.292	0.226
10000		1.426	1.164	0.966	0.722	0.390	0.302
12500		1.755	1.445	1.207	0.906	0.489	0.379
13000		1.805	1.502	1.255	0.944	0.510	0.395

TABLE 23. MAGNETIZATION TEMPERATURE (T) AND FIELD (H) DEPENDENCES OF AWS 330

Sample AWS 330 Magnetization v.s. Temperature v.s. Applied Field. Units=emu/gram page 1

H / T	4.2	10.0	15.0	20.0	25.0	30.0	35.0	38.0
10				0.120	0.128	0.138	0.144	0.142
20				0.238	0.280	0.318	0.323	0.318
30				0.367	0.440	0.488	0.502	0.490
50		0.233	0.619	0.619	0.722	0.803	0.814	0.786
100		0.588	1.144	1.275	1.412	1.526	1.532	1.492
200		1.412	2.186	2.357	2.517	2.665	2.642	2.568
300		2.380	3.086	3.268	3.439	3.570	3.490	3.382
500	1.435	4.059	4.498	4.634	4.771	4.828	4.669	4.526
667	2.010	5.039	5.397	5.494	5.591	5.597	5.392	5.227
1000	5.722	6.644	6.752	6.804	6.815	6.730	6.485	6.286
1111	5.961	7.231	7.140	7.174	7.174	7.003	6.764	
1250	6.223	7.572	7.515	7.515	7.515	7.345	7.060	
1429	6.530	7.971	7.971	7.971	7.914	7.743	7.458	
1667	6.889	8.483	8.483	8.483	8.369	8.199	7.857	
2000	7.743	9.110	9.110	9.053	8.939	8.711	8.369	
2500	8.825	9.850	9.850	9.736	9.622	9.337	9.053	
3333	10.362	10.875	10.818	10.704	10.533	10.248	9.907	
5000	12.127	12.298	12.127	12.013	11.785	11.501	11.159	
7500	13.664	13.721	13.550	13.380	13.152	12.867	12.526	
10000	14.746	14.746	14.518	14.348	14.120	13.892	13.494	
12500	15.543	15.543	15.315	15.145	14.917	14.632	14.291	
13200	15.771	15.714	15.543	15.372	15.145	14.860	14.518	

Units are: Magnetization, cm^3g^{-1}; Temperature, K; Magnetic field, Oe.

TABLE 23 continued

Sample AWS 330 Magnetization v.s. Temperature v.s. Applied Field. Units=emu/gram page 2

H / T	40.0	45.0	50.0	55.0	65.0	187.0	294.5
10	0.136	0.121	0.110	0.0945	0.0678		
20	0.309	0.279	0.240	0.203	0.132		
30	0.471	0.430	0.366	0.307	0.197		
50	0.769	0.692	0.585	0.494	0.313	0.0251	
100	1.435	1.287	1.105	0.928	0.597	0.0380	
200	2.477	2.220	1.913	1.623	1.082	0.0586	
300	3.262	2.955	2.562	2.198	1.503	0.0778	
500	4.395	3.997	3.519	3.097	2.215	0.113	0.0427
667	5.084	4.657	4.168	3.689	2.710	0.143	0.0540
1000	6.143	5.705	5.130	4.646	3.570	0.200	0.0752
1111	6.422	5.978		4.913	3.826	0.219	0.0826
1250	6.747	6.297		5.215	4.094	0.242	0.0922
1429	7.105	6.667		5.563	4.412	0.270	0.103
1667	7.515	7.066		5.995	4.788	0.310	0.118
2000	8.028	7.567		6.491	5.301	0.365	0.139
2500	8.654	8.199		7.145	5.944	0.446	0.171
3333	9.565	9.053		8.028	6.832	0.583	0.224
5000	10.818	10.362		9.337	8.199	0.854	0.330
7500	12.184	11.729		10.761	9.622	1.253	0.488
10000	13.152	12.753		11.785	10.704	1.628	0.647
12500	14.006	13.550		12.639	11.558	2.044	0.803
13200	14.177	13.778		12.867	11.785	2.141	0.848

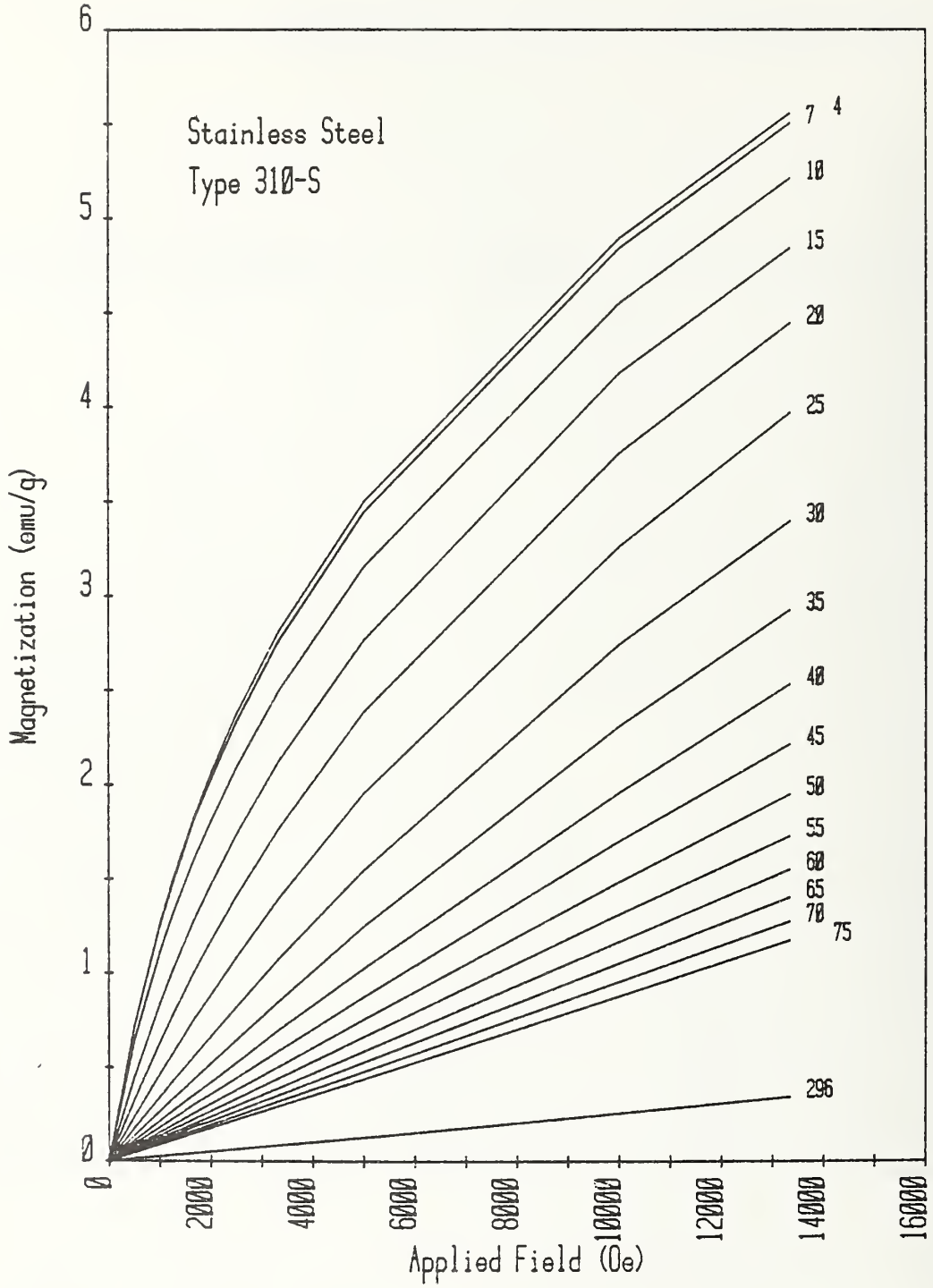

FIGURE 5. MAGNETIZATION FIELD AND TEMPERATURE DEPENDENCES OF AISI TYPE 310 S

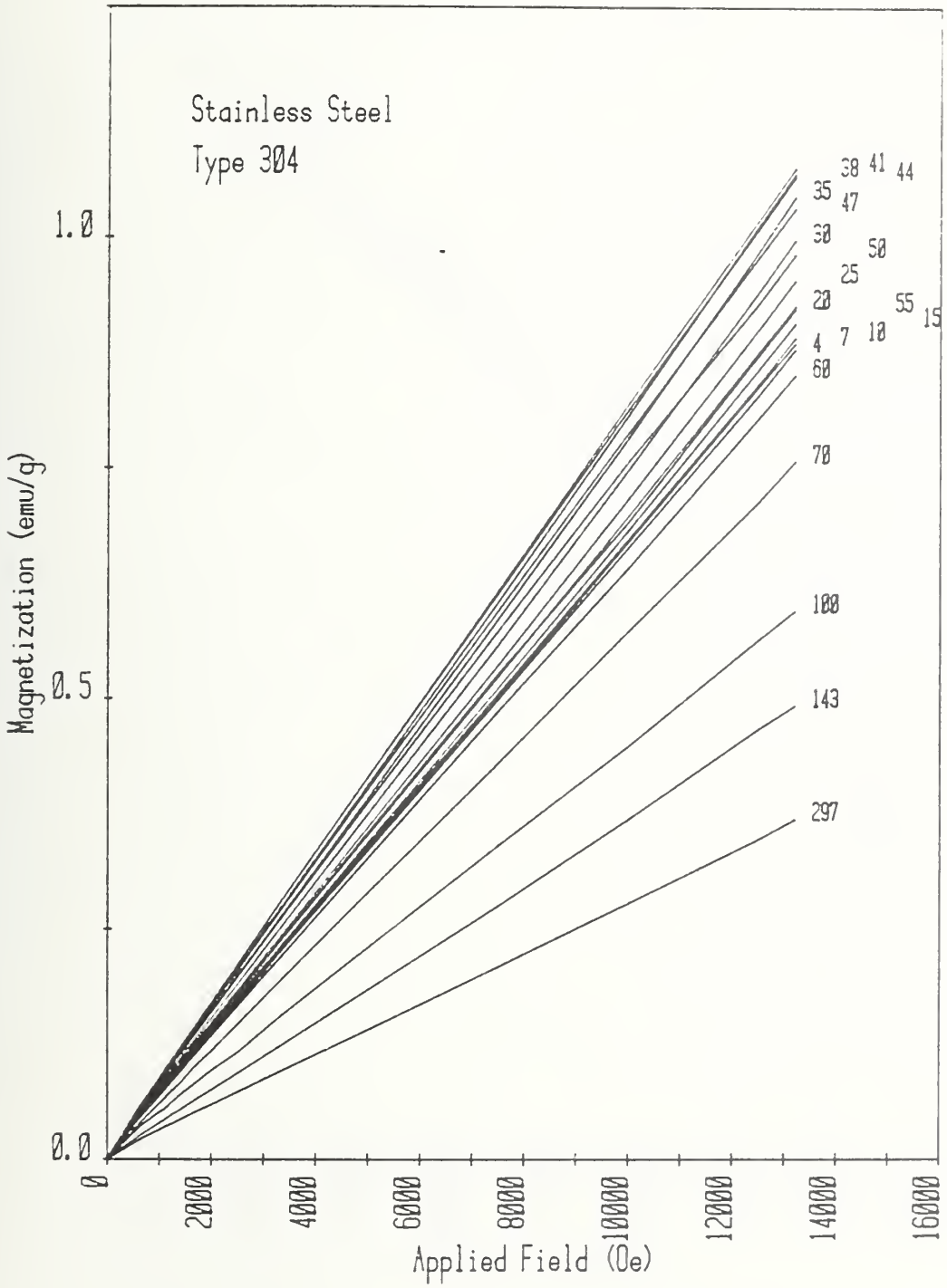

FIGURE 6. MAGNETIZATION FIELD AND TEMPERATURE DEPENDENCES OF AISI TYPE 304

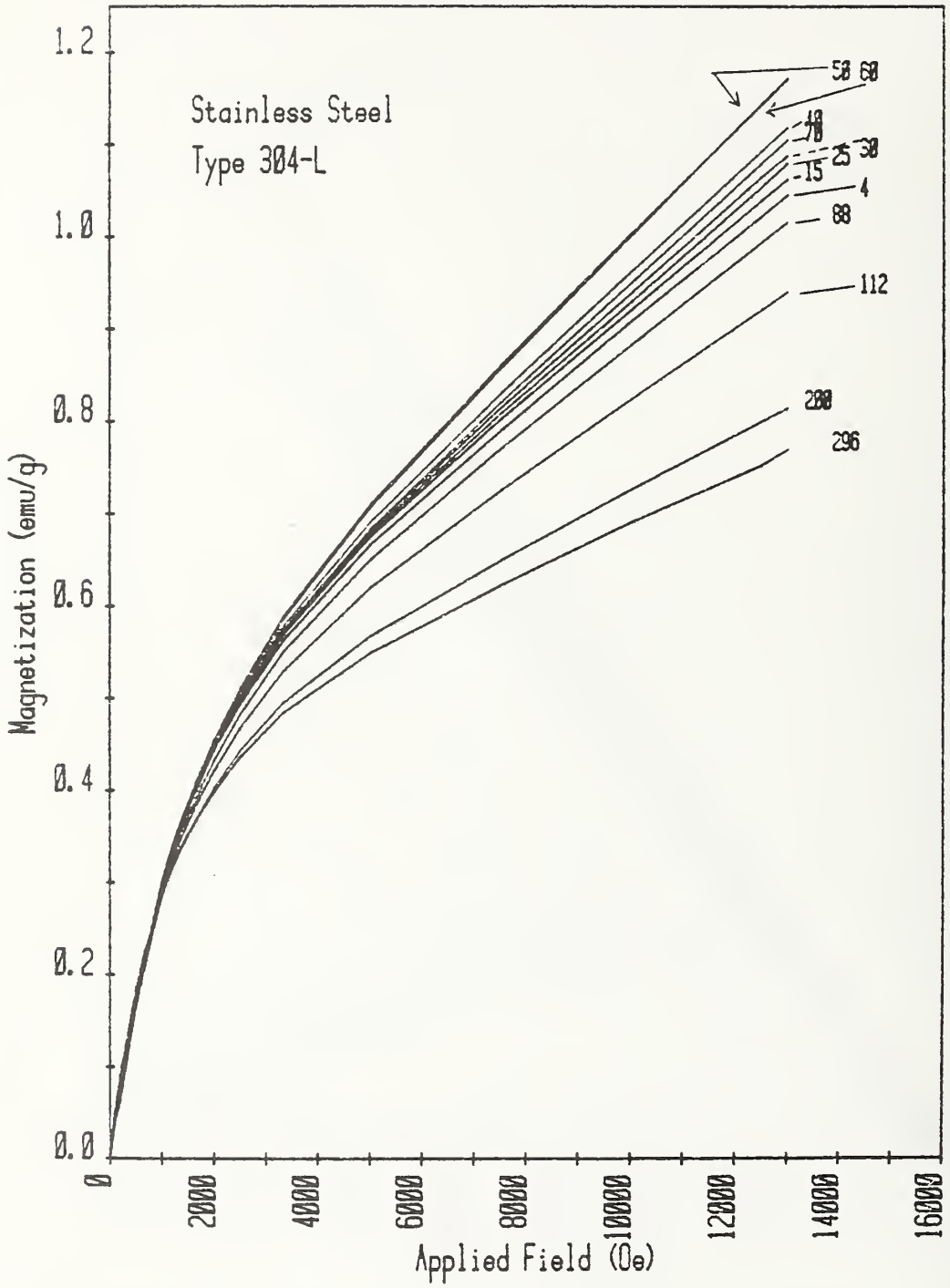

FIGURE 7. MAGNETIZATION FIELD AND TEMPERATURE DEPENDENCES OF AISI TYPE 304L

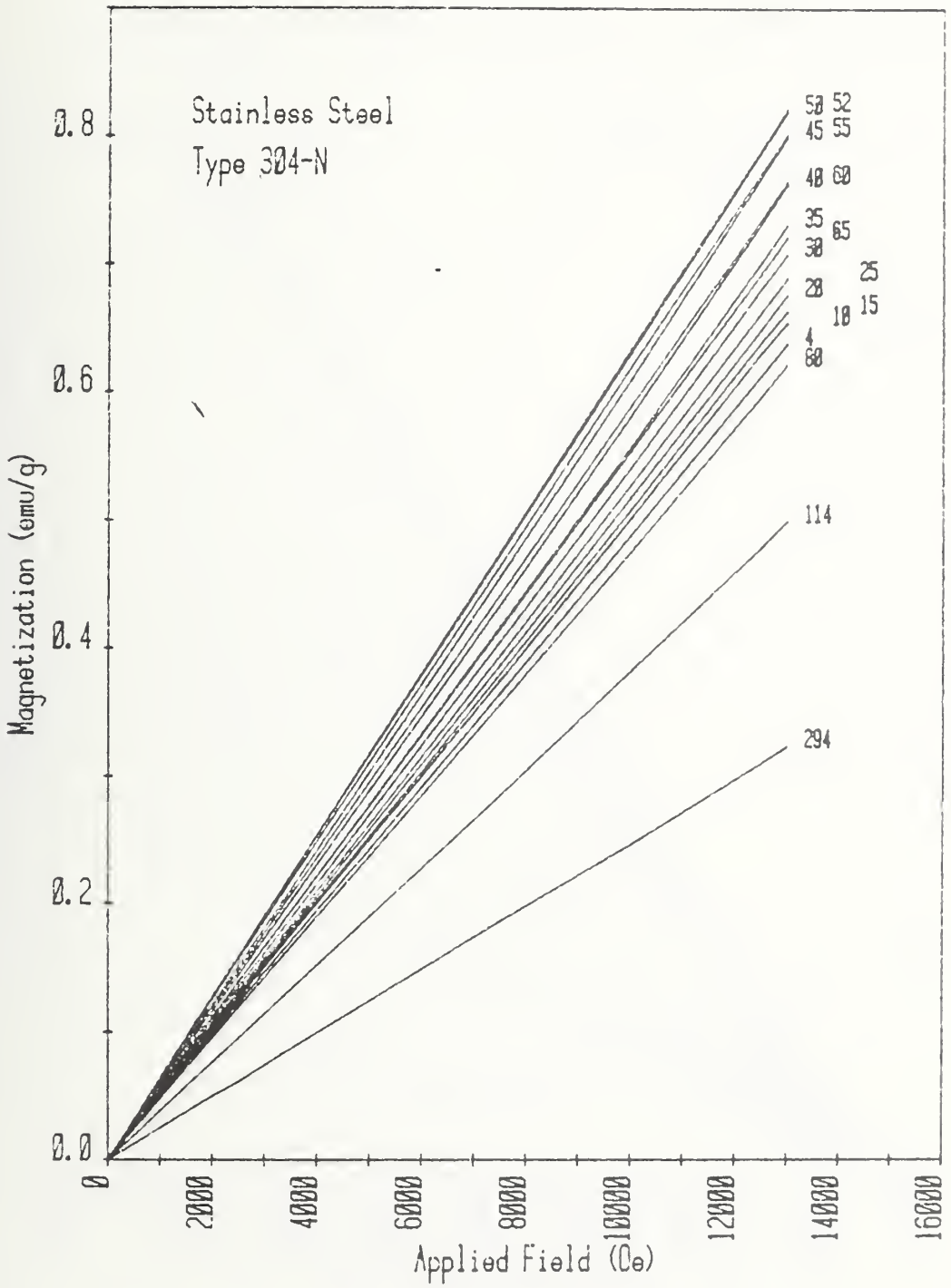

FIGURE 8. MAGNETIZATION FIELD AND TEMPERATURE DEPENDENCES OF AISI TYPE 304N

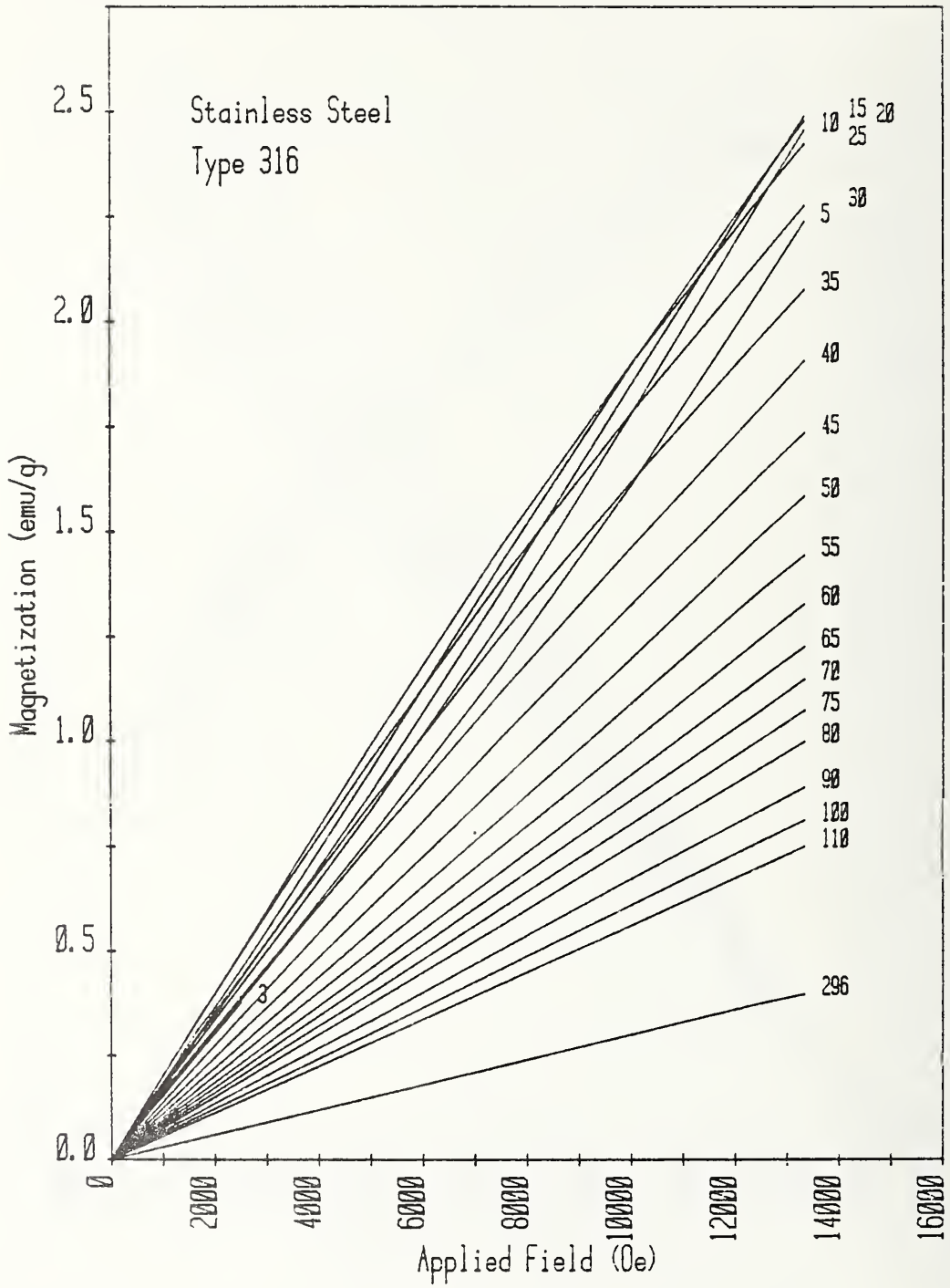

FIGURE 9. MAGNETIZATION FIELD AND TEMPERATURE DEPENDENCES OF AISI TYPE 316

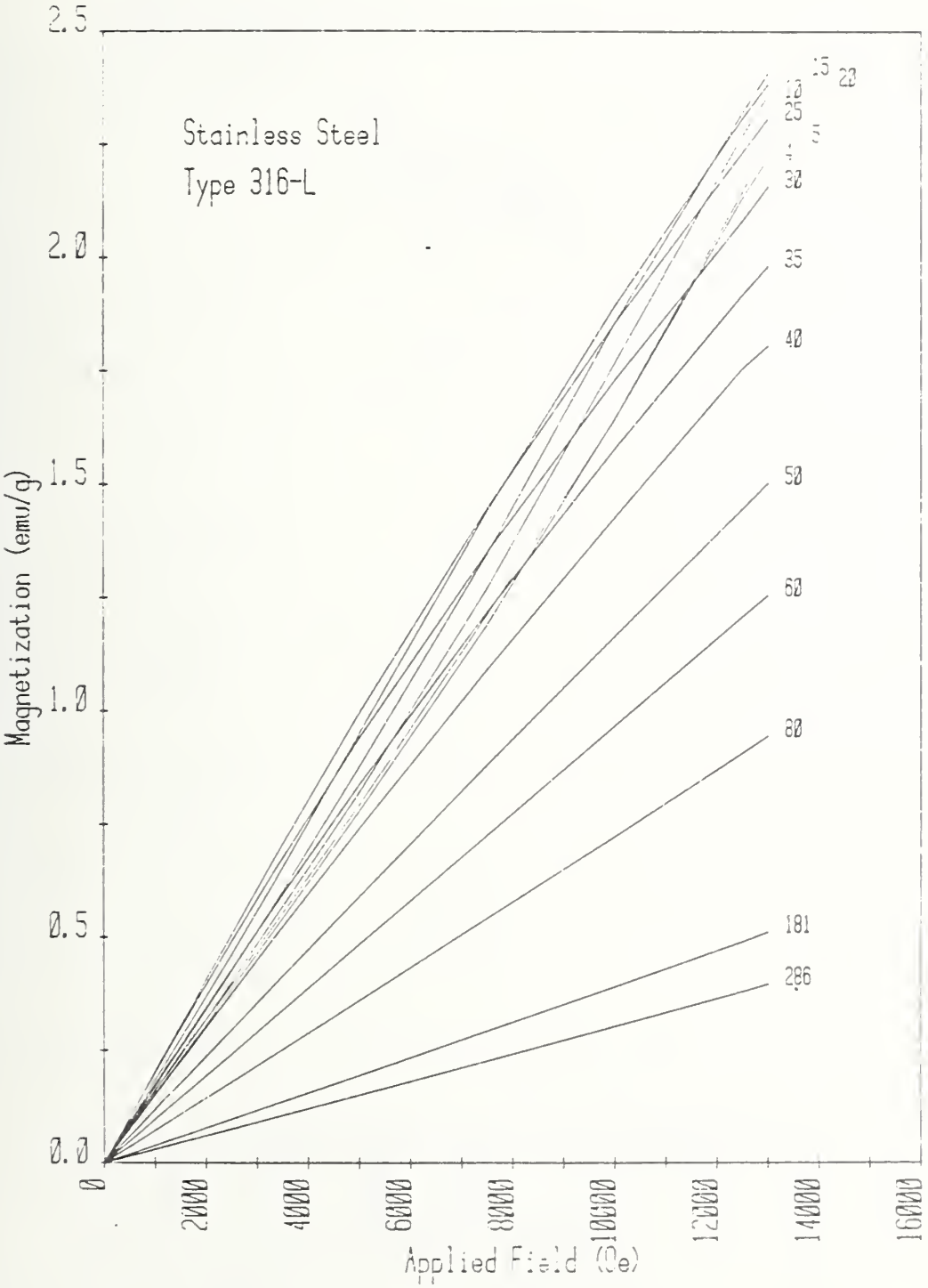

FIGURE 10. MAGNETIZATION FIELD AND TEMPERATURE DEPENDENCES OF AISI TYPE 316L

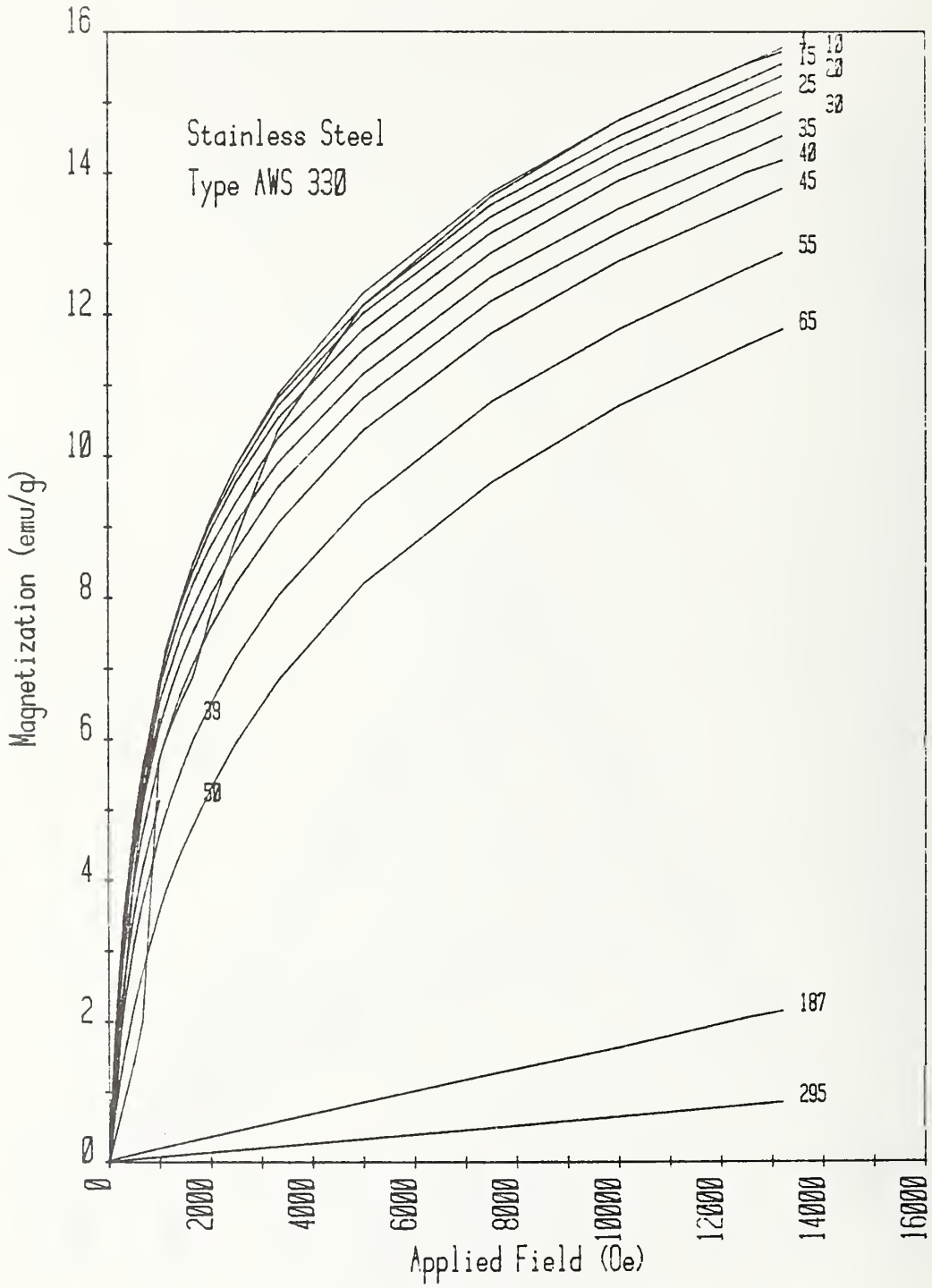

FIGURE 11. MAGNETIZATION FIELD AND TEMPERATURE DEPENDENCES OF AWS 330

Comments on the Magnetization Results

The interpretations of the significances of the several types of magnetization signatures encountered in Figures 5 through 11 are given in Table 24.

TABLE 24. MAGNETIZATION SIGNATURES

Characteristic	Example	Interpretation
concave downwards	310 S	superparamagnetism
linear over much of H,T range	304 316	paramagnetism over that range
concave upwards	304 316 at low temp.	result of the matrix-induced freezing of the giant moments
extreme downwards concavity when unexpected	304L	ferromagnetic contamination
maximum in M(T)	304 316 AWS 330	spin glass transition

An elaboration of these observations will be presented elsewhere.

Magnetic Susceptibility Temperature Dependences Derived from Magnetization Studies

Values of static magnetic susceptibility (M/H) were computed at low (i.e. 500 or 1000 Oe), intermediate, and high (i.e., about 13,000 Oe) magnetic fields for all of the alloys investigated. The results of this

work, displayed graphically in Figures 12 through 17 show clearly the effects of superparamagnetism, spin glass condensation, and these effects combined.

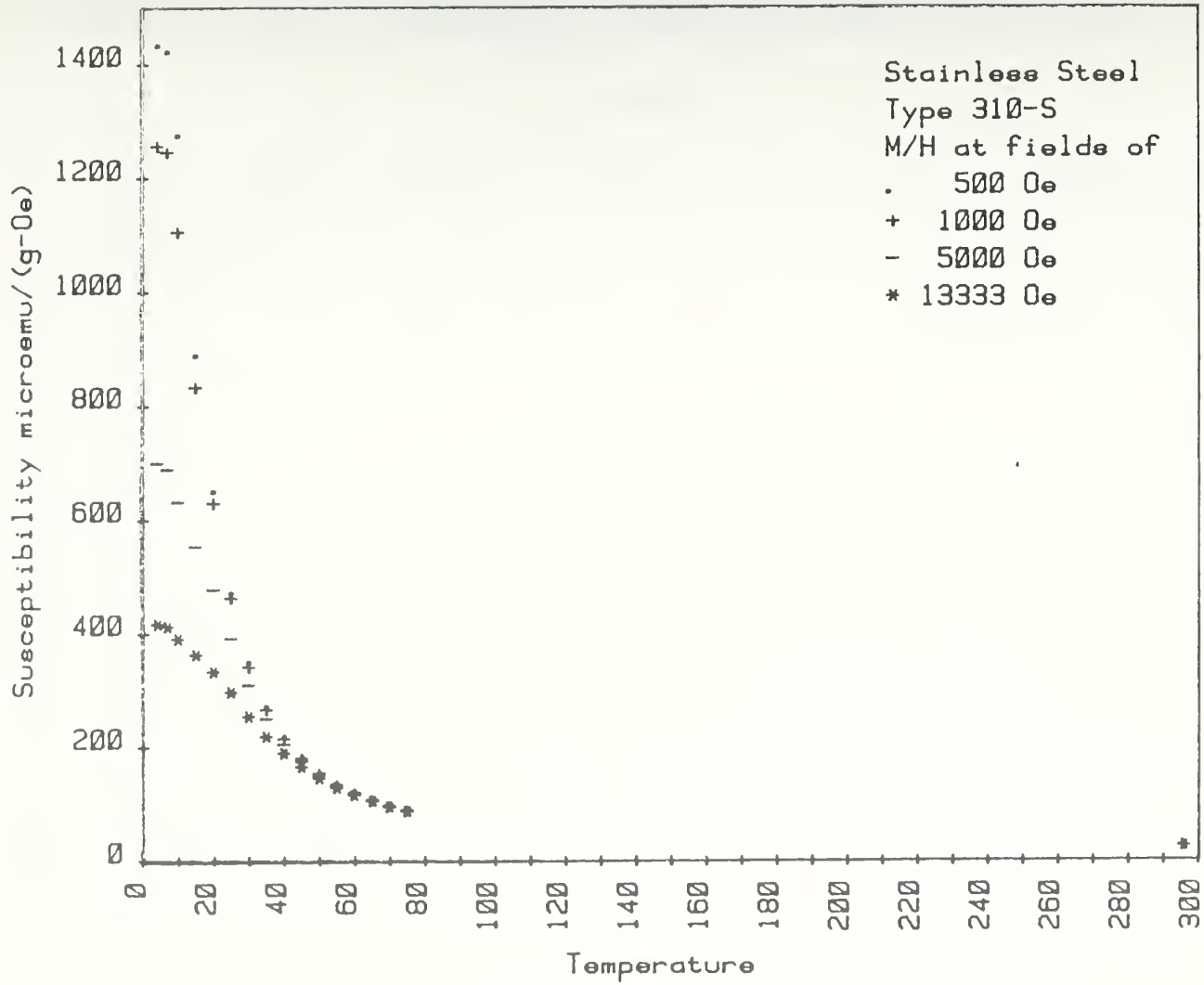

FIGURE 12. MAGNETIC SUSCEPTIBILITY TEMPERATURE DEPENDENCES OF AISI 310S AT LOW, INTERMEDIATE, AND HIGH MAGNETIC FIELDS

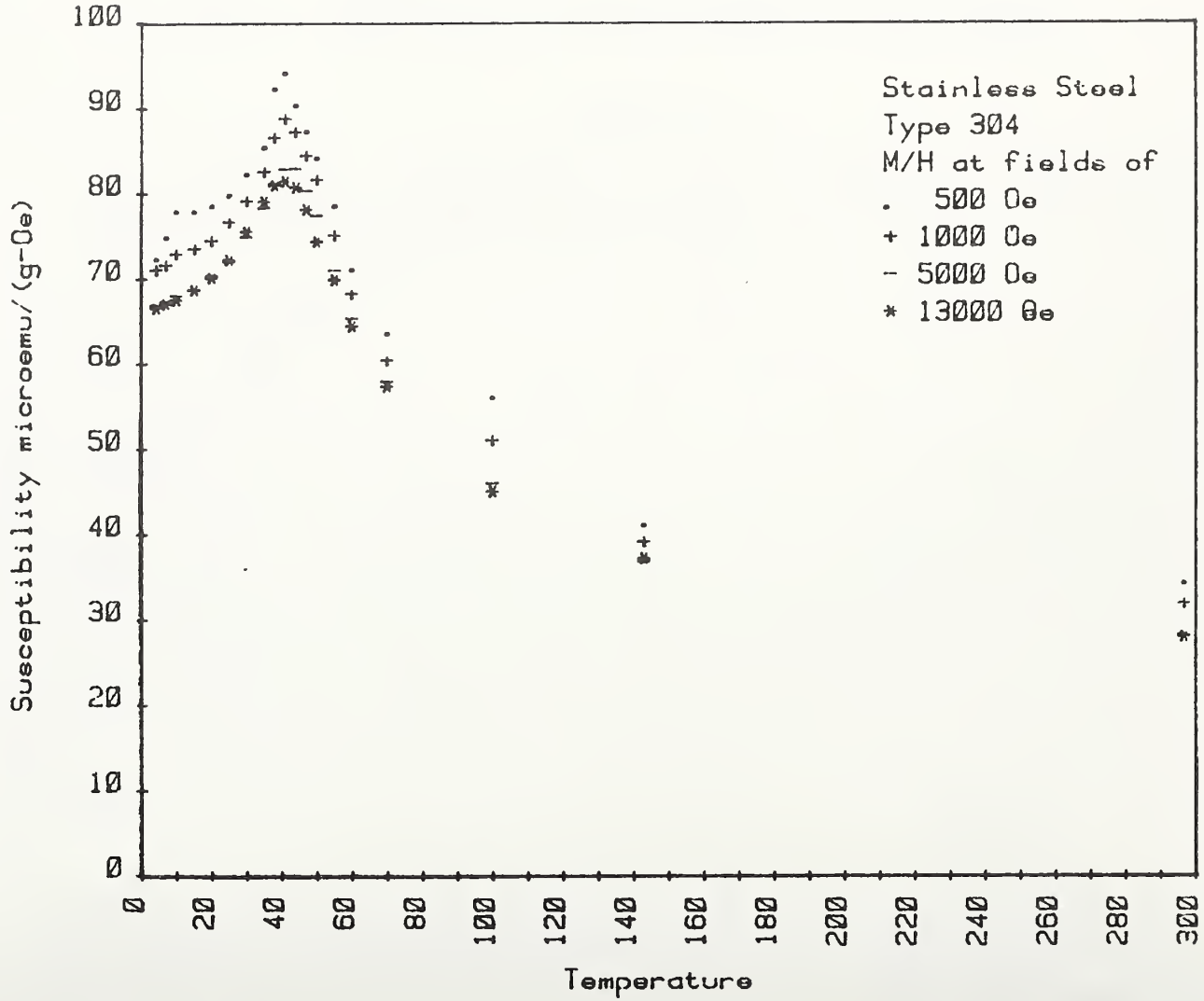

FIGURE 13. MAGNETIC SUSCEPTIBILITY TEMPERATURE DEPENDENCES OF AISI 304 AT LOW, INTERMEDIATE, AND HIGH MAGNETIC FIELDS

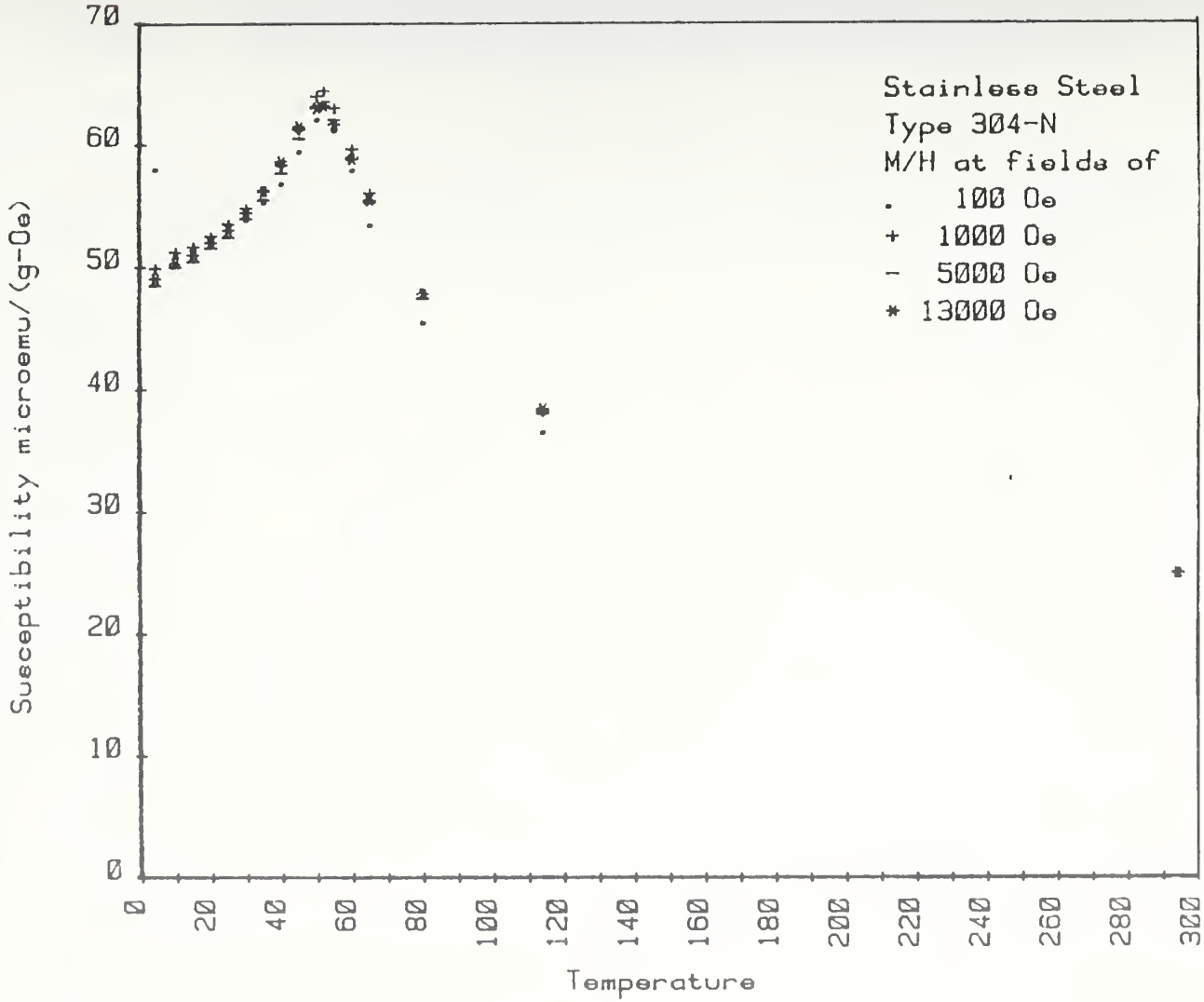

FIGURE 14. MAGNETIC SUSCEPTIBILITY TEMPERATURE DEPENDENCES OF AISI 304N AT LOW, INTERMEDIATE, AND HIGH MAGNETIC FIELDS

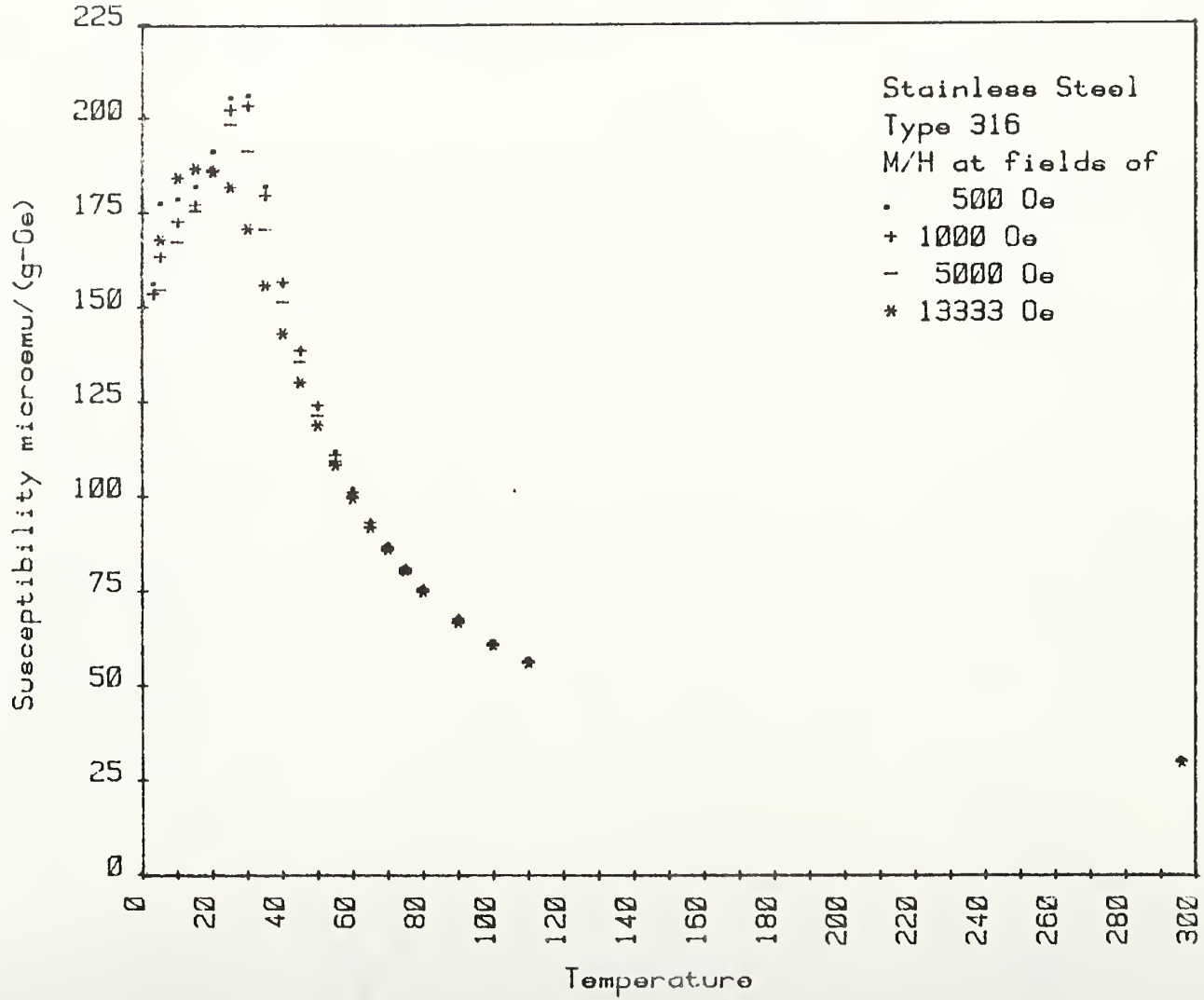

FIGURE 15. MAGNETIC SUSCEPTIBILITY TEMPERATURE DEPENDENCES OF AISI 316 AT LOW, INTERMEDIATE, AND HIGH MAGNETIC FIELDS

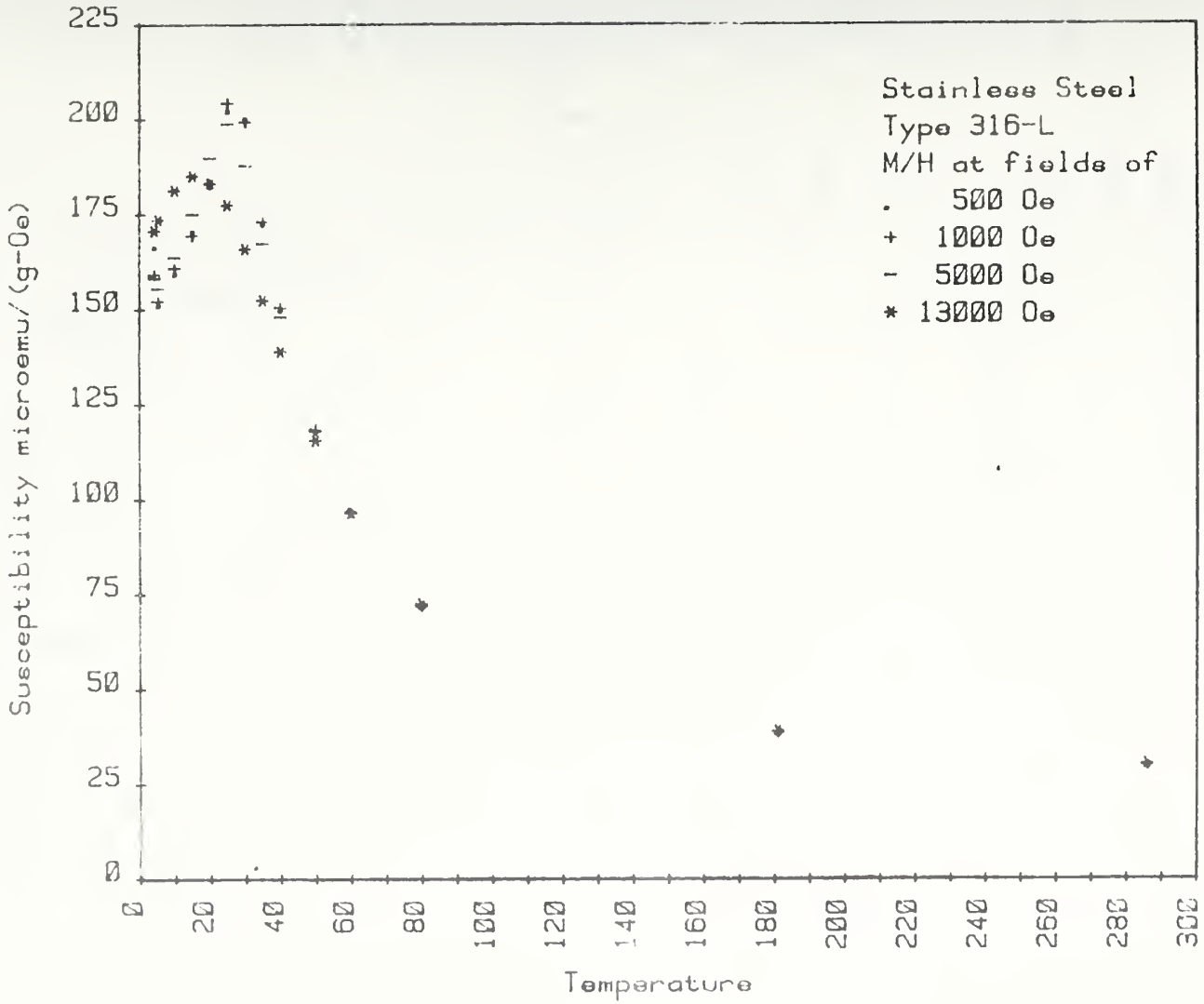

FIGURE 16. MAGNETIC SUSCEPTIBILITY TEMPERATURE DEPENDENCES OF AISI 316L AT LOW, INTERMEDIATE, AND HIGH MAGNETIC FIELDS

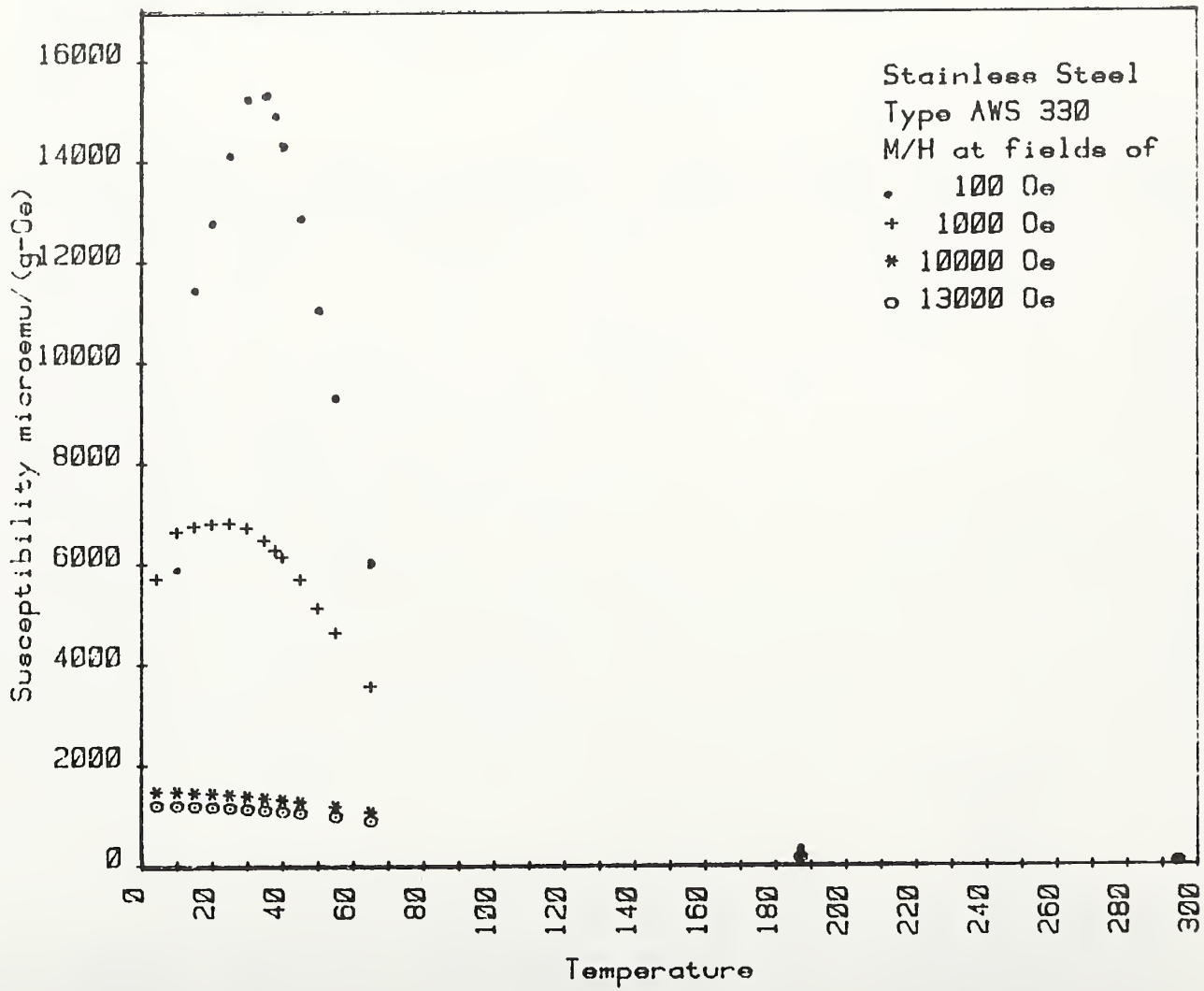

FIGURE 17. MAGNETIC SUSCEPTIBILITY TEMPERATURE DEPENDENCES OF AWS 330 AT LOW, INTERMEDIATE, AND HIGH MAGNETIC FIELDS

CONCLUSION

As a result of the magnetization study we have encountered in four types of austenitic stainless steel, selected for their metallurgical (low temperature strength and stability, and weldability) rather than magnetic interest four classes of magnetic material; they are:

Superparamagnetic (SPM)	AISI 310 S
Spin glass	304
Weakly SPM + spin glass	317
Strongly SPM + spin glass	AWS 330

Metal physics interpretations of these characteristics will be advanced in forthcoming research articles.

Magnetic Property Model

As a result of this study the following model for the magnetic properties of austenitic stainless steels is offered.

1. Stainless steels are not antiferromagnetic in the long-range ordered sense
2. At elevated temperature they are paramagnetic
3. As the temperature is decreased pre-existing chemical clusters acquire magnetic order (i.e. giant moments)--ferromagnetic in the low-Mn steels
4. The matrix within which the clusters are imbedded begins to undergo spin glass condensation, and finally does so at some temperature T_g at which there is a susceptibility and magnetization cusp
5. Cluster-matrix interaction tends to induce a frozen random order into the giant moment system but SPM exists well below T_g.

6. At very low temperatures the magnetization of the superparamagnetic (cluster) system is anomalously low due to induced "viscosity". As H increases magnetization of the giant cluster system increases more rapidly than H leading to an upwards concavity in M(H). This effect is also responsible for the exagerated shift to low temperatures of the susceptibility maximum in systems with extreme superparamagnetism.

LIST OF TABLES

Table 1. Temperature Ranges of the Susceptibility and Magnetization Studies . . . . . .

Table 2. Vendors and Available Specifications of the Alloys Investigated . . . . . .

Table 3. Vendor-Supplied Composition of Alloys Listed in Wgt Percent . . . . . .

Table 4. Degree of Etching and Specimen Weights in Magnetic Susceptibility and Magnetization Measurement . . . . . .

Table 5. Magnetic Susceptibility of AWS 330. Graphically Extrapolated χ_{∞} Values for the Temperature Range 414.5-129.5K . . . . . .

Table 6. Magnetic Susceptibility of AISI Type 304 in the Temperature Range 8.7-65.6K . . . . . .

Table 7. Index of Computer-Produced Susceptibility Temperature Dependence Data Tables . . . . . .

Table 8. Magnetic Susceptibility Temperature Dependence of AISI 310S Over the Temperature Range 77-414K . . . . . .

Table 9. Magnetic Susceptibility Temperature Dependence of AISI 304 Over the Temperature Range 77-408K . . . . . .

Table 10. Magnetic Susceptibility Temperature Dependence of AISI 304L Over the Temperature Range 77-410K . . . . . .

Table 11. Magnetic Susceptibility Temperature Dependence of AISI 304N Over the Temperature Range 77-403K . . . . . .

Table 12. Magnetic Susceptibility Temperature Dependence of AISI 316 Over the Temperature Range 77-407K . . . . . .

Table 13. Magnetic Susceptibility Temperature Dependence of AISI 316L Over the Temperature Range 77-413K . . . . . .

Table 14(a). Magnetic Susceptibility Temperature Dependence of Inconel 625 Over the Temperature Range 9-80K . . . . . .

Table 14(b). Magnetic Susceptibility Temperature Dependence of Inconel 625 Over the Temperature Range 77-412K . . . . . .

Table 15. Coefficients of the Susceptibility Temperature Dependences of Some 300-Series Stainless Steels and Inconel 625 . . . . . .

Table 16. Index of the Temperature and Magnetic Field Ranges Covered . . . . . .

Table 17. Magnetization Temperature (T) and Field (H) Dependences of AISI Type 310S . . . . . .

Table 18. Magnetization Temperature (T) and Field (H) Dependences of AISI 304 . . . . . .

Table 19. Magnetization Temperature (T) and Field (H) Dependences of AISI 304L . . . . . .

LIST OF TABLES
(Continued)

Table 20. Magnetization Temperature (T) and Field (H) Dependences of AISI 304N . . . . . .

Table 21. Magnetization Temperature (T) and Field (H) Dependences of AISI 316 . . . . . .

Table 22. Magnetization Temperature (T) and Field (H) Dependences of AISI 316L . . . . . .

Table 23. Magnetization Temperature (T) and Field (H) Dependences of AWS 330 . . . . . .

Table 24. Magnetization Signatures . . . . . .

LIST OF FIGURES

Figure 1(a). Magnetic Susceptibility of AWS 330. Reciprocal Field Plots for the Temperature Range 414.5-196.5K. The Gradual Development of "Ferromagnetic Slope" is Evident . . . . . .

Figure 1(b). Magnetic Susceptibility of AWS 330--Continued. Reciprocal Field Plots for the Temperature Range 185-77K. The onset of Superparamagnetism at Temperatures Near 100K is Evident. . . . . .

Figure 2. Magnetic Susceptibility Temperature Dependence of AISI Type 304, at Two Magnetic Fields Levels, Within the Temperature Range 8.7-65.6K . . . . . .

Figure 3. Algorithm for the Computer Reduction of Susceptibility Force Balance Data . . . . . .

Figure 4. Magnetic Susceptibility Temperature Dependences for AISI 310 S, AISI 304, AISI 316, AWS 330 and In 625 . . . . . .

Figure 5. Magnetization Field and Temperature Dependences of AISI Type 310 S . . . . . .

Figure 6. Magnetization Field and Temperature Dependences of AISI Type 304 . . . . . .

Figure 7. Magnetization Field and Temperature Dependences of AISI Type 304L . . . . . .

Figure 8. Magnetization Field and Temperature Dependences of AISI Type 304N . . . . . .

Figure 9. Magnetization Field and Temperature Dependences of AISI Type 316 . . . . . .

LIST OF FIGURES
(Continued)

Figure 10. Magnetization Field and Temperature Dependences of AISI Type 316L . . . . . .

Figure 11. Magnetization Field and Temperature Dependences of AWS 330 . . . . . .

Figure 12. Magnetic Susceptibility Temperature Dependences of AISI 310S at Low, Intermediate, and High Magnetic Fields . . . . . .

Figure 13. Magnetic Susceptibility Temperature Dependences of AISI 304 at Low, Intermediate, and High Magnetic Fields . . . . . .

Figure 14. Magnetic Susceptibility Temperature Dependences of AISI 304N at Low, Intermediate, and High Magnetic Fields . . . . . .

Figure 15. Magnetic Susceptibility Temperature Dependences of AISI 316 at Low, Intermediate, and High Magnetic Fields . . . . . .

Figure 16. Magnetic Susceptibility Temperature Dependences of AISI 316L at Low, Intermediate, and High Magnetic Fields . . . . . .

Figure 17. Magnetic Susceptibility Temperature Dependences of AWS 330 at Low, Intermediate, and High Magnetic Fields . . .

APPENDIXES A AND B

Discussions of the influence of α' martensite on the magnetic susceptibility and magnetization of Type 304 alloys.

APPENDIX A MAGNETIC EVALUATION OF MACHINING INDUCED DEFORMATION TRANSFORMATION IN AUSTENITIC STAINLESS STEELS

APPENDIX B MAGNETIZATION STUDIES OF MARTENSITE-BEARING AISI TYPE 304 STAINLESS STEELS

APPENDIX A

MAGNETIC EVALUATION OF MACHINING INDUCED DEFORMATION TRANSFORMATION IN AUSTENITIC STAINLESS STEELS

E. W. Collings

Accepted for publication in CRYOGENICS

ABSTRACT

Austenitic stainless steel alloys, particularly those with high M_d temperatures are prone to transform to ferromagnetic martensite during deformation. Prior to studying their magnetic properties, therefore, care must be taken to limit sample-preparation-induced damage to the surface layers, and then to remove these by severe etching before making the measurements. A magnetic technique for evaluating deformation-induced transformation is described and some experimental results are discussed.

INTRODUCTION

Before engaging on a program to study the low-temperature magnetic susceptibilities of a series of commercial stainless steel alloys it was recognized that some members of the series, particularly those with high (near room-temperature) M_d temperatures such as the 304's [1], would be prone to transform martensitically as a result of handling and machining during sample preparation. Two courses are open to remedy this situation -- the sample could be heat-treated in which case it would not longer be a true representative of the parent alloy; or it could be etched, a remedy effective only for surface damage, and one which possesses the possible disadvantage that

preferential etching might leave the surface rich in one or more of the ferromagnetic constituents (Fe or Ni).

Using 304N as sample, we applied the magnetic susceptibility technique itself to estimating semiquantitatively the degree of transformation which accompanied (a) bulk deformation (b) surface damage due to cutting, and (c) to examine the effectiveness of controlled etching in removing surface damage without deleterious side effects.

EXPERIMENTAL

The magnetic susceptibilities of small cube-shaped samples were measured by the Curie (magnetic buoyancy) technique in fields (H) of between 3.75 and 10.0 kOe (i.e., between 3.0 and 8.0 $10^5 Am^{-1}$). Assuming the sample to contain a mass-fraction f of ferromagnetic contaminent of specific magnetization σ, the magnetic susceptibility χ, is given by

$$\chi = (1-f)_{\chi 1} + f\,\sigma/H \ .$$

Thus, provided that the ferromagnetic component is always saturated in the measuring field ($H \geq 3.75$ kOe, i.e., $3.0.10^5 Am^{-1}$) such that σ = const., a plot of χ versus H^{-1} is linear with intercept $(1-f)_{\chi 1}$, where $_1$ is the susceptibility of the matrix and slope f σ. Thus, knowing σ one obtains f the fraction of ferromagnetic material present. In this work we assume for σ the saturation moment of α-Fe, viz. 221.9 $Oe.cm^3g^{-1}$,* thus acquiring a lower limit for the amount of transformed martensite. In the present measurements the standard error in slope is $\pm 0.14.10^{-2} Oe.cm^3.g^{-1}$.* "Zero Slope" thus represents an α-Fe content of ± 6.3 ppm.

The samples, which were removed from supplied stock material using a liquid-sprayed carborundum cut-off wheel, and which were

---

* 1 $Oe.cm^3.g^{-1} = (1/4\,\pi)\ A.m^2.kg^{-1}$.

measured both before and after etching with "glyceregia",** can be defined according to the following scheme:

Sample 1, (a) 24.75 mg, heavily deformed, measured; (b) etched to 18.03 mg, remeasured.

Sample 2, (a) 20.70 mg, as-cut, measured; (b) etched to 13.25 mg, remeasured.

Sample 3, (a) 5.70 mg, as-cut, measured; (b) etched to 4.37 mg, remeasured.

Thus, in Sample 1, we were dealing with both bulk and surface deformation, while in Samples 2 and 3 we examined surface effects only, at two different surface/volume ratios.

RESULTS

The results, in the format χ versus H^{-1} are presented in Figures 1(a) and (b) and summarized in Table 1.

DISCUSSION AND SUMMARY

Stainless steels such as the 304's with near-room-temperature M_d's [1] are subject to martensitic transformation during sample preparation. Local bulk plastic deformation in holding grips, and surface deformation in cutting or grinding induce sufficient transformation to cause serious measurement errors unless adequate precautions are taken. Material heavily deformed by compression can yield some 0.1 wgt% of transformation product, sufficient to increase the susceptibility at 5 kOe (4.10^5 Am^{-1}) by a factor of 7 above the true bulk value (from 26.5 to 182 10^{-6} cm^3 g^{-1} ($10^{-9} m^3 kg^{-1}$) at room temperature), Figure 1(a). With small (~ 6 mg) wheel-cut samples of 304N the α-Fe-

** 10 ml HNO_3, 20-50 ml HCL, 30 ml glycerol

equivalent contamination is 0.03 wgt%, which raises the 5 kOe (4.10^5 Am^{-1}) susceptibility by a factor of 1.5, Figure 1(b). Naturally, the cutting-induced relative surface damage decreases as the surface/volume ratio decreases.

Measurements made at a single value of magnetic field cannot, therefore, be relied upon to yield even an approximate value of magnetic susceptibility. Field-dependent measurements must be undertaken in order to determine, by extrapolation to $H^{-1} = 0$, the true bulk value, and to monitor the progress of any surface-damage-removal procedure. For some types of austenitic stainless steels, e.g., 310S, the magnetic susceptibility, as a result of superparamagnetism [2], becomes more and more field-dependent as the temperature is lowered, others transform structurally or magnetically. Thus, in order to be able to examine these phenomena properly all sources of spurious field-dependence at room temperature must be eliminated prior to commencing a series of low-temperature experiments.

ACKOWLEDGEMENTS

Sample preparation and magnetic measurements were carried out by R. D. Smith. The research was funded by the U.S. Department of Energy through the National Bureau of Standards, Boulder, CO, Dr. F. R. Fickett, Program Manager.

REFERENCES

[1] L.A.A. Warnes and H.W. King, Cryogenics, 16, 659 (1976)

[2] E.W. Collings, F. J. Jelinek, J. C. Ho and M.P. Mathur Advances in Cryogenic Eng., 28, 159 (1977).

TABLE A SEMIQUANTITATIVE EVALUATION OF DEFORMATION-INDUCED MARTENSITE

Sample Name	Mass (mg)	Sample Condition	Slope of χ versus H^{-1} ($Oe.cm^3.g^{-1}$) *	Equivalent α-Fe Content (wgt%)
1 (a)	24.75	cut plus heavily deformed	3.06×10^{-1}	13.8×10^{-2}
1 (b)	18.03	above plus etched	1.26×10^{-1}	5.7×10^{-2}
2 (a)	20.70	as-cut	4.40×10^{-2}	2.0×10^{-2}
2 (b)	13.25	above plus etched	$\pm 0.14 \times 10^{-2}$	$\pm 6.3 \times 10^{-4}$
3 (a)	5.70	as-cut	6.65×10^{-2}	3.0×10^{-2}
3 (b)	4.37	above plus etched	$\pm 0.14 \times 10^{-2}$	$\pm 6.3 \times 10^{-4}$

* $1\ Oe.cm^3.g^{-1} = (1/4\pi)\ A.m^2.kg^{-1}$

FIGURE A

FIGURE A (a) Reciprocal-field plots of magnetic susceptibility for heavily deformed 304N (greater than 50% by compression), and (b) reciprocal-field plots for as-cut and as-cut-plus-etched samples. Mass reduction of 20-40% by etching resulted in an undetectable slope, corresponding to a deformation-martensite α-Fe equivalent of $\pm$ 6.3 wgt.ppm. 20% mass reduction of a cube-shaped 6mg sample corresponds to the removal of surface to a depth of $\sim 1.5 \times 10^{-2}$mm.

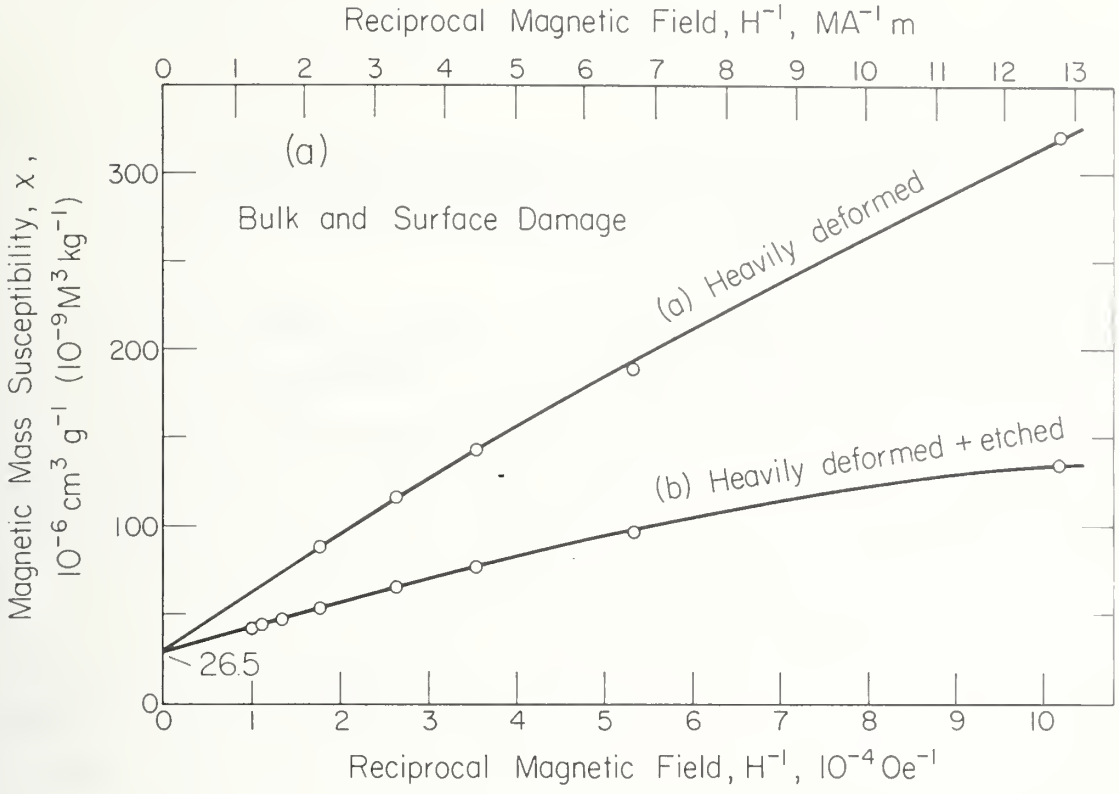
Reciprocal Magnetic Field, H^{-1}, $MA^{-1}m$
(a)
Bulk and Surface Damage
(a) Heavily deformed
(b) Heavily deformed + etched
26.5
Magnetic Mass Susceptibility, χ, $10^{-6} cm^3 g^{-1}$ ($10^{-9} M^3 kg^{-1}$)
Reciprocal Magnetic Field, H^{-1}, $10^{-4} Oe^{-1}$

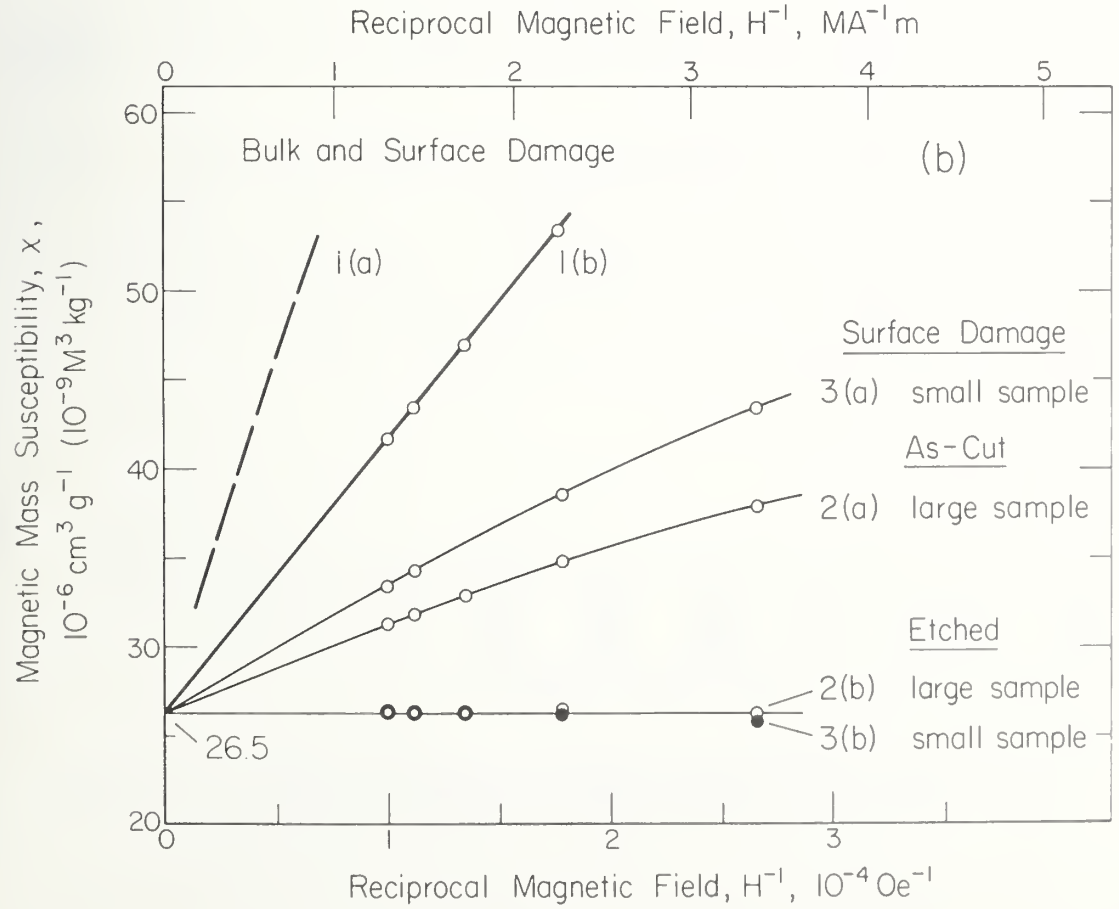
Reciprocal Magnetic Field, H^{-1}, $MA^{-1}m$
Bulk and Surface Damage
(b)
1(a)
1(b)
Surface Damage
3(a) small sample
As-Cut
2(a) large sample
Etched
2(b) large sample
3(b) small sample
26.5
Magnetic Mass Susceptibility, χ, $10^{-6} cm^3 g^{-1}$ ($10^{-9} M^3 kg^{-1}$)
Reciprocal Magnetic Field, H^{-1}, $10^{-4} Oe^{-1}$

APPENDIX B

MAGNETIZATION STUDIES OF MARTENSITE-CONTAINING AISI TYPE 304 STAINLESS STEEL

In Figures 6 and 8 we note the linearity in M versus H for 304 and 304N. On the other hand, Type 304L seems completely out of character, with extreme curvature to M(H). This apparent anomaly is resolved when we note that the high field slopes of M versus H for 304L are similar to the slopes (at corresponding temperatures) for the other alloys over the entire field range. Clearly Type 304L contains a saturable ferromagnetic contaminant (c.f. Appendix A).

It was initially supposed that the ferromagnetism noted was a result of cutting-induced surface damage. Accordingly, four more samples were prepared, very heavily etched, and measured at room temperature. As the following four curves (Figures B1 through B4) indicate, the ferromagnetic component (presumably martensite) was not confined to the surface, but was distributed throughout the bulk of the specimen as supplied. Further investigation would involve annealing and so on, but the effect is in principle solved.

This observation emphasizes that extreme care must be taken when dealing with marginally stable austenitic stainless steels (i.e. high $M_{s,d}$ temperatures). to ensure that the properties being measured are intrinsic to the alloy and are not being perturbed by the effects of parasitic precipitates and transformation products.

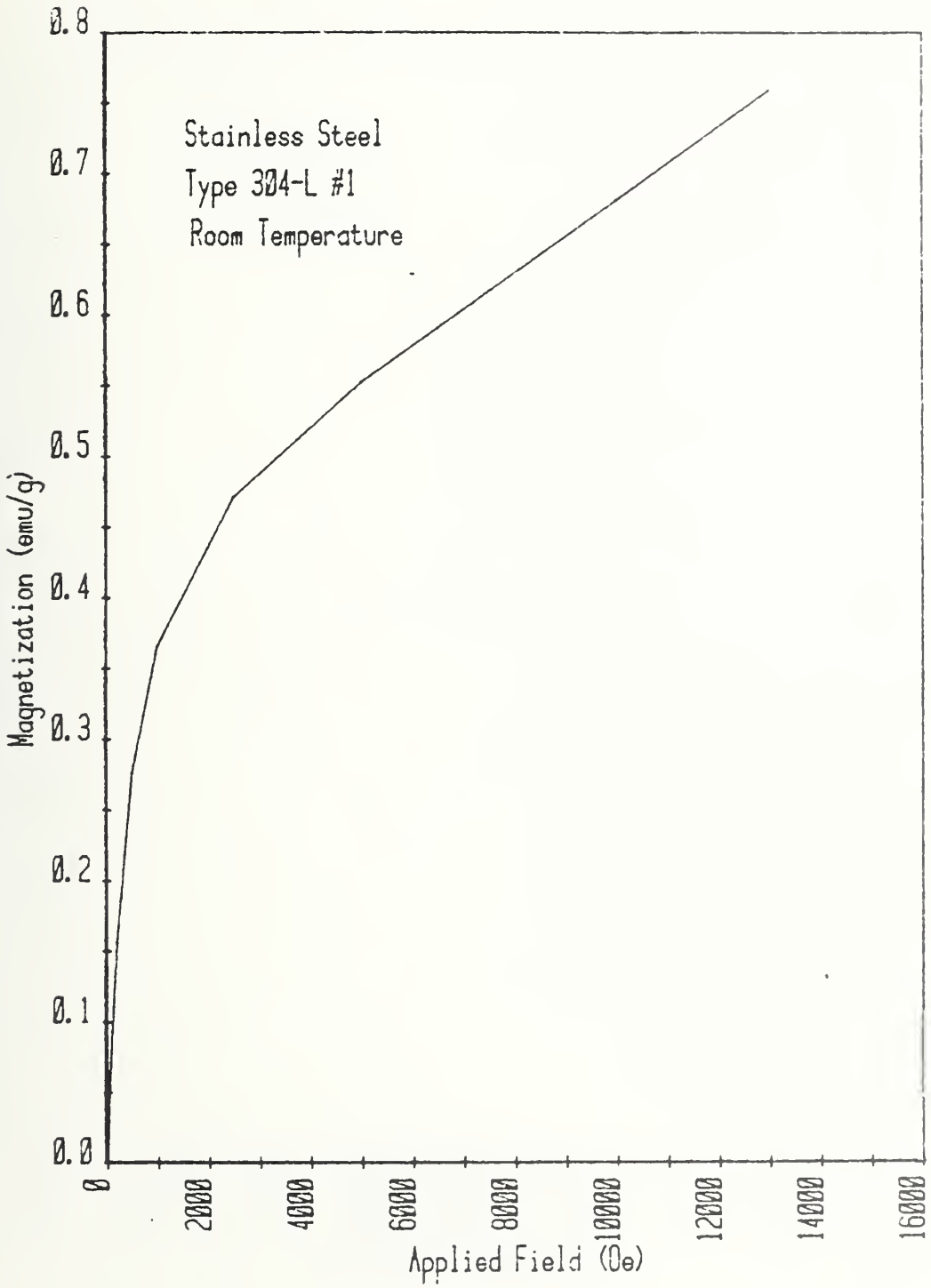

FIGURE B-1. FIELD DEPENDENCE OF ROOM TEMPERATURE MAGNETIZATION OF AISI TYPE 304L SAMPLE 1

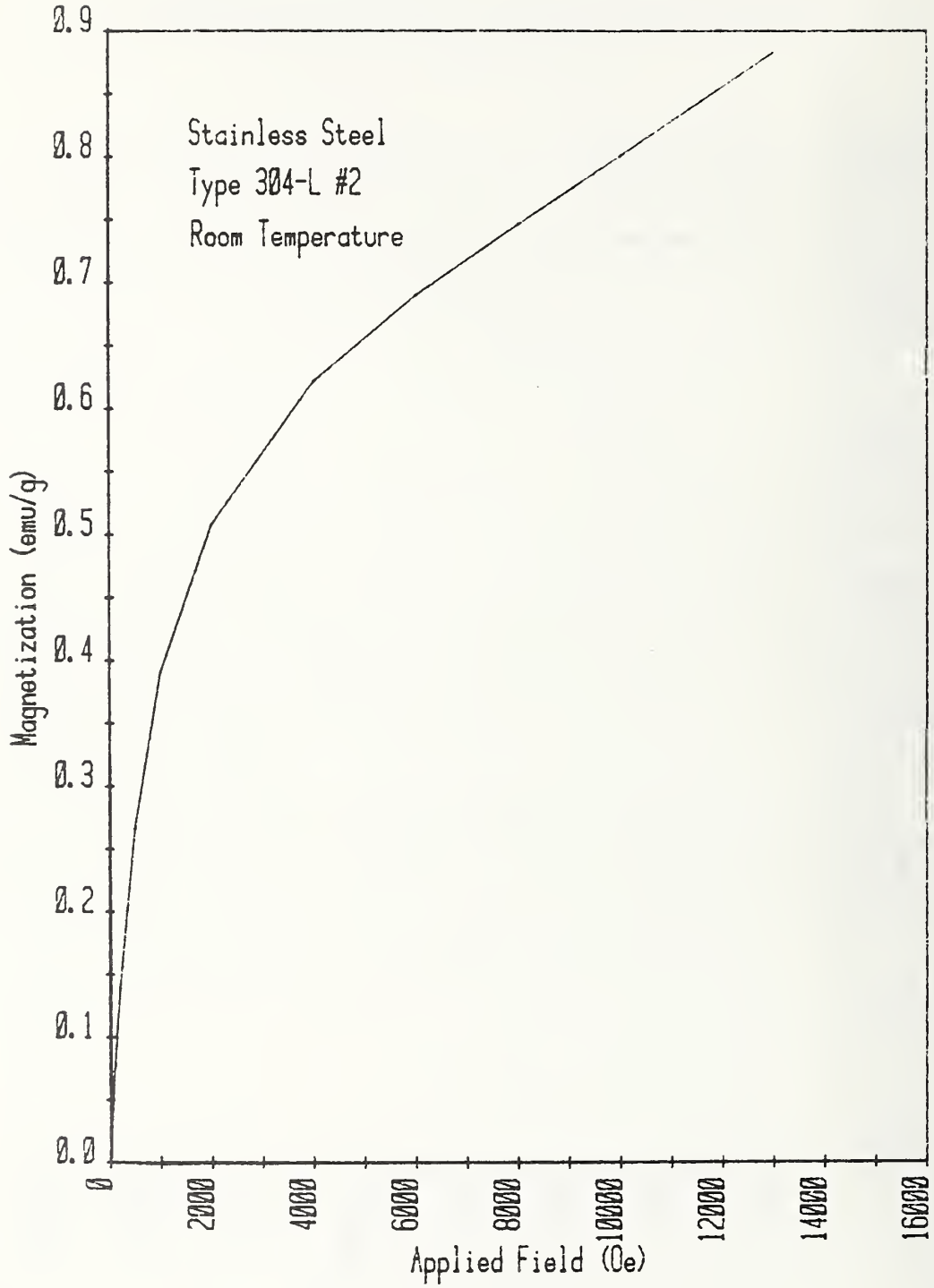

FIGURE B-2. FIELD DEPENDENCE OF ROOM TEMPERATURE MAGNETIZATION OF AISI TYPE 304L SAMPLE 2

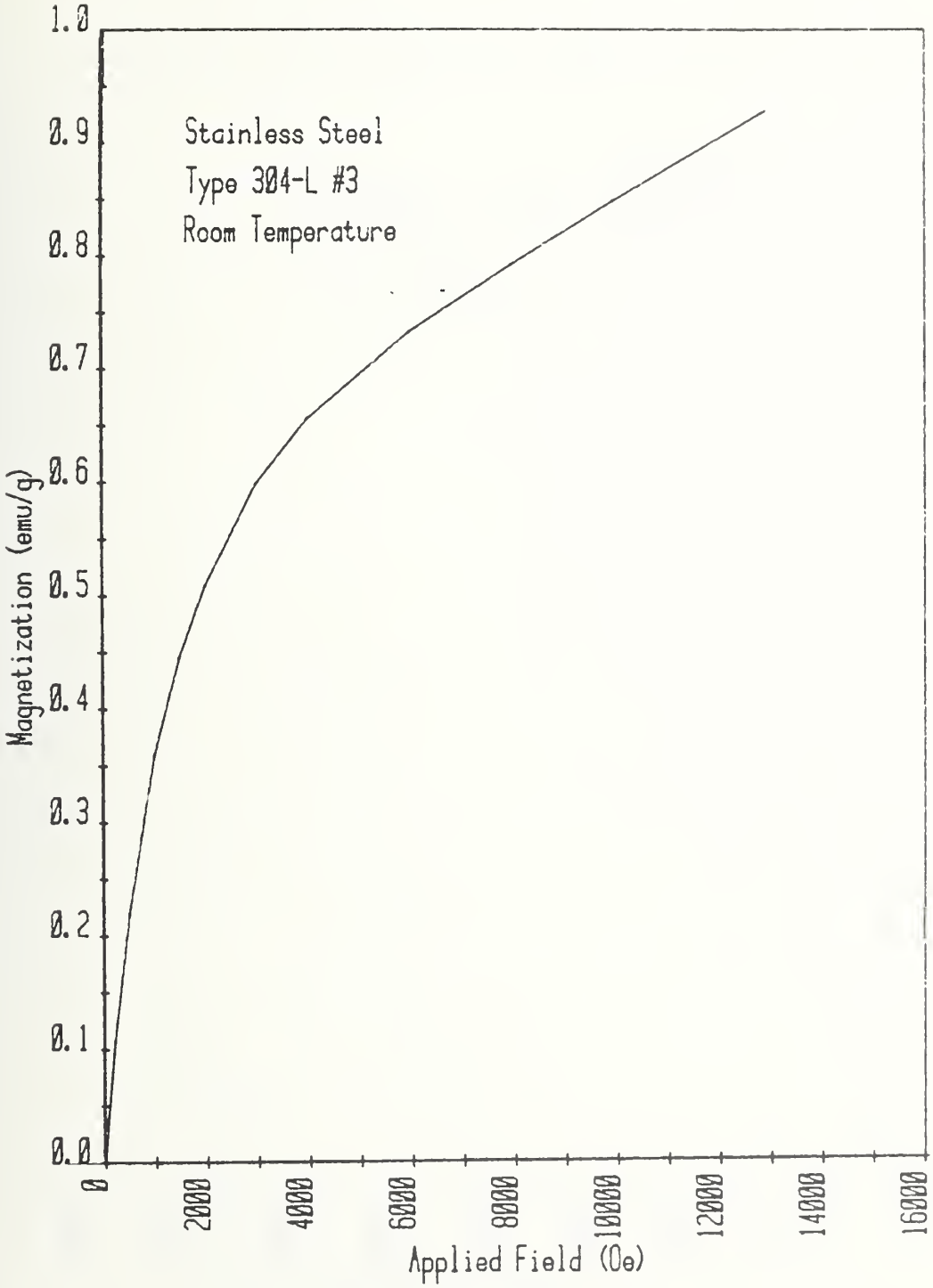

FIGURE B-3. FIELD DEPENDENCE OF ROOM TEMPERATURE MAGNETIZATION OF AISI TYPE 304L SAMPLE 3

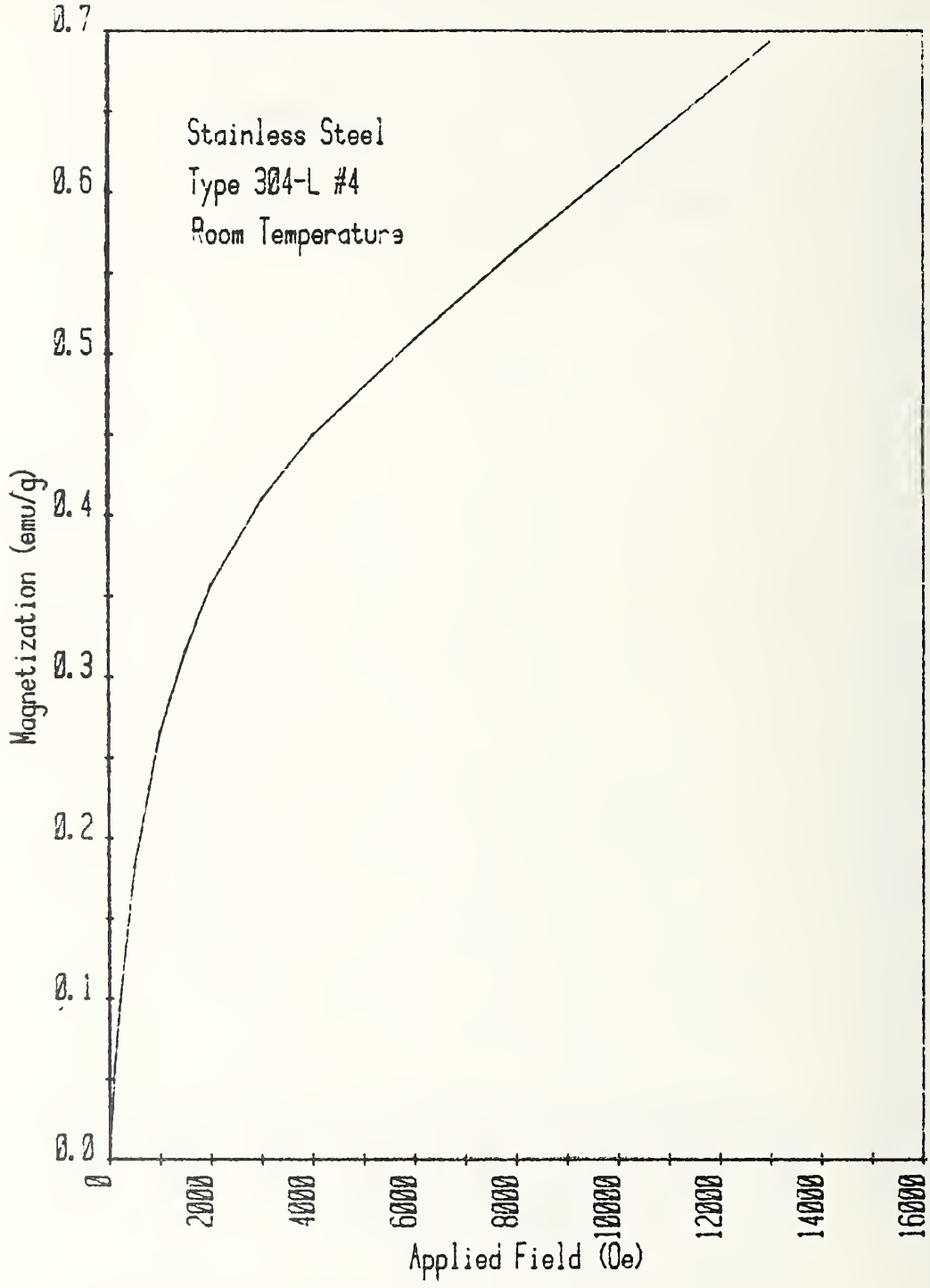

FIGURE B-4. FIELD DEPENDENCE OF ROOM TEMPERATURE MAGNETIZATION OF AISI TYPE 304L SAMPLE 4

SOME MAGNETIC PROPERTIES OF THE "NONMAGNETIC" STAINLESS STEELS

National Bureau of Standards

SOME MAGNETIC PROPERTIES OF THE "NONMAGNETIC" STAINLESS STEELS

F. R. Fickett
Thermophysical Properties Division
National Bureau of Standards
Boulder, CO 80303

ABSTRACT

The stainless steels proposed for low temperature service exhibit magnetic properties which are relatively complex functions of temperature. Welds in these metals also show complicated behavior. This paper discusses the magnetic properties of the "nonmagnetic" stainless steels as presented in the literature. The problems with using the permeability as a design parameter are outlined. Data are presented on the very low field susceptibility and the remanent magnetization of a large number of stainless steels measured at room temperature and at 4 K with a SQUID (Superconducting Quantum Interference Device) Magnetometer System.

INTRODUCTION

The austenitic stainless steels are, for practical purposes, paramagnetic materials at room temperature and above. However, as the temperature is lowered they all undergo transitions to other, more complex, magnetic states. The exact nature of these low temperature states is still open to some debate, but at present it appears that they form spin glass systems as discussed by Collings elsewhere in this report. The prior literature indicates that the state might also be one of antiferromagnetism or superparamagnetism. The actual state depends more on the interpretation of the data than it does on the material. The two measurements used to investigate these magnetic state properties are the variation of the magnetic susceptibility with temperature and the variation of the magnetization with applied field at fixed temperature. Graphs of these properties for representative austenitic steels are shown in Fig. 1 and Fig. 2.

Note that the magnetization at room temperature is linear with field giving a constant susceptibility ($\kappa = M/H$)* indicative of true paramagnetism. At 4 K, however, κ is strongly field dependent.

The location of the peak of the susceptibility curve (Fig. 1) depends strongly on the specific steel and may vary from 30 K to nearly room temperature. In the measurements shown (Ledbetter and Collings, 1978), any truly ferromagnetic components have been saturated out so that the data are for the austenitic phase alone.

While all this is very interesting from a metal physics viewpoint, in engineering applications one must be able to achieve a specific value of the relative magnetic permeability, μ_r. by an appropriate choice of material for service at (usually) a fixed temperature. The relative permeability, μ_r, is simply related to the susceptibility (in SI units) by

$$\mu_r / = \mu/\mu_o = 1 + \kappa. \qquad (1)$$

Unfortunately, it is conventional to give susceptibility values in units of emu/g. We call this quantity χ_ρ, the cgs mass susceptibility. χ_ρ must be multiplied by the material density to convert it to χ in units of emu/cm^3 which is, believe it or not, dimensionless. This quantity, multiplied by 4π is κ. The situation is only slightly less confusing if SI units are used throughout.

The use of permeability as a specification on stainless steel at low temperatures should only be done with a clear understanding of the implications of the M-H behavior shown in Fig. 2. The classical definition of μ is directly related to the slope of the line from the origin to the curve and thus can have

---

*κ is the symbol chosen to represent the SI susceptibility, which is dimensionless. The cgs susceptibility, represented by χ is also dimensionless, but $\kappa = 4\pi\chi$.

many values as shown. It is not a meaningful measure in general. However, the initial value of μ, i.e. that measured in fields $\lesssim$ 8 kA/m (100 Oe) is a useful number, if the shape of the full curve is kept in mind. Note that this is only a problem at low temperatures - at room temperature μ is a constant with field.

Another problem with the austenitic stainless steels, which is usually minor, is that truly ferromagnetic regions may exist in the steel due to a variety of causes, such as surface oxidation, formation of stress-induced or thermally-induced martensite, and ferrite formation which is particularly a problem in weldments. All of these cause the steel to show a magnetic remanence after magnetization which (rarely) may be significant in applications.

In this report we describe measurements of the magnetic remanence at room temperature and the susceptibility at both room temperature and 4 K for a variety of austenitic steels and some preliminary room temperature results on weld metals. Unless otherwise indicated, the measurements are made with a very sensitive magnetometer using a SQUID (Superconducting Quantum Interference Device) detector. This device is described by Fickett and Sullivan (1974). All susceptibility measurements are true initial susceptibilities. The base metal specimens are 20 mm long rods $\sim$ 3 mm square with rounded edges. The weld metal specimens are $\sim$ 5 mm diameter cylinders, also 20 mm long.

RESULTS

Remanent Moment

The results of room temperature measurements of the remanent magnetization after application and removal of a 358 kA/m (4.5 kOe) field are shown in Fig. 3. The as-machined (M) specimens show a significant variation from the annealed (A) ones, but with no systematic trend. The measurements which fall below the dashed line are probably of no significance to applications of the steels. They would give trouble in only the most demanding situations. The high value

for the machined 304 is most likely the result of martensite formed by deformation.

Susceptibility

The results of measurements of the initial susceptibility of the base metals at room temperature and at 4 K are shown in Fig. 4. Because this is a true initial susceptibility measured on previously unmagnetized material, the ferromagnetic components seen in Fig. 3 will also show up here as an increase in the susceptibility. They should not be very temperature dependent, however. It is clear that cooling to 4 K changes the susceptibility, usually significantly. This is what we would expect from the general behavior shown in Fig. 1 and, in fact, there is good agreement at both temperatures for the few cases in the literature where the χ vs T curves have been taken to 4 K. Also, it appears that the machining and annealing operations do not greatly alter the susceptibility except where ferromagnetic inclusions are apparently created.

Weld Metal Properties

Ferrite in weld metal is a ferromagnetic material and, as such, will show up both in the initial susceptibility and remanence measurements. We would not expect a strong temperature dependence. A preliminary measurement of the room temperature initial susceptibility of 316 and 316L weld metal specimens is shown in Fig. 5. The percent ferrite is determined by a Magnegage which measures the force required to pull a calibrated magnet from the metal. The susceptibility was determined by a two-coil induction device (Cristie and Symons, 1969) which applies a maximum field of 40 A/m (0.5 Oe). The specimens were measured transverse to the field and various calibration and correction factors were not determined in these preliminary measurements and, thus, only relative values of susceptibility are presented. Initial estimates indicate that, around 10% ferrite, the relative permeability may be as high as $\mu_r = 2$.

CONCLUSIONS

Austenitic stainless steels are not classical ferromagnets at any level and there is a danger of creating confusion by using a terminology appropriate to the ferromagnets. The most meaningful data for completely defining the magnetic properties of these metals at any temperature is a curve of magnetization versus applied field.

A remanent ferromagnetism due to inclusions and surface damage is found to exist in many of the stainless steels. The effect is usually negligible, but should be determined in some of the steels after machining or heat treatment if the application is at all critical magnetically.

The initial susceptibility is temperature dependent and depends also on the specific steel. It is not strongly affected by annealing or machining unless ferromagnetic particle formation occurs.

Weld metals are significantly more ferromagnetic than any of the base metals due to ferrite formation. More study is needed, particularly to determine if the magnetic properties are truly temperatue independent as we have assumed.

REFERENCES

Christie, K. W. and Symons, D. T. A. (1969). Apparatus for measuring magnetic susceptibility and its anisotropy. Geological Survey of Canada, paper 69-41.

Efferson, K. R. and Leonard, W. J. (1967). Magnetic properties of some structural materials used in cryogenic applications. Oak Ridge National Laboratory Report ORNL-4150, pp. 126-132.

Fickett, F. R. and Sullivan, D. B. (1974). Magnetic studies of oxidized impurities in pure copper using a SQUID system. J. Phys. F: Metal Phys. 4, 900-905.

Ledbetter, H. M. and Collings, E. W. (1978). Low-temperature magnetically induced elastic-constant anomalies in three manganese stainless steels. In: Metal Physics of Stainless Steels (TMS-AIME, New York) to be published.

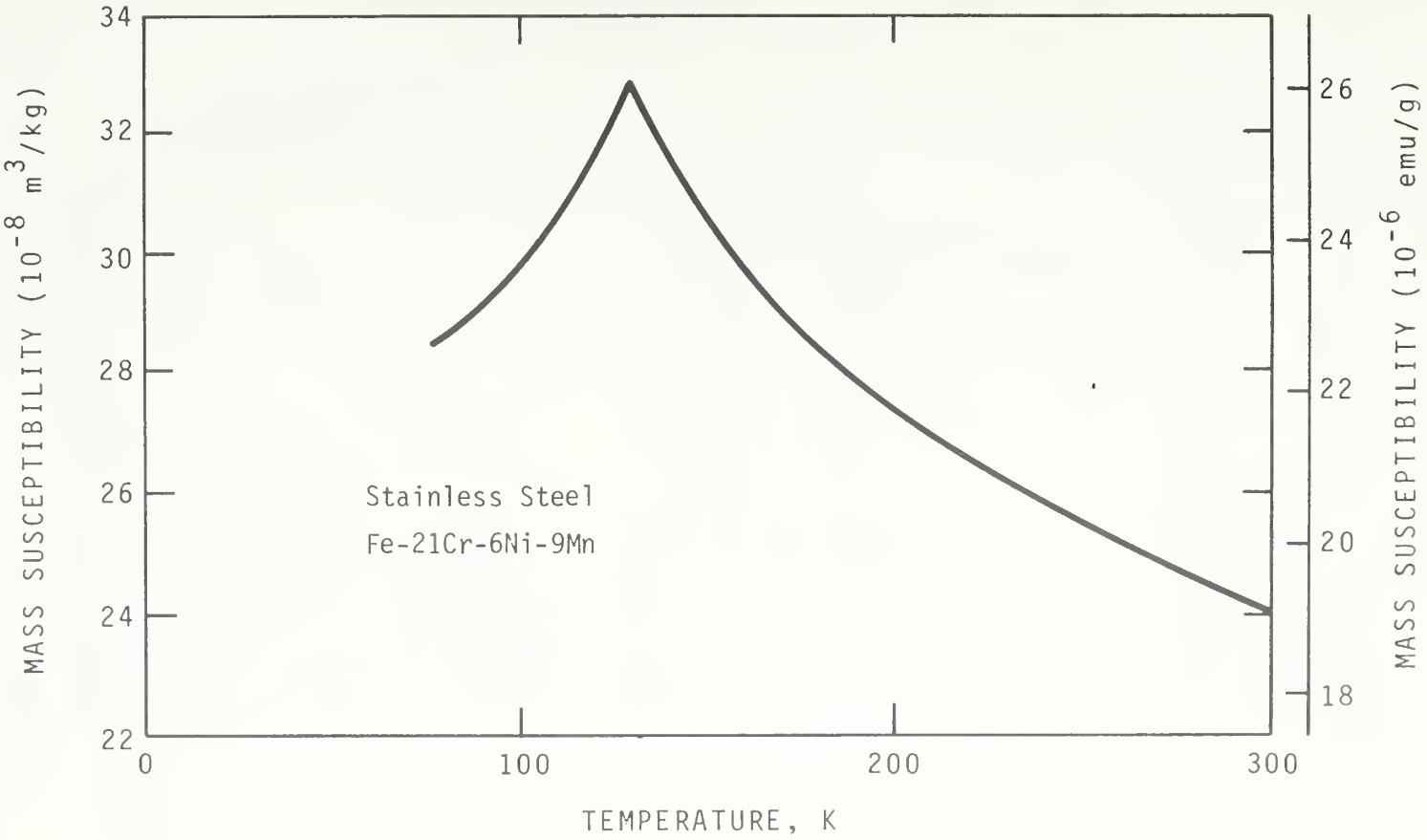

Figure 1. The variation of magnetic susceptibility as a function of temperature for the stainless steel Fe-21Cr-6Ni-9Mn. The behavior is typical of nearly all austenitic stainless steels, although the temperature of the peak varies with the steel. From Ledbetter and Collings (1978).

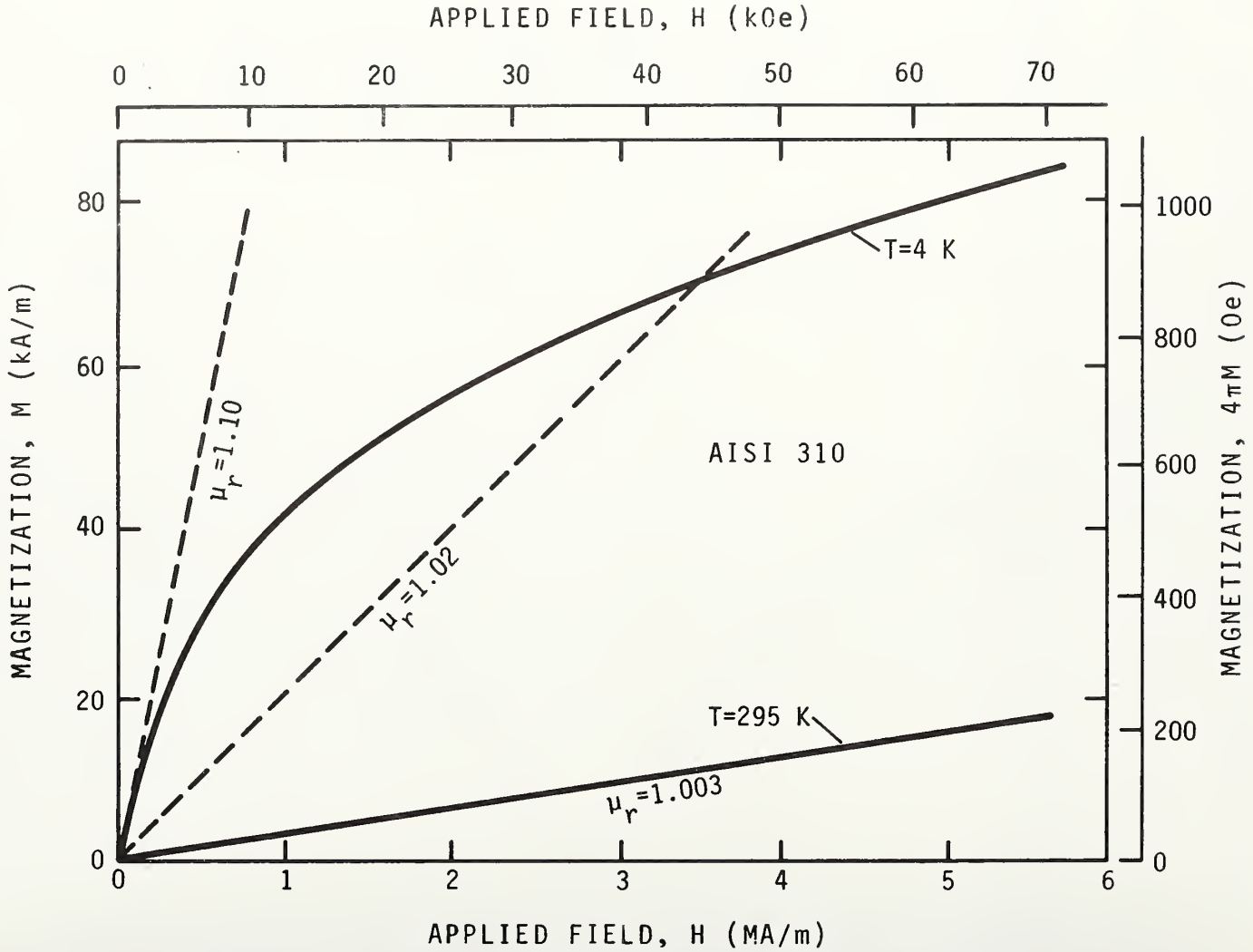

Figure 2. The magnetization of AISI 310 as a function of applied field. The behavior shown is typical of all austenitic stainless steels. The dashed lines indicate how the relative permeability is determined. Data from Efferson and Leonard (1967).

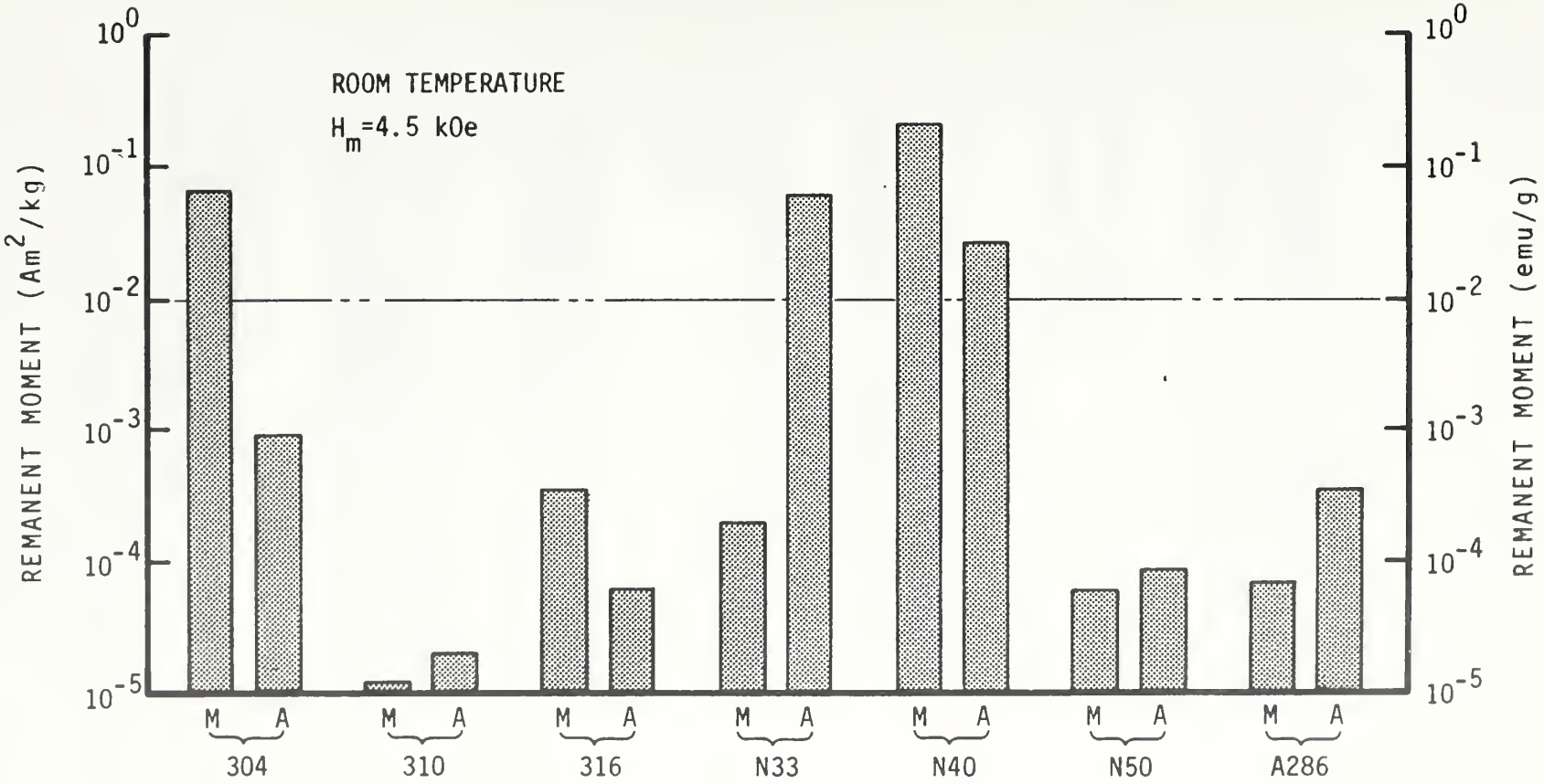

Figure 3. The remanent moment of austenitic stainless steels induced by application of a 358 kA/m (4.5 kOe) field. Specimens labeled M are machined from as-received stock. Those labeled A have been annealed after machining.

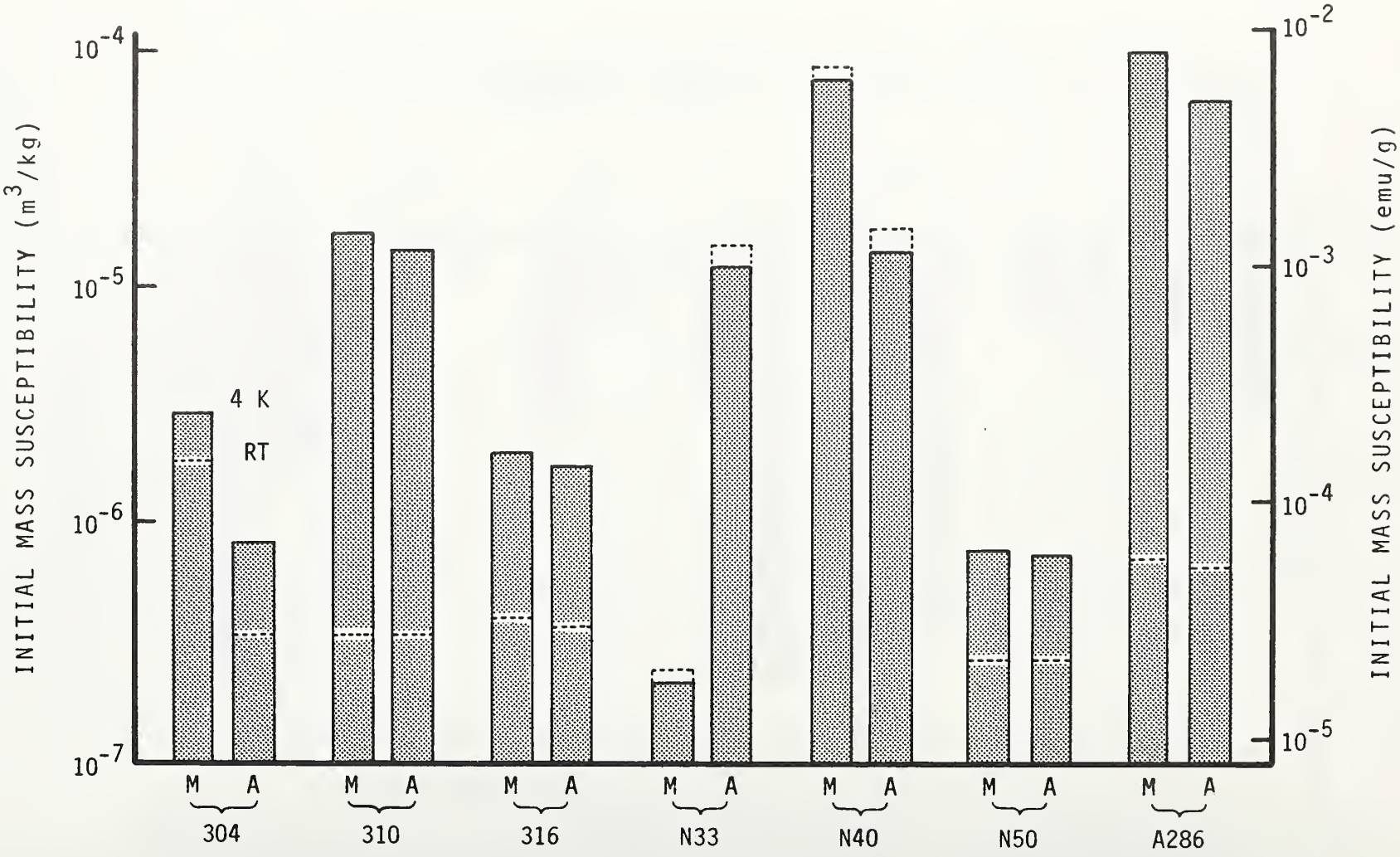

Figure 4. The initial susceptibility at 4 K and at room temperature for austenitic stainless steels.

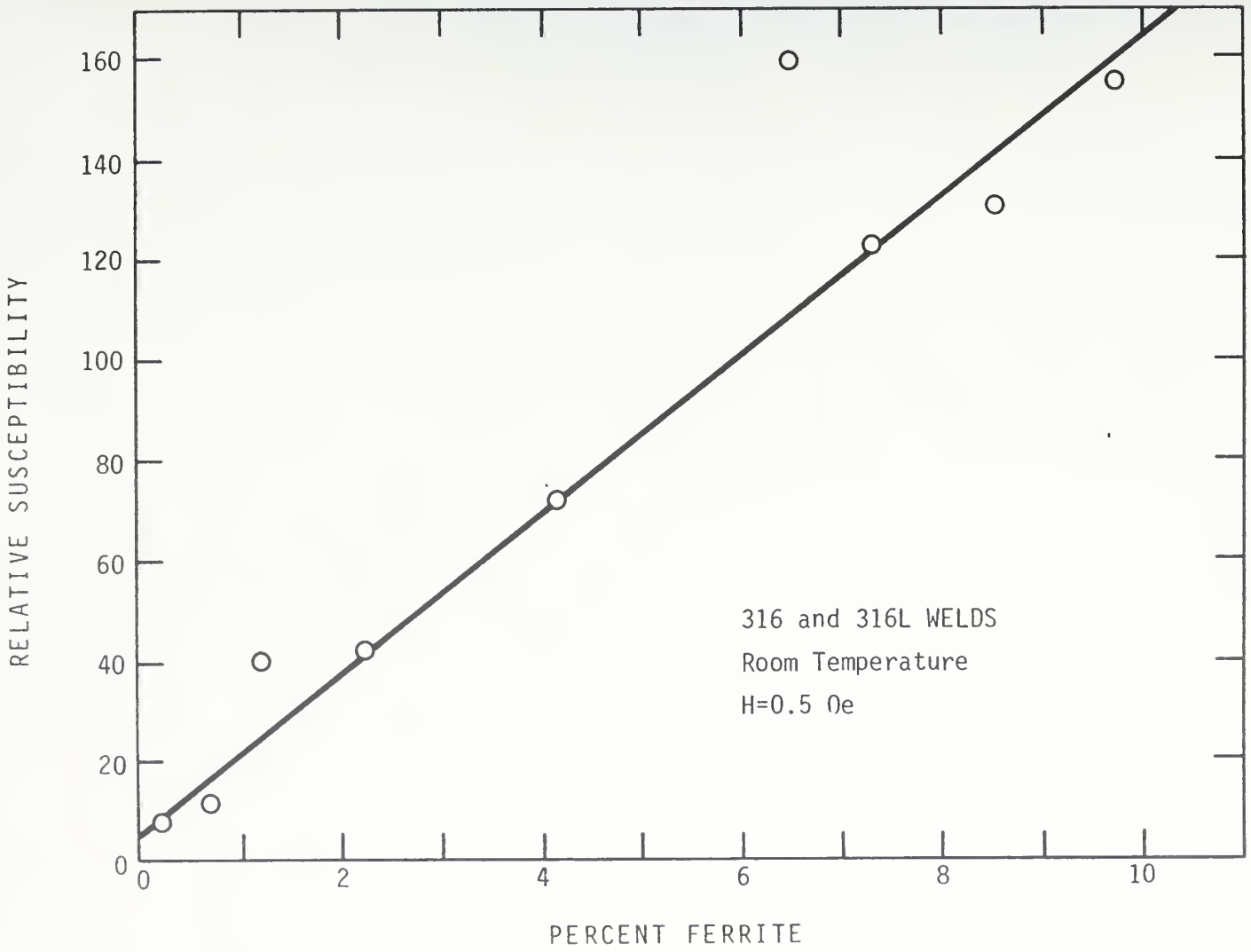

Figure 5. Preliminary results on the susceptibility of 316 and 316L welds measured at room temperature.

Stainless Steel Welding

EVALUATION OF STAINLESS STEEL WELD METALS AT CRYOGENIC TEMPERATURES

National Bureau of Standards

Evaluation of Stainless Steel Weld Metals at Cryogenic Temperatures

H. I. McHenry, D. T. Read and P. A. Steinmeyer
National Bureau of Standards
Boulder, Colorado 80303

The program to evaluate stainless steel weld metals for structural applications in superconducting magnet systems begun in FY 77 and was continued in FY 78. The objectives of the program are:

1. To investigate the metallurgical factors which affect the toughness of stainless steel weld metals.
2. To develop a high strength, high fracture toughness filler wire for welding nitrogen-strengthened stainless steels such as the 21Cr-6Ni-9Mn alloy.
3. To evaluate the fracture toughness of stainless steel welds at 4 K.

During FY 77, the first year of the program, three filler metal companies participated in the program(1). Arcos Corporation prepared a series of 10 test weldments to study the effect of ferrite content, ferrite morphology and sensitization on 316L weld metal deposited by the shielded metal arc (SMA) process. Armco evaluated the influence of nitrogen content on the strength and toughness of three experimental weld metals at 76 K: 13Cr-20Ni-9Mn-1.8Cb, 20Cr-10Ni-9Mn and 18Cr-16Ni-9Mn. Teledyne-McKay prepared SMA weldments with a 18Cr-34Ni-4.5Mn weld metal, a modified AWS 330 alloy. During FY 78, the Arcos and Teledyne-McKay weldments were received and the metallurgical and fracture toughness evaluations were completed. In addition, Armco completed the remaining work on the experimental alloys and work was started on a filler metal selection program in cooperation with General Electric's Large Coil Program. This report summarizes the results obtained in FY 78 and briefly outlines the plans for FY 79.

Metallurgical Effects on Toughness

The 316L welds supplied by Arcos were used to study the influence of ferrite content, ferrite morphology and sensitization on toughness at cryogenic temperatures, particularly 4 K. The metallurgical evaluation was conducted by the Colorado School of Mines and the results are presented in the attached report by Elmer, Steinmeyer and Olson. The fracture toughness tests were conducted by NBS and the results are presented in the attached report by Read, McHenry, Steinmeyer, and Thomas. The results clearly indicate that ferrite and sensitization cause significant reductions in toughness at 4 K.

High Strength Filler Wire Development

In the first year report(1), Armco presented the results of a program to evaluate the influence of nitrogen on the strength and toughness of three experimental filler wires at 77 K. The results, summarized in Figure 1, indicate that the strength of each alloy increases and the toughness decreases with increasing nitrogen content. Each of the alloys had marginal toughness at 77 K even at the lowest nitrogen level, and consequently plans for further testing at 4 K were cancelled.

The welds evaluated in the Armco Program were deposited by the SMA process. Stainless steel welds deposited by the SMA process generally have less toughness than similar welds deposited by either the gas tungsten arc (GTA) or gas metal arc (GMA) processes. For comparative purposes, a pulse-mode GMA weld was prepared for each experimental alloy. Nitrogen was kept to a minimum; however, the nitrogen levels were relatively high due to the nitrogen content of the wire. The chemistries of the as-deposited weld metals are shown in Table 1 and the mechanical properties at room temperature and 77 K are summarized in Table 2. The 13Cr-20Ni-9Mn-2Cb and 20Cr-10Ni-9Mn alloys had marginal toughness at 77 K and thus, further tests at 4 K are not planned. The 18Cr-16Ni-9Mn alloy had a

promising combination of strength and toughness at 77 K and consequently NBS will conduct fracture toughness tests at 4 K during FY 79.

Evaluation of AWS 330

The AWS 330 test plates prepared by Teledyne-McKay and described in last year's report(1) were fracture toughness tested at room temperature, 76 K and 4 K. The results, summarized in Table 3, indicate that AWS 330 has relatively good strength and toughness at 4 K. Microfissures were observed on the fracture surface; however, the microfissuring tendencies were not characterized or studied.

Electrode Selection Tests - 308L vs 316L

A series of test weldments were prepared by General Electric using the SMA process for an evaluation of three candidate electrodes: E308L, E316L (N = .044%) and E316L (N = .071%). The base metal was 316LN, one-inch-thick plate. Specimens were sent to NBS where the following tests were conducted on each weld: tensile properties at room temperature and 4 K and fracture toughness tests at 4 K. In addition GE conducted Charpy impact tests on each weld metal at room temperature and 77 K.

The welding procedures, and the weld deposit chemistries are summarized in Tables 4 and 5. Tensile tests were conducted on all-weld-metal specimens (specimen axis parallel to the weld) and on cross-weld specimens which included base metal, heat affected zone and weld metal in the test section. The results are summarized in Table 6. All of the cross-weld specimens failed in the weld indicating that the weld had lower strength than either the 316LN base plate or the heat affected zone. However, at 4 K, the strength level of the 316L weld metal was comparable to that of the 316LN base metal, particularly at the .071 N level where the joint efficiency was 89%.

The fracture toughness data at 4 K, presented in Table 7, indicate that 308L has better 4 K fracture toughness than 316L. The data of Table 7 may be compared with the results for the Arcos weldments, in the attached report by Read, McHenry, Steinmeyer, and Thomas. The toughness of 316L weld metal at 4 K measured on the Arcos weldments was 180 MPa$\sqrt{m}$ (164 ksi$\sqrt{in}$ at the zero ferrite level. In contrast, the GE 316L welds had values of 118 MPa$\sqrt{m}$ (107 ksi$\sqrt{in}$) (N = .044%) and 95 MPa$\sqrt{m}$ (86 ksi$\sqrt{in}$) (N = .071%). The only identified difference in the Arcos and GE welds other than minor variations in chemistry and weld procedures, was the electrode coating; titania coatings were used by Arcos and lime coatings were used by GE. Further work is needed to understand the cause of the large differences in toughness.

Further confusion arises when the 77 K Charpy impact data obtained by GE, Table 8, are compared with the data on the Arcos welds. The GE 316L welds had significantly higher Charpy impact values at 77 K (51J (38 ft-lb) at .044%N and 45J (33 ft-lb) at .071%N) than the Arcos welds (35J (26 ft-lb) at .04%N). In comparing the GE welds, 308L had the best toughness at 4 K and lowest Charpy impact energy (31J (23 ft-lb) at 77 K. Thus, use of a Charpy test at 77 K to estimate fracture toughness at 4 K does not appear useful.

Future Work

A. Multi-process study of 316L. Test weldments (AWS 316L filler metal, AISI 304L base plate) will be prepared by a subcontractor using each of the following processes: gas tungsten arc, gas metal arc and submerged arc. Initially, the welds will be evaluated by fissure-bend tests, room temperature tensile tests and Charpy tests at 76 K. Subsequently the welds will be evaluated at 4 K using tensile and fracture toughness test methods. All welding and initial testing will be done in FY 79. Testing will be completed in FY 80.

C. Aluminum Welding Program. Several fabricators will be asked to prepare test welds in 5083-O aluminum using 5183 filler wire obtained from a source of the fabricators choice. The weld procedures used and the resultant test welds will be qualified in accordance with ASME Boiler and Pressure Vessel Code requirements (Sections VIII and IX). The results will indicate if property variations at 4 K are significant enough to warrant more stringent qualification procedures for welds used in liquid helium applications.

D. Large Coil Project Support. Welds supplied by General Electric and General Dynamics will be evaluated at 4 K to develop data for use in designing superconducting magnets for the Large Coil Project.

Table 1. Chemical compositions of the gas metal arc weld deposits of three experimental alloys
Data provided by Armco (weight percent)

Alloy	Cr	Ni	Mn	C	N	P	S	Si	Other
20Cr-10Ni-9Mn Armco Heat 037026	19.6	8.9	8.4	.049	.09	.007	.026	.45	
13Cr-20Ni-9Mn-1.6Cb Armco Heat 036067	14.9	20.0	9.25	.045	.02	.006	.013	.57	Cb ÷ 1.98
18-Cr-16Ni-9Mn Armco Heat 037025	18.1	15.8	8.6	.049	.08	.004	.021	.44	

Table 2. Mechanical properties of gas metal arc weld deposits of three experimental alloys
Data provided by Armco

Alloy	Test Temperature	Tensile Properties				Charpy Impact	
		Ultimate Strength MPa (ksi)	Yield Strength MPa (ksi)	Elongation %	Reduction of Area %	Energy J(ft-lb)	Lateral Expansion mm (in)
20Cr-10Ni-9Mn	Room	737 (107)	439 (63.7)	25	35	99 (73)	1.5 (.059)
	77K	1392 (202)	971 (141)	17	39	24 (18)	.23 (.009)
13Cr-20Ni-9Mn-1.8Cb	Room	643 (93.3)	433 (62.8)	14	30	52 (38)	1.1 (.044)
	77K	903 (131)	710 (103)	8	20	29 (21)	.43 (.017)
18-Cr-16Ni-9Mn	Room	651 (94.5)	431 (62.6)	17	49	103 (76)	1.4 (.055)
	77K	1226 (178)	930 (135)	10	35	63 (46)	.66 (.026)

Table 3. Fracture toughness of AWS 330 weld metal shielded metal arc welds in one-inch-thick 304L plate

Sample	Temperature K	J_{Ic} kN/m	J_{Ic} lb/in	K_{Ic}* MPa$\sqrt{m}$	K_{Ic}* ksi$\sqrt{in}$
A-2 (diluted)**	295	289	1650	239	216
B-3 (diluted)	76	595	3400	356	322
WA-2 (undiluted)***	76	893	5100	436	394
WB-2 (undiluted)	76	543	3100	340	307
WA-3 (undiluted)	4	87.5	500	135	122
WB-3 (undiluted)	4	140	800	170	154

*Calculated from J_{Ic}: $K_{Ic} = (EJ_{Ic})^{\frac{1}{2}}$

**Double-Vee joint configuration

***AWS 5.4 joint configuration

Table 4. Chemical composition of shielded metal arc weld deposits in one-inch-thick 316LN plate
Data provided by the General Electric Company (weight percent)

Alloy	C	Mn	Si	Cr	Ni	Mo	N	Ferrite Number*
E308L-15	0.022	1.90	0.22	19.5	10.6	0.07	0.057	4.1
E316L-15	0.025	2.04	0.30	17.5	13.7	2.10	0.044	0.2
E316L-15	0.27	1.90	0.32	17.5	13.6	2.12	0.071	0

*Magna-gage

Table 6. Tensile properties of shielded metal arc weld deposits in one-inch-thick 316LN plate
Specimens supplied by the General Electric Company

Material	Specimen	Temperature K	Yield Strength MPa	(ksi)	Ultimate Strength MPa	(ksi)	Elongation (in 1")%	Reduction of Area %
316LN	Base Plate	295	279	(40.5)	615	(89.3)	57	72
	Base Plate	4	1025	(149)	1388	(201)	35	50
E308L-15	All-Weld	295	354		534		19	72
	All-Weld	295	408		543		20	62
	All-Weld	Avg	381	(55.3)	538	(78.1)	20	67
	All-Weld	4	598		1358		45	44
	All-Weld	4	709		1357		38	50
	All-Weld	Avg	654	(94.9)	1358	(197)	42	47
	Cross-Weld	295	407	(59.1)	568	(82.4)	27	57
	Cross-Weld	4	691		1376		31	43
	Cross-Weld	4	699		1401		30	49
	Cross-Weld	Avg	695	(101)	1388	(201)	31	46
E316L-15 N = .044%	All-Weld	295	322		484		41	65
	All-Weld	295	387		493		35	80
	All-Weld	Avg	355	(51.5)	488	(70.8)	38	72
	All-Weld	4	724		1217		41	55
	All-Weld	4	816		1192		29	33
	All-Weld	Avg	769	(112)	1205	(175)	35	44
	Cross-Weld	295	-		581	(84.3)	66	58
	Cross-Weld	4	823		1134		23	27
	Cross-Weld	4	792		1109		21	31
	Cross-Weld	Avg	807	(117)	1121	(163)	22	29
E316L-15 N = .071%	All-Weld	295	336		506		44	69
	All-Weld	295	385		532		17	51
	All-Weld	Avg	361	(52.4)	519	(75.3)	30	60
	All-Weld	4	829		1236		54	28
	All-Weld	4	929		1265		43	49
	All-Weld	Avg	879	(128)	1251	(182)	48	38
	Cross-Weld	295	399	(57.9)	536	(77.8)	17	40
	Cross-Weld	4	907		1111		43	26
	Cross-Weld	4	910		1263		31	37
	Cross-Weld	Avg	909	(132)	1187	(172)	37	32

Table 7. Fracture toughness of shielded metal arc weld deposits in one-inch-thich 316LN plate
Specimens supplied by the General Electric Company

Material	Temperature K	J_{Ic} k J/m	($in\text{-}\frac{lb}{in^2}$)	Average $K_{Ic}(J)$ MPa $m^{\frac{1}{2}}$	($ksi\sqrt{in}$)
E308L-15	4	102	(582)	156	(142)
	4	101	(577)		
E316L-15 .044%N	4	58	(331)	118	(107)
E316L-15 .071%N	4	28.4	(162)	95	(86)
	4	46.2	(264)		

Table 8. Charpy impact toughness of shielded metal arc weld deposits in one-inch-thick 316LN plate
Data provided by General Electric

Material	Condition	Temperature	Charpy Impact Toughness			
			Energy		Lateral Expansion	
			J	ft lb	mm	inch
E308L-15	as-welded	Room	81	59.5	1.60	.063
		Room	76	56	1.60	.063
		77K	28	20.5	0.30	.012
		77K	34	25	0.36	.014
	Annealed	77K	45	33	0.69	.027
		77K	46	33.5	0.71	.028
E316L-15	as-welded	Room	85	62.5	1.96	.077
N = .044%		Room	84	62	1.98	.078
		77K	50	37	0.81	.032
		77K	52	38	0.63	.025
	Annealed	77K	71	52	1.19	.047
		77K	68	50	1.27	.050
E316L-15	as-welded	Room	83	61	1.70	.067
N = .071%		Room	97	71	1.78	.070
		77K	42	31	0.69	.027
		77K	48	35	0.69	.027
	Annealed	77K	71	52	1.04	.041
		77K	67	49	0.97	.038

REFERENCE

1. Materials Studies for Magnetic Fusion Energy Applications at Low Temperatures — I (edited by F. R. Fickett and R. P. Reed), National Bureau of Standards, NBSIR 78-884 (April 1978).

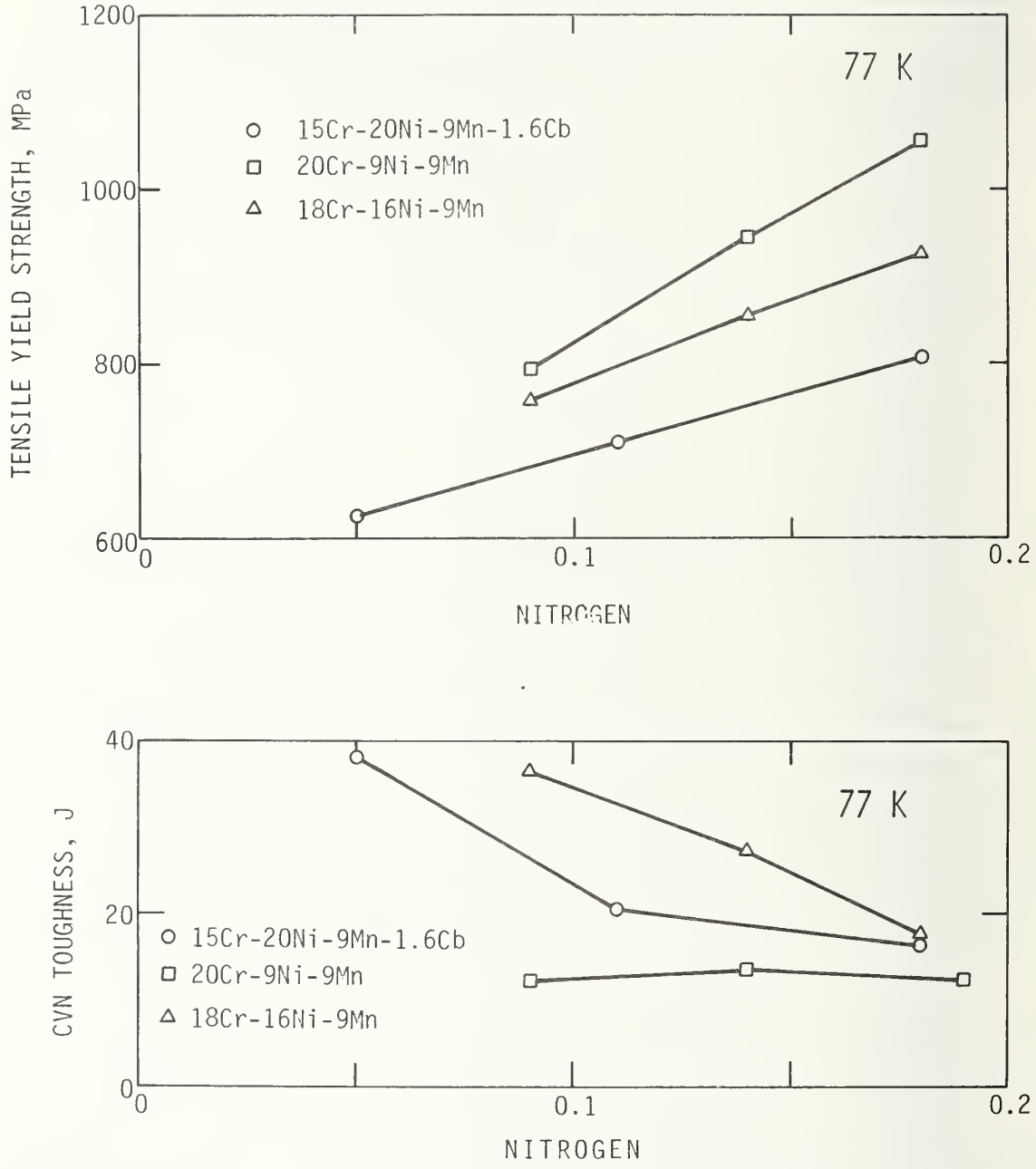

Figure 1. Influence of Nitrogen on the Strength and Toughness at 77 K of Three Experimental Filler Metals (SMA weld deposits).

METALLURGICAL FACTORS AFFECTING THE TOUGHNESS OF 316L SMA WELDMENTS AT CRYOGENIC TEMPERATURES

National Bureau of Standards

METALLURGICAL FACTORS AFFECTING THE TOUGHNESS OF 316L SMA WELDMENTS AT CRYOGENIC TEMPERATURES*

D. T. Read,[1] H. I. McHenry,[1] P. A. Steinmeyer,[2] and R. D. Thomas, Jr.[3]

[1]National Bureau of Standards
Boulder, CO 80303

[2]Colorado School of Mines
Golden, CO 80401

[3]Arcos Corporation
Philadelphia, PA 19143

*Work supported by the U. S. Department of Energy, Office of Fusion Energy. Contribution of NBS, not subject to copyright.

ABSTRACT

The effects of delta ferrite content, ferrite morphology, carbon content, and sensitization on the fracture toughness and tensile properties of AWS E316L and E316 shielded metal arc (SMA) weldments at 295, 76, and 4 K were investigated. Ten SMA test welds were evaluated, eight made with E316L and two with E316 electrodes. In four of the welds, the delta ferrite content was controlled over the range of 0 to 10.1% ferrite through slight variations in the chemical compositions of the electrode coatings. In three of the welds the ferrite morphology was varied in 8% ferrite welds deposited using the same electrode by varying heat input, preheat, and interpass temperature. One E316 weld with low ferrite content (1.2%) and the baseline welding parameters was used to assess the effect of carbon content. The two remaining welds were made with a low cooling rate, to study sensitization in the low ferrite, low (E316L) and regular (E316) carbon welds. Part of the E316 weld was deliberately sensitized at 675°C for 24 hours.

All of the weldments had excellent toughness at room temperature. However, at 76 K, only the E316L weld with low ferrite had acceptable (to ASME Standards) toughness. Large decreases in toughness at 76 and 4 K were related to increasing ferrite content. Decreases in Charpy impact energy at 76 K were also related to coarsened ferrite morphology caused by reduced cooling rates, to increased carbon content, and to the sensitization heat treatment. The tensile-yield strength increased with ferrite content, especially at 4 K. The effects of ferrite content on the ultimate tensile strength and the ductility were generally minor.

INTRODUCTION

Stainless steel weldments will be used for the main structural supports of the superconducting magnet systems needed for fusion energy devices.[1] The austenitic stainless steels have the best combination of strength, stiffness and toughness at 4 K, the operating temperature for superconducting magnets. The service experience with welded assemblies of these alloys has been satisfactory at cryogenic temperatures. A contributing factor to this success has been low design stresses; generally the stresses have been limited to 140 MPa(20 ksi); the ASME allowable stress for austenitic stainless steels at and below room temperature.

For large superconducting magnets, the enormous forces that must be contained and the limited space available for structure may necessitate operating at significantly higher stresses, stresses based on the strength of the alloy at the operating temperature. Many of the austenitic stainless steels exhibit excellent fracture toughness at temperatures down to 4 K in the base metal. Prior to this investigation, weld metal fracture toughness had not been determined at 4 K. Charpy impact results at 76 and 20 K [2,3,4,5] suggested that the toughness may be marginal at 4 K, particularly if the stress levels in the magnets are higher than current practice.

This paper addresses the question of the effect of delta (δ) ferrite content and morphology on weld toughness at low temperatures. Delta ferrite, a body-centered-cubic, ferromagnetic phase formed on weld solidification for a certain range of weld chemistries, is a prominent feature of the metallurgy of conventional stainless steel weld metals. From five to ten percent delta ferrite is often introducted to reduce

hot cracking, which occurs in many weld metals when ferrite is absent and renders them unacceptable. While δ ferrite has not been found deleterious to the room-temperature toughness of stainless steel weldments, it has been suspected of decreasing low-temperature weld toughness because of the well-known low temperature brittleness of body-centered-cubic materials such as mild steel. The ferrite morphology is of interest because isolated patches of a brittle phase should be far less harmful than a semi-conntinuous network that offers a path for crack propagation.

Consideration is also given to carbon content, E316L with .03%C vs. E316 with .06%C, and to sensitization. Again, these factors have a minor effect on toughness at room and elevated temperatures. Their possible significance at low temperatures is due to the increase in austenite strength, approximately two-fold, as temperature is reduced to 4 K. As matrix strength increases, additional sites, such as carbides, may nucleate voids and reduce toughness.

MATERIALS

Common filler metals for welding austenitic stainless steels for low temperature service are Types 308L and 316L. The 316L filler metal was chosen over 308L for this study because it has higher Charpy impact toughness at 77 K (-320F) [4,5], and slightly less susceptibility to microfissuring [6]. The test weldments were 2.5 cm (1 inch) thick plates of AISI 316 stainless steel welded with either AWS E316L-16 or E316-16 titania-coated electrodes using the shielded metal arc (SMA) process. The SMA process was chosen to permit systematic variation of the weld deposit chemistry by alloy additions to the coating. A single-vee (45° included angle) joint preparation with a 13 mm gap at the root

and a 6 mm-thick backing plate was used to avoid dilution by the base metal at the weld centerline.

Eight 316L and two E316 welds were evaluated. The welding parameters and weld deposit chemistries are given in Tables 1 and 2, respectively. The delta ferrite content was varied from 0 to 10% by altering the chemistry of the deposited weld metal within the limits for AWS E316L. The cooling rate of the weld was controlled by varying heat input, preheat, and interpass temperature. Four E316L weldments made with baseline welding parameters were used to investigate the effect of ferrite content. Three additional sets of parameters were used to make constant chemistry E316L welds with varying cooling rates, all with about 8% ferrite. One E316 weld with low ferrite content (1.2%) and the baseline welding parameters was used to assess the effect of carbon content. The two remaining welds were made with a low cooling rate to study sensitization in the low ferrite welds in both E316L and E316. In order to further study sensitization, part of the E316 weld (no. 10) was heat treated at 675°C for 24 hours. This weldment is subsequently designated number 11.

PROCEDURES

The weldments were evaluated using tensile, Charpy V-notch (CVN) and fracture toughness tests. Test environments included air at room temperature (approximately 295 K), liquid nitrogen at 76 K, and liquid helium at 4.2 K. The procedures are described in the following subsections.

Tensile: Tensile tests were conducted at 295, 76, and 4 K using 2.5 cm (1 in.) gage length and 0.64 cm (215 in.) diameter specimens. The specimens were oriented along the length of the weld such that the

entire sample was weld metal. The test procedures and the cryostat for the low temperature tests have been described by Reed [7].

Notch Toughness: Charpy V-notch impact toughness tests were conducted at 295 and 76 K using the procedures specified in ASTM E23. The specimen length was oriented perpendicular to the length of the weld with the notch at the weld centerline and perpendicular to the plate surface.

Fracture Toughness: Fracture toughness tests were conducted at 76 and 4 K using the ASTM E399 compact specimen with a 5.1 cm (2 in.) width and 2.5 cm (1 in.) thickness. The specimens were oriented such that loading was perpendicular to the weld and crack extension was along the weld centerline. The single specimen J-integral procedure [8] was used to determine J_{Ic}, the value of J at the onset of crack extension.

The plane strain fracture toughness, $K_{Ic}(J)$, was determined from J_{Ic} using the relationship proposed by Begley and Landes [9]:

$$K_{Ic}(J) = \left(\frac{J_{Ic} \cdot E}{1-\nu^2}\right)^{1/2}$$

where E is Young's modulus and ν is Poisson's ratio. Tests were conducted in an electrohydraulic fatigue machine equiped with a cryostat described by Fowlkes and Tobler [10].

In the single-specimen J-integral technique, the specimen is precracked in tension-tension fatigue to a crack length of 3 cm (1.2 in.). Subsequently, the specimen is loaded monotonically at a load-line-displacement rate 50 μm/s or less under displacement control to a point well within the elastic region. The curve of load vs. load-line displacement is recorded on an x-y plotter. A specimen is then partially unloaded, and the incremental compliance (load vs. displacement) curve

is recorded on a second x-y plotter with appropriate amplification and signal conditioning. A signal proportional to the change in load is electronically subtracted from the signal; the proportionality factor is adjusted so that the unloading compliance before crack extension is displayed as a vertical line on the graph of load change against load-line-displacement change. The specimen is incrementally extended, with several stops for recording the unloading compliance. Typically, ten to twenty unloading compliances are recorded. The magnitude of the decrease in load during the unloadings is restricted to ten percent of the total load. J-integral values are calculated from the load vs. load-line-displacement record at each unloading point using the Merkle-Corten [11] relation. Crack extension values, Δa, are calculated from all unloading compliance curves except the first one, which is used to evaluate the compliance at $\Delta a = 0$. The $(\Delta a, J)$ data are then plotted, and J_{Ic} is evaluated graphically as the intersection of a curve through the data with the theoretical blunting line given by $J = 2\bar{\sigma}\Delta a$ where $\bar{\sigma}$ is the arithmetic mean of the yield strength and the ultimate tensile strength.

RESULTS AND DISCUSSION

Ten test weldments were prepared to study the influence of ferrite content, ferrite morphology and sensitization on the toughness of stainless steel weld deposits.

Weldments 1 to 4 were welded with electrodes 1 to 4, respectively, to systematically vary the ferrite content between 0 and 12%. The weld-deposit chemistry of each electrode, summarized in Table 2, was within the chemistry limits specified for AWS E316L. The actual ferrite contents were 0.1, 4.1, 8.5 and 10.1% for weldments 1 to 4, respectively.

Ferrite content was measured with a Magne Gage* using standard procedures [12].

Weldments 3, 6, 7 and 8 were all welded with electrode 3 and the cooling rate was reduced by increasing the heat input from 6.4 kJ/cm to 20 kJ/cm. The cooling rate in weldment 8 was further reduced by using preheat and interpass temperatures of 315 ± 28°C (600 ± 50°F); a 107 ± 14°C (225 ± 25°F) interpass temperature was used for weldments 3, 6, and 7. The idea was to alter the ferrite morphology by reducing the cooling rate as suggested by Canonico, et. al. [13]. Metallographic examination of the welds, Figure 1, revealed a discontinuous ferrite network in the lowest heat input weld (weldment 6) and a nearly continuous ferrite network in the other three welds. It should be noted that the welds with 4.1% or less ferrite also had discontinuous ferrite networks. The higher heat input welds (weldments 7 and 8) had significantly coarser ferrite networks (and effectively, courser grain sizes) than the lower heat input welds. Cooling rates were calculated using the relationship suggested by Adams [14].

Weldments 1, 5, 9 and 10, which were nominally ferrite-free were used to investigate sensitization. Actual ferrite contents ranged from 0.1 to 2.2%. Sensitization was varied by increasing carbon content and by decreasing cooling rate. Carbon was varied by using electrodes with low carbon (Electrode 1, AWS E316L, C = 0.03%) for weldments 1 and 9, and higher carbon (Electrode 5, AWS E316, C = 0.06%) for weldments 5 and 10. Cooling rates were moderate (heat input of 10.1 kJ/cm and a

*This trade name is included for clarity only. No endorsement of this device by NBS is implied.

107 ± 14°C interpass temperature) for weldments 1 and 5, and slow (heat input = 20 kJ/in and a 315 ± 28°C interpass temperature) for weldments 9 and 10. A deliberate sensitization heat treatment, 675°C for 24 hrs, was given to a portion of weldment 10. The degree of sensitization in each of the weldments was not measured. The toughness of each weldment, which presumably reflects the extent of sensitization, is discussed below.

Tensile Properties

The tensile properties are summarized in Table 3. The tensile and yield strengths of weldments 1 to 4 are shown as a function of temperature in Figure 2. The lowest strengths were consistently obtained in the ferrite-free weld and strength increases of approximately 10% were obtained in the 8.5 and 10.1% ferrite welds. In the welds made with electrode 3 (weldments 3, 6, 7, and 8), yield strength increased with cooling rate as shown in Figure 3. The tensile strength varied ±5% with cooling rate, but did not increase systematically with cooling rate. The higher carbon welds (AWS E316, C = .06%) generally had higher tensile and yield strengths than the corresponding low carbon welds (AWS E316, C = .03%). Ductility of all the welds was satisfactory with elongation values ranging from 26 to 51% at room temperature and 20 to 40% at 4 K.

Charpy V-Notch Impact Toughness

The Charpy V-notch (CVN) impact test results are summarized in Table 4. Note that the results are given in terms of energy absorbed and lateral expansion. The ASME Boiler and Pressure Vessel Code requires .38 mm (.015 inch) lateral expansion in stainless steel weld

metals at the minimum design temperature. Welds made with each electrode and the deliberately sensitized weld easily passed this requirement at room temperature. However, at 76 K, only the AWS E316L weld with essentially zero ferrite (weldment No. 1) exceeded the .38 mm requirement. In the subsequent discussion of Charpy test results, the energy absorbed will be the indicator of toughness because of the excellent correlation of this parameter with the J-integral fracture toughness as discussed later.

As shown in Figure 4, the CVN toughness values drop sharply as the ferrite content is increased. The results agree with those previously reported by Szumachowski and Reid [4]. Comparison of the 76 K toughness weldments 1 and 5 and weldments 9 and 10 indicates that increasing the carbon content from .03% (E316L) to .06% (E316) also causes a substantial reduction in toughness at 76 K. A lesser drop in toughness occurs with reduced cooling rates. For weldments 3, 6, 7 and 8 lateral expansion was .16 ± 2 mm and varied linearly with the cooling rate through the sensitization temperature range, 550 to 800°C, as shown in Figure 5.

Fracture Toughness

Fracture toughness tests were conducted on Weldments 1 to 5 at room temperature, 76 and 4 K, and the results are summarized in Table 5. At room temperature, tests indicated that the toughness of each weld exceeded 275 MPa$\sqrt{m}$; specific toughness values were not obtained because the 2.5 cm-thick specimens did not meet the proposed size requirements [8] for $K_{Ic}(J)$ testing. As shown in Figure 6, the fracture toughness at 76 and 4 K decreased significantly as ferrite increased from 0 to 10%. These results confirm the trend observed in the 76 K CVN tests and indicate that toughness continues to decrease as temperature is reduced

to 4 K. For the 76 K tests, the J_{Ic} fracture toughness data correlated quite well with the CVN data as shown in Figure 7.

Fractography

One fracture toughness test was stopped after extensive sub-critical crack extension had occurred, but prior to fracturing the specimen. The specimen was sectioned in the plane perpendicular to the crack surface and in the direction of crack extension. The crack extension path was examined with a scanning electron microscope (SEM). The resulting SEM photomicrograph, Figure 8, indicates that cracking occurs preferentially along the ferrite phase rather than through the austenite matrix. It was not clear if the cracking occurred at the ferrite-austenite interface or through the ferrite phase. The fracture surfaces of 76 K Charpy specimens from Weldments 1 to 5 were examined with the SEM. The low ferrite weld (Weldment No. 1) had extensive ductile dimpling, Figure 9. The high ferrite welds had a relatively flat, brittle-appearing fracture surface with some regions of ductile dimpling, Figure 10. Isolated evidence of quasi-cleavage was found, but it cannot be conclusively stated that cleavage of the ferrite phase causes the reduced toughness. Visual examination (unmagnified) of the fracture surfaces of the 76 K Charpy specimens for weldments of each ferrite level revealed increased faceting with increased ferrite content. This observation coupled with the minimal evidence of cleavage fracture suggests that cracking progresses along the austenite/ferrite interface rather than through the ferrite.

The fracture surface of the 76 K Charpy specimen from the deliberately sensitized weld (Weldment 11) was also examined using the SEM. The fractographs, Figures 11 and 12, reveal that the fracture surface

was covered with a precipitate and extensive secondary cracking occurred perpendicular to the main fracture surface. Apparently, the fracture path follows the path defined by the localized carbide precipitation caused by the sensitization treatment.

Comparison with Base Metal Properties

The fracture toughness of the AWS 316L weldments at 4 K can be compared with annealed austenitic stainless steel plate [15]. As shown in Figure 13, weldments have significantly less fracture toughness than base metals at comparable yield strengths. This means that the weld zone is far more susceptible to fracture than the base metal in cryogenic structures. Clearly, further research to improve weld toughness at cryogenic temperatures is required.

SUMMARY AND CONCLUSIONS

Ten AISI 316 test plates were SMA welded with AWS E316L electrodes to evaluate the effect of ferrite content, ferrite morphology, carbon content, and cooling rate on the tensile properties, notch toughness, and fracture toughness at room and cryogenic temperatures. Each of the 10 test weldments easily passed the ASME Charpy toughness requirement of 0.38 mm (.015 inch) lateral expansion when the test was conducted at room temperature. However, when tested at 76 K, only the AWS E316L weld deposit with 0.1% ferrite that was welded using moderate heat input (10.5 kJ/cm) and interpass temperature (107 ± 14°C) exceeded the ASME requirement. Increasing the ferrite content to 4.1% or greater, increasing the interpass temperature to 315 ± 28°C, or increasing the carbon content to 0.06% (E316 instead of E316L) caused the toughness to fall below .38 mm. The following conclusions were drawn from the test results:

1. Increasing delta ferrite over the range 0 to 10% causes a sharp decrease in fracture toughness at 76 K and 4 K.

2. The ferrite morphology changes from isolated patches of ferrite at near zero ferrite to a nearly continuous ferrite phase at 7% ferrite.

3. Decreased cooling rate increases the ferrite dendritic spacing and the effective grain size of the austenite matrix, and it decreases the Charpy impact toughness at 76 K.

4. Increasing the carbon content from 0.03 to 0.06% decreased the fracture toughness at 76 and 4K.

5. Deliberate sensitization of an AWS E316 weld deposit caused a significant toughness loss at 76 K.

6. Fractography of failed CVN specimens suggests that fracture at 76 K progressed along the ferrite/austenite boundary.

7. The fracture toughness, $K_{Ic}(J)$, of E316L welds is approximately half of the $K_{Ic}(J)$ for AISI 300-series stainless steel plates.

ACKNOWLEDGMENTS

This work was sponsored by the U.S. Department of Energy; Dr. E. N. C. Dalder was the project monitor. The authors wish to thank J. W. Elmer and Professor D. L. Olson of the Colorado School of mines for metallographic examination of the weldments.

REFERENCES

1. H. I. McHenry and R. P. Reed, "Structural Alloys for Superconducting Magnets in Fusion Energy Systems," Nuclear Engineering and Design, forthcoming.

2. R. Castro and J. J. de Castenet, Welding Metallurgy of Stainless and Heat-Resisting Steels. Cambridge University Press, 1974, p. 122.

3. F. W. Bennett and C. P. Dillon, "Impact Strength of Austenitic Stainless Steel Welds at -320F —— Effects of Composition, Ferrite Content, and Heat-Treatment," J. Basis Eng. 88, 3, March 1966.

4. E. R. Szumachowski and H. F. Reid, "Cryogenic Toughness of SMA Austenitic Stainless Steel Weld Metals: Part I - Role of Ferrite," Welding Journal, Welding Research Supplement 57, 325-s to 333-s (1978).

5. W. T. DeLong, "Ferrite in Austenitic Stainless Steel Weld Metals," Welding Journal, Welding Research Supplement 53 273-s to 286-s (1974).

6. C. D. Lundin and D. F. Spond, "The Nature and Morphology of Fissures in Austenitic Stainless Steel Weld Metals," Welding Journal, Welding Research Supplement 55, 356-s to 367-s (1976).

7. R. P. Reed, "A Cryostat for Tensile Tests in the Temperature Range 300 to 4 K," in Advances in Cryogenic Engineering, Vol. 7, Plenum Press, New York, 1962, pp. 448-454.

8. G. A. Clarke, W. R. Andrews, P. C. Paris, and D. W. Schmidt, in Mechanics of Crack Growth, Proceedings of the 1974 National Symposium on Fracture Mechanics, ASTM STP 590, American Society for Testing and Materials, Philadelphia, PA (1976), p. 27-42.

9. J. A. Begley and J. D. Landes, in Fracture Toughness, Proceedings of the 1971 National Symposium on Fracture Mechanics, Part II, ASTM STP 514, American Society for Testing and Materials, Philadelphia, PA (1972), 1-20.

10. C. W. Fowlkes and R. L. Tobler, "Fracture Testing and Results for a Ti 6Al-4V Alloy at Liquid Helium Temperatures," Engineering Fracture Mechanics, Vol. 8, 1976, pp. 487-500.

11. J. G. Merkle and H. T. Corten, "A J-Integral Analysis for the Compact Specimen, Considering Axial Force as well as Bending Effects," Journal of Pressure Vessel Technology, Trans. ASME, 1974, pp. 286-292.

12. W. T. DeLong, "Calibration Procedure for Instruments to Measure the Delta Ferrite Content of Austenitic Stainless Steel Weld Metal," Welding Journal, Vol. 52, 1973, pp. 69-s to 72-s.

13. D. A. Canonico, "Materials and Their Application in the Nuclear Industry," Metallography, Vol. 9, 1976, pp. 459-481.

14. C. M. Adams, Jr., "Cooling Rates and Peak Temperatures in Fusion Welding," Welding Journal Vol. 37, 1958, pp. 210-s to 215-s.

15. D. T. Read and R. P. Reed, "Fracture and Strength Properties of Selected Austenitic Stainless Steels at Cryogenic Temperatures," to be published.

LIST OF TABLES

Table 1. AWS E-316L and E-316 Test Weldments.

Table 2. Chemical Composition of Weld Deposits of the Test Electrodes.

Table 3. Tensile Properties of the AWS E316L Weldments.

Table 4. Charpy V-Notch Impact Test Results.

Table 5. Fracture Toughness of the AWS 316L Weldments at 76 and 4 K.

Table 1. AWS E-316L and E-316 Test Weldments.

Weldment No.	Electrode Type	Electrode No.	Welding Parameters Current Amps.	Volts	Travel cm/s	Interpass (ipm)	°C	Temp. °F	No. of Passes	Ferrite % Ave.*	Ferrite No. FN Ave.*
1	E316L	1	130	24	15-20	(6-8)	93-121	(200-250)	31	0.13	0.12
2	E316L	2	130	24	15-20		93-121		25	4.1	4.5
3	E316L	3	130	24	15-20		"		29	8.5	9.2
4	E316L	4	130	24	15-20		"		33	10.1	11.0
5	E316	5	130	24	15-20		"		33	1.2	1.3
6	E316L	3	100	24	20-25	(8-10)	"		39	6.5	7.1
7	E316L	3	160	24	10-15	(4-6)	"		26	9.7	10.5
8	E316L	3	160	26	10-15		288-343	(550-650)	17	7.3	7.9
9	E316L	1	160	26	10-15		"		22	0.67+	0.73+
10	E316	5	160	26	10-15		"		23	2.2	2.4
11°											

*12 Readings
+Fissures observed on surface
°Weldment 11 was part of Weldment 10 that was given a sensitization heat treatment of 675°C for 24 hours

Table 2. Chemical Composition of Weld Deposits of the Test Electrodes.

Electrode No.	WRC Ferrite No. Diagram	Measured	Composition, Weight Percent C	Mn	Si	S	P	Cr	Ni	Mo	Cb	N
1	2	0.5	.031	1.72	.58	.011	.033	18.47	13.97	2.25	.14	.042
2	4.5	3.5	.030	1.72	.56	.012	.034	18.64	12.97	2.29	.14	.046
3	10	9.0	.034	1.70	.57	.009	.034	19.20	12.01	2.32	.15	.042
4	12.5	12.0	.028	1.76	.59	.008	.029	19.66	11.06	2.18	.15	.067
5	3	0.6	.059	1.75	.56	.009	.033	18.69	12.85	2.25	.15	.044

NOTE: Weld deposit chemistry per AWS specification 5.4.

Table 3. Tensile Properties of the AWS E316L Weldments.

Weldment No.	Ferrite %	Temp. K	Yield Strength, 0.2% Offset MPa(ksi)	Ultimate Tensile Strength MPa(ksi)	Elongation in 4-d %	Reduction of Area %
1	.13	295	392 (56.9)	535 (77.6)	38	58
	"	76	659 (95.6)	983 (143)	19	28
	"	4	694 (101)	1222 (177)	20	28
2	4.1	295	396 (57.5)	552 (80.1)	35	57
	"	76	657 (95.3)	1064 (154)	30	32
	"	4	798 (116)	1331 (193)	38	42
3	8.5	295	452 (65.6)	578 (83.9)	45	63
	"	76	753 (109)	1183 (172)	20	42
	"	4	886 (129)	1294 (188)	28	32
4	10.1	295	429 (62.3)	590 (85.6)	38	66
	"	76	725 (105)	1203 (175)	40	32
	"	4	881 (128)	1373 (199)	38	47
5*	1.2	295	405 (58.8)	555 (80.6)	32	56
	"	76	680 (98.7)	914 (133)	12	24
	"	4	924 (134)	1364 (198)	32	40
6	6.5	295	509 (73.9)	609 (88.4)	26	52
	"	76	793 (115)	1261 (183)	55	34
	"	4	936 (136)	1325 (192)	36	32
7	9.7	295	441 (64.0)	564 (81.9)	46	64
	"	76	736 (107)	1179 (171)	58	48
	"	4	817 (119)	1369 (199)	39	54
8	7.3	295	412 (59.8)	585 (84.9)	51	51
	"	76	678 (98.4)	1175 (171)	57	48
	"	4	792 (115)	1263 (183)	40	46
9	.67	295	343 (49.8)	514 (74.6)	48	59
	"	76	639 (92.7)	996 (145)	30	30
	"	4	745 (108)	1157 (168)	26	26
10*	2.2	295	417 (60.5)	597 (86.6)	44	55
	"	76	711 (103)	1250 (181)	46	29
	"	4	847 (123)	1158 (168)	26	26

*AWS E316 electrode.

Table 4. Charpy V-Notch Impact Test Results.

Weldment No.	Electrode	%F	Room Temperature Energy J	Room Temperature Energy ft lb	Room Temperature Lateral Expansion mm	Room Temperature Lateral Expansion in	76 K Energy J	76 K Energy ft lb	76 K Lateral Expansion mm	76 K Lateral Expansion in
1	1	0.1	90	66	1.40	.055	35	26	.41	.016
2	2	4.1	103	76	1.63	.064	28	21	.34	.013
3	3	8.5	84	62	1.24	.049	19	14	.20	.0079
4	4	10.1	76	56	1.30	.051	12	9	.12	.0046
5	5	1.2	86	63	1.40	.055	23	17	.24	.0096
6	3	6.5	92	68	1.27	.050	21	15	.16	.0063
7	3	9.7	84	62	1.42	.056	17	12	.13	.0050
8	3	7.3	88	65	1.37	.054	15	11	.15	.0058
9	1	0.7	92	68	1.70	.067	31	23	.32	.0126
10	5	2.2	82	60	1.55	.061	20	15	.21	.0083
11	5	---	74	54	1.45	.057	11	8	.09	.0036

Note: Data are average values for four tests.

Table 5. Fracture Toughness of the AWS 316L Weldments at 76 and 4 K.

Weldment No.	%Ferrite	Temp K		J_{Ic} KJ/m^2	J_{Ic} in-lb/in^2	K_{Ic} MPa$\sqrt{m}$	K_{Ic} ksi$\sqrt{in}$
1	0.1	76		196	1120		
		76		152	870		
		76	Average	174	995	203	184
		4		109	625		
		4		160	914		
		4	Average	135	770	179	162
2	4.1	76		126	720		
		76		150	857		
		76	Average	138	788	180	164
		4		64	368		
		4		105	599		
		4	Average	85	484	141	128
3	8.5	76		99	564		
		76		74	424		
		76	Average	86	494	143	130
		4		47	267		
		4		34	197		
		4	Average	41	232	108	98
4	10.1	76		62	352		
		76		24	139		
		76	Average	43	246	98	90
		4		47	267		
		4		34	197		
		4	Average	41	232	98	90
5*	1.2	76		95	544		
		76		118	675		
		76	Average	107	610	159	144
		4		544	400		
		4		675	763		
		4	Average	610	582	154	140

LIST OF FIGURES

Figure 1. Photomicrographs showing the morphology of δ-ferrite in an austenitic matrix in 316L weld metal deposited by the SMA process at four heat input levels.

Figure 2. Temperature dependence of the yield and tensile strengths of E316L weldments with 0 to 10% ferrite.

Figure 3. Cooling rate dependence of the yield strengths of E316L weldments with 8 ± 2% ferrite at room temperature, 76 and 4 K.

Figure 4. Charpy V-notch impact energy at 76 K as a function of ferrite content for E316L weldments.

Figure 5. Charpy V-notch impact energy at 76 K as a function of cooling rate for E316L weldments with 8 ± 2% ferrite.

Figure 6. Fracture toughness, $K_{Ic}(J)$ at 76 and 4 K as a function of ferrite content for E316L weldments.

Figure 7. Correlation of the critical J-integral, J_{Ic}, with Charpy V-notch impact energy for E316L weldments at 76 K.

Figure 8. SEM photomicrograph showing the crack propagation path in a 316L weldment with 10% ferrite (2000X, reduced 55% for re production).

Figure 9. SEM photomicrograph of the fracture surface of a 76 K Charpy V-notch impact specimen from an E316L weldment with 0.1% ferrite (550X).

Figure 10. SEM photomicrograph of the fracture surface of a 76 K Charpy V-notch impact specimen from an E316L weldment with 10% ferrite (550X).

Figure 11. SEM photomicrograph of the fracture surface of a 76 K Charpy V impact specimen from an E316 weldment that was deliberately sensitized at 675°C for 24 hours (550X).

Figure 12. SEM photomicrograph of the fracture surface of a 76 K Charpy V impact specimen from an E316 weldment that was deliberately sensitized at 675°C for 24 hours ((a) 200X and (b) 550OX).

Figure 13. Fracture toughness at 4 K of E316L weldments as a function of yield strength. Also shown is a best fit line for the stainless steel plate of fracture toughness in yield strength.

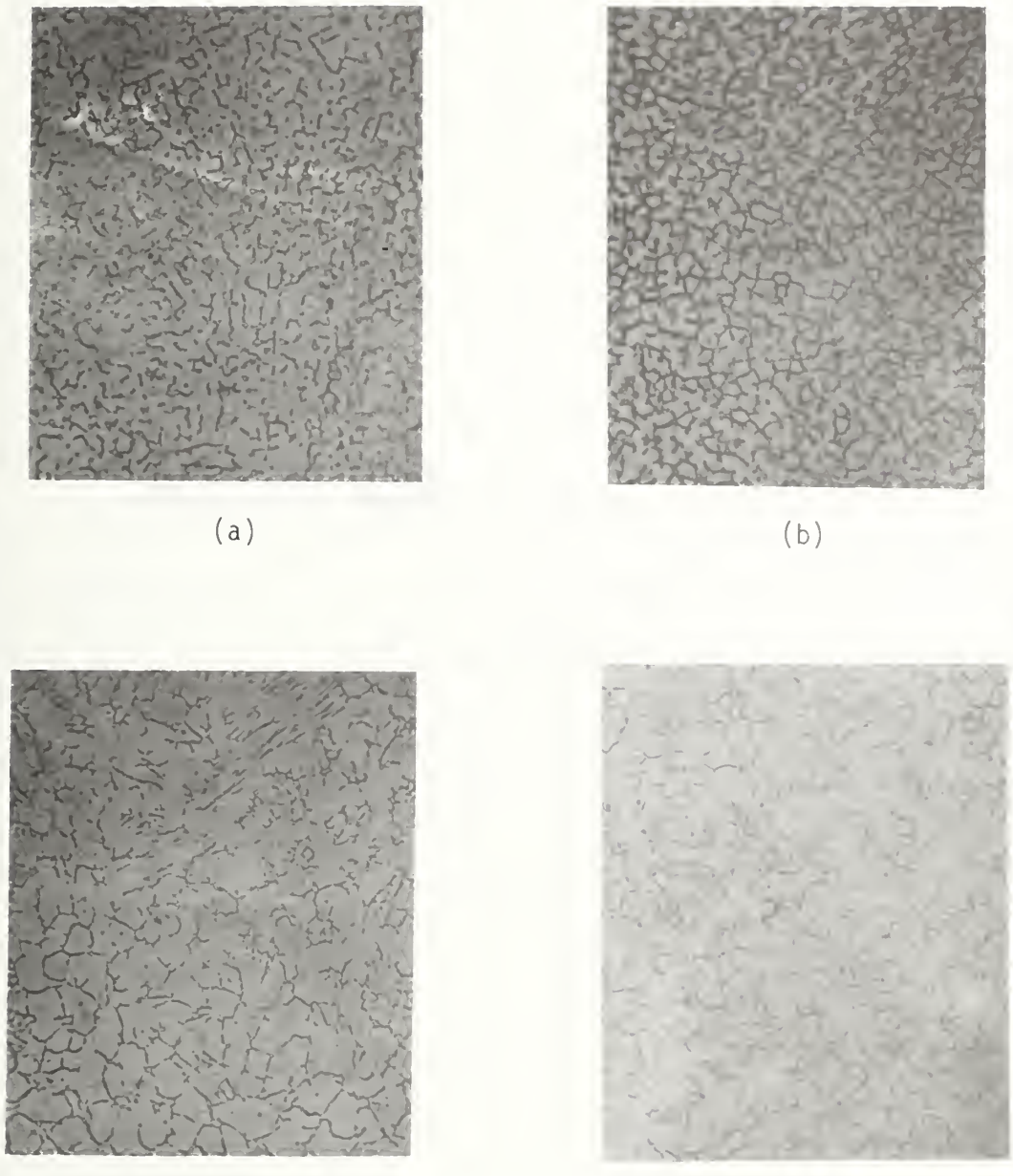

Figure 1. Photomicrographs showing the morphology of delta-ferrite in an austenitic matrix in 316L weld metal deposited by the SMA process at four heat input levels:: 5.3, 10.5, 18.1, and 19.6 kJ/cm in photomicrographs (a), (b), (c), and (d), respectively. 330 X.

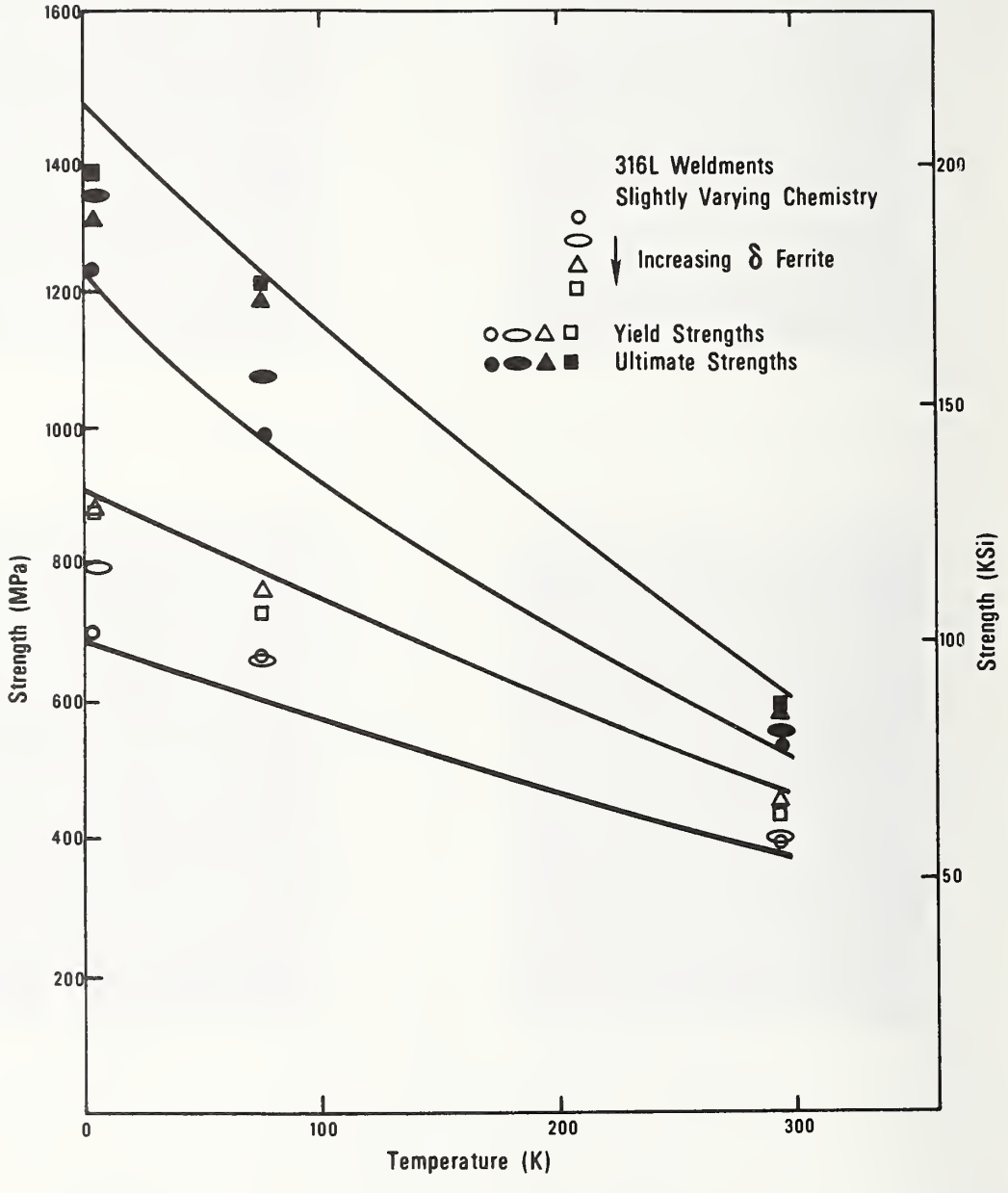

Figure 2. Temperature dependence of the yield and tensile strengths of E316L weldments with 0 to 10% ferrite.

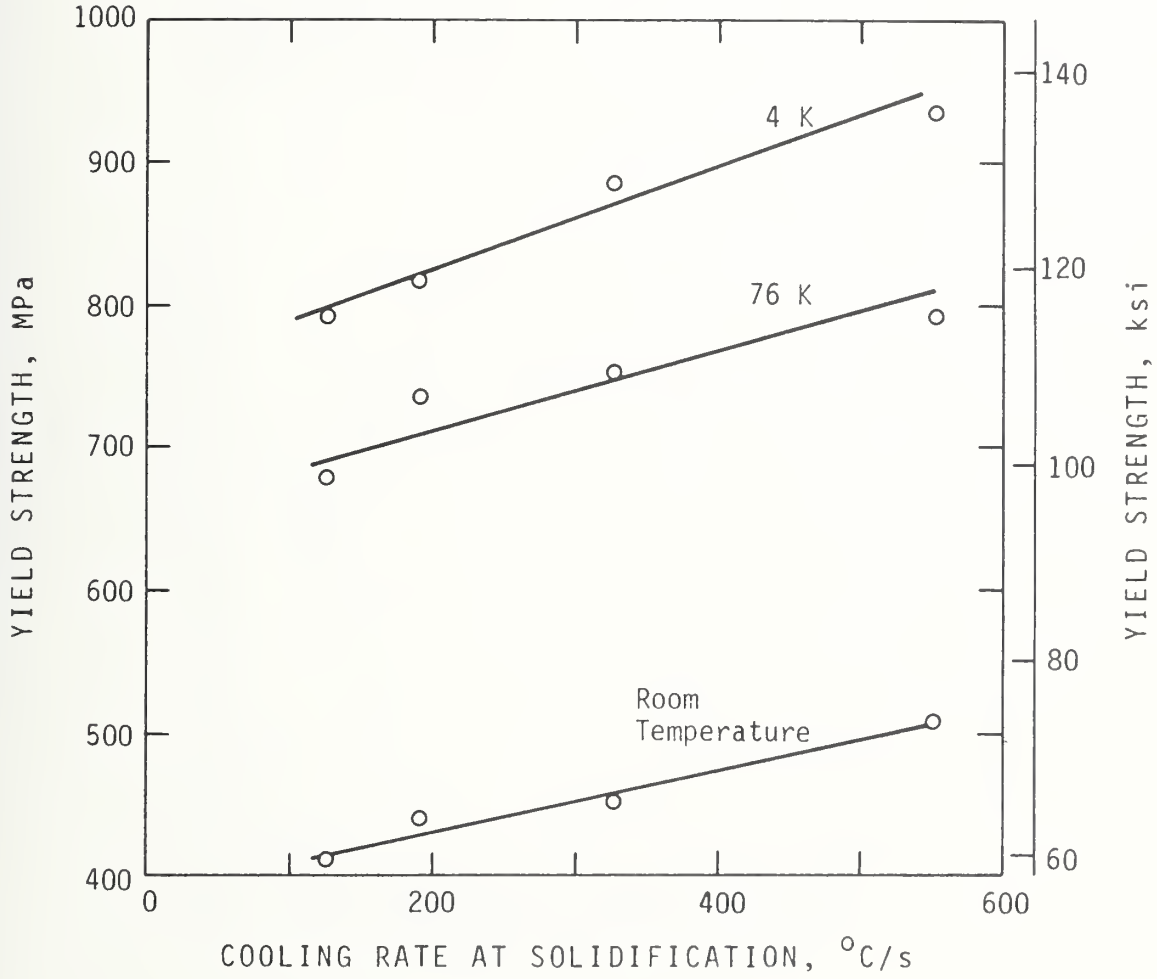

Figure 3. Cooling rate dependence of the yield strengths of E316L weldments with 8 ± 2% ferrite at room temperature, 76 and 4 K.

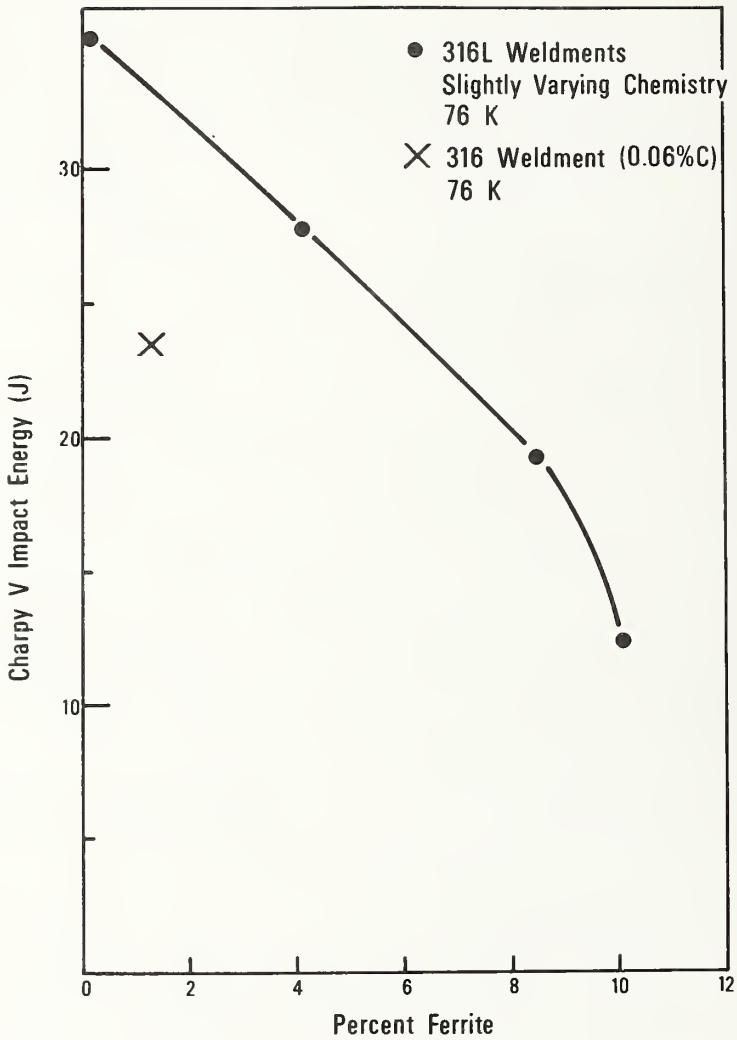

Figure 4. Charpy V-notch impact energy at 76 K as a function of ferrite content for E316L weldments.

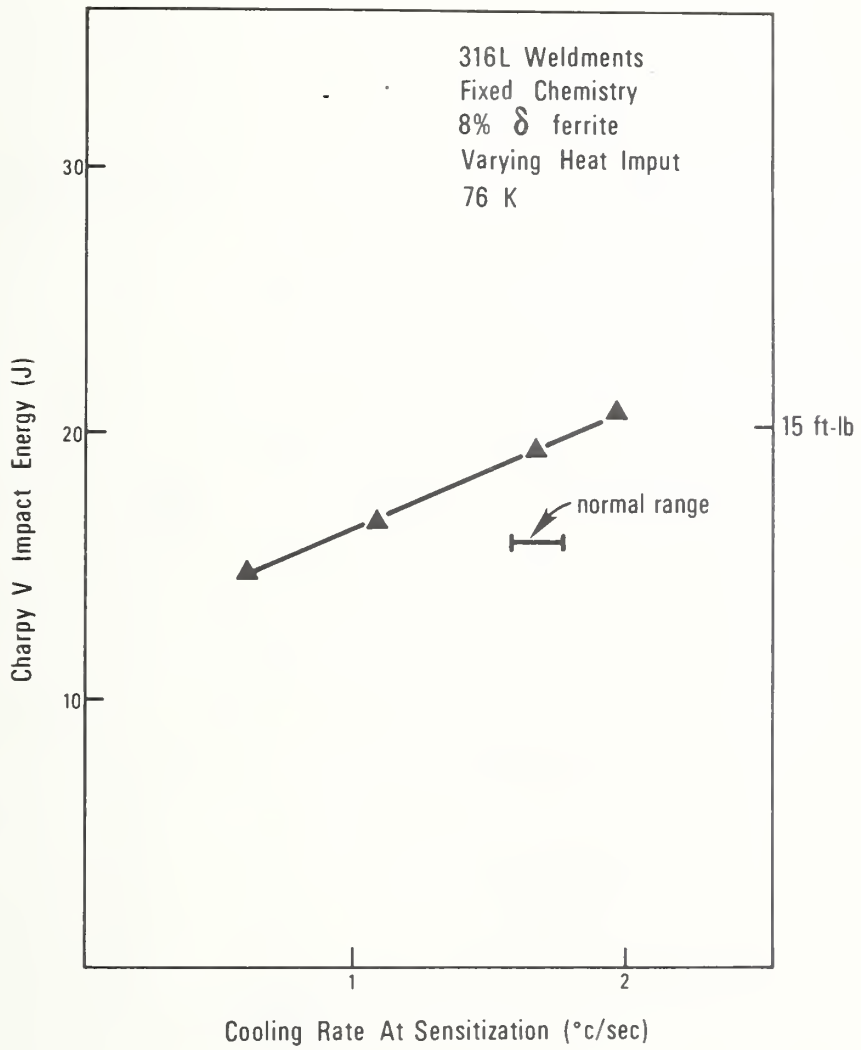

Figure 5. Charpy V-notch impact energy at 76 K as a function of cooling rate for E316L weldments with 8 ± 2% ferrite.

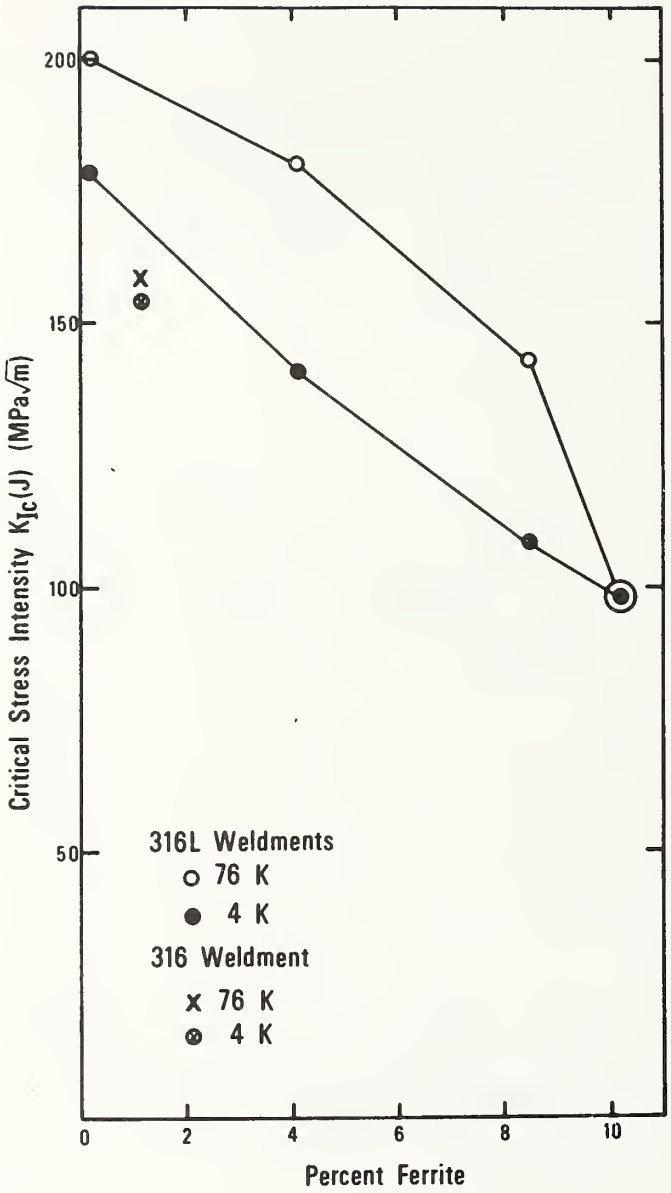

Figure 6. Fracture toughness, $K_{Ic}(J)$ at 76 and 4 K as a function of ferrite content for E316L weldments.

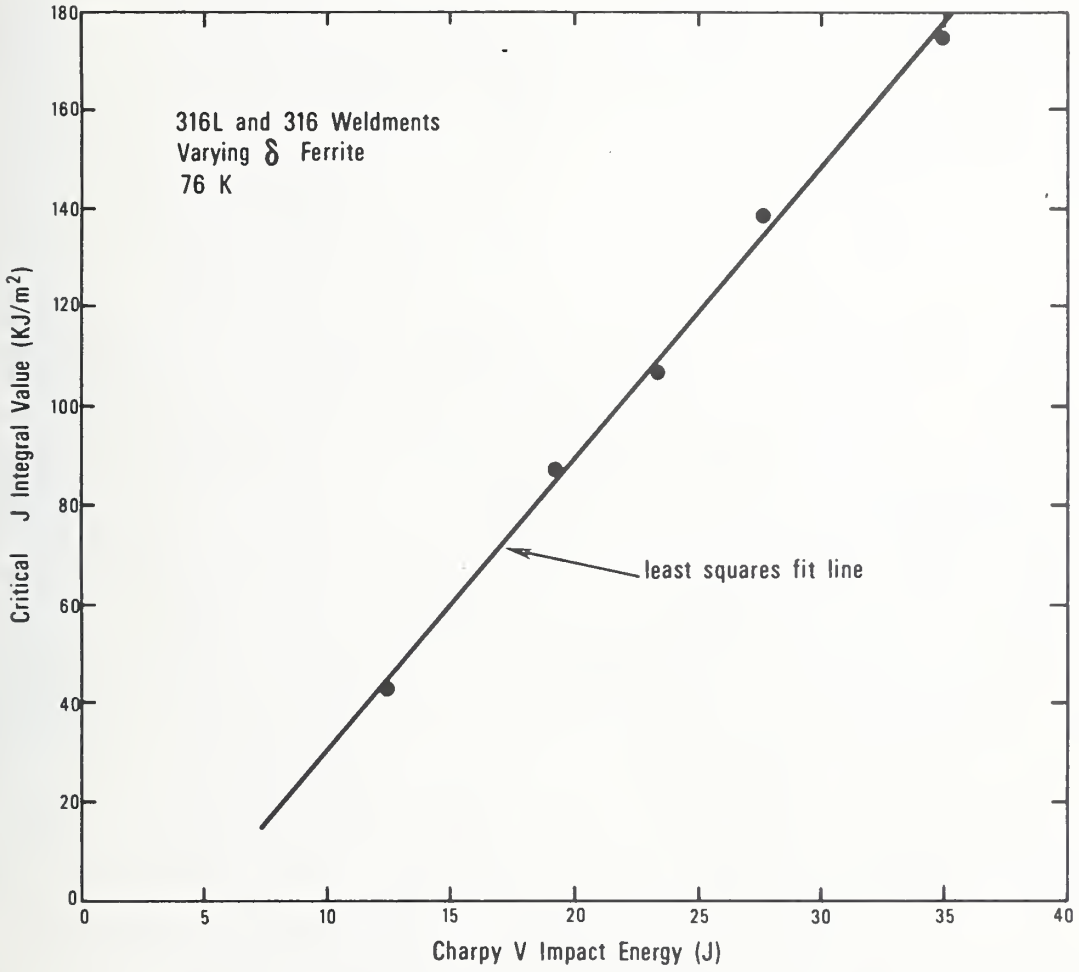

Figure 7. Correlation of the critical J-integral, J_{Ic}, with Charpy V-notch impact energy for E316L weldments at 76 K.

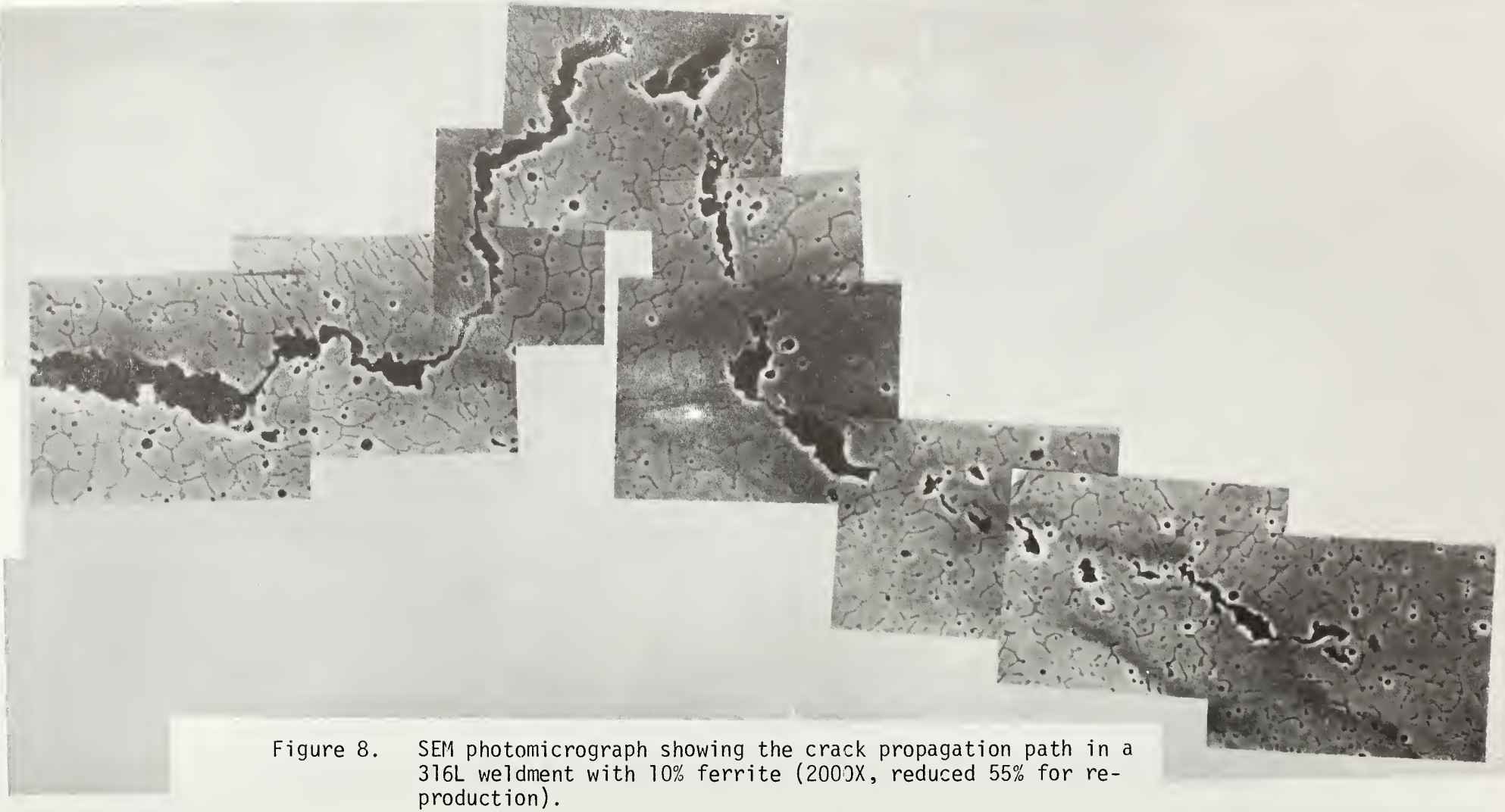

Figure 8. SEM photomicrograph showing the crack propagation path in a 316L weldment with 10% ferrite (2000X, reduced 55% for reproduction).

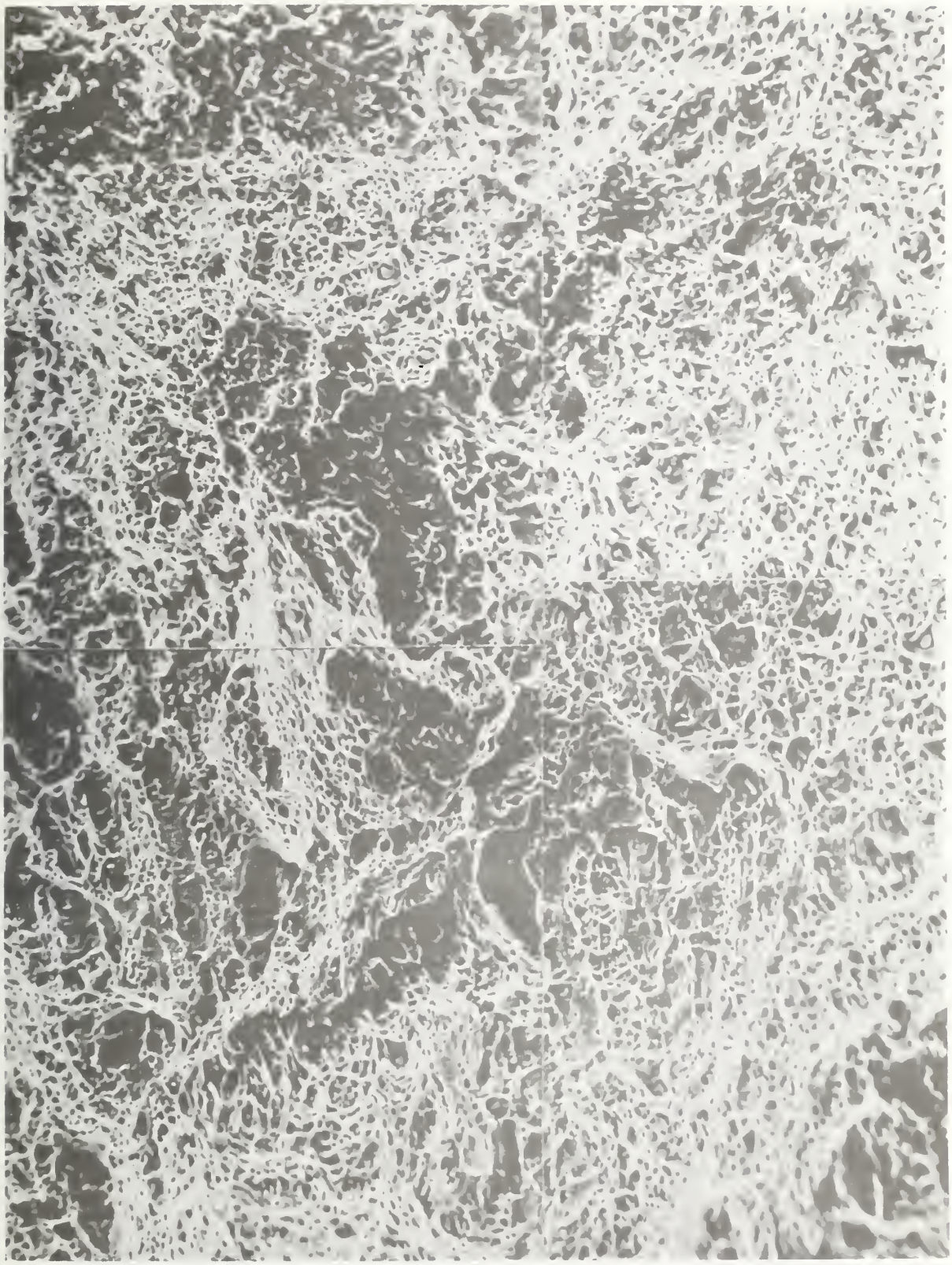

Figure 9. SEM photomicrograph of the fracture surface of a 76 K Charpy V-notch impact specimen from an E316L weldment with 0.1% ferrite (550X).

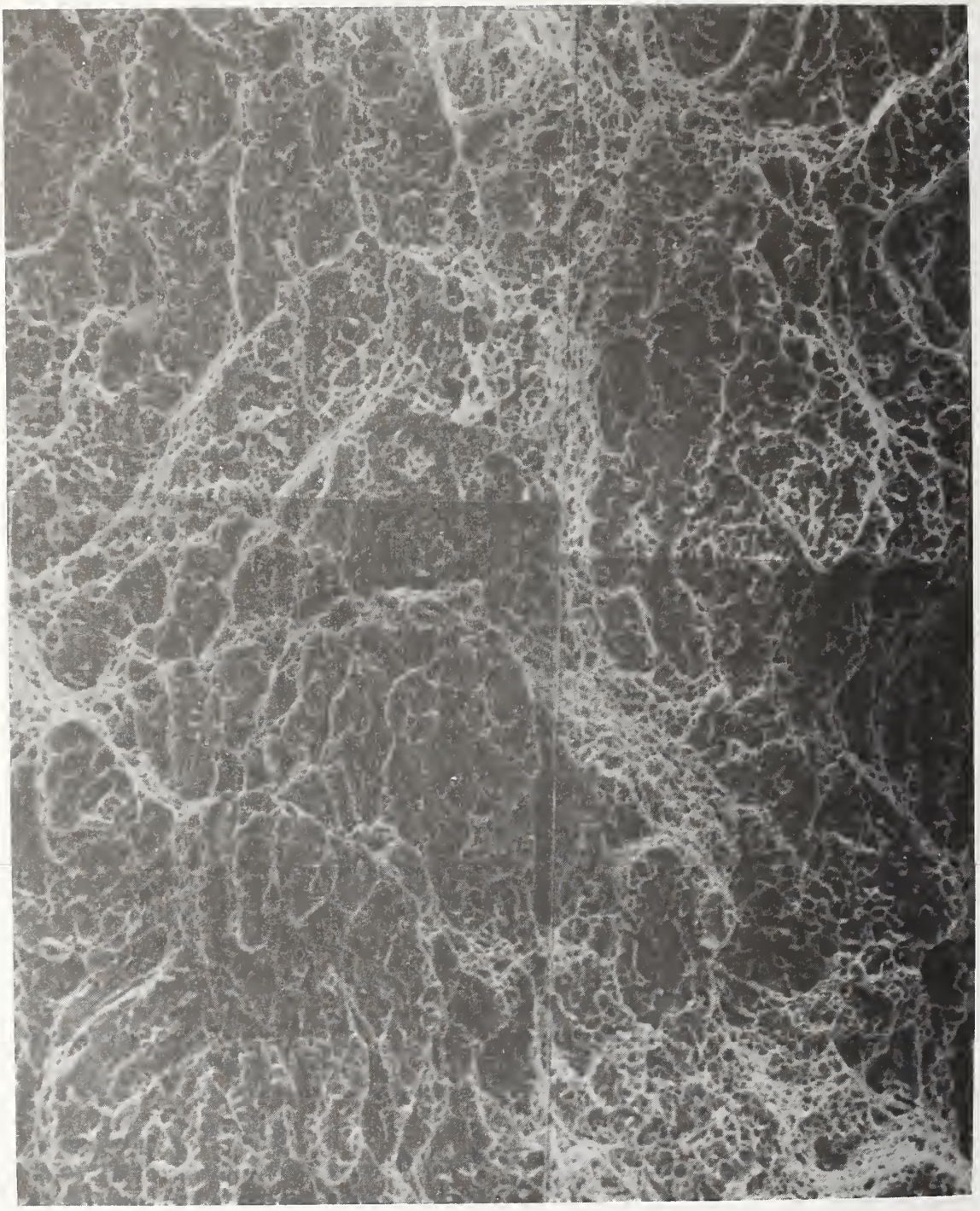

Figure 10. SEM photomicrograph of the fracture surface of a 76 K Charpy V-notch impact specimen from an E316L weldment with 10% ferrite (550X).

Figure 11. SEM photomicrograph of the fracture surface of a 76 K Charpy V impact specimen from an E316 weldment that was deliberately sensitized at 675°C for 24 hours (550X).

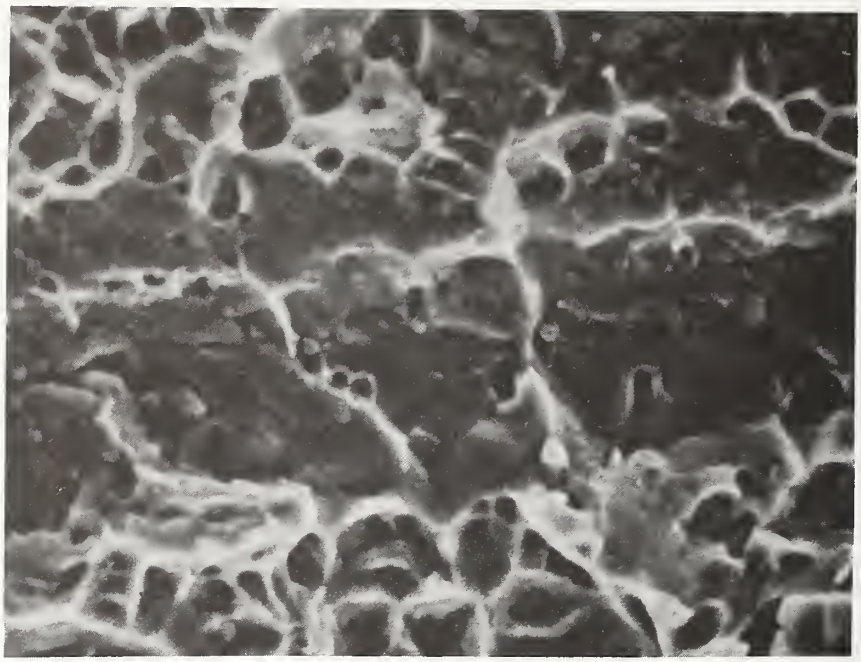

(a)

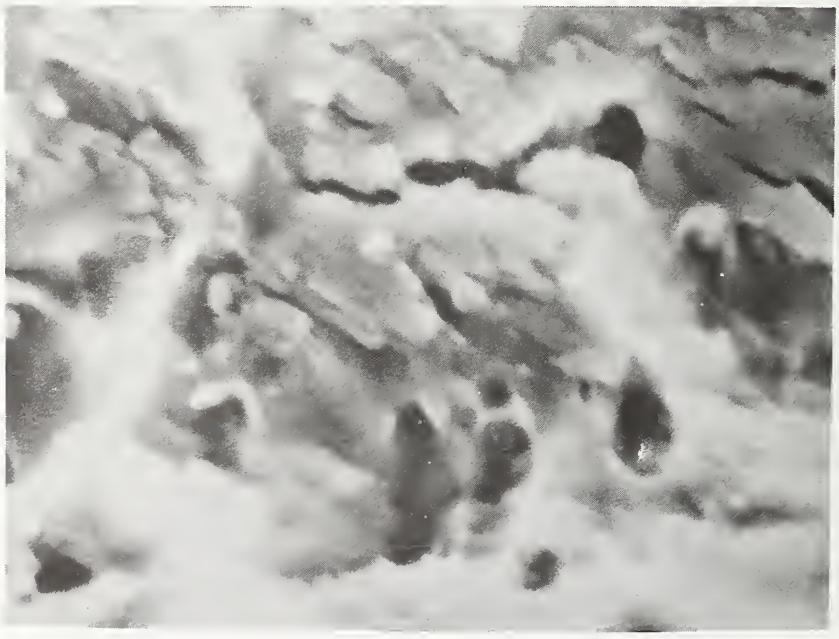

(b)

Figure 12. SEM photomicrograph of the fracture surface of a 76 K Charpy V impact specimen from an E316 weldment that was deliberately sensitized at 675°C for 24 hours ((a) 2200X and (b) 5500X).

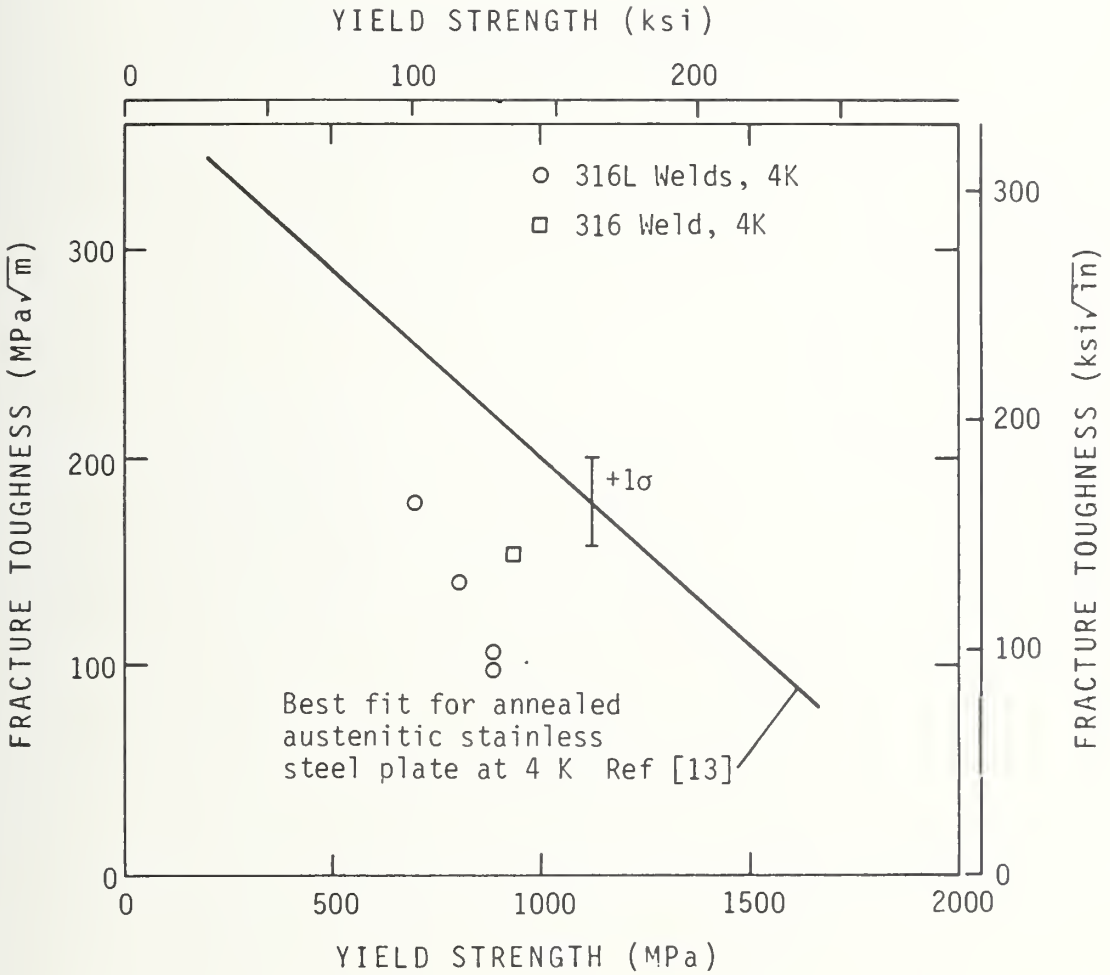

Figure 13. Fracture toughness at 4 K of E316L weldments as a function of yield strength. Also shown is a best fit line for the stainless steel plate of fracture toughness in yield strength.

MICROSTRUCTURE OF SPECIFIC STAINLESS STEEL WELDMENTS BEING EVALUATED FOR CRYOGENIC SERVICE

Colorado School of Mines

FINAL REPORT

"MICROSTRUCTURE OF SPECIFIC STAINLESS STEEL WELDMENTS BEING EVALUATED FOR CRYOGENIC SERVICE"

J. W. Elmer, P. A. Steinmeyer and D. L. Olson

Department of Metallurgical Engineering
Colorado School of Mines
Golden, Colorado 80401

Submitted to:

National Bureau of Standards

Cryogenic Laboratory

Boulder, Colorado

November 28, 1978

INTRODUCTION

Stainless steels derive their corrosion resistance from the presence of specific alloying elements; the major addition is chromium which, when present in amounts in excess of 11%, forms a protective chromium-oxide layer on the surface of these alloys in corrosive environments. Other alloying elements added to stainless steels are Ni, Mo, Mn, Ti, Nb, Cu, and N. Each influences the microstructure in a specific manner.

The microstructure of stainless steel greatly influences its mechanical and corrosion behavior.[1-3] Welding will change its microstructure to such an extent that the weld will have properties different from either the base or the filler metal. During the welding process on most stainless steels, the molten metal solidifies into a microstructure with two phases: austenite and/or ferrite[4-17]. The relative amounts of each structure depend on several variables such as welding heat input[18-19], welding technique[19-23], and weld metal composition[24-27]. Martensitic structure, with a c/a ratio approaching one may also form with mechanical working or with an extremely low quenching temperature.

Much work has been performed to relate the microstructure of the weld metal to its composition. The first of such work was published in 1949 by Schaeffler[8] with his constitution diagram for stainless steel welding (Figure 1). The Schaeffler diagram provided a means to determine the weld deposit ferrite content by combining the effects of the austenitic stabilizing elements Ni, C, and Mn with the ferrite stabilizing elements Cr, Mo, Si, and Nb.

Seferian[12] has also proposed a mathematical expression for ferrite content. His equation is derived from the Schaeffler diagram, and allows the calculation of ferrite content of an austenitic stainless steel weld

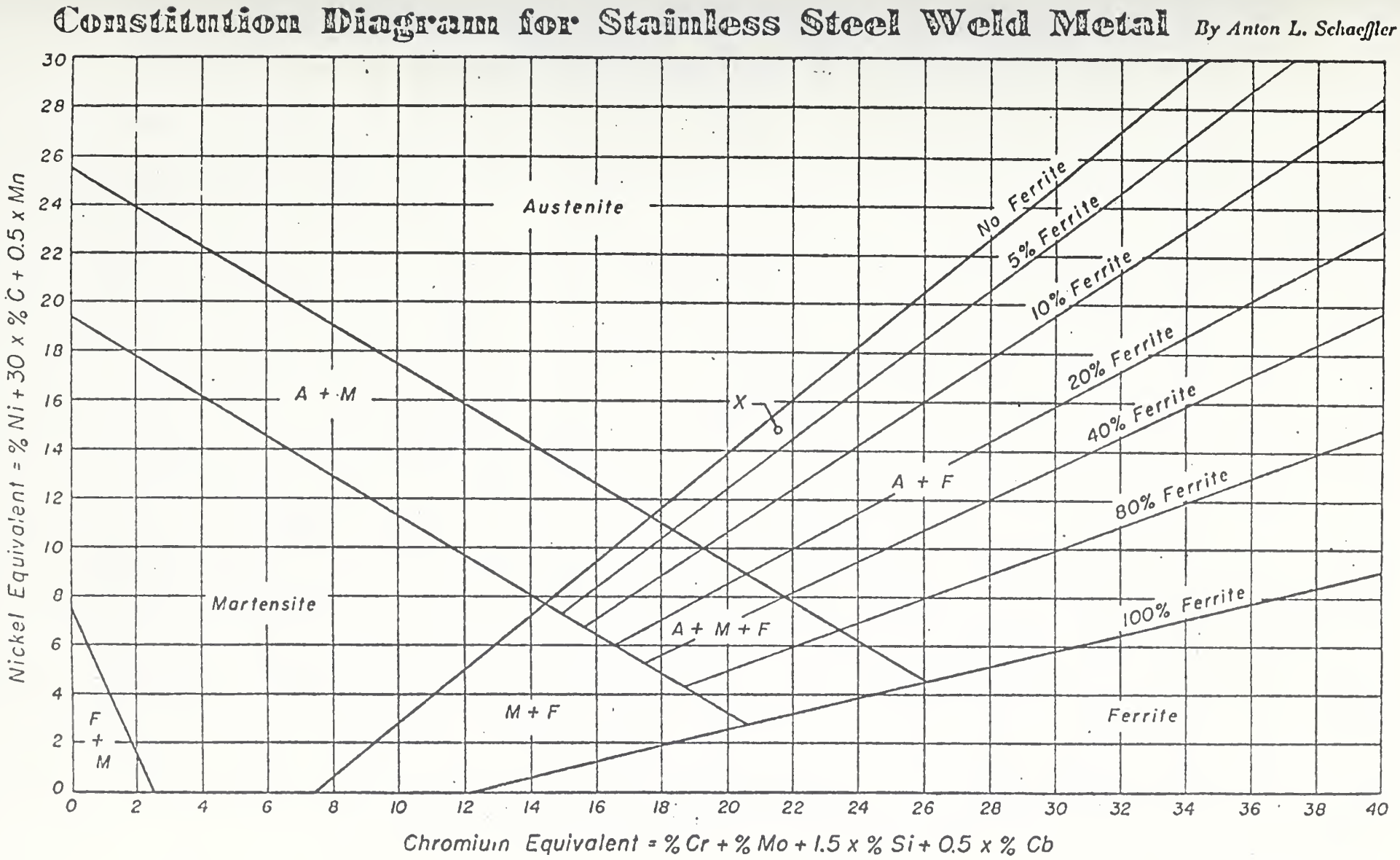
Constitution Diagram for Stainless Steel Weld Metal
By Anton L. Schaeffler
Austenite
A + M
Martensite
F + M
M + F
A + M + F
A + F
Ferrite
X
No Ferrite
5% Ferrite
10% Ferrite
20% Ferrite
40% Ferrite
80% Ferrite
100% Ferrite
Nickel Equivalent = % Ni + 30 x % C + 0.5 x Mn
Chromium Equivalent = % Cr + % Mo + 1.5 x % Si + 0.5 x % Cb
0 2 4 6 8 10 12 14 16 18 20 22 24 26 28 30 32 34 36 38 40
0 2 4 6 8 10 12 14 16 18 20 22 24 26 28 30

Figure 1: The Schaeffler diagram for stainless steels which provides a means to measure weld deposit Ferrite content based on weldment composition.

deposit as follows:

$$\% \text{ ferrite} = 3\{Cr_{eq} - .93\ Ni_{eq} - 6.7\}$$

In 1956, DeLong[9] expanded on the Shaeffler diagram to include the strong austenitizing effects of nitrogen (Figure 2).

Recently Hull[10] has modified the DeLong diagram to include the inversion behavior of manganese from an austenitic to a ferritic stabilizer at high manganese levels (4% of larger). The Hull diagram is compared with these other diagrams in Figure 3. Notice the various expressions for the nickel and chromium equivalents. The tendency for other alloying elements to act as austenite or ferrite stabilizers has also been studied. For example, the presence of copper has been found to increase austenite stability in stainless steels, although its effectiveness is only about 0.6 times that of nickel. Thus, in the expression for nickel equivalent, copper has a coefficient of 0.6. Similarly, the effect of tungsten (a ferrite stabilizer) is accounted for in the chromium equivalent expression by assigning it a coefficient of 0.5, while titanium has been reported to have a coefficient varying from 2 to 5.

In recent years the role of delta ferrite has become an important factor in explaining the behavior of weldments[1,30-33]. Some of the general effects that delta ferrite has on weldments are:

1. The ability to control hot cracking at 3 to 8% ferrite.
2. An increase in tensile strength with higher ferrite contents.
3. Reduction of stress corrosion cracking at high ferrite levels[57].
4. At high temperatures (1000°F) the delta ferrite transforms to the more brittle sigma phase reducing ductility, strength and corrosion resistance of the steel[41,58,59].

The DeLong Constitution Diagram

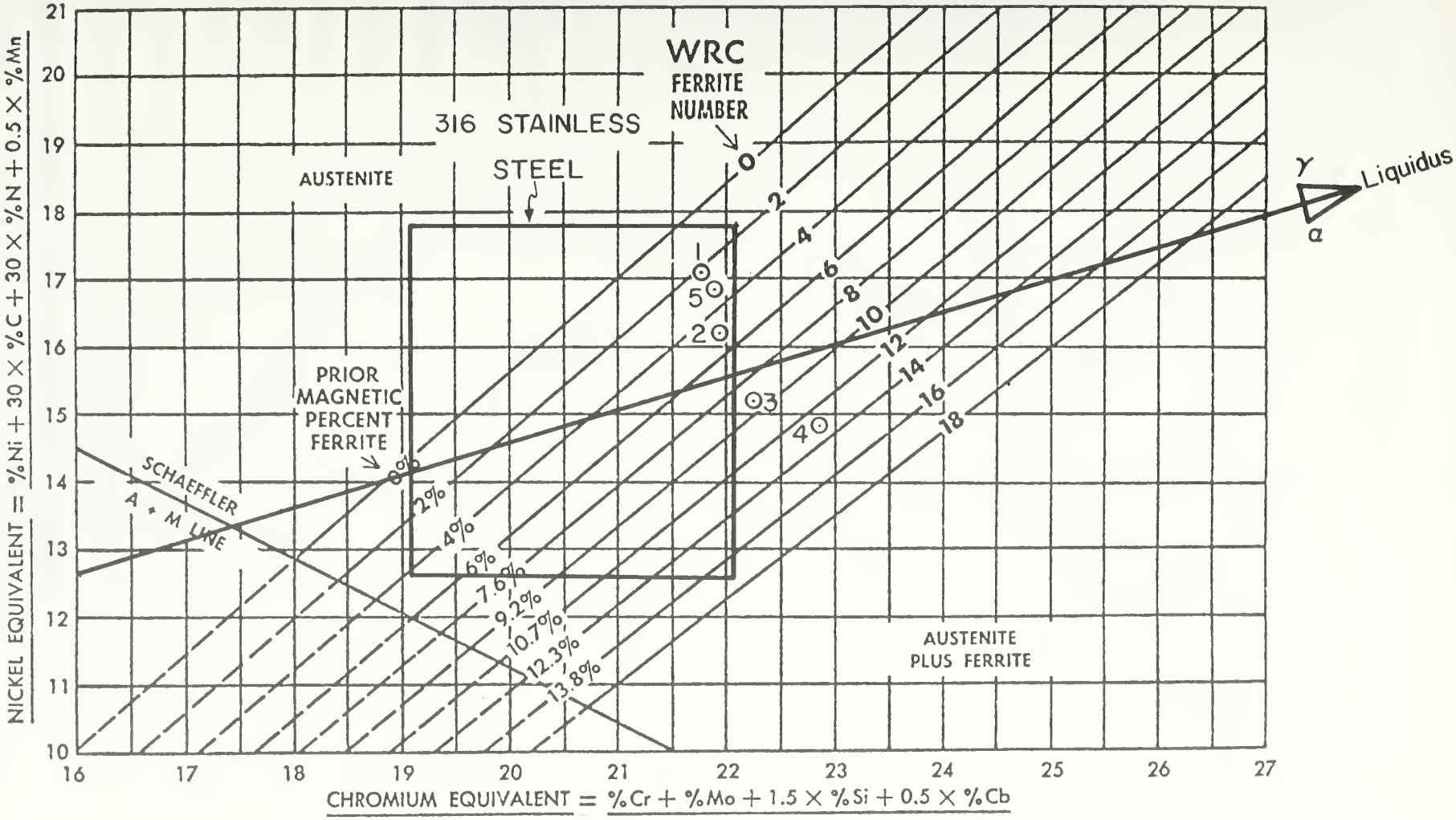

Figure 2. The DeLong diagram. This is based on the Schaeffler diagram, but is revised to include the strong austenitizing effect of nitrogen. The boxed-in area indicates the range of compositions allowed for 316L stainless steel. The heavy line sloping upward from left to right is the liquidus line.

A.

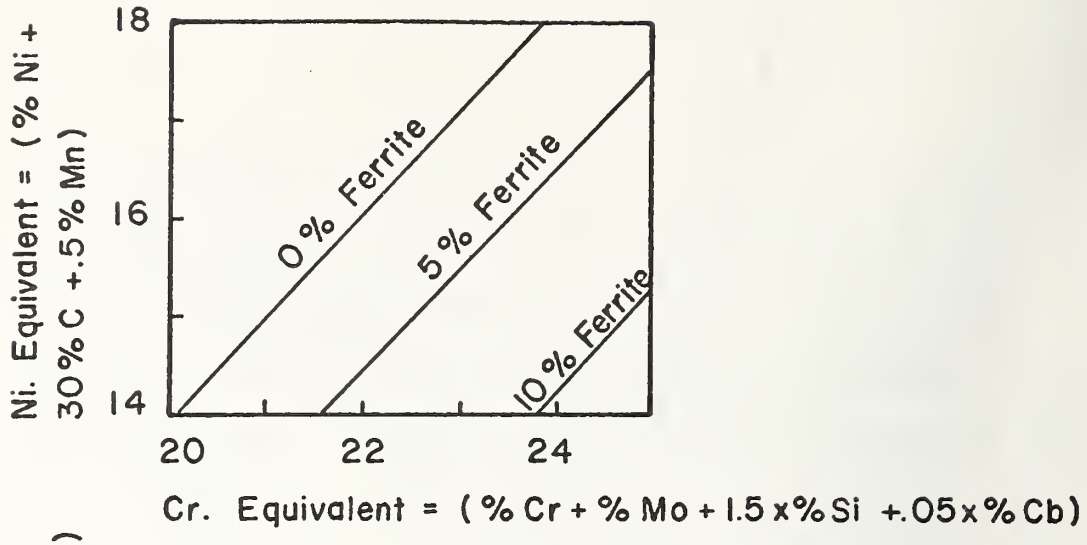

B.

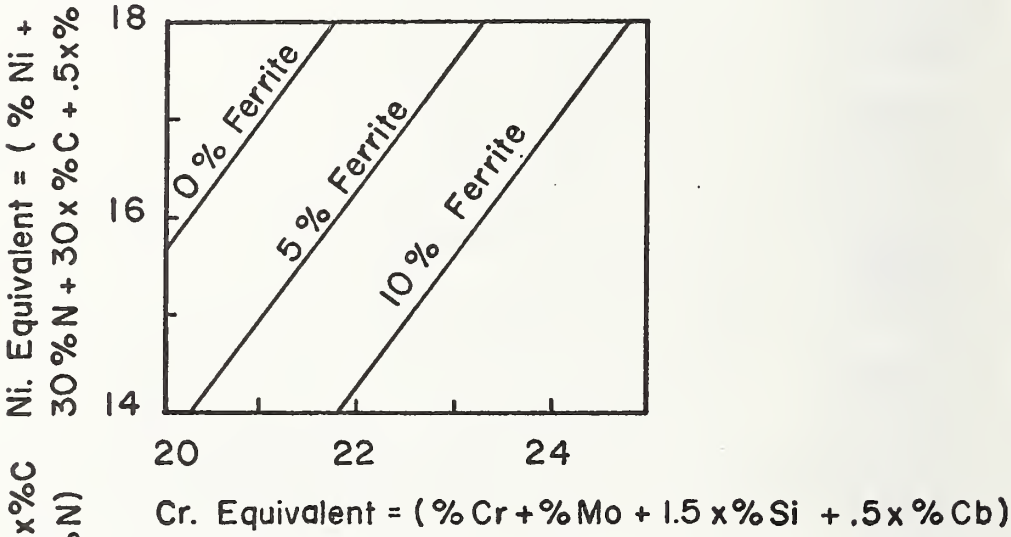

C.

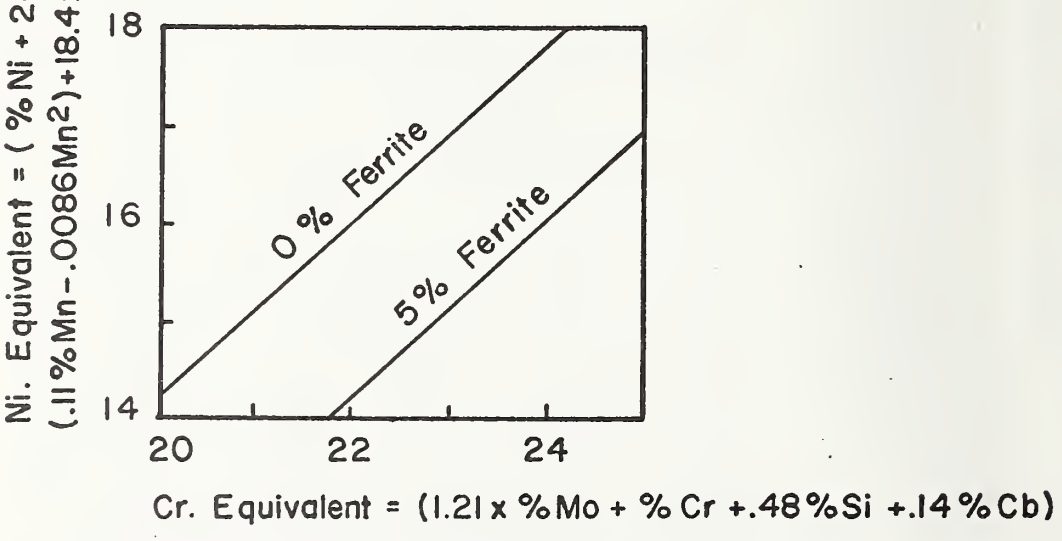

Figure 3. Comparison of the three constitution diagrams.
A) Schaeffler Diagram, B) DeLong Diagram, C) Hull Diagram

5. Increases the susceptability of stainless steel weldments to porosity.

Lundin and Spond[1] have reported on the nature and morphology of the fissures found in stainless steel with low ferrite levels. They found that fissures occur primarily along grain boundaries in the heat affected zone of the previously deposited pass. The fissuring tendency is enhanced by multiple thermal cycling in the heat affected zone and is invariably more pronounced in ferrite-free areas. They also found that the fissures form by a liquation mechanism. Average fissure length was found to be 0.004 in. (0.1 mm) in stainless steel weldments. These fissures were found to be resistant to propagation at room temperature even at strains of up to 20%.

Sulfur and phosphorus tend to promote liquation in stainless steel, and may result in fissuring[34-36]. Sulfur has been reported by Bernstein et al[26] to have more influence than phosphorus on mechanical properties; sulfur level should be kept below 0.015% for critical applications. Honeycombe and Gooch[37] have found that manganese additions reduce cracking but also must be controlled, as manganese may have deleterious effects on corrosion resistance. They showed that additions between 2% and 6% manganese produced crack-free welds.

Brooks and Lambert[36] also report that the amount of ferrite necessary to prevent cracking is directly related to the impurity level (P + S). They report that stainless steel welds with ferrite contents greater than ferrite number 13 to 14 were able to accommodate large amounts of phosphorus and sulfur without cracking. Haddrill and Baker[38] have reported that increasing the carbon content apparently reduces the cracking tendency in austenitic stainless steel. Furthermore, the use of a large-diameter electrode decreases the fissuring tendency.

The presence of controlled amounts of delta ferrite in austenitic stainless steel weldments, although beneficial in reducing microfissuring, may have an adverse effect on mechanical properties. The influences of delta ferrite on high-temperature mechanical properties have been studied by a number of investigators[30,39-45]. King et al[41] reported that anisotropic deformation behavior occurs that can be related to the orientation of the solidification microstructure of the weld. Transverse weld metal specimens were found to be consistently stronger than longitudinal specimens. During creep testing the original ferrite transforms to sigma phase. The resulting hard precipitates of sigma phase were aligned with the solidification substructure making high temperature deformation anisotropic. Type 316 stainless steel welds with controlled amounts of residual elements (CRE) such as boron, phosphorous, and titanium have shown good strength and ductility at 649C in both short-term tensile tests and creep tests lasting up to about 6000 hr. Shahinian et al[43,46] evaluated the fatigue behavior of stainless steel weldments at 25°C, 427°C, and 593°C, and found type 316 stainless steel weld metal to have better resistance to fatigue crack growth than type 308 stainless steel weld metal. They also found that 304 stainless steel weld metal had better resistance than 316 stainless steel base metal. Thomas[33] reported that optimum creep resistance at 600C occurs at approximately 5% ferrite content. Thomas[33] also found that at high ferrite levels (~10% ferrite), the ferrite forms a continuous network, significantly increasing creep resistance.

Charpy V-notch and J_{IC} data (as determined from single-specimen J integral tests) have shown a marked decrease in toughness with increasing ferrite content. When the amount of ferrite was increased from 0.13% to 10.1%, the 76K CVN energy dropped from 35.2J to 12.6J, while

the 76K J_{IC} fracture toughness decreased from 174KJ/m^2 to 43.0KJ/m^2. Fracture toughness tests at 4K showed the same trend, J_{IC} dropping from 135kj/m^2 to 41KJ/m^2. Tensile tests showed only slight increases in yield strength at higher ferrite levels.

The loss of toughness at high ferrite contents in austenitic stainless steel weld-metals is believed to be due to the brittle behavior of the ferrite at lower temperatures. Transmission and scanning electron fractography indicates that high ferrite samples fracture by a cleavage mechanism, while low ferrite fracture is characterized by microvoid coalescence. The SEM micrograph of Figure 4 depicts a crack in a 4K single specimen fracture-toughness test sample; the specimen has been partially cracked, unloaded, and sectioned. The dark areas in the figure are delta ferrite dendrites. It is seen that the ferrite influences the crack propagation behavior: cracking occurs more readily along ferrite regions than through the more ductile austenite matrix.

Ekerot et al[47] have found that the nature and number of pores formed in austenitic stainless steel weldments can also be related to the stainless steel microstructure. They reported that primary precipitation of pores occurs on ferrite dendrites.

There are four major factors which control the amount and morphology of ferrite in the weldment. These are heat input[61], amount of applied strain, composition and history[60]. Williams[19] reported that higher peak temperatures resulted in higher ferrite contents. Also, the applied strain during the thermal cycle of welding has been reported to influence the amount of ferrite. These results suggest that the size of the weld deposit, which has an effect on the amount of shrinkage, is likely to influence the amount and morphology of the ferrite.

A number of investigators[20-25, 47, 48] have evaluated the influence of the electrode coatings on the amount of ferrite formed

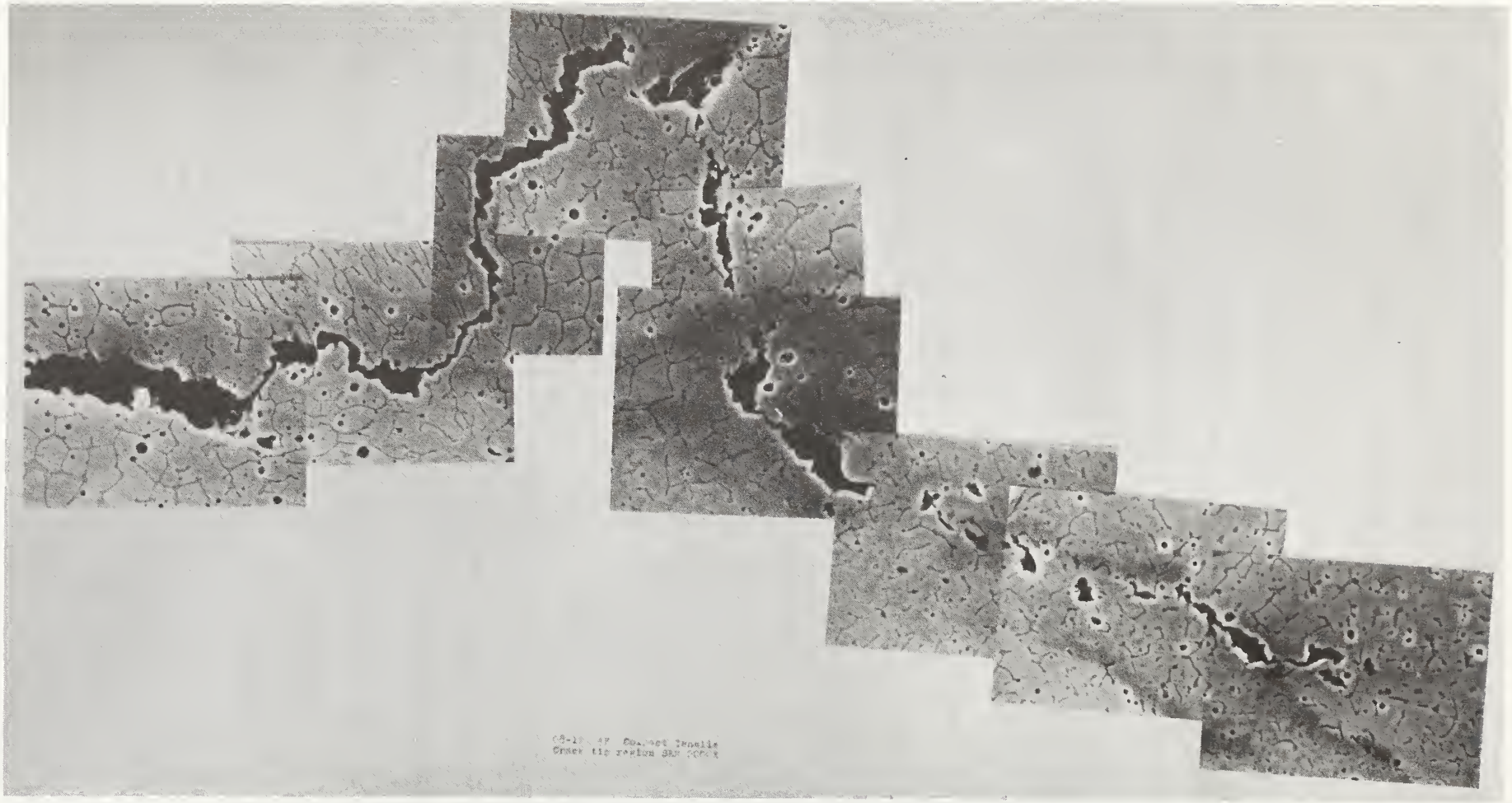

Figure 4. Crack tip region of compact tensile specimen sectioned from 316L weldment (FN = 11), showing crack propagation behavior affected by presence of delta ferrite. Fracture at 4K, SEM micrograph, 2000x. Reduced 55% for reproduction.

and solidification cracking resistance. Binkley et al[25] studied weldments made with 308 stainless steel electrodes with lime, lime-titania and titania based flux and found lime-covered electrode deposits to be weaker in creep rupture testing at 1200F than either lime-titania or titania covered electrode deposits. Daemen[20] and Zvanut and Farmer[23] have also been developing stainless steel electrode materials.

Many investigators[15,34,49,50,51,62,63,64] have performed research to determine ferrite levels needed to control hot cracking. It is well-known that hot cracking may be eliminated by residual ferrite contents as small as 2 to 3%.

Recent work has shown that hot cracking is not only a function of the residual ferrite content, but of the primary phase to solidify; if the primary phase is austenite, then fissuring occurs, but if the primary phase is ferrite, no cracks form. The explanation lies in the fact that sulfur and phosphorus are retained in the primary ferrite, thereby controlling liquation if ferrite forms first. But if austenite is the primary phase, then sulfur and phosphorus are left in the interdendritic liquid where liquation can occur. Thomas[4] explains the role of the primary dendritic phase by studying the liquidius diagram for the iron-chromium-nickel ternary system (Figure 5) and looking at a constant iron isopleth (Figure 6). From these diagrams, weldments can be classified as having primary ferritic or austenitic dendrites. This means that weld metals on the austenite side of the liquidus line are susceptable to hot cracking whereas weld metal on the ferrite side does not promote liquation along the dendrite boundaries.

Because of the importance of delta ferrite in weldments, a number of devices have been developed to measure residual ferrite content. These instruments - the Severn gauge, Magne-gauge, and Forrester ferrite content meters are all based on the same principle--the measurement of the magnitude

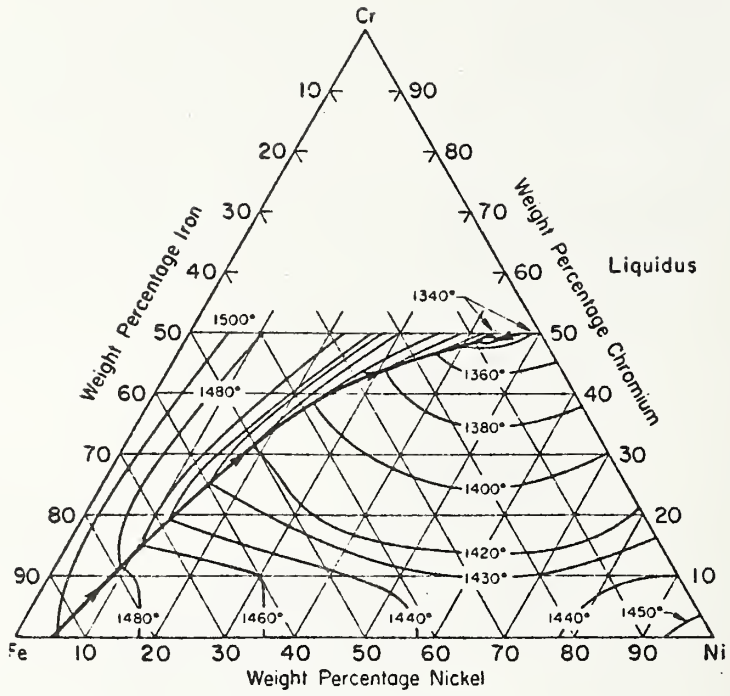

Figure 5: Iron-Chromium-Nickel ternary phase equilibra diagram.

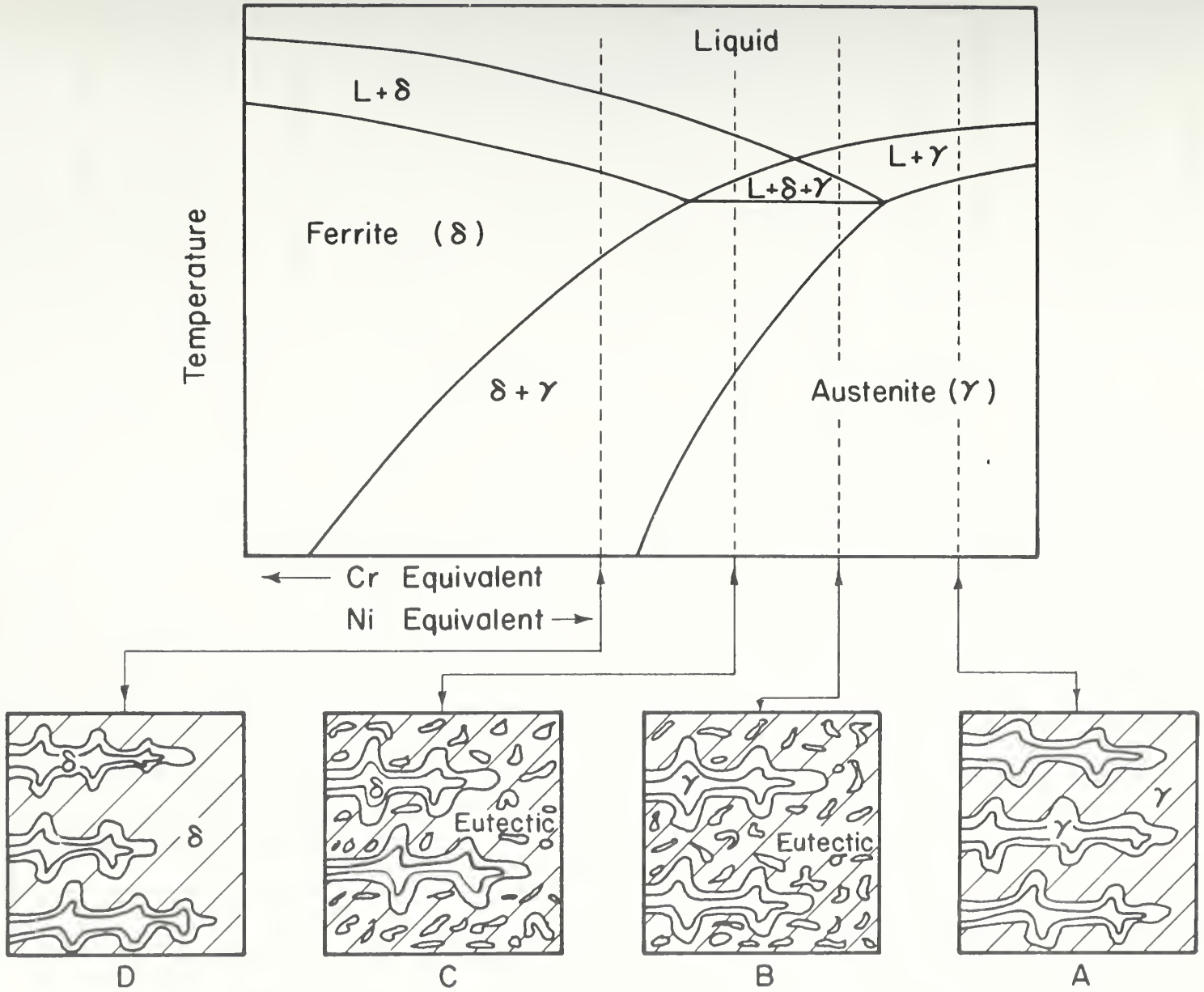

Figure 6. The four different solidification structures which occur at the indicated compositions. A constant percent iron is assumed and the structures are drawn at a temperature directly below their respective solidus, before appreciable transformation has taken place.

of magnetic attraction in the steel. This attraction is due to the ferromagnetic nature of the ferrite. These ferrite meters measure the volume percent ferrite in the steel. However, due to different calibration methods and interest differences associated with each type of meter, accurate ferrite readings have been difficult to obtain. To solve this problem, a standardized calibration technique has been agreed upon by the welding community[52]. The method agreed upon was to replace the percent ferrite with the ferrite number (FN), where the ferrite number is a magnetic response obtained from test blocks with various non-magnetic coating thicknesses produced by the National Bureau of Standards.

Goodwin et al[7] have shown that variation in ferrite distribution is related to weld heat input; this variation can cause difficulty with ferrite content measurement. Binkley et al[25] also have shown that even variation within AWS compositional specification limits produced significant variation in mechanical properties. Although the ferrite readings taken using the ferrite number give a more accurate means of comparing data, the problem still exists with reproducing a weld with the same ferrite level because the retained ferrite is not only a function of composition but also a function of the selection of the welding process and parameters[53-55].

Lindin et al[49] determined the minimum ferrite contents necessary for the elimination of fissures in several weld metals. They found that 316L stainless steel weld metal required a ferrite number (FN) of 1.5, while 316 stainless steel required an FN of 2.5. While it is known that at least 2% delta ferrite is necessary for elimination of microfissuring, there still is little information as to the mechanical behavior when the delta ferrite content is above 10%. Above 10% ferrite, the delta ferrite may be continuous in the solidification direction. These weldments with

the continuous delta ferrite phase will most likely pass through the ductile-brittle transition on cooling and have very limited mechanical properties.

The purpose of this investigation was to assist in the characterization of the microstructure of a set of stainless steel weldments which have been extensively mechanically tested for cryogenic service. Each weldment has experienced either a different filler metal or welding procedure.

Experimental Procedure

Materials and Test Matrix

The weldments were prepared using a one inch, 316L stainless steel plate; all welds were multipass, covered electrode butt welds. Five electrodes were used. Each was designed to give a different ferrite level in the weldment. The compositions of the electrodes and base metal are listed in Table I. The experimental test matrix is separated into two sets of five weldments, the first five weldments being welded with constant welding parameters but using each of the five separate electrodes; the second set of five weldments was welded with select electrodes varying the welding parameters to produce weldments with differing energy inputs. The welding parameters for all ten weldments are listed on Table II.

Weldment Preparation

In order to determine information about the welds before they were sectioned, a nitric-sulfuric acid macro etch was prepared and the as received weldments were placed in the boiling etch. The weldments were observed periodically over a 72 hr. exposure to the etch. This preliminary procedure gave little microstructural information, but was of assistance in the determination of proper sectioning. The weldments were then sectioned, ground, and polished. To bring out the microstructure a 10% oxalic acid

TABLE I

Weld Metal Composition

Electrode	Composition %										Nickel[+] Equivalent	Chromium[+] Equivalent	Ferrite	
	C	Ni	N	Mn	Cr	Mo	Si	Cb	S	P	Ni_{eq}	Cr_{eq}	%[++]	Fn[++]
1	.031	13.97	0.42	1.72	18.47	2.25	.58	.14	.011	.033	17.02	21.66	.13	.12
2	0.30	12.97	.046	1.72	18.64	2.29	.58	.14	.012	0.34	16.11	21.84	4.1	4.5
3	.034	12.01	.042	1.70	19.20	2.32	.57	.15	.009	.034	15.14	22.45	8.5	9.2
4	.028	11.06	.067	1.76	19.66	2.18	.59	.15	.008	.029	14.79	22.80	10.1	11.0
5	.059	12.85	.044	1.75	18.69	2.25	.56	.15	.009	.033	16.82	21.86	1.2	1.3
316L Base Plate	.018	12.84	.027	1.71	18.54	3.00	.27	---	----	----	14.55	21.95	0	0

[+]Using DeLong equation (Reference 9)

[++]Magna-gage measurements

TABLE II

Welding Parameters

Weldment		Ferrite			Welding Parameters				
Plate Number	Electrode Number	% + Avg	Fn + Avg	Current (Amps)	Volts	Speed (in/min)	Weld Temp °F	# of Passes	Heat Input (kj/in)
T12005R	1	0.13	0.12	130	24	6-8	225	31	26.7
T12006R	2	4.1	4.5	130	24	6-8	225	25	26.7
T12007R	3	8.5	9.2	130	24	6-8	225	29	26.7
T12008R	4	10.1	11.0	130	24	6-8	225	33	26.7
T12009R	5	1.2	1.3	130	24	6-8	225	33	26.7
T12007 R-II	3	6.5	7.1	100	24	8-10	225	39	16.0
T12007 R-III	3	9.7	10.5	160	24	4-6	225	26	46.1
T12007 R-IV	3	7.3	7.9	160	26	4-6	600	17	49.9
T12005 R-IV	1	.67	.73	160	26	4-6	600	22	49.9
T12009 R-IV	5	2.2	2.4	160	26	4-6	600	23	49.9
316L	-	0	0	---	--	----	---	--	----

+ Magna-gage measurements

electroetch was used operating at a current of 2 amp. for 30 secs. This etch worked extremely well in delineating the fusion zone between individual weld beads, as well as the solidification structure. The oxalic acid etch was used throughout the remainder of the experiment because of its etching ability and because of the control of the etching parameters. Metallographic procedures for stainless steel weldments are given by White and LeMay[56].

Macro and Microstructure

After the welds had been sectioned, polished and etched, a macro photograph was taken of each weld at a 1.5x magnification. To compare the microstructure of each weldment a series of ten photomicrographs was taken across the weld bead at 100x magnification. The welds were then examined from a direction looking down on the top of the weld bead by sectioning along the weldment. This section was then mounted in bakelite, polished, and etched in oxalic acid. A light oxalic acid etch (.5 amp/cm^2 for 20 sec.) was used in order to bring out the microstructure of the delta ferrite. The Forrester ferrite content meter was used on each weldment to measure the percent of delta ferrite. This instrument allows measurement of the ferrite in each bead of the weldment. It was found that weld beads which had melted the parent metal were usually lower in ferrite content than beads in the interior of the weldment. The averaged measured values agreed well with the Magne-gauge measured values given in Table I. The microstructure was thoroughly characterized using both optical and scanning electron microscopy.

Two ASTM corrosion tests were performed on the weldments to bring out better microstructural characterization of these weldments; the Streicher oxalic acid test and the Huey nitric acid test. The Streicher test was

performed on the polished sample, which included the entire fusion zone, heat affected zone and base metal. The electroetching was performed in an electropolisher with a constant size etching aperture; the current density was 1 amp. per sq. cm. of aperture. The Huey test was performed on two identical sets of samples, corroded in separate vessels so that a means existed to verify the data taken from each vessel. The two samples were prepared by sectioning them out of the center of the fusion zone using an abrasive cutoff wheel. The samples were then boiled in a 65 weight percent nitric acid solution for five consecutive periods of 48 hours each. At the end of each time period the samples were removed, cleaned, dried and accurately weighed to determine the weight loss.

Results and Discussion

Macrostructure

In the polished and etched weldments, the individual beads are readily distinguishable in the fusion zone as shown in a representative macrograph of one of the weldments (Figure 7). In this macrograph, epitaxial growth is apparent, and the grains seem to grow in a preferred orientation which is perpendicular to the fusion front. It is also apparent that the grains not only grow in a preferred orientation, but they also grow in a sequential manner from bead to bead, thus giving the weldment the appearance of having large columnar grains growing in from the base metal towards the top center of the fusion zone. It is expected that such an orientation of the solidification structure will strongly affect mechanical properties. This suggests that special orientation is necessary for the extraction of mechanical specimens.

Figure 7. Macro Photograph. 1.5x mag. 07-IV Rod 3. Showing individual beads in the fusion zone and epitaxial growth in a large columnar type structure.

Microstructure

A series of microphotographs was taken across each of the etched weldments to compare the microstructures; a representative micrograph is shown in Figure 8. Several observations can be made by comparing these photomicrographs. There is an apparent decrease in dendrite arm spacing with increasing ferrite content. This decrease in dendrite arm spacing can be attributed to a large number of ferritic dendrites at high ferrite compositions which have nucleated and grown. This reduction in dendrite arm spacing has little or no effect on the sequential grain growth from bead to bead, as was found by comparing the microstructure of the high and low percent ferrite weldments. Such sequential growth suggests a weakness in the weld by allowing crack propagation across individual beads. Another observation was the large variation in the nature of the microstructure at different positions across the weldment.

Delta Ferrite

In an attempt to determine the solidification nature of the ferrite the original weld samples were sectioned in a direction perpendicular to the top plane of the weld bead and etched to show the ferritic structure. The micrographs of Figure 9 illustrate the appearance of the ferrite structure at three levels of ferrite content. Notice the increasing continuous ferrite network with increasing ferrite content. Figure 9C contains 4.1% ferrite (4.5 FN) and can be considered only semicontinuous when compared with the structures of Figure 10 which range from 6.5% (7.1 FN) to 9.7% (10.5 FN) ferrite, all containing a nearly continuous ferrite network.

Figure 9A provides an insight into the nature of the solidification mechanism of the stainless weld metal. In this picture the dark areas are retained ferrite. Surrounding the ferrite is a light gray phase which is

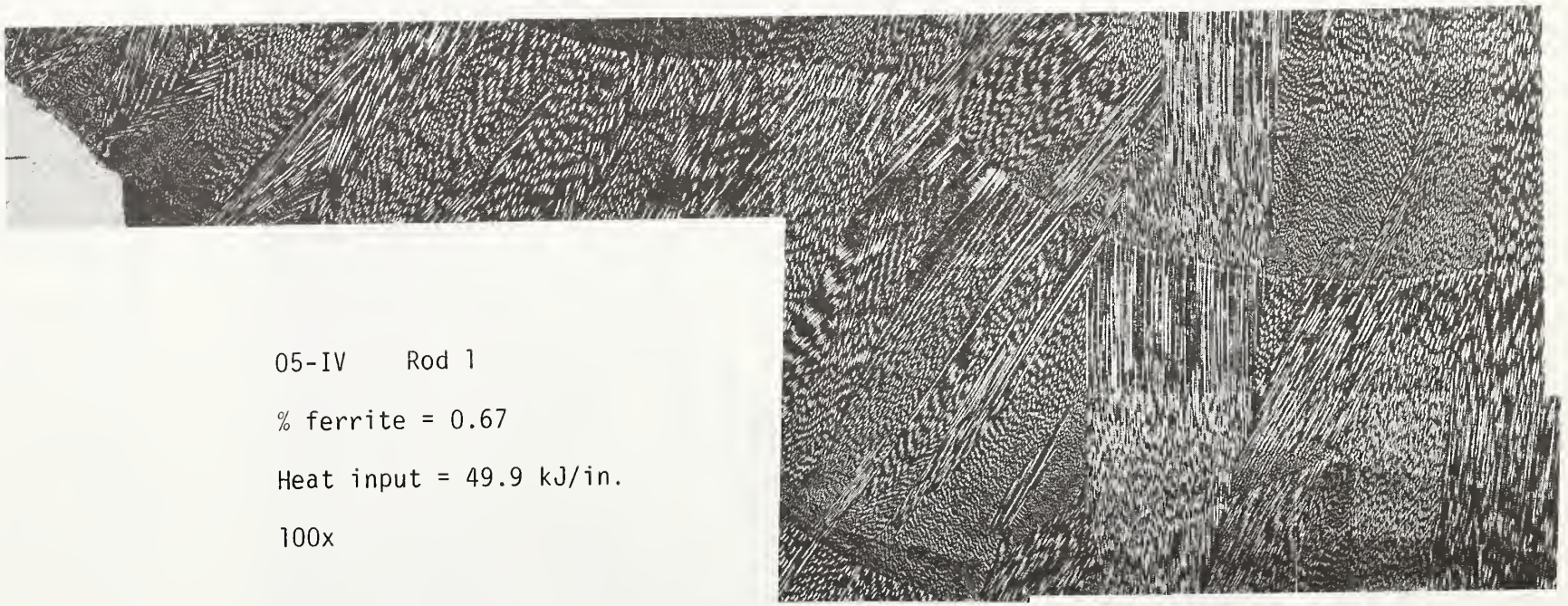

Figure 8. Sequential grain growth from bead to bead in the weldment.

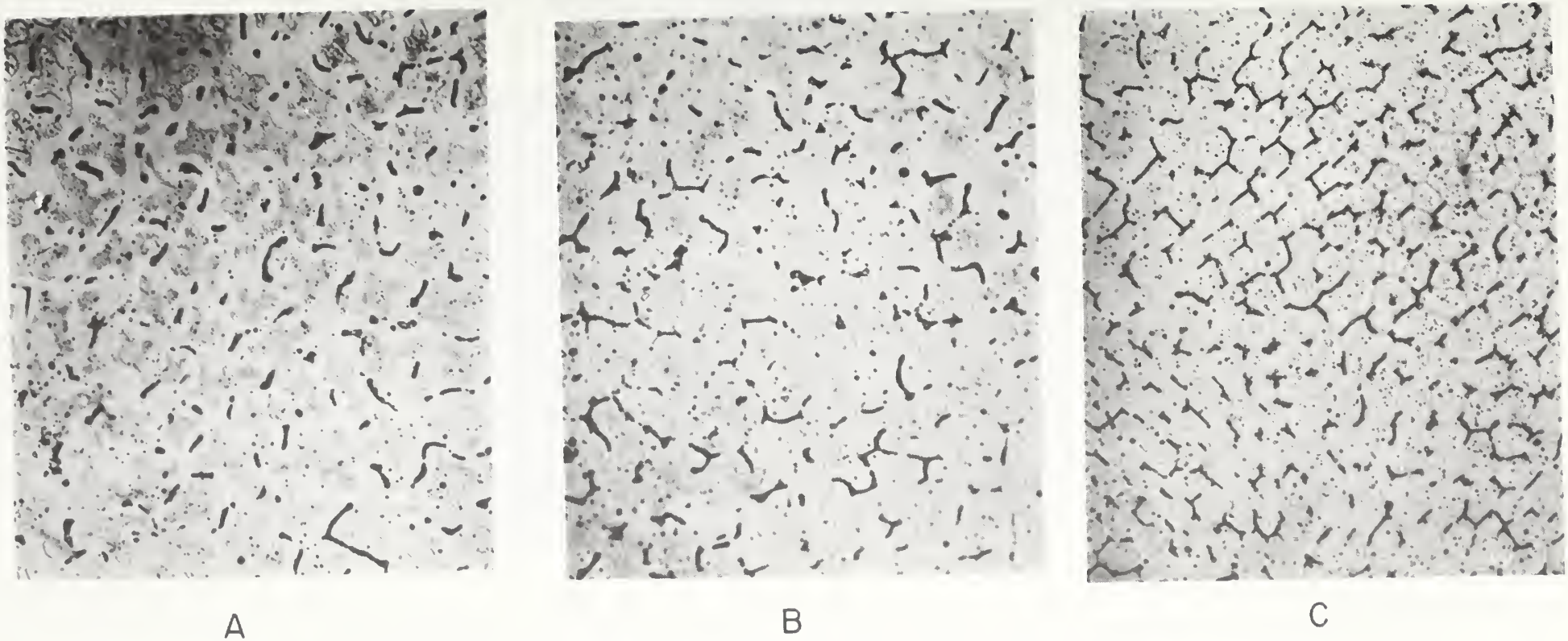

Figure 9. Photomicrographs showing the formation of a continuous network of δ-ferrite with increasing ferrite content, 500x, oxalic acid electroetch.

a) 09-IV Rod 5 0.67% ferrite

b) 05-Iv Rod 1 2.2 % ferrite

c) 02-I Rod 6 4.1 % ferrite

the austenite that transformed from the original primary ferrite as the stainless steel cooled below the solidus temperature. The remaining dark gray area is the austenite resulting from the transformation in ferritic-austenitic eutectic structure which solidified directly from the molten steel. This solidification pattern shown in Figure 9A is predicted from the isopleth of the iron-chromium-nickel ternary phase equilibrium of Figure 5.

Figure 10 shows micrographs of weldments made using the same electrode, but welded with varying welding parameters. The microstructure which results from increasing the energy (heat) input into the weld is illustrated in Figure 10A to Figure 10D as indicated. The ferrite content varies from 6.5% (7.1 FN) to 9.7% (10.5 FN), but was not found directly related to heat input suggesting that the variation in ferrite is due to variations in the specific welding parameters and conditions rather than the calculated energy input. What is to be noticed from these micrographs is the increasingly continuous ferrite network with increasing energy input. Since ferrite may become brittle at low temperatures or will transform to the more brittle sigma phase at high temperatures, a less continuous ferrite network is desirable. This would suggest that a lower energy input would be advantageous. Another observation from this series of micrographs is that a general increase in dendritic ferrite spacing occurs as heat input is increased, effectively increasing the grain size of the weldment. This increase in grain size is not advantageous either, since it results in a somewhat weaker weld. This trend also supports the use of a lower heat input.

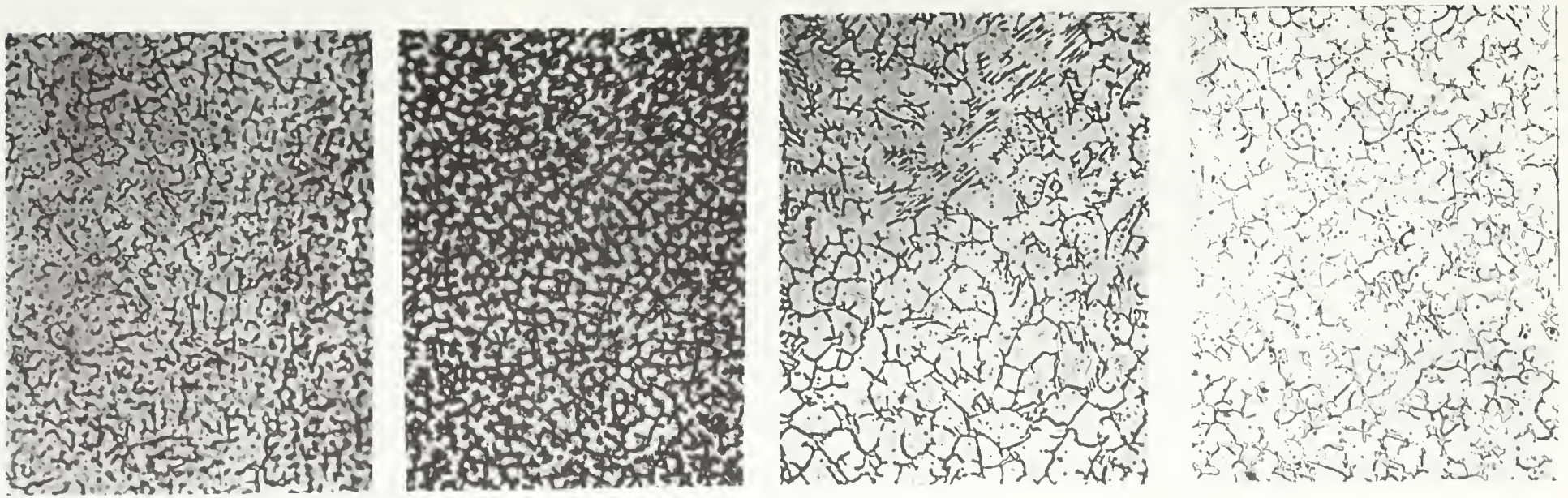

Figure 10. Photomicrographs showing the growth of ferrite into a continuous network having a larger interdendritic spacing with increasing heat input.

a) 7-II Rod 3 16.0 KJ/in.

b) 7-I Rod 3 26.7 KJ/in.

c) 7-III Rod 3 46.1 KJ/in.

d) 7-IV Rod 3 49.9 KJ/in.

Streicher Corrosion Test

The Streicher (oxalic acid) test was performed as a preliminary corrosion test to the more quantitative Huey test. Three representative micrographs of the Streicher test results are shown in Figure 11. Figure 11A shows the step structure which is characteristic of the 316L austenitic stainless steel base metal. The base metal is the only sample which formally passed the Streicher test. Figure 11B shows a ditched structure partially surrounding the primarily dendritic microstructure of this weld. This micrograph also shows the large variation in dendrite widths which can occur from bead to bead in the weldments. Figure 10C shows a heavily ditched structure surrounding the cellular microstructure occurring in this weldment. This series of micrographs also shows the tremendous variation in microstructure that occurs in the same weldment. It is apparent that the Streicher test, being a test to determine the susceptability of stainless steel to sensitization (and thus to intergranular corrosion) cannot be applied to weldments containing ferrite. Because of the severity of the etch, it is difficult to determine whether the attack is associated with a chromium depleted region adjacent to the grain boundaries or confined to the ferrite phase itself.

Huey Corrosion Test

The Huey test determines the corrosion rate as a function of time. The weight loss data was converted to weight loss per surface area of the sample, and is plotted as weight loss vs. time^2 for all weldments and base metal on Figure 12 and 13. The t^2 time dependence was found to give the overall rate law and suggests an accelerated corrosion behavior in the weldments.

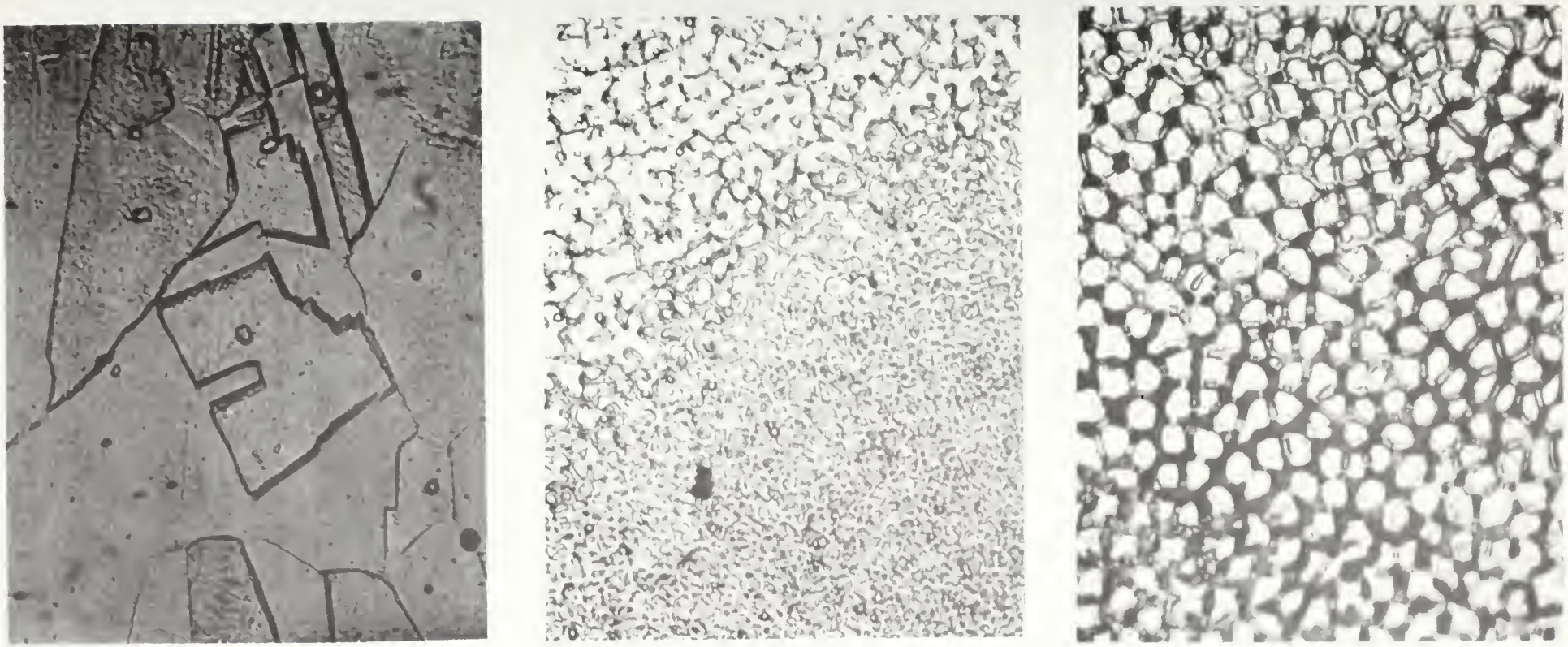

A B C

Figure 11. Results of the Streicher test, 570x.

a) base metal - step structure

b) 05-I Rod 1 - ditched structure and variation of grain size from bead to bead

c) 07-I Rod 3 - heavily ditched cellular structure

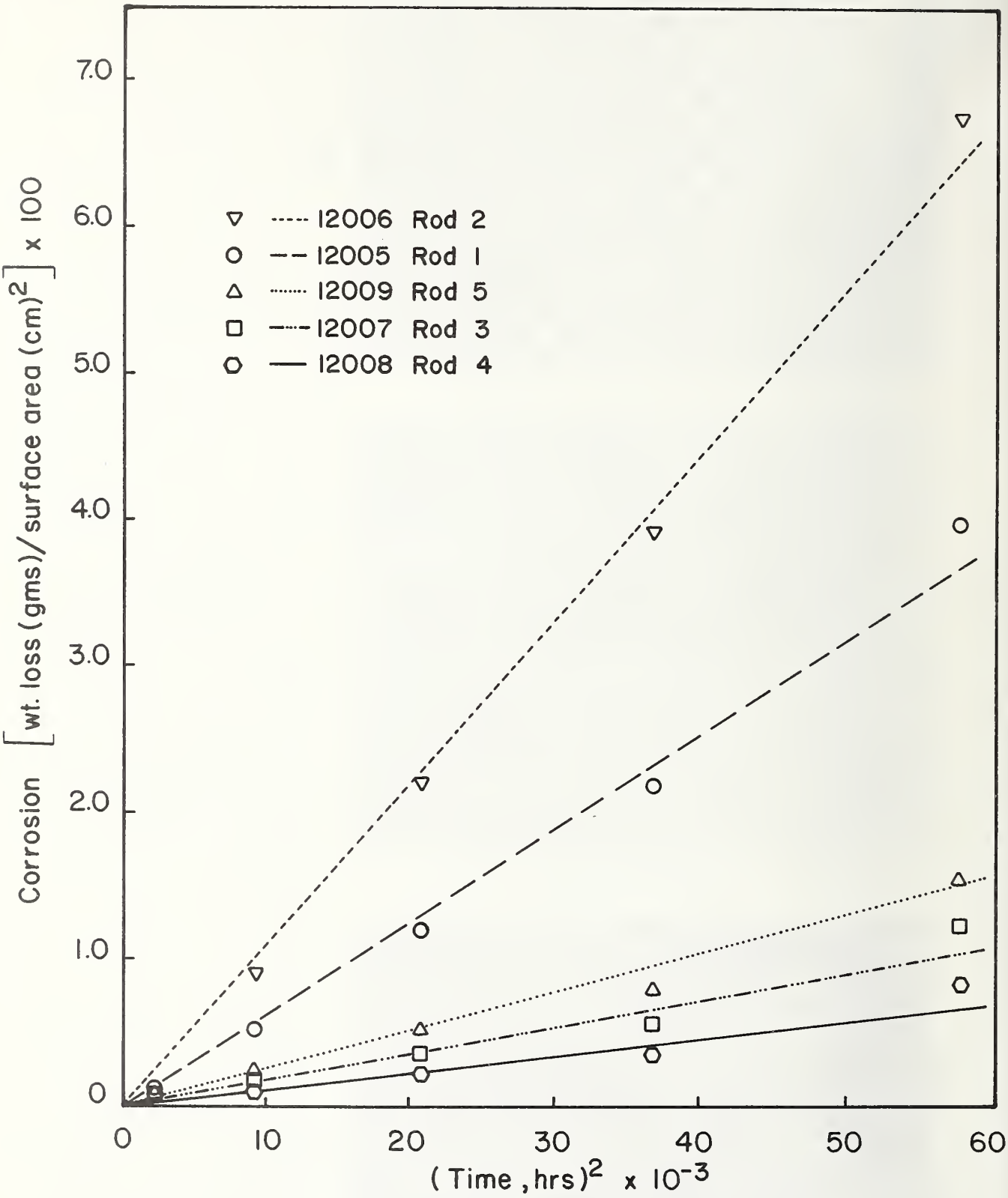

Figure 12. Corrosion rate versus time^2 for the Huey test data taken on five weldments, welded at a constant energy input but with different electrodes.

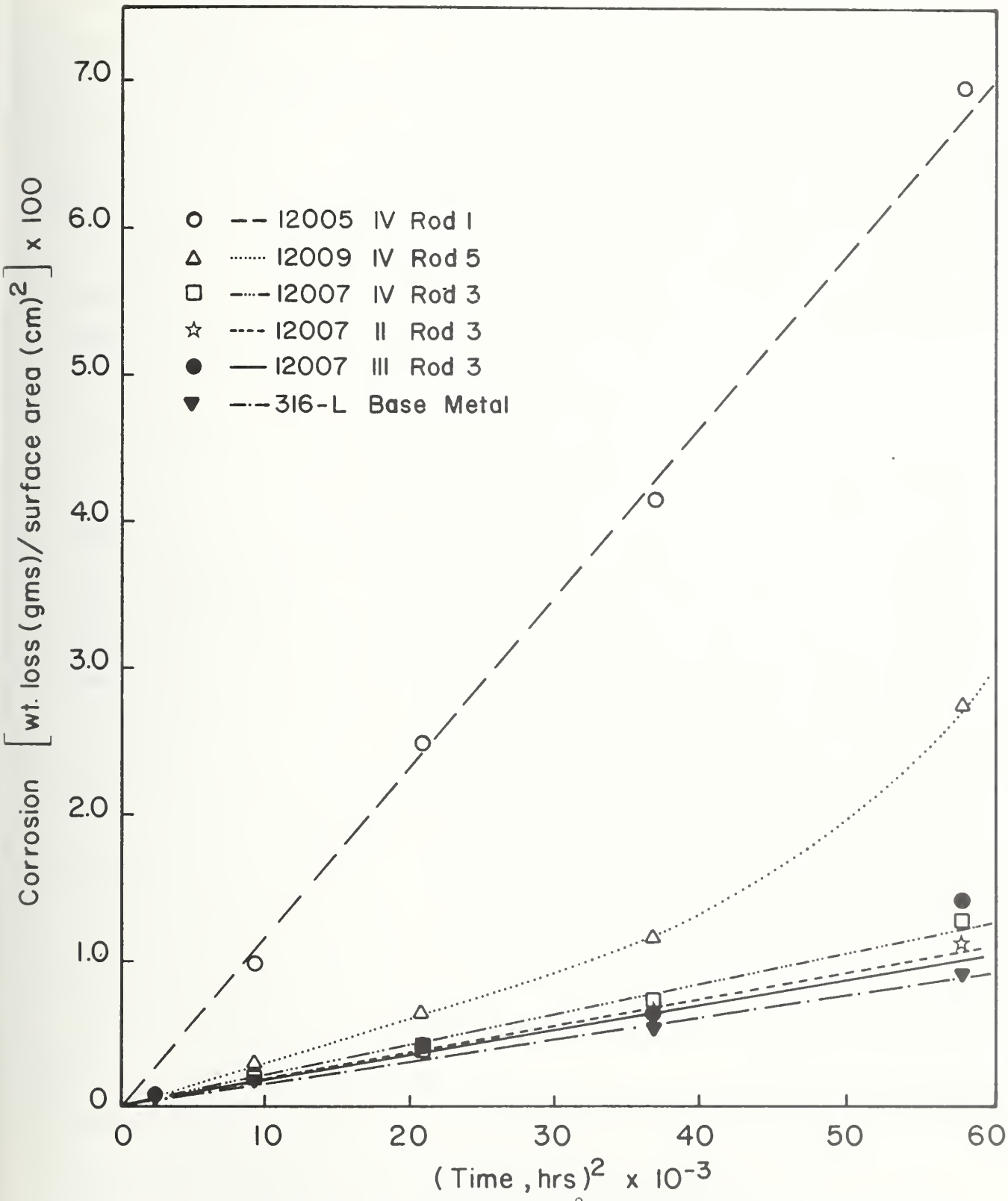

Figure 13. Corrosion rate versus Time^2 for the Huey test data taken on five weldments, welded with select electrodes and different energy inputs. The 316-L base metal is also included on this graph.

A general relationship between corrosion behavior and weldment ferrite content can be seen in Figure 14 for the 240 hr. corrosion weight loss data plotted as a function of % ferrite. The rate of corrosion rapidly increases with % ferrite up to a ferrite value of 6%, but then drops off to a relatively constant rate independent of ferrite and comparable in corrosion rate to the base metal itself. Since this data was taken from welds with various welding parameters, a more representative plot of the data is shown on Figure 15 which shows the 240 hr. corrosion vs. % ferrite for the first five weldments, welded with the same energy inputs. This figure also illustrates the same type of behavior.

To explain this corrosion behavior, the diagram shown in Figure 4 is applied. Weight loss vs. chromium and nickel equivalent is plotted in Figure 16 for the five different electrodes. A bar graph is also included on Figure 17 showing the weight loss in 240 hours for each electrode. The two points with low corrosion on the high chromium side of the dashed line are from the high ferrite weldments while the other three points represent the low ferrite containing weldments. Figure 16 shows that the corrosion behavior changes drastically as the weldment composition crosses the liquidus line. Thus the corrosion behavior is dependent on whether ferrite or austenite is the proeutectic dendritic phase. Two forms of corrosion may be responsible for the corrosion behavior of the stainless steel weldments: intergranular corrosion and galvanic corrosion. Intergranular corrosion may occur as the result of the formation of grain boundary or interdendritic carbides which deplete the adjacent matrix of chromium. The chromium carbides first form along the ferrite-austenite boundaries, then around the austenite grain boundaries. Referring to Figure 6, which shows schematically the predicted microstructure for four specific electrode compositions, a material with composition 'A' would solidify having only austenite grain boundaries

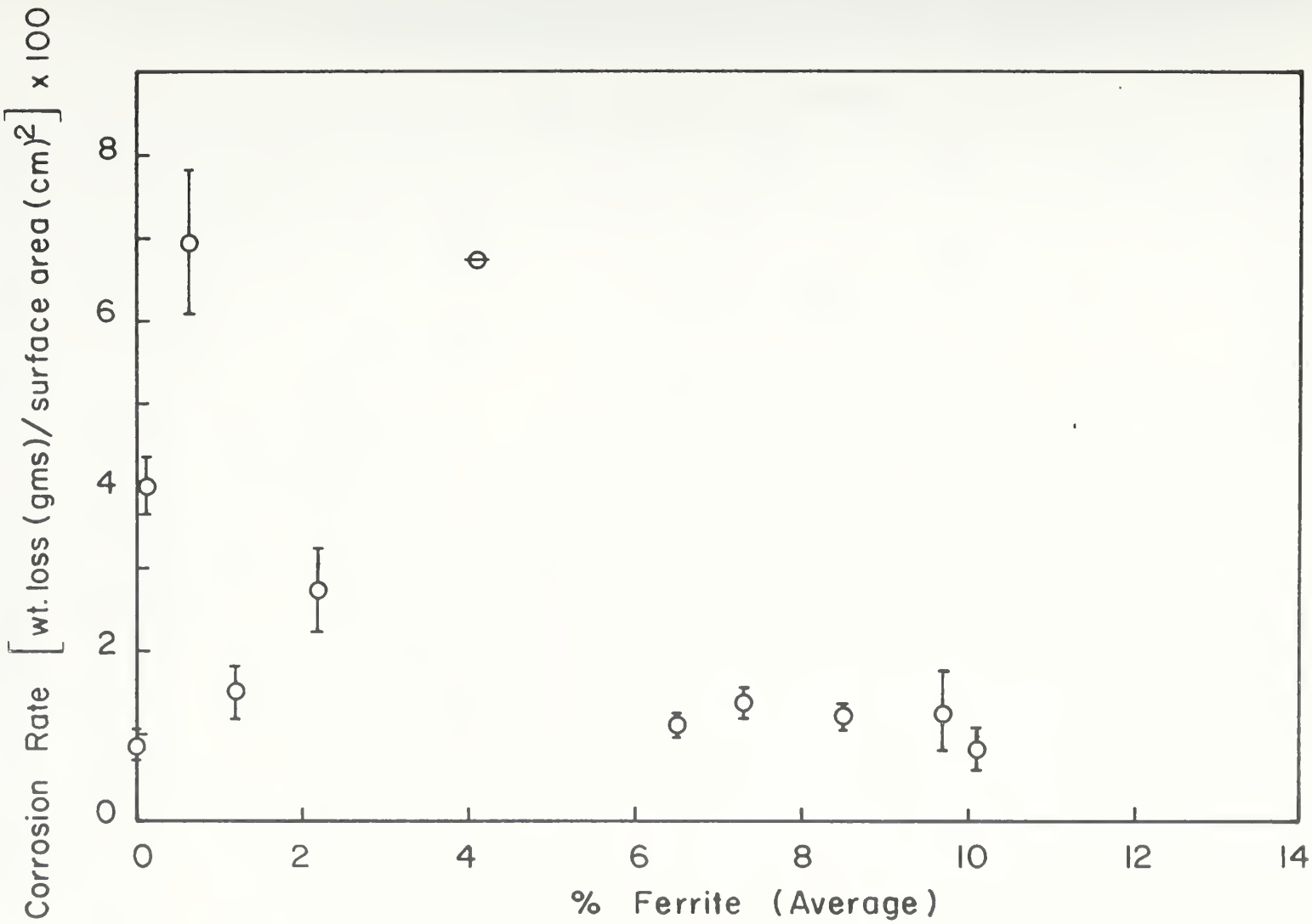

Figure 14. Corrosion rate and 316-L base metal vs. % Ferrite for all ten weldments.

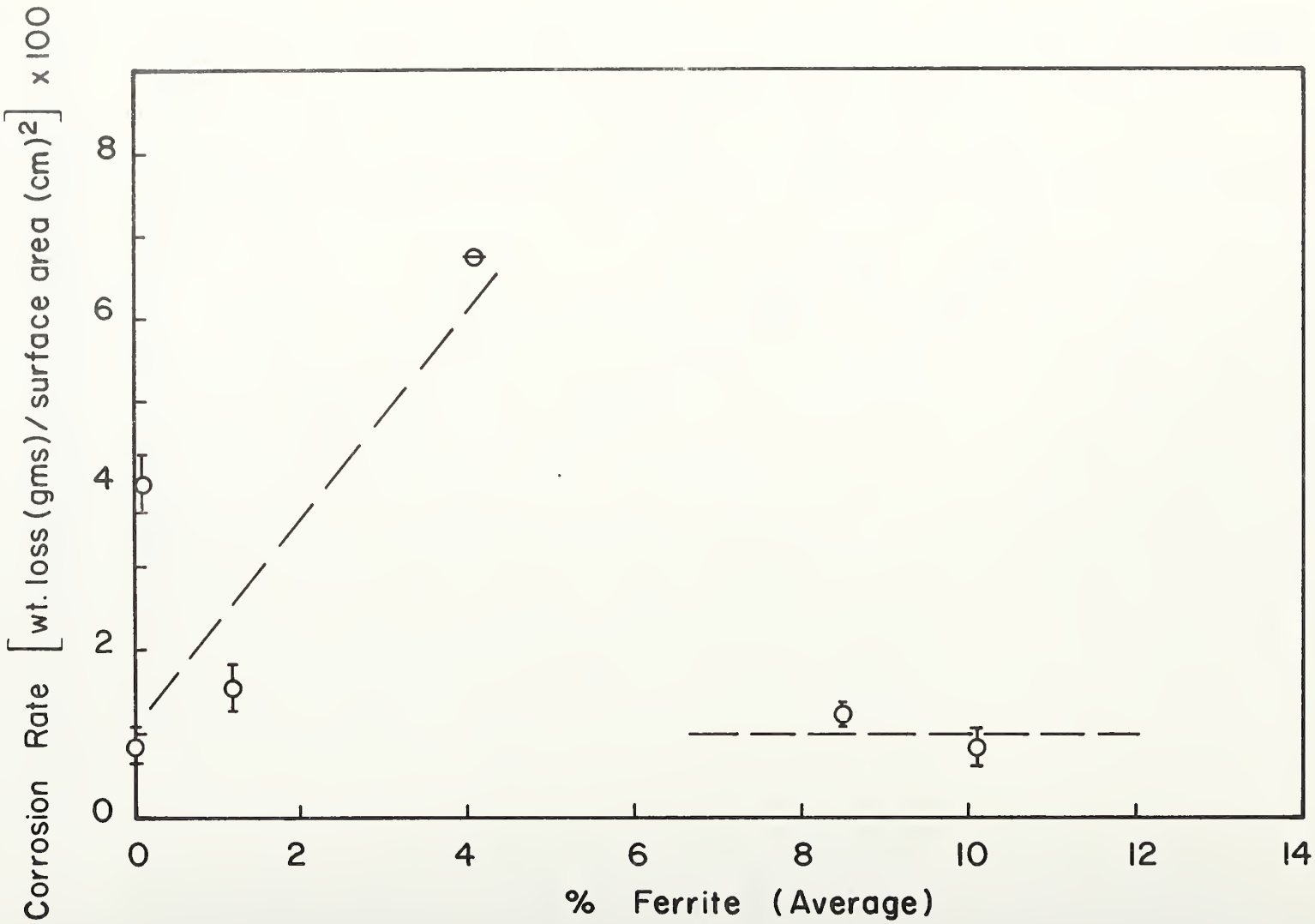

Figure 15. Corrosion rate vs. % Ferrite for the first five weldments, welded with a constant energy input.

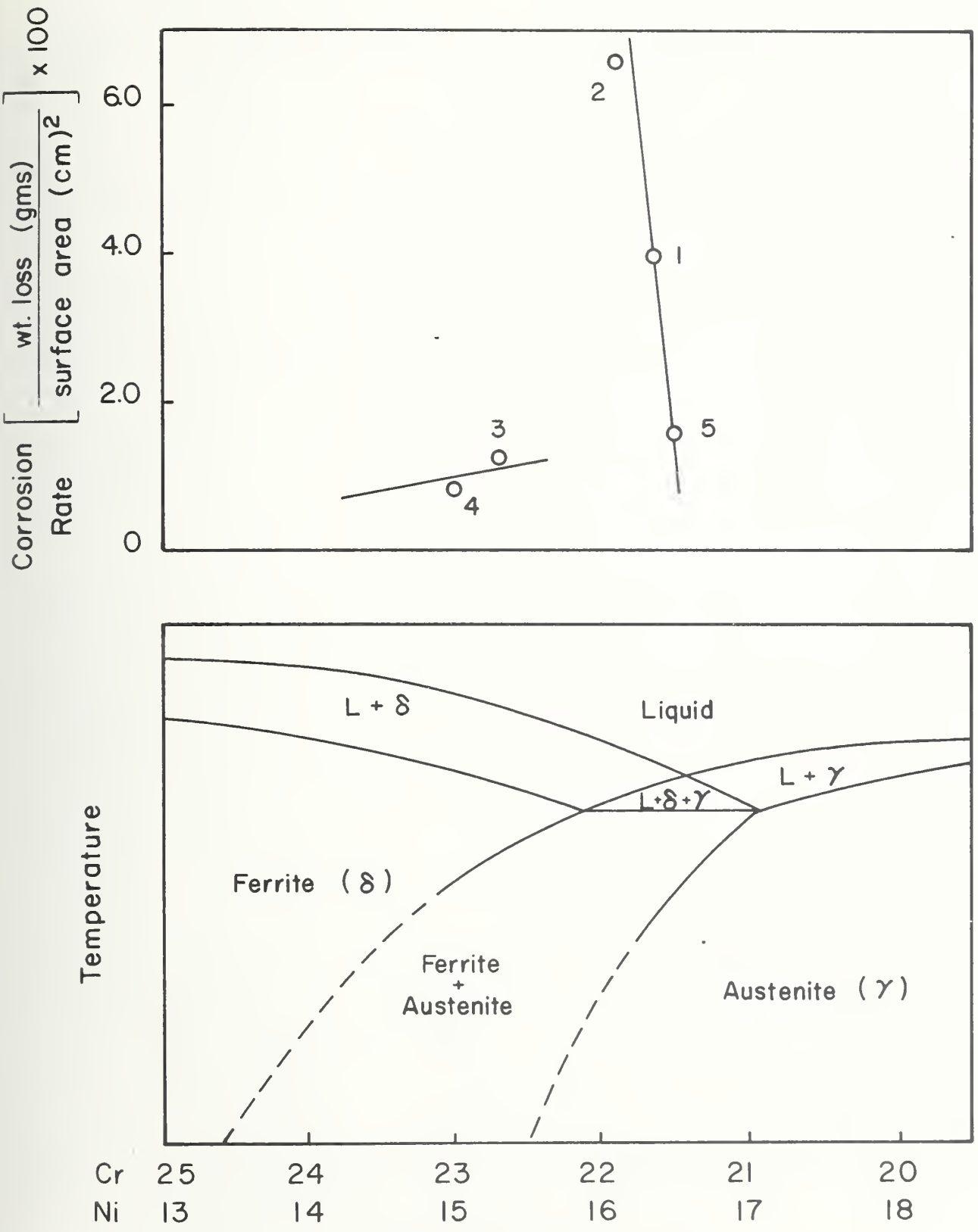

Figure 16. Fe-Cr-Ni ternary phase diagram, above which is plotted the corrosion rate of the first five weldments, welded at a constant energy input.

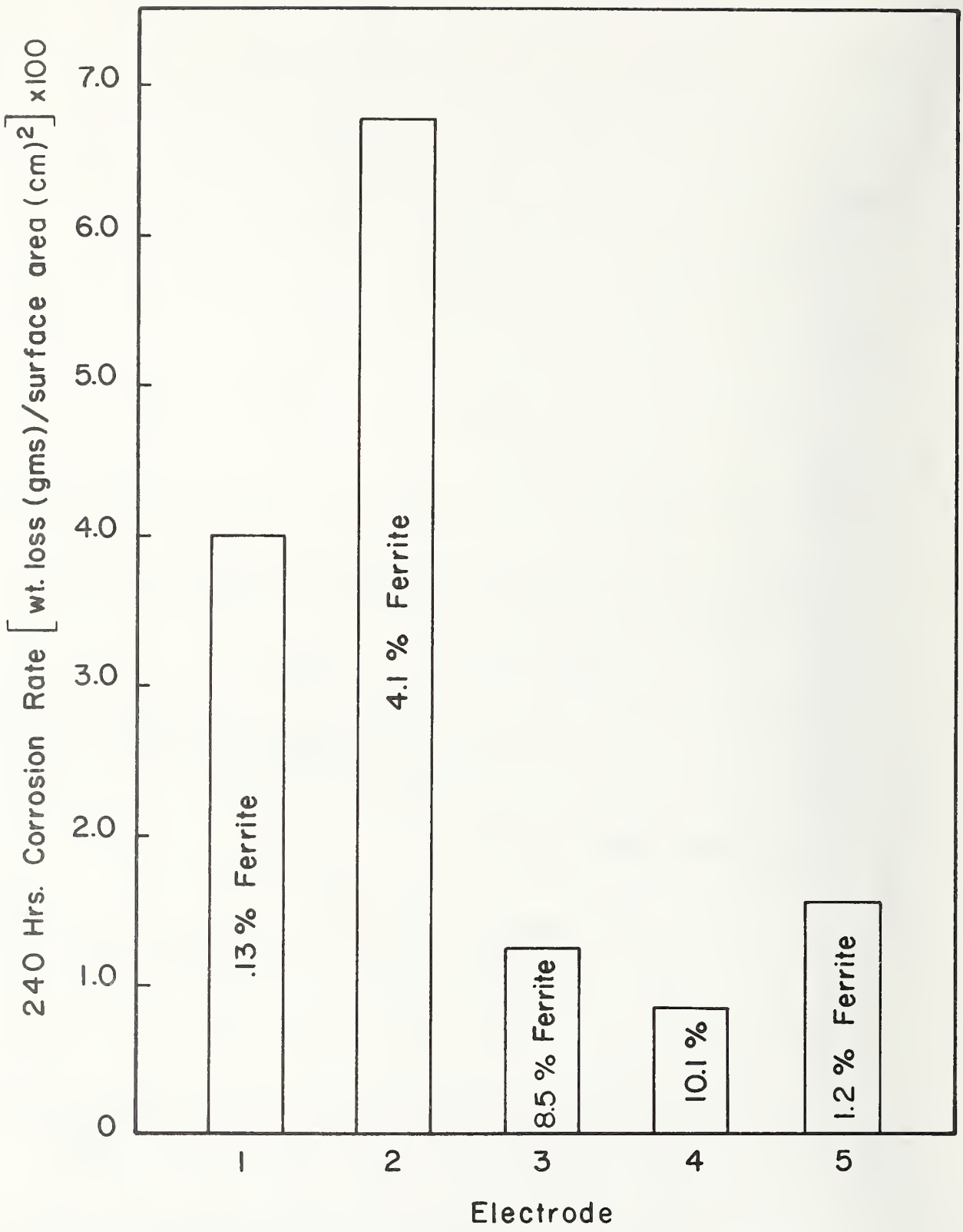

Figure 17. Bar graph showing the relative corrosion rates of the five separate electrodes. Each electrode producing the indicated amount of residual ferrite.

available for carbide precipitation; for a composition 'B' which passes through the eutectic portion of the diagram, finely distributed ferrite exists scattered throughout the matrix, producing a large area for carbide precipitation; for composition 'C', ferrite is the primary phase to solidify giving additional area for carbide precipitation; and finally for composition 'D' there will exist only a small amount of austenite-ferrite grain boundary surface area, since the structure solidifies entirely as ferrite. Thus assuming that only intergranular corrosion is responsible for the corrosion behavior, the corrosion rate would increase from composition 'A' to 'B' to 'C' but then drop off for composition 'D', explaining the corrosion behavior of the weldments welded with the five separate electrodes as shown in Figure 16.

An alternate model can be suggested to explain the corrosion behavior based on the use of the DeLong diagram shown in Figure 2. The line plotted on the diagram represents the liquidus line of the portion of the phase diagram of interest, Fe-Cr-Ni. On one side of the line, austenite is the primary phase to solidify while on the other side, ferrite is the primary phase to solidify. This line passes through a rectangular region outlining the composition limits of 316 stainless steel. The five points plotted on this diagram represent the compositions of the five electrodes used in this study. Notice that the electrodes with high corrosion rates, electrodes 1,2, and 5 lie on the austenite side of the liquidus line while the electrodes with the low corrosion rates, electrodes 3 and 4 lie on the ferrite side of the line. Thus suggesting that liquating elements, sulfur, phosphorus, etc., play a role in the behavior as they do with the hot cracking behavior. Hot cracking is more probable when austenite is the primary phase to solidify.

The second form of corrosion to consider, galvanic corrosion, may occur when a potential difference exists between two dissimilar alloys or phases. This potential difference causes electron flow between the two phases.

Usually the more corrosion resistant (more noble) material is protected at the expense of the less corrosion resistant, more active material. The stainless steel of Figure 5a has almost no ferrite; there would be little galvanic corrosion. The steel of Figure 5b has a higher ferrite content spread out in the eutectic structure and being distributed as it is, the ferrite is high in area and in close contact with the austenite, providing a means for galvanic corrosion. Figure 5c has a higher cathode to anode area ratio providing an even more accelerated attack. The sample in Figure 5d has a high ferrite content, but the ferrite is not distributed as well as in the other microstructures, thus reducing the galvanic corrosive effect. In summary, corrosion explanations could be used to explain the increase in corrosion rate with increasing chromium equivalent (ferrite content) up to a ferrite content of 5 to 6% and then the corrosion rates drop off for higher ferrite levels as experimentally determined in the Huey test.

A series of micrographs taken on a scanning electron microscope is shown in Figure 18 showing the corrosion behavior as a function of residual ferrite content. Figure 18a clearly indicates the intergranular corrosion of the ferrite-free base metal. The weldment of Figure 18b contains 2.2% ferrite (2.4 FN) and has a composition just on the high chromium side of the apex of the three phase region. The weld shown in Figure 18c has 4.1% ferrite (4.5FN) and has a composition at the high chromium end of the three phase region. Notice the massive attack in some regions of the sample. The structure of Figure 18d contains 101% ferrite (11.0 FN) and has a composition such that ferrite is the only phase to solidify. This structure then, has a low corrosion rate.

Figure 19 is a series of SEM micrographs showing the effects of energy input on the weldment microstructure. These four weldments were all made using electrode number 3; the energy input increases from Figure 19a to Figure 19d. All of these welds have a high ferrite content which solidified

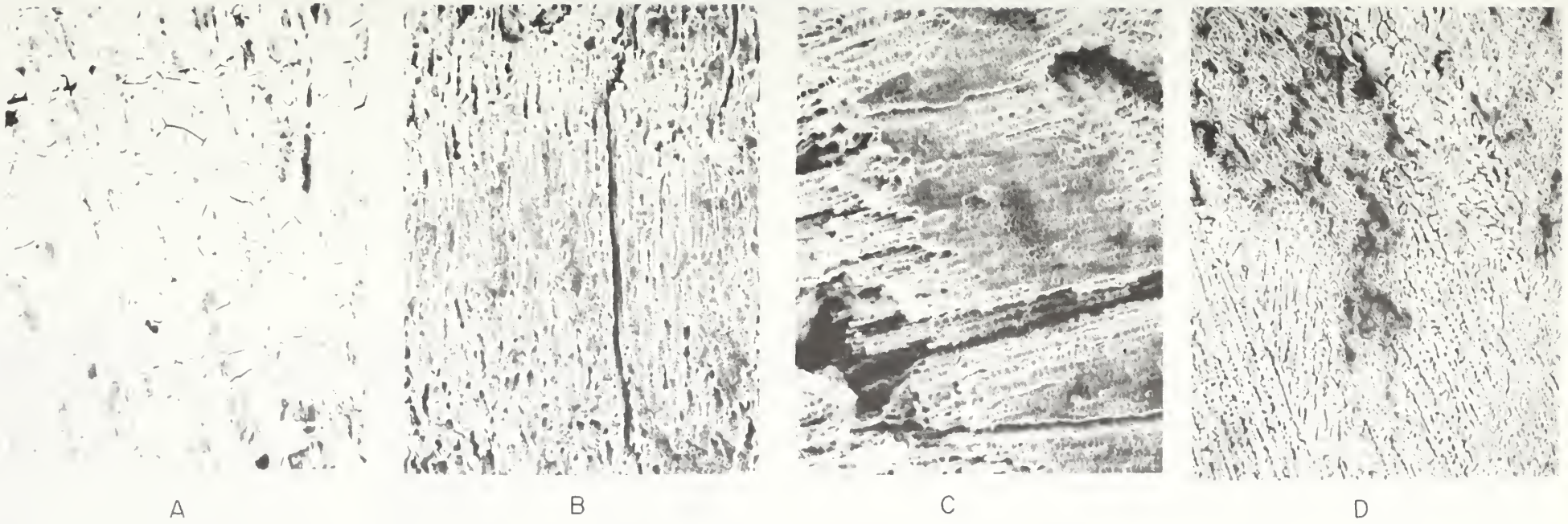

Figure 18. Photomicrographs of Huey corrosion samples A) 200x, B,C and D) 500x. Taken on SEM, showing various corrosion attacks.

A)	Base metal	0% ferrite
B)	09-IV Rod 5	2.2% ferrite
C)	06-I Rod 2	4.1% ferrite
D)	08-I Rod 4	10.1% ferrite

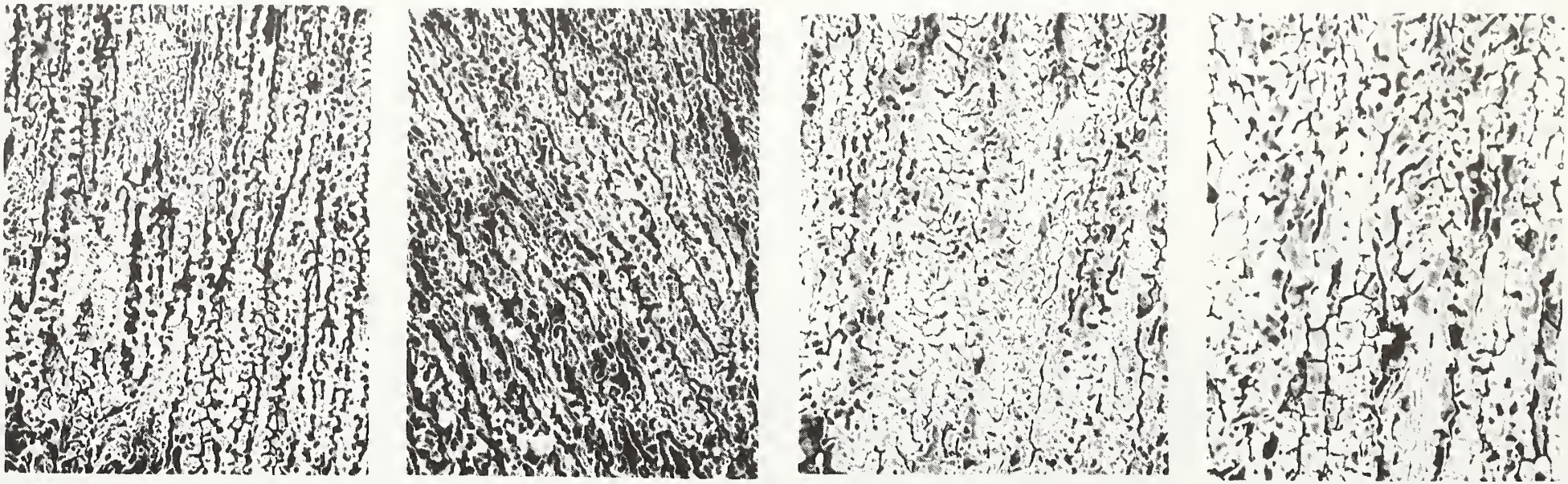

Figure 19. Photomicrographs of Huey corrosion samples taken on the SEM @ 500x mag. Showing the increasing dendritic size with increasing heat input.

a) 7-II Rod 3 16.0 KJ/in.

b) 7-I Rod 3 26.7 KJ/in.

c) 7-III Rod 3 46.1 KJ/in.

d) 7-IV Rod 3 49.9 KJ/in. with large preheat

as high chromium-containing dendrites, leaving a chromium-depleted inter-dendritic liquid to solidify last. Notice how this chromium-depleted phase, last to solidify, is selectively corroded leaving the dendritic solidification pattern.

An important observation from these micrographs is that dendrite size is sensitive to weld heat input, dendrite size increasing at higher energy inputs.

REFERENCES

1. C. D. Lundin and D. F. Spond, "The Nature and Morphology of Fissures in Austenitic Stainless Steel Weld Metals," Welding Journal 55, 356S (1976).

2. S. B. Melkumov, "Influence of Specific Heat Input on the Corrosion Resistance of the Metal of the Heat Affected Zone if Ferritic-Austenitic Stainless Steel," Svar. Proiz, No. 4, 25 (1976).

3. K. E. Pinnow and A. Moskowitz, "Corrosion Resistance of Stainless Steel Weldments," Welding Journal, 49, 278S (1970).

4. R. David Thomas, Jr., "Ferrite in Austenitic Stainless Weld Metal," Arcos Corporation report - March 3, 1978.

5. W. T. DeLong, G. A. Ostrom, and E. R. Szamachowski, "Measurement and Calculation of Ferrite in Stainless Steel Weld Metal," Welding Journal, 35, 521S (1956).

6. C. J. Long and W. T. DeLong, "The Ferrite Content of Austenitic Stainless Steel Weld Metal," Welding Journal, 52, 281S (1973).

7. G. M. Goodwin, N. C. Cole, and G. M. Slaughter, "A Study of Ferrite Morphology in Austenitic Stainless Steel Weldments," Welding Journal, 51 (1972).

8. A. L. Schaeffler, "Constitution Diagram for Stainless Steel Weld Metal," Metal Progress, 56, 680 (1949).

9. W. DeLong, G. Ostrom, and E. Szumachowski, "Measurement and Calculation of Ferrite in Stainless Steel Weld Metal," Welding Journal, 35, 526S (1956).

10. F. C. Hull, "Delta Ferrite and Martensite Formation in Stainless Steel," Welding Journal, 52, 193S (1973).

11. R. Castro and J. J. De Cadenet, "Welding Metallurgy of Stainless and Heat-Resisting Steels," Cambridge University Press, London (1975).

12. D. Seferain, "Metallurge de la Foudure," Dunod, Paris (1959).

13. V. N. Zemzin and G. L. Petrov, "Influence of Ferrite Content on the Properties of Austenitic Weld Metal," Svar. Proiz., __, No. 5,6 (1967).

14. H. C. Campbell, "The Ferrite Problem," Welding Journal, 54, 867 (1975).

15. H. F. Reid and W. T. DeLong, "Making Sense Out of Ferrite Requirements in Welding Stainless Steels," Metal Progress, 84, 73 (1973).

16. G. M. Goodwin, N. C. Cole, and G. M. Slaughter, "A Study of Ferrite Morphology in Austenitic Stainless Steel Weldments," Welding Journal, 51, 425S (1972).

17. G. E. Linnert, "Welding Characteristics of Stainless Steels" Source Book on Stainless Steels; Section VI: Welding, p. 226, American Society for Metals, Metals Park, Ohio (1976).

18. D. J. Kotecki, "Welding Parameter Effects on Open-Arc Stainless Steel Weld Metal Ferrite," Welding Journal, 57, 109S (1978).

19. N. T. Williams, "Influence of Welding Cycles on the Ferrite Content of Type 321 Austenitic Steel," British Welding Journal, 12, 435 (1965).

20. R. A. Daemen, "High Recovery Electrodes for Welding Stainless Steel," British Welding Journal, 14, 550 (1967).

21. A. L. Schaeffler, "Selection of Austenitic Electrodes for Welding Dissimilar Metals," Welding Journal, 26, 601S (1947).

22. I. A. Zaks and R. S. Zhorova, "Effect of Various Fluxes on the Solidification Cracking Resistance and Properties of Austenitic Weld Metals," Svar. Proiz, __, No. 7,32 (1974).

23. A. J. Zvanut and H. N. Farmer, Jr., "Self-Shielding Stainless Steel Flux Cored Electrodes," Welding Journal, 51, 775 (1972).

24. B. S. Payne, G. J. Dormer, and L. R. Haslip, "Lime Coated vs Titanium Coated Stainless Steel Electrodes," Welding Journal, 41, 115 (1962).

25. N. C. Binkley, R. G. Berggren, and G. M. Goodwin, "Effects of Slight Compositional Variations on Type E308 Electrode Deposits," Welding Journal, 53, 91S (1974).

26. A Bernstein, J. Carlen, and L. Rick, "Influence of Phosphorus and Sulfur on the Properties of the Weld Metal in Certain Austenitic Stainless Steels," Welding Journal, 44, 504S (1965).

27. C. V. Shirwaikar and G. P. Reddy, "Purging with Nitrogen in the Welding of Austenitic Stainless Steels," Welding Journal, 54, 12S (1975).

28. B. C. Odegard, "Some Observations of the Formation of Surface Martensite in 304L Stainless Steel," Metallography, 7, 129 (1974).

29. T. Suzuki, H. Kojima, K. Sutaki, T. Hashimoto, and M. Ichihara, "An Experimental Study of the Martensite Nucleation and Growth in 18/8 Stainless Steel, Acta Met, 95, 1151 (1977).

30. R. G. Berggren, N. C. Cole, G. M. Goodwin, J. O. Stiegler, G. M. Slaughter, R. J. Gray, and R. T. King, "Structure and Elevated Temperature Properties of Type 308 Stainless Steel Weld Metal with Varying Ferrite Contents," Welding Journal, 57, 167S (1978).

31. J. R. Hawthorne and B. H. Menke, "Influence of Delta Ferrite Content and Welding Variables on Notch Toughness of Austenitic Stainless Steel Weldments," Naval Research Laboratory Report, Washington, DC.

32. R. T. King, J. O. Stiegler, and G. M. Goodwin, "Relation Between Mechanical Properties and Microstructure in CRE Type 308 Weldments," Welding Journal, 53, 307S (1974).

33. R. G. Thomas, "The Effect of Delta-Ferrite on the Creep Rupture Properties of Austenitic Weld Metals," Welding Journal, 57, 232S (1978).

34. Y. Arata, F. Matsuda, and S. Katayama, "Solidification Crack Susceptability in Weld Metals of Fully Austenitic Stainless Steels (Report II)--Effect of Ferrite, P, S, C, Si, and Mn on Ductility Properties of Solidification Brittleness," Transactions Japanese Welding Research Institute, 6, (1977).

35. Y. Arata, F. Matsuda, and S. Katayama, "Solidification Crack Susceptability in Weld Metals of Fully Austenitic Stainless Steels--Fundamental Investigation of Solidification Behavior of Fully Austenitic and Duplex Microstructures and Effect of Ferrite on Microsegregation," Transactions Japanese Welding Research Institute, 5, 135 (1976).

36. J. A. Brooks and F. J. Lambert, Jr., "The Effects of Phosphorus Sulfur and Ferrite Content of Weld Cracking of Type 309 Stainless Steel," Welding Journal, 57, 139S (1978).

37. Mrs. J. Honeycombe and T. G. Gooch, "Effect of Manganese on Cracking and Corrosion Behavior of Fully Austenitic Stainless Steel Weld Metals," Metal Const. and British Welding Journal, 4, 456 (1972).

38. D. M. Haddrill and R. G. Baker, "Microcracking in Austenitic Weld Metal," BWRA Report B5/20/63 (1963).

39. M. O. Malone, "Sigma and 885F Embrittlement of Chromium-Nickel Stainless Steel Weld Metals," Welding Journal, 46, 241S (1967).

40. D. P. Edmonds, R. T. King, and G. M. Goodwin, "Residual Elements Have Significant Effects on the Elevated Temperature Properties of Austenitic Stainless Steel Welds," ORNL Report TM-6177 (1978).

41. R. T. King, N. C. Cole, and G. M. Goodwin, "Creep Behavior of SMA Type 316 Weld Metal with Controlled Residual Elements," J. Pressure Vessel Technology, 98, 194 (1976).

42. L. A. James, "Crack Propagation Behavior in Type 304 Stainless Steel Weldments at Elevated Temperatures," Welding Journal, 52, 173S (1973).

43. P. Shahinian, H. H. Smith, and J. R. Hawthorne, "Fatigue Crack Propogation in Stainless Steel Weldments at High Temperatures," Welding Journal, 51, 527S (1972).

44. R. T. King, D. A. Canonico and C. R. Brinkman; "Elevated Temperature Weldment Behavior as Related to Nuclear Design Criteria," Welding Journal, 54, 265S (1975).

45. G. H. Rowe and J. R. Stewart, "Creep-Rupture Behavior of Type 316 Stainless Steel Weldments Prepared With and Without Restraint," Welding Journal, 41, (1962).

46. P. Shahinan, "Fatigue and Creep Crack Propagation in Stainless Steel Weld Metal," Welding Journal, 57, 87S (1978).

47. S. Ekerot, F. Bruk, and H. Fredriksson, "Pore Formation in the Mechanism of Stainless Steel Weld Metals," Metallographic Dept. Royal Institute of Technology, Stockholm, Sweden.

48. N. C. Binkley, G. M. Goodwin, and D. G. Harman, "Effects of Electrode Coverings on Elevated Temperature Properties of Austenitic Stainless Steel Weld Metal," Welding Journal, 52, 306S (1973).

49. C. D. Lundin, W. J. DeLong, and D. F. Spond, "Ferrite-Fissuring Relationship in Austenitic Stainless Steel Weld Metals," Welding Journal, 54, 241S (1975).

50. J. C. Borland and R. N. Yonger, "Some Aspects of Cracking in Welded Cr-Ni Austenitic Steels," British Welding Journal, 7, 22 (1960).

51. H. Frediks and L. J. Vander Toorn, "Hot Cracking in Austenitic Stainless Steel Weld Deposits," British Welding Journal, 15, 178 (1968).

52. W. T. DeLong, "Calibration Procedure for Instruments to Measure the Delta Ferrite Content of Austenitic Stainless Steel Weld Metal," Welding Journal, 52, 69S (1973).

53. R. A. Huseby, "Stress Relieving of Stainless Steels and the Associated Metallurgy," Welding Journal, 37, 304S (1958).

54. N. C. Code, G. M. Goodwin, and G. M. Slaughter, "Effect of Heat Treatments on the Microstructure of Stainless Steel Weld Metal," Microstructural Science, 3, 789 (1975).

55. E. M. Pronina et al, "The Effect of Strain Aging on the Susceptibility of Austenitic Steel KH25N16G7AR (E1835) to Cracking in the Heat Affected Zone of the Welded Joint," Suar. Proiz. __, No. 6,23 (1977).

56. W. E. White and I. LeMay, "Metallographic Observation on the Formation and Occurrence of Ferrite, Sigma Phase, and Carbides in Austenitic Stainless Steel," Metallography, 3, 51 (1970).

57. W. A. Baeslack, III, D. J. Duquette, and W. F. Savage, "Stress Corrosion Cracking in Duplex Stainless Steel Weldments," Welding Journal, 57, 175S (1978).

58. L. R. Poole, "An Unwanted Constituent in Stainless Weld Metal," Met. Prog., 65, 108 (1954).

59. O. H. Henry, M. A. Cordovi, and G. J. Fischer, "Sigma Phase in Austenitic Stainless Steel Weldments," Welding Journal, 34, 75S (1955).

60. W. A. Petersen, "Fine Grained Weld Structures," Welding Journal, 52, 74S (1973).

61. R. J. Traman and D. Hardwick, "Some Effects of Heat Treatment on the Rupture Properties of Three Stainless Steels," Iron and Steel Institute Publication, 97 (1967).

62. H. F. Reid and W. T. DeLong, "Making Sense Out of Ferrite Requirements in Welding Stainless Steels," Met. Progress, 103, 73 (1973).

63. R. D. Thomas, "Crack Sensitivity of Chromium-Nickel Stainless Weld Metal," Metal Progress, 50, 474 (1946).

64. R. S. Brown and J. B. Koch, "Development of a Solidification Crack Resistant Weld Filler Metal for a Stabilized, Fully Austenitic Alloy," Welding Journal, 57, 85S (1978).

65. D. M. Haddrill and R. G. Baker, "Effect of Cobalt on Susceptibility of Welded Austenitic Steels to Heat Affected Zone Cracking During Heat Treatment," B.W.R.A. Report, C104/1 (1964).

66. Mrs. J. Honeycombe and T. G. Gooch, "Effects of Microcracks on Mechanical Properties of Austenitic Stainless Steel Weld-Metals," Metal Construction and British Welding Journal, 5, 140 (1973).

67. J. Durnin and K. A. Ridal, "Determination of Retained Austenite in Steel by X-Ray Diffraction," J. Iron and Steel Institute, 206, 60 (1968).

68. F. C. Hull, "Effects of Composition on Embrittlement of Austenitic Stainless Steels," Welding Journal, 50, 104S (1973).

69. C. L. Choi and D. C. Hill, "A Study of Microstructural Procession in As-Deposited Weld Metal," Welding Journal, 57, 232S (1978).

70. N. I. Kakhovski and A. M. Solokha, "A Cr-Ni Steel Containing Nitrogen with a Low Carbon Content," Auto. Weld, 21, 81 (1968).

71. J. K. Pokhodnya and A. P. Paltsevich, "Absorption of Nitrogen During the Welding of Type 18Cr-9Ni Steel," Auto Weld, 23, 9 (1970).

72. H. Astrom, B. Loberg, B. Bengtsson, and K. E. Easterling, "Hot Cracking and Micro-Segregation in 18-10 Stainless Steel Welds," Metal Science, __, 225 (1976).

73. M. C. T. Bystram and M. F. Stuchfield, "Nickel Base Electrodes for Plant Operating at Low and High Temperatures," British Welding Journal, 11, 427 (1964).

74. E. H. Schmidt, "Low Temperature Impact of Annealed and Sensitized 18-8," Metal Progress, 52, 698 (1948).

75. J. R. Hawthorne and H. E. Watson, "Notch Toughness of Austenitic Stainless Steel Weldments With Nuclear Irradiation," Welding Journal, 52, 255S (1973).

76. W. T. DeLong, "Ferrite in Austenitic Stainless Steel Weld Metal," Welding Journal, 53, 273S (1974).

77. R. Espy, "What Weld Metal for Type 316L Stainless Steel," Metal Prog. 86, 109, (1964).

78. R. Gunia and G. Ratz, "The Measurement of Delta Ferrite in Austenitic Stainless Steels," WRC Bulletin 132, August (1968).

79. I. Masumoto, K. Tamaki, and M. Katsuna, "Hot Cracking of Austenitic Steel Weld Metal," J. Japan Weld. Soc., 41, 1300 (1972).

Nonmetallics for Magnet Structures

NONMETALLICS FOR MAGNET SYSTEMS

National Bureau of Standards

NONMETALLICS FOR MAGNET SYSTEMS

M. B. Kasen, J. G. Hust and H. M. Ledbetter
Fracture and Deformation Division
and
Thermophysical Properties Division
National Bureau of Standards
Boulder, CO 80303

INTRODUCTION

NBS, in cooperation with the U.S. laminating industry, has arranged for commercial availability of special grades of NEMA type G-10 and G-11 glass-epoxy industrial laminates intended for use in cryogenic magnet structures. These materials, designated G-10CR and G-11CR, differ from conventional G-10 and G-11 products only in that they are produced to a specification covering all aspects of components and procedures, thereby minimizing product variability. The CR-grade laminates are commercial products meeting current NEMA G-10 and G-11, MIL-P-18177C and Federal LP-509 specifications. G-10CR is a heat-activated, amine-catalyzed bisphenol A solid type epoxy resin laminate reinforced with continuous-filament E-glass fabric, silane finished. G-11CR os an aromatic-amine hardened bisphenol A liquid type epoxy resin laminate reinforced in the same manner. The G-10CR formulation was selected because of its proven performance in cryogenic structures. The G-11CR formulation was selected to provide an alternative aromatic-amine cured laminate which is expected to provide higher resistance to radiation damage.

This action was taken because variability in cryogenic properties among conventional proprietary G-10 and G-11 laminates has caused concern as to their suitability for demanding MFE applications in superconducting magnet structures. Property variability problems arise because the room-temperature electrical performance specifications, which conventional proprietary laminates are required to meet, may be met by different laminate compositions and manufacturing processes. Thus, G-10 and G-11 laminates produced by different

companies can and do differ in the type of glass reinforcement, in the weave of the glass fabric, in the epoxy system used and in other ways which affect the cryogenic performance of the laminates. These problems are eliminated by the CR grades.

Specifications for producing the CR grade laminates have been distributed to all U.S. laminating companies through the Industrial Laminates Subcommittee of the National Electrical Manufacturing Association, Washington, D.C. Specifications will remain proprietary within NEMA. Inquiries regarding details of the specifications should be addressed to Mr. H. Colin Smith of NEMA.

The CR grades may be produced by any laminating firm wishing to compete for the market. They are presently available in commercial quantities.

CR-grade laminates are produced to a natural beige color, as the dye required to produce the familiar green color of proprietary G-10 and G-11 laminates is only cosmetic and has an unknown effect on radiation resistance. Standard laminated sheets range from 18 to 50 inches in width and 24 to 120 inches in length. Standard thicknesses range from 1/64 inch to 2 inches. Laminated tubes are available in a variety of diameters and lengths. Both CR-grades are available in rod forms produced by molding or by matching from square sheet stock.

Both G-10CR and G-11Cr are woven glass cloth composites. The warp fibers are those which emerge from the loom, while the fill fibers are

those woven across them at right angles. The yarn count per inch is 43 ± 3 for warp and 32 ± 2 for fill. The normal direction of the composite is perpendicular to the cloth ply plane.

This report summarizes the results of cryogenic mechanical, thermal, elastic and electrical property characterization of G-10CR and G-11CR laminates manufactured in the pilot plant of one industrial laminating firm. A continuing study is examining the variability in properties which might occur in normal plant production and among the products produced by different firms to the same specifications.

The tolerance of G-10CR and G-11CR to neutron and gamma radiation at 4 K is being studied in an independent program at ONRL. Inquiries should be directed to Mr. C. J. Long at that facility.

MECHANICAL PROPERTIES, THERMAL CONTRACTION, AND ELECTRICAL PROPERTIES OF G-10 CR AND G-11CR

M. B. Kasen

MECHANICAL PROPERTIES

The effect of cryogenic temperatures on the mechanical properties of G-10CR and G-11CR laminates are summarized in Table 1 and are plotted as a function of temperature on Fig. 1(a-g). Cooling to cryogenic temperatures is clearly beneficial -- tensile and compressive strengths increase 70-100%, Young's moduli increase about 30%, ultimate tensile failure strain is increased 140% and interlaminar (guillotine) shear strengths increase 30-70%. In this test series, the G-10CR product was found to be mechanically superior to the G-11CR grade in all except Young's modulus. There is also some indication that cooling below 76 K may be deleterious to several of the G-11CR properties. These data do not consider the factor of radiation resistance. If as expected, amine-catalyzed epoxy system of the G-11CR product suffers less degradation

Table 1.

INITIAL MECHANICAL PROPERTY VALUES OF G-10 CR AND G-11 CR
(MANUFACTURER A)

Temperature	Young's Modulus, E (Tensile-W)		Poisson's Ratio, ν	Tensile Strength σ^{TU}(W)		Compressive Strength, σ^{CU}(W)		Compressive Strength, σ^{CU}(N)		Shear Strength σ^{SI} (Short Beam-W)		Shear Strength σ^{SI}(Guillotine-W)		Strain to Failure ε^{TU}
(K)	$N/M^2 \times 10^9$	PSI$\times 10^6$		$N/M^2 \times 10^6$	PSI$\times 10^3$	$N/M^2 \times 10^6$	PSI$\times 10^3$	$N/M^2 \times 10^6$	PSI$\times 10^3$	$N/M^2 \times 10^6$	PSI$\times 10^3$	$N/M^2 \times 10^6$	PSI$\times 10^3$	%
							G-10 CR							
295	27.18	3.943	.1579	411.2	59.64	357.7	51.88	384.7	55.79	59.90	8.63	44.88	6.51	1.85
	28.35	4.112	.1568	414.3	60.09	369.7	53.62	459.7	66.66	58.61	8.50	43.50	6.31	1.75*
	28.56	4.142	.1338	419.9	60.91	386.3	56.03	415.0	60.18	61.23	8.88	38.47	5.58	1.64*
						387.4	56.18			61.02	8.85			
Average	28.03	4.066	.1495	415.1	60.21	375.2	54.42	419.8	60.88	60.05	8.71	42.28	6.13	1.75
76	34.41	4.991	.1861	785.0	113.9	790.4	114.6	696.9	101.0	124.3	18.03	59.22	8.59	3.15*
	34.07	4.941	.1848	848.3	123.0	832.6	120.7	719.0	104.3	131.2	19.03	60.74	8.81	3.66*
	32.73	4.747	.1978	840.6	121.9	877.5	127.3	645.6	93.6	138.0	20.01	63.91	9.27	3.49*
								708.6	102.7					
Average	33.73	4.893	.1896	824.6	119.6	833.5	120.9	692.5	100.4	131.1	19.02	61.27	8.89	3.44
4	36.23	5.256	.2253	889.2	129.0	854.5	123.9	845.3	122.6			73.84	10.71	3.97*
	35.86	5.201	.2006	870.2	126.2	849.9	123.2	662.0	96.0			71.22	10.33	3.78*
	35.62	5.166	.2071	825.2	119.7	881.9	127.9	701.6	101.7			72.74	10.55	3.25*
								785.7	113.9					
Average	35.91	5.208	.2110	861.8	125.0	862.1	125.0	748.6	108.6			72.57	10.53	3.65
							G-11 CR							
295	32.93	4.776	.1300	478.7	69.44	383.3	55.58	430.0	62.36	69.84	10.13	39.09	5.67	1.79
	32.08	4.653	.1585	476.3	69.09	395.1	57.35	463.7	67.25	73.57	10.67	40.88	5.93	1.83
	30.97	4.492	.1813	453.0	65.71	410.6	59.55	489.8	71.03	72.33	10.49	41.85	6.07	1.85
Average	31.99	4.640	.1566	469.4	68.08	396.4	57.49	461.2	66.88	71.91	10.43	40.61	5.89	1.82
76	37.80	5.483	.2352	791.1	114.7	850.9	123.4	800.8	116.1	119.7	17.36	56.33	8.17	3.32*
	36.22	5.253	.2110	840.5	121.9	740.8	107.4	785.0	113.8	118.4	17.17	57.02	8.27	3.27*
	37.88	5.494	.2237	848.1	123.0	819.7	118.9	810.3	117.5	121.5	17.63	56.19	8.15	3.04*
Average	37.30	5.410	.2233	826.7	119.9	803.8	116.6	798.7	115.8	119.8	17.38	56.51	8.20	3.21
4	37.80	5.482	.2008	874.0	126.8	708.4	102.7	784.3	113.7			59.09	8.57	2.85*
	38.62	5.601	.1931	823.8	119.5	735.7	106.7	849.4	123.2			55.23	8.01	3.75*
	41.82	6.064	.2416	918.3	133.2	745.7	108.2	694.9	100.8			54.40	7.89	3.81*
Average	39.41	5.716	.2118	872.2	126.5	739.3	105.9	776.2	112.6			56.23	8.16	3.52

(W) = Warp direction of reinforcement
(N) = Normal to reinforcement
* = Calculated values

under irradiation than does the G-10CR formulation, the performance ranking of the two products might substantially change.

In common with conventional G-10 and G-11 products, the G-10CR and G-11CR laminates are reinforced with an unbalanced glass fabric, the glass content in the fill direction of the fabric being about 75% of that in the warp direction. The tensile and compressive properties in the fill direction should, to a first approximation, be 75% of those reported on Table 1 for the warp direction. This remains to be verified.

Interlaminar shear properties (resistance to shear between layers of the laminates) are important in superconducting magnet designs in which the windings nest in slots machined into the laminates or in other designs in which the electromagnetic forces place the laminates in shear. The relevant data appear in Table 1 under the heading "Shear Strength (Guillotine)." Data designated "Shear Strength (Short Beam)" is not a relevant property for this application, as this test method does not provide a true measure of interlaminar shear.

Interlaminar shear strength is a difficult property to measure accurately because the defined test conditions -- pure shear stress without tensile or compressive stresses on the shear plane -- can only be approximated. The discrepancy noted on Fig. 1(g) between "unsupported" and "side-supported" test methods indicates the possible error that can occur even though the tests comply with an existing ASTM method which is currently under revision. Data appearing on Table 1 and identified as "side-supported" on Fig. 1(g) reflect improved methods developed at NBS-Boulder and are believed to reflect the most accurate available data.

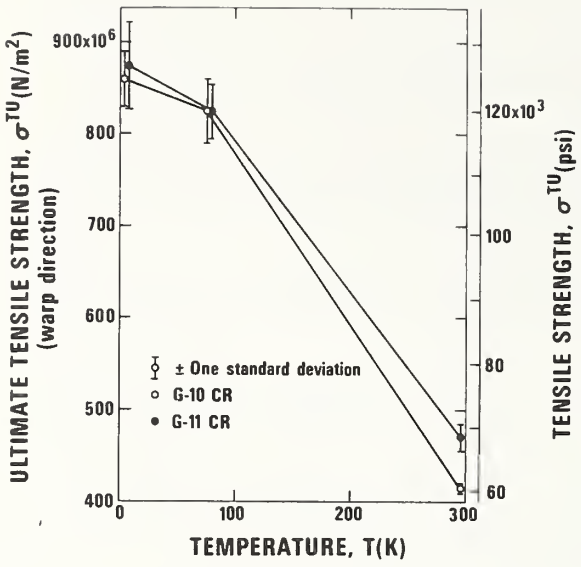

(a) Temperature dependence of ultimate tensile strength, warp direction.

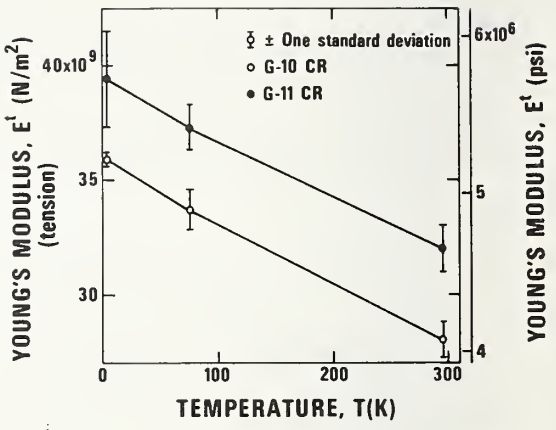

(b) Temperature dependence of Young's modulus in tension, warp direction.

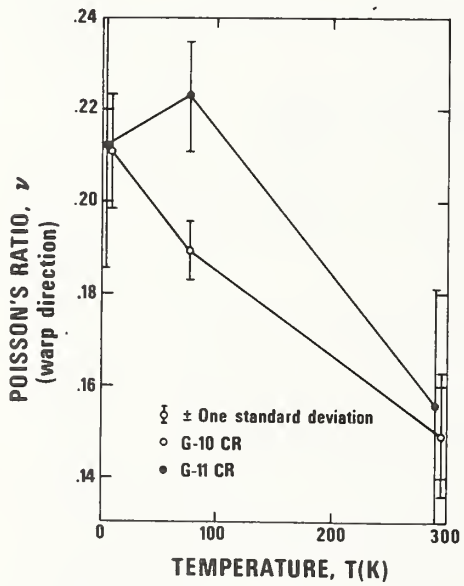

(c) Temperature dependence of Poisson's ratio in tension, warp direction.

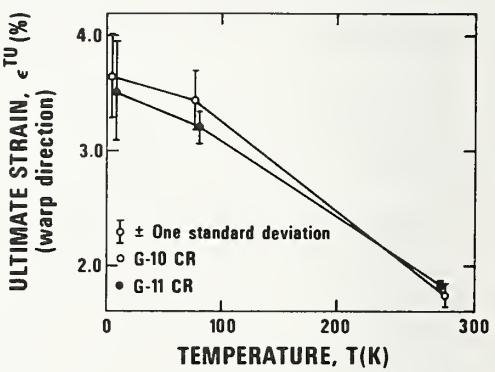

(d) Temperature dependence of ultimate tensile strain, warp direction.

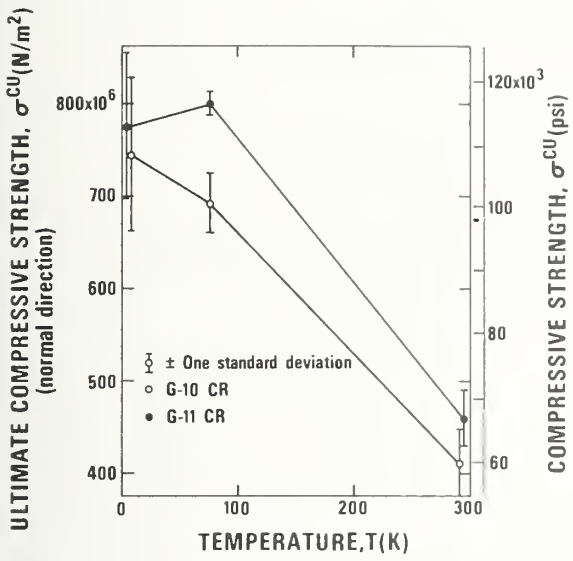

(e) Temperature dependence of ultimate compressive strength normal to the reinforcement.

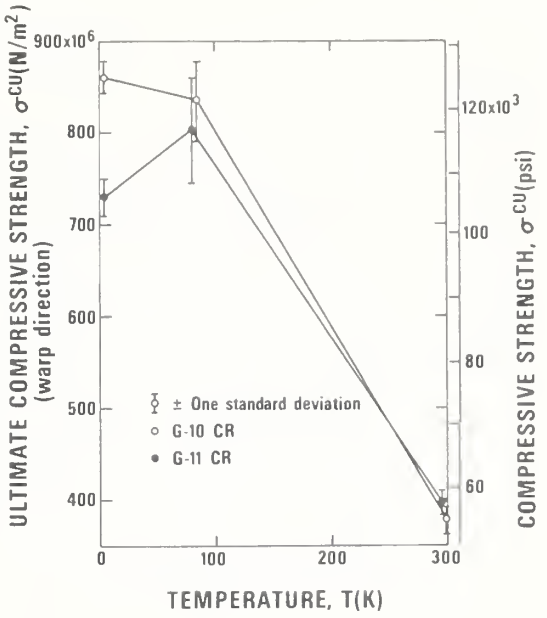

(f) Temperature dependence of ultimate compressive strength, warp direction.

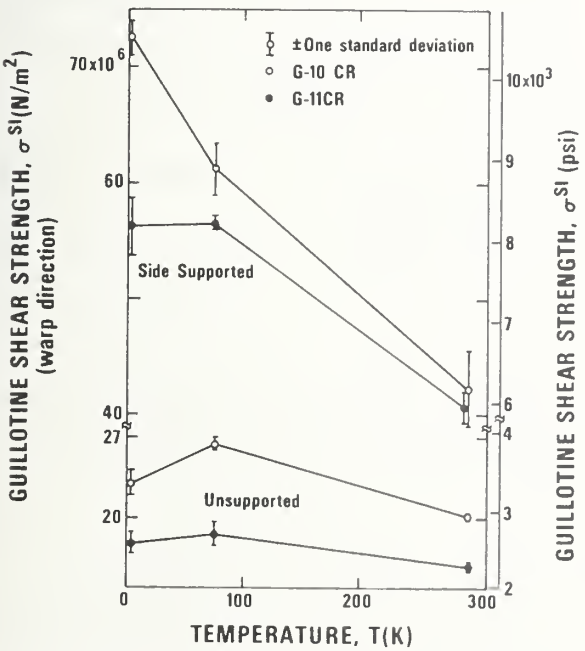

(g) Temperature dependence of interlaminar shear (guillotine), warp direction. Unsupported data are invalid. See text.

Fig. 1. Temperature-dependence of mechanical properties of G-10CR and G-11CR high-pressure, glass-epoxy industrial laminates. Initial data, supplier A, three specimens per data point. Warp/fill ratio = 43/32. NBS-Boulder data.

The "short beam" shear strength data appearing on Table 1 are primarily indicative of overall laminate quality. The data indicate that the tested laminates were equal in quality to the best commercial products. Interlaminar shear strength values obtained with this test cannot be equated with values obtained by the guillotine method because the three-point flexure method of testing subjects the specimen to tensile and compression stresses as well as shear with the state of stress continually changing throughout the test. These data were obtained as part of a series of test evaluating the effect of changing from a methacrylate chromium chloride (Volan) glass finish to a silane finish as required by recent EPA directives. The results, summarized on Fig. 2 indicate that the change of finish on the glass has substantially improved the quality of both CR-type laminates.

The ability of the laminates to withstand severe thermal shock in thick sections is of interest since cracking or delamination caused by such shock could adversely affect the performance of the laminates in magnet structures. The ability of G-10CR and G-11CR to withstand thermal shock was evaluated by repeatedly cycling one-inch cubes of each material between 76 K and 390 K, after which degradation was assessed by comparing the short-beam shear strength of specimens taken from the surface layers of cycled specimens with that of similar specimens taken from uncycled cubes. The results, summarized on Table 2, suggest that the CR-grade laminates are highly resistant to thermal shock.

The FY-79 nonmetallics mechanical test program will complete the characterization of the G-11CR and C-10CR products in the fill direction. A set of laminates received from a second manufacturer will be evaluated to assess the variability in mechanical properties which might exist

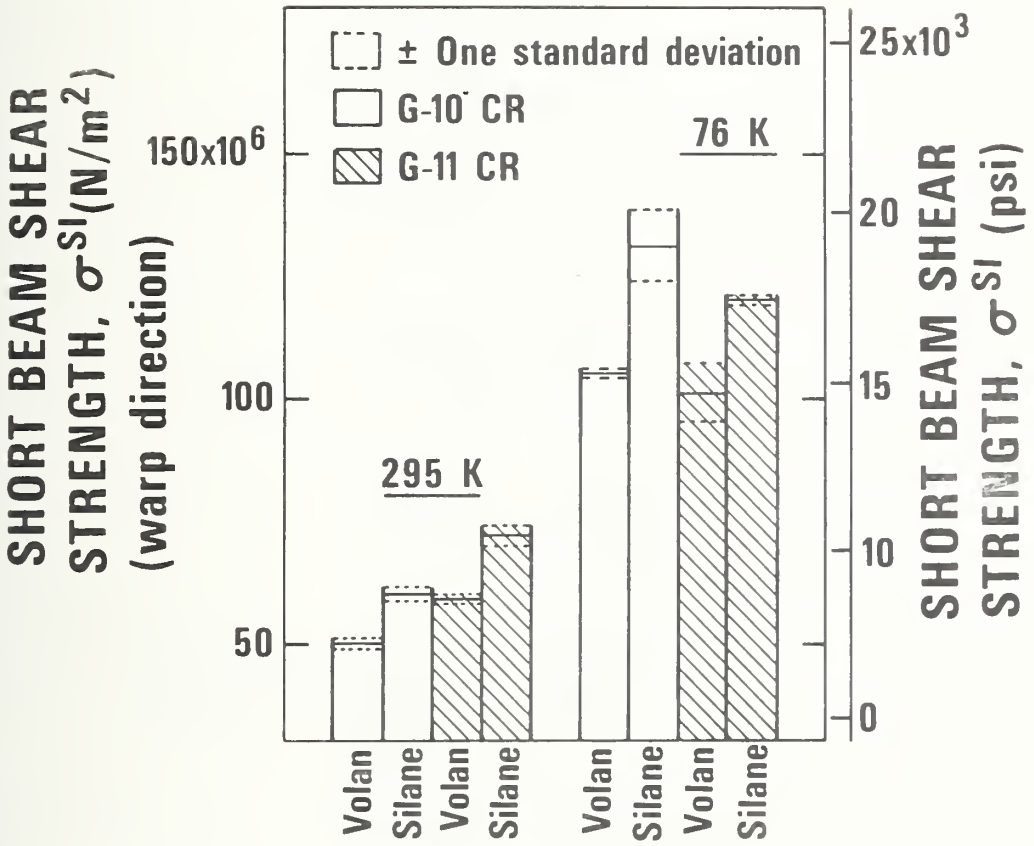

Fig. 2. Comparison of short-beam shear strengths of G-10CR and G-11CR laminates produced with glass fiber having volan (methacrylate chromium chloride) and silane finishes.

Table 2.

EFFECT OF THERMAL CYCLING ON WARP DIRECTION
SHORT-BEAM SHEAR STRENGTH OF G-10 CR AND G-11 CR
(MANUFACTURER A)

Temperature (K)	G-10 CR Control (10^3 PSI)	G-10 CR Control (MPa)	G-10 CR Thermally Cycled* (10^3 PSI)	G-10 CR Thermally Cycled* (MPa)	G-11 CR Control (10^3 PSI)	G-11 CR Control (MPa)	G-11 CR Thermally Cycled* (10^3 PSI)	G-11 CR Thermally Cycled* (MPa)
	8.733	60.21	8.232	56.76	10.11	69.70	9.229	63.63
295	8.840	60.94	8.161	56.27	9.806	67.61	9.551	65.85
	8.602	59.31	8.180	56.40	9.376	64.65	9.407	64.86
Average	8.725	60.16	8.191	56.48	9.760	67.29	9.396	64.78
	18.67	128.7	19.16	132.1	14.19	97.84	14.71	101.4
76	19.07	131.5	19.05	131.3	12.56	85.60	14.97	103.2
	19.57	134.9	18.18	125.3	16.09	110.9	16.81	115.9
Average	19.10	131.7	18.80	129.6	14.28	98.46	15.50	106.9

*10 cycles 76 K to 390 K

between laminates produced to the same specification at different plants. Additionally, the mechanical properties of laminates produced to the same specification but containing boron-free E-glass reinforcement will be screened. Samples of these laminates will be provided to ORNL for 4 K radiation testing to determine if increased radiation resistance due to reduction in boron content is sufficient to justify additional development of this variant.

THERMAL CONTRACTION

The available data on contraction of G-11CR and G-10CR laminates are summarized on Table 3. These data, independently provided to NBS by the Los Alamos Scientific Laboratory (R. I. Schermer), reflect total thermal contraction from 295 K to 75 K.

A more complete characterization of thermal contraction is scheduled during FY-79.

Table 3.

TOTAL THERMAL CONTRACTION 295 K TO 75 K OF G-10CR AND G-11CR HIGH-PRESSURE, GLASS-EPOXY INDUSTRIAL LAMINATES.(1)

Direction	ΔL/L, mm/meter G-10CR	G-11CR
Warp	2.35 ± 0.00(2)	2.19 ± 0.07
Fill	2.69 ± 0.03	2.43 ± 0.03
Normal	7.30 ± 0.15	6.20 ± 0.18

(1) Private communication, Los Alamos Scientific Laboratory, 14 April 1978.

(2) Standard deviation of the mean of the measurements.

ELECTRICAL PROPERTIES

Available data on the effect of cryogenic temperatures on the volume electrical resistivities of G-10CR and G-11CR laminates are summarized

on Table 4. Data on the effect of cryogenic temperatures on the electrical strengths are summarized on Table 5. These data were provided by the Westinghouse Research and Development Center (R. N. Sampson) under contract from NBS.

A more complete report on this work is being prepared by Westinghouse.

Table 4.

VOLUME RESISTIVITIES OF G-10 AND G-11 LAMINATES
AT LOW AND ROOM TEMPERATURES

Sample	Thickness, Mils	Volume resistivity, ohm-cm 298K	77K	4K
G-10	14.4	8.9×10^{15}		4.0×10^{17}
G-10	20	9.3×10^{14}	1.5×10^{17}	4.1×10^{17}
G-11	12	7.3×10^{15}		2.0×10^{17}
G-11	20	1.3×10^{15}	6.1×10^{16}	2.0×10^{17}

Table 5.

ELECTRIC STRENGTHS OF G-10 AND G-11 LAMINATES
AT LOW AND ROOM TEMPERATURES

Measurements with 60 Hz voltage at 0.5 kV/sec. rise,
0.5 in. and 1.5 in. diam. electrodes

Sample	Thickness, Mils	Breakdown voltage stress, kV/mil at 298K	63K	4K
G-10	11	.87, Two > 1.52	1.66,1.60 1.63 av.	
G-10	14	1.16		1.26,1.19 1.23 av.
G-11	12	1.23		
G-11	12.5			1.18
	11.7			1.25
				1.22 av.

Thermal Conductivity of G-10CR and G-11CR Industrial Laminates at Low Temperatures

by

J. G. Hust

ABSTRACT

The thermal conductivity of G-10CR and G-11CR is reported for temperatures from 2 to 300K. These materials are produced by a standardized manufacturing specification designated by the suffix CR. Measurements were conducted in two directions: (a) Normal to the glass fabric plane and (b) in the plane of the fabric (warp direction). The measurements and analysis were conducted by the thermal conductivity integral method with an uncertainty of about $\pm$ 5%.

I. INTRODUCTION

As part of the continuing cryogenic materials program, NBS, in cooperation with the U. S. laminating industry, has arranged for commercial production of component-specified NEMA/ASTM type G-10 and G-11 industrial laminates for cryogenic insulation and structural applications. This action was taken because variability in cryogenic properties of conventionally produced proprietary G-10 and G-11 laminates has caused concern in the demanding specifications of superconducting magnets for magnetic fusion energy applications. The cryogenic variability in G-10 and G-11 laminates occurs because the room temperature NEMA specifications can be met by different glass reinforcements, weaves of the fabric, types of epoxy, and cure agents, as well as the fabrication procedures. The component-specified laminates investigated are designated as G-10CR and G-11CR.

NBS is performing a thorough low temperature electrical, thermal, and mechanical properties characterization of G-10CR and G-11CR. This report describes the thermal conductivity measurements performed on these laminates in two directions (to determine the anisotropy) and temperatures from 2 to 300 K.

II. MATERIAL AND SPECIMEN CHARACTERIZATION

G-10CR and G-11CR are composites of fiber glass fabric and epoxy. The fabric is woven from type E glass threads with 43 threads per inch (17 per cm) in the warp direction and 32 threads per inch (12 per cm) in the fill direction. The thread is composed of 75 filaments each of 0.00018 inch diameter (0.00046 cm). The density of E glass is 2.4 g/cm^3. The resin Y-2000, used in G-10CR, has an uncured density of 1.10 ± 0.01 g/cm^3. The resin, HMS-2002 used in G-11CR, has an uncured density of 1.04 ± 0.01 g/cm^3. The densities of the cured resins are not known.

The thermal conductivity specimens are 3/4 inch cubes. The G-10CR specimen has a density of 1.904 g/cm^3 and the G-11CR specimen 1.956 g/cm^3 with an uncertainty of $\pm$ 0.002 g/cm^3. The finished G-10CR laminate contains 33-35% resin and G-11CR 27-31% by weight.

Using the above measured densities and weight fractions of the resins, a value of 1.25 $\pm$ 0.01 g/cm^3 is calculated for the cured resin density for both resins. This corresponds to a fiber content of 53% for G-10CR and 58% for G-11CR by volume. These calculations were performed using the following equations:

$$\rho_c = \rho_r WF_r + \rho_g WF_g$$
$$V_c = V_r VF_r + V_g VF_g$$

where ρ and V are density and specific volume ($V=1/\rho$), WF and VF are weight fraction and volume fraction, and the subscripts designate composite (c), resin (r), and glass (g).

Table 1. Dimensions, volumes, weights and densities of the G-10CR and G-11CR specimens

	Dimensions (cm)					
Material	Normal to fabric	Warp direction	Fill or woof direction	volume (cm^3)	weight (g)	density (g/cm^3)
G-10CR	1.910	1.890	1.919	6.93	13.188	1.904
G-11CR	1.915	1.913	1.910	7.00	13.684	1.956

Thermal conductivity of each of these specimens was measured in the normal and warp directions.

III. EXPERIMENTAL PROCEDURE AND DATA ANALYSIS

The thermal conductivity of the test blocks is determined in a modified "fixed-point" apparatus. This apparatus has been used previously to determine thermal conductivity values near the fixed-points of cryogenic baths (liquid helium, 4K; liquid nitrogen, 76K; dry ice-alcohol mixture, 194K; and ice-water mixture, 273K) for relatively rapid measurement to an accuracy of 10% or better. Modifications, as described by Hust and Arvidson [1], were made to perform closely spaced measurements at temperatures from 2 to 300K. The specimen chamber of this apparatus is shown in Figure 1.

A measurement is performed as follows: the chamber is placed into a temperature controlled bath and the lower block heater is energized to generate a fixed temperature difference, ΔT, between the two blocks with a constant heater power, $\dot{Q}$. From a previous calibration experiment, the amount of heat, $\dot{Q}_r$, flowing through the compression bolts under these conditions is known. The heat flow through the specimen of cross-sectional area, A, and length, ℓ, is thus calculated as $\dot{Q}_s = \dot{Q} - \dot{Q}_r$. If the temperature gradient is sufficiently small, the thermal conductivity, k, can be calculated from,

$$k = \dot{Q}_s \ell / A \, \Delta T \qquad \text{Eq. 1}$$

This relationship yields the correct value of k at $T = (T_1 + T_2)/2$, regardless of the magnitude of $\Delta T = T_2 - T_1$ if k is either independent of temperature between T_1 and T_2 or a linear function of temperature, $k = aT$. In this experimental arrangement it is necessary to use large temperature differences in order to obtain data from 2 to 300K, thus, Eq (1) would not yield correct values of k.

To circumvent this discrepancy we first resort to the defining equation for k(T) for one-dimensional heat flow,

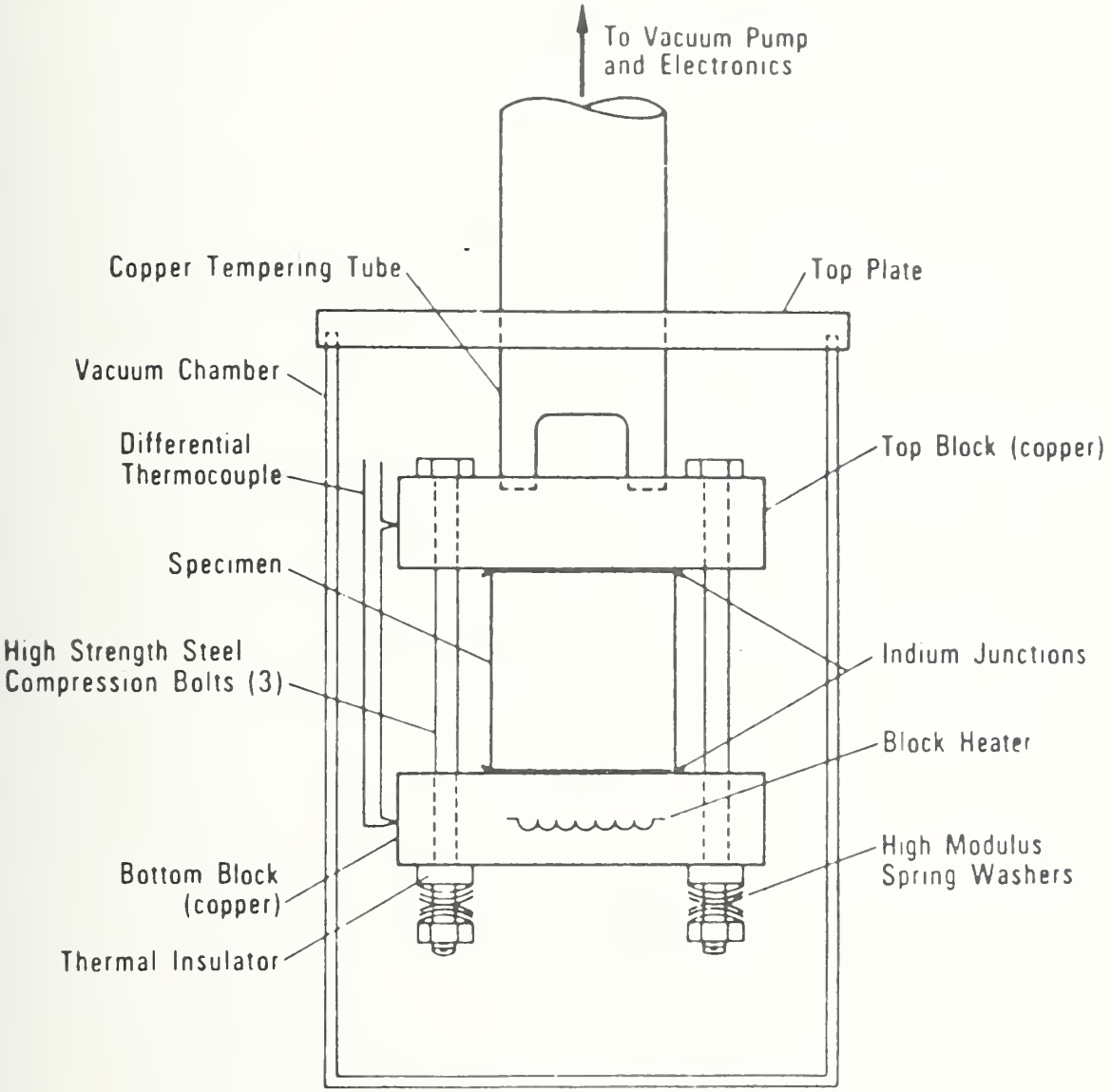

Figure 1. Specimen chamber of compression "fixed-point" thermal conductivity apparatus.

$$\dot{Q}_s = k(T)A\ dT/dX \qquad \text{Eq. 2}$$

where dT/dX is the temperature gradient at any position along the specimen and k(T) is thermal conductivity at that temperature. Integrating this equation from T_1 to T_2 we obtain

$$\dot{Q}_s\ell/A = \int_{T_1}^{T_2} k(T)dT \qquad \text{Eq. 3}$$

Assuming some integrable functional form df(T dT for k(T) we obtain

$$\dot{Q}_s\ell/A = f(T_2) - f(T_1) \qquad \text{Eq. 4}$$

For convenience the function k(T) is chosen to be an appropriate linear series containing a number of undetermined parameters,

$$k(T) = \sum_{i=1}^{n} a_i\ df_i(T)/dT \qquad \text{Eq. 5}$$

Thus, we obtain

$$\dot{Q}_s\ell/A = \sum_{i=1}^{n} a_i(f_i(T_2) - f_i(T_1)) \qquad \text{Eq. 6}$$

Only the linear parameters a_i are unknowns in this equation. Thus, a least squares fit of several experimental runs can be performed to determine the a_i and, consequently, k(T) can be calculated from Eq. (5). It is necessary to have at least as many independent runs as there are parameters but considerably more are obtained in actual practice. The latter method (Eqs.(5) and (6)) is referred to as the thermal conductivity integral method, while the former (Eq. (1)) as the finite difference method. Both of these methods are used here to analyze the experimental data.

Further details of the experimental setup, determination of Q_r, thermocouple calibration, and the operating procedure have been described in a previous sponsor report by Hust and Arvidson [1]. A calibration measurement on a standard reference material is also included in the report by Hust and Arvidson [1]. The measurements on the standard reference material (SRM 735) indicate an overall system accuracy of about $\pm$ 3% up to 100K and $\pm$ 6% above 100K.

IV. RESULTS AND DISCUSSION

The direct experimental data on the two specimens in two directions are available from the author. These data were analyzed by both the difference method and the thermal conductivity integral method. The results of these calculations are illustrated in Figures 2, 4, 6 and 8. The deviations of the direct experimental data from the integral method calculations are illustrated in Figures 3, 5, 7 and 9. the function chosen for k(T) in the integral method is

$$k(T) = \sum_{i=1}^{6} a_i [\ln(T+1))]^i \qquad \text{Eq.7}$$

The resulting values of a_i for the four specimens are presented in Table 2. Tabular values, as calcualted from eq. 7, are given in table 3.

It is noted that these four sets of thermal conductivities are the same to within about $\pm$ 20%. Because of this, a least squares fit was also performed for the entire set of data and the results are presented in Figures 10 and 11, the parameters are given in Table 2 and calculated values in table 3. Figure 12 illustrates the smoothed data for each of the four specimens. This plot reveals that G-10CR and G-11CR exhibit essentially the same thermal conductivity, but the warp directions has a conductivity about 20% higher in both cases.

Table 2. Values of the parameters, a_i, of equation 7 for the four sets of data on G-10CR and G-11CR and for all of the data taken as a single set (composite mean).

	G-10R		GR-11CR		Composite Mean
	Normal	Warp	Normal	Warp	
1	-122251.92	-29802.969	-28757.138	17929.675	-77070.427
2	255195.80	80143.031	73864.094	-22689.905	171354.28
3	-159650.69	-23413.583	-28560.501	54878.220	-94121.693
4	50450.437	1551.1046	6340.1721	-25877.220	26281.670
5	-7798.5477	404.43393	-841.94250	4781.6591	-3613.2451
6	473.39836	-38.341244	59.450845	-298.89669	204.51475

NOTE: All values have been multiplied by 10^6.

Table 3. Values of thermal conductivity for the normal and warp directions of G-10CR and G-11CR as calculated from equation 7 and the parameters in table 2.

Temp (K)	Thermal Conductivity (W m^{-1} K^{-1})x10^3				
	Normal	Warp	Normal	Warp	Composite mean
2.2	28.7	40.5	31.5	38.6	35.0
2.4	33.3	45.1	35.2	42.6	39.5
2.6	37.6	49.5	38.8	46.6	43.8
2.8	41.6	53.8	42.2	50.5	47.9
3.0	45.4	57.8	45.5	54.2	51.7
3.5	53.9	67.4	53.3	63.3	60.5
4	61.2	76.1	60.5	71.7	68.3
5	73.5	91.4	73.1	86.7	81.5
6	83.6	104	83.9	99.5	92.5
8	99.6	126	102	120	110
10	113	143	116	136	124
15	139	175	143	163	152
20	160	200	163	182	173
30	192	241	193	211	209
40	218	276	216	236	240
50	238	308	237	260	266
60	256	338	255	284	291
80	286	395	289	331	336
100	312	448	321	378	376
120	336	498	352	423	414
140	361	545	382	466	450
160	386	590	412	507	486
180	413	633	442	546	520
200	440	674	471	582	553
240	500	752	529	649	620
280	565	823	587	708	685
300	600	857	-----	735	717

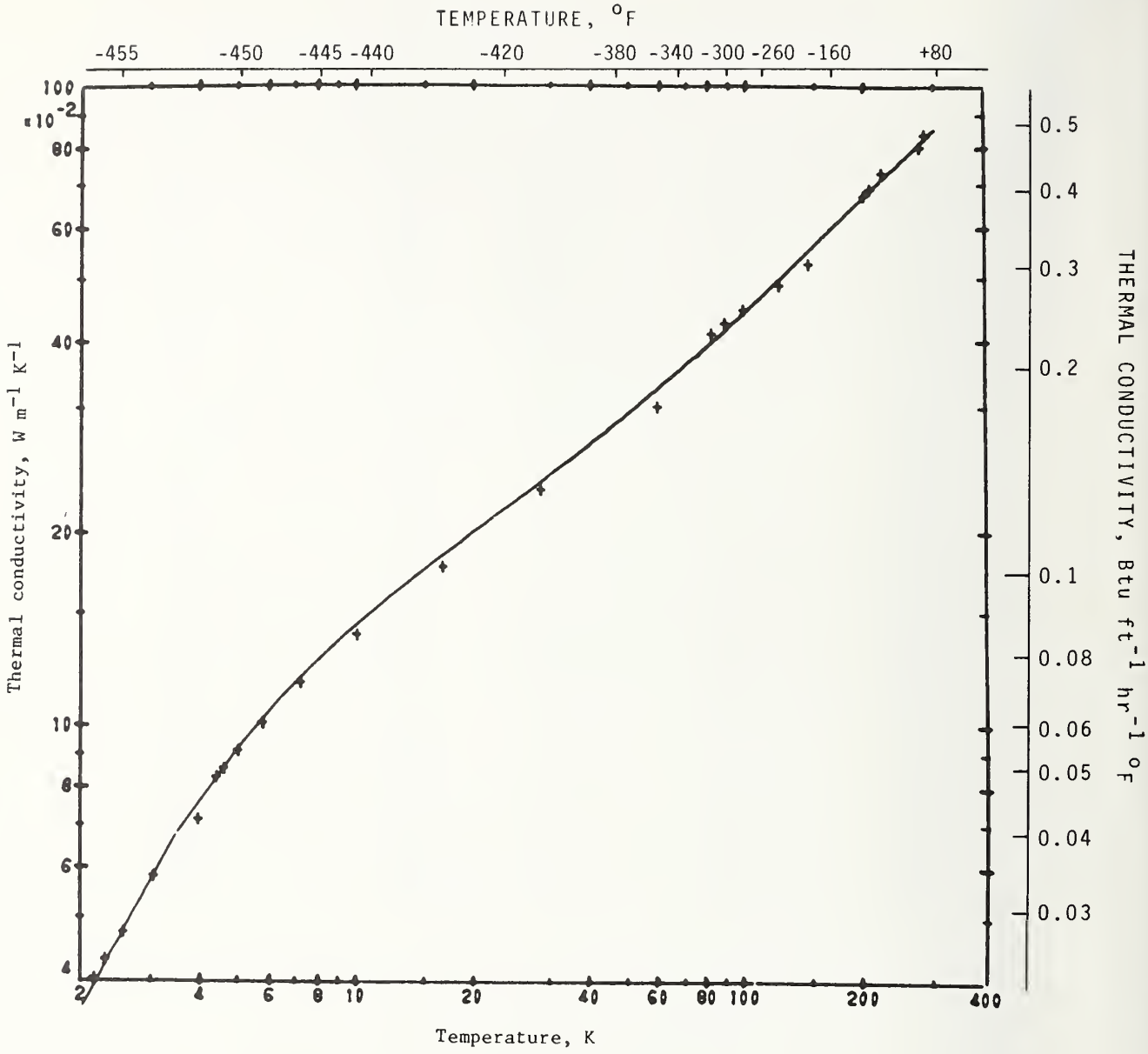

Figure 2. Thermal conductivity values form G-10CR, warp direction (+ obtained by difference methods; ---- obtained from integral method)

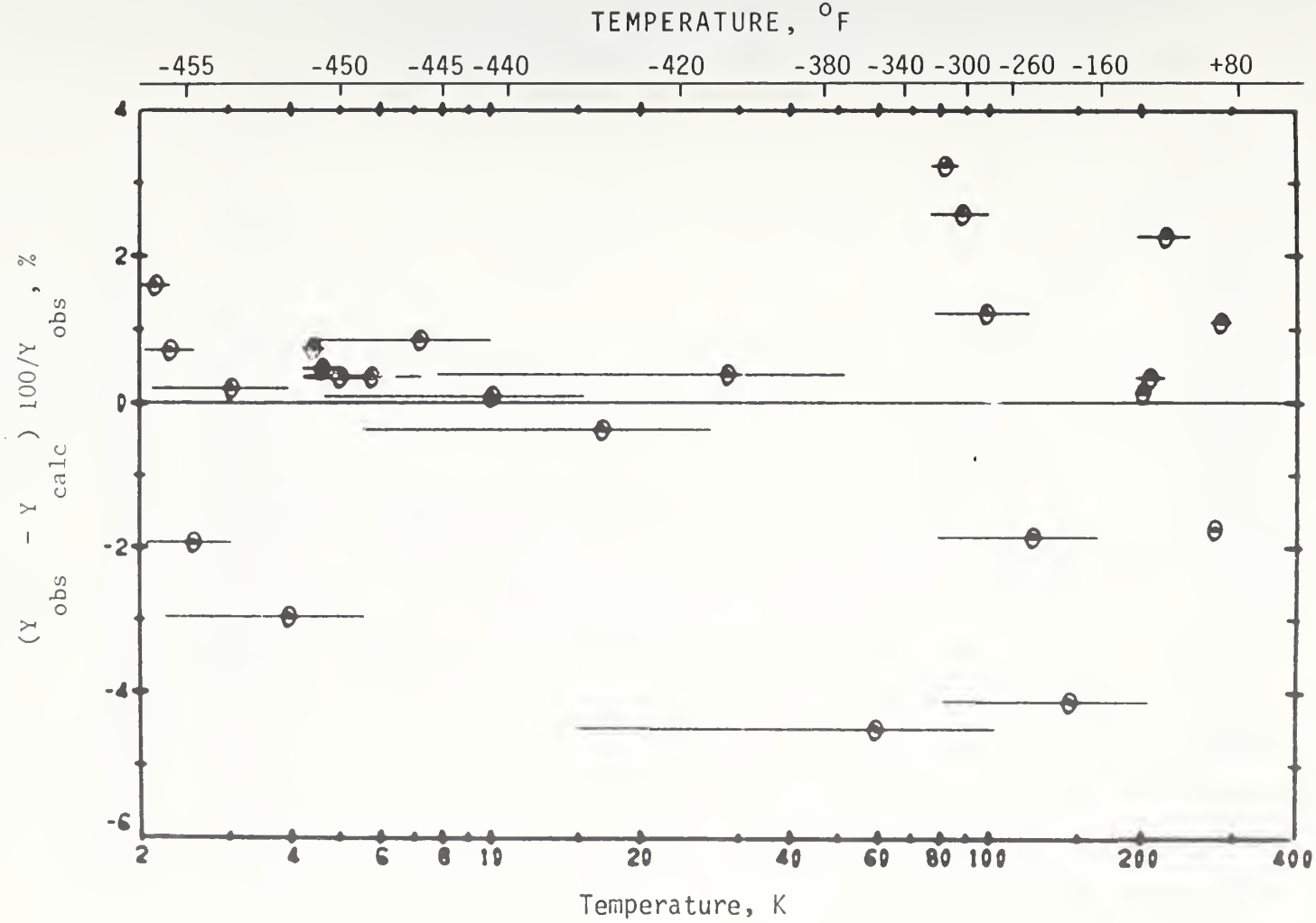

Figure 3. Deviations of observed thermal conductivity integrals (Y) from least squares fit of data for G-10CR (warp direction)

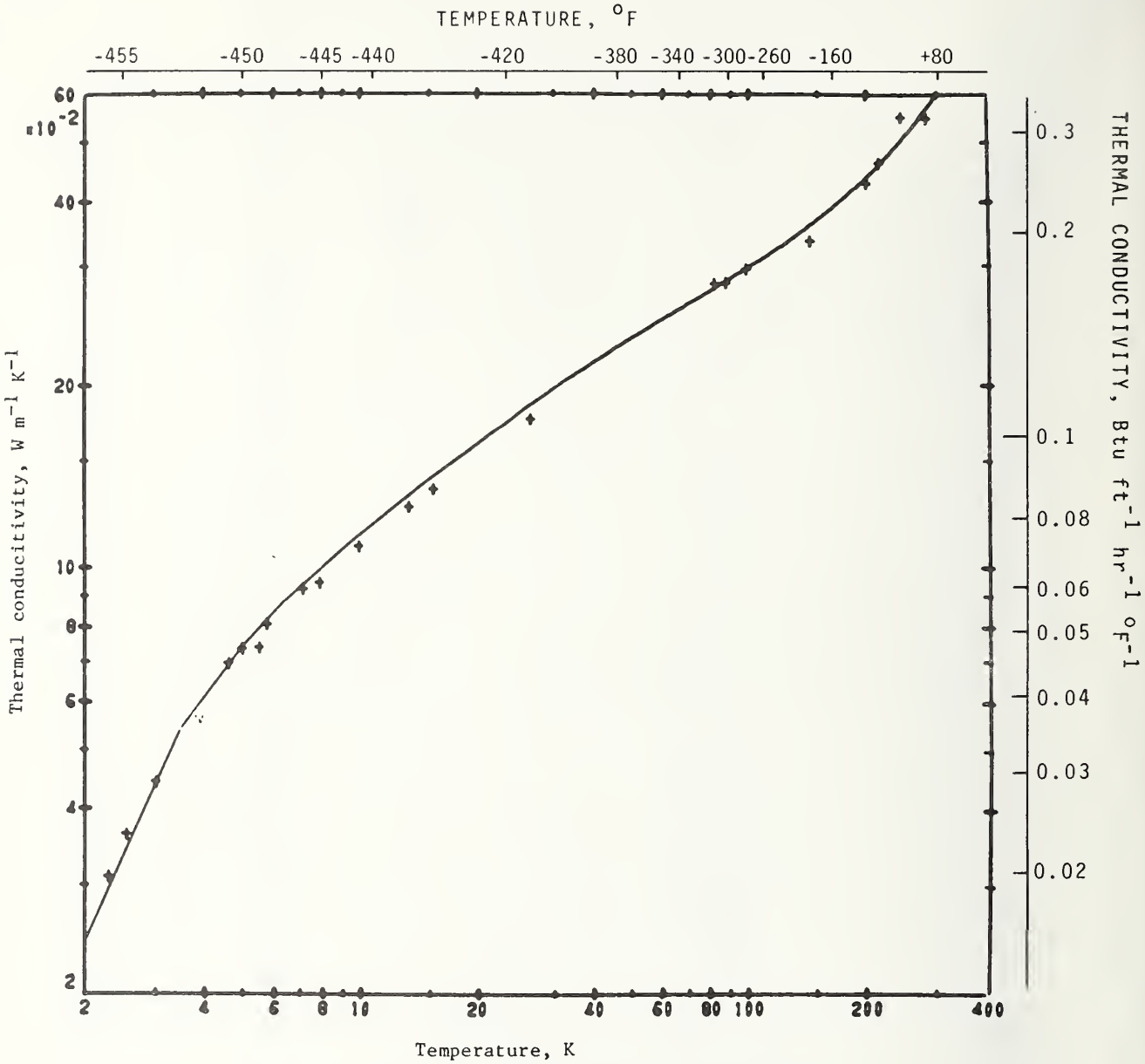

Figure 4. Thermal conductivity values for G-10CR, normal to fabric (+ obtained by difference methods; ----obtained from integral method)

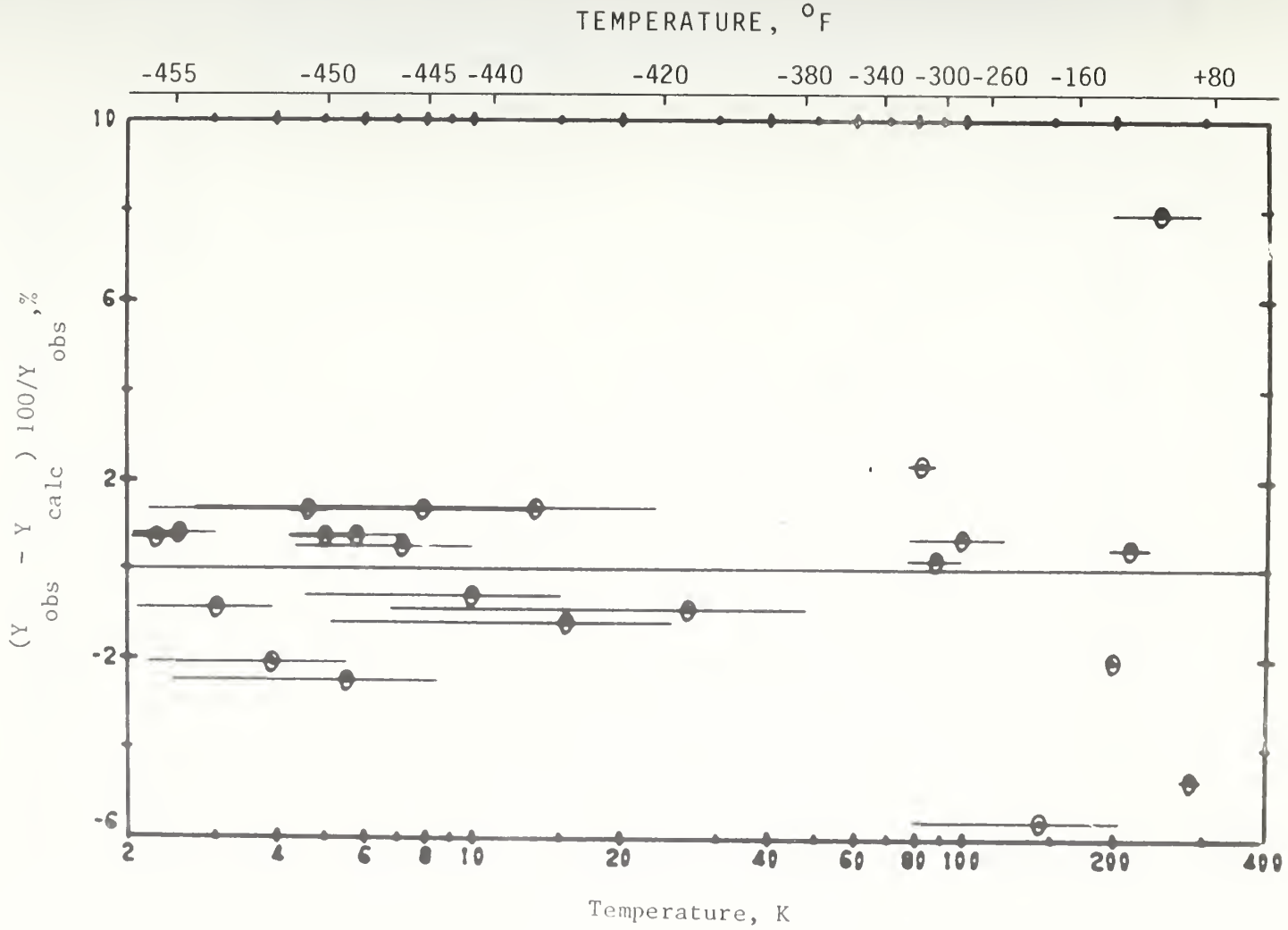

Figure 5. Deviations of observed thermal conductivity integrals (Y) from least squares fit of data for G-10CR (normal to fabric)

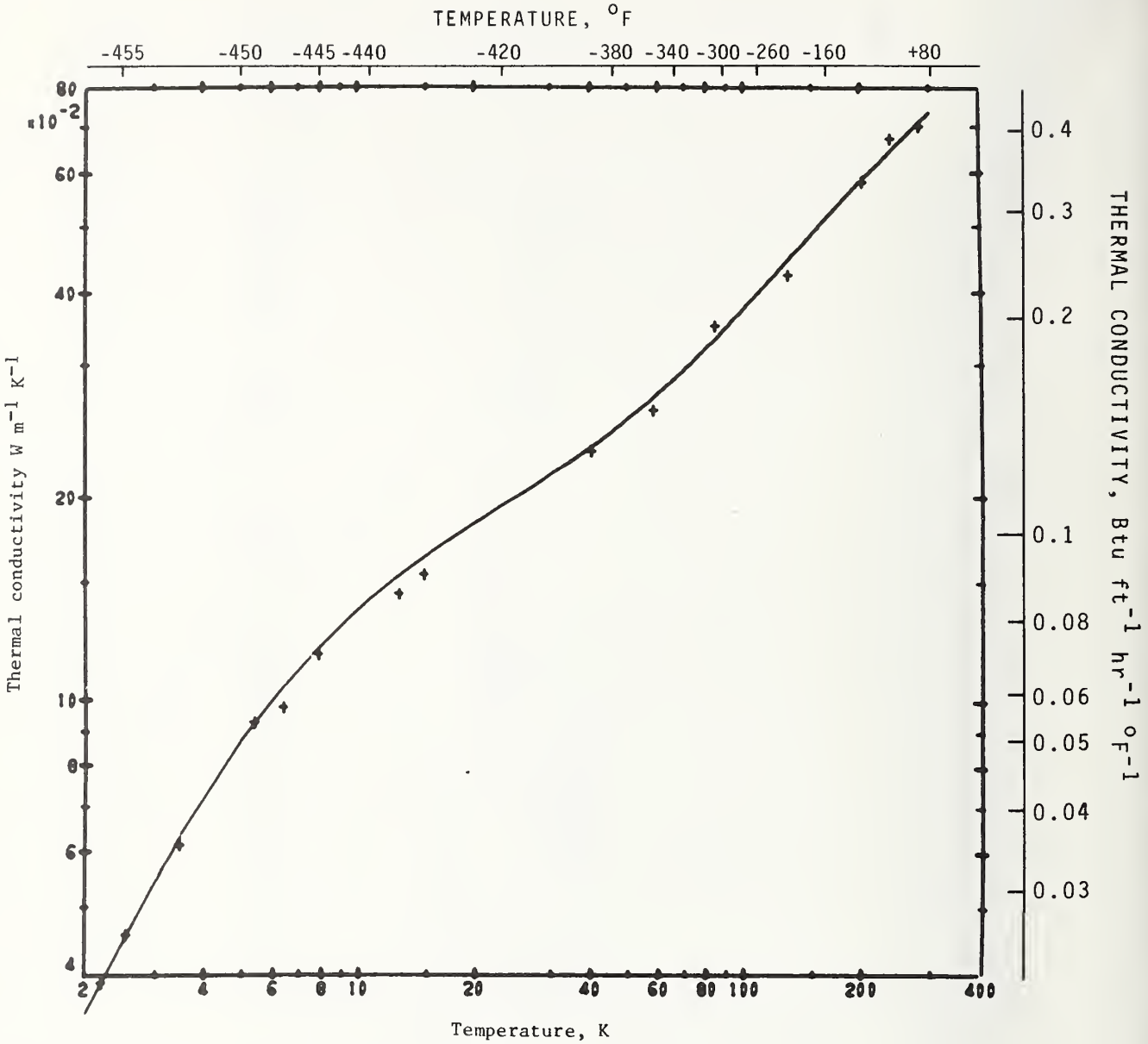

Figure 6. Thermal conductivity values for G-11CR, warp direction (+ obtained by difference methods; ----obtained from integral method)

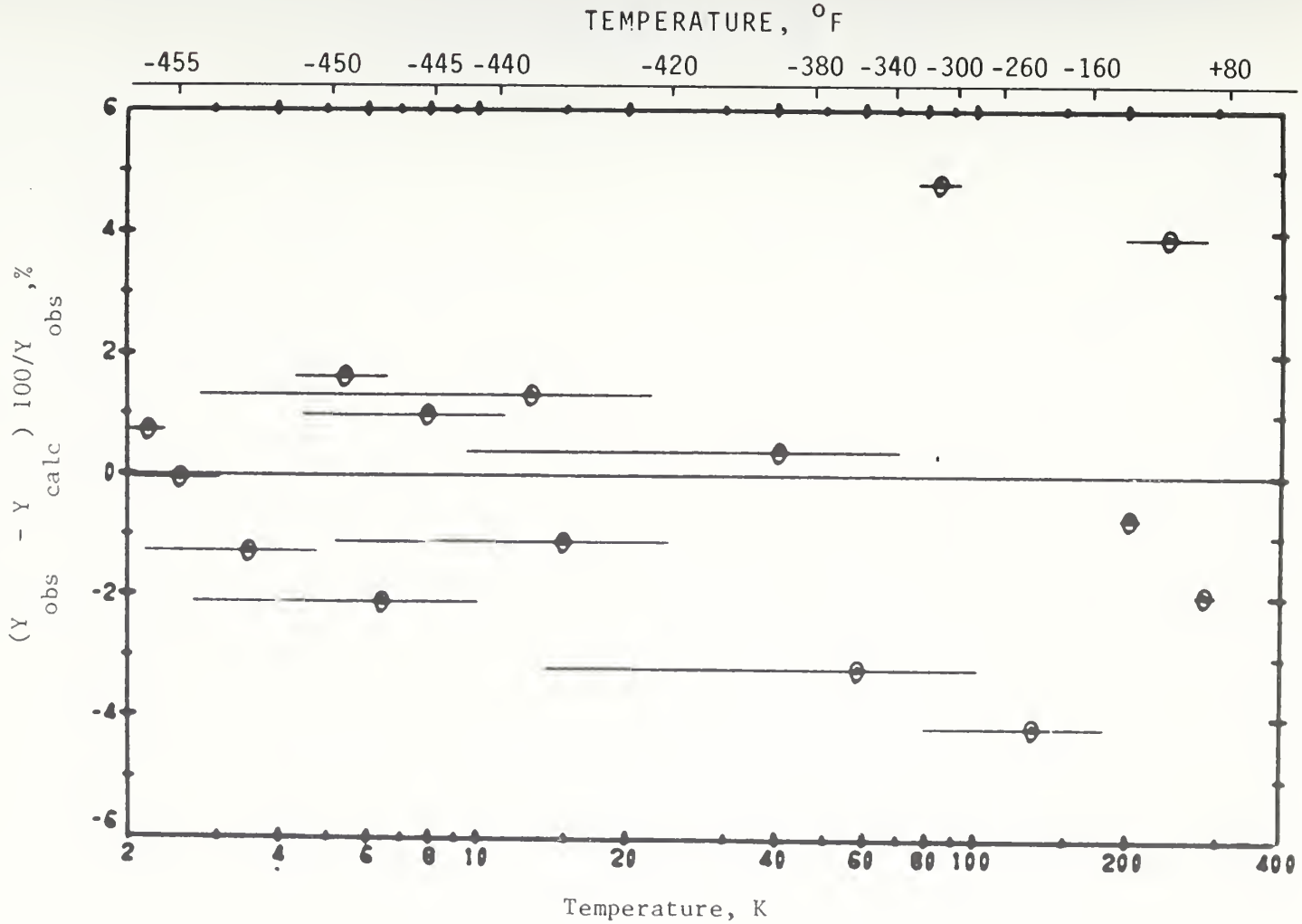

Figure 7. Deviations of observed thermal conductivity integrals (Y) from least squares fit of data for G-11CR (warp direction).

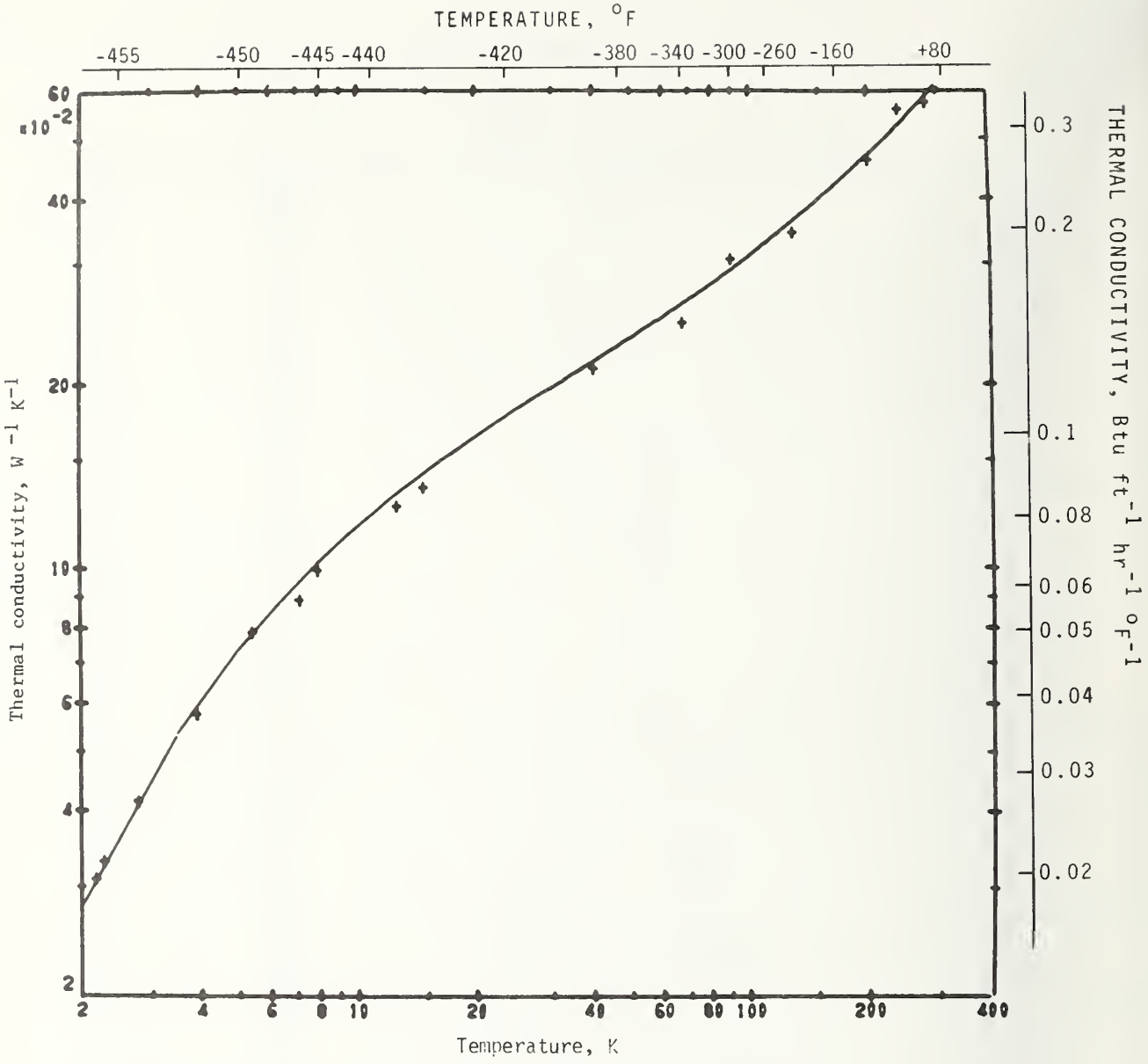

Figure 8. Thermal conductivity values for G-11CR, normal to fabric (+ obtained by difference method; ---- obtained from integral method)

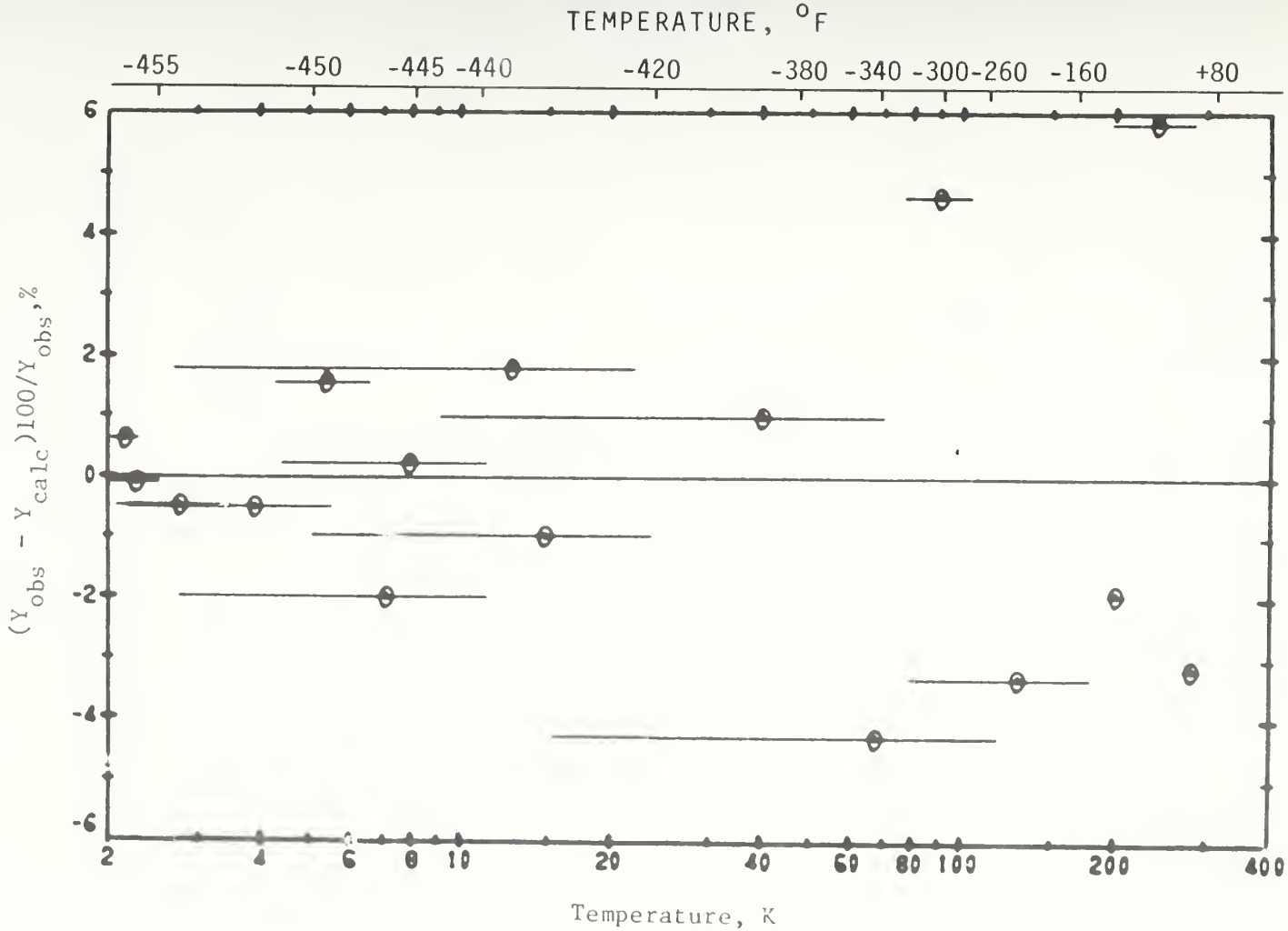

Figure 9. Deviations of observed thermal conductivity integrals (Y) from least squares fit of data for G-11CR (normal to fabric)

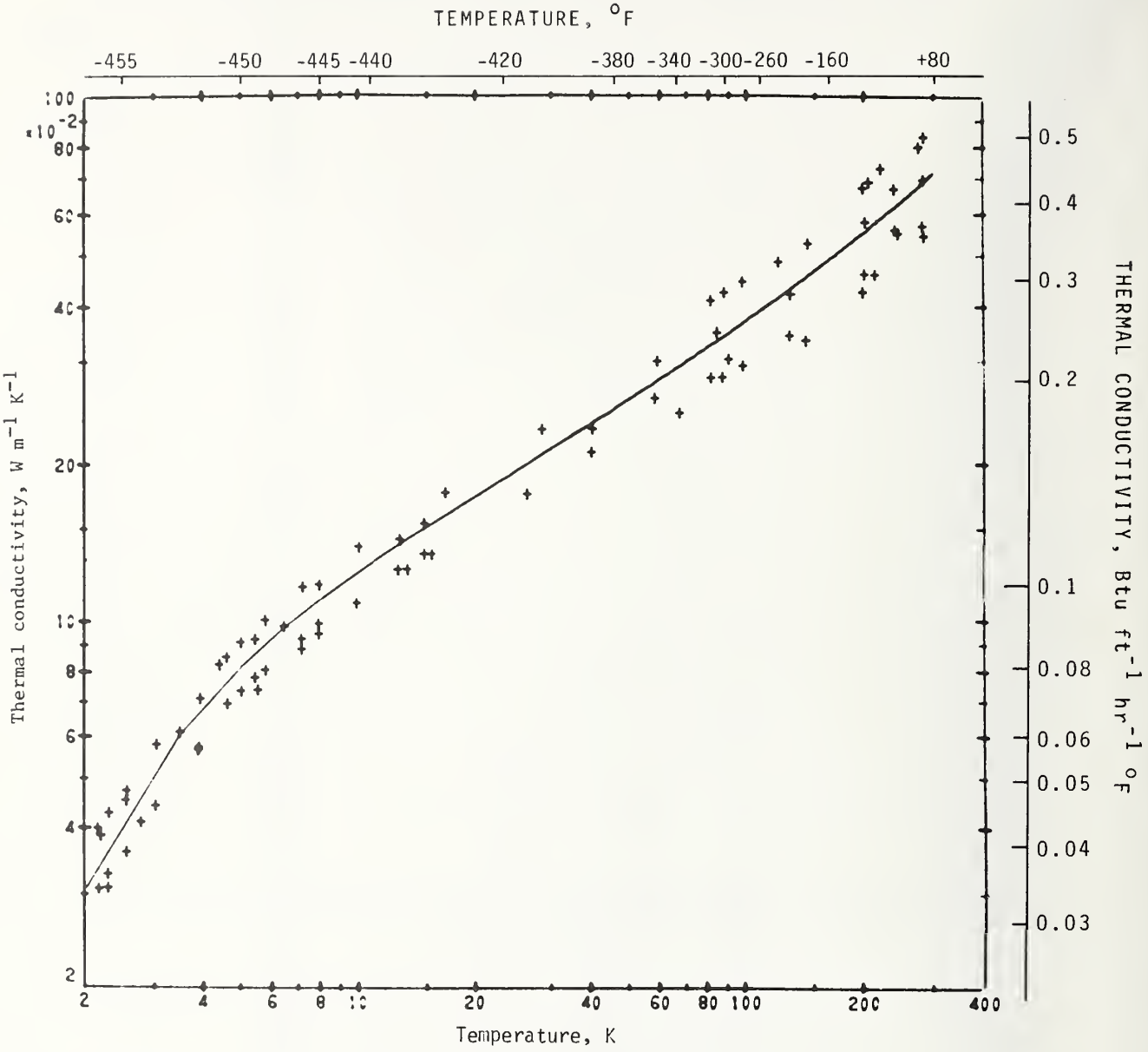

Figure 10. Thermal conductivity values for G-10CR and G-11Cr, both normal and warp directions (+ obtained by difference methods; ----mean values obtained by integral method)

-18-

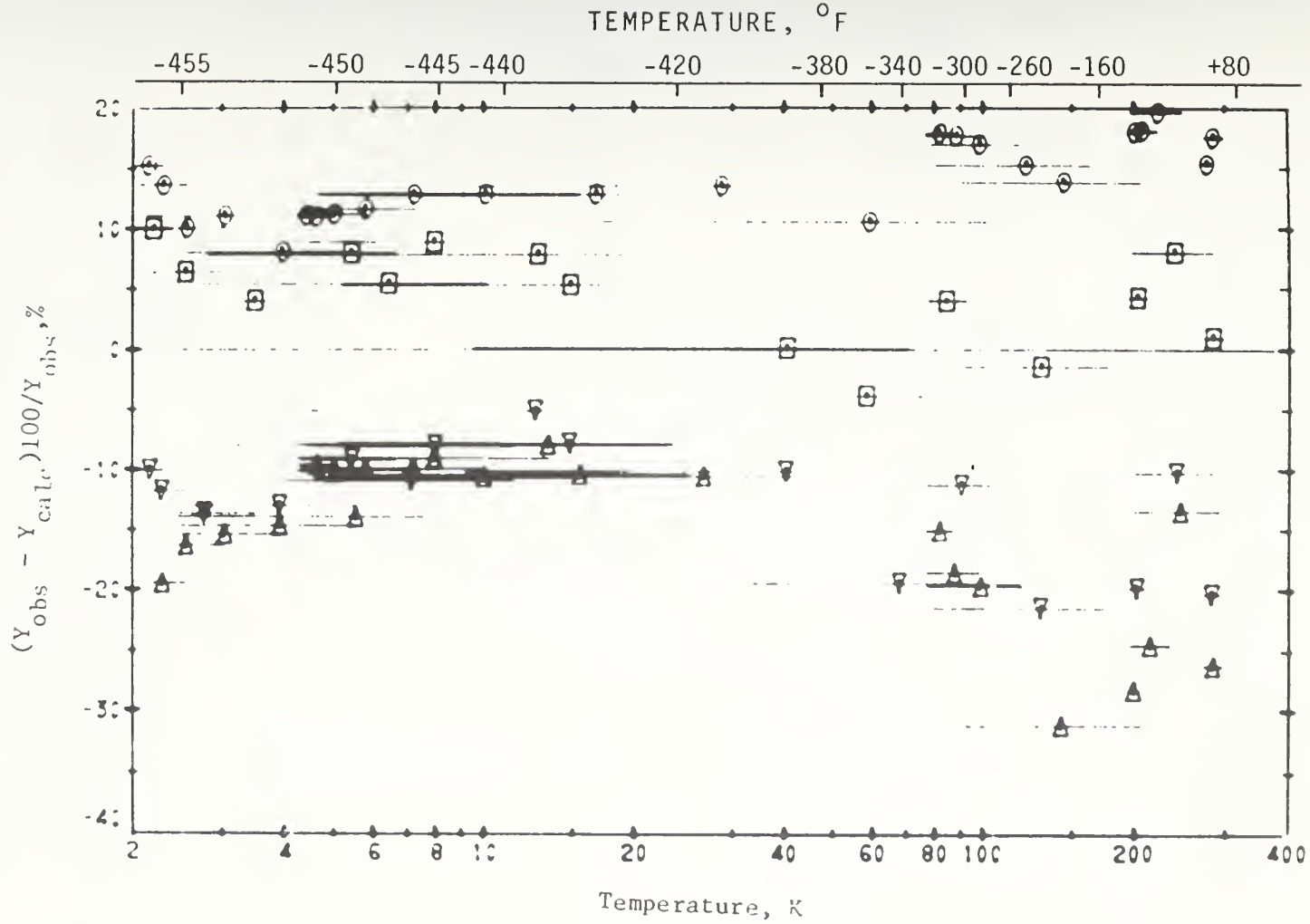

Figure 11. Deviations of observed thermal conductivity integrals (Y) least squares fit of all data on G-10CR and G-011Cr, both normal and warp directions.

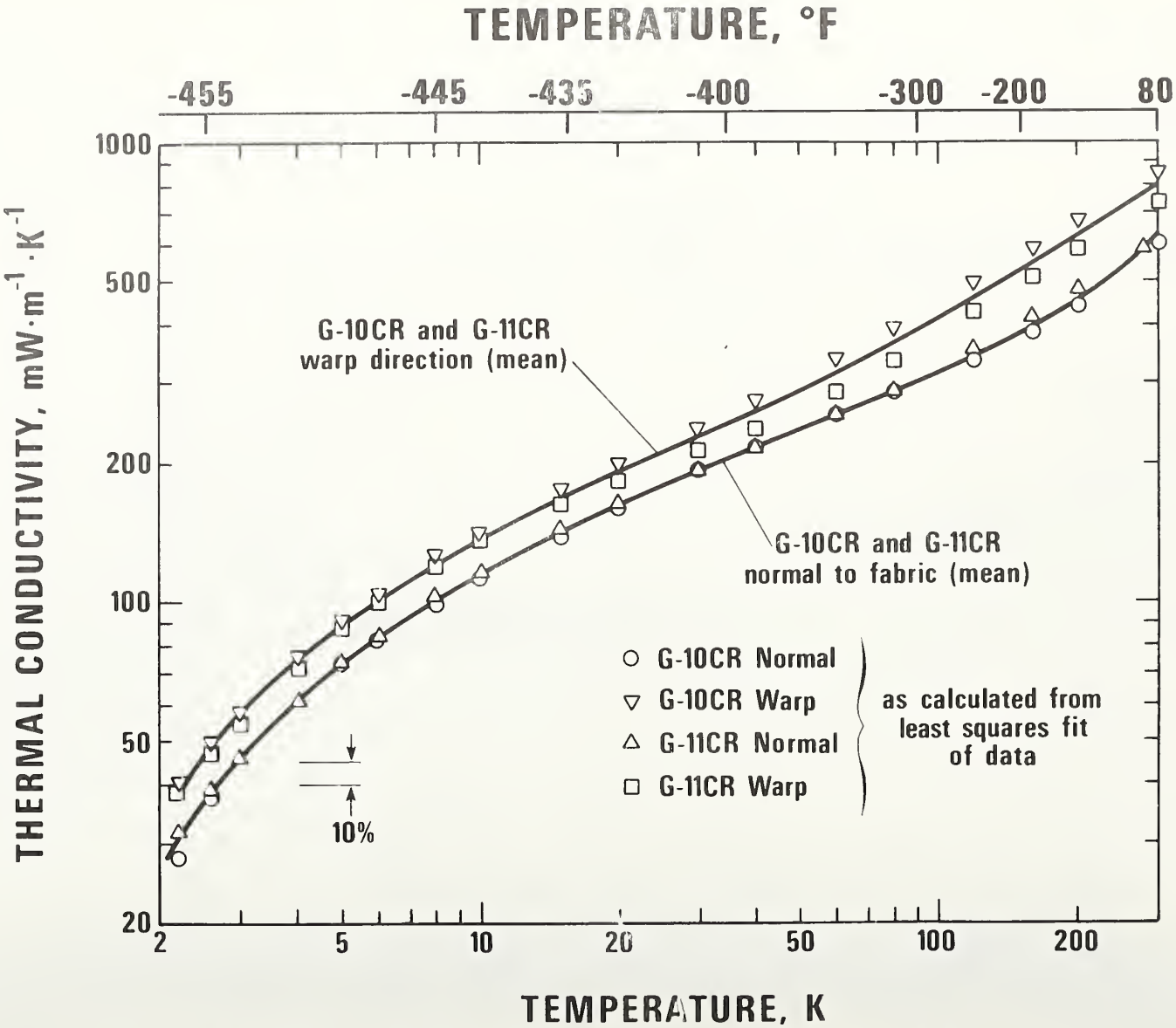

Figure 12. Thermal conductivity from 2 to 300 K of G-10CR and G-11CR in the warp and normal directions.

Dynamic Elastic Modulus and Internal Friction in G-10CR and G-11CR Fiberglass-Cloth-Epoxy Composites*

H. M. Ledbetter

Fracture and Deformation Division, NBS, Boulder, Colorado, USA

ABSTRACT

Young's moduli were determined dynamically for two fiberglass-cloth-epoxy composites in the warp, fill, and normal directions between room temperature and liquid-nitrogen temperature. Dynamic internal friction relates inversely to dynamic modulus in the studied materials. The experimental arrangement consisted of a Marx three-component oscillator at frequencies between 40 and 90 kHz.

Key Words: Composites; elastic constants; glass-epoxy; internal friction; Young's modulus.

*Contribution of NBS, not subject to copyright.

INTRODUCTION

Solid-state elastic constants fill many needs. Engineering design calculations require them for estimating load-deflection and thermoelastic stress. Derived from fundamental interatomic forces, elastic constants index both cohesion and strength. They relate to other physical properties such as specific heat and thermal expansion, all of which help define a solid's equation of state.

A composite's elastic constants serve further purposes. Their accurate measurement permits tests of theories relating composite properties to constituent properties. Their tensor character permits detecting fiber-induced mechanical anisotropy. Elastic constants may also facilitate quality control[1] and incipient-failure detection.[2] For some composites, empirical relationships exist between elastic constants and important mechanical properties.[3]

A composite's internal friction, which is a companion property to the elastic constants, has several possible sources:

1. fiber properties
2. matrix properties
    a. intrinsic (for example, "molecular engineering" in the case of resins)
    b. Extrinsic (for example, fillers)
3. fiber-matrix interface
    a. relative displacement
    b. localized stress
4. cracks and voids

Besides depending on direction, internal friction usually varies with both deformation mode (flexure, torsion, etc.) and frequency. The

present study used an extensional, or Young's-modulus-type, deformation, which has alternating uniaxial tensile and compressive regions with corresponding transverse Poisson contractions or expansions. Internal friction not only characterizes composites, but it may serve to detect incipient failure.[2] In engineering design, higher internal friction improves dimensional stability by minimizing stress-induced deflections.

The presently reported study had two principal purposes. First, apply to composites an experimental technique used previously almost exclusively for noncomposites[4] for determining dynamic Young's modulus and internal friction. Second, determine for G-10CR and G-11CR composites their room-temperature Young's moduli and the change of these moduli with decreasing temperature.

The experimental technique, using a three-component oscillator, offers several possible advantages over static methods: relatively small, simple-geometry specimens; simple and relatively small experimental arrangement, reducing refrigeration costs during cooling experiments; readily obtained one-percent inaccuracies; elastic-constant changes due to temperature, pressure, magnetic field, etc., easily measured to a few parts in 10^5; nearly simultaneous internal-friction measurements. However, the technique does not yield accurate dilatation-type elastic constants, such as Poisson's ratio and the bulk modulus, compared with directly measured shear-type elastic constants such as Young's modulus and the torsional modulus.

EXPERIMENTAL

Materials

Table 1 summarizes studied-material properties. Materials were received as green plates 2.5 cm (1 in) by 20.3 cm (8 in) by 20.3 cm from manufacturer A.

Specimens

The experiments used circular rods, 0.40 and 0.48 cm diameter. Lengths varied from 2 to 5 cm depending on material, fiber orientation, and chosen resonance frequency. Three specimens were studied for each material and orientation.

Elastic-Constant Measurements

Determining Young's modulus, E, required measuring the sound velocity, v, and the mass density, ρ, and using the relationship

$$E = \rho v^2 = \rho f_s^2 \lambda^2 \tag{1}$$

where f_s denotes specimen resonance frequency and λ denotes resonance wavelength. At half-wave resonance, $\lambda = 2l_s$ (where l_s denotes specimen length), and

$$E = 4\rho f_s^2 l_s^2 \tag{2}$$

A Marx[5,6] oscillator (shown schematically in Fig. 1) yielded the experimental resonance frequency according to

$$m_o f_o^2 = \sum_i m_i f_i^2 \tag{3}$$

where m denotes mass, o denotes the complete oscillator, and i denotes oscillator components: quartz-crystal driver, quartz-crystal gage, and specimen. It follows simply from Eq. (3) that

$$f_s^2 = f_o^2 + (f_o^2 - f_q^2)\, m_q/m_s \tag{4}$$

where subscript q denotes quartz crystals. The quartz-crystal length fixes f_q. A maximum voltage V_g, corresponding to a maximum strain amplitude at the gage-crystal midpoint, detects f_o. Sweeping frequency f_q reveals the voltage maximum. Extensional elastic waves were launched along the rod axis by using -18.5° X-cut quartz crystals. Multiplying the right side of Eq. (2) by the well-known Rayleigh factor

$$R = \left[1 + \left(\frac{n\pi\nu d}{4l_s}\right)^2\right]^2 \qquad (5)$$

introduced the necessary short-rod correction, where $n = 2l_s/\lambda$, ν denotes Poisson's ratio, and d denotes either the diameter of circular rods or $d^2 = \frac{2}{3}(a^2 + b^2)$ for axb rectangular rods. Detecting resonance at the first and third harmonics and extrapolating to zero yielded the zero-frequency Young's moduli.

Internal-Friction Measurements

For a sharp, Lorentzian resonance peak (as shown schematically in Fig. 2) the composite oscillator's intenal friction, Q_o^{-1}, is

$$Q_o^{-1} = (f_2 - f_1)/f_o \qquad (6)$$

the resonance-peak width at $1/\sqrt{2}$ of maximum in a strain (proportional to V_g) versus-frequency plot. Equation (6) holds for $\phi = Q^{-1}$ up to 0.1 or 0.2, where ϕ relates the complex, real, and imaginary elastic moduli as shown in Fig. 3. Experimentally one observes M*, the modulus in phase with strain. But one usually seeks M_{real}, the usually more-relevant storage modulus. For zero internal friction, $M_{real} = M^*$.

Similar to Eq. (3),

$$m_o Q_o^{-1} = \sum_i m_i Q_i^{-1} \qquad (7)$$

Thus, a relationship similar to Eq. (4) yields the specimen's internal friction

$$Q_s^{-1} = Q_o^{-1} + (Q_o^{-1} - Q_q^{-1})\, m_q/m_s \qquad (8)$$

RESULTS

Table 2 contains room-temperature and liquid-nitrogen-temperature internal-friction values and Young's moduli at the quartz-crystal resonant frequency (40 to 90 kHz). Table 3 and Figs. 4 and 5 show Young's modulus versus temperature for the two composites.

DISCUSSION

Several observations follow from the results of this study:

1. Young's modulus can be measured more accurately dynamically than statically, as shown by the average dynamic-case uncertainty of 3 percent.

2. Young's-modulus anisotropy, E(max)/E(min), was about two, a surprisingly low value. In-plane anisotropy was even lower.

3. Internal-friction anisotropy was about three. Internal friction was always higher in the normal direction, which tends to sample the matrix. In-plane internal friction was higher in the fill direction than in the warp direction.

4. Higher Young's modulus always corresponds to lower internal friction, and vice versa.

5. All Young's moduli show regular behavior during cooling to 76 K: linearity at higher temperatures, steady increase, continuously decreasing slope, tending toward zero slope at zero temperature.

6. During cooling, Young's modulus changes most in the normal direction and least in the warp direction.

7. Internal friction decreased with low temperatures to a value at 76 K about 10 to 20 percent of its room-temperature value.

ACKNOWLEDGMENT

This study was supported in part by the U.S. Department of Energy. R. E. Schramm and M. B. Kasen furnished materials for study and provided unpublished data. M. Austin and G. Maerz made the measurements.

REFERENCES

1. K. Thomas, D. E. Meyer, E. C. Fleet, and M. Abrams, J. Phys. D. (Appl. Phys.) 6, 1336-1352 (1973).

2. L. E. Nielsen, J. Compos. Mater. 9, 149-156 (1975).

3. A. Vary and K. J. Bowles, NASA Tech. Memo. TMX-73646 (1977).

4. W. H. Robinson, S. H. Carpenter, and J. L. Tallon, J. Appl. Phys. 45, 1975-1981 (1974). References 4-12 therein.

5. J. Marx, Rev. Sci. Instrum. 22, 503-509 (1951).

6. W. H. Robinson and A. Edgar, IEEE Trans. Son. Ultrason. SU-21, 98105 (1974).

7. A. S. Nowick and B. S. Berry, Anelastic Relaxation in Crystalline Solids, Academic, New York (1972), p. 18.

Table 1. Properties of studied materials.

Material	Fiber	Matrix	Mass Density (g/cm^3)	Fiber Volume Fraction
G-10CR	7628 E-glass cloth	bisphenol epoxy	1.90	0.64-0.68
G-11CR	7628 E-glass cloth	bisphenol A, aromatic amine	1.95	0.64-0.68

Table 2. Dynamic Young's moduli, E, and internal friction, Q^{-1}, of G-10CR and G-11CR.

Temp (K)	Direction	G-10CR E(GPa)	G-10CR $Q^{-1}(10^{-4})$	G-11CR E(GPa)	G-11CR $Q^{-1}(10^{-4})$
295	warp	29.5±1.0	68.3±6.6	31.4±0.4	147.0±34.9
	fill	26.8±1.0	114.0±7.8	27.7	161.3
	normal	14.0	228.6	15.6±0.6	406.5
76	warp	34.5	14.6	37.6	33.4
	fill	33.3	17.3	--	--
	normal	21.8	19.6	23.4	--
76/295 dimensionless ratios	warp	1.17	0.21	1.20	0.23
	fill	1.24	0.15	--	--
	normal	1.56	0.09	1.50	--

Table 3. Dynamic Young's moduli of G-10CR and G-11CR at selected temperatures in units of GPa.

Temp	G-10CR warp	G-10CR fill	G-10CR normal	G-11CR warp	G-11CR normal
295	29.5	26.8	14.0	31.4	15.6
290	28.9	27.3	14.5	31.9	15.9
280	29.2	27.8	15.0	32.3	16.3
270	29.5	28.4	15.5	32.7	17.1
260	--	28.9	16.0	33.1	17.6
250	30.2	29.4	16.5	33.4	17.8
240	30.5	29.8	17.0	33.7	18.5
230	30.8	30.2	17.4	34.0	19.0
220	31.1	30.6	17.9	34.3	19.4
210	31.3	30.8	18.1	34.5	19.6
200	31.8	31.5	18.8	34.9	20.1
190	31.0	31.7	19.2	35.1	20.5
180	32.3	32.0	19.7	35.2	20.8
170	32.6	32.2	19.9	35.5	21.1
160	32.9	32.4	20.2	35.8	21.4
150	33.1	32.6	20.5	36.0	21.5
140	33.2	32.7	20.6	36.1	21.6
130	33.5	32.9	21.0	36.4	21.9
120	33.6	32.9	21.2	36.5	22.1
110	33.7	33.0	21.3	36.7	22.4
100	33.9	33.0	21.5	36.9	22.3
90	34.0	33.0	21.6	37.0	22.6
80	34.3	33.1	21.7	37.2	22.7
76	34.5	33.3	21.8	37.6	22.8

Figure Captions

Fig. 1. Marx composite oscillator for determining standing-wave (resonant) sound velocities.

Fig. 2. Forced-vibration Lorentzian-shaped resonance peak. Adapted from Nowick and Berry.[7]

Fig. 3. Complex-plane diagram showing vector relationships among stress, strain, M* = complex modulus, $M_1 = M_{real}$ = storage modulus, $M_2 = M_{imaginary}$ = loss modulus, and ϕ = loss angle = internal friction. Adapted from Nowick and Berry.[7]

Fig. 4. Temperature variation of three principal Young's moduli of G-10CR glass-cloth-epoxy composite.

Fig. 5. Temperature variation of two principal Young's moduli of glass-cloth-epoxy composite.

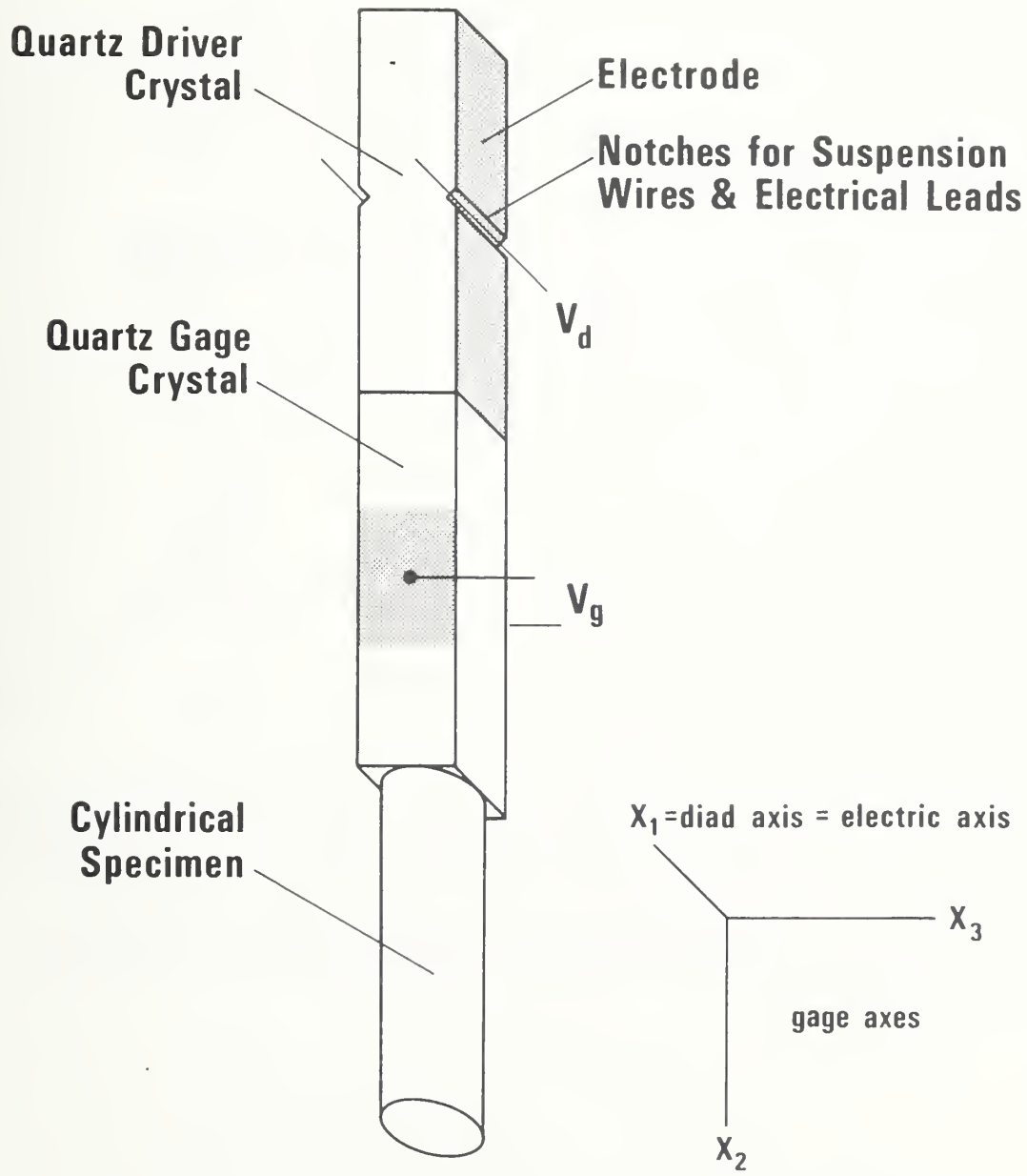

Fig. 1. Marx composite oscillator for determining standing-wave (resonant) sound velocities.

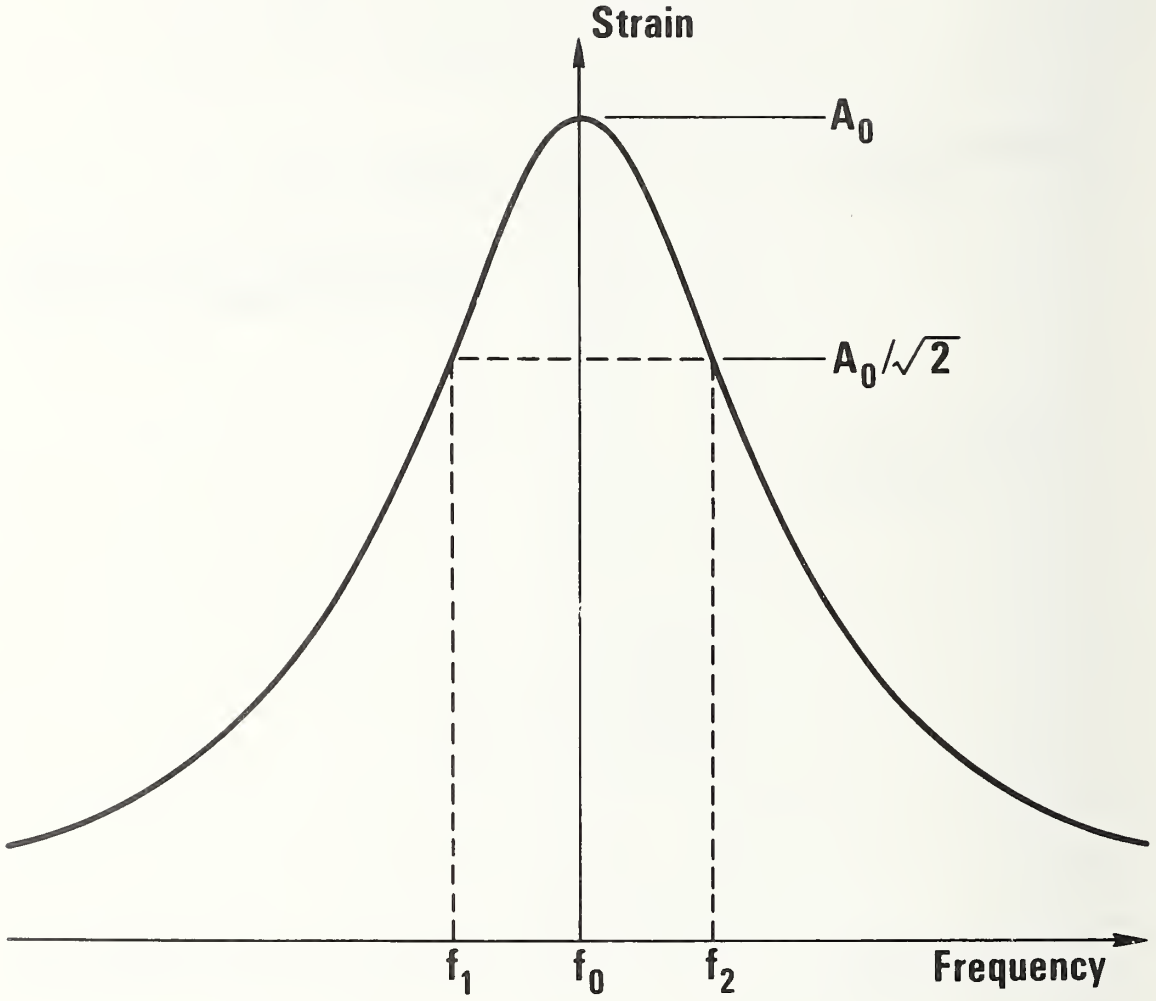

Fig. 2. Forced-vibration Lorentzian-shaped resonance peak. Adapted from Nowick and Berry.[7]

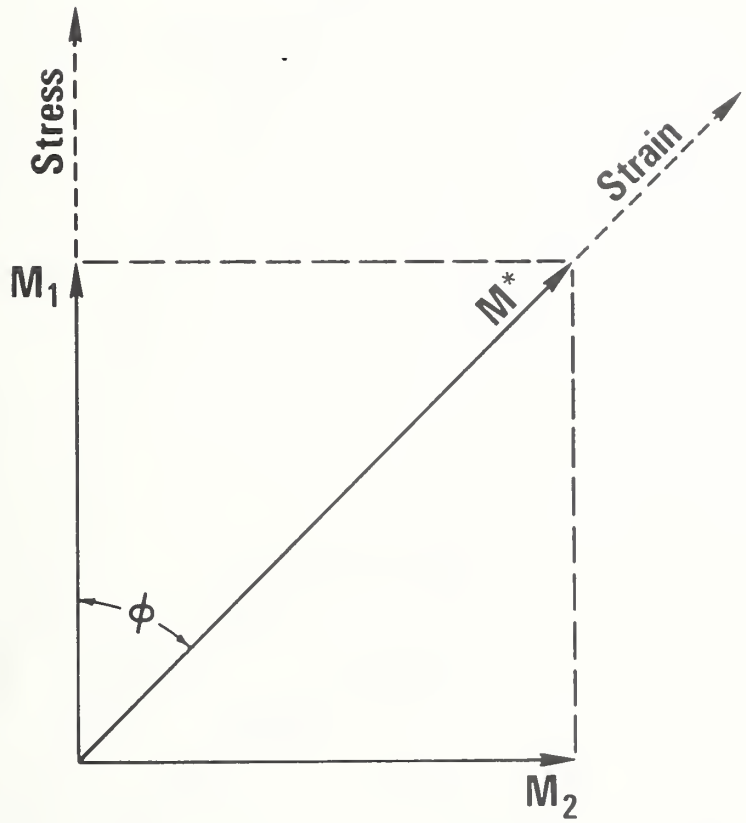

Fig. 3. Complex-plane diagram showing vector relationships among stress, strain, M* = complex modulus, $M_1 = M_{real}$ = storage modulus, $M_2 = M_{imaginary}$ = loss modulus, and ø = loss angle = internal friction. Adapted from Nowick and Berry.[7]

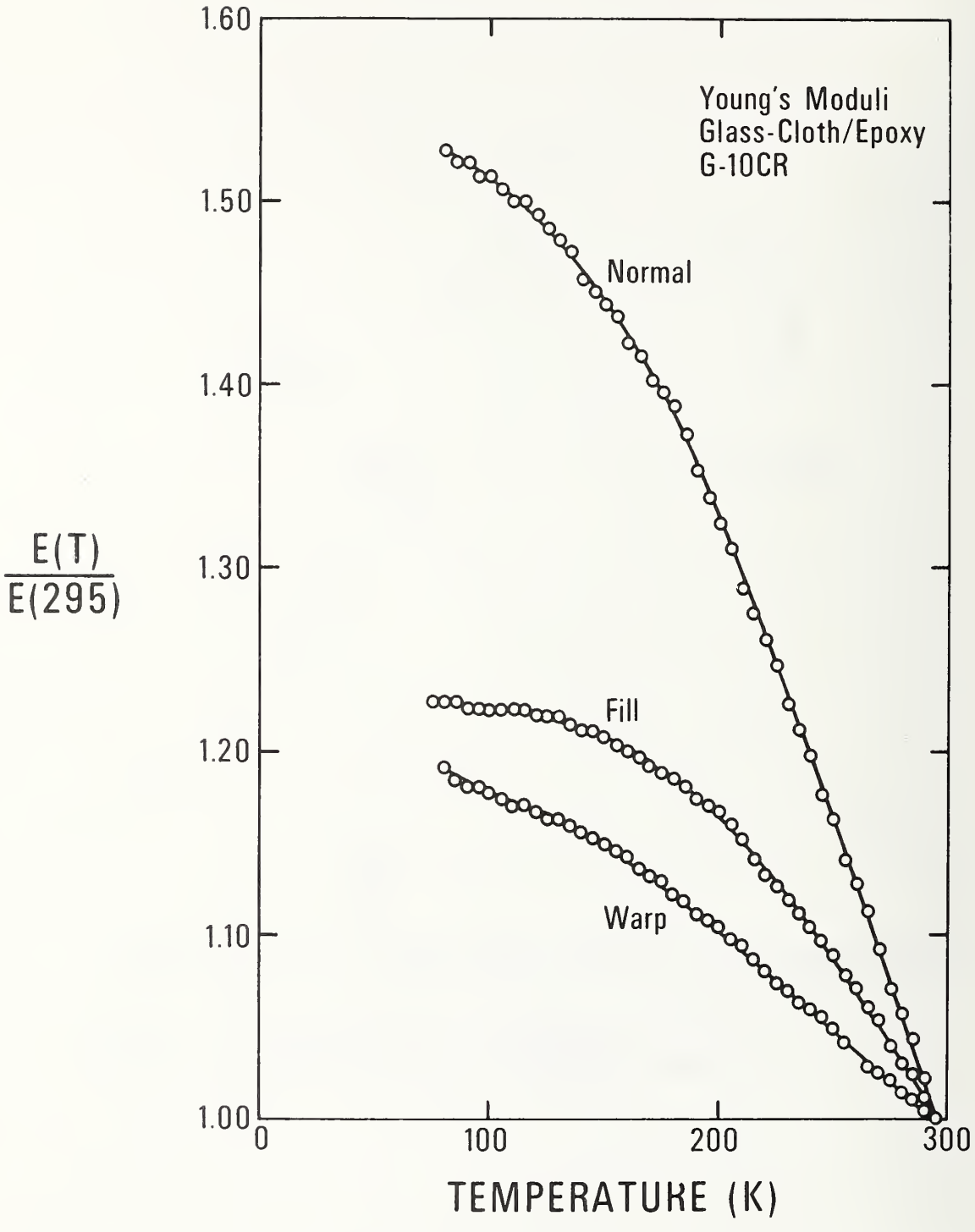

Fig. 4. Temperature variation of three principal Young's moduli of G-10CR glass-cloth-epoxy composite.

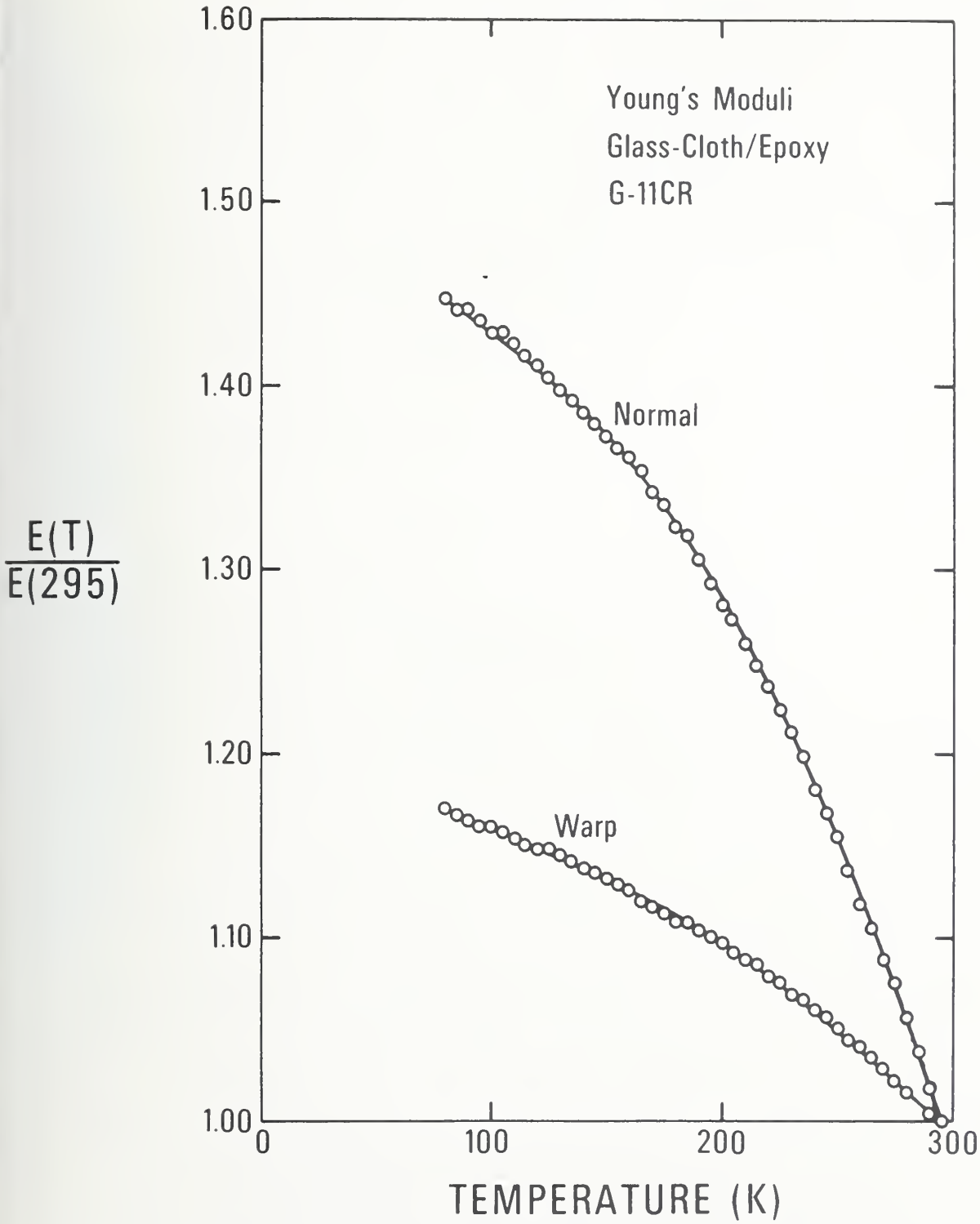

Fig. 5. Temperature variation of two principal Young's moduli of G-11CR glass-cloth-epoxy composite.

Technology Transfer

STRUCTURAL ALLOYS FOR SUPERCONDUCTING MAGNETS IN FUSION ENERGY SYSTEMS

National Bureau of Standards

Structural Alloys for Superconducting Magnets in Fusion Energy Systems*

H. I. McHenry and R. P. Reed
Fracture and Deformation Division
National Bureau of Standards
Boulder, Colorado 80303

*Publication of NBS, not subject to copyright.
Submitted for publication in Nuclear Engineering and Design.

ABSTRACT

The behavior of selected alloys for superconducting magnet structures in fusion energy systems is reviewed with emphasis on the following austenitic stainless steels (AISI grades 304, 310S and 316), nitrogen-strengthened austenitic stainless steels (types 304LN, 316LN and 21Cr-6Ni-9Mn) and aluminum alloys (grades 5083, 6061 and 2219). The mechanical and physical properties of the selected alloys at 4K are reviewed. Welding, the properties of weldments and other fabrication considerations are briefly discussed. The available information suggests that several commercial alloys have adequate properties at 4K and sufficient fabrication characteristics for the large magnet structures needed for fusion energy systems.

Key Words: Aluminum alloys, cryogenics, elastic properties, fabrication, fatigue, fracture, fusion energy, stainless steel, superconducting magnets, tensile properties, thermal properties, welding.

1. Introduction

Alloys will be used for the main structural members of the superconducting magnet systems needed for fusion devices. Designs of tokamak and mirror machines that require superconducting magnets are currently in the conceptual stage (except for MFTF), but many design features that strongly influence materials selection are reasonably well established. The principal features governing alloy selection for structural applications are the enormous size and stored energy of the magnet systems, the extremely high forces exerted by the magnets, the massive structural elements needed to restrain these forces, the limited space available for the structure, and the need for accessability to install and periodically remove the blanket and shield systems--systems that are completely surrounded by magnets and the support structure. These features result in the need for alloys with sufficient strength and stiffness to perform the required structural functions within the space available, sufficient fatigue and fracture resistance to operate safely, and sufficient fabricability to permit manufacture and assembly of the components.

The choice of materials is further restricted by the adverse operating environment of the magnet system. The alloys are subjected to temperatures down to 4K and must not be susceptible to low temperature embrittlement. The presence of high magnetic fields of controlled shape cautions against the use of ferromagnetic materials in certain applications because they would be subjected to higher forces due to the magnetic field and would result in field distortion. The rapid magnetic field changes associated with cyclic operation of the poloidal field coils cause heat inputs to the structure from eddy current losses. Consequently, alloys with high electrical resistivity are usually preferred. The radiation environment eliminates use of alloying elements, such as cobalt, which transmute to long half life products. With this exbeption, radiation does not appear to be a significant factor in the selection of structural alloys because dosage levels sufficient to degrade structural performance probably cause unacceptable deterioration of other system materials. Finally, the microstructure of the material must be stable when exposed to the operating strains, temperature, and radiation; e.g. the martensite transformation in metastable austenitic stainless steels produces a brittle, ferromagnetic phase and the attendant volume expansion causes localized areas of stress concentration.

The constraints on materials selection caused by size requirements, space limitations and operating environment significantly reduce the number of candidate alloys. Further limitations arise due to considerations related to experience, cost and availability. Currently, the leading candidates are the austenitic stainless steels and aluminum alloys. In this paper, the properties of the alloys considered most suitable for liquid helium applications are reviewed with emphasis on their properties at 4K and on their fabrication characteristics relevant to fusion magnet systems.

This review draws heavily on research conducted at the National Bureau of Standards; particularly a three-year program on materials for superconducting machinery sponsored by the Defense Advanced Research Projects Agency (1), a survey of low temperature materials for magnetic fusion energy (2) and a continuing program on materials for fusion energy magnets (3) sponsored by the Office of Fusion Energy of the U. S. Department of Energy. For background relating to the properties discussed the reader is referred to reviews by Fickett (4) on the physical basis for each property and by McHenry (5) on fracture mechanics and its application to cryogenic structures.

2. Annealed Austenitic Stainless Steels

Austenitic chromium-nickel stainless steels, including the nitrogen strengthened grades discussed in more detail in Section 3, are the most widely proposed alloys for structural applications in superconducting magnet systems. These steels have the best combination of strength, stiffness and toughness at 4K. The physical properties also offer advantages over competing materials. Specifically, the modulus is high, the thermal expansion is close to that of the copper-stablized conductor, magnetic permeability is low and the electrical and thermal conductivities are low. The principal disadvantages are the high cost of construction and problems arising from microstructural stability and control.

The AISI 300-series stainless steels, particularly types 304 and 304L, are widely used in cryogenic applications. The designations and

compositions of commonly used grades are summarized in Table 1. These grades have moderate strength, excellent toughness, good fabrication characteristics and are available in a variety of product forms. The ASTM specifications for the various product forms are listed in Table 2. Several 300-series grades not listed in Table 1 are covered by ASTM specifications and can meet ASME Pressure Vesels Code requirements for cryogenic vessels. These grades are not described in this chapter because they offer no particular advantage for superconducting magnet structures and consequently their service experience and property data at 4K are limited.

The alloys listed in Table 1 can be compared with respect to AISI-304, the basic 19Cr-9Ni stainless steel. AISI 316 contains 2-3% Mo and slightly higher nickel and thus has greater austenite stability than AISI 304. AISI 304L and 316L are low carbon modifications of 304 and 316 respectively; low carbon is desirable to avoid sensitization, the grain boundry precipitation of Cr-carbides. Type 310S is a 25Cr-20Ni alloy that has lower carbon (.08%C) than AISI 310 (.25%C). The high alloy content provides austenite stability and greater strength and thus 310S is useful where dimensional stability, non-magnetic behavior and higher strength are desireable.

The low temperature properties of the 300-series austentitic stainless steels have been compiled in cryogenic handbooks (6,7), in a review article by Brickner and Defilippi (8) and in suppliers publications (9,10). In this section, the general trends in strength, toughness and fatigue resistance are summarized as a function of temperature. Care should be taken in using the data presented here or in data compilations because there are significant heat-to-heat variations in the mechanical properties of the 300-series stainless steels, particularly in the yield strength and toughness. The principal causes of these variations are interstitial content, i.e. carbon and nitrogen, and mechanical deformation history, i.e. resulting grain size. The influence of nitrogen within the limits of 0 to 0.08 weight percent is particularly significant with the higher nitrogen contents causing substantial increases in yield strength.

2.1 Tensile Properties

The yield and ultimate strengths of AISI grades 304, 310 and 316 are compared in Figure 1 for temperatures ranging from 4 to 300K. Notice that type 304 has the lowest yield strength and the highest ultimate strength at all temperatures. This is due in part to the martensite transformation which occurs more readily in 304 than in 316 or 310. Since the transformation is strain induced, the yield strength is not significantly influenced by martensite, but the ultimate strength is increased.

The yield and ultimate strengths of AISI grades 304 and 304L are compared in Figure 2. Type 304 exhibits a slightly greater increase in strength than type 304L as temperature is reduced. The loss of strength associated with reduced carbon content is considered to be characteristic of all the stainless steels, i.e. 304L vs 304, 316L vs 316 and 310S vs 310, and is attributed to the strengthening effect of carbon.

The ductility of the annealed 300-series stainless steels is generally excellent at cryogenic temperatures. Elongation and reduction-of-area tend to drop with decreasing temperatures, but values generally exceed 30%.

2.2 Toughness

The austenitic stainless steels retain excellent toughness at cryogenic temperatures. The Charpy V-notch impact toughness does decrease with temperature but in all cases known to the authors the toughness far exceeds the 0.38mm lateral expansion requirement of the ASME Boiler and Pressure Vessel Code (11) and a ductile-to-brittle transition is not exhibited. The minimum temperature for Charpy testing is about 20K, becaure adiabatic heating causes specimen temperatures in excess of 20K even when the test temperature is 4K.

Slow-strain-rate tests using notched tensile specimens indicate that notch sensitivity does not develop at 4K (6). The data summarized in Figure 3, indicate that the notch-to-unnotched ratio of tensile strengths is approximately equal to 1 and the ratio of notched tensile strength to unnotched yield strength generally exceeds 2.

Tobler (12) used J-integral methods to measure the fracture toughness of AISI grades 310 and 316 at temperatures to 4K. The toughness, $K_{Ic}(J)$, at 4K is 230 MPa $\sqrt{m}$ for 310S and 460 MPa$\sqrt{m}$ for 316, and in both alloys the toughness at 4K exceeds the toughness at room temperature. The ratio of toughness to yield strength is sufficiently high to assure gross ductile deformation prior to fracture.

2.3 Fatigue

Strain cycling fatigue properties at 300, 76 and 4K have been measured for AISI grades 304L and 310 by Nachtigall (13) and for grades 304L and 316 by Shepic and Schwartzberg (14). The results for 304L which were essentially the same in both investigations and for 316 are shown in Figure 4. The fatigue resistance of 310 and 316 were superior to that of 304L, particularly in low cycle fatigue (less than 10^4 cycles). For each alloy, the fatigue resistance at low temperatures is superior to the fatigue resistance at room temperature except at the highest strain ranges where failure occurred in less than 1000 cycles.

The fatigue crack growth behavior of AISI grades 304, 304L, 310S and 316 has been determined at 295, 76 and 4K by Tobler and Reed (15). The data for 304L are shown in Figure 5. Notice that the growth rates are essentially the same at 76K and 4K; similar behavior was observed in each of the other alloys. Also, the growth rates at 76K and 4K are slower than those at room temperature. The best-fit lines through the 304L data at 295K and at 76K and 4K form the approximate scatter bands for the data on 304, 310S and 316 at 295, 76 and 4K. Thus, it can be concluded that alloy content and temperature have minimal influence on the fatigue crack growth behavior of the 300-series stainless steels.

2.4 Physical Properties

The physical properties of the 300-series stainless steels at 295, 76 and 4K are summarized in Table 3. The thermal properties have been taken from the best-fit lines used in the LNG Materials Handbook (7), and the original sources are given for the elastic properties (16), electrical resistivity (17) and magnetic permeability (18).

3. Annealed Nitrogen-Strengthened Austenitic Stainless Steels

Nitrogen has a pronounced effect on the yield strength of austenitic stainless steels, particularly at cryogenic temperatures. For example, the yield strength of 304N (AISI 304 with deliberate additions of nitrogen) is approximately three times greater than the yield strength of 304 at 76K, the ultimate strengths are approximately equal and the elongation of the 304N is superior at temperatures below 220K (20). This remarkable improvement in mechanical properties occurs in many nitrogen strengthened grades. Consequently, significant interest is developing in these alloys for future applications in superconducting magnet systems.

The designations and compositions of the commercially available grades that offer promise for liquid helium applications are summarized in Table 4. Several other nitrogen strengthened grades have been developed and are covered by ASTM specifications such as A240 and A412. However, the availability and property data on these grades are limited. Several additional grades are commonly used in Europe where nitrogen is deliberately added to several of the common Cr-Ni 300-series stainless steels. The equivalent AISI designations for these European grades are 304LN and 316LN.

Two basic types of nitrogen strengthened stainless steels are suitable for cyrogenic service: the Cr-Ni-N and the Cr-Ni-Mn-N alloys. The Cr-Ni-N alloys are 300-series stainless steels with deliberate additions of nitrogen. In the U.S. specifications, the nitrogen range is 0.10 to 0.16% for 304N and 316N. The corresponding European specifications permit nitrogen levels to 0.25%. The manganese in Cr-Ni-Mn-N alloys

provides austenite stability and can thus be used to replace part of the Ni content. Manganese also increases the solubility of nitrogen in austenite and thus permits higher nitrogen levels-0.4% maximum nitrogen is typical.

3.1 Tensile Properties

The yield and ultimate strengths of the Cr-Ni-N 300-series stainless steels are summarized in Figure 7. The solid lines and the broken lines represent the data of Randak et al.(21) for 304LN and 316LN, respectively. The various symbols depict the data for seven other investigations (20,22-27), each on one of the following alloys: 304LN, 304N and 316LN. As is the case for 304 and 316, Figure 1, alloys 304N and 304LN have approximately 20% greater ultimate strength at cryogenic temperatures than alloy 316LN. All three alloys have essentially the same yield strength at and below room temperature. There is relatively little scatter in the yield strength data considering that data on 17 heats from a variety of sources are plotted. The nitrogen contents of the 17 heats range from 0.09 to 0.17%.

Of the four nitrogen-strengthened Cr-Ni-Mn stainless steels listed in Table 4, the 21Cr-6Ni-9Mn alloy has been most thoroughly evaluated (28-32). The tensile and yield strength data are summarized in Figure 6. This alloy typically has about 25% greater yield strength than the Cr-Ni-N alloys. Representative tensile data on the other N-strengthened Cr-Ni-Mn alloys that have been tested at 4K indicate that yield strength increases and ductility decreases with decreasing temperature; and thus, fracture resistance must be considered when selecting these alloys for liquid helium service.

3.2 Toughness

The N-strengthened stainless steels have excellent toughness at room temperature. However, as shown in Figure 8, significant toughness losses generally occur as the temperature is reduced (25). Read and Reed (25) observed significant variations in the toughness of a single piece of

21Cr-12Ni-5Mn alloy. As received mill-annealed material having an intergranular micro-constituent had a plane strain fracture toughness at 4K at 111 MPa$\sqrt{m}$. A high temperature (1177 C, 1.5 h) anneal dissolved the micro-constituent and increased the toughness to 176 MPa$\sqrt{m}$. Thus, certain N-strengthened grades can be used at 4K, but care should be taken to assure that the alloy selected has satisfactory toughness at 4K for the applicable melting practice, product form and heat treatment.

3.3 Fatigue

The strain cycling fatigue behavior of 21Cr-6Ni-9Mn has been measured at 295, 76 and 4K by Shepic and Schwartzberg (14). The results at 4K, shown in Figure 4, indicate that the 21Cr-6Ni-9Mn alloy has fatigue strength better than 304L but not as good as 316. Thus, the significantly higher strength of the N-strengthened grade does not result in a comparable improvement in fatigue life.

The fatigue crack growth behavior of several N-strengthened grades has been studied at cryogenic temperatures (25,28). The results for the high nitrogen Cr-Ni-Mn alloys depend largely on the relative austenite stability of the alloys. For the least stable alloy evaluated, 18Cr-3Ni-13Mn, the fatigue crack growth rates at 4K are 50 times faster than those for the most stable alloy evaluated, 21Cr-12Ni-5Mn, and 10 times faster than the growth rates for 21Cr-6Ni-9Mn. For the 21Cr-12Ni-5Mn alloy, the fatigue crack growth rates fall within the same scatter band as the 300 series ($N < .08\%$) alloys at 4K. For the Cr-Ni alloys, comparison of 304 and 304L with 304N and 304LN shows that the nitrogen-strengthened alloys have growth rates at 4K about 4 to 5 times higher than the lower nitrogen grades. In contrast, the 316 alloy, which has greater austenite stability than 304, has essentially the same growth rates at 4K as the 316LN alloy.

3.4 Physical Properties

In general, the physical properties of the N-strengthened stainless steels are similar to the 300-series alloys as summarized in Table 3. In general, the nitrogen contributes to austenite stability and thus reduces the magnetic permeability induced in some alloys by deformation at low temperatures. Anamolous behavior has been observed in high manganese

alloys by Ledbetter (33) in the elastic behavior and by Ledbetter and Collings (34) in the magnetic susceptibility.

4. Fabrication Characteristics of Austenitic Stainless Steels

The fabricability of austenitic stainless steels is certainly sufficient for fusion magnet systems as attested by the widespread use of stainless steels in a variety of industries. Fabrication characteristics that should receive special consideration for fusion magnet applications are briefly reviewed in this section.

4.1 Welding

The austentitic stainless steels, with and without nitrogen strenthening, are readily weldable by all of the common welding processes, providing the appropriate consummables and procedures are used. The service experience with welded assemblies of the alloys has been satisfactory at cryogenic temperatures. The American Welding Society, AWS, designation system, which is similar to the AISI system for wrought products, is generally used to classify stainless steel filler metals. The AWS designations and chemical compositions of the filler metals commonly used for cryogenic applications are summarized in Table 5. The strength of stainless steel welds at 4K generally exceeds the corresponding base metal strength, but toughness is usually significantly lower. Three phenomena that affect the strength and toughness of the as-deposited weld metal take on added significance at cryogenic temperatures: sensitization, ferrite content and nitrogen pickup. In addition, heat treatment generally has a stronger influence on the weld metal than the base metal.

Sensitization, the grain boundry precipitation of Cr carbides reduces weld metal toughness at low temperatures (35). Consequently, weld metals with extra low carbon, such as 308L and 316L, are commonly used for cryogenic applications. Sensitization is most extreme if the weldment is given prolonged exposure in the temperature range of 500 to 800C. However, the underlying weld beads in multipass weldments may receive sufficient exposure to these temperatures to cause significant toughness reductions in stainless steels with greater than 0.03% carbon.

Subsequent annealing of the welds at temperatures greater than 950C dissolves the carbides and improves the toughness.

The ferrite content of as-deposited weld metals can be estimated by using the Schaeffler constitution diagram. To avoid microfussuring the weld metal chemistry is generally balanced to provide 4 to 10% ferrite. However, for cryogenic service, there is concern that the ferrite, which is a bcc phase and therefore brittle at low temperatures, may embrittle the weld metal. Szumachowski and Reid (36) have shown that ferrite reduces toughness at 76K for a wide range of stainless steel weld metals. Read, McHenry and Steinmeyer (35) have evaluated the effect of ferrite content on the fracture toughness of shielded metal arc welds of AWS 316L; the results at 76K and 4K are shown in Figure 9.

Nitrogen increases the yield strength and decreases the toughness of stainless steel weld metals. When conventional (low N) filler metals are used, nitrogen variations in the range 0.04 to 0.13% may occur depending on the amount of air which enters the arc shielding medium. The greatest variations in N-pickup are associated with gas metal arc welding where the N content ranges from 0.04 to 0.13% depending on the type of gas coverage and the electrode stickout. Smaller variations are attributed to electrode coatings; lime coatings generally give better coverage and less N pickup than titania coatings.

4.2 Heat Treatment

One of the principal advantages of annealed austenitic stainless steels is that heat treatment is generally not required. The possible exceptions are annealing at 1000 to 1100C following severe forming operations and stress relief at 420 to 480C to reduce peak residual stresses and improve dimensional stability.

Heat treatment of stainless steel welds has been studied by Bennett and Dillon (37) for AWS types 308, 308L and 310. Heat treating or slow cooling in the sensitization range causes significant toughness loss at

76K in types 308 and 310, but does not affect 308L. Stress relieving at 840C followed by furance cooling causes about a 50% toughness loss in each alloy (20-32J as-welded and 8-20J stress-relieved). Stress relieving at 950C followed by furnace cooling caused a 50% toughness loss in 310, no change in 308L and mixed results (± 40% toughness change) in 308. Annealing at 1070C followed by water quenching improved the toughness of 308 and 308L, but decreased the toughness of 310. The beneficial effect of a full anneal on toughness at 76K has also been reported by Krivobok and Thomas (38), McConnell and Brady (39) and DeLong (40).

4.3 Castings

The austenitic stainless steels are widely used for manufacturing corrosion resistant castings. The casting alloys equivalent to AISI types 304 and 316 are ACI (Alloy Casting Institute) types CF8 and CF8M respectively. The ferrite content of these alloys may vary from 0 to 40% due to chemistry variations within the allowable ranges. Ferrite levels in this range are likely to be unacceptable because of low fracture toughness and high permeability. Ferrite-free castings require use of higher nickel content alloys such as ACI grades CK 20 (corresponding to AISI grade 310). A 16Cr-20Ni-10Mn-2.2Mo alloy has been used for liquid hydrogen (41) and liquid helium bubble chambers (42,43); the alloy retains excellent strength (550 MPa yield strength) and ductility at temperatures to 2.5K (43).

4.4 Machining, Forming and Forging

Machining: Annealed austenitic stainless steels are more difficult to machine than carbon steels or aluminum alloys because of their relatively high tensile strength, work hardening rates, and low thermal conductivity. These properties cause poor finishes, heat buildup and excessive tool wear. As a result, it is necessary to use heavier feeds, slower speeds, better quality tool bits, more rigid machines and more power.

Forming: The candidate stainless steels have excellent formability. Alloys with more austenite stability than types 304 or 316 may be needed if severe forming operations are required. The nitrogen-strengthened

21Cr-6Ni-9Mn alloy is reported to have excellent austenite stability; even after 60% reduction at room temperature, the permeability is less than 1.02 (44).

Forging: The austenitic stainless steels can be forged into shapes suitable for many magnet applications, e.g. forged pancake billets for ring rolling coil forms. Stainless steels are more difficult to forge than most common structural alloys because of their high strength at elevated temperatures. Within the family of austenitic stainless steels, the forgeability of types 304 and 316 is rated good (45).

4.5 Inspection

During fabrication of fusion magnet systems, the stainless steel material and components are likely to be inspected using conventional methods. The only problem peculiar to the proposed designs is the need for heavy-section stainless steel welds. These welds cannot be effectively inspected for the presence of cracks or crack-like defects. Radiography is of limited use because of its inability to reliably detect cracks. Ultrasonic methods do not work effectively because of the high noise levels and large and variable attenuation arising from the large-grain-size welds. Standards are needed to assure that the defect sizes that can be reliably detected do not adversely affect structural integrity.

5. Aluminum Alloys

Aluminum alloys have been proposed for many structural applications in fusion magnet systems. Their princhpal advantages are: low as-fabricated cost, light weight, non-magnetic behavior, stable microstructure, and good retention of strength and toughness at cryogenic temperatures. The main disadvantages of aluminum alloys are low strength in weldments, high electrical and thermal conductivity and an unfavorable elastic modulus (too low) and thermal expansion (too high) for many applications.

For fusion magnet structures, the preferred aluminum alloys are 5083, 2219 and 6061. The composition ranges for these alloys are summarized in Table 6. Alloy 5083 is generally used in the annealed condition (5083-0) and has a typical yield strength of 171 MPa (25 ksi) at 4K. Alloy 2219 is generally used in a heat treated condition (T 851, T 87 etc.), and in the T 851 temper has a typical yield strength of 482 MPa (70 ksi) at 4K. Alloy 6061 is usually used in the heat treated condition (T 6, T 651, etc.), and in the T-6 temper has a typical yield strength of 380 MPa (55ksi) at 4K. Although each of these alloys is readily weldable, only 5083 retains full strength in the welded condition and is the best choice for most large welded components. Alloy 2219 has the highest strength of the three alloys and is recommended for bolted construction where space or weight need to be conserved.

Several other aluminum alloys have excellent properties at 4K and may be used for special applications. Commercially pure aluminum (alloy 1100) and the 3003 alloy have excellent formability. Alloy 3003 has been widely used for cryogenic applications and is the best choice when brazing is used for joining. The high strength alloys such as 2014 and 7005 may be used for nuts and bolts.

The ASTM specifications for aluminum mill products of alloys 5083, 2219 and 6061 are summarized in Table 7. For a more complete listing of specifications refer to the Aluminum Standards and Data Book (46). Procurement of heavy sections may require additional specification requirements on through-thickness ductility (47).

The low temperature properties of aluminum alloys have been compiled in cryogenic handbooks (6,7), in a review article by Kaufman and Wanderer (48) and in suppliers publications (49). In this section, the general trends in strength, toughness and fatigue resistance are summarized, particularly the data for room temperature and 4K. The data are taken on relatively few lots of material, but generally the lot-to-lot variations in the mechanical properties of aluminum alloys are relatively small (with respect to stainless steel).

5.1 Tensile Properties

The mechanical properties of alloys 5083, 6061 and 2219 at room temperature and 4K have been determined by Kaufman, Nelson and Wanderer (50) and the results are summarized in Table 8. Notice that in all cases the tensile strengths, and to a lesser extent the yield strengths are superior at 4K and the ductility values are not significantly changed. The alloys retain good notched-tensile properties at 4K.

Aluminum alloys having a wide range of strength levels are suitable for liquid helium applications. The yield strengths of commercially pure (CP) aluminum (types 1100-0 and 1099-H14) and the preferred alloys are shown as a function of temperature in Figure 10 (42). The yield strengths of each alloy gradually increase with decreasing temperature. Strength increases in the following order: annealed CP (1100-0), cold worked CP (1099-H14), solution-strengthened Al-Mg alloy (5083-0), cold worked Al-Mg alloy (5083-H321), precipitation hardened Al-Mg-Si alloy (6061-T651) and precipitation hardened Al-Cu alloy (2219-T851). Still higher yield strengths are available in several other alloys including 2014-T651, 2024-T851 and 7005-T5351.

5.2 Toughness

Aluminum alloys generally retain excellent toughness at cryogenic temperatures. A useful measure of aluminum alloys toughness at 4K is the notch-yield ratio, i.e., the ratio of notched tensile strength to unnotched yield strength (51). Ratios substantially greater than one, say 1.5, indicate that the alloys retain the ability to plastically deform and resist crack initiation in the presence of sharp stress concentrations. As shown in Table 9, the 5083 and 6061 alloys have notch-yield ratios greater than 1.6 and the higher-strength 2219-T851 and T87 alloys have notch-yield ratios of about 1.4. Significantly lower ratios (1.0 to 1.25) occur in other high strength alloys such as 2014-T651 and 2024-T851 and in most 7000 series alloys (7005 is an exception), where the ratio is sometimes below 0.4 at cryogenic temperatures (52).

Limited toughness test data are available on aluminum alloys at 4K. Tobler and Reed (53) measured the fracture toughness of 5083-0 (4.3 cm thick plate) using J-integral procedures and found that toughness increased with decreasing temperature. The $K_{Ic}(J)$ was 47 MPa$\sqrt{m}$ at 4K in the transverse (TL) orientation. Shepic (54) measured the toughness of 2219-T87 (3.8cm thick plate) using ASTM E399 plane strain fracture toughness testing procedures. The K_{Ic} for 2219-T87 at 4K was 45.5 MPa$\sqrt{m}$ in the transverse (TL), 47.7 MPa$\sqrt{m}$ in the longitudinal (LT) and 28.6 MPa$\sqrt{m}$ in the through-thickness (SL) orientations.

5.3 Fatigue

Strain cycling fatigue tests have been conducted by Nachtigal (13) on 2219-T851 and 2014-T6 alloys at room temperature, 77K and 4K. For a given strain level, the fatigue lives of both alloys were greater at 4K than at the higher temperatures for endurances greater than about 500 cycles. The results for 2219-T851 are shown in Figure 11. The Manson-Hirschberg (55) method of universal slopes gave reasonable predictions of fatigue behavior based on the tensile properties at the test temperature.

The fatigue crack growth behavior of 5083-0 (53), 2219-T87 (54) and an Al-6Mg (56) alloy have been determined at 4K. In each case, the results indicate that the growth rates at 4K are slower than the rates at room temperature.

5.4 Physical Properties

The physical properties of the candiate aluminum alloys are summarized in Table 9. The thermal properties have been taken from the best-fit lines used in the LNG Materials Handbook (7) and from the compilation on thermal conductivity by Childs, Ericks and Powell (57). Original sources are given for the elastic properties (58,59) and electrical resistivity (17).

With the exception of magnetic susceptibility, the physical properties of aluminum alloys are not as good as those of stainless steels for

fusion magnet applications at 4K. The elastic modulus is relatively low, and thus when used for coil case applications, more of the load must be carried by the conductor assembly. The thermal and electrical conductivities are relatively high, resulting in incrased thermal loads particularly from eddy current losses.

6. Fabrication Characteristics of Aluminum Alloys

The relative ease of fabricating large aluminum structures is the principal advantage of aluminum over stainless steels. In addition the lower weight of aluminum structures may facilitate assembly and erection of the large magnet structures anticipated for fusion energy systems. Fabrication characteristics that should receive special consideration for fusion magnet systems are briefly reviewed in this section.

6.1 Welding

Alloys 5083, 6061 and to a lesser extent 2219 are readily weldable by the gas metal-arc and gas tungsten-arc processes. The compositions of aluminum welding rods and electrodes for these processes are summarized in Table 10. Annealed 5083 alloy retains full strength in the as-welded condition, but the cold worked and precipitation hardened alloys are weakened by welding. Part of the strength of precipitation hardened alloys can be restored by a post weld heat treatment.

The tensile properties of aluminum alloy weldments were determined by Nelson, Kaufman and Wanderer (60) and the results for selected alloys at room temperature and 4K are summarized in Table 11. Notice that part of the strength obtained by cold working (5083-H321) and by precipitation hardening (6061-T6 and 2219-T851) is retained by the welded joint. This strength increase is not reflected in design-code allowable stresses (11) which assume as-welded aluminum alloys are in the fully annealed condition. The tensile properties of 6061-T6 and 2219-T62 welds that were subsequently solution treated and aged indicate that substantial strengthening can be achieved by post-weld heat treatments. For most fusion magnet structures, the solution treatment and quenching are not considered practical. The data in Table 11 also indicate that the

ductility of 2219 weldments is quite low due to localized deformation in the heat affected zone; the ductility and notch-yield ratio of 5556 and 4043 filler metals (as-welded) are low at 4K; and the best ductility and notch-yield ratios in the as-welded condition at 4K are provided by the 5083 and 5356 alloys.

6.2 Heat Treatment and Temper Designations

Aluminum alloys are supplied in a wide range of tempers, and for large complex structures, subsequent heat treatments are not generally performed by the fabricator. The tempers are designated by a letter followed by one to three digits. The letter is the basic temper designation: O-annealed, H-strain hardened and T-thermally treated. For the strain hardened tempers, the first digit indicates the hardening operations: H1-strain hardening only, H2-strain hardened and partially annealed and H3-strain hardened and stabilized. The second digit (e.g. H18 is strain-hardened by a cold reduction of 75%) indicates the degree of strain hardening and the third digit is sometimes used for specified variations. For the thermally treated tempers, the first digit indicates the specific sequence of basic treatments; for example T6 designates solution heat treated and then artificially aged and T8 designates solution heat treated, cold worked and then artificially aged. Subsequent digits indicate specific variations, such as x51 stress relieved by stretching as in T651 or T851. The reader is referred to the Aluminum Association Handbook (46) for a complete description of the temper designation system.

6.3 Castings

Aluminum alloy castings can be produced by a variety of processes and generally are satisfactory for non-structural applications at low temperatures. The ASME Code (11) permits use of Al-5 Si (Type 43) and Al-7Si-0.3Mg (Type 356-T6) for non-welded structural applications. Nelson, Kaufman and Wanderer (60) evaluated the tensile properties at 4K of several combinations of castings welded to wrought alloys; in general, superior properties were obtained when the properties of the cast and wrought components were nearly equal.

6.4 Machining, Forming and Forging

Machining: Aluminum alloys, particuarly the heat treated grades, have excellent machinability. Machined and bolted assemblies of high strength aluminum alloys can replace more costly welded stainless steel assemblies. Care should be taken when using steel bolts because the thermal contraction of aluminum alloys on cooling to 4K exceeds that of steel.

Forming: Aluminum alloys have excellent formability in the annealed or the solution treated conditions.

Forging: Aluminum alloys have the best forgeability of all structural alloys because of their very low strength at forging temperatures of 370 to 510°C. The size limit on aluminum forgings is significantly greater than that on stainless steels because of the reduced pressures required.

6.5 Inspection

Aluminum alloys and their weldments are readily inspectable by conventional methods: dye-penetrant, ultrasonics and radiography.

7. Alternative Alloys

Alternative alloy systems do not provide candidate structural materials for superconducting magnets in fusion energy systems. Consider the following systems:

Nickel base alloys are ferromagnetic, expensive and frequently difficult to fabricate. However, many of these alloys have excellent combinations. of strength and toughness at 4K and may be suitable for special applications (61).

Titanium alloys are brittle at 4K, expensive and difficult to fabricate (62).

Cobalt base superalloys transmute to long half-life reaction products and are expensive and difficult to fabricate.

Carbon and alloy steels including the ferritic and martensitic stainless steels are ferromagnetic and brittle at 4K. Even the cryogenic nickel steels are brittle at 4K (63) except for a specially processed 12Ni alloy (64).

Copper alloys are acceptable, but generally not competitive with the austenitic stainless steels or aluminum alloys.

8. Summary Comments

This review suggests that there are several commercially available alloys that are suitable for construction of large superconducting magnet structures for fusion energy systems. These alloys include annealed austenitic stainless steels, nitrogen strengthened austenitic stainless steels where greater strength is needed, an annealed Al-Mg alloy for welded aluminum construction and precipitation-hardened aluminum alloys for bolted assemblies. For each of these alloys, there are enough experimental data and fabrication experience to provide reasonable assurance that the alloys have sufficient strength, ductility and toughness in the liquid helium environment; that the alloys can be fabricated into support structures for superconducting magnets; and finally, that the fabricated structure will retain adequate properties during operation of the fusion energy device.

It should be realized, however, that the depth of understanding, the degree of characterization, and the extent of related experience for these alloys in the fusion-magnet environment are extremely limited. More work is needed on material behavior at 4K, particularly in the areas of material variability, processing effects on properties, and the fabrication and mechanical behavior of large, complex, thick-section components.

9. Recommendations

The accumulated knowledge of materials for fusion energy systems should eventually result in a code for the design, construction and inspection of fusion magnets. Adherence to this code should provide assurance that the magnet system provides the intended field and operates in a safe, reliable and efficient manner. Establishment of such a code for large magnets must await further developments in the technology, particularly the experience gained from prototype systems and greater material characterization. However, parts of the code should be set forth as preliminary guidelines to facilitate the orderly development of materials technology for magnet systems.

Design guidelines needed for selection of materials should identify operating loads and conditions and criteria for establishing allowable working stresses for candidate materials. For magnet systems, description of the operating loads should include the anticipated load history for normal operation, loads due to credible fault conditions and procedures for treating combined loads. The operating conditions of interest are the thermal environment, radiation dosage, magnetic field profile and design life. Allowable working stresses should account for the materials strength variability, the fatigue strength for a specified scatter factor on fatigue cycles, fracture mechanics analysis and a factor of safety based on uncertainties in the loads and stress analysis.

Material procurement and processing should be controlled by a set of specifications which are sufficient to preclude use of materials in the magnet systems which have properties inferior to those assumed in design. Inspection specifications and standards are needed to provide a high degree of confidence that no defects are present in the raw materials, or introduced during fabrication, which could cause unsatisfactory performance of the magnet system.

References

1. R. P. Reed, A. F. Clark and E. C. van Reuth, in: Advances in Cryogenic Engineering, Vol. 22, Plenum Press, New York (1976) p. 1.

2. R. P. Reed, F. R. Fickett, M. B. Kasen and H. I. McHenry, in: Materials Studies for Magnetic Fusion Energy Applications at Low Temperatures - 1, NBSIR 78-884, National Bureau of Standards, Boulder, CO (1978) p. 243.

3. F. R. Fickett, M. B. Kasen, H. I. McHenry and R. P. Reed, in: Advances in Cryogenic Engineering, Vol. 24, Plenum Press, New York (1979).

4. F. R. Fickett, Properties of Non-superconducting Technical Solids at Low Temperatures, Proc. Fourth Internatinal Conference on Magnet Technology, Brookhaven, NY (1972) p. 498.

5. H. I. McHenry, in: Advances in Cryogenic Engineering, Vol. 22, Plenum Press, New York (1976)p.9.

6. Handbook on Materials for Superconducting Machinery, Metals and Ceramics Information Center, MCIC-HB-04, Battelle, Columbus, OH (1977).

7. D. B. Mann, editor, LNG Materials and Fluids, National Bureau of Standards, Boulder, CO (1978).

8. K. G. Brickner and J. D. Defilippi, in: Handbook of Stainless Steels, McGraw-Hill, New York (1977) p. 20-1.

9. Low Temperature and Cryogenic Steels, Materials Manual, U. S. Steel Corp., Pittsburgh, PA (1966).

10. Materials for Cryogenic Service-Engineering Properties of Austenitic Stainless Steels, International Nickel Limited, London (1974).

11. ASME Boiler and Pressure Vessel Code, Section VIII, Pressure Vessels, American Society of Mechanical Engineers, New York (1977).

12. R. L. Tobler, in: Fracture 1977, Vol. 3, Proc. Fourth International Conference on Fracture, Waterloo, Canada (1977) p. 839.

13. A. J. Nachtigall, in: Properties of Materials for Liquefied Natural Gas Tankage, ASTM STP 579, American Society for Testing and Materials (1975) p. 378.

14. J. A. Shepic and F. R. Schwartzberg, in: Materials Studies for Magnetic Fusion Energy Applications at Low Temperatures-1, NBSIR 78-884, National Bureau of Standards, Boulder, CO (1978) p. 13.

15. R. L. Tobler and R. P. Reed, in: Advances in Cryogenic Engineering, Vol. 24, Plenum Press, New York (1979).

16. H. M. Ledbetter, W. F. Weston and E. R. Naimon, Journal of Applied Physics, Vol. 46, 9 (1975) p. 3855.

17. A. F. Clark, G. E. Childs and G. H. Wallace, Cryogenics, 10 (1970) p. 295.

18. K. R. Efferson and W. J. Leonard, Magnetic Properties of Some Structural Materials Used in Cryogenic Applications; ORNL-4150, Oak Ridge National Laboratory, Oak Ridge, TN (1976) p. 126.

19. Metals Handbook, Vol. 1, Eighth Edition, American Society for Metals, Metals Park, OH (1967).

20. G. P. Sanderson and D. T. Llewellyn, Journal Iron and Steel Institute, London, Vol. 27 (1969) p. 1129.

21. V. A. Randak, W. Wessling, H. E. Bock, H. Steinmaurer and L. Faust, Stahl and Eisen, Vol. 91 (1971) p. 1255.

22. R. Voyer and L. Weil, in: Advances in Cryogenic Engineering, Vol.11, Plenum Press, New York (1966) p. 447.

23. D. C. Larbalestier, Private Communication, U. of Wisconsin, Madison, WI (1977).

24. C. E. Spaeder, Jr., and W. F. Domis, Cryogenic and Elevated-Temperature Mechanical Properties of a High-Nitrogen Type 304 Stainless Steel, Project 44.012-062(2), U. S. Steel Corp., Pittsburgh, PA (1969).

25. D. T. Read and R. P. Reed, in: Materials Studies for Magnetic Fusion Energy Applications at Low Temperatures-1, NBSIR-78-884, National Bureau of Standards, Boulder, CO (1978) p. 91.

26. D. B. A. Macmichael, M. Liddle and J. S. H. Ross, Superconducting AC Generators Trial Rotor Forging Investigation, International Research and Development Co. Ltd., Newcastle upon Tyne, England (1978).

27. D. T. Read and R. P. Reed, in: Materials Studies for Magnetic Fusion Energy Low Temperature Applications-II, National Bureau of Standards, Boulder, CO (1979).

28. R. L. Tobler and R. P. Reed, in: Elastic Plastic Fracture, ASTM STP xxx, American Society for Testing Materials, Philadelphia, PA, forthcoming.

29. P. F. Scardigno, M. S. Thesis, Naval Postgraduate School, Monterey, CA, NTIS AD/A-004555(1974).

30. P. R. Landon, Unpublished Data, Lawrence Livermore Laboratories, Livermore, CA (1975).

31. R. D. Masteller, NASACR-82638, Martin Marietta Corp., Denver, CO (1970).

32. C. O. Malin, NASA SP-5921(01), Technology Utilization Office, NASA, Washington, D.C. (1970).

33. H. M. Ledbetter, Materials Science and Engineering, 29 (1977) p. 255.

34. H. M. Ledbetter and E. W. Collings, in: Metal Physics of Stainless Steels, TMS AIME, New York, Forthcoming.

35. D. T. Read, H. I. McHenry and P. A. Steinmeyer, in: Materials Studies for Magnetic Fusion Energy Low Temperature Applications - II, National Bureau of Standards, Boulder, CO (1979).

36. E. R. Szumackowski and H. F. Reid, Welding Journal, Vol. 57 (1978) p. 325-s.

37. V. N. Krivobok and R. D. Thomas, Jr., Welding Journal, Vo. 29, (1950) p. 493-s.

39. J. H. McConnell and R. R. Brady, Chemical Engineering, Vo. 67 (1960) p. 125.

40. W. T. DeLong, Welding Journal, Vol. 53 (1974) p. 273-s.

41. C. L. Goodzeit, in: Advances in Cryogenic Engineering, Vol. 20, Plenum Press, New York (1965) p. 26.

42. D. F. Shaw, Cryogenics, Vol. 4 (1964) p. 193.

43. A. B. Miller, Cryogenics Vol. 5 (1965) p. 320.

44. Armco Nitronic 40 Stainless Steel Sheet and Strip, Armco Steel Corp., Baltimore, MD (1976).

45. J. E. Jenson, editor, Forging Industry Handbook, Forging Industry Association, Cleveland, OH (1966).

46. Aluminum Standards and Data, Aluminum Association, Inc. Washington, D. C. (1976).

47. H. I. McHenry. Metals Progress, Vol. 93, 3 (1968) p. 62.

48. J. G. Kaufman and E. T. Wanderer, in: Aluminum: Vol. II, Design and Applications, American Society for Metals, Metals Park, OH (1967) 297.

49. Alcoa Aluminum - The Cryogenic Metal, Alcoa, Pittsburgh, PA (1971).

50. J. G. Kaufman, K. O. Bogardus and E. T. Wanderer, in: Advances in Cryogenic Engineering, Vol. 13, Plenum Press, New York (1968), p. 294.

51. J. G. Kaufman and E. W. Johnson, in: Advances in Cryogenic Engineering, Vol. 8, Plenum Press, New York (1963) p. 678.

52. M. P. Hanson, G. W. Stickley and H. T. Richards, in: Low Temperature Properties of High-Strength Aircraft and Missile Materials, ASTM STP 287, American Society for Testing and Materials, Philadelphia, PA (1961) p.3.

53. R. L. Tobler and R. P. Reed, Journal of Engineering Materials and Technology, Vol. 99 (1977) p. 306.

54. J. A. Shepic, in: Materials Studies for Magnetic Fusion Energy Low Temperature Applications-II, National Bureau of Standards, Boulder, CO (1979).

55. S. S. Manson, Experimental Mechanics, Vol. 5 (1965) p. 193.

56. H. I. McHenry. S. E. Naranjo, D. T. Read and R. P. Reed,in: Advances in Cryogenic Engineering, Vol. 24, Plenum Press, New York (1979).

57. G. E. Childs, L. J. Ericks and R. L. Powell, Thermal Conductivity of Solids at Room Temperature and Below, NBS Monograph 131, National Bureau of Standards, Boulder, CO (1973).

58. E. R. Naimon, H. M. Ledbetter and W. F. Weston, Journal of Materials Science, Vol. 10 (1975) p. 1309.

59. D. T. Read and H. M. Ledbetter, Journal of Engineering Materials and Technology, Vol. 99 (1977) p. 181.

60. F. G. Nelson, J. G. Kaufman and E. T. Wanderer, in: Advances in Cryogenic Engineering, Vol. 14, Plenum Press, New York (1969) p. 71.

61. J. M. Wells, R. Kossowsky, W. A. Logsdon and M. R. Daniel, in: Materials Research for Superconducting Machinery VI, (NTIS No. ADA 036919), National Bureau of Standards, Boulder, CO (1976).

62. R. L. Tobler, in: Cracks and Fracture, ASTM STP 601, American Society for Testing and Materials, Philadelphia, PA (1976) p. 346.

63. R. L. Tobler, in: Materials Research for Superconducting Machinery VI, (NTIS No. ADA 036919) National Bureau of Standards, Boulder, CO (1976).

64. S. Jin, S. K. Hwang and J. W. Morris, Jr., Met. Trans., Vol. 6A (1975) p. 1569.

Table 1 - Compositions of Austenitic Stainless Steels Suitable for Liquid Helium Service

AISI Type No.	Composition, % Cr	Ni	C,max	Other
304	18-20	8-10.5	.08	
304L	18-20	8-12	.03	
316	16-18	10-14	.08	2-3 Mo
316L	16-18	19-22	.03	2-3 Mo
310	24-26	19-22	.25	1.5 Si, max
310S	24-26	19-22	.08	1.5 Si, max

For each grade Mn = 2.0 max S = .030 max
Si = 1.0 max P = .045 max

Table 2. ASTM Specifications for Various Product Forms of Austenitic Stainless Steels

Product Form	ASTM Specifications
Plates, sheet and strip	A240
Forgings	A473
Bars and sections	A479
Seamless tubes	A213
Welded tubes	A249
Seamless and welded tubes	A269
Small diameter tubing	A632
Bolts, screws, studs	A320
Nuts	A194

Table 3. Physical Properties of Austenitic Stainless Steels

Property	Units	AISI 304 295K	AISI 304 4K	Ref	AISI 310 295K	AISI 310 4K	Ref	AISI 316 295K	AISI 316 4K	Ref
Density	g/cm^3	7.9	--	19	7.9		19	8.0		19
Young's Modulus	GN/m^2	189	204	16	184	199	16	217	234	16
Shear Modulus	GN/m^2	740	800	16	700	770	16	830	910	16
Poisson's Ratio	--	.290	.271	16	.307	.296	16	.298	.281	16
Thermal Conductivity	W/m.K	13	0.3	7	Nearly the same 304, 310 and 316 Thermal					
Expansion	$cm/cm/K^{-1} x 10^{-6}$	15.8	10.2	7	Nearly the same for 304, 310 and 316					
Specific Heat	J/Kg.K	480	0.5	7	Nearly the same for 304, 310 and 316					
Electrical Resistivity	u Ω cm	70.4	49.6	17	87.3	68.5	17	75.0	53.9	17
Magnetic Permeability (Initial)		1.02	1.09	18	1.003	1.10	18	1.003	1.02	18

Table 4. Compositions of Nitrogen-Strengthened Austenitic Stainless Steels Suitable for Liquid Helium Service

Type	Nominal Composition, %					
	Cr	Ni	Mn	C, max	N	Other
AISI 304N	18-20	8-10.5	2.0, max	.08	.10-.16	-
304LN	18-20	8-12	2.0, max	.03	.10-.16	-
AISI 316N	16-18	10-14	2.0, max	.08	.10-.16	-
316LN	16-18	10-14	2.0, max	.03	.10-.16	-
ASTM XM11*	18-21	5-7	8-10	.04	.15-.40	-
ASTM XM19*	20.5-23.5	11.5-13.5	4-6	.06	.20-.40	Cb .10-.30 V .10-.30 Mo 1.5-3.0

*ASTM A412

Table 5 - Compositions of Filler Metals for Welding
Austenitic Stainless Steels

AWS Type	Composition, %			
Covered Electrodes	Cr	Ni	C, max	Other
E308	18-21	9-11	.08	
E308L	18-21	9-11	.04	
E310	25-28	20-22.5	.20	.75 Si, max
E16-8-2	14.5-16.5	7.5-9.5	.10	.50 Si, max; 1-2 Mo
E316	17-20	11-14	.08	2-2.5Mo
E316L	17-20	11-14	.04	2-2.5Mo
E330	14-17	33-37	.25	
Rod and Bare Electrodes				
ER308	19.5-22	9-11	.08	
ER308L	19.5-22	9-11	.03	
ER310	25-28	20-22.5	.08-.15	
ER316	18-20	11-14	.08	2-3Mo
ER316L	18-20	11-14	.03	2-3Mo

For Covered Electrodes: Mn = 2.5, max; Si = 0.9, max; P = .04, max; S = .03 max
For Rod and Bare Electrodes: Mn = 1.0-2.5; Si = .25-60; P = .03, max; S = .03, max

Table 6. Compositions of Aluminum Alloys Suitable for Liquid Helium Service (46)

Type	Composition, %								
	Si max	Fe max	Cu	Mn	Mg	Cr	Zn max	Ti	Others
1100	1.0	Si + Fe,max	.05-.20	.05,max	--	--	0.10	--	99.00Al,minimum
2219	0.2	0.3	5.8-6.8	.20-.40	.02,max	--	0.10	.02-.10	.05-15V; .10-.25Zr
3003	0.6	0.7	.05-.20	1.0-1.5	--	--	0.10	--	
5083	0.4	0.4	0.1,max	.40-1.0	4.0-4.9	.05-.25	0.25	.15,max	
6061	.4-.8	0.7	.15-.40	.15,max	.08-1.2	.04-.35	0.25	.15,max	

Table 7. ASTM Specifications and Availability of Aluminum Mill Products (46)

Product Form	Specification ASTM	Availble Alloys 5083	6061	2219
Sheet and plate	B209	x	x	x
Wire, rod, bar; rolled or cold finished	B211		x	x
Wire, rod, bar,shapes,tube	B221	x	x	x
Structural shapes	B308		x	
Pipe	B241		x	
Forgings and forging stock	B247	x	x	x
Structural pipe and tube; extruded	B249		x	

Table 8. Tensile Properties of Aluminum Alloys at Room Temperature and 4K (50)

Alloy and Temper	Plate Thickness	Orientation	Temp	TS Tensile Strength	JYS Joint Yield Strength	Elongation in 4D	Reduction of areaa	NTS Notch Tensile Strength	NTS/TS	NTS/JYS
	mm		K	MPa	MPa	%	%	MPA		
5083-0	25	L	RT	322	141	19.5	26	372	1.16	2.65
			4	557	178	32	33	429	0.77	2.42
5083-H321	25	L	RT	335	235	15	23	421	1.26	1.80
			4	591	279	29	33	508	0.86	1.82
6061-T651	25	L	RT	309	291	16.5	50	477	1.54	1.64
			4	483	379	25.5	42	619	1.28	1.63
		T	RT	309	278	15.2	42	467	1.51	1.68
			4	485	363	23	33	601	1.24	1.66
2219-T851	25	L	RT	466	371	11	27	547	1.12	1.48
			4	659	484	15	26	703	1.06	1.48
		T	RT	457	353	10.2	22	531	1.16	1.50
			4	659	481	13	21	665	1.01	1.38
2219-T87	25	L	RT	464	387	11.8	28	567	1.22	1.46
			4	674	511	15	23	690	1.03	1.37
A356-T61	19	Casting	RT	287	208	8.8	10	354	1.23	1.70
Casting			4	455	331	7.1	9	495	1.09	1.50

Table 9. Physical Properties of Aluminum Alloys

Property	Units	5083 (Annealed) 295K	4K	Ref	Precipitation Hardened 6061 295K	4K	Ref	Precipitation Hardened 2219 295K	4K	Ref
Specific Gravity	g/cm^3	2.66			2.70			2.83		
Young's Modulus	GN/m^2	71.5	80.9	58	70.1	77.7	7	77.4	85.7	59
Shear Modulus	GN/m^2	26.8	30.7	58	26.4	29.2	7	29.1	32.5	59
Poisson's Ratio		.333	.318	58	.338	.327	7	.330	.318	59
Thermal Conductivity	W/m.K	120	3.3	7	120-160	3.-6.	50	120-160	3.-6.	50
Thermal Expansion	$K^{-1}x10^{-6}$	23	14.1	7	120-160	14.1	7	120-160	14.1	7
Specific Heat	J/Kg.K	900	.28	7	120-160	.28	7	.28	.28	7
Electrical Resistivity	$\mu\Omega cm$	5.66	3.03	17	3.94	1.38	17	5.7	2.9	17

Table 10. Compositions of Aluminum Welding Rods and Electrodes for Liquid Helium Service (46)

Type	Composition, % (max unless range given)										Suggested for Welding
	Cu	Mg	Mg	Cr	Si	Fe	Zn	Ti	Be	Other	
1100	0.20	--	0.05	--	Si+Fe=1.0,max					99.0-99.5Al	1100,3003
2319	5.8-6.8	0.02	0.20-0.40	--	0.20	0.30	0.10	0.10-0.20	0.0008	0.10-0.25Zr	2219
4043	0.03	0.05	0.05	--	4.5-6.0	0.80	0.10	0.20	0.0008	0.05-0.15V	1100,6061
5183	0.10	4.3-5.2	0.50-1.0	0.05-0.25	0.40	0.40	0.25	0.15	0.0008		5083
5356	0.10	4.5-5.5	0.05-0.20	0.05-0.20	Si+Fe=0.5,max		0.10	0.06-0.20	0.0008		5083,6061
5556	0.10	4.7-5.5	0.5-1.0	0.05-0.20	Si+Fe=0.4,max		0.25	0.05-0.20	0.0008		5083,6061

Table 11. Tensile Properties of Aluminum Alloy Weldments at Room Temperature and 4K (60)

Alloy and Temper	Plate Thickness	Filler Alloy	Post-Weld Thermal Treatment	Temp	TS Tensile Strength	JYS Joint Yield Strength	Elongation in 4D	Reduction of Area	Joint Efficiency	Location of Failure	NTS Notch Tensile Strength	NTS / TS	NTS / JYS
	mm			K	MPa	MPa	%	%	%		MPa		
5083-0	25	5183	No	RT	293	138	21.5	--	100	WM	308	1.05	2.22
				4	381	174	27	37	69	BM	371	0.98	2.14
5083-H321	25	5183	No	RT	305	179	14	39	96	HAZ	376	1.23	2.10
				4	455	246	9.0	14	80	WM	405	0.89	1.65
5083-H321	25	5356	No	RT	286	167	13.5	47	90	WM	371	1.30	2.22
				4	455	235	9.0	17	80	HAZ	398	0.87	1.69
5083-H321	25	5556	No	RT	306	176	14	36	97	WM	370	1.21	2.10
				4	474	238	13	17	83	WM	399	0.84	1.68
6061-T6	25	4043	No	RT	214	144	6.0	19	69	HAZ	234	1.10	1.63
				4	338	259	4.5	9	63	WM	275	0.81	1.06
			Yes	RT	298	247	11	44	96	BM	396	1.31	1.57
				4	452	309	15	16	84	WM	463	1.02	1.50
6061-T6	25	5356	No	RT	225	156	8.0	31	73	WM	323	1.44	2.07
				4	398	243	13.5	24	74	WM	367	0.92	1.50
			Yes	RT	279	202	9.5	33	90	BM	---	----	----
				4	476	307	19	24	89	WM	419	0.88	1.37
2219-T851	32	2319	No	RT	225	185	2.0	5	50	HAZ	280	1.24	1.52
				4	411	277	2.5	10	62	HAZ	363	0.88	1.31
2219-T62	25	2319	Yes	RT	395	277	7.5	7	99	HAZ	439	1.11	1.58
				4	496	355	3.5	5	80	HAZ	570	1.15	1.61

Note: Location of Failures
WM - Weld metal
BM - Base metal
HAZ - Heat affected zone

List of Figures

1. Tensile and yield strengths of three austenitic stainless steels - AISI types 304, 310 and 316 - at temperatures between 4K and 300K (6).

2. Tensile properties of two austenitic stainless steels - AISI types 304 and 304L - at temperatures between 4K and 300K(6).

3. Notched tensile properties of five austenitic stainless steels - AISI types 304, 304L, 310,310S and 316 - at 4K (6). K_T is the stress concentration factor of the notch.

4. Fatigue behavior of three austenitic stainless steels - AISI types 304 and 316 and a 21Cr-6Ni-9Mn alloy - at 4K (14).

5. Fatigue crack growth rates of AISI type 304L austenitic stainless steel at 295, 76 and 4K (15).

6. Tensile and yield strengths of nitrogen-strengthened 300-series stainless steels at temperatures between 4K and 300K (20-27).

7. Tensile and yield strengths of 21Cr-6Ni-9Mn stainless steel at temperatures between 4K and 300K (28).

8. Fracture toughness of four nitrogen-strengthened austentitic stainless steels at temperatures between 4K and 300K (25).

9. Fracture toughness of AWS 316L weld metal at 4K as a function of ferrite content (35).

10. Yield strengths of six aluminum alloys at temperatures between 4K and 300K (50).

11. Fatigue behavior of 2219-T851 aluminum alloy at temperatures of 300, 77 and 4K (13).

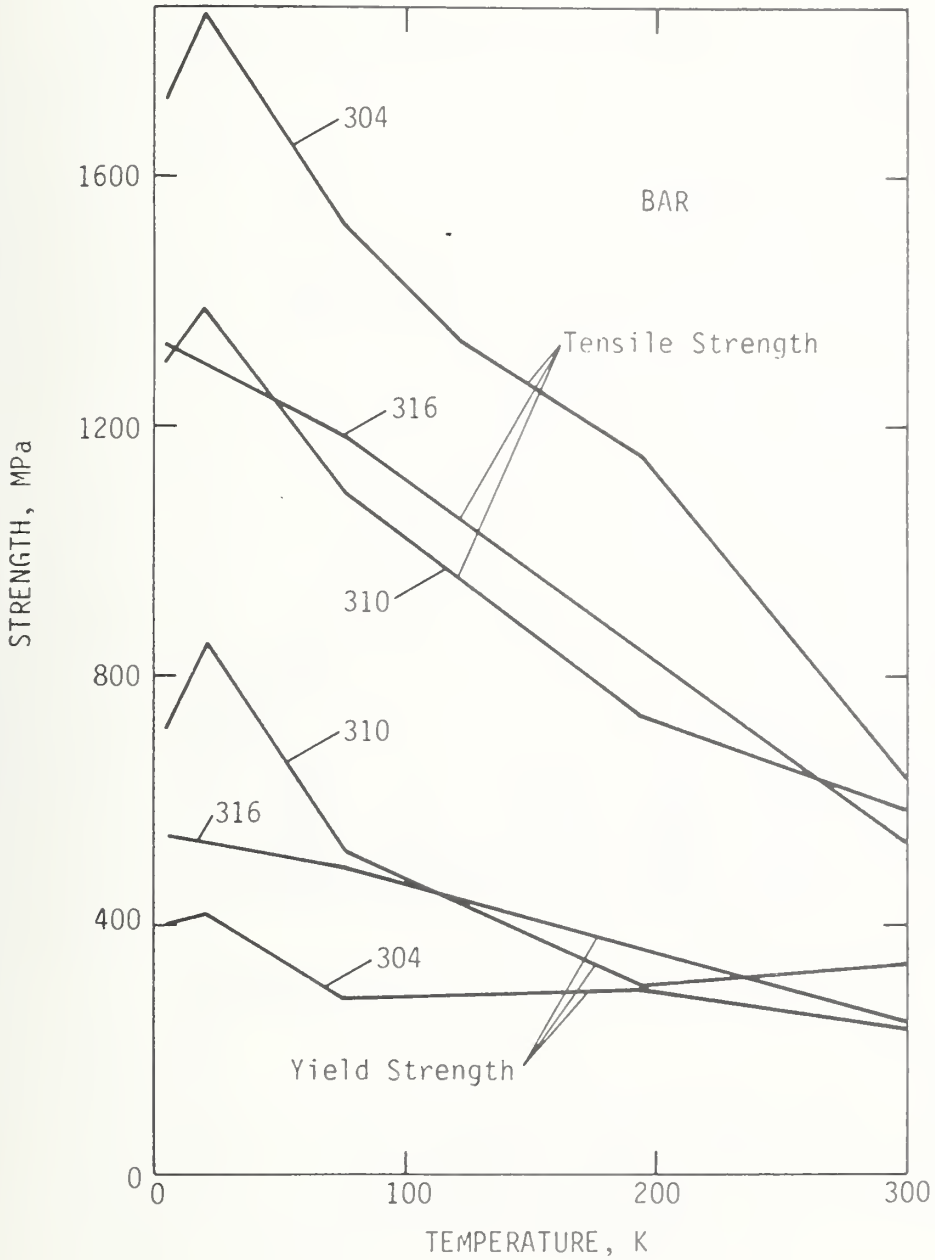

1. Tensile and yield strengths of three austenitic stainless steels - AISI types 304, 310, and 316 - at temperatures between 4K and 300K (6).

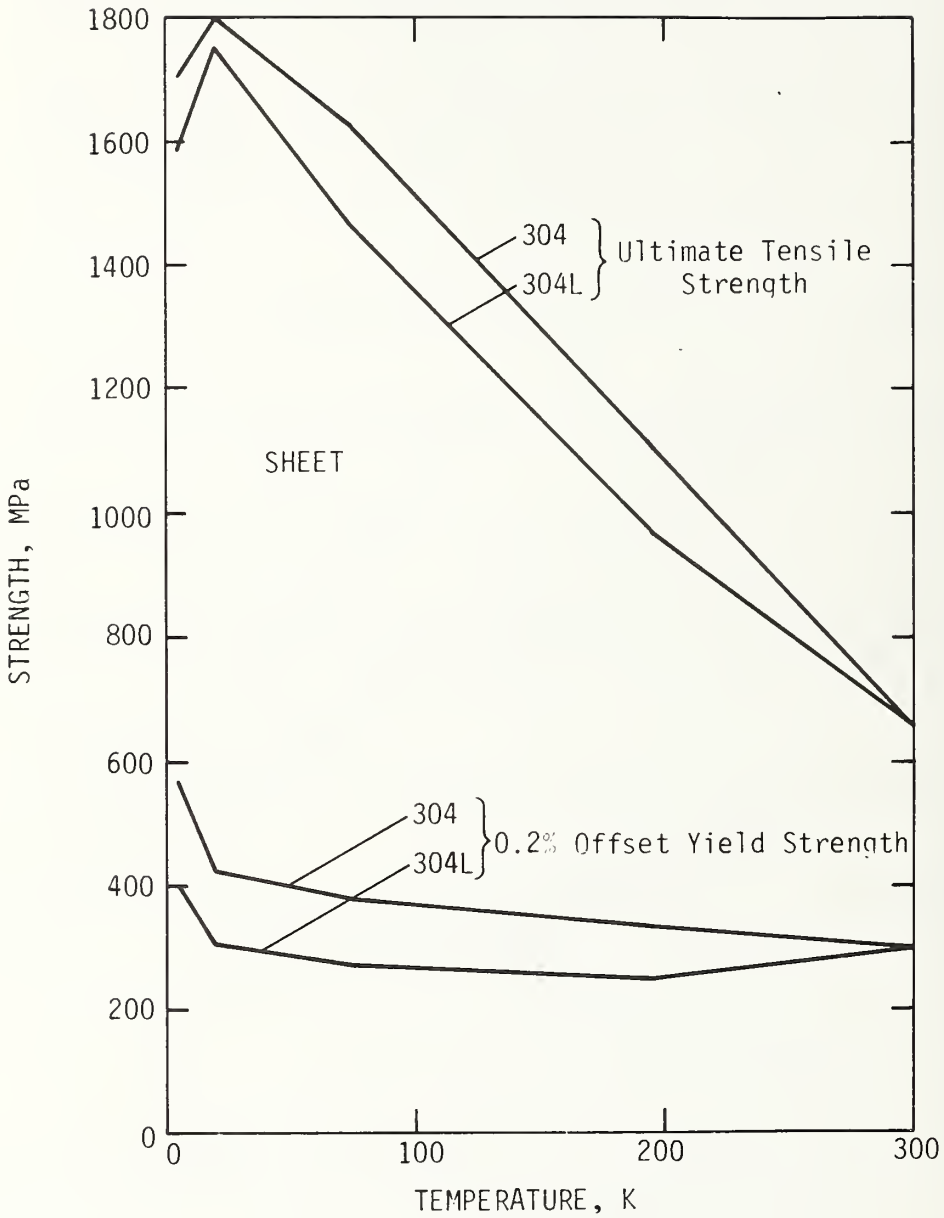

2. Tensile properties of two austenitic stainless steels - AISI types 304 and 304L - at temperatures between 4K and 300K (6).

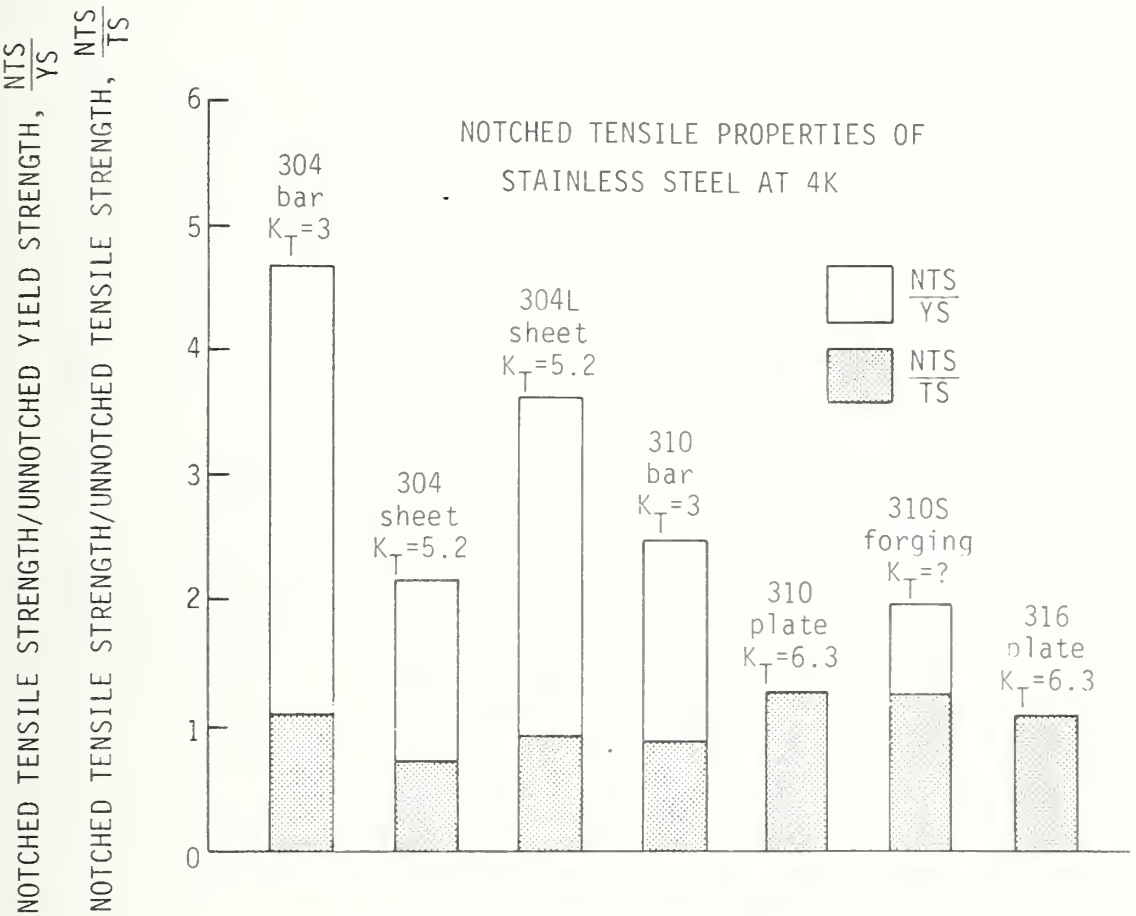

3. Notched tensile properties of five austenitic stainless steels - AISI types 304, 304L, 310, 310S, and 316 - at 4K (6). K_T is the stress concentration factor of the notch.

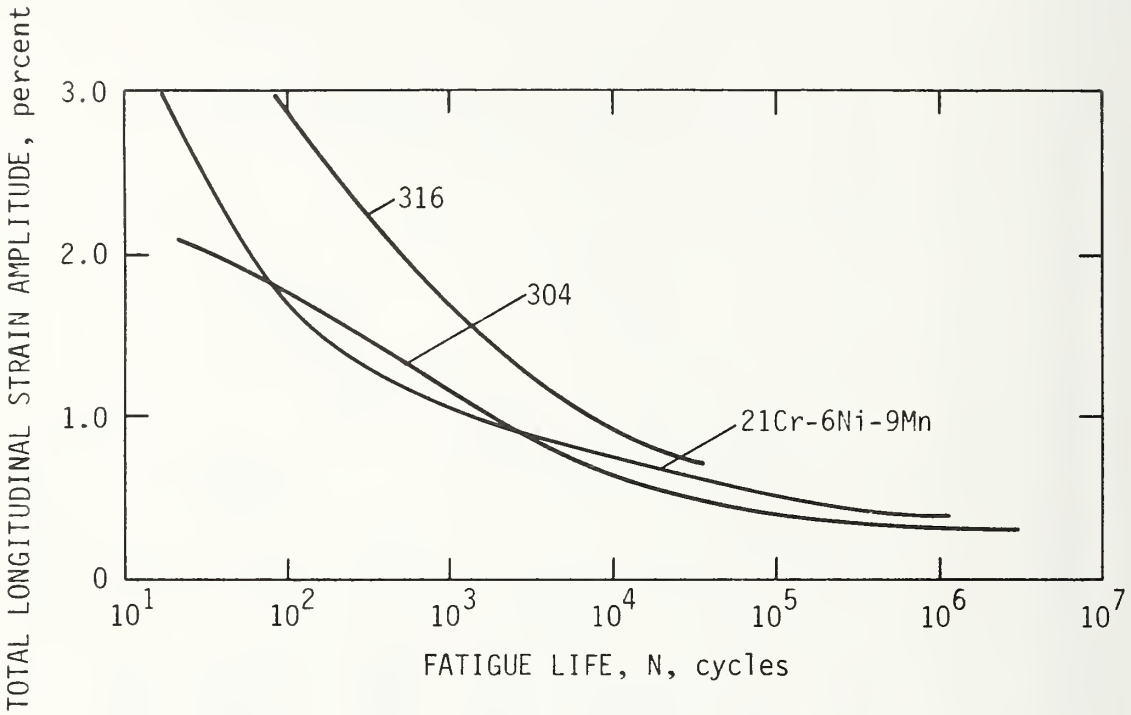

4. Fatigue behavior of three austenitic stainless steels - AISI types 304 and 316 and a 21Cr-6Ni-9Mn alloy - at 4K (14).

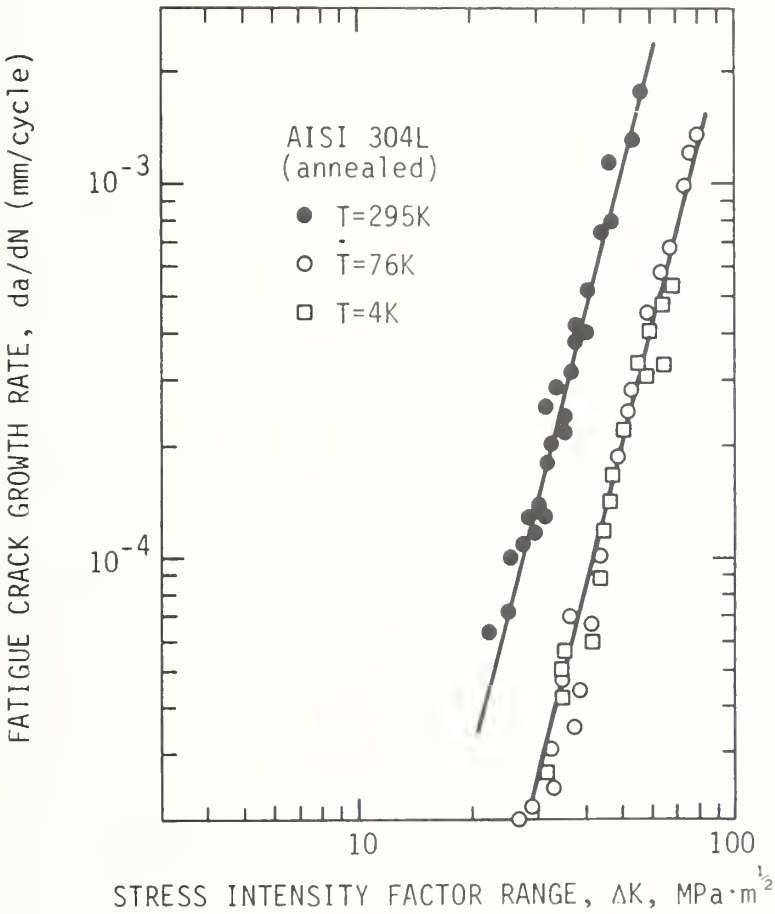

5. Fatigue crack growth rates of AISI type 304L austenitic stainless steel at 295, 76 and 4K (15).

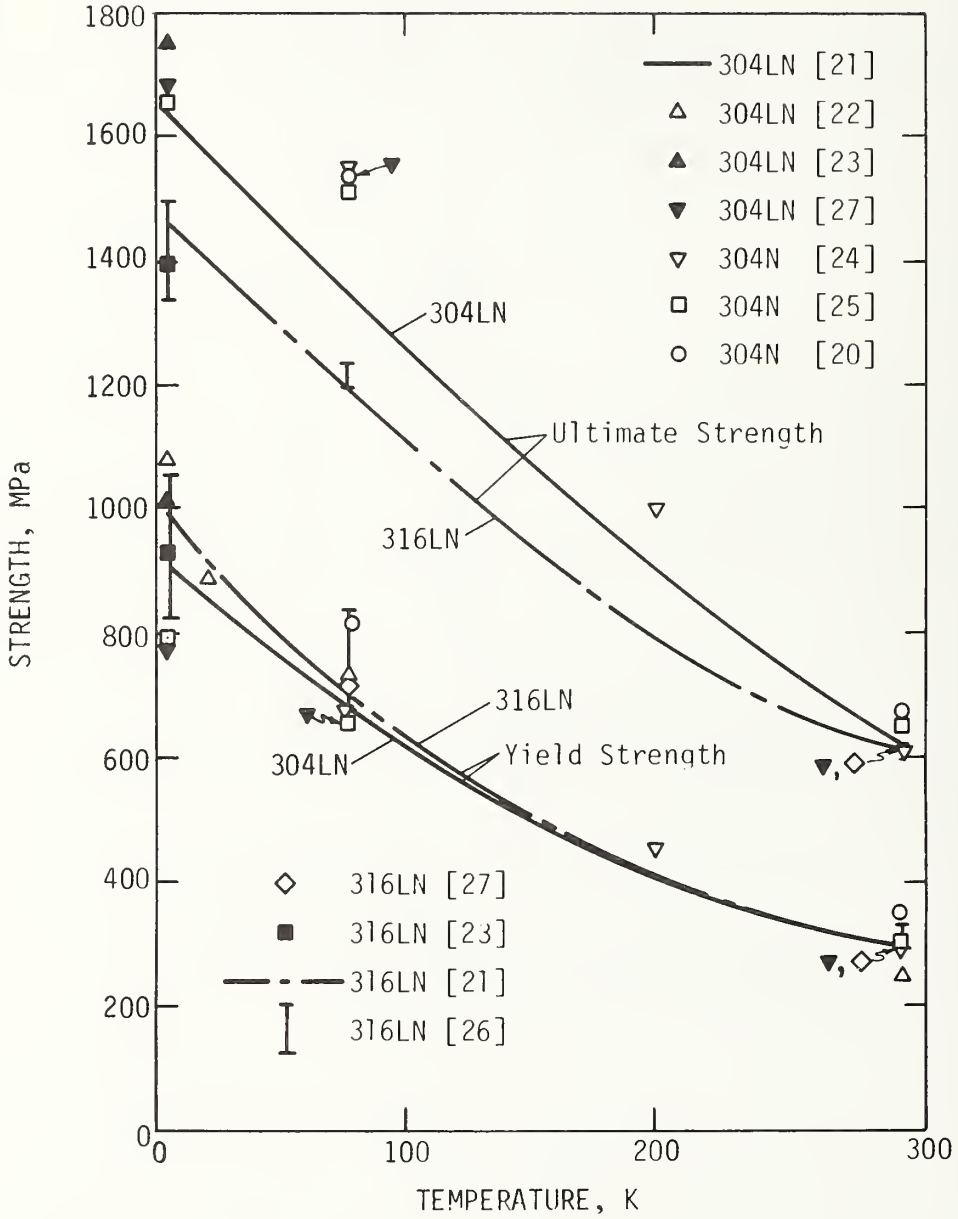

6. Tensile and yield strengths of nitrogen-strengthened 300-series stainless steels at temperatures between 4K and 300K (20-27).

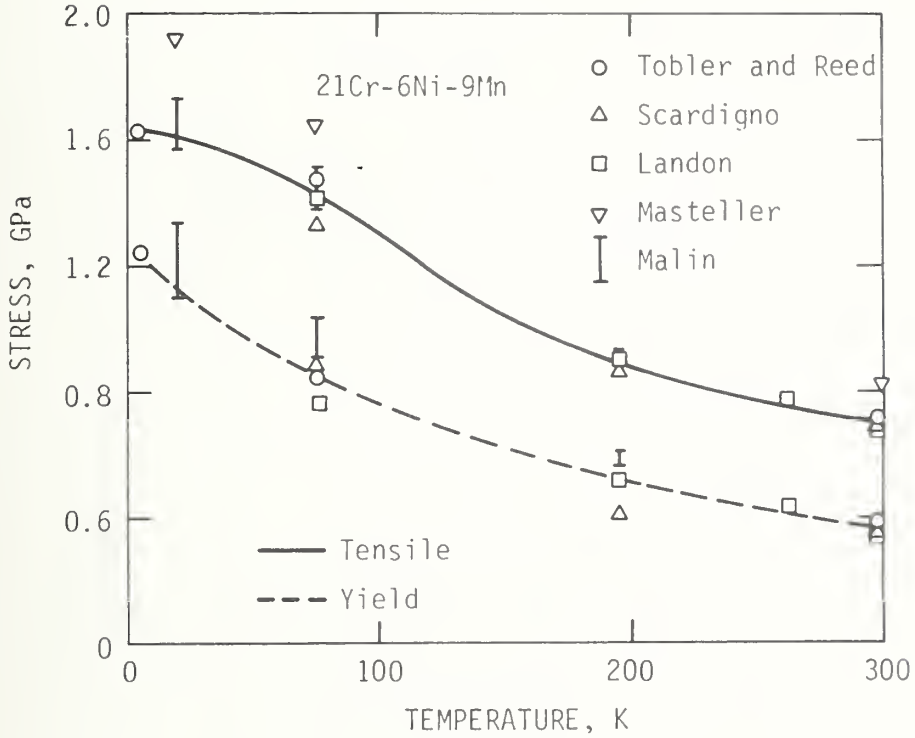

7. Tensile and yield strengths of 21Cr-6Ni-9Mn stainless steel at temperatures between 4K and 300K (28).

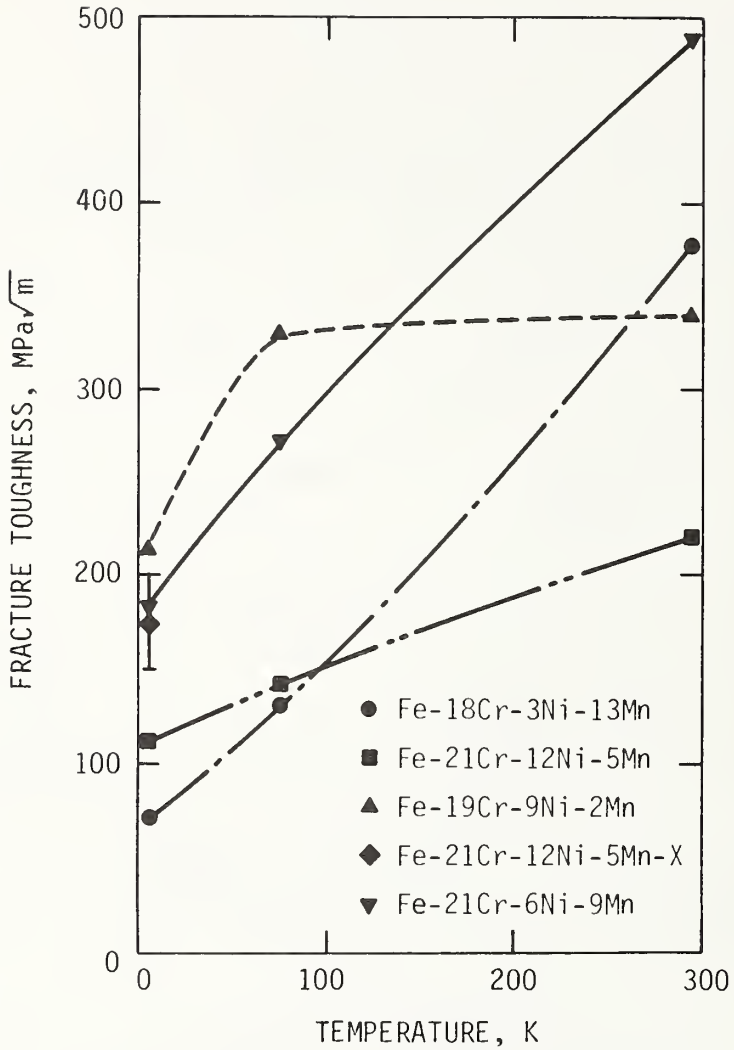

3. Fracture toughness of four nitrogen-strengthened austenitic stainless steels at temperatures between 4K and 300K (25).

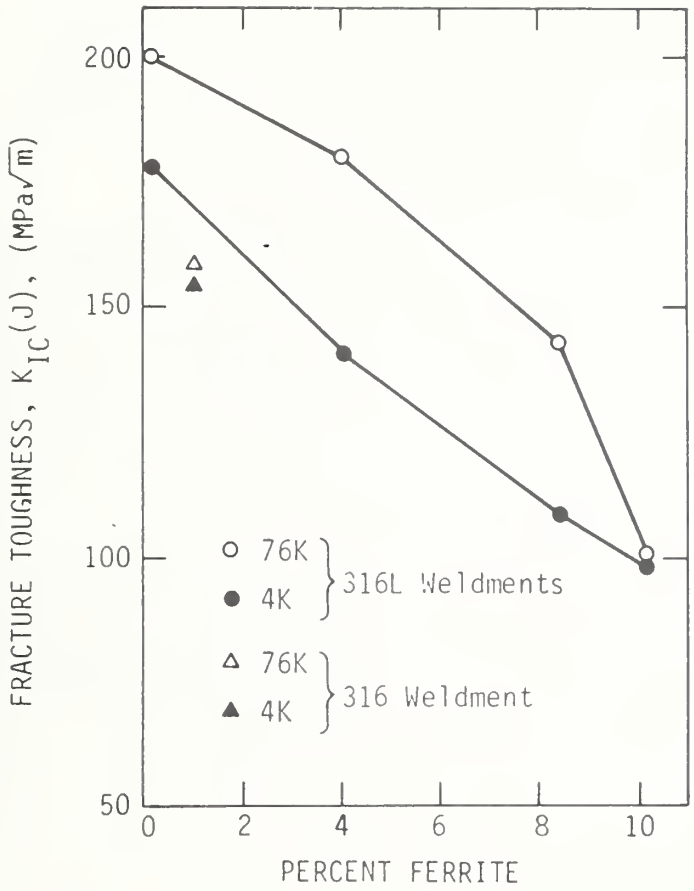

9. Fracture toughness of AWS 316L weld metal at 4K as a function of ferrite content (35).

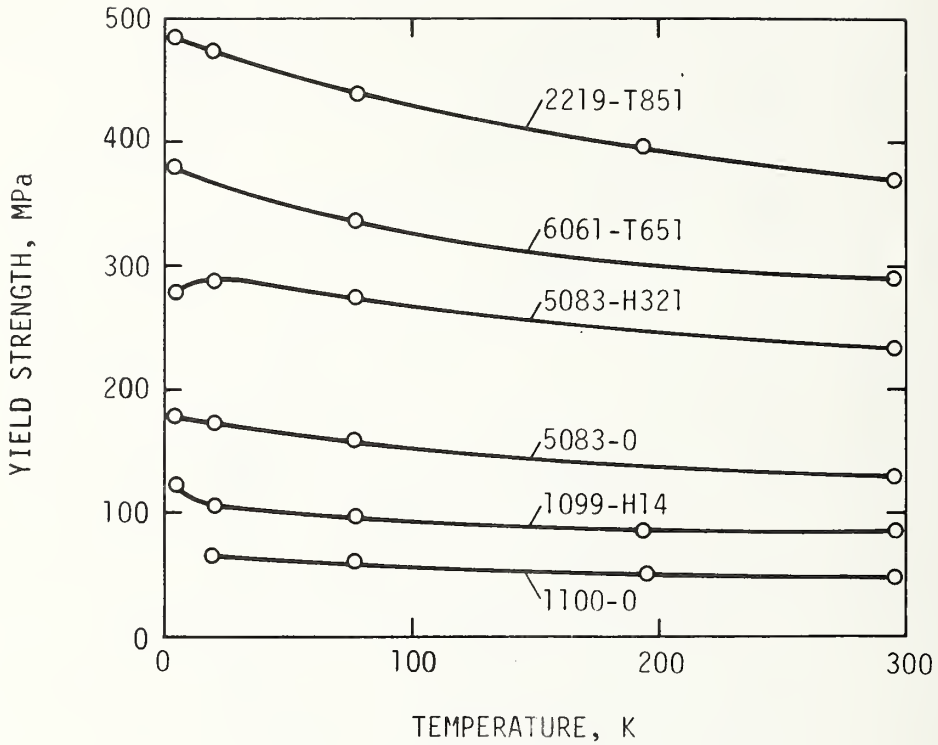

10. Yield strengths of six aluminum alloys at temperatures between 4K and 300K (50).

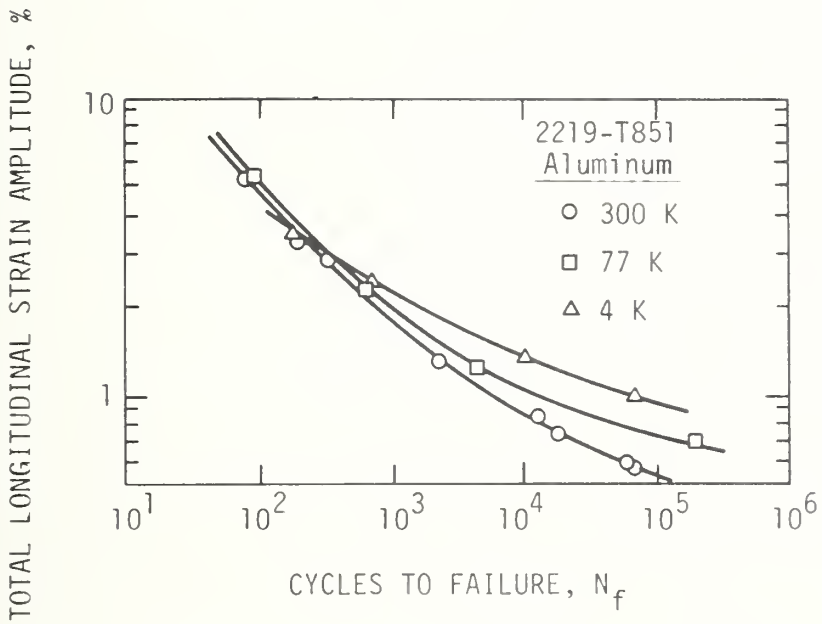

11. Fatigue behavior of 2219-T851 aluminum alloy at temperatures of 300, 77 and 4K (13).

HANDBOOK PREPARATION

Mechanical Properties Data Center

National Bureau of Standards

HANDBOOK PREPARATION

F. R. Fickett
Thermophysical Properties Division
National Bureau of Standards

The handbook is being produced jointly by the Mechanical Properties Data Center (MPDC) of Traverse City, MI and the staff of the NBS-Thermophysical Properties Division. The literature searching and document acquisition is done by NBS. MPDC extracts the data and prepares worksheet graphs and characterization tables which are then evaluated by the NBS staff to determine "best value" curves and appropriate error bands. The handbook presents "best value" curves for properties in two catagories listed in Table 1. For the category A properties we give an error band which indicates the spread that one might expect due to material variability, experimental error, etc. A typical graph is shown in Fig. 1. The published graphs will have SI units primary, but common units will be shown also. Each A category property presentation also contains a characterization table giving the appropriate information (different for physical and mechanical properties) on each of the original data sources used in constructing the best value curve. A preliminary version of the table is shown as Table 2. Another table is given for the "A" properties which provides a tabular listing of the best value curve (see Table 3). The B category properties are presented in smaller graphs as shown in Fig. 2. Error and variability estimates are also shown for these properties where possible. For all properties a complete bibliography is included. Each chapter (one for every material) starts with a detailed discussion of the material including: composition limits, designations, product forms, heat treatment, melting and casting, fabrication, welding, and chemical properties.

The materials being processed for inclusion in the first edition of the handbook are: stainless steels - 316, 304, 21/6/9 (and L and N modifications) and aluminum alloys - 5083, 2219 and 6061.

We have completed and evaluated the final draft of the first chapter (AISI 316) and it will be printed soon. The handbook covers have been received and our plan at present is to start distribution as soon as the first chapter is ready. Computer runs and evaluation of the output have been done for the second chapter (21/6/9). The data for the other chapters has been extracted from the easily-obtainable literature and entered into the computer system at MPDC. We are now evaluating more obscure documents and reports prior to doing the initial computer runs on these materials.

Table 1. Properties presented in the handbook. A given property is included only if low temperature data exist.

A (primary)	B (secondary)
Coefficient of thermal expansion	Bulk modulus
Crack growth rate	Compression
Fatigue strength	Creep
Fracture toughness	Electrical resistivity
Tensile strength	Impact strength
Tensile yield strength	Magnetic permeability
Thermal conductivity	Poisson's ratio
Young's modulus	Shear modulus
	Specific heat capacity
	Stress-strain
	Tensile elongation
	Tensile reduction in area
	Thermal diffusivity

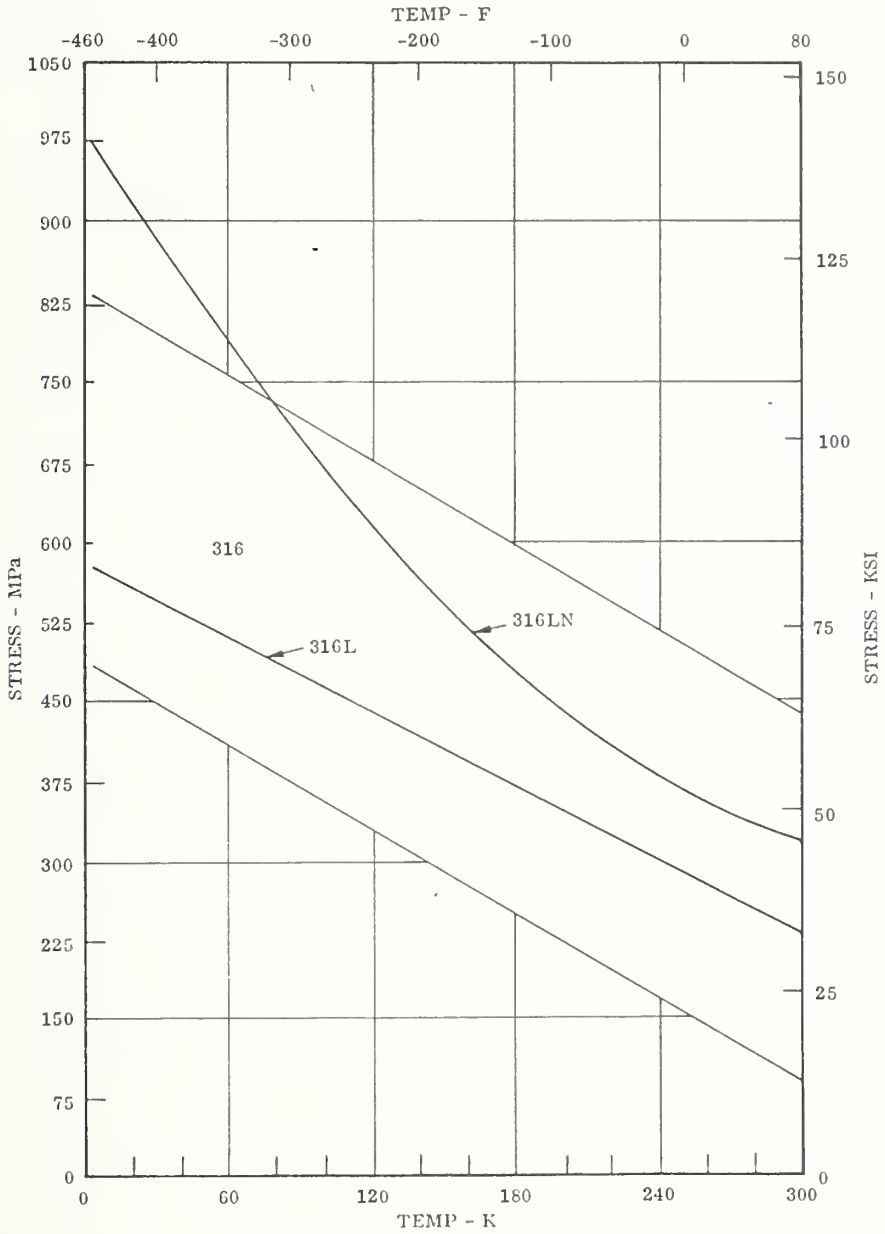

THE YIELD STRENGTH OF ANNEALED TYPE 316, 316L, AND 316LN STAINLESS STEEL (1, 2, 5, 6, 7, 8, 9, 10, 11, 12)

Figure 1. A typical handbook graph - A-category property. Colored shading is used in the actual handbook. 2.03

REFERENCE NO.	6	7	8	9	10	11	12
Composition	316	316	316	316LN	316LN	316LN	316L
CR	17.52		17.47	17.70	17.73 17.98		17.8
NI	13.48		13.40	13.63	11.70 13.08		13.9
MO	2.34		2.28	2.78	2.55 2.77		2.3
MN	1.86		1.67	0.86	1.35 1.63		1.96
SI	0.58		0.45	0.62	0.33 0.20		0.41
N	0.03		-	0.15	0.163 0.17		-
C	0.057		0.058	0.023	0.018 0.027		0.027
P	0.024		0.018	0.018	- -		-
S	0.019		0.022	0.020	- -		-
FE	Bal.		Bal.	Bal.	Bal. Bal.		Bal.
Others	.02 TI, .02 CO		.11 CU				
Heat Treatment	Annealed	Annealed	Annealed	Annealed	Annealed	Annealed	Annealed
Average Grain Size	ASTM 5						
Hardness	R_B79						
Product Form	Round Bar	Sheet 0.1016 cm thick	Rod	Forging			
Specimen Type	Round	Flat	Round Button Head	Round (b)			
Min. Width or Dia.	0.381 cm dia.	0.508 cm Wide		0.564 cm dia.			
Thickness		0.1016 cm					
Reduced Sec. Lg.				3.5 cm			
Gage Length	2.54 cm	5.08 cm		5D			
Notch Type							
Included Angle							
Root Radius							
KT Factor							
Strain Rate	0.0508 cm/min.	0.01 cm/cm/min.	0.05 cm/min. & 254 cm/min.				
Total Spec. No.	3	6	7	28	7 2	5	2

Remarks

(b) Specimens taken from various locations of the forging and with different orientations.

CHARACTERIZATION TABLE FOR THE TENSILE PROPERTIES OF ANNEALED TYPE 316 STAINLESS STEEL

MECHANICAL PROPERTIES DATA CENTER - 1978

2.00.1 Table 2. A small part of the characterization table for the tensile properties of AISI 316.

TABULAR PRESENTATION OF THE "BEST VALUE CURVE" FOR THE YIELD STRENGTH OF ANNEALED TYPE 316 STAINLESS STEEL

NUMBER OF DATA POINTS: 35
TOLERANCE FACTOR A: 259.5
TOLERANCE FACTOR B: 149.8

Temp K	Temp °F	MPa	KSI	Temp °F	Temp K	KSI	MPa
4.2	(-452.1)	657.8	(95.41)	-452	(4.2)	96.84	(657.7)
20	(-423.7)	636.9	(92.37)	-420	(22.04)	91.98	(634.2)
40	(-387.7)	610.3	(88.52)	-390	(38.71)	88.76	(612.0)
60	(-351.7)	583.8	(84.67)	-360	(55.37)	85.56	(589.9)
77	(-321.7)	561.2	(81.39)	-330	(72.04)	82.35	(567.8)
80	(-315.7)	557.2	(80.81)	-320	(77.59)	81.28	(560.4)
100	(-279.7)	530.7	(76.97)	-300	(88.71)	79.15	(545.7)
120	(-243.7)	504.2	(73.13)	-270	(105.4)	75.94	(523.6)
140	(-207.7)	477.6	(69.27)	-240	(122.1)	72.74	(501.5)
160	(-171.7)	451.1	(65.43)	-210	(138.7)	69.52	(479.3)
180	(-135.7)	424.5	(61.57)	-180	(155.4)	66.31	(457.2)
200	(- 99.67)	398.0	(57.72)	-150	(172.0)	63.11	(435.1)
220	(- 63.67)	371.5	(53.88)	-120	(188.7)	59.90	(413.0)
240	(- 27.67)	344.9	(50.02)	- 90	(205.4)	56.69	(390.9)
260	(8.33)	318.4	(46.18)	- 60	(222.1)	53.49	(368.8)
273	(31.7)	301.1	(43.67)	- 30	(238.7)	50.27	(346.6)
280	(44.33)	291.8	(42.32)	0	(255.4)	47.06	(324.5)
300	(80.33)	265.3	(38.48)	30	(272.0)	43.86	(302.4)
				60	(288.7)	40.65	(280.3)
				80	(299.8)	38.51	(265.5)

2.04 Table 3. Tabular presentation of the best-value curve for the AISI 316 data shown in Fig. 1.

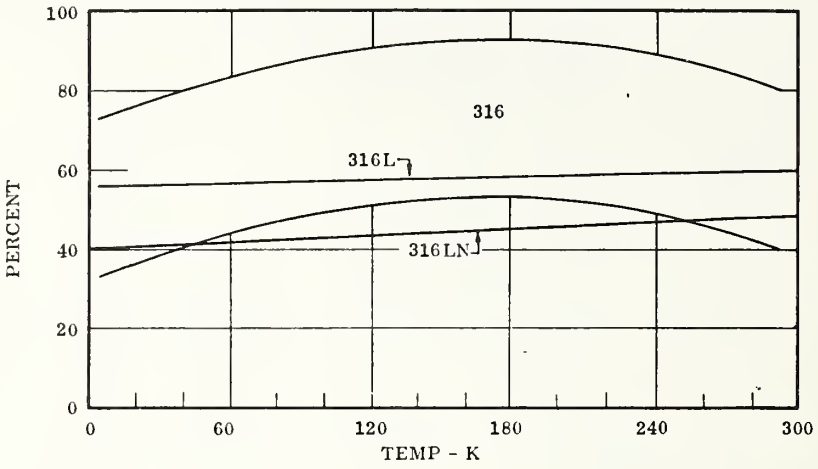

THE ELONGATION OF ANNEALED TYPE 316, 316L, 316LN STAINLESS STEEL (1, 2, 3, 4, 6, 7, 9, 10, 11, 12)

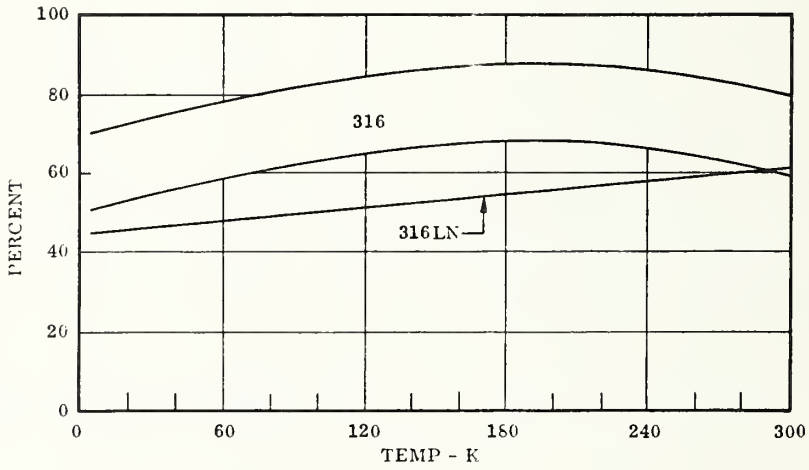

THE REDUCTION IN AREA OF ANNEALED TYPE 316, AND 316LN STAINLESS STEEL (1, 2, 3, 4, 6, 9, 10, 11)

Figure 2. A typical handbook graph - B-category property. 2.05

VAIL WORKSHOP

VAIL WORKSHOP

F. R. Fickett
Thermophysical Properies Division
National Bureau of Standards

A major aspect of the technology transfer part of the program is the workshop. These meetings are held each year with the goal of bringing together representatives from all parts of the materials community who are involved with low temperature applications. The attendees at this year's workshop, held at Vail, CO, October 24-26, represented just such a diverse group including: industry, national labs, MFE projects and universities. The following pages give the attendance list and the program for the workshop. No proceedings are published, but extended abstracts of the presentations were provided to the attendees. In addition a review of the workshop will be presented at the First Topical Meeting on Fusion Reactor Materials, January 29-31, 1979.

PROGRAM FOR NBS-DOE WORKSHOP ON
MATERIALS AT LOW TEMPERATURES
Vail, Colorado October 24-26, 1978

Tuesday, Oct. 24

I. INTRODUCTION (8:30-9:30), E. N. C. Dalder, Chairman

Welcome	F. R. Fickett	NBS
OFE overview	E. N. C. Dalder	DOE
NBS program	R. P. Reed	NBS
Handbook project	T. Moore/B. Gilmore	MPDC

II. DESIGN I (10:00-12:00), F. R. Fickett, Chairman

Large coil project	C. J. Long	ORNL
	E. Belkin/T. Leax	Westinghouse
	F. Mazandarany	General Electric
	J. Christian	General Dynamics

III. DESIGN II (2:00-4:30), F. R. Fickett, Chairman

MFTF	J. Hodges	LLL
MHD magnets	R. Shaw	MIT
Pulsed magnets	Z. N. Sanjana	Westinghouse
	S. T. Wang	ANL
TFTR	G. Brown	PPPL

Wednesday, Oct. 25

IV. ALLOYS FOR LOW TEMPERATURE SERVICE (9:00-12:00), R. P. Reed, Chairman

Fatigue	J. Shepic	Martin Marietta
Fracture & tensile	D. T. Read	NBS
Production	H. Espy	Armco
Elastic properties	H. M. Ledbetter	NBS
Magnetic properties	T. Collings	Battelle
	F. Fickett	NBS

V. THICK SECTION WELDING FOR LOW TEMPERATURE APPLICATIONS (2:00-5:00), H. I. McHenry, Chmn.

Stainless steel weld metallurgy	D. Olson	Colo. School of Mines
Cryogenic toughness of stainless steel weld metals	H. Reid	Teledyne-McKay
Influence of delta ferrite on toughness	D. T. Read	NBS
Nickel-based weld metals	C. Witherell	LLL
NBS/DOE welding program	H. I. McHenry	NBS

EVENING (6:00-8:00) Fluid flow studies in the lobby bar area (cocktail party)

Thursday, Oct. 26

VI. NONMETALLICS FOR MAGNET STRUCTURES (8:30-12:00), M. B. Kasen, Chairman

ICMC Munich Conference review	A. F. Clark	NBS
NBS/DOE composites program	M. B. Kasen	NBS
Composite production	J. Benzinger	Spaulding Fiber
Radiation damage	C. J. Long	ORNL
Composites testing	E. Erez	MIT
Elastic properties	H. Ledbetter	NBS
Friction and wear of polymers	R. Tobler	NBS

ATTENDANCE AT NBS/DOE VAIL WORKSHOP
October 24-26, 1978

1. John Arvidson, National Bureau of Standards
2. Ed Belkin, Westinghouse
3. James Benzinger, Spaulding Fibre Co.
4. John Bronson, Los Alamos Scientific Lab.
5. Graham Brown, Princeton Plasma Physics
6. William Burns, Lawrence Berkeley Lab.
7. James Bywater, Argonne
8. Sheree Chen, Lawrence Berkeley Lab.
9. Jack Christian, General Dynamics
10. Al Clark, National Bureau of Standards
11. Ted Collings, Battelle Columbus
12. Ray Conder, Beech Aircraft Corp.
13. Donald Cornish, Lawrence Livermore Lab.
14. Ed Dalder, Department of Energy
15. Dan Deis, Lawrence Livermore Lab.
16. David Dew-Hughes, Brookhaven National Lab.
17. James Dwyer, Permali, Inc.
18. Elena Erez, MIT
19. Harry Espy, Armco
20. Fred Fickett, National Bureau of Standards
21. Lyle Genens, Argonne
22. Bryce Gilmore, Mechanical Properties Data Ctr.
23. Ted Hartwig, University of Wisconsin
24. Carl Henning, Lawrence Livermore Lab.
25. Edwin Hodge, Battelle Columbus
26. Jeff Hodges, Lawrence Livermore Lab.
27. Takehumi Horiuchi, Kobe Steel, Japan
28. John Horvath, General Dynamics/Convair
29. Bud Kasen, National Bureau of Standards
30. Dennis Keiser, INEL
31. S. H. Kim, Argonne
32. Kazunori Kitamura, Tokyo Shibaura Electric Co., Japan
33. Damian Kotecki, Teledyne-McKay
34. Dick Kropschot, National Bureau of Standards
35. Tom Leax, Westinghouse
36. Hassell Ledbetter, National Bureau of Standards
37. Ks Lee, Brookhaven National Lab.
38. Mark Leininger, Fermilab
39. Carl Linkinhoker, General Electric
40. Joseph Long, Oak Ridge National Lab.
41. Farad Mazandarany, General Electric
42. Tom Moore, Mechanical Properties Data Ctr.
43. Harry McHenry, National Bureau of Standards
44. Ralph Niemann, Argonne
45. Michael Olmstead, MIT
46. Dave Olson, Colorado School of Mines
47. Walter Pelczarski, Argonne
48. Wayne Pollard, Lawrence Livermore Lab.
49. John Porter, Lawrence Berkeley Lab.
50. Dave Read, National Bureau of Standards
51. Dick Reed, National Bureau of Standards
52. Harry Reid, Teledyne-McKay
53. William Roden, General Dynamics
54. Stan Sangdahl, Chicago Bridge & Iron
55. Zal Sanjana, Westinghouse
56. Robert Shaw, MIT
57. John Shepic, Martin Marietta
58. Earl Stone, U. of Wisconsin
59. Lowell Stuebinger, Westinghouse
60. Ralph Tobler, National Bureau of Standards
61. Dick Vandervoort, Lawrence Livermore Lab.
62. Bert Wang, Argonne
63. Roger West, Lawrence Berkeley Lab.
64. Deb Wilson, National Bureau of Standards
65. Chuck Witherell, Lawrence Livermore Lab.
66. Phil Sanger, Airco
67. Willard Hanson, Fermilab

Figure 1. NBS/DOE Vail Workshop Attendees.

1. W. Pelczarski
2. C. Henning
3. E. Dalder
4. H. Reid
5. S. Sangdahl
6. M. Leininger
7. J. Christian
8. J. Bywater
9. J. Long
10. R. Tobler
11. S. Chen
12. D. Wilson
13. J. Bronson
14. B. Burns
15. E. Belkin
16. R. West
17. D. Reed
18. E. Hodge
19. L. Stuebinger
20. T. Leax
21. T. Moore
22. E. Erez
23. D. Dew-Hughes
24. S. Kim
25. F. Mazandarany
26. E. Collings
27. J. Porter
28. K. Kitamura
29. D. Kotecki
30. C. Witherell
31. H. Espy
32. R. Shaw
33. J. Benzinger
34. M. Olmstead
35. B. Kasen
36. L. Genens
37. J. Hodges
38. F. Fickett
39. W. Roden
40. D. Keiser
41. T. Hartwig
42. J. Dwyer
43. J. Arvidson
44. B. Gilmore
45. H. McHenry
46. J. Horvath
47. Z. Sanjana
48. R. Niemann
49. K. Lee
50. D. Kropschot
51. D. Deis
52. C. Linkinhoker
53. D. Cornish
54. G. Brown
55. W. Pollard
56. J. Shepic
57. E. Stone
58. R. Conder
59. T. Horiuchi
60. D. Read

Figure 2. Identification of attendees shown in Fig. 1.

NBS-114A (REV. 9-78)

U.S. DEPT. OF COMM. BIBLIOGRAPHIC DATA SHEET	1. PUBLICATION OR REPORT NO. NBSIR 79-1609	2. Gov't. Accession No.	3. Recipient's Accession No.

4. TITLE AND SUBTITLE

Materials Studies for Magnetic Fusion Energy Applications at Low Temperatures - II

5. Publication Date: June 1979

6. Performing Organization Code

7. AUTHOR(S)

F. R. Fickett and R. P. Reed, Editors

8. Performing Organ. Report No.

9. PERFORMING ORGANIZATION NAME AND ADDRESS

NATIONAL BUREAU OF STANDARDS
DEPARTMENT OF COMMERCE
WASHINGTON, DC 20234

10. Project/Task/Work Unit No. 7360531

11. Contract/Grant No.

12. SPONSORING ORGANIZATION NAME AND COMPLETE ADDRESS *(Street, City, State, ZIP)*

Department of Energy
Office of Fusion Energy
Washington, D.C. 20545

13. Type of Report & Period Covered

14. Sponsoring Agency Code

15. SUPPLEMENTARY NOTES

☐ Document describes a computer program; SF-185, FIPS Software Summary, is attached.

16. ABSTRACT *(A 200-word or less factual summary of most significant information. If document includes a significant bibliography or literature survey, mention it here.)*

The reports presented here summarize the work of the low temperature materials research project for the second year of the program. The various projects are outlined and the research results are presented. The major thrust of the measurements has been the evaluation of the low temperature mechanical and physical properties of stainless steel base metal and welds, with particular emphasis on the nitrogen strengthened stainless steels. Aluminum alloys have received some consideration also. Work has been done on the production of nonmetallics, primarily industrial laminates for low temperature applications and on the measurement of their properties at cryogenic temperatures. The second NBS/DOE Vail workshop was held in October 1978. A brief description is given of that program.

17. KEY WORDS *(six to twelve entries; alphabetical order; capitalize only the first letter of the first key word unless a proper name; separated by semicolons)*

Alloys; fiberglass; mechanical properties; nonmetallics; physical properties; stainless steel.

18. AVAILABILITY

☒ Unlimited

☐ For Official Distribution. Do Not Release to NTIS

☐ Order From Sup. of Doc., U.S. Government Printing Office, Washington, DC 20402, SD Stock No. SN003-003-

☒ Order From National Technical Information Service (NTIS), Springfield, VA. 22161

19. SECURITY CLASS (THIS REPORT)	21. NO. OF PRINTED PAGES
UNCLASSIFIED	496
20. SECURITY CLASS (THIS PAGE)	**22. Price**
UNCLASSIFIED	$12.50

U.S. GOVERNMENT PRINTING OFFICE:1979—677-072 / 1291

USCOMM-DC